Geophysical Study of the Abandoned Gullbridge Mine Tailings Management Facility, Central Newfoundland

by

© Andrew Gordon Blagdon

submitted to the School of Graduate Studies

in partial fulfillment of the requirements

for the degree of

Master of Science (Geophysics)

Department of Earth Sciences
Memorial University of Newfoundland

Summer 2021

St. John's, Newfoundland and Labrador

Abstract

As part of an ongoing dam monitoring study, this research aims to assist in the closure of the Gullbridge Tailings Facility in Central Newfoundland using geophysical survey methods. Centered over a volcanogenic massive sulfide ore deposit, the Gullbridge mine produced 94,000 tonnes of copper concentrate from 2.8 million tonnes of ore from 1967-1972. The facility deploys an earth-filled dam separating a valley impoundment reservoir containing 1.8 million m^3 of subaqueously deposited copper tailings from an adjacent wetland. Historical seepage of tailings water through the embankment is concerning as it poses a risk of seepage related erosion, a likely failure mechanism which, combined with poor dam foundations, contributed to a breach in December 2012. Relevant variations in the material properties of the dam can be detected by geophysical methods. Spontaneous-potential (SP), direct-current resistivity and ground-penetrating radar and magnetics were deployed for surveying the embankment, particularly over a known seepage location. SP data points to irregular seepage of tailings water through the embankment in the known seep area and in the northern part of the dam. DCR surveys indicate there is a 1-2 m thick dry layer, thickening northward, over the main seep. GPR data suggests flow of tailings water through the embankment is constrained to poorly compacted core materials surrounding an historic inlet channel, the location of which is indicated by magnetic data. As a secondary focus, an adjacent wetland was surveyed using an electromagnetic ground conductivity meter. The conductivity data delineate areas of elevated copper resulting from the distribution of tailings sediment along a dammed stream

bed and along a discharge channel where water exits the reservoir and into the wetland via a spillway.

General Summary

This project involved using non-destructive geophysical methods to study an earth-filled tailings dam at the abandoned Gullbridge mine site in central Newfoundland. “Tailings” are mining waste. They are commonly stored under water to prevent reactions with the air, which can lead to environmentally damaging acid mine drainage. In December 2012, a section of dam collapsed**,** releasing an estimated 500 m^3 of solid Cu-Zn tailings into an adjacent wetland. It is suspected the collapse was triggered by an unstable foundation and internal erosion of the dam resulting from seepage of water through the embankment. Multiple methods including electrical, electromagnetic, and ground penetrating radar were carried out over the dam to identify changes in the physical properties of the embankment, and thus delineate seepage related erosion channels and other potential failure mechanisms. An electromagnetic survey of the wetland identified regions of enhanced metal concentrations.

Acknowledgements

This work was generously funded by Hibernia Management and Development Company Ltd. We would like to express our sincerest gratitude to Hibernia for the financial assistance provided during the entirety of this project and for their continued support of geophysics graduate students in Newfoundland and Labrador pursuing a career in natural resource exploration.

This thesis was written under the supervision of Dr. Alison Leitch and with the support and guidance of Dr. Abigail Steel of the Newfoundland and Labrador Department of Natural Resources. Dr. Steel has overseen post-operation mining activities in Gullbridge since the beginning of this research and has contributed invaluable advice leading to the effective closure of the mine.

We would like to acknowledge Peter Bruce for his continued commitment to assisting students at Memorial University with computer software such as ArcGIS. Peter selflessly takes time to answer students' questions regarding mapping techniques regarded as fundamental for a career in natural resource development.

Lastly, it is essential that we acknowledge the efforts of our field assistants Nick Lynch, Joey Pittman and Jacob Newman. All students demonstrated an ability and passion for geophysics that was inspirational and refreshing during long, laborious field days accompanied by uncooperative weather conditions.

Table of Contents

Abstract i

General Summary i

Acknowledgements ii

1 Introduction 1

1.1 Gullbridge Mine Tailings Facility 1

1.2 Objectives 4

1.3 Location and Access 7

1.4 Regional Geology 10

1.5 Local Geology 12

2 The Gullbridge Tailings Facility 16

2.1 Tailings Management 16

2.2 Construction History 20

2.2.1 Initial Construction 20

2.2.2 1993-1999: Failure, Assessment and Remediation 22

2.2.3 2010-2012: Assessment and Remediation 22

2.2.4 2012-2014: Failure, Assessment and Remediation 27

2.3 Dam Properties 38

2.3.1 Dam Materials from Borehole Data 40

2.3.2 Depth of Water Table 47

2.3.3 Drainage System 48

2.4 Dam Design 50

2.4.1 Failure Mechanisms 50

2.4.2 Outflow Design 53

2.5 Reservoir Properties 55

2.5.1 Surface Water Samples 56

2.5.2 Tailings Samples 58

2.5.3 Tailings Test Pits ... 62
2.6 Wetland Properties ... 66
2.6.1 Bog Probes and Boreholes ... 68
2.6.2 Passive Mitigation Processes ... 70
2.6.3 Surface Water Samples ... 71
2.6.4 Soil Samples ... 74
3 Methods ... 76
3.1 Theory ... 76
3.1.1 Spontaneous Potential ... 76
3.1.2 Magnetics ... 80
3.1.3 Direct-Current Resistivity and Induced Polarization ... 86
3.1.4 Ground-Penetrating Radar ... 98
3.1.5 Electromagnetic Ground Conductivity and Magnetic Susceptibility ... 103
3.1.6 Bog and Water Sample Analysis ... 111
3.2 Field Methods ... 112
3.2.1 Spontaneous Potential ... 114
3.2.2 Magnetics ... 121
3.2.3 Direct-Current Resistivity and Induced Polarization ... 124
3.2.4 Ground-Penetrating Radar ... 130
3.2.5 Electromagnetic Ground Conductivity and Magnetic Susceptibility ... 135
3.2.6 Bog and Water Sample Analysis ... 140
3.3 Data Processing ... 143
3.3.1 Spontaneous Potential ... 143
3.3.2 Magnetics ... 145
3.3.3 Direct-Current Resistivity and Induced Polarization ... 149
3.3.4 Ground-Penetrating Radar ... 155
3.3.5 Electromagnetic Ground Conductivity and Magnetic Susceptibility ... 165
3.3.6 Bog and Water Sample Analysis ... 166
4 Results ... 169

4.1 Spontaneous Potential 169
4.1.1 June 2016 Along the Embankment 169
4.1.2 July 2018 Seep Grid 175
4.2 Magnetics 183
4.3 Direct-Current Resistivity and Induced Polarization 188
4.3.1 June 2016 Along the Embankment 188
4.3.2 Seep Surveys 192
4.4 Ground-Penetrating Radar 207
4.4.1 July & September 2016, Along the Embankment 211
4.4.2 July 2016 Northern Grid 224
4.4.3 November 2016 Seep Grid 231
4.4.4 June 2017 Seep Grid 237
4.4.5 Wetland: September 2016 (GPR LINE05) 261
4.4.6 Wetland: February 2017 262
4.5 Electromagnetic Ground Conductivity 265
4.5.1 EM Along the Embankment 267
4.5.2 EM31 over the Reservoir, September 2016 271
4.5.3 EM31 June 2017 Seep Grid 273
4.5.4 EM31-MK2 Wetland Survey Lines 278
4.6 Bog and Water Sample Analysis 284
4.6.1 Water Samples 284
4.6.2 Properties of Bog Samples 287
5 Summary and Discussion 291
References 307
Appendices 323

List of Figures

Figure 1.1: Aerial view of the Gullbridge Tailings Facility 2

Figure 1.2: Schematic illustrating seepage related erosion through an embankment dam..4

Figure 1.3: Location of Gullbridge, Newfoundland 7

Figure 1.4: Location of the Gullbridge TMA 8

Figure 1.5: Regional Geological Map of Newfoundland.. 10

Figure 1.6: Map of Notre Dame Subzone indicating location of Gullbridge and several other VMS deposits occupying rocks of the Robert's Arm 11

Figure 1.7: Plan view and cross-section of the Gullbridge deposit 13

Figure 2.1: Downstream construction phases of a raised embankment design. 21

Figure 2.2: Shallow slope failure looking north along the downstream slope of the Gullbridge Dam. 23

Figure 2.3: Aerial view of the Gullbridge Tailings Facility indicating the locations of boreholes and bog probes drilled along the dam and wetland respectively 25

Figure 2.4: Gullbridge Dam breach looking northeast on December 17th, 2012............ 28

Figure 2.5: Aerial view of the Gullbridge TMA following the December 2012 breach outlining the suspected debris path in the wetland.. 29

Figure 2.6: Construction of temporary berm and settling pond on December 19th, 2012 immediately following the breach 30

Figure 2.7: TMA test pit, ground water and material sample locations. 32

Figure 2.8: Compaction of second lift on November 20th, 2013 36

Figure 2.9: Seepage area drainage system constructed during November 2013 repair work. 37

Figure 2.10: “Before and After” section of material encountered over the Gullbridge Dam before rehabilition in 2013. 39

Figure 2.11: Borehole stratigraphy over BH3 of the Gullbridge embankment dam from (a) 0 – 10 m and (b) 10 – 19.7 m. 43-44

Figure 2.12: Borehole stratigraphy over BH/MW4 of the Gullbridge embankment dam from (a) 0 – 10 m and (b) 10 – 13.4 m. 45-46

Figure 2.13: Image of Gullbridge TMA dam spillway with connecting sedimentation ponds, berm and spoil location 49

Figure 2.14: Illustration of the development of seepage related erosion channelsthrough earth-filled embankments 53

Figure 2.15: Streambed carrying tailings sediment through the impoundment reservoir. 56

Figure 2.16: Image of TP-2 shortly after caving on July 10th, 2013 65

Figure 2.17: Looking west into the wetland from the southern toe of the dam 66

Figure 2.18: Graph of peat thickness versus distance along the dam for three profiles ... 69

Figure 2.19: Locations of DNR surface water samples collected in July 2013 and dam spill material samples collected in December 2013 73

Figure 3.1: Generation of streaming potentials between soil grains 78

Figure 3.2: Schematic of the general array for a DCR survey 86

Figure 3.3: Diagram depicting the conventional geometry of the Schlumberger DCR array 89

Figure 3.4: (a) Pseudo-section generated from Schlumberger DCR array (b) increasing a-spacing about the potential pair at the center of the array demonstrating increasing depth level *n* 91

Figure 3.5: Diagram depicting the conventional geometry of the Wenner DCR array 91

Figure 3.6: (a) Pseudo-section generated from Wenner DCR array (b) increasing a-spacing about the center of the array demonstrating increasing depth level *n* 93

Figure 3.7: Graph of the decay of induced potentials within a conducting material in the time-domain 96

Figure 3.8: Generation of induced potentials within the pore channels of a rock grain ... 97

Figure 3.9: Illustration showing the GPR surveying process 98

Figure 3.10: Induction currents in a homogeneous half-space 105

Figure 3.11: a) Contributions of *Hs* (φ) generated from horizontal current loops in a thin horizontal half-space slice dz at depth z for VMD and HMD orientations b) Cumulative response of the secondary magnetic field $R_V(z)$ versus depth for all materials below a specific normalized depth for VMD and HMD dipole orientations 109

Figure 3.12: Example of SP survey set-up 115

Figure 3.13: Diagram of kaolinite clay/CuSO4 SP electrode pot. 116

Figure 3.14: Equipment used in SP surveys over the Gullbridge Dam during the June 2016 research trip 117

Figure 3.15: Clay electrode pot connected to a multi-meter over Gullbridge 120

Figure 3.16: Equipment used in magnetics survey 122

Figure 3.17: DCR survey setup over the Gullbridge Dam 125

Figure 3.18: Illustration of DCR/IP spreads, segments and survey parameters 126

Figure 3.19: Automatic sequence creation window in Iris Instruments Electre II 127

Figure 3.20: GPR survey conducted over the Gullbridge Dam in June 2016 131

Figure 3.21: February 2017 winter GPR assembly operating a snowmobile attached to a GPR assembled in a towed sled 134

Figure 3.22: Andrew Blagdon conducting an EM31-MK2 electromagnetic ground conductivity survey over the wetland adjacent to the Gullbridge TMA .... .136

Figure 3.23: Andrew Blagdon and field assistant Jacob Newman collecting a sample over bog site #1 .... .141

Figure 3.24: Diurnal magnetic drift over the Gullbridge TMA on July 17th, 2016 ...... .146

Figure 3.25: June 2017 2 m Schlumberger survey with north extensions superimposed over the June 2017 GPR grid 151

Figure 3.26: Arrangement of blocks in rectilinear mesh in RES2DINV with corresponding pseudo-section data point distribution 154

Figure 3.27 GPR LINE05 collected with 100 MHz antennae in September 2016 displayed in “LineView” mode 155

Figure 3.28: GPR LINE05 with application of local background subtraction filter....... 160

Figure 3.29: Average frequency spectrum plot over LINE05 161

Figure 3.30: CMP over bog area... 163

Figure 3.31: GPR LINE05 collected over the limestone berm of the Gullbridge wetland in September 2016 with active interpretations... 164

Figure 4.1: Map image indicating the locations of rover pot stations along SP Line 1 and SP Line 2 collected over the Gullbridge Dam from June 19th-20th, 2016.................... 170

Figure 4.2: Electric Potential (mV) over SP Line 1 (wetland side) collected over the Gullbridge Dam in June 2016. 171

Figure 4.3: Electric Potential (mV) over SP Line 2 (reservoir side) collected over the Gullbridge Dam in June 2016. 171

Figure 4.4: Profiles of electric potential over SP Line 2 and the July 18th, 2016 repeatability check over SP Line 2 174

Figure 4.5: Map image indicating location of SP electrodes collected over the seep area of the Gullbridge Dam on July 14th, 2018... 176

Figure 4.6: SP contour map over the July 2018 grid overlaying the drone imagery of the Gullbridge Impoundment.. 177

Figure 4.7: Profiles of SP over (a) YLINE00 and (b) YLINE05 178

Figure 4.8: SP contour map over the July 2018 grid 179

Figure 4.9: Graph displaying three profiles of the drift over time (dV/dt) measured at stationary rover electrodes over three different stations of the June 2018 SP grid .... .181

Figure 4.10: SP dV/dt$_0$ (mV/min) contour map over the July 2018 grid SP grid 182

Figure 4.11: Residual magnetic field over the Gullbridge region.................................. 184

Figure 4.12: Map image indicating Magnetics Line 1 and 2 stations collected over the Gullbridge Dam on July 17th, 2016.. 185

Figure 4.13: Corrected TMI (nT) collected S-N along the Gullbridge Dam. 186

Figure 4.14: Corrected VMG (nT/m) collected S-N along the Gullbridge Dam............ 186

Figure 4.15: Map image indicating locations of midpoints for each DCR spread conducted over the Gullbridge TMA in June 2016 189

Figure 4.16: Profiles of ρ_a versus x for a-spacings of 5m and 10m obtained from DCR Wenner CST survey along the middle of the Gullbridge Dam in June 2016. 190

Figure 4.17: 2D Inversion model generated from DCR Wenner CST data plotted in Figure 4.16 190

Figure 4.18: Electrode positions of DCR Schlumberger spreads conducted over the Gullbridge Dam seep area in November 2016 and June 2017....................................... 193

Figure 4.19: Log-linear graph displaying profiles of ρ_a versus x for 5 pseudo-depths acquired from 2 m Schlumberger DCR survey collected S-N over YLINE02 of the seep grid in November 2016 195

Figure 4.20: 2D inversion performed in RES2DINV on 2 m Schlumberger DCR data collected S-N over the seep in November 2016.. 195

Figure 4.21: Profiles of apparent chargeability versus x for 5 pseudo-depths acquired from 2 m IP survey collected S-N over YLINE02 of the November 2016 seep grid..... 197

Figure 4.22: Graph of profiles of apparent resistivity versus y for different pseudo-depths obtained from the 2 m DCR surveys collected S-N over the June 2017 seep grid......... 198

Figure 4.23: Inversion model generated from Schlumberger DCR data from three overlapping spreads shown in Figure 4.16 198

Figure 4.24: Schlumberger VES modelling of 2 m Schlumberger DCR data at position (10,26) over the “2 m Central” survey assuming a 2-layer system 200

Figure 4.25: Schlumberger VES modelling of 2 m Schlumberger DCR data at position (10,52) over the “2 m Central” survey assuming a 2-layer system 200

Figure 4.26: Inversion model of combined Schlumberger and Wenner DCR results over the 2 m Central spread. 202

Figure 4.27: Selected points of ρ_a versus *y* profiles acquired over the “4 m Central” Schlumberger DCR survey collected S-N over the seep grid in June 2017 203

Figure 4.28: Inversion model generated from Schlumberer DCR data using values of ρ_a up to a=14 over the “4 m Central” survey line. 203

Figure 4.29: Smoothed ρ_a versus *y* profiles acquired over the “2 m East” Schlumberger DCR survey with the central artifact removed.. 205

Figure 4.30: Inversion model generated from Schlumberger DCR data over the “2 m East” survey line. 205

Figure 4.31: Schlumberger -1-D VES model of “2 m East” ρ_a data at position y=58 m along YLINE07 over the June 2017 seep grid assuming a 2-layer system... 206

Figure 4.32: Map image indicating locations of GPR surveys collected over the Gullbridge TMA between July 2016 and February 2017... 208

Figure 4.33: Profiles of three GPR survey lines collected S-N over the Gullbridge Dam along the reservoir side, center of the dam, and wetland side. 212

Figure 4.34: S-N profile of GPR LINE00 collected in September 2016 along the center of the Gullbridge Dam between y=0 m and y=243 m. 214

Figure 4.35: S-N profile of GPR LINE00 collected in September 2016 along the center of the Gullbridge Dam between y=250 m and x=493 m. 217

Figure 4.36: S-N profile of GPR LINE00 collected in September 2016 along the center of the Gullbridge Dam between y=500 m and y=743 m. 220

Figure 4.37: S-N profile of GPR LINE00 collected in September 2016 along the center of the Gullbridge Dam between y=730 m and y=973 m. 221

Figure 4.38: GPR profiles of y-line surveys collected S-N over the July 2016 grid. 225

Figure 4.39: GPR profiles of x-line surveys collected W-E over the July 2016 Northern grid. 227

Figure 4.40: July 2016 grid generated in GFP edit outlining the surface location where the radar pulse has attenuated. 229

Figure 4.41: Reflection amplitude slice over the July 2016 GPR grid taken at a depth of 4.25 m 230

Figure 4.42: S-N GPR profiles collected over the November 2016 seep grid.............. 232

Figure 4.43: W-E GPR profiles collected across the dam crest over the November 2016 seep grid 234

Figure 4.44: (a) Depth slice generated in Ekko_Project over the November 2016 GPR grid between z= 4.00 m and z= 4.25 m and (b) z= 4.50 m and z= 4.75 m. 236

Figure 4.45: Map image indicating location of June 2017 GPR survey grid over the seep area of the Gullbridge Dam.......... 238

Figure 4.46: November 2016 grid location relative to the June 2017 GPR grid 239

Figure 4.47: S-N profiles collected over the June 2017 seep grid using 250 MHz antennae. 241-242

Figure 4.48: Depth contour map of the water table surface over the June 2017 seep grid. 244

Figure 4.49: S-N profiles collected over the June 2017 seep grid using 100 MHz antenna frequency.......... 246-247

Figure 4.50: S-N profiles collected over the June 2017 seep grid using 50 MHz antenna frequency.......... 249-250

Figure 4.51: Reflection amplitude slice between z= 3.0 m and z=3.5 m over the June 2017 seep grid collected using the 50 MHz antennae.......... 251

Figure 4.52: Reflection amplitude slices between (a) z= 2.5-3.0 m (b) z=7.0-7.5 m and (c) z=10.5-11 generated from y-line data over the June 2017 seep grid using the 50 MHz antennae. 252

Figure 4.53: W-E profiles over the June 2017 seep grid collected using the 250 MHz antennae. 254

Figure 4.54: W-E profiles over the June 2017 seep grid collected using the 100 MHz antennae. 255

Figure 4.55: W-E profiles over the June 2017 seep grid collected using the 50 MHz antennae. 256

Figure 4.56: Voxler isosurface models generated using y-line data over the 50 MHz June 2017 GPR grid 258

Figure 4.57: Profile of GPR LINE05 collected over the limestone barrier encompassing sediment pond 2 in the wetland. 261

Figure 4.58: S-N oriented profile over GPR LINE06 collected in the wetland. 262

Figure 4.59: S-N oriented profile over GPR LINE07 collected in the wetland. 262

Figure 4.60: S-N oriented profile over GPR LINE08 collected in the wetland. 264

Figure 4.61: S-N oriented profile over GPR LINE09 collected in the wetland. 264

Figure 4.62: Map image indicating locations of EM31-MK2 survey lines and bog sample locations collected over the Gullbridge TMA between September 2016 and July 2018.266

Figure 4.63: S-N profiles of σ_a versus station spacing along EM LINE00 collected using VMD and HMD orientations and a S-N instrument orientation. 268

Figure 4.64: S-N profile GEM2 LINE00 displaying the quadrature component of $\vec{H}_s$ for three different operating frequencies 270

Figure 4.65: S-N profile GEM2 LINE00 displaying the in-phase component of $\vec{H}_s$ for three different operating frequencies 270

Figure 4.66: N-S profiles of the EM31 Quadrature component of $\vec{H}_s$ collected using VMD and HMD dipole orientations over the tailings reservoir 272

Figure 4.67: VMD Quad. phase apparent conductivity contour map over the June 2017 seep grid. 274

Figure 4.68: HMD Quad. phase apparent conductivity contour map over the June 2017 seep grid. 275

Figure 4.69: Profiles of σ_a versus station spacing over YLINE05 of the June 2017 seep grid collected S-N using the VMD orientation, with the boom aligned in two directions 276

Figure 4.70: Profiles of σ_a versus station spacing over XLINE10 of the June 2017 seep grid collected W-E using VMD and HMD orientations aligned S-N 277

Figure 4.71: EM31 VMD ground-conductivity contour map over the Gullbridge embankment and wetland 279

Figure 4.72: Elevation contour map over the wetland adjacent to the Gullbridge Tailings impoundment. 280

Figure 4.73: Profiles of concentrations versus core depths at bog site locations GB-01 and GB-03. 288

Figure 5.1: Aerial view of the Gullbridge Tailings Facility with main features of the impoundment indicated. 292

Figure 5.2: S-N section over YLINE05 of the June 2017 seep grid conducted over the main seep area of the Gullbridge Dam. 297

Figure 5.3: Delineation of suspected seepage flow paths compiled from SP and GPR surveys conducted over the main seep area 299

Figure 5.4: Coordinates of an elevation profile collected W-E across the Gullbridge Dam 302

Figure 5.5: W-E cross-section of the Gullbridge Dam over the elevation profile indicated in Figure 5.4 303

List of Tables

Table 2.1: NL Regulation 65/03 Schedule A concentrations 19

Table 2.2: Water table depths measured from the crest of the dam................................. 47

Table 2.3: Concentrations of key elements calculated from two samples within the impoundment collected at unknown locations... 60

Table 2.4: Elevations and depths of the July 2013 test pit programs key features 63

Table 2.5: Peat thicknesses under the embankment and in the adjacent wetland from borehole and bog probe data 68

Table 3.1: Magnetic susceptibility values for common materials found at Gullbridge.... 84

Table 3.2: Table of field schedule at the Gullbridge Tailings Facility 112-113

Table 3.3: Parameters used for DCR/IP surveys conducted over the Gullbridge TMA. 128

Table 3.4: Survey parameters used for EM31-MK2 surveys conducted over the Gullbridge TMA 137

Table 3.5: Drift measurements and correction calculations along section 1-2 and 3-4 of SP Line’s 1 and 2 collected in June 2016 along the Gullbridge Dam 144

Table 3.6: Example spreadsheet of DCR data uploaded from Syscal Junior resistivity unit in Prosys processing software.. 149

Table 3.7: Table of GPR processing procedures 156-158

Table 3.8: Excel spreadsheet of exported interpretation point data along GPR LINE05 collected in the wetland in September 2016 164

Table 4.1: Selected GPR surveys at the Gullbridge Tailings Facility 207

Table 4.2: Comparison of depths to major interfaces obtained from BH and GPR LINE00 data 223

Table 4.3: Elemental concentration, pH and conductivity of reservoir surface water and seep samples.. 285

List of Abbreviations

ABA – Acid Base Accounting

AGC – Automatic Gain Control

APP – Assisted Picking Processing

BL – Baseline

CDA – Canadian Dam Association

DCPT – Dynamic Cone Penetration Test

DCR – Direct-Current Resistivity Survey Method

DSR – Dam Safety Review

FOS – Factor of Safety

GPR – Ground-Penetrating Radar Survey Method

GWT – Groundwater Table

HMD – Horizontal Magnetic Dipole

ICP-MS – Inductively Coupled Plasma Mass Spectrometry

ICP-OES – Inductively Coupled Plasma Optical Emission Spectrometry

IP – Induced Potential

LCS – Laboratory Control Sample

m asl – Meters Above Sea-Level

NLDNR – Newfoundland and Labrador Department of Natural Resources

NPR – Neutralization Potential Ratio

PMT – Photomultiplier Tube

ppb – Parts Per Billion

ppm – Parts Per Million

RSD – Relative Standard Deviation

RX – Receiver

SP – Spontaneous-Potential Survey Method

SPT – Standard Penetration Test

TCH – Trans-Canada Highway

TMA – Tailings Management Area

TMI – Total Magnetic Intensity

TSS – Total Suspended Solids

TX – Transmitter

VES – Vertical Electrical Sounding

VMD – Vertical Magnetic Dipole

VMG – Vertical Magnetic Gradient

1 Introduction

1.1 Gullbridge Mine Tailings Facility

In recent years the use of non-invasive, geophysical survey methods in dam monitoring studies has been recognized in identifying and mitigating failure mechanisms responsible for destabilization and large-scale breaching. These methods were deployed to characterize material changes in the Gullbridge Tailings Dam following a December 2012 breach.

The Gullbridge Mine is an orphaned and abandoned property in Central Newfoundland centered over a volcanogenic massive sulfide ore deposit containing mainly copper-zinc ore. It operated between 1967 and 1971. During this time, the mine produced 94,000 tonnes of copper concentrate from 2.8 million tonnes of ore (Upadhyay & Smitheringale, 1972).

The Tailings Management Facility at the former Gullbridge Mine (Figure 1.1) lies at the site of a valley impoundment in which tailings were deposited from a stream into a reservoir impoundment enclosed by an earth-filled dam constructed from a local till. The dam acts as a barrier retaining tailings from an adjacent wetland. It was estimated from topographic survey data and test pit data acquired by AMEC in July 2013 that the reservoir contains approximately 1.8 million m^3 of subaqueously deposited sulfide bearing tailings. However, most of the tailings in the impoundment are subaerial at the present time. Water

Figure1.1: Aerial view of the Gullbridge Tailings Facility with main features of the impoundment indicated.

exits the reservoir via an armoured spillway before flowing through two sedimentation ponds and an armored discharge channel into the wetland (Figure 1.1) (AMEC, 2014).

Despite best efforts to manage water levels at the Gullbridge TMA, concerns have been raised in recent years over the stability of the tailings dam. The original structure was washed out in 1996 and rehabilitated in 1999 (Stantec Consulting Ltd., 2012).

Then, during repair work in December 2012 as part of Stantec Consulting's design to increase the slope stability, a large section of dam embankment in the south collapsed resulting in a significant decrease in pond water elevation exposing previously submerged tailings. NLDNR agreed to a closure option, carried out by AMEC Environment and Infrastructure, in which the dam crest would be lowered, and the downstream and upstream slopes reshaped. This closure option was successful, and the dam has been stable since remediation work was completed. However, the decrease in pond water elevation has resulted in the exposure of 235,000 m^2 of tailings in the impoundment in the present day, with water cover limited to areas adjoining the upstream slope of the dam in the west in the present day (AMEC, 2014).

Without continued maintenance and repair earth-filled dams are almost always subject to destabilization with age (Vick, 2001). Failures such as the Gullbridge Mine Tailings Dam breach are not an uncommon occurrence for abandoned and orphaned mines. Even facilities that are closely monitored and deploy the costliest closure options are at risk for several failure mechanisms over time. It is suspected that the main mode of failure responsible for the breach of the Gullbridge Dam was seepage of supernatant pond water

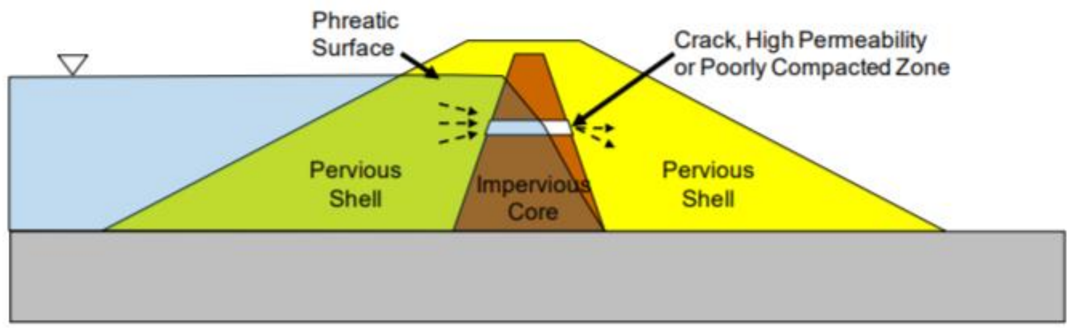

Figure 1.2: Schematic illustrating seepage related internal erosion through an embankment dam (U.S. Department of the Interior Bureau of Reclamation, 2019).

through the embankment as a consequence of rising pond water in the reservoir and poorly compacted zones within the dam material. Researchers have identified several locations along the base of the dam where seepage is suspected to be associated with internal erosion (AMEC, 2014).

The internal performance of a TMA can be analyzed by monitoring changes in the tailings seepage (Engels, 2017). Figure 1.2 illustrates the generation of seepage pathways as a result of water levels in the reservoir rising above a threshold elevation. Flow of tailings water is normally constrained to cracks or areas of poorly compacted material (U.S. Department of the Interior Bureau of Reclamation, 2019).

1.2 Objectives

The objective of this thesis was to carry out geophysical surveys at the Gullbridge Mine tailings facility as part of ongoing monitoring with the aims of determining the internal structure of the dam – particularly in locations of leakage and potential failure – and mapping areas of tailings concentration in the wetland.

Over time it is expected that the physical properties of a dam change significantly. These changes may lead to physical instabilities that geophysical survey methods can detect. Geotechnical investigations deploying geophysics are becoming increasingly popular in long-term dam monitoring investigations.

This study involves the application of multiple non-invasive geophysical survey methods over the Gullbridge Tailings Dam in order to delineate seepage related erosion pathways and other potential failure mechanisms. The spontaneous potential (SP) survey method is of great importance to dam monitoring studies as it is the only method that responds directly to fluid flow. Seepage can generate electric "streaming" potentials in embankment dams which are characterized in general by local anomalous highs on the downstream side and anomalous lows near the upstream side (Minsley, et al., 2011). Electrical methods such as the Direct-Current Resistivity (DCR) survey are effective at locating conductive seepage paths which may cause internal erosion and are often combined with other surveys such as ground penetrating radar (GPR) for locating voids in embankments. Magnetic surveys were deployed to identify buried iron structures such as historic pipes or culverts. Electromagnetic survey methods were conducted to measure lateral and vertical changes in conductivity that assisted in the identification of conductive seepage pathways through the dam. The most heavily studied location in the study area lies to the south where leaking of pond water at the base of the downstream slope has been identified. The focus at this site was to delineate the flow of pond water through the internal structure of the embankment.

Another nearby site of significance is where an old stream once flowed through the area before the construction of the dam. Discoloured orange-brown tailings water was observed discharging from the base of the downstream slope along a NE-SW impression in the wetland where the old stream once flowed (labeled “Depression” in Fig. 1.1). This research suggests that the foundation materials overlying the old stream may have been eroded by historical seepage of water beneath the dam along this depression during periods of rising pond water elevation (e.g. precipitation events)..

A secondary focus of this study was the wetland to the west of the dam. Research conducted in the wetland involved electromagnetic ground conductivity surveys as a means of mapping elevated concentrations of metals. Metal ions dissolved in water generate a conductive signature that electromagnetic induction methods can detect even at relatively low concentrations.

1.3 Location and Access

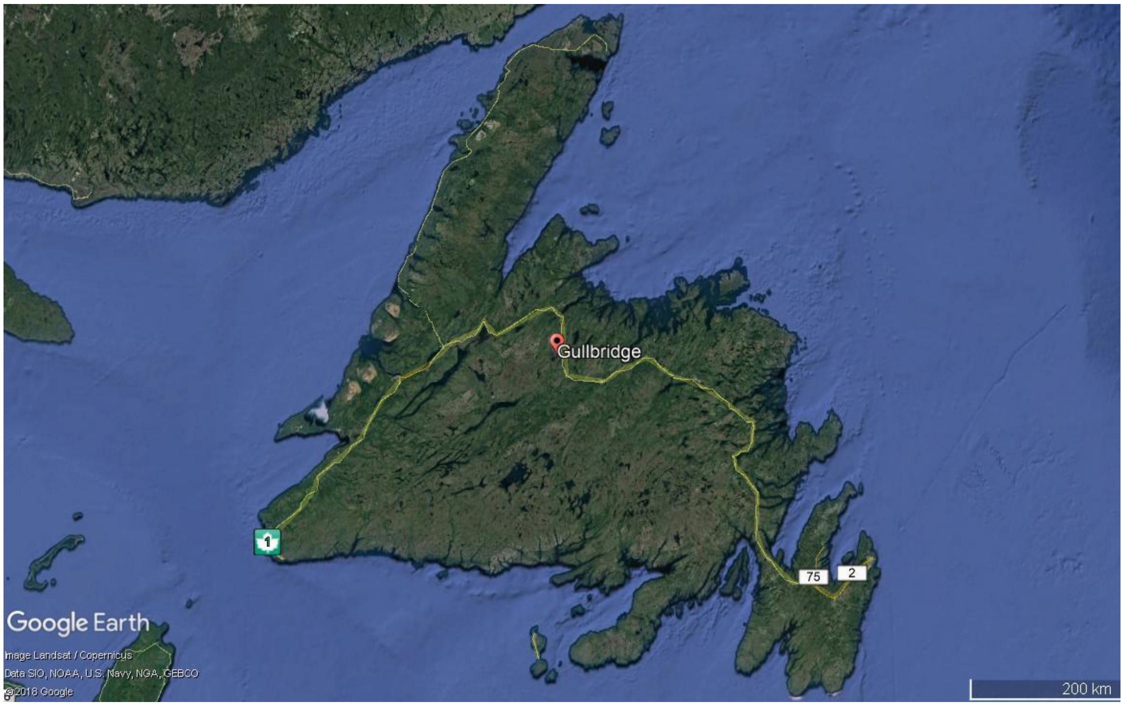

Figure 1.3: Location of Gullbridge, Newfoundland (Google Earth, 2018).

The Gullbridge TMA, encompassing an area of 267,000 m^3, is located between the towns of Badger and South Brook in north-central Newfoundland (Figure 1.3) on the western shore of Great Gull Pond (Figure 1.4) (AMEC, 2014).

Figure 1.4 below displays the location of and access to the Gullbridge TMA. The field site is accessed by a 5 km gravel road heading west from the Trans-Canada Highway (green star) approximately 30 km north of the town of Badger.

The Gullbridge TMA is located at the end of a westward turnoff path from the main gravel access road (Fig. 1.4). The path is navigable by vehicle to the northern section of the dam. A yellow star indicates the location of a gravel berm that was excavated sometime

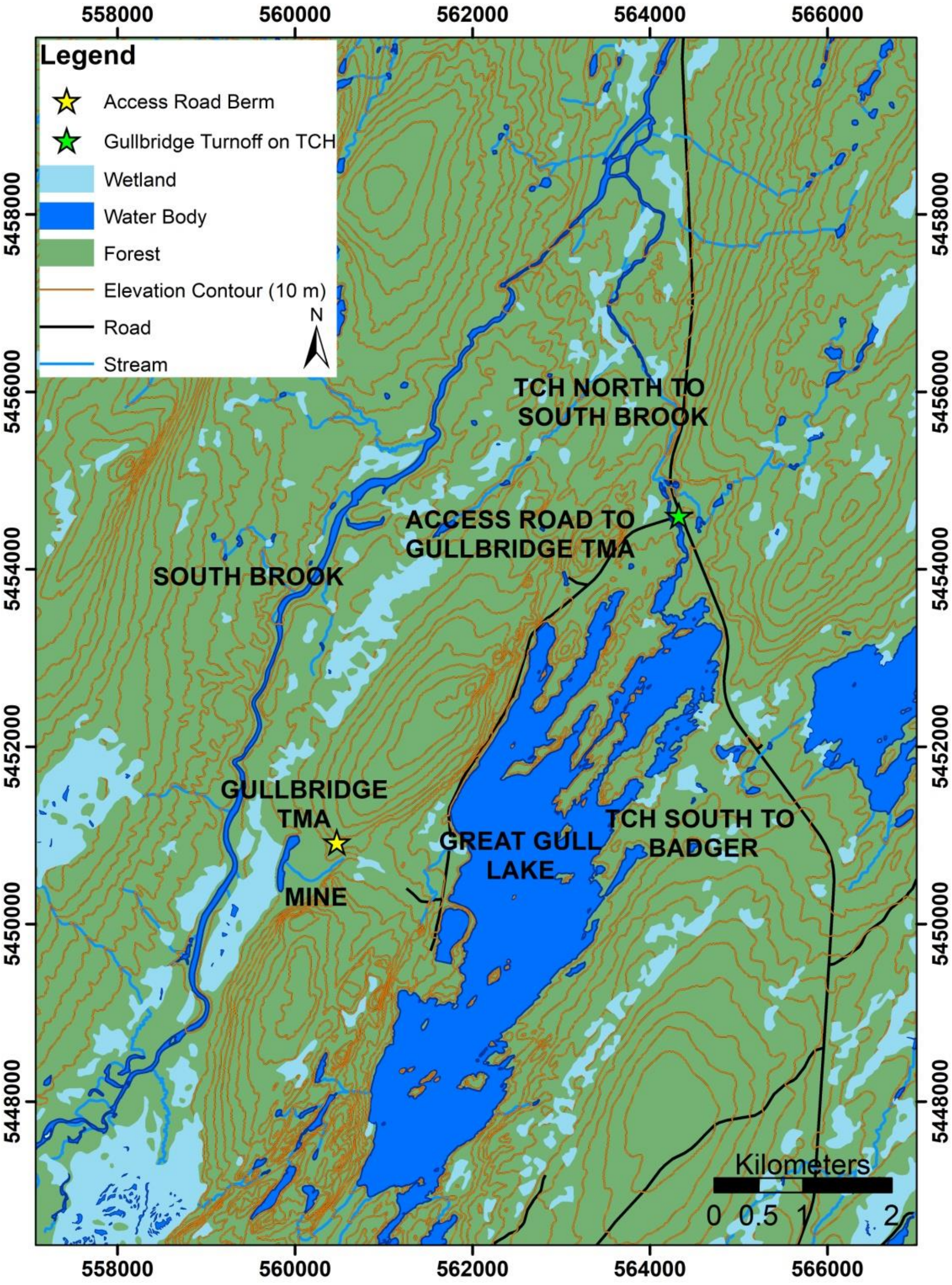

Figure 1.4: Location of the Gullbridge TMA on a topographic map generated in ArcGIS from data acquired by Natural Resources Canada.

between July and November 2017. The location of the berm in Figure 1.4 marks the entrance to the TMA. During winter months, the site is accessible only by snowmobile.

Light brown elevation contour lines separated by intervals of 10 m indicate the topographic relief over the region. Near the Gullbridge TMA, isolines on either side of a small stream, named South Brook, mark 140 masl. The mine shaft is located on a topographic high of 220 m observed ~ 1 km southeast of the impoundment where tailings sediment were pumped into an east-west oriented stream that feeds into a reservoir located at the base of the valley.

A wetland occupies the area immediately to the west of the Gullbridge TMA. The ground over this area is composed mainly of peat. Approximately 400 m downstream of the embankment dam, ground and surface water from the wetland feeds into South Brook. There are several small ponds and riverlets within the wetland. The wetland is heavily water saturated with scattered dense coverings of trees or bushes making it a difficult surface to survey in the summer months: frozen ground serves as a better platform for field work. However, deep snow cover in the winter field season made trudging over the wetland a hardship, so that electromagnetic ground conductivity surveys conducted both in the summer and winter were difficult (AMEC, 2014).

The climate in the area is continental with short mild summers and long cold winters. Precipitation in the area calculated by Natural Resources Canada ranges from 900 mm to 1600 mm annually. The area is surrounded by a densely vegetated forest and little exposed bedrock (AMEC, 2013).

1.4 Regional Geology

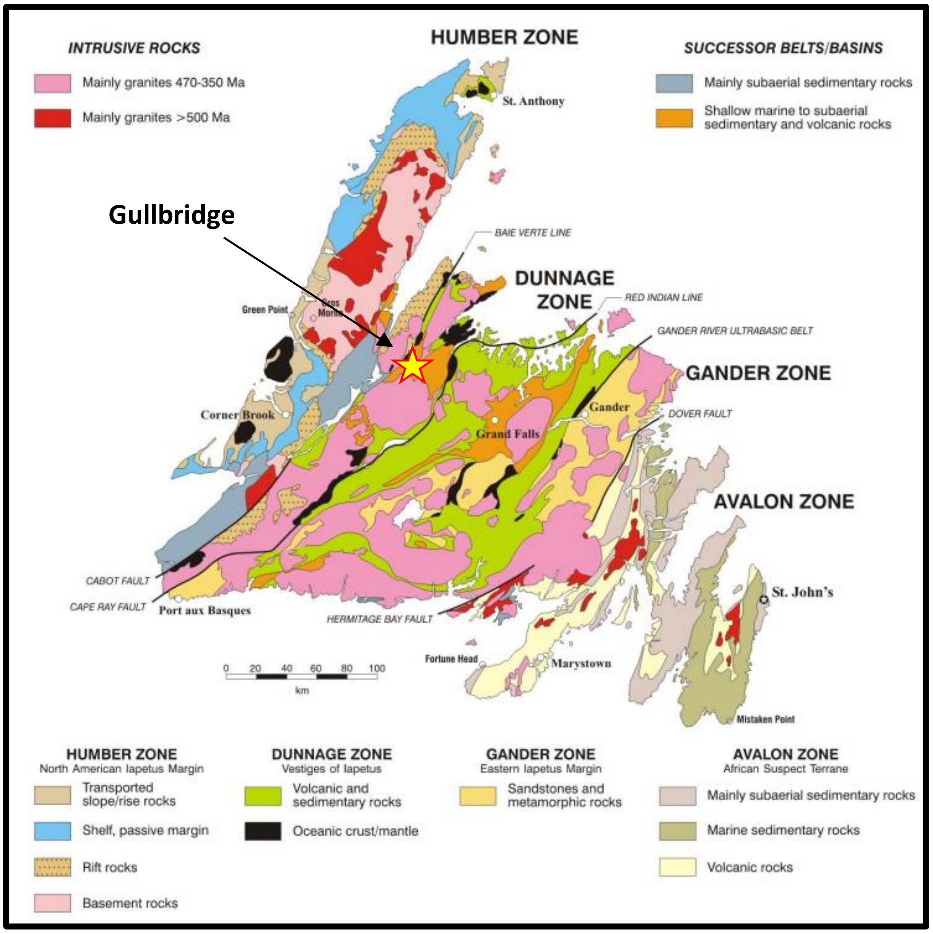

Figure 1.5: Regional Geological Map of Newfoundland (Geological Association of Canada).

The Gullbridge deposit lies in the central Appalachian orogenic belt within the Notre Dame subzone of the Dunnage zone (Fig. 1.5) (Dec et al., 1997). The Notre-Dame subzone is bordered by the Exploits subzone, to the west of the Red Indian Line, which juxtaposes rocks formed on either side of the former Iapetus Ocean (Rogers et al., 2007).

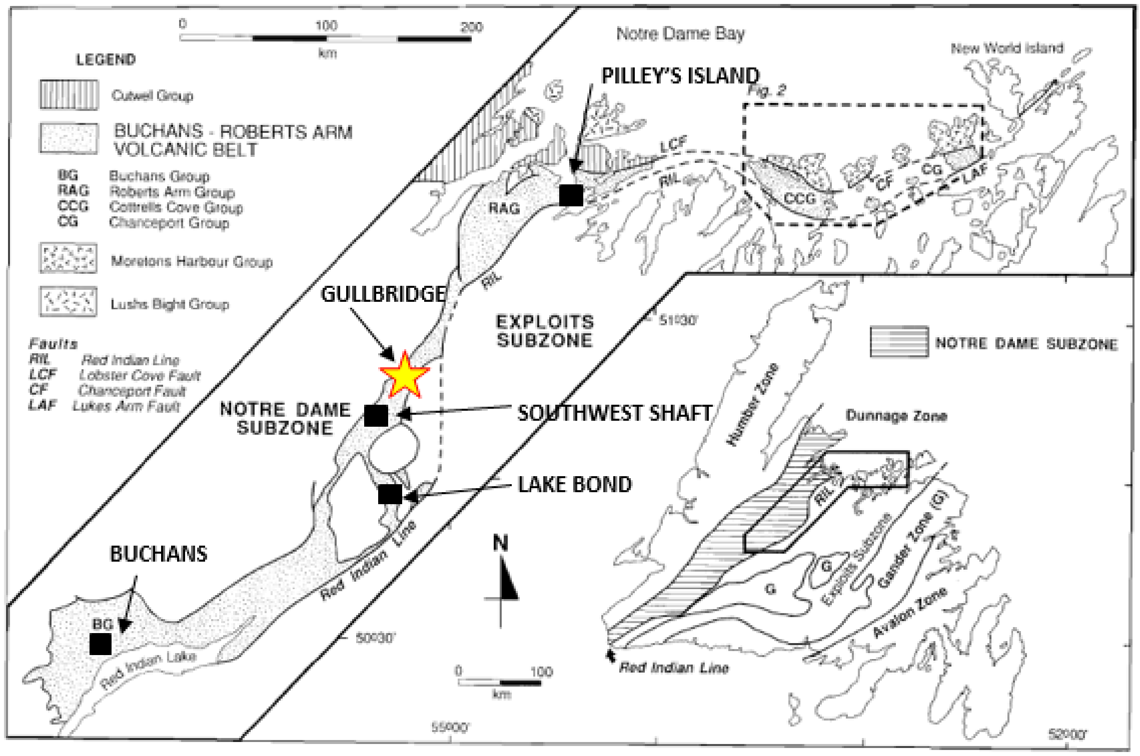

Figure 1.6: Map of Notre Dame Subzone indicating location of Gullbridge and several other VMS deposits occupying rocks of the Robert's Arm **(**Modified from Dec et al., 1997).

Gullbridge hosts one of many pyritic VMS ore deposits occupying volcanic host-rocks of the Buchans-Roberts Arm Belt (473-464 Ma), which formed along a regionally extensive tectonic setting within the Dunnage zone between the Notre Dame and Exploits subzones (Figure 1.6; Rogers et al. 2007). The deposits are suspected to have formed during the existence of the Cambro-Ordovician Iapetus Ocean in a mature volcanic island-arc setting. One hypothesis is that this arc sequence accreted to older Dunnage Zone rocks on the Laurentian margin during the later stages of the Taconic Orogeny (O'Brien, 2007; Upadhyay & Smitheringale, 1972).

The Roberts Arm Group is comprised of a regionally extensive sequence of lower Ordovician marine volcanic and epiclastic rocks that are divided into two main units: calc-alkalic basaltic massive pillow sequences with tuffaceous inclusions, and pyroclastic volcanic rocks. To the east and west of Gull Pond the Roberts Arm Group has undergone contact metamorphism from gabbroic to granitic intrusive plutons, and this has clouded the origins of the Gullbridge deposit (Upadhyay & Smitheringale, 1972; Hudson & Swinden, 1990; Dec et al., 1997).

1.5 Local Geology

The Gullbridge mine is centered over a pyritic VMS ore deposit containing mainly copper-zinc ores with bedrock exposures consisting of volcanic and clastic sediments. The deposit is located 30 km south of the Luke Arm Fault, an E-W oriented fault zone centered on the Red Indian Line suture zone. Between 1967 and 1972 the Gullbridge mine produced 3 million tonnes of ore averaging approximately 1.1 % copper (Upadhyay & Smitheringale, 1972; AMEC, 2014).

The exact origins of the Gullbridge deposit have been clouded by hydrothermal and metamorphic deformational events which produced an assemblage of varying mineralogy such as mafic greenschists and mineralized mafic flows (Dec et al. 1997). These alteration zones were catalyzed by the post-tectonic intrusion of the South Brook pluton consisting of granodiorite, granite and syenite (O'Brien, 2007). Host rocks contain small quantities of magnetite and pyrrhotite which contribute to the high magnetic signature of the VMS deposits in the area. However, what sets the host rocks of the Gullbridge deposit apart

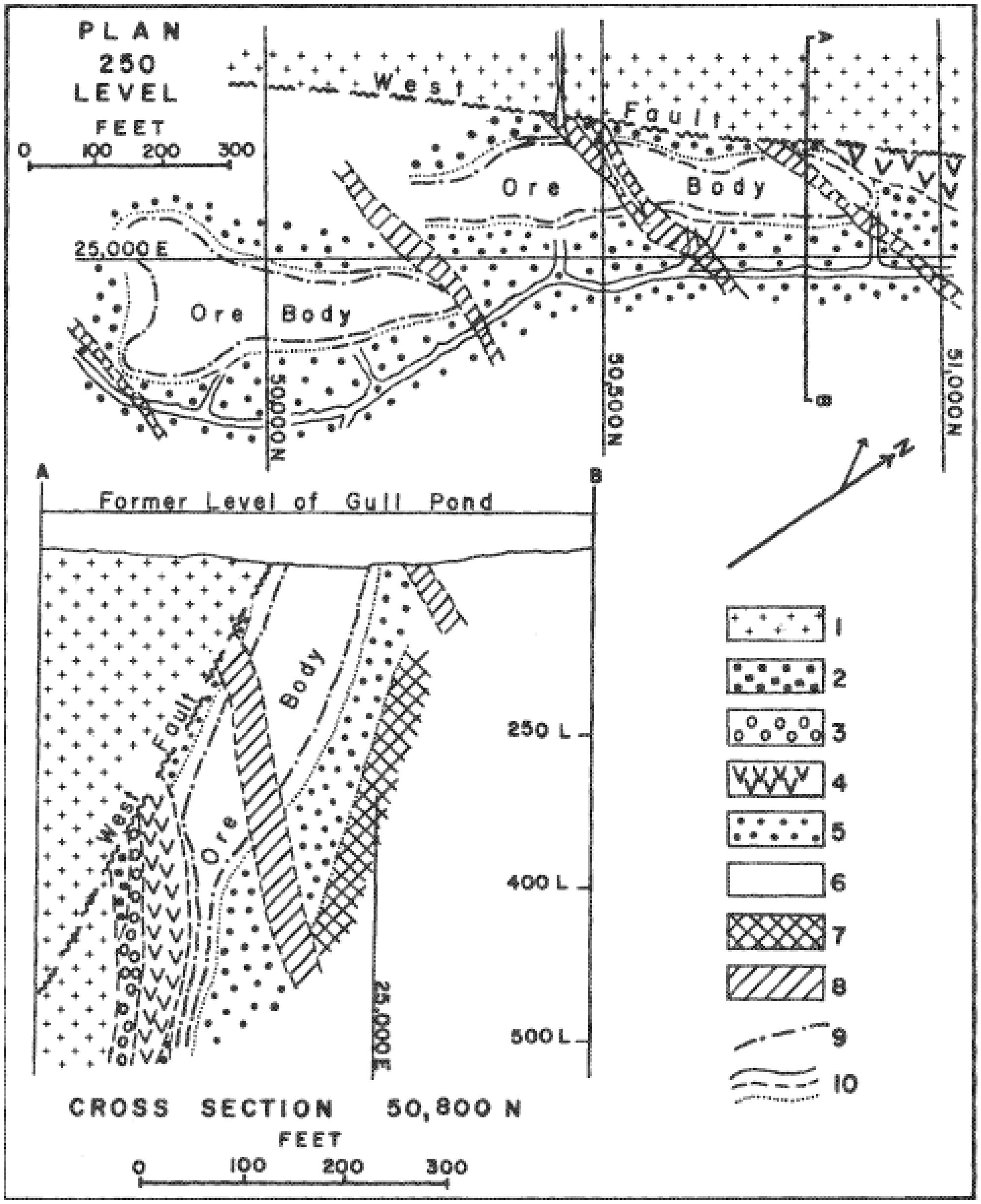

Figure 1.7: Plan view and cross-section of the Gullbridge deposit. Key: (1) Rhyolite; (2) Quartz-sericite phyllite; (3) Iron formation; (4) Metabasalt; (5) Cordierite-anthophyllite rock; (6) Cordierite-andalusite-chlorite schist (ore body host rock); (7) Silicic hornfels (with thin units of metabasalt); (8) Composite dike; (9) Outline of ore body; (10) Geological contact (Upadhyay & Smitheringale, 1972).

is that they contain andalusite, cordierite and anthophyllite thought to have grown as a result of a "post-main schistocity thermal metamorphic overprint" (Hudson & Swinden, 1990; Upadhyay & Smitheringale, 1972).

Figure 1.7 illustrates a plan view and cross-section of the Gullbridge ore deposit. The plan view taken from Upadhyay & Smitheringale (1972) measures a length of approximately 400 m and the NW-SE section AB displayed at the bottom is ~120 m wide.

The ore body was composed of tabular lenses dipping 70^0-90^0 to the northwest with an average thickness of 30 m. The longitudinal section of the ore body had a decreasing strike length with depth and its deepest section reached a depth of approximately 210 m (Upadhyay & Smitheringale, 1972).

The ore body (Fig. 1.7) is overlain by a thick layer of rhyolite (unit 1) adjacent to a northwestward dipping longitudinal fault. The fault cuts the rocks of the hanging wall as well as intrusive composite dikes (unit 8) penetrating the deposit in the north. The west fault zone acts as a boundary between thick rhyolite flow rocks and a quartz-sericite phyllite zone (unit 2). The phyllite component is generated from slates metamorphosed on the boundary of the western fault. The ore deposit is enveloped by the foliated ore-bearing cordierite-andalusite-chlorite schist host rock (unit 6) which is also intruded by dikes generated from historical volcanic activity. The northern section of the ore deposit is overlain by a section of metabasalts (unit 4) that thicken to the north. The metabasalt contains hornblende and cloudy plagioclase that were generated by contact metamorphism due to the composite dikes of basaltic rocks. The dikes are primarily diabase in composition, accompanied by some felsite and andesite. There is a presence of magnetite within the ore body occurring as grain fragments that that are suspected to have been generated through replacement of chromite (Upadhyay & Smitheringale, 1972).

2 The Gullbridge Tailings Facility

2.1 Tailings Management

During upstream mining operations, ore material is typically milled and partitioned into high-grade concentrates and low-grade byproducts. The rejected byproducts, known as tailings, are a mixture of fine sand-to-silt-sized rock particles, water and processing reagents. Tailings management is an indispensable preliminary measure in the design and operation of mining activities across Canada, necessary for the mitigation of environmental impacts (Natural Resources Canada, 2013).

If attempts to contain tailings safely over time are unsuccessful, adverse environmental and socio-economic consequences may result. If sulfide minerals within tailings become exposed to oxygen, they produce sulfuric acid. This increase in acidity may lead to an increase in the solubility of heavy metals, resulting in high concentrations of dissolved (leached) heavy metals within the pond water. Conventional tailings storage methods require acid generating and or metal leaching tailings be submerged underwater or stored underground in large containers where oxygen gas is unable to penetrate the pore space of the tailings (Blowes et al., 2003; Fitzpatrick A. , 2013; Fey, 2003).

Typically, mining facilities in Canada deploy a Tailings Management Area (TMA) to contain tailings and mitigate the effects of acid-generation and metal leaching. Tailings sediment is normally transported from the mine shaft by pipeline and deposited subaqueously in a large reservoir where sedimentation occurs, and tailings water is separated from solid tailings. Valley impoundments such as Gullbridge utilize natural mechanisms such as streams to transport tailings sediment from the processing plant to the reservoir. Pond water is normally contained in the reservoir by a man-made barrier known as a “tailings dam”. The elevation of the water column in the reservoir is maintained by utilities such as decant structures and spillways that regulate drainage during heavy periods of rainfall and storm-surge events. Decant structures generally consist of pipes joining the upstream and downstream sides of a dam (Engels, 2017;(Stantec Consulting Ltd., 2012).

Maintaining a stable water level in the reservoir plays a vital role in the performance of a TMA. If the elevation of the water is too high, barrier seepage or overtopping can occur; if it is too low, dusting and acid-generation can occur due to sub-aerial exposure of tailings. Historically when a tailings management facility fails to reach its full operational capacity, it can usually be attributed to mismanagement of ponded water in the reservoir (Engels, 2017).

With time, the material aspect ratio (height:width) and slope angles of the dam must change to accommodate the increase in tailings volume and the rise in pond water. If the height of the dam is raised, the downstream and upstream slopes must be adjusted to ensure the stability of the structure (AMEC, 2013).

The Canadian Dam Association (CDA) is an organization committed to guiding the safe design and operation of dams across the country. The CDA has developed a set of guidelines that classifies dams based on their hazard potential. The classification scheme, ranging from low to extreme, is based on several factors including slope angles, population at risk, environmental and economic losses, and data collected from various geotechnical investigations. Ideal facilities take precautions to ensure the dam is “low risk” provided there is no population at risk, with minimal potential for environmental and economic losses (Parsons & Warford, 2008).

Acid Base Accounting (ABA) is an analytical technique used to assess the degree to which acid generation may occur calculated by the balance between acid-production and acid-neutralizing potential (Mills, 2017). A key result of ABA, which is referred to frequently in this chapter, is the Neutralization Potential Ratio (NPR). A material with NPR less than 1 is considered potentially acid generating (Appendix A2.2).

Mining facilities analyze physical properties of tailings and water such as total suspended solids (TSS) and total metals. Table 2.1 on the following page displays a list of the Newfoundland and Labrador Regulation 65/03 Schedule A physical parameters. Water samples in compliance with Schedule A concentrations limit the possibility of acid generation and metal leaching. This range of values has come to be the accepted standard for the safe release of water into aquatic environments in Newfoundland. For the purpose of this discussion, the parameters relevant to this research are pH (5.5-9), Total Suspended Solids (30 mg/L), Total Copper (300 μg/L), Total Iron (10000 μg/L) and Total Zinc (500 μg/L) (AMEC, 2013).

Table 2.1: NL Regulation 65/03 Schedule A concentration regulations for several parameters tested at the Gullbridge TMA (AMEC, 2013).

Physical Parameters	**Units**	**Schedule A***
pH	pH	5.5 – 9.0
Conductivity	uS/cm	
Total Suspended Solids	mg/L	30
Nitrate (N)	mg/L	10
Anions		
Dissolved Chloride (Cl)	mg/L	
Nitrogen (Ammonia Nitrogen)	mg/L	2
Orthophosphate (P)	mg/L	
Dissolved Sulphate (SO4)	mg/L	
Metals		
Total Arsenic (As)	ug/L	500
Total Barium (Ba)	ug/L	5000
Total Boron (B)	ug/L	5000
Total Cadmium (Cd)	ug/L	50
Total Chromium (Cr)	ug/L	50
Total Copper (Cu)	ug/L	300
Total Iron (Fe)	ug/L	10000
Total Lead (Pb)	ug/L	200
Total Nickel (Ni)	ug/L	500
Total Selenium (Se)	ug/L	10
Total Silver (Ag)	ug/L	50
Total Zinc (Zn)	ug/L	500

2.2 Construction History

2.2.1 Initial Construction

Historical documentation on construction, maintenance, and remediation of the Gullbridge Tailings Facility prior to 1993 was not obtainable. It is uncertain whether the dam was constructed as a rolled-earth cut-off trench dam, or a rolled-earth core dam (Stantec Consulting Ltd., 2011; Gedeon, 2004). A rolled-earth dam is constructed in layered phases and compacted using a roller or rolling equipment. A cut-off dam reduces seepage losses from underneath the dam by utilizing a trench, extending the length of the embankment at its base, that is filled with soil overlying compacted clay. A core dam consists of a fine-grained, clay-rich impervious earth-filled core with an outer shell of rock less susceptible to erosion flanking each of the slopes and covered with fill material (State of Tasmania, 2008). Based on assessments of the dam structure by the author and NLDNR, it is thought the Gullbridge dam was initially a core dam. Then, during mining operations, the height of the dam was increased in phases using fill materials sourced from a local till collected along the access road leading into the impoundment.

The embankment and pond water elevation were raised several times over the years to accommodate the increase in tailings. Test pit data (section 2.5.3) suggest that during the dam height adjustments, and before the required modifications which would allow for the increase in pond water elevation, tailings were periodically exposed and deposited on the upstream slope of the dam and may have been oxidizing over the last 40 years.

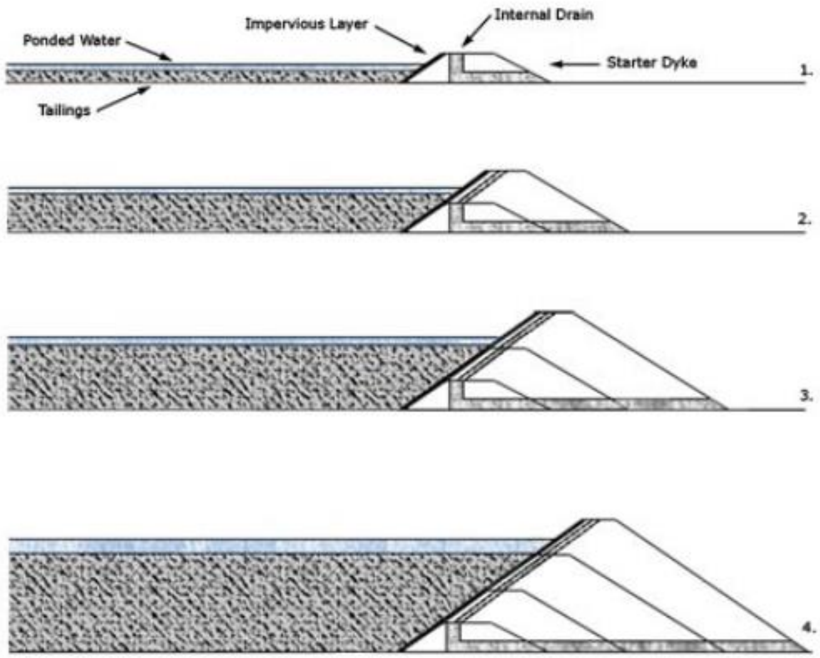

Figure 2.1: Downstream construction phases of a raised embankment design (Engels J., 2017).

Based on geotechnical investigations by Stantec and AMEC, the Gullbridge dam evolved according to a raised downstream embankment design, as depicted in Figure 2.1. The dam is extended upward and in the downstream direction, while on the upstream side beached tailings adhere to the slope. At each stage, the new dam material is compacted. The core was made during the first construction phase and was not modified during the raises (A. Steel, pers. comm. 2021; Boak & Sibbick, 2014; Engels, 2017b).

2.2.2 1993-1999 Failure, Assessment and Remediation

The earliest performance issues concerning the Gullbridge dam were reported in 1993 when there was a failure on the northern section (Boak & Sibbick, 2014). The cause of this failure is unclear.

In 1996 an original decant structure acting as the main discharge outlet for the facility was washed out and subsequently repaired. There is no documentation concerning this repair work, or the design or location of the original structure. It is uncertain whether the repaired decant was decommissioned or not (Engels, 2017;(Stantec Consulting Ltd., 2012). Following the washout, sometime after 1996 a new discharge outlet in the form of 12 m long, 900 mm diameter corrugated steel twin culverts was installed in the northwest corner of the dam, allowing pond water at a discharge elevation of 151.14 m asl to flow freely into the wetland (AMEC, 2013).

The former mine site location was rehabilitated in 1999, which process included the removing of unnecessary buildings and production materials as well as the sealing of mine shafts (Stantec Consulting Ltd., 2012).

2.2.3 2010-2012: Assessment and Remediation

On June 10th, 2010 NLDNR visited the Gullbridge site to conduct a visual inspection of the embankment. Most notably, a longitudinal crack on the downstream slope was observed. On October 10th, 2010 Stantec Consulting Ltd. were hired by NLDNR to generate a Dam Safety Review (DSR) of the Gullbridge Tailings Dam as part of preliminary efforts to design a long-term closure option (Stantec Consulting Ltd., 2011).

On November 29th, 2010 Stantec Consulting Ltd. visited the Gullbridge site to inspect the dam design, operation, and maintenance. Some of the major findings included seepage at the downstream toe, cracks on the upstream slope related to the freeze-thaw cycle (‘ice-jacking’), and shallow erosion of the downstream slope suspected to be due to sloughing previously reported in June 2010 (Fig. 2.2).

Figure 2.2: Shallow slope failure looking north along the downstream slope of the Gullbridge Dam on June 10th, 2010 (Stantec Consulting Ltd., 2011).

Two potentially historical outlet structures were observed on the upstream slope. One was in the form of a wooden frame and standpipe, and the other was an inlet channel "with timber" proposed by Stantec to have been installed during the initial phases of the dam construction and served as a decant to allow for water to flow freely beneath the embankment without eroding the dam fill materials. Historical data on the origins of these decants are not available. The coordinates for some of the features observed on this trip are included in Table A2.1 (Stantec Consulting Ltd., 2011).

Dam material was observed downstream of the culverts in the north. This displaced material was the result of both a washout of the original decant structure in 1996 and a recent localized failure related to repair work conducted by DNR in November 2010 where regions of the dam disturbed by construction resulted in the loosening of dam material (Stantec Consulting Ltd., 2011).

On March 2nd, 2011, a preliminary DSR reported the dislodging of large stones (rip rap) placed on the upstream slope of the dam to retard erosion, tension cracks, and shallow slope failures on the downstream slope (Stantec Consulting Ltd., 2011 (b)).

On September 10th, 2011 Stantec Consulting Ltd. conducted hydrological and hydrotechnical field studies. This involved further visual inspection of the dam and tailings reservoir as part of a slope stability analysis as well as measuring flow rates at various locations for determination of the capacity of the discharge structures (Stantec Consulting Ltd., 2012).

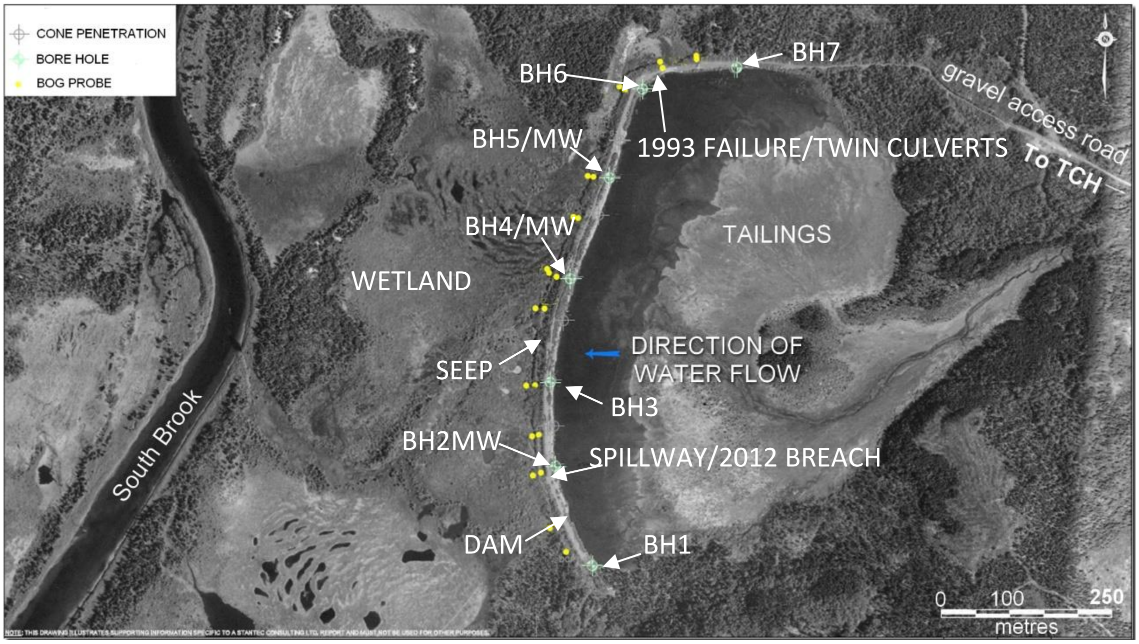

Figure 2.3: Aerial view of the Gullbridge Tailings Facility indicating the locations of boreholes and bog probes drilled along the dam and in the wetland respectively (Stantec Consulting Ltd., 2012). This aerial photograph was captured before the installation of the spillway, sedimentation ponds and limestone lined berm. The legend in the top-left corner indicates the marker legend for cone penetration, bore hole and bog probe positions recorded from data collected by Stantec Consulting Ltd.

From October 19th to 25th, 2011, seven boreholes designated BH1 to BH7 were drilled along the top of the dam (Figure 2.3). At this time, monitoring wells (MW) were installed in BH2, BH4, and BH5 to measure the height of the water column (Stantec Consulting Ltd., 2012).

Between November 7th and 9th, 2011, 13 Penetration Tests (Appendix A2.3) were carried out over the dam, providing shearing resistance and density data to supplement corresponding borehole data.

At the same time, 24 bog probes were conducted immediately downstream of the toe of the dam (Figure 2.3). On November 9th, 2011 water level measurements in the dam were made at the monitoring wells (Stantec Consulting Ltd., 2012).

On November 16th, 2011 in a follow up geotechnical field investigation, post-operation failures along the dam in the form of scarps at the toe and corresponding voids of undisclosed size at the crest were observed. Seepage was also reported at various locations along the length of the dam. In particular seepage was observed at the locations of the twin-culverts, at the downstream slope above the old stream and at the southern end of the dam near the tree line (AMEC, 2014) (Stantec Consulting Ltd., 2012).

The locations of the bog probes, boreholes, twin-culverts, and main seep are indicated in the air photo in Figure 2.3. An image of the twin-culverts prior to their removal is presented in Appendix A2.1.

On April 13th, 2012, a hydrotechnical report assessed that the culvert system in the north was blocked, deteriorated and inoperable and that it could no longer serve as the main discharge feature of the facility. NLDNR reported that occasionally the culverts were blocked due to beaver activity, giving rise to variable pond water elevations over the reservoir (AMEC, 2014; Boak & Sibbick, 2014). The culverts were severely corroded due to iron oxidation, seepage was observed under their base, and there was loss of dam material around the culverts due to wave action erosion. It was recommended that an armored spillway with erosion protection be installed over the dam (Stantec Consulting Ltd., 2012 (b)).

On October 26th, 2012, in a follow up report of the preliminary DSR, Stantec Consulting determined that the Gullbridge Dam required modifications to achieve an acceptable "factor of safety", which is a measure of the embankment stability determined by the ratio of the ultimate strength of a material and the allowable stress subjected to it. Proof that the dam would be safe after the recommended modifications was based on watershed delineation and flow modeling, intrusive testing, assessment of outlet structures, and hydraulic assessment of the spillway. The remediation work was completed in the fall of 2012 (Stantec Consulting Ltd., 2012; Engineers Edge, 2017).

NLDNR reviewed the DSR and changed the dam classification from low risk to significant risk, based on environmental concerns due to the proximity of the tailings dam to South Brook. In response, on December 12th, 2012 Stantec submitted a supplementary report in which they determined, based on a 1:100 year Inflow Flood Design model, that the remedial measures proposed in October 2012 would be adequate. Slope stability analysis conducted along both the upstream and downstream slopes also supported the proposed remedial measures (Stantec Consulting Ltd., 2012 (c)).

2.2.4 2012-2014 Failure, Assessment and Remediation

The initial part of the remediation involved placing a rock fill berm downstream of the dam to define the new extent of the downstream slope. On December 17th, 2012 at 7:45 am, while excavating a peat/bog layer prior to the placement of this berm, the dam breached. A section of the embankment, 35 m long and the full height and width of the dam (7 m high, 25 m wide) collapsed (Fig. 2.4). The tailings pond drained over the hours

Figure 2.4: Gullbridge Dam breach looking northeast on December 17th, 2012 (Government of Newfoundland and Labrador, 2018).

following the breach resulting in a 1 m decrease in pond water elevation. Given this decrease in pond water elevation it is estimated 100,000 m^3 of pond water was released from the reservoir exposing to the air previously submerged tailings in the reservoir. Based on the water volume leaving the impoundment it was estimated 7,000 m^3 of dam debris and 500 m^3 of tailings were cast into the wetland (AMEC, 2014; Government of Newfoundland and Labrador, 2018; NLDNR, 2012 (b)).

Figure 2.5 displays an aerial photograph over the Gullbridge TMA overlain by information on the breach and subsequent modifications to the facility. The area outlined in red indicates the assumed debris flow path established by AMEC in 2014. Material connected with the breach covered an area of approximately 4 ha over the wetland and was observed as far as 400 m from the embankment. Occasional patches of grey sand and gravel mixed with bog material were observed. Tailings were likely deposited in the wetland as small, consolidated chunks or as fines in high velocity waters near the breach (AMEC, 2014;NLDNR, 2012 (b)).

Following the breach, an additional 60,000 m^2 of tailings were exposed to the air. Consolidated tailings immediately upstream of the breach contained small erosion channels associated with high velocity waters from the breach (Boak & Sibbick, 2014). There was

Figure 2.5: Aerial view of the Gullbridge TMA following the December 2012 breach. The suspected debris flow path is outlined in red, as well as other important modifications to the facility **(**AMEC, 2014**)**.

a decrease in pond water elevation from 151.14 m asl at the discharge elevation of the twin culverts to 150.0 m asl (AMEC, 2014;NLDNR, 2012 (b)).

Repairs at the breach location began on December 19th, 2012. The initial repairs involved constructing a small temporary berm to contain tailings advancing from the small amount of water that continued to trickle from the breached section into a temporary settling basin (NLDNR, 2012 (b)).

On December 20th, 2012, a helicopter inspection was conducted by the Department of Environment and Conservation and the town of South Brook. Along the spill zone, a

Figure 2.6: Construction of temporary berm and settling pond on December 19th, 2012 immediately following the breach (Government of Newfoundland and Labrador, 2018).

layer of grey sand and gravel debris as well as tailings were photographed from the air (Figure 2.6). Larger chunks of tailings and dam material were enclosed by the temporary berm. A large volume of consolidated tailings was still confined to the impoundment: at the base of the breached area, tailings were observed 2-2.5 m above the lowest breach elevation. Looking upstream from the spill site, the tailings had a layered appearance (NLDNR, 2012 (b)).

In March 2013, a fordable spillway was installed over the breached area. Water flows regularly through the spillway, except in the summer months when it dries occasionally. Limestone lined berms constructed from blast rock were installed, encircling two sedimentation ponds excavated immediately downstream of the spillway. In constructing the berms, limestone blast rock was placed over the spill material. Spill/spoil material within the berms was then removed to create space for the two sedimentation ponds, and this material was relocated a short distance south of the sedimentation ponds outside the berm. Water from the larger, second settling pond flows over a limestone lined berm and into an adjacent armoured discharge channel before being discharged into the wetland.

The location of the settling ponds (Sediment Ponds 1 and 2) are given below in Figure 2.7: the armoured discharge channel is labelled "outflow" and indicated by the blue circle. To further mitigate effects of the advancing debris flow, 100 tonnes of limestone gravel was added to the debris flow path upstream of the berm to neutralize potential acid-drainage (AMEC, 2013).

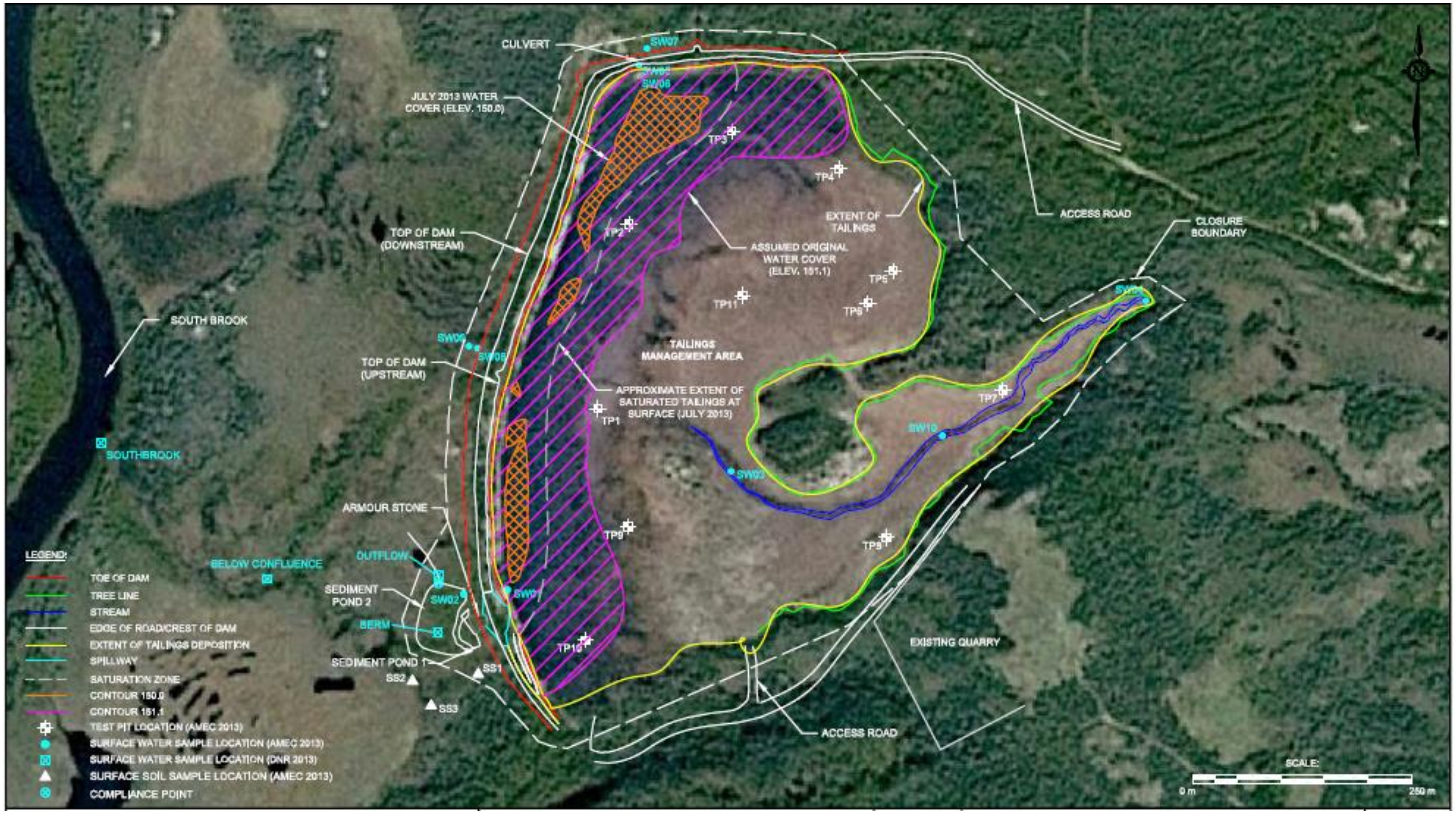

Figure 2.7: TMA test pit, ground water and material sample locations at Gullbridge. Significant boundaries include the toe of the dam (red), the tree line (green), the extent of the tailings deposition (yellow), the spillway (light blue), and the tailings creek (blue) (AMEC, 2013 (c)).

In May 2013, AMEC were hired by NLDNR to assist in the preparation of several closure options for the abandoned mine. As part of the continued dam monitoring efforts, water quality testing of discharge at Sediment Pond 2 by NLDNR continued through the summer months (AMEC, 2013).

Figure 2.7 displays the locations of surface water samples of the July 2013 sampling program, as well as the locations of 3 samples collected in December 2013 by AMEC. Thefigure displays several significant boundaries (AMEC, 2014; Hollett, 2014). Figure 2.7 also displays the locations of 11 test pits (TP) collected on July 10^{th} and 11^{th}, 2013 11 dug at spaced intervals in the reservoir using a Caterpillar 320B (AMEC, 2013).

Figure 2.7 also displays the water cover in the reservoir before the breach (purple hatched area), and the water cover and approximate extent of the water-saturated tailings in July 2013 (Hollett, 2014). The difference in water cover reflects the decrease in water elevation from 151.1 masl before the breach to 150 masl after installation of the spillway (AMEC, 2013).

AMEC collected 9 surface water samples within the tailings impoundment, near the breach, and in the wetland, as indicated in Figure 2.7 by the blue circles. Sediment pond 2 was not actively discharging during this time, so no samples were collected there (AMEC Environment and Infrastructure, 2013). The samples were submitted to Exovus Accutest for laboratory analysis.

NLDNR collected ground water samples (blue crossed squares in Figure 2.7) from Sediment Pond 2 ('BERM'), from the outflow site ('OUTFLOW'), from a point in the wetland where surface streams have converged ('BELOW CONFLUENCE') and at the bank of South Brook. The samples were submitted to SGS Canada for laboratory analysis. The 'OUTFLOW' location is a 'compliance point' which is routinely tested to ensure that the water composition complies with environmental regulations (Hollett, 2014).

During July 2013 sampling, AMEC and NLDNR personnel observed a continuous and thin (2-3 cm) fine-grained layer of grey sediment in the wetland downstream of the dam sandwiched between underlying wetland peat and an overlying thin layer of peat (2-5 cm). This sediment layer is suspected to be material deposited as a result of undocumented spills or discharge from historical decants prior to the breach of 2012. It was discovered when high velocity pond water from the 2012 failure washed away part of the surface cover of peat. Thus, samples collected at the spill/spoil area are representative of the breach sample, whereas sediment in the wetland is likely representative of deposition over the course of 20 years (AMEC, 2014).

On October 20th, 2013 AMEC submitted a final report concluding that, based on water quality modeling and slope stability analysis, the best closure solution involved a phased remediation of the impoundment beginning with the rehabilitation of the dam. This involved lowering the crest of the dam and flattening the downstream slope, while maintaining the post-breach pond water elevation of 150 m asl. The embankment's steep downstream slope and poor foundation, combined with loose dam material and seep related erosion, was likely a contributing factor in the failure mechanism behind the 2012 breach. Water quality sampling in the reservoir indicated the majority of all sample parameters were in compliance with Schedule A concentrations, therefore it was decided this pond elevation was adequate as a long-term solution (AMEC, 2013;Burridge, 2014).

The elected rehabilitation model, Closure Option 1C, included several remedial phases designed to prevent future failures. It entailed the removal of vegetation on the downstream slope, then lowering the height of the dam to an average elevation of 151 masl, and using excavated material cut from the crest to extend and flatten the downstream slope. A rock fill toe-berm was constructed starting from the spillway and extending into the wetland to stabilize the bog and support construction (AMEC, 2013;AMEC, 2013 (b)).

Modifications of the spillway installed in March 2013 would involve excavation of till fill and other fill materials, and the installation of a geotextile filter fabric, which was to extend 1.5 m past the lowered crest and be covered with a fine rock fill material. Furthermore, since the new pond water elevation was below the elevation of the inoperable twin-culverts, they would be removed (AMEC, 2014).

Between November 12th and Dec. 5th, 2013, a modified version of Closure Option 1C was carried out along ~800 m of the Gullbridge dam. Prior to reconstruction, the average width of the crest was ~ 13.5 m and its average elevation was 152.8 masl. The average downstream and upstream height of the crest were 5.6 m and 1.3 m respectively. In the south, the dam reached maximum heights of up to ~ 10 m (Stantec Consulting Ltd., 2012 (c)) (AMEC, 2013).

Following emplacement of an initial 1 m thick layer, the downstream slope of the dam was built up in a series of layers 30 cm thick known as “lifts” or “benches” until the

Figure 2.8: Compaction of second lift on November 20th, 2013 (AMEC, 2014)

crest was reached. Each lift was compacted by a road roller before the next was added (Fig. 2.8). When 2 m of lifting was reached, new lifts were ‘keyed’ into the existing structure. For every 3 lifts (90 cm) the key into the existing structure was 1 m in the horizontal. The benches provided a rigid platform for transportation of construction equipment along the slope. Figure 2.8 below displays the second lift from the base being compacted under static loading (AMEC, 2014). This indicates the dam was raised in phases, which assists in the interpretations of the geophysical data.

After lowering the crest of the dam by ~ 1 m (A. Steel, pers. comm. 2021), its average width was 25m and on the downstream side it was extended by a meter to the west.

Because of bog displacement, and the resulting depression (by ~1m) of the ground surface, the downstream toe was extended further than initially planned, typically 4-5 m, in order to provide the requisite slope angle. Material excavated from the crest was also used to reshape and extend the upstream slope at this time (Stantec Consulting Ltd., 2012) (AMEC, 2014).

An area of seepage (Fig. 2.9) identified at the base of the downstream slope north of the spillway, and a major focus of this study, was repaired by the placement of a drainage system consisting of washed drainage rock wrapped in a permeable filter fabric (Boak & Sibbick, 2014).

Figure 2.9: Image captured by the author in November 2016 identifying the coarse drainage system rocks covering the seep looking west from the toe of the downstream slope.

Samples of dam material were collected and analyzed in December 2013. A sample of dam material was collected at the new crest elevation (ED-1), two samples were collected in the wetland southwest of the sediment ponds using a shovel at depths of ~ 200-300 mm (SS2, SS3), and one sample was collected from the spill site of excavated material from the sediment ponds (SS1). Sample locations with the exception of ED-1 are indicated in Figure 2.7. Attempts were made to collect samples within the debris flow area, however due to weather conditions sampling locations were limited to a localized region near the breach. The purpose of these samples was to gain an understanding of the physical properties of the dam material.

Water levels in the reservoir are historically lower than ever since repairs were made in November 2013 (Engineers Edge, 2017). Dam monitoring studies have been ongoing since this repair work. Ground water samples were collected by NLDNR in November 2016 in the impoundment and at the seep location.

2.3 Dam Properties

Historically tailings, soil or waste rock were used for building a dam. The material used to construct the Gullbridge dam was largely a local glacial till soil from a quarry ~ 1 km northeast of the impoundment (Stantec Consulting Ltd., 2012).

The embankment is approximately 1,050 m long. The width at the crest varies from 8 m in the north to 30 m in the south. The height of the dam from the crest to the toe of the downstream slope varies between 2.2-8.2 m with an average height of 5.6 m across the dam with an average crest elevation of 151 masl (AMEC, 2014).

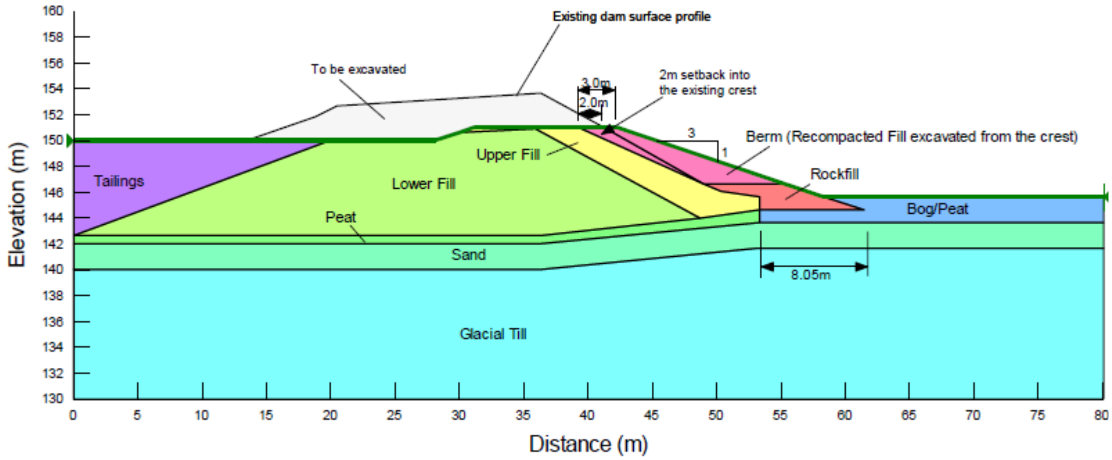

Figure 2.10: "Before and After" section of the Gullbridge Dam before rehabilitation in 2013 drawn from borehole data collected by Stantec Consulting Ltd. (AMEC, 2013 (c)).

The abutments of an earth-filled dam refer to the portion where the ends of the dam wall join the natural ground along the slopes of a valley impoundment (U.S. Army Corps of Engineers, 2004). The coordinates of the south and northeast abutment locations for the Gullbridge Dam are listed in Appendix A2.1.

Figure 2.10 displays a proposed "before and after" section of the Gullbridge Dam rehabilitation, produced by AMEC (2013), before rehabilitation in 2013. It shows dam fill, foundation, and subsurface materials. Note the core materials of the dam, located within the lower fill unit have not been considered in this image. Note also that due to the unforeseen circumstances described in section 2.2.4, many features of this section – in particular the structure of the downstream slope – differ from the present embankment.

The white area denotes the excavated material taken from the top of the crest at a previous dam height elevation ranging between 153 and 154 masl. Two metres of preexisting material was to be cut from the downstream crest edge, and the downstream slope was subsequently flattened and extended 3 m towards the wetland, for an overall 1 m extension of the crest to the west. During actual construction, an average of ~ 1 m of the dam crest was excavated and used to flatten the dam (A. Steel, pers. comm. 2021). The pink unit in Figure 2.10 denotes material cut from the crest deposited onto the upper fill shell rock flanking the slope (yellow unit). The purple unit denotes the submerged tailings and overlying pond water, to an elevation of 150 masl (AMEC, 2013 (c)).

The slope angle along the downstream slope is indicated as 3H:1V in Figure 2.10. The downstream slope was actually constructed to 4H:1V as a result of the bog displacement during construction (AMEC, 2013 (c)).

2.3.1 Dam Materials from Borehole Data

The 7 boreholes drilled over the crest of the dam in 2011 (BH1 to BH7, Figure 2.3) are analyzed here to facilitate the identification of material interfaces in the GPR data. The depths of the boreholes ranged between 6.7 and 19.7 m and the height of the fill material of the embankment was between 4.2 and 10.6 m before excavation of the crest in November 2013. Borehole data indicated that the dam material was subdivided into two distinct units classified largely by density and volume of fines (Stantec Consulting Ltd., 2012 (c)).

The upper unit (yellow and grey in Fig. 2.10) ranging in thickness between 1.8 – 2.6 m, was on average a loose to compact, poorly graded to well graded sand with gravel with varying amounts of silt. This unit occasionally contained cobbles, boulders, and organic debris such as wood and roots. A large volume of the original upper fill material was excavated during the November 2013 rehabilitation and cast onto the downstream slope (Figure 2.10) (Stantec Consulting Ltd., 2012 (c)). Sample ED-1 of the upper dam material was collected for chemical analysis by AMEC in December 2013. (Its location was not given in AMEC's reports.) It was determined to have a significantly high pH of 8.7, and an NPR (Appendix A2.2) of 15, therefore the dam fill material is considered non-acid producing (AMEC, 2014).

The downstream slopes constructed during the successive dam lifts are likely composed of the same materials as the upper unit described above. To mitigate the impacts of erosion, a coarse layer of erosion resistant rip rap was placed over the entire downstream slope (Stantec Consulting Ltd., 2012).

The lower unit (green unit in Fig 2.10) in contrast is composed of a very loose sand and gravel material with relatively high fines used in the original construction of the dam. The lower fill unit encompasses the relatively very loose internal core localized along the base of the dam of identical composition used in the original construction of the embankment (Stantec Consulting Ltd., 2012). The core consists of a relatively high amounts of fines implemented to slow down advancing seepage through coarser overlying lower fill material.

Underlying the dam fill material almost all boreholes encountered organic peat topsoil (lime green unit in Figure 2.10) with thicknesses ranging from 0.15 – 1.6 m. This peat has been compressed by the dam fill material over the years and is thinner than the organic material associated with the adjacent wetland (Stantec Consulting Ltd., 2012).

A ~ 2m layer of compact sand underlies the peat (light blue unit in Figure 2.10). It is a "grey to brown, poorly graded sand with varying amounts of silt" with average undrained shear strength of 50 kPa, which is typical of a stiff substrate. This layer effectively stabilizes the bog layer, serving as the foundation material for the overlying dam fill material. It is assumed this layer thickens to the north based on borehole data (Stantec Consulting Ltd., 2012). In the case of BH1, organic peat soils are not present, and this sand unit lies directly below the dam fill material.

A thick unit of glacial till (aqua unit in Figure 2.10) underlies the sand unit. The till is comprised of a dense, grey to brown, silty sand with gravel. Small zones of sandy silt can be found scattered throughout the till accompanied by occasional cobbles and boulders. This material was observed in all boreholes, except BH3, at depths below the crest of the dam varying from 4.15 m in BH1 to 11.8 m in BH4 (Stantec Consulting Ltd., 2012).

Figure 2.11 and Figure 2.12 display the borehole logs of BH3 and BH4 respectively, with lithological descriptions on the left and shear strength on the right. The seep area is approximately centered between these two boreholes. The seep area material is likely most representative of the data displayed from BH3, as this area has remained undisturbed by construction since 2011 (Stantec Consulting Ltd., 2012). The stratigraphy charts for BH1, BH2/MW, BH5/MW, BH6 and BH7 are included in the Appendix (A2.4).

Figure 2.11 indicates the upper unit encountered over BH3 was a 2.4 m thick, very loose to compact, well-graded, silty sand and gravel with occasional cobbles. The lower unit consisted of a similar material 7.7 m thick, described as being very loose to loose

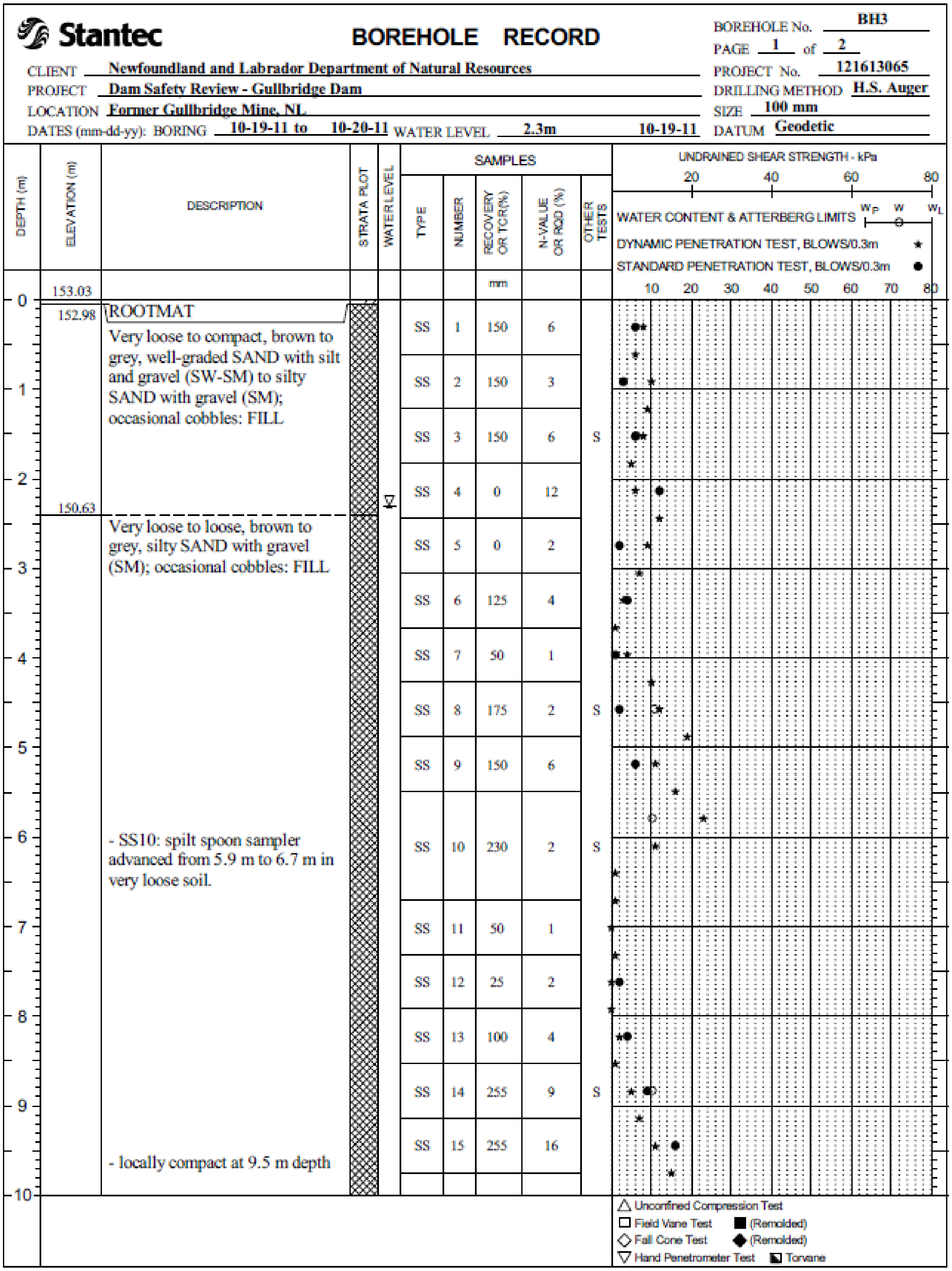

Figure 2.11 (a): Borehole stratigraphy over BH3 of the Gullbridge embankment dam (0 – 10 m) (Stantec Consulting Ltd., 2012).

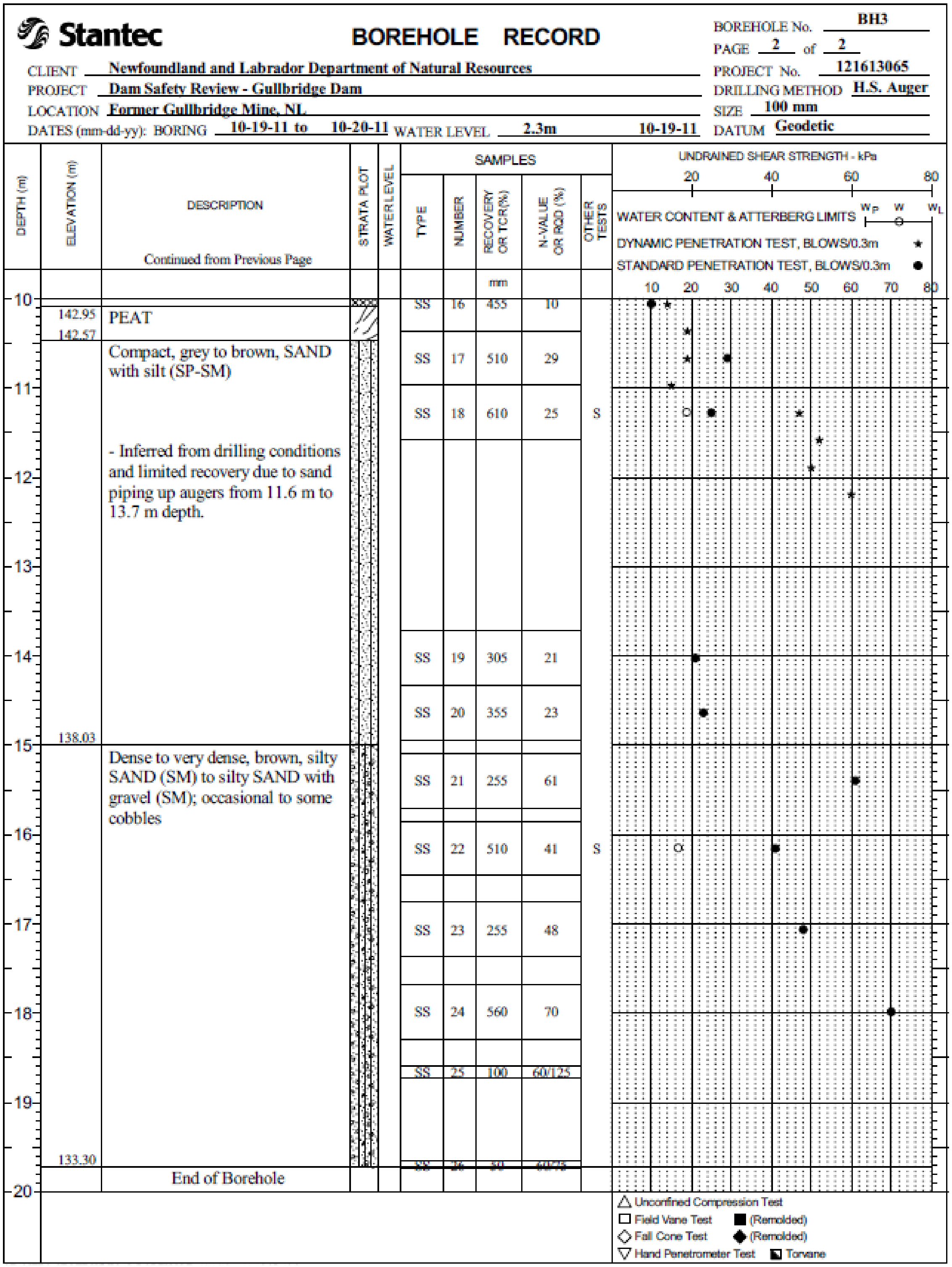

Figure 2.11 (b): Borehole stratigraphy over BH3 of the Gullbridge embankment dam (10 – 19.7 m) (Stantec Consulting Ltd., 2012).

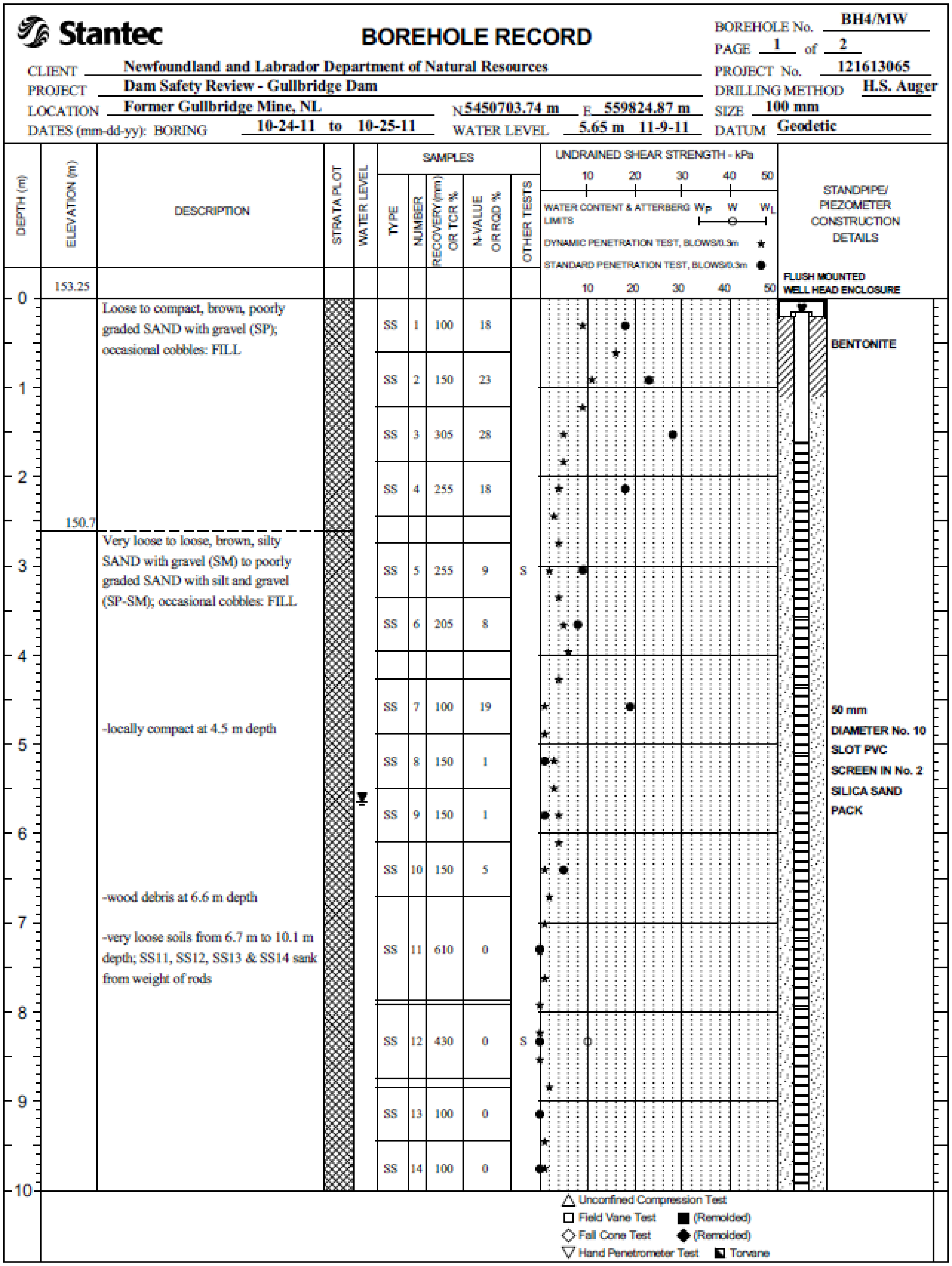

Figure 2.12 (a): Borehole stratigraphy over BH4/MW of the Gullbridge embankment dam (0 – 10 m) (Stantec Consulting Ltd., 2012).

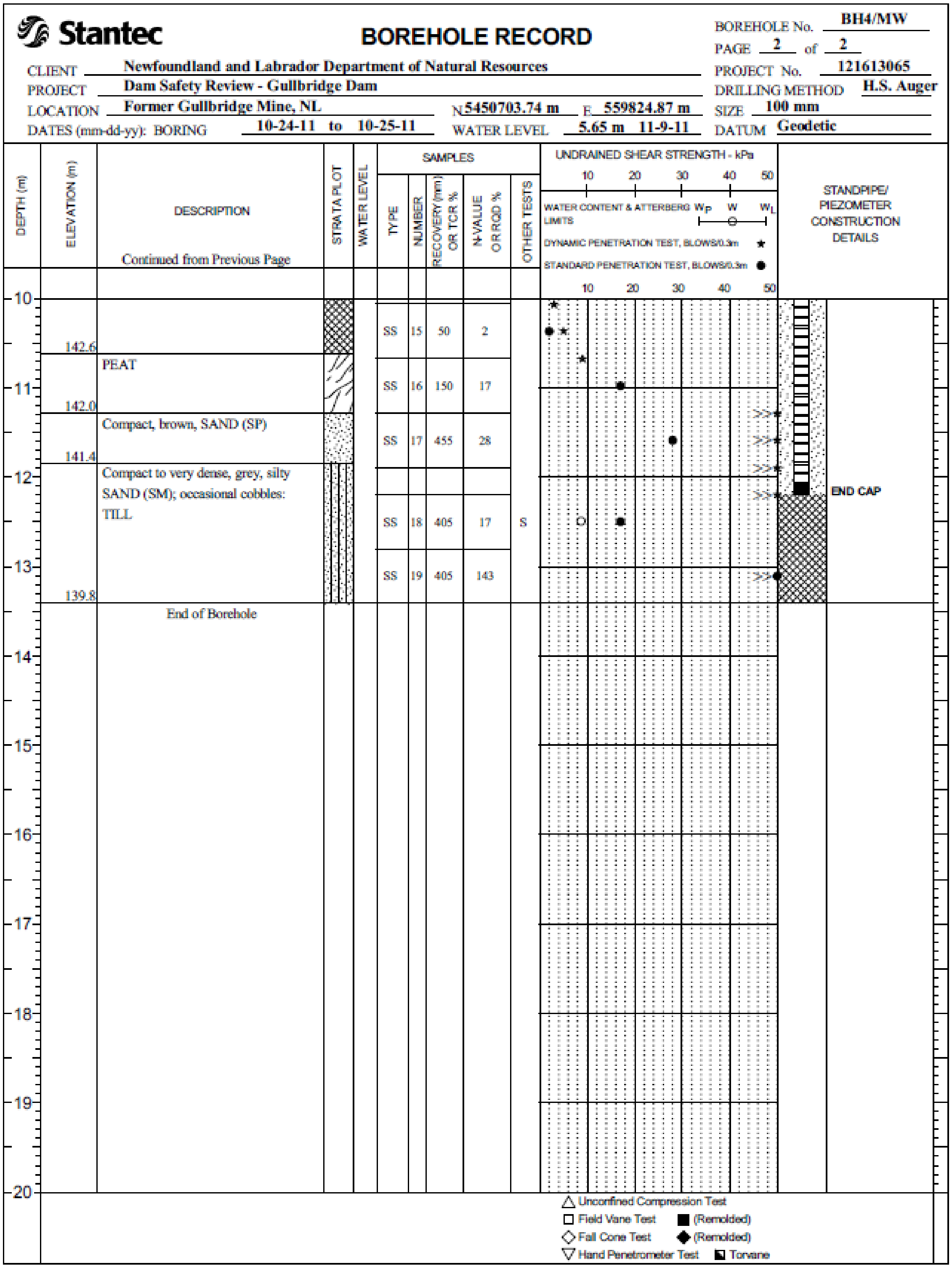

Figure 2.12 (b): Borehole stratigraphy over BH4/MW of the Gullbridge embankment dam (10 – 13.4 m) (Stantec Consulting Ltd., 2012).

though locally compact at 9.5 m in depth. The lower unit rests on 0.4 m thick organic peat layer overlying a ~4.5 m thick unit of grey-brown sand with silt. The lower most unit encountered was a similar layer of dense to very dense brown silty sand with occasional cobbles (Stantec Consulting Ltd., 2012).

Figure 2.12 displays the stratigraphy chart for BH4 north of the seepage area. The upper fill unit consists of a 2.6 m thick loose to compact poorly graded sand with gravel and occasional cobbles. An 8 m thick layer of lower dam fill material was determined to be comprised of very loose to loose brown silty sand with gravel and occasional cobbles. The material became locally compact at a depth of 4.5 m, and wooden debris was found scattered at a depth of 6.6 m. It was also noted that very loose soils were scattered throughout the lower fill material from 6.7 m – 10.1m of depth. A 0.7 m thick peat layer was encountered at the base of the fill at a depth of 10.6 m, and is underlain by a thin layer of compact brown sand overlying a thick unit of glacial till (Stantec Consulting Ltd., 2012).

2.3.2 Depth of Water Table

Table 2.2 Water table depths measured from the crest of the dam. *=inferred.

Borehole	BH1	BH2	BH3	BH4	BH5	BH6	BH7
Crest Elevation (masl)	153.38	152.99	153.03	153.25	153.31	152.62	152.76
Distance (m)	0	168	289	450	606	742	886
Water Table (m)	1.8*	3.3	2.3*	5.7	2.7	1.5*	1.5*

On November 9th, 2011, the depth of the water table was measured using piezometers installed in boreholes BH2, BH4, and BH5 (Figure 2.3), and inferred from borehole data for the other boreholes. Results are shown above in Table 2.2.

With the November 2013 excavations of the crest, it is expected that the water table is now located at shallower depths below the crest. These data suggest that the area with the most efficient drainage through the embankment would be near BH4 where the water table is lowest. (Stantec Consulting Ltd., 2012). Note that most of the water table readings are inferred, which does not provide confidence in the Stantec conclusion.

2.3.3 Drainage System

The fordable spillway constructed over the breach area in the south serves as the main discharge outlet for the TMA. The top surface of the spillway is at an elevation of 150 masl, approximately 1 m deeper than the top of the dam, and has a width of 38 m. When water in the reservoir rises above 150 masl, the spillway discharges water into sediment pond 1 indicated in Figure 2.13 (blue star) where fines from the tailings water are allowed to settle. Water flows from sediment pond 1 to sediment pond 2 (green star) where additional fines settle, and from there over a berm and through an armored discharge channel into the wetland. The yellow star indicates a tailings spoilage where excavated tailings were placed during winter 2013 breach repairs. This spoil pile was covered with excess materials used for the repair of the breached section.

The outer coarser dam material consisting of sand, gravel and shell rocks flanking the downstream slope allow for the movement of seepage water through the embankment

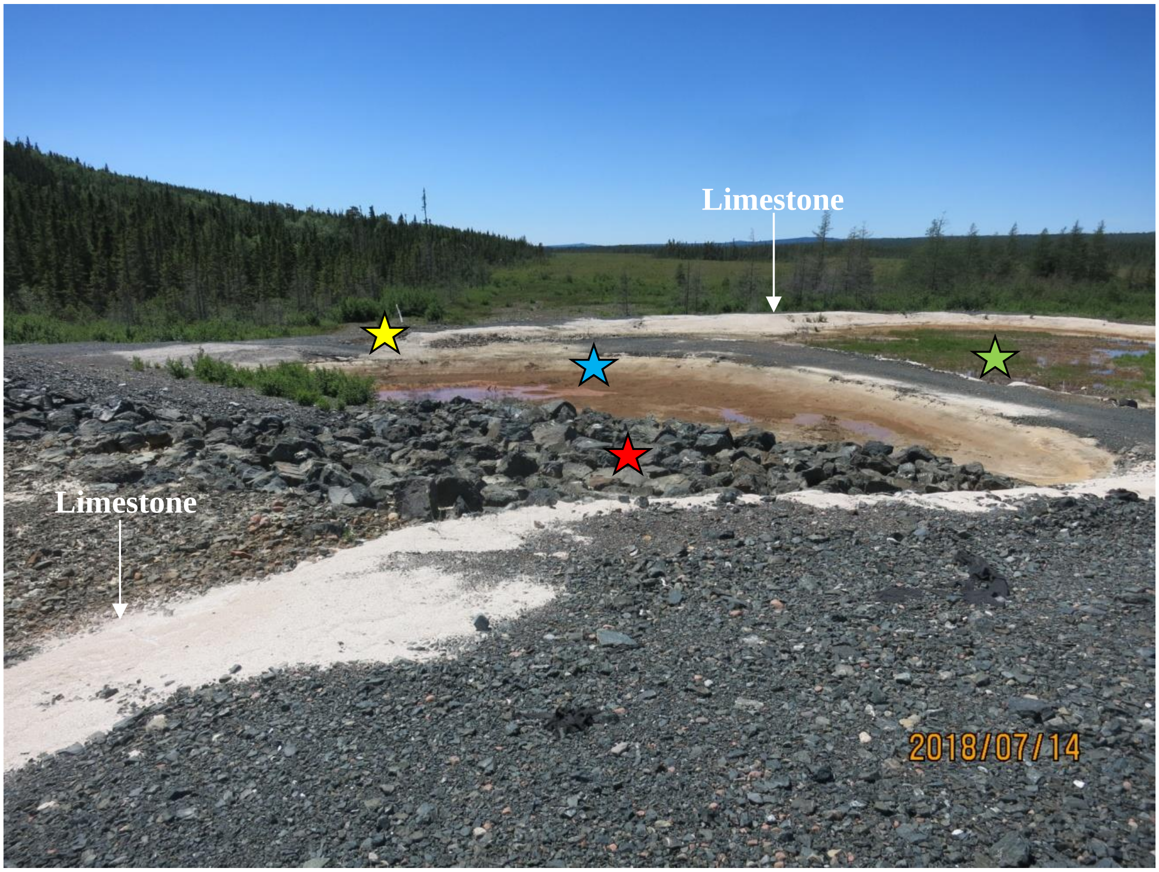

Figure 2.13: Spillway of Gullbridge Dam lined with erosion resistant rip-rap (red star) with connecting sedimentation ponds 1 (blue star) and 2 (green star), berm and spoil location (yellow star) indicated. This image was captured by the author on July 14th, 2018 standing on the dam crest looking southwest into the wetland. Note that water is not flowing over the berm due to dry weather conditions.

due to the permeability of the materials. This permeable outer material likely serves as a "drainage blanket", a seepage control method that permits free flow of water within the dam along a controlled path designed to maintain a safe phreatic surface elevation below the downstream toe. A higher phreatic surface may result in increased pore water pressure and seepage in the downstream portion of the dam, resulting in sliding and erosion of the downstream slope (i.e., piping) (Stantec Consulting Ltd., 2012; Calamak et al., 2016; Durham University, 2021; U.S. Department of the Interior Bureau of Reclamation, 2012).

2.4 Dam Design

In order for the dam to work at full operational capacity while reducing environmental losses, several factors need to be considered in the preliminary design stages. As such, proper flood-routing analysis and dam stability calculations must be conducted to determine dam and discharge outlet geometries.

2.4.1 Failure Mechanisms

Some common failure mechanisms thought to have contributed to the 2012 breach of the Gullbridge Dam are surface erosion, slope and foundation instability, and internal erosion and piping (Stantec Consulting Ltd., 2012).

The slopes of the Gullbridge Dam are particularly vulnerable to surface erosion due to events such as overtopping and ice-jacking in the winter. Ice-jacking can create large cracks in the slopes that can create periodic sloughing. Frost action observed over the crest of the dam risks the creation of conduits that trap surface run-off. However, it is unlikely that ice-jacking contributed to the 2012 breach due to the width of the core (Stantec Consulting Ltd., 2011 (b); Engels J. , 2017 (b)).

Human activities at Gullbridge such as vehicle traffic and removal of vegetation on the downstream slope have contributed to erosion of the crest and downstream slopes respectively (Stantec Consulting Ltd., 2012).

One of the major factors contributing to the failure at Gullbridge was slope instability. This occurs when the activating shear stress on the slopes exceeds the maximum shear resistance of the material. A combination of the steepness of the downstream slope prior to the breach and the relatively high elevation of the pond water posed a risk for structural failures over areas with loose fill material. This type of slope failure can occur at any time throughout the dam's life even under normal load bearing conditions. Slope failure can also occur during rapid reservoir drawdown or significant seismic events (Stantec Consulting Ltd., 2012).

In earth-filled embankments one of the most frequent modes of failure is seep-related internal erosion (Adam et al., 2020). When water stored in tailings reservoirs advances through the pore space of fill materials it can potentially create high seepage pathways leading to the destabilization of the embankment. This is also a common occurrence in dam abutments, foundations and in the space surrounding drainage systems of the dam. Generally, the process is slow and progressive. Monitoring changes in the seepage effluent can be an effective tool in measuring the internal performance of the TMA (Engels, 2017b).

The probability of failure in earth-filled dams is highly influenced by the degree to which internal seepage has occurred within the embankment. Seepage can begin as early as just after the dam's construction, and can continue to occur for years. It is not initially obvious to visual inspection. Left unchecked, it can lead to internal erosion causing destabilization of the structure and ultimately breaching of large sections (Stantec Consulting Ltd., 2012). Historically, a dam is most vulnerable during construction, likely a result of disturbing dam material over areas where internal erosion is most prevalent.

Internal erosion is the likely failure mode at Gullbridge due to the very loose to loose nature of the internal core . It is suspected that pervasive seepage through the dam is due to poor foundation materials and the “zoning” of two distinct materials. It is possible that during the December 2012 breach the foundation materials failed first. Seepage may intensify through cracks in the structure which develop as a result of uneven settlement of fill materials due to varying elastic behaviour of the foundation materials along the base of the embankment (Adamo et al., 2020). Large embankments such as the Gullbridge Dam are generally “zoned” meaning fines (silt/clay) are compacted within the core to impede the flow of water, and coarser rocks such as sand, gravel and fill (shell rocks) are used along the upstream and downstream slopes for strength and stability (UC Davis, 2020). It was suggested that during construction over time core materials were covered over with coarser, more permeable fill in layered phases (A. Steel, pers. comm. 2021). It was determined from borehole results that the dam contains an internal core consisting of high amounts of fines that normally act to slow down advancing seepage from the phreatic surface. However, due to zoning and the very loose nature of the core, water readily advances through loose sediment creating seepage pathways.

Figure 2.14 illustrates the pond water flow path from a reservoir infiltrating the pore space of a dam. The water initially occupies the space surrounding the loose core material, and develops high porosity flowage channels that advance to an unprotected exit (U.S. Department of the Interior Bureau of Reclamation, 2014).

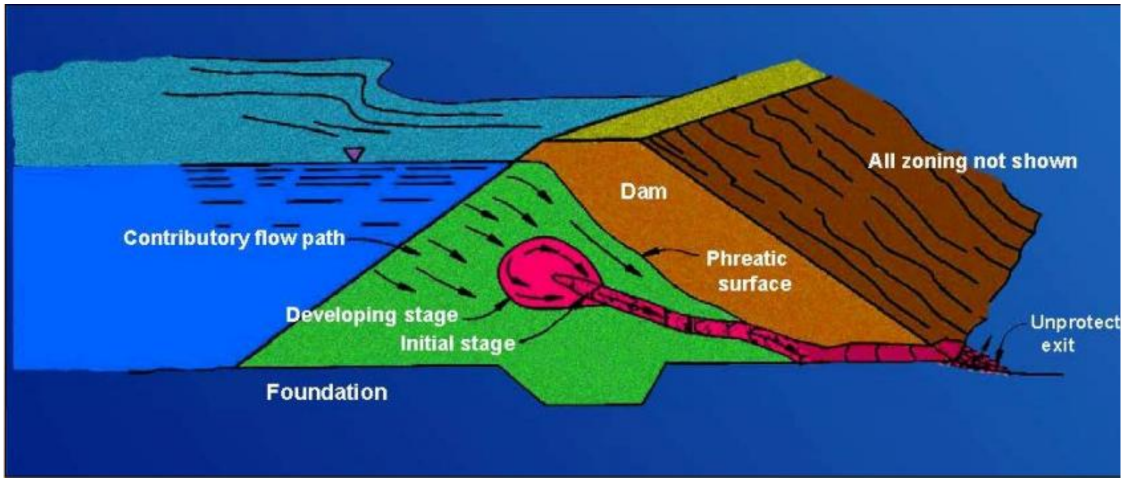

Figure 2.14: Illustration of the development of seepage related erosion channels through earth-filled embankments (U.S. Department of the Interior Bureau of Reclamation, 2014).

It is unlikely that, during the construction of the Gullbridge Dam, there was a filter fabric used to separate the materials of the internal core and the coarser downstream sand and gravel. Zoning combined with a high phreatic surface gradient and subsequent high exit gradients further risk the potential for seepage related erosion.

2.4.2 Outflow Design

CDA assigns approximate IDF's (Inflow Design Flood) (Appendix A2.5) based on their hazard classification. According to their guidelines, if a dam has a "low" hazard potential, the dam can accommodate a 1:100 year storm event without flooding and overtopping.

The peak discharge of the pond water through the spillway for a 1:100 year storm event was calculated to be 5.6 m^3/s, using computer software deploying the Rational Formula (Appendix A2.6) (AMEC, 2014 (b)). In fact, the 2013 rehabilitation at Gullbridge was designed to service the TMA well in exceedance of a 1:1000 year storm (Stantec Consulting Ltd., 2012 (c)).

Some of the materials used in the rehabilitation work of the dam were chosen to mitigate the impact of potential tailings seepage into the wetland. Analysis of the chemistry of surface water samples collected at Gullbridge suggest that a combination of the wetland, settling ponds and limestone berm are mitigating the water quality to parameters below Schedule A compliance.

The spillway was designed to be fordable so that maintenance crews would be able to walk through shallow water passing over the base, and has properly graded armored rocks with the capacity to discharge excess water at slow non-erosive velocities to prevent flooding and overtopping (AMEC, 2014 (b)).

The settling ponds were designed to sequester fines at the base of the ponds where they are temporarily stored before their eventual relocation. The discharge water analyzed at sediment pond 2 is composed of tailings pond water plus surface water. It is regularly monitored as it is the ‘point of compliance’ (located next to the OUTFLOW in Figure 2.7). Water samples from this location indicate that the armored spillway, sedimentation ponds and limestone berm effectively neutralize the potential acid drainage. Concentrations of metals as well as TSS and pH values are in compliance with Schedule A at this location (AMEC, 2014).

The limestone may play a role in improving the quality of the discharge into the wetland, however this is not a long-term solution as the limestone is coated by metal-oxide precipitant (AMEC, 2013).

It is suspected the spillway is the primary outlet structure to which tailings fines are transported into the wetland. Therefore, it is necessary to determine the extent to which the armor rocks have prevented erosion, and whether the limestone lining the spillway has effectively buffered potential acid generating tailings travelling into the wetland.

2.5 Reservoir Properties

The reservoir contains submerged tailings under limited water cover in the west, tailings deposited near the upstream slope of the dam and a large area of sub-aerial "beached" tailings in the east. The tailings are mostly covered by cm thick algal mats capable of preventing wind erosion of subaerial exposures (Stantec Consulting Ltd., 2012).

Presently, a surface stream runs through the middle of the tailings pond (Figure 2.15) and along the edges of the tailings pond before exiting through the spillway. A seep was identified immediately east of the mouth of the surface stream referred to as the "tailings outflow location". The orange discolouration of the impoundment water is due to iron precipitates formed during the oxidation of sulfide minerals (Fitzpatrick A. , 2013) AMEC, 2014 (c)).

The water depth in the impoundment generally varies and is usually lowest in July and August. Based on a visual assessment of the pond water elevation of 150 masl, in July

Figure 2.15: Streambed carrying tailings sediment through the impoundment reservoir captured in July 2013 (AMEC Environment and Infrastructure Ltd., 2014 (c)).

2013 it was estimated that the average pond depth of the water in the reservoir was 0.25 m with a maximum pond depth of 0.5 m. These numbers have likely been reduced since 2013 to the present day (AMEC, 2014 (c)).

2.5.1 Surface Water Samples

Several water samples were collected from the reservoir after the 2012 breach of the Gullbridge embankment. The locations are indicated by the cyan dots in Figure 2.7. These were surface pond water samples SW-01and SW-05 as well as samples collected from the tailings creek (Figure 2.15) SW-03, SW-04 and SW-10 in July 2013**.** A water sample labelled “impoundment” was also collected from on November 2nd, 2016 at an undisclosed location. It is not required that water stored in the tailings pond meet Schedule

A concentrations. However, water discharging at the compliance point (Figure 2.7) must meet Schedule A concentrations. Most of the parameters tested in the chemical analyses (see Appendix A2.7) met the regulations of Schedule A. However, there were several exceptions.

Samples collected on the upstream side of the dam, SW-01 and SW-05, were acidic and high in copper, reporting pH levels of 4.3 and 3.9 and copper concentrations of 706 μg/L and 733μg/L respectively. All other concentrations were within Schedule A regulations (AMEC, 2013).

Sample SW-04 collected on the eastern extent of the tailing's creek (Figures 2.15) was determined to be in compliance with Schedule A. Base metal concentrations in SW-10 were in compliance with Schedule A, however SW-03 exceeded the copper and iron concentrations at 442 μg/L and 20,900 μg/L respectively. These samples indicate decreasing water quality moving downstream in the tailing's creek (Figure 2.7) (AMEC, 2013).

A sample collected on November 2nd, 2016 at an undisclosed location within the impoundment was analyzed by Maxxam labs and was calculated to have an acidic pH of 3.72, accompanied by a very high copper concentration of 2700 μg/L (Maxxam, 2016).

2.5.2 Tailings Samples

Tailings sediment in the Gullbridge reservoir is comprised mostly of low porosity sand and silt including insoluble copper derived from the rejected byproducts from processing of ore. The iron concentration in the tailings is high as the mining wastes of copper at Gullbridge are iron sulfides, including potentially acid generating sulfides such as pyrite. In addition to this, the tailings contain elevated levels of copper, zinc, chromium and several other elements.

A large volume of the tailings in the impoundment are sub-aerial. In May 2014, 235,000 m^2 of tailings were sub-aerial, and only 32,000 m^2 of tailings had water cover. Before the breach, 175,000 m^2 of tailings were sub-aerial. Aerial photos of the mining facility indicate there has been minimal pond water cover largely confined to the eastern edge of the upstream slope since 1975 (AMEC, 2014 (c)).

Before the breach, tailings were periodically exposed due to fluctuations in the pond surface elevation. Based on historic air photos over the impoundment compared with visual assessment in 2013, the historic pond water elevation ranged between 150.2-151.5 m asl. This fluctuation was likely triggered by different mechanisms including beaver blockage of the decant, dry periods, historic failures like in 1993, and increasing tailings volume. When the thickness of the tailings in the reservoir exceeded the pond water elevation, the tailings would remain sub-aerial until the embankment was raised (AMEC, 2014 (c)) (NLDNR, 2012).

On the eastern part of the reservoir, some tailings have been exposed and oxidizing for the last 40 years. The highest pond water elevation was suggested in AMEC's closure options analysis to have been 151.5, and elevations over the eastern edge of the of the tailings surface are as high as 155.3 masl and 153.4 (TP-7 and TP-8 respectively in Figure 2.7). Generally, if tailings reach a thickness exceeding an elevation of 151.5 masl, they are considered to have been permanently exposed.

In the evolution of a mine site, there are typically 3 stages of acid drainage (AMEC, 2014 (c)). In the initial stages, primary sulfide minerals in the tailings at the surface are consumed due to dissolution and oxidation, with the rate controlled by the water table and moisture content, and secondary iron and aluminum hydroxide minerals form at a much slower rate. The presence of primary minerals in the surficial tailings at Gullbridge indicates that the tailings are in this first stage of acidic drainage. It is assumed that acidic conditions will remain in the tailings at Gullbridge in the second stage, in the absence of sulfide minerals, as equilibrium dissolution of secondary minerals buffers low pH values. In the third stage there is no acidic drainage as both the primary and secondary minerals are completely exhausted and less reactant minerals begin to dissolve very slowly.

Two samples of tailings from depths of 5-60 cm at unknown locations within the impoundment were acquired in 2012 to provide information on the potential impacts of the tailings released during the 2012 breach. The samples were tested for trace metals and major element oxides, and were determined to be similar with moderate variability. As a

Table 2.3: Concentrations of key elements calculated from tailings and till samples (NLDNR, 2012).

Element	Range (tailings); ppm unless stated otherwise	Range (tills)
As	4-9	6-8
Ba	288-560	385-464
Cd	0.2-0.7	-
Cr	260-361	54-73
Cu	230-1926	27-41
Fe	19.74-30.94%	4.0-4.3%
Pb	4-7	6-10
Mg	6.49-7.12%	0.6-0.7%
Mn	1281-1504	586-764
Ni	28-170	13-18
U	0.6-1	0.9-1.7
Zn	68-221	38-49

background check, 5 till samples from within 2 km of the tailings were analyzed (NLDNR, 2012). Table 2.3 provides the results of the chemical analyses.

It is assumed that the tailings across the reservoir are fairly homogeneous, and the two samples are representative. The samples consist mostly of silicate minerals, with ~ 40-52% silica oxides (NLDNR, 2012).

Several of the element concentrations in the tailings samples were very high relative to the local background concentrations in the till, most notably copper, magnesium and chromium. Copper in the tailings samples is 10 to 50 times higher than in the till samples. Chromium in the tailings samples is 4.8 to 4.9 times higher than in the till samples, and magnesium in the tailings samples is 10.2 to 10.8 times higher than in the till samples. This is not surprising given copper tailings have been settling in the reservoir since the beginning of the TMA's operation (NLDNR, 2012).

Elements that are elevated relative to background levels but do not pose risks of environmental impacts include nickel, magnesium and iron. These metals were likely concentrated in the ore during mining operation (NL Department of Resources Mineral Development Division, 2016). The high iron content in the tailings sample is expected as VMS deposits like Gullbridge generally contain high levels of iron- and base-metal-sulfide minerals (Taylor et al. 1995).

The concentrations of some elements (As, Ca, Cd, Pb, U) in the tailings samples were found to be below or similar to the background values in the till. Calcium in the reservoir is suspected to be insoluble and occurring as calc-silicate minerals which, unlike the limestones used in the wetland surrounding the sedimentation ponds, are incapable of neutralizing acid generation (NLDNR, 2012).

Acid-Base Accounting was conducted on the tailings samples (Appendix A2.2). Not surprisingly, the NPR values were below 1, indicating the material was capable of contributing to harmful acid drainage in the area (NLDNR, 2012).

In September 2012 six tailings samples were collected from the impoundment and analyzed for major element oxides and trace metals. The results of the tailings samples are included in Appendix A2.8. The samples indicated that, as a result of weathering and metal release, the tailings solid phase metal concentrations nearest the surface were lower than at depth. The majority of tailings in the Gullbridge reservoir have been periodically oxidizing for over 40 years due to fluctuations in the water level, however given that long time scale, metal leaching and oxidation rates have likely stabilized in recent years. All samples contained chromium, copper, iron, magnesium, sodium, nickel and zinc elevated above average continental crust concentrations. Potassium levels were found to be much lower in all the tailings samples than the average crustal levels (AMEC, 2013).

One tailings sample was collected after the breach in December 2012 from the impoundment and subjected to ABA testing. The sample had an NPR value of 0.79, indicating the tailings had the potential to undergo acid generation in the future. However, the sample's pH was calculated to be slightly basic at 8.1 (AMEC Environment and Infrastructure Ltd., 2014 (c)).

2.5.3 Tailings Test Pits

In July 2013, 11 tailings test pits (white crossed squares in Figure 2.7) were dug with an excavator to depths between 2.5 m and 7 m. The depth was limited by either early caving in a weak subsurface or by the maximum depth of the excavator. It is important to note that all test pits were terminated in the tailings pond and therefore the depth and quantity of tailings could not be determined. Properties are indicated in Table 2.4. The total metal contents of the tailings solids are summarized in Appendix A2.8.

The elevation of the test pits range from 155.3 to 150.8 m asl due to the natural topography over the valley impoundment. TP-7 on the western extent of the reservoir had an elevation of 155.3 m asl, while TP's 2 and 3, nearest the upstream slope of the dam in the west, had elevations 4 to 4.5 m lower.

Table 2.4: Elevations and depths of the July 2013 test pit programs key features (m[1] “based on observed oxidation depth, observable degree of tailings saturation, and elevation of tailings surface, m[2] “based on caving of test pit, or maximum extent of excavator”) (AMEC, 2013).

Test Pit	Test Pit Elevation (masl)	Depth of Oxidized Tailings (m)	Estimated Water Table Depth (m)[1]	Estimated Water Table Elevation (masl)	Test Pit Depth (m)[2]
TP1	151.3	0.0 - 0.2	0.2	151.1	2.5
TP2	150.8	0.0 - 0.2	0.2	150.6	3.0
TP3	150.8	0.0 - 0.1	0.1	150.7	3.0
TP4	151.5	0.0 - 0.2	0.2	151.3	7.0
TP5	152.2	0.0 - 0.1	0.5	151.7	2.5
TP6	152.5	0.0 - 0.15	0.5	152.0	7.0
TP7	155.3	0.0 - 0.5	>1.0	<154.3	7.0
TP8	153.4	0.0 - 0.2	1.0	152.4	4.0
TP9	151.3	0.0 - 0.3	0.3	151.0	5.0
TP10	151.1	0.0 - 0.3	0.3	150.8	3.0

The top layer of the tailings is oxidized to depths from 0.2 to 0.5 m. Generally, tailings are submerged in water to prevent oxidation and acid generation. For most test pits, the depth to oxidation is just above the water table. Close to the current water cover, it is likely that the thickness of the oxidized tailings is 10-30 cm, provided the pond water elevation is stable at 150 m asl.

For test pits in the east at higher elevation (TP-5 to TP-8) the water table is several cm deeper than oxidized layer. The oxidation rate depends on water content which was found to be quite variable. The concentration of oxygen gas in the pore space of the tailings at depth decreases as oxygen gas is reduced by sulfide oxidation. With increasing depth the water saturation in the tailings also limits the ability of oxygen to penetrate the tailings (AMEC, 2014 (c)).

Samples that were not predominately under water were periodically exposed to the air since deposition and have been oxidizing over the last 40 years. In the east the oxidized layers are much thicker as they were exposed during regression of pond water as well as periods of lowered elevation during construction phases when the embankment was raised to accommodate an increase in tailings (AMEC, 2014 (c)).

The increase in the estimated water table elevation in the west (Table 2.4) indicates a hydraulic gradient of the water table to the east, likely influenced by topography, as well as infiltration of precipitation and tailings permeability. The water table is about 1 m below the surface of tailings in the east and higher than the pond elevation. It was also determined from the test pits that, above the water table, water content increases with depth (AMEC, 2014 (c)). Reservoir pits produced variable results particularly in degree of saturation at depth.

At TP-2 in the west (Figure 2.16), drillers encountered a cm thick red-orange algal mat. Underlying the algal mat was a layer of 0.2 m orange-brown sandy tailings with cm-size fragments of hardpan less than 1 cm thick containing dark red cement. From 0.2-3 m a layer of fine grained silty grey tailings was observed. Both these layers were sampled for geochemical analysis. The pH increased with depth from the orange-brown layer (3.7) to the grey silt layer (6.4). The water content increased with depth, and the native ground was not encountered as the test pit was shallow: it terminated at 3m due to caving (AMEC, 2013). An image of TP-7 drilled on the eastern extent of the reservoir is provided in Appendix A2.8.

In total 22 samples were collected from the test pits at several different depths within the reservoir and geochemically analyzed. Solid tailings samples that were collected from the surface of the test pits had acidic pH levels ranging between 3.7- 4.5, and were all

Figure 2.16: Image of TP-2 shortly after caving on July 10th, 2013 (NL. AMEC Environment & Infrastructure, 2014).

acid generating with NPR values less than 1. The surface solid phase metal concentrations were all similar and less than those at depth. It is thought that periods of weathering and heavy rainfall washed away some of the original elements from the tailings at the surface (AMEC, 2014 (c)).

The tailings samples collected at depths greater than 30 cm within the test pits in the reservoir had generally neutral pH values, however NPR values indicated that all samples were potentially acid generating if exposed to oxidizing conditions.

In comparing the samples collected at the surface and those collected at depths greater than 30 cm within the reservoir test pits, the chemical composition showed minor variability. However, due to differences in water saturation, oxygen diffusivity, and periods of exposure to the air and submersion in water, there was a distinct geochemical difference in oxidation rates. However, it is postulated that tailings once submerged and now exposed at the surface due to the recent fall in pond water elevation, and permanently exposed tailings have similar oxidation and metal leaching rates (AMEC, 2014).

2.6 Wetland Properties

Figure 2.17 is an image captured of the wetland west of the embankment. Tailings pond water from the reservoir is discharged into the wetland through the spillway and seepage related erosion channels in the dam. The wetland conveniently utilizes poor drainage and many small natural ponds, which impedes advancing tailings pond water to the west (Ford, 2003). On field trips made to the Gullbridge TMA an orange-red discharge

Figure 2.17: Looking west into the Gullbridge wetland from the southern toe of the dam. Pictured are field assistant Jacob Newman (left) and Dr. Alison Leitch (center).

has been observed flowing through the spillway and into the wetland. Similar tailings pond water has been observed flowing through the seep area.

A stream that once flowed through the wetland was dammed during the construction of the Gullbridge TMA. The stream was once a source of fresh water into the wetland. The stream bed now appears as a large depression in the wetland, periodically containing surface runoff and seepage through the dam. It is being proposed that this stream has caused disturbances in the structural integrity in the overlying dam in this area, as tailings water may flow both beneath and partially through the embankment in this area.

Wetlands such as the one in Gullbridge are intermediate between aquatic and terrestrial environments and contain significant water channels and ponds. They are areas that are saturated with water long enough to promote hydrophytic vegetation which is indicated by poorly drained soils. The wetland at the Gullbridge site is an organic wetland which is composed mainly of peat.

2.6.1 Bog Probes and Boreholes

Table 2.5: Peat thicknesses under the embankment and in the adjacent wetland in Gullbridge TMA, from borehole and bog probe data. Distance is measured along the dam crest to the north from BH1. Modified from (Stantec Consulting Ltd., 2012).

	Embankment		Toe of Dam		Downstream	
Distance	Station	Depth	Station	Depth	Station	Depth
0	BH1	0				
32			BP-24	0.6		
76			BP-1	1.5	BP-2	1.5
151			BP-3	2.1	BP-4	1.7
168	BH2	1.6				
205			BP-22	1.5	BP-23	1.7
278			BP-5	1.8	BP-6	1.5
289	BH3	0.4				
393			BP-7	1.8	BP-8	1.8
435			BP-9	1.8	BP-10	3
450	BH4	0.6				
534			BP-20	1.5	BP-21	3
595			BP-12	1.5	BP-13	1.8
606	BH5	0.2				
731			BP-14	1.2	BP-15	0.6
742	BH6	0.7				
780			BP-16	1.8	BP-17	2
830			BP-18	1.8	BP-19	1.8
886	BH7	0.6				

Table 2.5 indicates the results of the 24 bog probes (yellow dots in Figure 2.3) conducted by Stantec Consulting in 2011. The probes were carried out to determine the thickness of the peat layer in the wetland immediately downstream of the toe of the embankment. Wetlands naturally mitigate the impact of mining wastes so tailings impoundments such as Gullbridge ideally favour thick mats of peat. The results show significant peat thickness variability from 0.6 to 3 m. Peat thickness is an important factor

in the mitigation of mining waste as increasing organic content contributes to greater retention of tailings water (Stantec Consulting Ltd., 2012).

The BP's were generally collected in pairs (e.g. (BP-1/BP-2), (BP-3/BP-4)) along the edge of the downstream toe of the dam and about 10 to 15 meters into the wetland (see Figure 2.3). Exceptions are BP-24 which was an individual probe and BP-9,10 and 11 in which three BP's were collected west of the dam. "Distance" for the bog probes in Table refers to their position extrapolated perpendicular to the dam crest. UTM positions are given in Appendix A2.9.

Figure 2.18 is a graph of the data presented in Table 2.5. Peat beneath the embankment (blue profile) is thinnest due to compression from the overlying material.

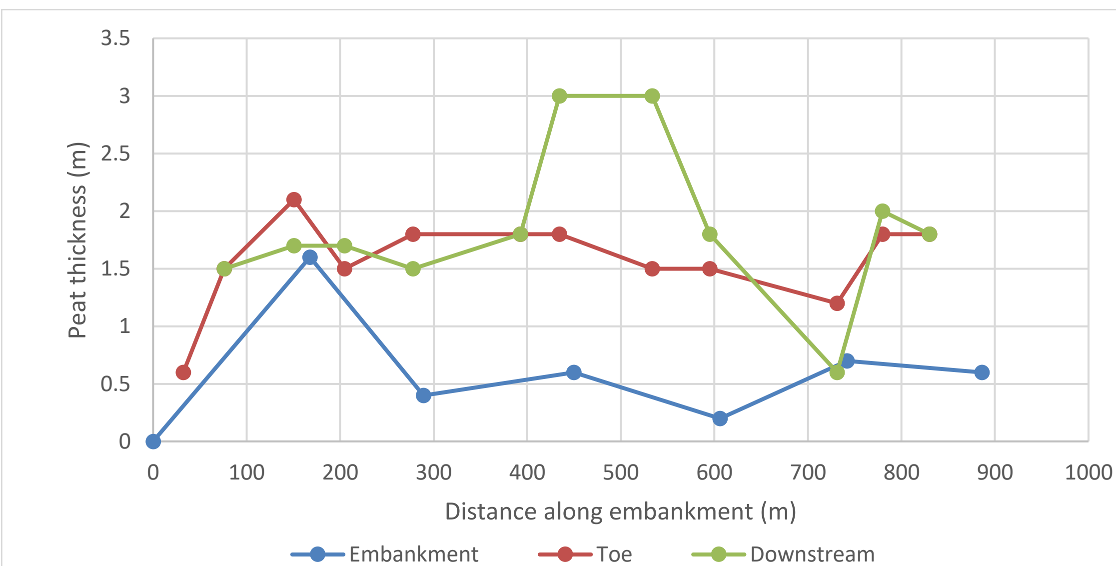

Figure 2.18: Graph of peat thickness versus distance along the dam for three profiles: under the embankment (blue), in the wetland along the edge of the downstream slope (brown), and several meters downstream of the toe (green). Data from Table 2.5.

Along the edge of the dam (brown profile) the peat thickness is fairly even, with an average thickness of approximately 1.8 m. To the west, peat thickness is more variable with greatest thickness in the middle near the old stream bed.

2.6.2 Passive Mitigation Processes

Wetlands have been known to naturally mitigate the impact of mining wastes. Wetlands can enhance groundwater quality through several physical, chemical and biological processes. Natural processes responsible for mitigating wastewater principally involve sedimentation and filtering of suspended solids. At the Gullbridge TMA, tailings water advances slowly west through the wetland and solid material in the advancing water is impeded by soil and sediment, acting as a filter material removing suspended solids from the water through straining (Dordio, Carvalho, & Pinto, 2008). In addition to this, during floods the wetland can store water and impede the flow of water west to South Brook.

Chemical processes in wetlands responsible for mitigating wastewater are completed primarily through sorption and precipitation. The degree to which chemicals within the advancing water are retained by absorption in the peat soil as well as plant roots at the surface is dependent on several characteristics of the substrate including composition and ion exchange properties. Precipitation of insoluble compounds assists in the decrease in the waters ion concentration, and is mostly dependent on pH and redox conditions (Dordio, Carvalho, & Pinto, 2008).

Biological processes such as sulfate-reducing bacteria effectively lower the concentration of sulfates, which are in wastewater as a consequence of acid-mine drainage.

Sulfate reducing bacteria obtain their energy anaerobically by coupling oxidizing organic compounds to the reduction of sulfate to sulfide (Camacho et al., 2009).

2.6.3 Surface Water Samples

Surface water samples collected in the wetland area during AMEC's July 2013 sampling program are SW-08 (Tailings Seepage), SW-02 (Sediment Pond 2) and SW-07 (Northern downstream toe) and SW-09 (Diluted Seepage downstream) (Figure 2.7). All metal concentrations were within Schedule A compliance with the exception of SW-02 which yielded a high total iron concentration of 13,700 μg/L. This, however, was attributed to the presence of iron precipitate inadvertently included in the sample. All pH values were within Schedule A compliance with the exception of the seepage sample SW-08 which had a pH of 4.68: this compares with the still more acidic values within the tailings pond (4.3 and 3.9 for SW-01 and SW-05 respectively). The results for all water samples are indicated in Appendix A2.7. Sample SW-09 collected less than 10 m from SW-08 reported a neutral pH value 7.1 indicating water quality quickly improves downstream of the embankment (AMEC, 2014 (c)). The measured conductivities of the tailings seepage and diluted seepage were 280 μS/m and 210 μS/m respectively, indicating the seepage becomes less conductive as it is diluted by the wetland downstream of the embankment toe. The measured conductivities along the downstream toe in the north (SW-07) and near the seep (SW-02) were 67 μS/m and 340 μS/m respectively, indicating the surface water near the seep region is elevated in conductivity as a result of the settling of tailings fines.

In addition to sample SW-02, other samples not indicated in Figure 2.7 were collected in and around sedimentation pond 2 in May 2013. Samples were collected on the north and south end and the discharge point of sediment pond 2. All these samples had neutral pH levels indicating the limestone berm was effectively neutralizing tailings water flowing from the spillway. They also reported lower sulfate, boron, barium, cadmium, nickel and zinc compared to the tailings pond, due to the lower solubility of these metals at higher pH. Metal concentrations were below Schedule A, indicating improving water quality along the flow path between the tailings pond and the compliance point at the sediment pond 2 outflow location (AMEC, 2014 (c)).

In July 2013 NLDNR collected an additional 4 water samples. The locations are indicated in Figure 2.19 below. The image displays the present-day limestone lined berm constructed during Winter 2013 repairs encompassing sediment pond 2 (dashed black line) and the temporary dam (bold black line) constructed in December 2012 following the breach designed to control discharge in the south before completion of remediation work in the fall. All sample parameters were within Schedule A compliance with the exception of the concentration of dissolved chloride, which was high in all samples (AMEC, 2013).

The properties of a water sample collected by NLDNR at the seep site in 2016 were within Schedule A except for the pH which was slightly acidic at 4.35 and copper concentrations which were very high at 1,800 μg/L. The results of the 2016 sampling can be found in Appendix A2.10 (AMEC, 2014 (c)).

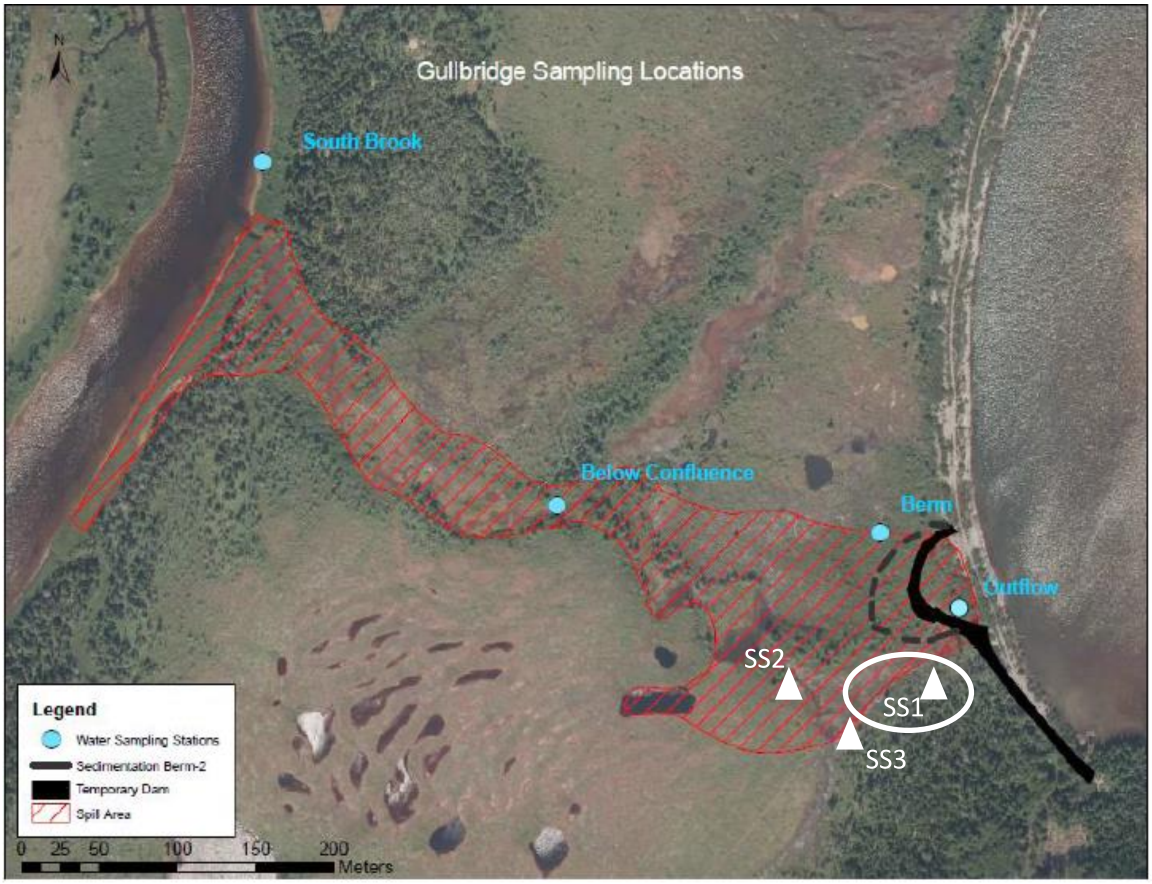

Figure 2.19: Locations of DNR surface water samples collected in July 2013 (blue circles) modified to include spilled dam material samples (white triangles) collected in the spoil pile (white circle) and the wetland in Dec. 2013 (AMEC, 2013).

The water sampling results from the wetland downstream of the dam indicate that the water quality before and after the collapse of the dam are similar. All metal concentrations were below Schedule A with the exception of copper (AMEC, 2014 (c)).

2.6.4 Soil Samples

The washout in 2012 caused sediment to be transported downstream from the dam into the bog. Thin layers of sand, gravel and tailings can be observed downstream of the sedimentation ponds near the spillway. In a 2011 Stantec report, it was theorized that a large-scale dam failure would not result in the movement of tailings to South Brook. This is due to the wetlands flat, boggy terrain with moderate tree coverage between the dam and South Brook (Stantec Consulting Ltd., 2011). In agreement with this, no reports from site visits since the breach in 2012 document transport of tailings to South Brook.

Spill area soil samples were collected in December 2013 (white triangles in Fig. 2.19). Sample SS-1 from the spoil reported a neutral pH of 7.3, and the fine grey material samples SS-2 and SS-3 from the wetland were slightly acidic at 6.1 and 5.3 respectively. Compared to the dam material sampled (Section 2.3) the wetland samples were determined to be much more acidic, as the dam material had a pH of 8.7 (AMEC, 2014 (c)).

Acid Base Accounting was performed on the samples to determine whether the samples were potentially acid generating. Both wetland samples (SS-2 and SS-3) reported NPR values less than 1 (0.8 and 0.39) indicating there is a potential for acid drainage. Sample SS-1 in the spoil had an NPR value greater than 1, like the dam material (AMEC, 2014 (c)).

Metal concentrations in the samples were within Schedule A parameters. Comparing the wetland samples (SS-2 and SS-3) to the spoil zone (SS-1) and dam material (ED-1), the copper concentrations in the wetland exceeded the dam soil by more than three times and contained copper concentration greater than 2 times the spoil sample (AMEC, 2014). It is suspected copper fines are being transported from the reservoir into the wetland along seepage pathways beneath the dam along the old streambed, through the dam to an unprotected exit at the site of the drainage system, and through the spillway to a discharge location at the compliance point.

3 Methods

3.1 Theory

3.1.1 Spontaneous Potential

The spontaneous potential survey method measures the naturally occurring electrical potential voltage differences resulting from charge separation due to geological, geochemical and hydrological interactions in the ground.

Self-potentials may arise from thermoelectric, electrochemical, bioelectrochemical and electrokinetic mechanisms. The two primary mechanisms in which self-potentials are generated over the Gullbridge Dam are electrochemical and electrokinetic. Electrochemical potentials can be generated from charge separation due to the diffusion of ions (with differing mobilities) across a concentration gradient maintained between two regions. Diffusion potentials arise when electrolytes with differing concentrations in the ground come into contact with one another. The movement of ions in the direction of the concentration gradient creates a convection current, leading to a charge imbalance that is balanced by a resultant conduction current in the opposite direction. The resultant voltage drop in response to the conduction current is the measured diffusion potential anomaly. Diffusion potentials may arise from concentration differences in groundwater for example (Mainali, 2006). Electrochemical potentials also arise when charge separation occurs due to the presence of a semipermeable interface which impedes the diffusion of ions. Electrochemical redox potentials have characteristic negative SP anomalies used to delineate the redox fronts of contaminant plumes (Jouniaux et al., 2009; Naudetet al., 2003).

Several different sources may generate electrochemical potentials over the Gullbridge site. Diffusion potentials may occur within the embankment between groundwater affected by tailings and ground water or between tailings imbued dam sediments and non-tailings imbued sediments. Corrosion potentials on steel may arise as a consequence of oxidation of buried utilities submersed in electrolytic solution (tailings water). Redox potentials may occur in the embankment due to transfer of electrons through conductive bodies (tailings sediment). Electrochemical potentials may also occur within the embankment at the interface between two different materials. The measured voltage differences may be generated from static charge accumulation over mineral interfaces (mineral potentials), buried tree roots and metallic objects (Corry, DeMoully, & Gerety, 1980).

A “streaming potential” is an electrokinetic potential difference that may arise when fluids interact with earth materials creating a charge separation between them. Figure 3.1 is an illustration of how streaming potentials are generated by fluid flow between soil grains. The soil grains are characterized by negatively charged surfaces (typical of most earth materials with typical pH and ion concentrations), and an outer layer of positively charged ions. The negative surface charges result from chemical interactions between the soil and the fluid where mostly hydroxyl (OH^-) ions are adsorbed and tightly bound to the soil grain. The outer loosely bound diffuse layer of positive ions (H^+ or other positive ions)

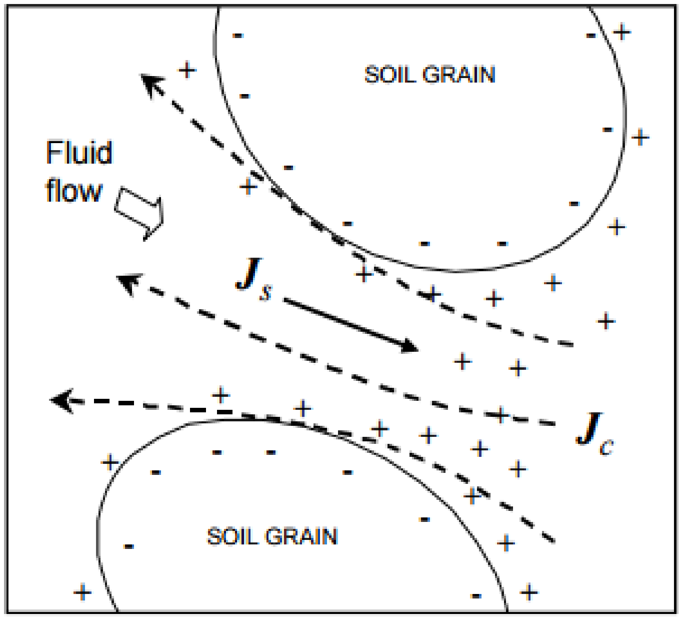

Figure 3.1: Generation of streaming potentials between soil grains (Sheffer, 2007).

is attracted to the surface by electrostatic forces. Due to diffusion (and thermal agitation in the presence of a temperature gradient), the outer layer extends a certain distance from the surface of the soil grain with the concentration of positive ions decreasing with distance. Thus, the electrical potential within the diffuse layer falls off with distance from the soil grain surface. Under static conditions this ‘electrical double layer’ is balanced and electrically neutral. The innermost part of the diffuse layer is strongly attracted to the soil grain surface due to electrostatic forces. However, fluid passing through the soil can displace mobile positive ions in the outer region of the diffuse layer beyond the “shear plane” allowing for the development of macroscopic charge separations that give rise to potential differences which represent spontaneous potentials of electrokinetic origin. (Mainali, et al., 2015; Hunter, 1981; Gillis, 2016; Lowrie, 2007).

Fluid flow indicated by the arrow in Figure 3.1 pulls positive ions in its direction, creating a streaming current ***Js***, leading to a charge imbalance giving rise to an opposing conduction current ***Jc*** due to the generation of the potential difference, which manifests itself as the measurable self-potential on the earth's surface. A net "streaming potential" arises as a result of this current imbalance (Minsley, et al., 2011).

The electric potential gradient is generally in the direction opposite to the hydraulic gradient. Therefore, increasingly positive self-potentials are measured in the direction of the fluid flow**.** Consequently, streaming potentials generated by seepage through earthenware embankments such as Gullbridge are expected to be more positive near the downstream slope/drainage blanket and more negative near the upstream slope/inflow area (Minsley, et al., 2011).

Variations in the measured SP response are also influenced by changes in fluid and rock chemistry. That is, streaming potentials generated by seepage through a dam will differ from one porous medium to the next (e.g., tailings, dam soil) (Minsley, et al., 2011).

Streaming potentials are of importance in dam monitoring as SP is the only geophysical method that responds directly to fluid flow. Flow of water through the structure may occur along several pathways including cracks, loose embankment material, and the downstream slope (drainage blanket) resulting in an increased rate of seepage. If seepage velocities become sufficiently high, they can cause internal erosion of fines, leading to eventual piping and dam failure. This makes SP one of the most important methods for delineating seepage flow for this study (Stantec Consulting Ltd., 2012)..

Naturally occurring potential differences in the ground are measured between a stationary ‘base’ and a mobile ‘rover’ electrode pot both coupled to the ground surface. A pot is a ceramic or plastic container with a porous base, containing a copper conducting rod submersed in an electrolytic solution (e.g., $CuS0_4$, kaolinite clay). Seepage through the wide, porous base establishes good electrical connection with the ground. The measurements may be subject to fluctuations unrelated to the subsurface target of interest to the surveyor, such as pot drift and telluric drift.

The “pot drift” refers to drift in the electrical potential between the base and rover electrode due to natural processes as associated with chemical and temperature variations in the electrolyte solution.

Time-varying electric fields within the crust originate when solar winds interact with the Earth’s natural magnetic field causing geomagnetic disturbances and erratic fluctuations in SP measurements known as telluric drift.

To mitigate the effects of pot drift and telluric currents repeat measurements are generally required along several surveys of the profile grid or line (Wynn & Sherwood, 1984). Drift checks between the base and rover pots as well as actual monitoring of the telluric fields may be conducted as well (Corwin, 1990).

3.1.2 Magnetics

Magnetic surveys have a broad set of applications. The total magnetic intensity (TMI) measured by a magnetometer is the sum of the contributions made by the Earth’s core, upper crust, and ionosphere. The geomagnetic field is generated by convective currents in the Earth's outer core (Morgan, 2010).

The Earth's geomagnetic field can be approximated by the field of a theoretical magnetic dipole near the centre of the Earth inclined at about 11.5° to the axis of rotation. As it is approximately dipolar, the magnetic intensity of the geomagnetic field in units of nanoTesla (nT) varies significantly from the equator to the poles. At the Earth's surface the magnetic intensity varies from 22,000 nT at the equator to 67,000 nT at the poles (Macmillan, 2004; Kearey, Brooks, & Hill, 2002).

Magnetic anomalies, that is, variations from the geomagnetic field, are due to crustal magnetism (spatial anomalies) or ionospheric currents (temporal anomalies). The ionosphere is a region of the upper atmosphere where atoms have been ionized by solar and cosmic rays resulting in the generation of an electrically conducting medium. Upper atmospheric winds move this electrically conducting medium through the Earth's magnetic field resulting in the generation of electromotive forces that drive electric current flow. These currents generate magnetic noise that can be detected by a magnetometer on the Earth's surface. Typically, a base-station sensor is deployed to measure diurnal variations associated with these external source magnetic anomalies. The diurnal drift is time-synced to the data acquisition times and subtracted from the dataset. Gradiometer data is free of anomalies associated with distant sources, given the gradient signal of the magnetic field falls off with the 4^{th} power of the distance (Prouty, Hrvoic, & Vershovski, 2013; Richmond A. D., 2016; Richmond A. , 1979).

Diurnal variations of the Earth's magnetic field occur as a result of the electric currents in the Earth's ionosphere resulting from plasmas associated with solar winds interacting with the magnetosphere. A geomagnetic storm is a disturbance of the Earth's magnetic field generated by intensified solar winds interacting with the Earth's magnetosphere. This may result in the rapid variation of the Earth's magnetic field intensity (TMI) by 10's to 100's of nT's. Although these disturbances are infrequent, it is in good practice to check the global geomagnetic activity at the time of the survey. Magnetic surveys should not be conducted during geomagnetic storms (Nagatsuma, 2002) (Mickus, 2014).

Crustal magnetic anomalies give insight into the concentration of magnetized rock forming minerals, as well as ferrous man-made objects such as buried utilities.

All magnetic fields are created by electric charges in motion. Any magnetized material on an atomic scale contains magnetic dipoles in the form of tiny current loops of electrons orbiting about a nucleus and spinning around their own axes. When a magnetic field is applied to a particular material it may acquire an induced magnetization in which the dipoles of the material align themselves with the applied field.

When a material becomes magnetized as the result of an inducing field, the strength and direction of this induced magnetic field is quantified by the dipole moment per unit volume or the magnetization vector $\vec{M}$.

The relationship between the degree of magnetization $\vec{M}$ and the applied magnetic field $\vec{H}$ can be written as the following assuming isotropic media:

$$\vec{M} = \chi\vec{H} \tag{3.1}$$

The magnetic susceptibility χ is a dimensionless quantity. Magnetic materials are generally classified into three main groups based on their susceptibilities: Diamagnetic, Paramagnetic and Ferromagnetic materials (Brittanica Encyclopedia, 2017; Oliver, 2015; Fitzpatrick R. , 2006).

Ferromagnetic materials have atomic dipoles that readily align with the direction of an applied magnetic field and retain this orientation in the absence of the applied field. In nature only several materials are known to be ferromagnetic such as magnetite and other iron oxides (Magnet Academy, 2015; Oliver, 2015).

Paramagnetic, materials are characterized by small positive susceptibilities sometimes smaller than 1 ppt. Like ferromagnets, paramagnets have dipoles (in the form of unpaired electron spins) that align themselves with the direction of an applied field, but in a much weaker manner. (Griffiths, 1999; Oliver, 2015; Syltie, 2002).

Diamagnetic materials are characterized by small negative susceptibilities. When the paired electrons of diamagnets are placed in an external field, they precess and begin to orbit faster around the nucleus of an atom, generating a magnetic force that opposes the applied field $\vec{H}$. All materials are diamagnetic, however the diamagnetic response is

Table 3.1: Magnetic susceptibility values in SI units for common materials found at Gullbridge (Schenck J. F., 1996) (Skrede, 2012).

Material/Substance	Magnet Type	Susceptibility χ ($\times 10^{-6}$)
Copper	Diamagnetic	-9.63
Zinc	Diamagnetic	-15.7
Water	Diamagnetic	-9.05
Pyrite (FeS_2)	Paramagnetic	1.5×10^3
Pyrrhotite (Fe_7S_8)	Ferromagnetic	3.2×10^6

generally overwhelmed by larger ferromagnetic and paramagnetic effects (Oliver, 2015; University of Birmingham, 2019; Salim, 2012).

Table 3.1 gives examples of susceptibility values in SI units for various materials and substances found at the Gullbridge Tailings Impoundment (Schenck J. F., 1996; Syltie, 2002).

The Gullbridge Tailings Impoundment is surrounded by diamagnetic copper-zinc concentrated water occupying the wetland to the west and the reservoir pool on the eastern edge of the embankment(Schenck J. F., 1996).

The most common paramagnetic material found over the Gullbridge impoundment is pyrite contained in the tailings. A paramagnetic material that will yield small positive susceptibility measurements not mentioned in Table 3.1 is gravel and sandstone, the materials used in the construction of the Gullbridge Tailings Impoundment. However, these magnetic susceptibilities are all very small and it is likely they would not be detected in a magnetic survey (Syltie, 2002).

Ferromagnetic iron is highly concentrated in the tailings contained within the reservoir. Dissolved iron and iron hydroxides in the tailings water may also contribute to the magnetic signature of the reservoir. In addition to this, some ferromagnetic materials that may generate isolated anomalous susceptibility highs are magnetite rich iron oxides, pyrrhotite contained in host rocks of the Gullbridge deposit and various buried metallic objects(Syltie, 2002).

Magnetic surveys have been proven successful for locating buried metallic objects such as decants responsible for transporting contaminated water through a dam(University of St. Andrews, 1997).

Vertical magnetic gradient (nT/m) is a measure of the spatial variation in the magnetic field strength between two magnetic field sensors mounted vertically. The VMG operates by eliminating long wavelength components of the magnetic signal associated with the regional total field resulting in an increasing resolution. However, in doing so, reduces the amplitude of the signals received (Byrd, 1967).

In exploration geophysics the VMG is particularly useful for characterizing shallow, near source metallic objects, in particular, defining the lateral boundaries of buried metallic objects. At Gullbridge, comparing the TMI and VMG data helped to distinguish whether magnetic anomalies were due to the shallow lithology in the area or an anthropogenic object which are similarly amplified in the magnetic gradient data (Mickus, 2014; Byrd, 1967).

3.1.3 Direct-Current Resistivity and Induced Polarization

Direct-Current Resistivity

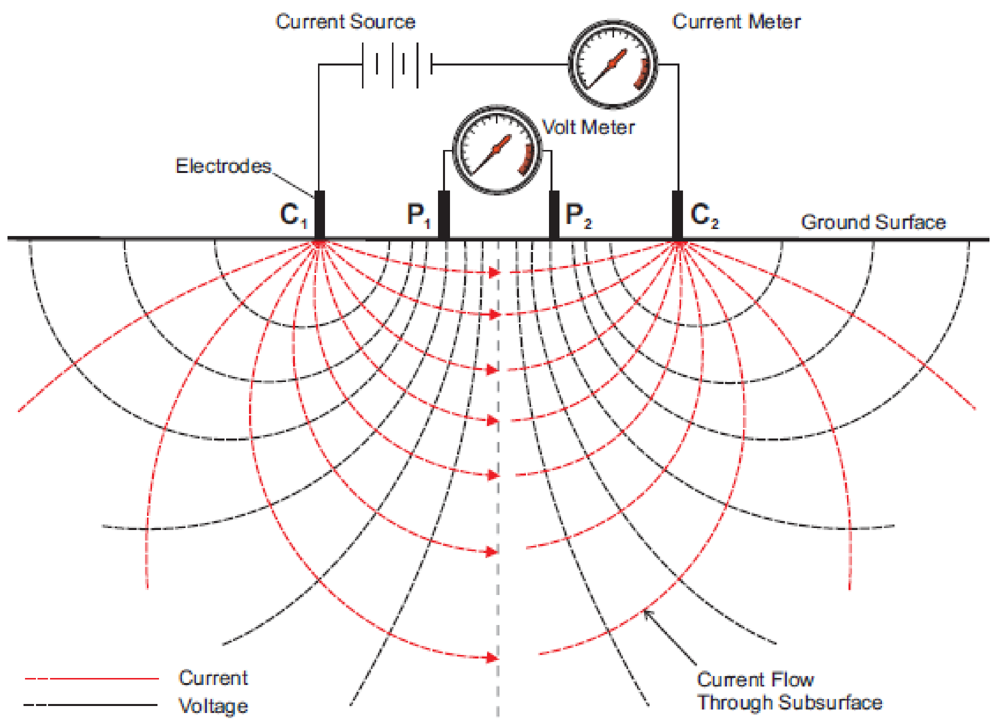

Figure 3.2: Schematic of the general array for a DCR survey indicating the positions of the current electrodes (C_1 and C_2) and the potential electrodes (P_1 and P_2) (Sharma, 1997). Note the volt and current meters in this image should not read zero when current is circulating between C_1 and C_2.

The direct-current resistivity method (DCR) (Figure 3.2) is a widely used technique that measures the apparent resistivity of the subsurface by injecting current through one pair of "current" electrodes and measuring the potential difference between another pair of "potential" electrodes. These four electrodes are referred to as a "quadrupole". The relative locations of current and potential electrodes define an "array" (Mainali, et al., 2015; Reynolds, 1997).

Figure 3.2 displays an image of a typical DCR survey array over a homogeneous half-space. As Figure 3.2 displays, current (red lines) is pumped through the ground as a current density J (A/m^2) from a source connected to the electrodes into the ground from C_1 to C_2 which subsequently generates a set of equipotential (voltage) surfaces about the current electrode positions. The response (the electrical potential drop ΔV) is measured between the potential pair P_1 and P_2 (University of St. Andrews, 1997; Reynolds, 1997). This relationship can be understood as a generalization of Ohm's Law for current flow I through a resistance R:

$$\Delta V = IR \tag{3.2}$$

which states that the potential drop ΔV is proportional to the product of the total current flowing through the circuit I and the electrical resistance R. During a DCR survey, the direction of the current is regularly reversed in intervals typically between 0.5 and 2s, in a square wave pattern. The regular reversals of current are used to cancel any steady potentials (SP) present, and the relatively long time interval allows for transients to pass before the potential is measured.

For circuit-elements of uniform cross-sectional area A perpendicular to the direction of current flow:

$$R = \frac{\rho L}{A} \tag{3.3}$$

where ρ represents the resistivity, L represents the length of the circuit element and A (m^2) represents the cross-sectional area of the element. The resistivity ρ (Ω*m) differs from the resistance R as it is a material property, whereas the resistance of an element depends on both its resistivity and the geometry of the object relative to the direction of current flow (Reynolds, 1997).

By substituting equation (3.3) into equation (3.2), it can be seen that if a small potential (ΔV) is measured between the potential pair M and N (Figure 3.2), the material is relatively conductive (inverse of resistive). Similarly, if this measured potential is large, the material is relatively resistive (Reynolds, 1997) (Kilfoil, et al., 2018).

The measurements of resistance that are recorded in the subsurface are converted to measurements of the 'apparent' resistivity of the ground beneath the array, calculated under the assumption that the ground is homogeneous. In the absence of sharp lithological changes, such as vertical boundaries, this is a weighted average of the resistivity values in the vicinity of the array. The equation used to calculate apparent resistivity ρ_a is:

$$\rho_a = K \frac{\Delta V}{I} \tag{3.4}$$

where K is a geometric factor depending on the electrode configuration.

The survey investigation depth is dependent on the spacing of the current electrodes C_1 and C_2. Successively increasing the spacing between the current electrodes increases the depth of penetration of current through the subsurface and allows for measurements of resistivity in materials at greater depths. Measurements of resistivity are recorded at different pseudo-depths based on the spacing AB of the current electrodes. For uniform ground, half the current flows deeper than a depth of *AB/2*, and the other half remains nearer the surface. As the pseudo-depth of the measurements increases, if the distance between the potential electrodes does not increase, the signal to noise ratio decreases as the current is diluted over a larger volume through the subsurface and a smaller percentage of the potential drop is detected between the potential pair (Reynolds, 1997; Kearey, Brooks, & Hill, 2002).

The two array types used during this research were Schlumberger and Wenner. They were combined to improve spatial resolution and sensitivity over the seep area.

Figure 3.3 illustrates the geometry and naming convention for a DCR Schlumberger array. The current electrodes, C_1 and C_2 at positions A and B respectively are placed on the outside of the potential electrodes P_1 and P_2 at positions M and N. Measurement locations are at the center of the array x. The b-spacing is the distance between the potential electrodes.

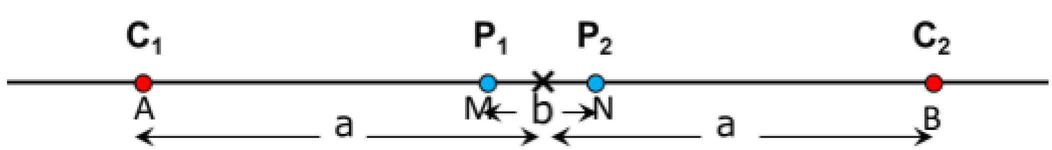

Figure 3.3: Diagram depicting the conventional geometry of the Schlumberger DCR array conducted over the Gullbridge seep.

The a-spacing in a Schlumberger array is the distance between the current electrodes and the center of the array x, which also gives an indication of the penetration depth of the current. As the ratio a/b increases, a smaller signal-to-noise is encountered.

The geometric factor used for calculating apparent resistivity (see Eqn (3.4)) for the Schlumberger array is:

$$K = \pi\left(\frac{a^2}{b}\right)\left(1 - \frac{b^2}{4a^2}\right) \tag{3.5}$$

Pseudo sections, where measurements of apparent resistivity are plotted versus x and a (pseudo depth), are generated by varying x and a (and sometimes b) along a survey line. Figure 3.4 (a) demonstrates how a pseudo-section is generated using 24 electrode positions, arranged in Schlumberger arrays. To generate the first row of measurements (n=1) the first quadrupole is located at (A,M,N,B = 1,2,3,4) and the last at (A,M,N,B = 21,22,23,24). Figure 3.4 (b) illustrates how the current electrodes are expanded about the potential pair at the middle of the array to "see" deeper. Quadrupoles (A,M,N,B = 2,3,4,5) and (A,M,N,B = 1,3,4,6) are both centered between electrodes 3 and 4, however (A,M,N,B = 1,3,4,6) "sees" deeper given the increased a-spacing. The plot locations for these two measurements are indicated in Figure 3.4 (a) by the red rectangle. Expansion about electrode positions 12 and 13 generate the maximum depth level (n=11) attainable by 24 electrode locations in a line (blue rectangle in Figure 3.4(a)). A total combination of 121 quadrupoles are attainable using the aforementioned system.

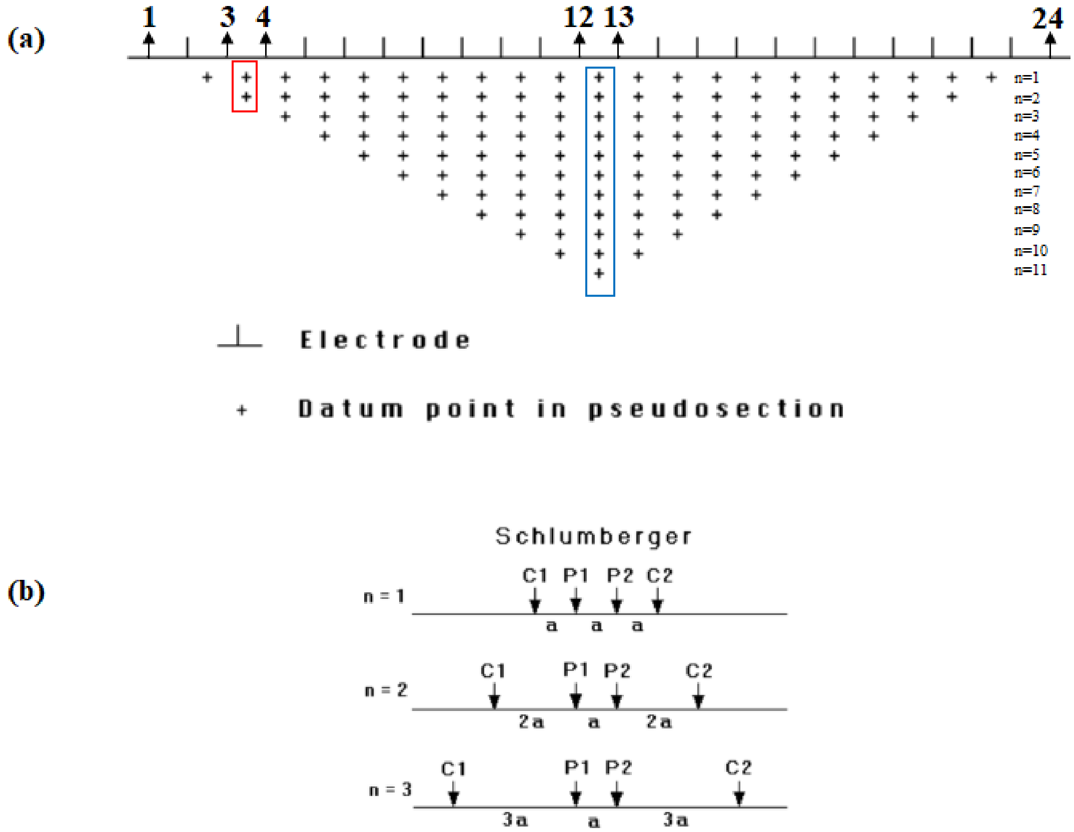

Figure 3.4: (a) Pseudo-section generated from Schlumberger DCR array (b) increasing a-spacing about the potential pair at the center of the array demonstrating increase in depth level *n*. Adapted from (Geotomo Software, 2010).

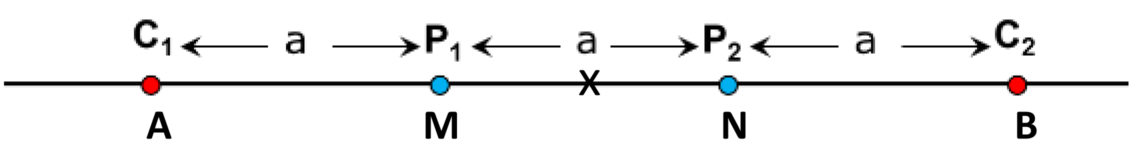

Figure 3.5: Diagram depicting the conventional geometry of the Wenner DCR array (Leitch A. , 2016).

Figure 3.5 illustrates the Wenner array configuration. For a Wenner array, the a-spacing is equal to the distance between each electrode.

The geometric factor (see Eqn (3.5)) for the Wenner array is:

$$K = 2\pi a \tag{3.6}$$

The expanding Wenner configuration (Figure 3.5) works by gradual expansion of the electrodes about the midpoint x while maintaining an equal spacing between each of the electrodes (Goyal, Niwas, & Gupta, 1991)..

Figure 3.6 (a) demonstrates how a pseudo-section is generated when 24 electrode locations are available for Wenner arrays, cycling through all the possible electrode configurations where the distance between AM, MN and NB are the same. The first measurement (red rectangular box) is taken with quadrupole (A,M,N,B=1,2,3,4). The second measurement (blue rectangular box) is collected using quadrupole (A,M,N,B = 2,3,4,5).The third measurement (green rectangular box) using quadrupole (A,M,N,B = 1,3,5,7) is plotted at a depth level of n=2 given the increase in a-spacing (2×a). Figure 3.6 (b) illustrates how the array is expanded to "see" deeper. A total of 4 Wenner quadrupoles can be utilized to record measurements over the center of the array (orange box). (A,M,N,B = 1,3,5,7), (A,M,N,B = 8,11,14,17), (A,M,N,B = 5,10,15,20) and (A,M,N,B = 2,9,16,23) indicate a, 3×a, 5×a and 7×a respectively. Hence, the 24-electrode system utilizes a maximum depth level of 7 when deploying the Wenner array geometry. A total combination of 84 quadrupoles are attainable using this system. In comparison to the

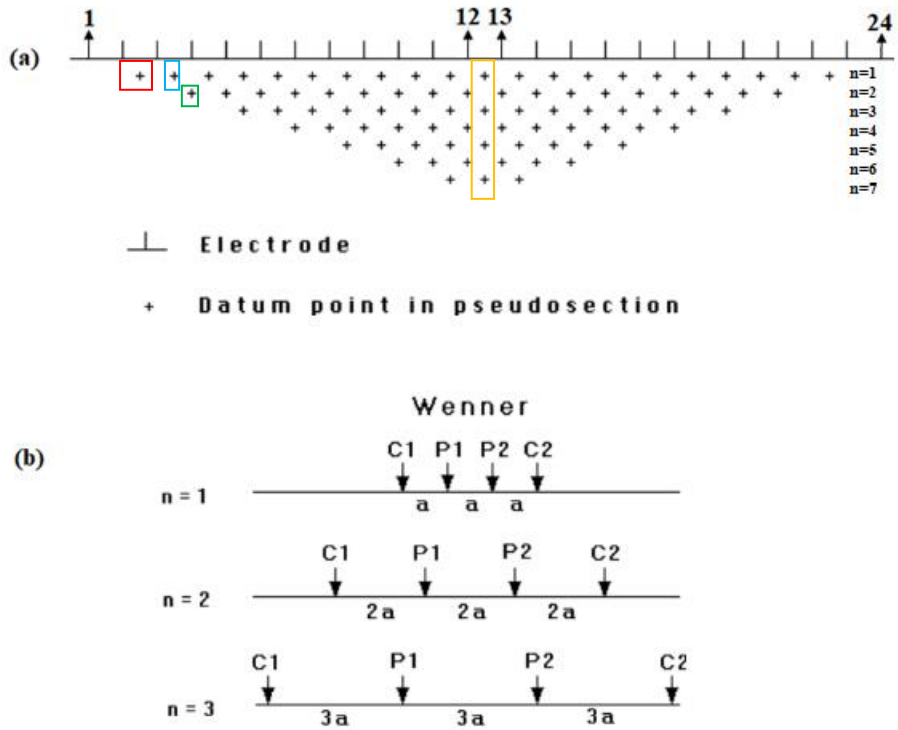

Figure 3.6: (a) Pseudo-section generated from Wenner DCR array (b) increasing a-spacing about the center of the array demonstrating increase in depth level *n*. Adapted from (Geotomo Software, 2010).

Schlumberger array, the Wenner provides better signal to noise, but fewer, shallower measurements.

The use of direct-current resistivity surveys in dam monitoring has been effective in previous studies because of relationships between electrical properties and fluid content in the embankment structure. Electrical surveys over tailings dams are effective at locating seepage causing internal erosion and are often combined with other surveys such as ground penetrating radar and spontaneous potential as a means to estimate water content and porosity (Mainali, et al., 2015). Because of dissolved ions, water is usually conductive, and therefore resistivity values over areas with a high degree of saturation will appear relatively low. The conductivity of the water depends on the concentration of dissolved ions. The Gullbridge dam overlies a thin veneer of peat, which may have low values of resistivity due to the increased water content. It is expected that near the surface of the dam there will be high resistivity values corresponding to unsaturated quarry rock materials. Unsaturated materials normally have a higher resistivity because the resistivity of air is extremely high even when compared with fresh water, therefore areas over coarse fill materials will be much more resistive than saturated areas of the dam (University of St. Andrews, 1997).

DCR surveys were used in this study to estimate the depth of the water table, determine thicknesses of dam fill (sand and gravel) to qualitatively estimate clay content and porosity, and detect areas where the dam sediment is saturated. Dry sand and gravel have high resistivity (greater than 200 $\Omega * m$) and saturated sands have a relatively lower electrical resistivity depending on the resistivity of the water (Lucius, Langer, & Ellefsen, 2006). The resistivity of a saturated sand can be estimated using Archie's Law:

$$\rho_r = F\rho_w \tag{3.7}$$

which states that the resistivity of a water-saturated rock ρ_r is equal to the formation factor $F = \phi^{-m}$, a function of porosity ϕ and the cementation factor m related to the pore geometry, multiplied by the resistivity of the water saturating the pore space ρ_w (Glover, 2016; Lyons, 2010). The measured conductivity σ of the tailings water in 2018 was 35.1 mS/m, and since $\sigma = 1/\rho$ the resistivity of the water saturating the pore space ρ_w is approximately equal to 28.5 $\Omega * m$. Assuming a cementation factor of m=1.3 typical of unconsolidated sands (Lyons, 2010) and a porosity of 40% typical of unconsolidated sands (Earle, 2019), the calculated formation factor F=3.3. Therefore, the estimated resistivity of the saturated dam soil within the Gullbridge Dam is approximately ρ_r=94 $\Omega * m$.

Induced Polarization

Induced-Polarization (IP) surveys are carried out with the same equipment and at the same time as DCR surveys, however instead of simply reversing the direction of current flow, for time-domain IP the current is switched off between current pulses. IP surveys involve measuring the decay in electric potential ΔV after the current in the resistivity array is switched off, and give an indication of the capacitance of the ground, that is, the materials ability to store electric charge.

Figure 3.7 displays a graph of the measured potential over a 10 second current cycle. The potential *Vc* is the measured potential difference just before the current is switched off, or the maximum potential at which charge accumulation in the ground is greatest. The potential *V* is shown dropping immediately, before steadily decaying as the charges disperse. The inset of Figure 3.7 displays the potential drop over an off cycle. The potential is measured at several small-time intervals (V_1, V_2, V_3) from the time the current was shut off. This information is used to calculate the chargeability *M* measured in (ms) of the material:

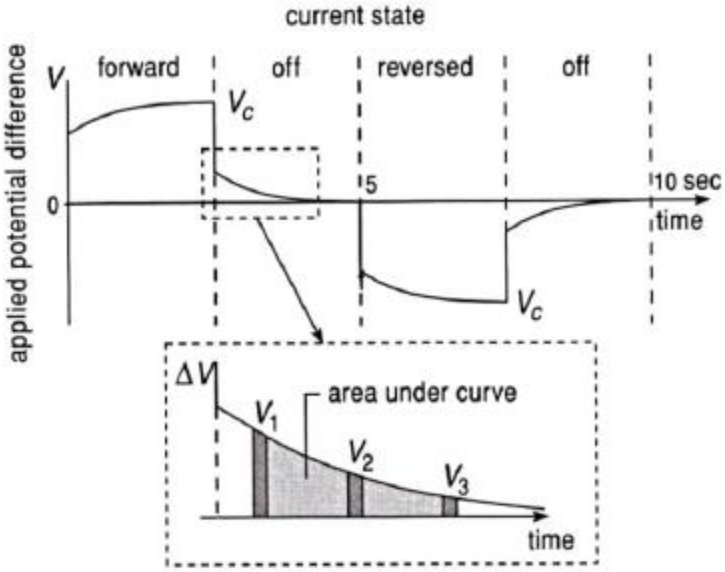

Figure 3.7: Measuring the decay of the induced potential (capacitance of a material) in the time-domain simultaneously during DCR survey (Mussett & Khan, 2000).

$$M = \frac{A}{\nabla V} = \frac{1}{\nabla V}\int_{t1}^{t2} v(t)dt \qquad (3.8)$$

This is just one of the equations used to calculate chargeability in the time-domain (UBC, 2007) (Srigutomo, 2016).

The Induced-Polarization method is best known for detecting disseminated ores within a non-conducting matrix (Figure 3.8). When the current is switched on, dissolved ions move through the pore space of rock grains by movement within the groundwater through small channels due to the electric field generated by the array. If blockages in the pore space are at insulators, the particles are forced to move around the blockage given ions will not adhere to their surface. However, if the blockage is a conductor (Figure 3.8), charged particles build up on the surface of the conductor and electrons may pass through

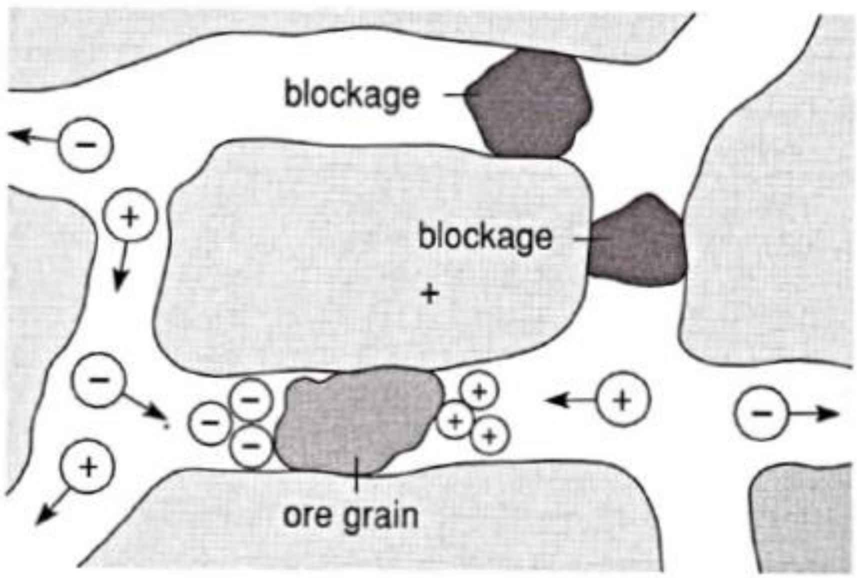

Figure 3.8: Generation of induced potentials within the pore channels of a rock grain (Mussett & Khan, 2000).

the material. These conductors in effect work as small capacitors throughout the non-conducting matrix. The transfer of electrons across the grain boundary is relatively slow, so there is a small buildup of charge within the grain due to the accumulation of charged particles on either side. This is a process known as “electrode polarization” (Mussett & Khan, 2000).

If electronic conductors (e.g. metallic sulfide minerals) are present in the material, the induced potential drop may take several seconds to reduce completely to zero. The larger the concentration of electronic conductors, the longer this decay in electric potential resulting in greater values of the calculated chargeability (Srigutomo, 2016) (UBC, 2007). Clay minerals like metallic minerals also behave as capacitors and generate accumulations of charge that are dispersed when the current is switched off (Mussett & Khan, 2000).

The intent of using IP surveys over the Gullbridge TMA is to determine the clay content of the earth-filled dam material. If clay is present in the pore space of the dam fill, IP's will be generated due to the accumulation of charge at the blockage when the current is switched on.

3.1.4 Ground-Penetrating Radar

The ground penetrating radar (GPR) technique (Figure 3.9) is a non-intrusive high-resolution method that produces detailed images of the subsurface by emitting radio

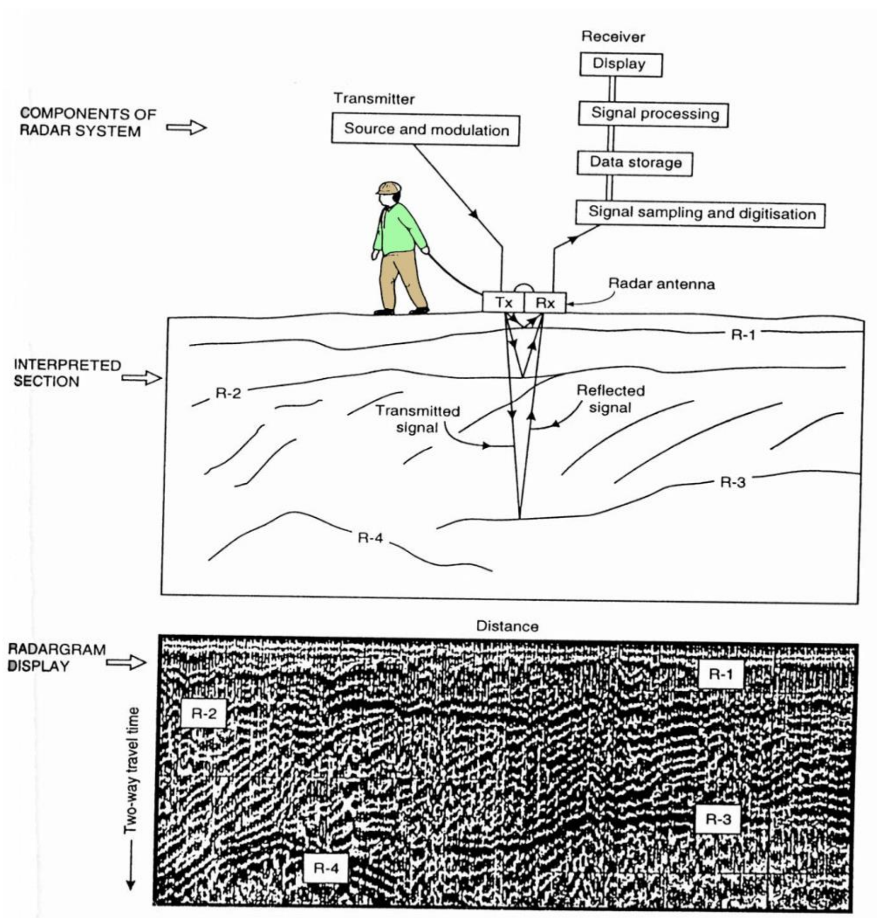

Figure 3.9: Illustration showing the GPR surveying process (Reynolds, 1997).

frequency pulses of electromagnetic (EM) energy through a transmitting antenna and detecting the reflections from interfaces by a receiving antennae. As the surveyor pushes the instrument along the surface the transmitter and receiver distanced at a constant separation continually collect and record reflection traces at regular intervals as two-way travel time. The electromagnetic energy is reflected and refracted at interfaces in the ground where there are changes in electrical properties, more specifically changes in the electrical permittivity (ε), the relative magnetic permeability (μ), and/or the electrical conductivity (σ) of a material. These reflections build an image of the subsurface, giving depth, material, and geometrical information. The frequency of the antenna chosen is based on a trade-off between resolution and investigation depth. Lower frequency antennas generate waves that penetrate to greater depths but produce lower resolution profile images, as the spatial resolution is nominally one quarter of a wavelength (Reynolds, 1997).

GPR can be used to determine the dimensions of layers of soil, rock, concrete, wood and anything non-metallic (Sensors and Software Inc., 2016). Areas over metallic bodies will produce a significant ringing of the signal, generating artifacts in the dataset.

The theory behind GPR imaging is based on signal propagation of electromagnetic waves. The general electromagnetic wave equations in a linear medium in one dimension (Griffiths, 1999) are:

$$\frac{\partial^2 \vec{E}}{\partial z^2} = \mu\varepsilon \frac{\partial^2 \vec{E}}{\partial t^2} + \mu\sigma \frac{\partial \vec{E}}{\partial t} \tag{3.9a}$$

$$\frac{\partial^2 \vec{B}}{\partial z^2} = \mu\varepsilon \frac{\partial^2 \vec{B}}{\partial t^2} + \mu\sigma \frac{\partial \vec{B}}{\partial t} \tag{3.9b}$$

where $\vec{E}$ is the electric field component and $\vec{B}$ is the magnetic field component of the electromagnetic wave, z is the vertical distance and t is the time (Griffiths, 1999). The electromagnetic properties that govern the behaviour of a radio pulse are σ, ε, and μ. The electrical conductivity σ relates to how easily current flows through a material, the permittivity ε relates to how easily the material becomes polarized in the presence of an applied electric field, and the magnetic permeability μ relates to how easily a material becomes magnetized. In most cases, the magnetic permeability μ is constant and its effects on the propagation of the EM wave are negligible. This holds true for most sedimentary rocks (Gullbridge Dam fill), as they do not generally contain magnetite and therefore do not become significantly magnetized in the presence of an external magnetic field.

The plane wave solutions to equations 3.9a and 3.9b are written as attenuating waves:

$$\vec{E}(z,t) = \overrightarrow{E_0} e^{-\kappa z} \cos\left(kz - \omega t + \delta_E\right) \hat{x} \tag{3.10a}$$

$$\vec{B}(z,t) = \overrightarrow{B_0} e^{-\kappa z} cos(kz - \omega t + \delta_E + \phi)\, \hat{y} \tag{3.10b}$$

where ω is the angular frequency, κ is the decay rate, k is the wave number, δ_E is the initial phase angle of the electric field and ϕ is the phase delay of the magnetic field $\phi = tan^{-1}(\kappa/k)$.

The electric and magnetic field components of the EM wave are polarized respectively in the $\hat{x}$ and $\hat{y}$ directions along the z-axis, given the oscillations of the two fields are mutually orthogonal to one another (Griffiths, 1999).

For a plane wave in a conducting medium:

$$k \equiv \omega\sqrt{\frac{\varepsilon\mu}{2}}\left[\sqrt{1+\left(\frac{\sigma}{\varepsilon\omega}\right)^2}+1\right]^{\frac{1}{2}} \tag{3.11a}$$

$$\kappa \equiv \omega\sqrt{\frac{\varepsilon\mu}{2}}\left[\sqrt{1+\left(\frac{\sigma}{\varepsilon\omega}\right)^2}-1\right]^{\frac{1}{2}} \tag{3.11b}$$

The decay rate κ describes the rate at which the electromagnetic signal attenuates through the ground as it dissipates into heat energy resulting in decreasing amplitude with increasing z.

The dielectric constant ε_r is defined as the ratio of the charge storage capacity of a material in the presence of an electric field (i.e. permittivity) to the permittivity of free space (Martinex & Byrnes, 2001).

$$\varepsilon_r = \varepsilon/\varepsilon_0 \tag{3.12}$$

When an EM wave encounters an interface between two materials with differences in σ, ε, or μ, some energy is reflected. GPR is most successful in situations where the factor

$P = \sigma/\varepsilon\omega$ in equations (3.11) is low ($P < 0.5$). Derivation of the low-loss forms of the equations for GPR wave velocity and reflection coefficient can be found in (GeoSci Developers, 2017).

The amplitude of the reflected wave in proportion to the incident wave is known as the reflection coefficient. For radio waves, the reflection coefficient depends on how different the dielectric properties of the two materials are. In materials such as dam soils, the water table interface results in large values of the reflection coefficient given its large value of relative permittivity (GeoSci Developers, 2017), and therefore can present as a bright reflection in GPR data. However, the strength of a signal at a GPR receiver also depends on other factors: **w**hen a radar pulse travels through the subsurface it loses amplitude due to (1) geometrical spreading, (2) intrinsic attenuation and scattering due to heterogeneity (Lucius, Langer, & Ellefsen, 2006).

The degree of clay content and water saturation heavy influences the attenuation rate of the radar pulse. GPR signals over boundaries between the dam fill and water and/or clay content are limited in their depth of penetration due to increased conductivity σ. Differences in dielectric permittivity ε also result in a large amount of the signal reflecting at the boundary and so less signal available to reflect from deeper interfaces.

The GPR technique has been deployed in past dam monitoring and diagnostic studies as it is a non-invasive technique that allows for the investigation of dams without affecting their structure (Loperte et al., 2011). The GPR serves as a method to detect and localize fluid flow, as the electrical properties of water differ significantly from the quarry rocks used to build the dam. The most common reflections in a GPR profile are from heterogeneities and changes in water content due to the large contrasts in the electromagnetic properties from those of sediment grains and air. Changes in water content are generally associated with variations in textural characteristics that influence water retention. The GPR technique also has the ability to locate voids, lithological discontinuities or fracture zones embedded within the embankment that threaten the physical stability of the dam (Lucius et al., 2006). If the dam is in fact heavily saturated, then ground-penetrating radar may have the capability of mapping the permeable layers of the embankment (van Dam, 2001).

Ground-Penetrating Radar can be used in earth-filled embankments such as Gullbridge to detect to the top of the water table, the top of lenses of fine gravel as well as thickness of units of varying dielectric properties. GPR cannot distinguish between sand and gravel given the small differences in their dielectric properties. The amplitude of the reflected wave at an interface between saturated and non-saturated sand and gravel is large given the large differences in the values of relative permittivity and conductivity. Therefore, the water table of an earth-filled dam should be in most cases the most clearly imaged boundary. If conductive layers of clay are present in an area, the GPR signal will not image below them (Lucius, Langer, & Ellefsen, 2006).

3.1.5 Electromagnetic Ground Conductivity

Electromagnetic geophysical surveys measure the ground conductivity by electromagnetic induction. The theory behind electromagnetic induction can be described by Faraday's Law, Ampere's Law and Ohm's Law. Faraday's Law, (Equation 3.13) states that a time-variant magnetic field will induce an electric field equal to the rate of change of the magnetic flux or vice-versa (Griffiths, 1999).

$$\nabla \times \vec{E} = -\frac{\partial \vec{B}}{\partial t} \tag{3.13}$$

Ampere's Law states that the curl of the magnetic field is equal to the current density $\vec{\mathrm{J}}$ and the time-varying electric field $\frac{\partial \vec{\mathrm{E}}}{\partial \mathrm{t}}$ multiplied by the permittivity of free space ε_0 all multiplied by the magnetic permeability of free space μ_0 (Griffiths, 1999).

$$\nabla \times \vec{\mathrm{B}} = \mu_0 \vec{\mathrm{J}} + \mu_0 \varepsilon_0 \frac{\partial \vec{\mathrm{E}}}{\partial \mathrm{t}} \tag{3.14}$$

Rewritten in terms of $\vec{H}$ – the usual variable representing the magnetic field in geophysics – where

$$\vec{B} = \mu_0 \vec{H} + \vec{M} \tag{3.15}$$

and assuming that magnetization $\vec{M}$ is negligible, Ampere's Law becomes:

$$\nabla \times \vec{\mathrm{H}} = \vec{\mathrm{J}} + \frac{\partial \vec{\mathrm{D}}}{\partial \mathrm{t}} \tag{3.16}$$

where $\vec{D}$ is the electric displacement, generally also assumed negligible in ground conductivity measurements.

Ohm's Law

$$\vec{J} = \sigma\vec{E} \quad (3.17)$$

states that the total current density in the conductive body $\vec{J}$ in A/m^2 is equivalent to the product of the conductivity σ in Siemens/m and the electric field in units of volts/meter (University of British Columbia Geophysical Inversion Facility, 2014).

Electromagnetic surveys are performed by passing an AC current through a coil of wire (transmitter) and generating an electromagnetic field (Jika & Mamah, 2014). Time-varying electrical currents $\vec{J}$ in the transmitter coil generate a time-varying primary magnetic field $\vec{H_p}$ (Eqn (3.16)) with its axis along the axis of the coil. This primary magnetic field $\vec{H_p}$ propagates through the subsurface causing secondary electrical field which drives currents in conductive bodies $\vec{J_s}$ known as "eddy currents". The strength of the currents is proportional to the conductivity of the ground (Eqn (3.17)).

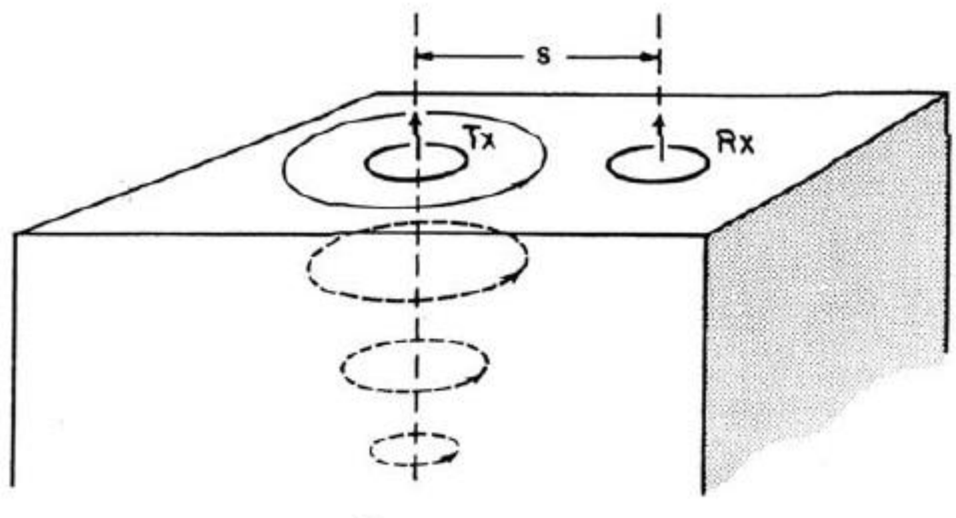

Figure 3.10: Induction currents in a homogeneous half-space generated by an electromagnetic survey instrument (McNeill, 1980).

Figure 3.10 depicts the generation of secondary current loops in a homogeneous half-space from a transmitter (Tx) with its coil axis perpendicular to the ground. These concentric current loops generated by the transmitter Tx are displayed circling about the horizontal in a direction determined by the right-hand rule, with magnitudes falling off with distance from the transmitter (McNeill, 1980).

These current loops generate a secondary magnetic field $\vec{H}_s$ (Eqn (3.16)) that is measured by the receiver. The receiver measures the sum of the primary and secondary fields in frequency-domain systems, and bucks out the primary field (University of St. Andrews, 1997; University of British Columbia Geophysical Inversion Facility, 2014).

The EM31-MK2 instrument used in this study ideally operates under a low induction number (LIN) condition. Inductance describes the tendency for a conductor to

oppose a change in the electrical current running through it, and it is significant if the ground is highly conductive or contains large conductors.

The induction number β is defined as the ratio of the intercoil spacing s to the skin depth δ:

$$\beta = \frac{s}{\delta} = \frac{s}{\sqrt{\frac{2}{\sigma_a \omega \mu}}} \tag{3.18}$$

The skin depth is defined as the depth at which an electromagnetic plane wave propagating into the subsurface has decayed to $e^{-1}$of its initial magnitude. (However, this definition does not apply to the dipole "near field" generated by the transmitter because it is not a plane wave detached from its source.) For instruments operating assuming the LIN approximation in a homogeneous half-space (Figure 3.10), the transmitter frequency is typically low, and the terrain conductivity normally should not exceed 100 mS/m. The EM31 instrument operates with a coil spacing of 3.66 m at a frequency of 9800 Hz (McNeill, 1980), so the induction number corresponding to an apparent conductivity of σ_a=100 mS/m (and the LIN condition) is:

$$\beta = \frac{s}{\delta} = \frac{s}{\sqrt{\frac{2}{\sigma_a \omega \mu_0}}} = \frac{3.66\,m}{\sqrt{\frac{2}{(0.1\,S/m)(2\pi(9800\,Hz)(4\pi \times 10^{-7})}}} = \frac{3.66}{16} = 0.22$$

The electromagnetic ground conductivity meter computes the ground conductivity from the ratio of the secondary magnetic field to the primary magnetic field at the instrument receiver. The secondary magnetic field at higher frequencies is a complex function of s, σ_a and ω. However, when the instrument operates at low induction numbers in a homogeneous half-space, the equation for the secondary magnetic field takes the simple form linearly proportional to the (uniform) ground conductivity:

$$\frac{H_s}{H_p} \cong \frac{i\omega\mu_0\sigma s^2}{4} \tag{3.19}$$

As typical in EM, i indicates there is a phase shift of $\pi/2$ between H_s and H_p, hence H_s is in quadrature (McNeill, 1980).

Given equation (3.19), the apparent ground conductivity in mS/m is computed at the receiver by the following:

$$\sigma_a = \frac{4}{\omega \mu_0 s^2}\left(\frac{H_s}{H_p}\right) \tag{3.20}$$

In addition to the quadrature component in ground conductivity measurements, in-phase measurements can also be acquired by the Geonics EM31 meter. The in-phase component of H_s/H_p is due to ground inductance resulting in an extra phase shift. The in-phase component of the secondary field actually has a phase shift of 180^0 (upside down) relative to the primary field and is given as a ratio, in ppt, of the amplitude of the secondary field which is in-phase with the primary field to the amplitude of the primary field, at the receiver. The benefits of integrating in-phase data with quadrature ground conductivity is that it allows the interpreter to determine whether an anomaly is caused by a metallic debris or increased moisture and tailings concentration (Reynolds International, 2011). Two primary factors that control the exploration depth of a terrain conductivity meter are the coil spacing s and the coil orientation. The EM31 operates using a fixed s, and measures two values of ground conductivity distinguished by the coil orientation relative to the ground surface. (Risch & Robinson, 2001; Reynolds International Ltd., 2011). The vertical magnetic dipole (VMD) orientation refers to when the plane of the Tx and Rx coils are parallel to the ground, and the horizontal magnetic dipole (HMD) refers to when the plane of the coils are normal to the ground.

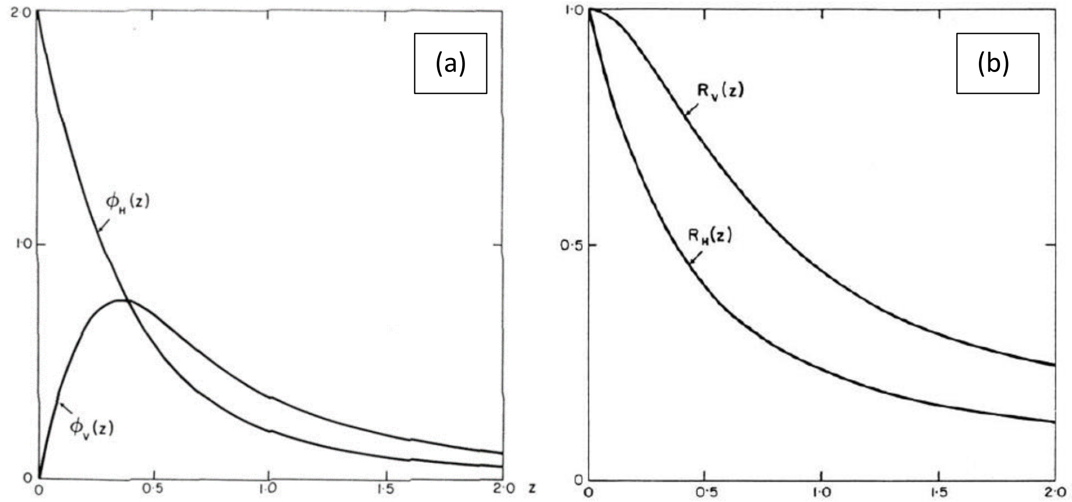

Figure 3.11: a) Contributions of Hs (ϕ) generated from horizontal current loops in a thin horizontal half-space slice dz at depth z for both the vertical dipole orientation (ϕ_v) and the horizontal dipole orientation (ϕ_H) b) Cumulative response of the secondary magnetic field $R_V(z)$ versus depth for all materials below a specific normalized depth for both the VMD and HMD dipole orientations (McNeill, 1980).

Figure 3.11a illustrates the sensitivity function ϕ(z) which describes the contributions of H_s versus depth normalized by the intercoil spacing *s* for both the VMD orientation (ϕ_v) and the HMD orientation (ϕ_H). The penetration depth is proportional to the intercoil spacing and limited by the fall off of the field from the current loops with distance from the transmitter.

The contributions to the secondary magnetic field using the VMD orientation (ϕ_v) are at a maximum at a depth equal to 0.4 s. The function then begins to gently slope to near-zero contributions with depth, however there is still a significant amount of the secondary magnetic field generated at a depth of 2s.

The HMD (ϕ_H) profile in Figure 3.11a indicates the contributions of the induced currents to Hs decrease monotonically with depth.

When dealing with a multi-layered system, a ground conductivity meter at low induction numbers finds the cumulative response of all the layers. The following function,

$$R_{\substack{V\\H}}(z) = \int_{z}^{\infty} \phi_{\substack{V\\H}}(z)dz \tag{3.21}$$

gives the cumulative response of the secondary magnetic field for all materials above a given normalized depth $Z = z/s$ plotted in Figure 3.11b (McNeill, 1980).

The maximum exploration depth achievable by an EM31-MK2 system with an intercoil spacing $s =$3.66 m is ~6 m and ~3 m for VMD and HMD orientations, respectively (Geonics Training, 2013). However, Figure 3.11b indicates that 25% of $\vec{H}_s$ received is below an exploration depth equal to double the coil spacing (~7.3 m). It is expected that a significantly conductive layer at this depth would be detected by the instrument.

The electromagnetic ground conductivity has some advantages over convention resistivity methods such as DCR. For DCR, ground conductivity anomalies near the electrodes can cause significant noise in the measurements. For small near-surface ground conductivity anomalies near the transmitter of the EM31, the current density may be large but the radius of the current loops are small and distant from the receiver and therefore they do not couple well magnetically thus the effect of localized resistivity inhomogeneities are small (McNeill, 1980).

Electromagnetic surveys have been deployed previously for dam monitoring studies to observe lateral and vertical changes in conductivity in dam embankments, as well as generating terrain conductivity (contamination) maps, delineating seepage conduits and locating anthropogenic conductors such as pipes (University of St. Andrews, 1997; McNeill, 1980).

3.1.6 Bog and Water Sample Analysis

Two bog core samples in the wetland and two water samples in the reservoir and seep area were collected at the Gullbridge site in July 2018. The bog samples were subjected to ICP-OES (Inductively Coupled Plasma Optical Emission Spectroscopy) analysis of major elements and the water samples were subjected ICP-MS (Inductively Coupled Plasma Mass Spectrometry) analysis. A detailed description of the methods is provided in Appendix A3.2. The samples were collected to determine whether concentrations of metals were within Schedule A compliance, and to aid in the interpretation of ground conductivity data collected in the wetland, as increased concentrations of iron, copper, and zinc have an associated conductive signature.

3.2 Field Methods

Table 3.2 indicates the date, survey method, survey area and weather over the duration of the field work conducted from June 2016 to July 2018 at the Gullbridge TMA.

Table 3.2: Table of field schedule at the Gullbridge Tailings Facility (* data lost, ** imprecise positioning, data not used).

Date	Technique	Survey Line	Weather Conditions
June 19th, 2016	SP	L1+00 – L1+400 L2+00 – L2+400	Sunny
June 20th, 2016	SP DCR	L1+400 – L1+760 L2+400 – L2+760 L1+00 – L1+160	Sunny with overcast
June 21st, 2016	DCR	L1+160 – L1+795	Sunny
June 22nd, 2016	GPR	*Several lines over dam and CMP in bog area.	Overcast
July 16th, 2016	GPR	10 m x 20 m grid over dam, CMP in bog area. **3 lines over full length of dam,	Overcast
July 17th, 2016	Mag.	L1+00 – L1+790 L2+00 – L2+820	Sunny
July 18th, 2016	SP	L2+35 – L2+230	Sunny
September 24th, 2016	GEM2	L0+00 – L0+810	Overcast
September 25th, 2016	EM31 GPR	L0+00 – L0+760 LINE00. **LINE02, LINE03, LINE05	Overcast
November 26th, 2016	DCR GPR	YLINE02 with 24 m extension N 50 m x 20 m Seep Grid	Overcast & Occasional Snow
February 20th, 2017	GPR	Wetland LINE6-LINE9	Overcast

Table 3.2: Table of field schedule at the Gullbridge Tailings Facility (* data lost, ** imprecise positioning, data not used).

February 21rst, 2017	EM31	B.L.+00 –B.L.+180	Overcast
June 25th, 2017	DCR	Seep Grid – Start: YLINE04 - End: YLINE05, 5 m east of YLINE05	Sunny and Windy
June 26th, 2017	GPR	100 MHz Seep Grid Survey Lines (Full)	Rainy
June 27th, 2017	GPR	250 MHz Seep Grid and Old Stream Extension Survey Lines (Full), 50 MHz Old Stream Extension Survey Lines (0,5) - (140,5) YLINE00-06, no x-lines)	Sunny with Clouds
June 28th, 2017	GPR	50 MHz Old Stream Grid Survey Lines (Full), 100 MHz Old Stream Grid Survey Lines	Overcast
June 30th, 2017	GPR EM31	100 MHz Old Stream Grid Survey Lines (Full) Seep Grid – XLINE00, 25, 50, 75, 100 & 120. YLINE00, 05 & 09	Sunny
November 10th, 2017	EM31	L1+00-L1+530, L2+00-L2+550	Calm Winds with Overcast
November 11th, 2017	EM31	L3+00-L3+~430	Overcast with Strong Winds
July 14th, 2018	SP	(60x20) Seep Grid Survey Lines	Overcast
July 15th, 2018	EM31 Bog and Water Sampling	LINE04 & LINE05 Bog Site #1, #2, and Seep and Reservoir Water Samples.	Overcast

Locations of all survey stations were obtained using a Topcon Hiper V Real Time Kinetic (RTK) system with the exception of instances when the RTK batteries failed due to overuse or extreme weather. In this case a handheld Garmin GPS was used to acquire coordinates over measurement stations.

RTK digital GPS measurements were collected, relative to a base-station collecting static data at a fixed position, using a rover sensor over the Gullbridge TMA. All measurements were base-station corrected using the true base-station location acquired from static data processed by Natural Resource Canada's *Precise Positioning System* (Natural Resources Canada, 2019).

3.2.1 Spontaneous Potential

Over the course of this research three different survey designs were introduced to acquire SP data over the Gullbridge Dam. SP data was collected over two parallel lines along the top of the dam between June 19th and 20th, 2016. On July 18th, 2016, a repeat line of the June surveys was conducted over the spillway in the south. On July 14th, 2018, SP data was collected along a grid consisting of 5 lines centered over the seep area. The field procedures and equipment used differed slightly between the three trips given their different objectives.

Figure 3.12 displays a schematic of the general field setup for an SP survey. A base station is established at the beginning of a line in an area where cultural disturbances and tampering do not pose a problem for obtaining data. The rover is moved from station to station along a survey line or grid and placed in a small depression in the surface dug by

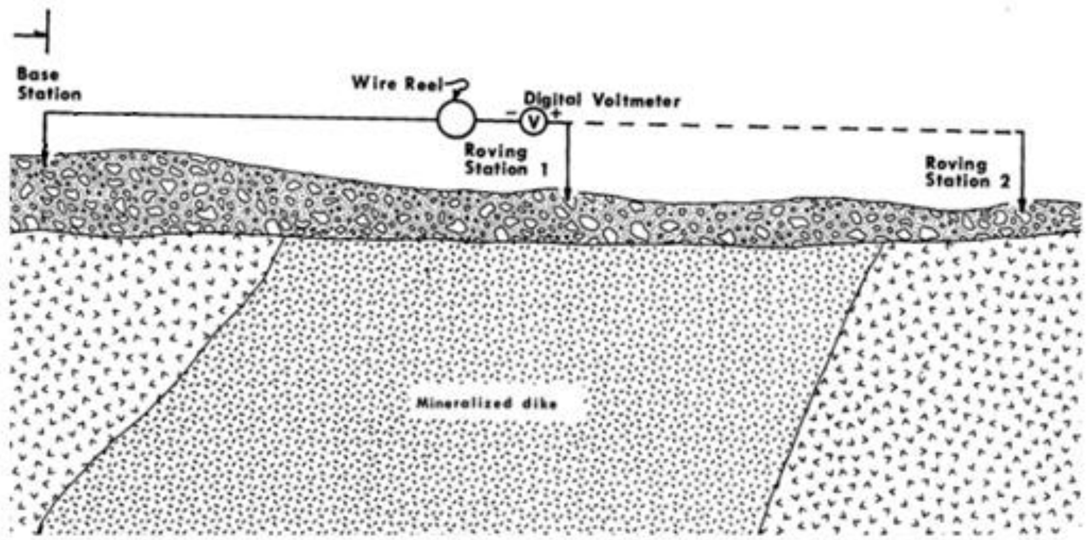

Figure 3.12: Example of SP survey set-up over a mineralized dike (Corry, DeMoully, & Gerety, 1980).

the surveyor to ensure the electrode has good contact with the ground (Corry, DeMoully, & Gerety, 1980).

This study deployed both commercial SP electrodes and electrodes of a different design built by Nicholas Lynch as a part of his B.Sc. (Honours) project under the supervision of Alison Leitch.

The commercial electrode pots used consisted of plastic pots containing a copper conducting rod submersed in a copper-sulfate solution. They make contact through a porous porcelain base that effectively couples the electrodes to the ground establishing an electric connection over a wide area, reducing unwanted contact potentials generated between the electrode and the ground (Zogala, Mendecki, Zuberek, & Robak, 2012).

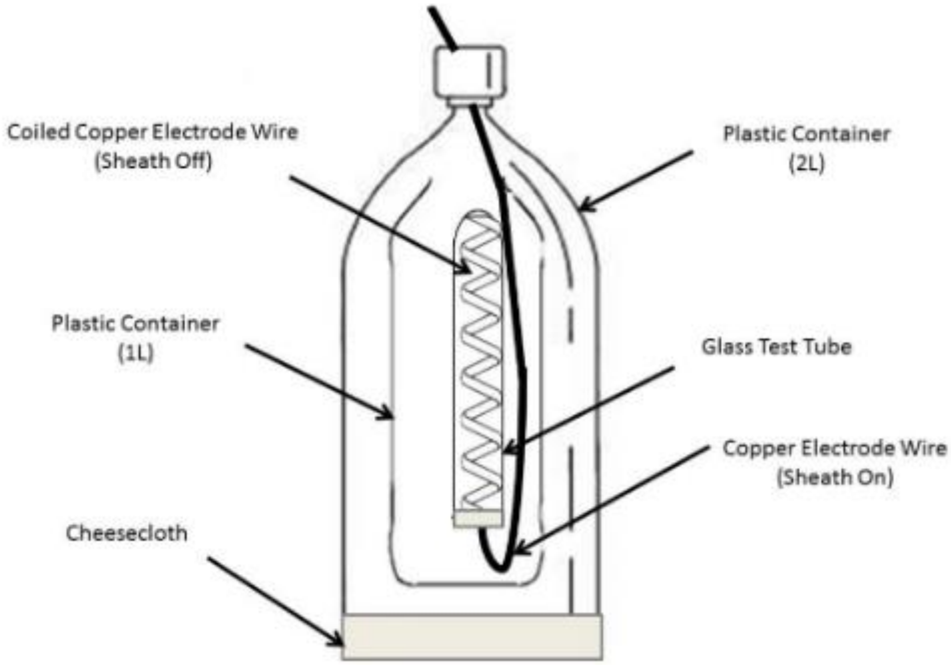

Figure 3.13: Diagram of kaolinite clay/$CuSO_4$ SP electrode pot (Lynch N. , 2017).

A special clay electrode manufactured by Nicholas Lynch following a design provided by Dr James MacRae from Melbourne's RMIT University was used for the majority of the SP surveys (Figure 3.13). This electrode consists of a 2L plastic bottle outer shell with the base cut and sanded, a second 1L plastic bottle inside the shell containing a coiled conducting copper wire encased by a glass test tube, and a connecting copper wire fed through the top cap of the bottle and connected to the coiled wire. The electrical connection with the ground is established with kaolinite clay immersed in $CuSO_4$ solution. A cheese cloth is wrapped around the bottles base and serves as a semi-permeable membrane for the material establishing ionic contact (Lynch N. , 2017).

Figure 3.14 indicates the survey equipment and field setup used during the June 2016 trip to acquire 151 self-potentials measurements over two survey lines labelled SP Line 1 (nearest the wetland) and SP Line 2 (nearest the reservoir) collected S-N extending 760 m along the embankment. The equipment used in June 2016 includes two clay rover electrodes, a clay base station electrode, a wire spool with two wires measuring a total length of 195 m, a Keithley 2700 desktop digital multimeter, and a laptop computer that displayed electrical potential measurements. A tape measure was used to mark each of the survey stations at a spacing of 5 m along each line, and blue flags were used to mark each station. The station coordinates were acquired with a Garmin Handheld GPS. Note the

Figure 3.14: Equipment used in SP surveys over the Gullbridge Dam during June 2016 research.

rover electrodes are not visible in Figure 3.14. Andrew Blagdon is observed standing in the distance moving the rover pots from station to station while Nick Lynch (not shown) recorded measurements near the multimeter. The black commercial pots were deployed to measure any voltages produced by telluric currents in the region. It was determined there was little geomagnetic activity during the survey period. Therefore, the correction for telluric drift was negligible (Corry, DeMoully, & Gerety, 1980) (Burr, 1982).

Each 755 m line was completed in 4 S-N "sections" given the limited length of the wire, between June 19th and 20th, 2016. Sections 1-2 were completed on the first day. Section 1 consisted of 38 measurement stations spanning 190 m in length over both lines. Section 2 consisted of 37 measurement stations (39-75) which ran from 195-375 m along the extended survey line. Section 3 consisted of 38 measurement stations (75-112) extending from 380 m – 565 m of the previous line. Section 4 consisted of 39 measurement stations (113-151) and continued from section 3 at 570 m – 760 m along both lines.

During the initial field set up for each "section" extension in June 2016, a single base station was connected to the negative terminal of the volt meter by the yellow wire around the spool on the far right (Figure 3.14). This base electrode was positioned at a location centered between the last stations of the previous lines, rather than being placed over the positions of the last stations of the previous lines as recommended. This means that there may be a small offset in the readings between each section.

The rover pots over each survey line were connected to the positive terminal of the volt meter one at a time by the red wire along the spool on the far right (Figure 3.14), and reeled along each line at a station spacing of 5 m. Once the roving electrode was carefully placed in the ground, the SP operator used hand signals to contact the base station operator to ready for a measurement. The measurement was recorded both digitally and in a field book at time-intervals of up several minutes to allow the electrodes to stabilize, and the roving electrode was moved to the next station. After each measurement, the red wire around the spool on the far right (Figure 3.14) was disconnected from the rover and moved to the rover on the corresponding station of the of the adjacent survey line. Both rovers used this same wire. This process was repeated until the end of the wire was reached, and a secondary base station established.

Immediately before and after each line, or whenever the base electrode was moved to another location, a measurement of the pot drift was made using the normal polarization set up. The pot difference in this study were established by placing both pots within proximity of one another in a copper sulfate tote bath and recording a value of potential difference at the beginning of each line and at the end of each line. This allows the interpreter to determine the exact amount of pot drift that has occurred so it may be removed from the dataset. The drift voltage should be less than +/- 5 mV. (Corry, DeMoully, & Gerety, 1980).

On July 18th, 2016 repeat measurements were conducted, as a quality check, between L2+35 to L2+255 over the spillway in the south using a station spacing of 5 m. The equipment used for this survey consisted of a rover and base clay electrode pot, two 220 m long wires attached to a spool, and a fluke handheld digital voltmeter. Measurements were recorded when the multimeter stabilized. The base station was located on station L2+30 of the previous June survey. No pots were deployed to monitor telluric drift during this survey.

On July 14th, 2018 SP surveys were conducted over a grid consisting of 5, 60 m S-N lines (y-lines) centered over the seep area. The rover pot used over this grid was connected to a base electrode located on the center of the grid (0, 0).The station spacing along each line was 2 m with exception to the easternmost line nearest the reservoir, in which 4 measurement stations were collected over a 60 m S-N line. Each of the y-lines was separated by a distance of 5 m.

The equipment used in July 2018 consisted of clay electrodes connected through a Fluke handheld digital voltmeter. Figure 3.15 displays the clay rover electrode attached to

Figure 3.15: Clay electrode pot connected to a multi-meter over Gullbridge.

the Fluke multimeter over a measurement station of the grid. The electrodes were connected to the multimeter by a long single-stranded house wire with a banana plugs at the multimeter end and a banana or alligator clip at the electrode end.

The station drift over each of the stations $\Delta V/\Delta t$ was recorded in the survey field book. The 'drift' referred to here is the amount of change with time between the first two readings at each station, which were taken every 30 seconds (ΔV/min). The rover electrode was allowed to sit for as little as 50 seconds and as long as 14 minutes depending on how long it took the electrical potential to stabilize over that particular area. It was apparent that this was greatest where the SP was changing in space. Once the potential stabilized over two readings the measurement was recorded. The difference between the first reading at a station and the last reading of the previous station was also recorded. It was thought that this may be linked to the drift, but this was not apparent and therefore these measurements were not included in the results.

3.2.2 Magnetics

The equipment used for this survey was a GEM GSM-19 Overhauser magnetometer (Figure 3.16). The gradiometer back-pack configuration consists of two magnetic sensors mounted on a pole connected to a backpack carried by the surveyor. The instrument works as both a magnetometer collecting total magnetic intensity (TMI) data in nT, and a gradiometer collecting vertical magnetic gradient (VMG) data in nT/m. The surveyor monitors a hands-free console (strapped to the backpack) that records up to five readings a

Figure 3.16: Equipment used in magnetics survey. This picture was taken on a separate field trip in Gros Morne, NL captured in July 2017.

second. The magnetometer also has an integrated GPS option that records the surveyor's location across survey transects.

The magnetometer has a 'walkgrad' function where the surveyor walks along the survey line as the magnetometer continuously collects high sensitivity data at discrete time intervals, accompanied by a corresponding GPS measurement (GEM Systems Inc., 2008). This method is practical for long survey distances such as the Gullbridge dam. The cycling time chosen for the surveys at the Gullbridge site was 0.5 seconds. A graph of TMI data is produced on the console in real-time, allowing the surveyor to identify magnetic anomalies at the instant they are measured by the magnetometer. The console allows the surveyor to create fiduciary markers over areas of interest on the real-time graph. The gradiometer sensors are separated vertically by a distance of 56 cm. The gradient is calculated from the difference in the TMI between the two sensors.

A base station GEM GSM-19 Overhauser magnetometer was established in the southern section of the dam to monitor diurnal variations and disturbances in magnetic activity. The base station must be positioned in a quiet area free of cultural noise. The southern section of the dam was determined to be the best location due to the lack of human activity, as locals occasionally would drive over the embankment using all-terrain vehicles. During the survey setup the rover and base station consoles were time-synced in Greenwich Meridian Time ensuring there was a correlation in temporal variations of the magnetic field and the ambient local field. The base station was programmed to obtain a total magnetic field measurement every 4 seconds (Riddihough, 1971; Conrad, 2011; GEM Systems Inc., 2008).

The magnetometer utilizes an A/C filter used to remove unwanted noise associated with electrical signals normally set to 60 Hz. However, due to the remote location of the Gullbridge Dam this filter was not necessary.

A background magnetic field value (International Geomag. Ref. Field for a point in the survey area) was programmed into the modem during the initial tuning of the magnetometer. The regional background field at the time of surveying for any area located in Canada can be found on the Natural Resources Canada website. Anomalous values in the local total magnetic field were then recorded with respect to the regional background field.

A total of 2 survey lines were conducted along the length of the Gullbridge Dam. Line 1 is ~ 816 m in length and is closest to the downstream slope of the tailings embankment, while Line 2 is a total length of ~ 790 m and is closest to the tailings pond. The location coordinates were acquired by an integrated Garmin GPS system every 1 s. Mag. Line 1 and 2 are coincident with SP Line 1 and 2. Line 1 was collected from 18:34:16 – 18:44:54 for a duration of 10 minutes and 37.5 seconds. Line 2 was collected from 18:22:22 – 18:33:17 for a duration of 10 minutes and 55 seconds.

3.2.3 Direct-Current Resistivity and Induced Polarization

Equipment

The equipment used for the DCR method is indicated in Figure 3.17. An Iris Instruments Syscal Junior Resistivity Meter was used to compute values of resistivity and chargeability. The resistivity unit has a maximum voltage of up to 400 V, a maximum current of 1.250 A and a maximum power of 100 W using a 12 V battery (Geomatrix Earth Science Ltd., 2021). Two 120 m long multi-core cable segments were connected to the control box, and were laid out one on each side of the control box with call-out connections supplied at every 10 m of cable. A stainless-steel electrode was attached to each call-out using a short length of wire with a bull-dog clip at each end. Each multi-core cable accommodates 12 electrodes. There is a great advantage of using the automated system with the multicore cables, as it is far less time consuming than a mode of operation where

Figure 3.17: DCR survey setup over the Gullbridge Dam. Note Andrew Blagdon sleeping during the survey. Depending on the sequence used, some DCR surveys can take up to 45 minutes.

data is logged manually as the cable is moved from electrode to electrode. Electrodes were hammered into the ground at a chosen interval (≤ 10 m) in a straight line. As mentioned in section 3.1.3, each VES requires a quadrupole (4 electrodes) which are arranged in sequence along the multi-core cables at a designated spacing. The control box can be programmed to take a sequence of measurements using different combinations of the 24 electrodes depending on the specified array type. With the exception of the June 2016 surveys, an external power source option was utilized: the resistivity unit was connected to a 12V car battery by alligator clips to increase the current signal to 2 A. However, it is uncertain whether the unit could inject 2 A of current into the dam given the high contact resistance between the current electrodes and the sand/gravel. To ensure minimal contact resistance associated with the dry, highly resistive materials of the upper 2 m of the dam, the electrodes (30 cm long) were driven into the dam crest as far as possible, and water from the tailings pond and in some cases copper-sulfate solution was poured over the electrodes to establish electrical contact with the ground. It is important that the machine be sheltered from extreme heat that could overload the console and reduce the quality of data recorded. This was done so by means of an umbrella on a couple of occasions.

Each programmed sequence of measurements was taken using a 24 electrode “spread” over two multicore-cable lengths. Given the limited length and call-out connections of the cables, to extend the length of the survey it was carried out in a number of segments. As an example, Figure 3.18 displays a DCR survey consisting of two segments for a total of 36 electrode positions. Rather than moving the entire spread, only the first half was moved to ensure there was significant overlap of data (i.e. quadrupoles between electrode 12 and 24). For the November 2016 2 m DCR survey, there was no overlap between the two. In contrast, during the June 2016 5 m Wenner DCR survey, the

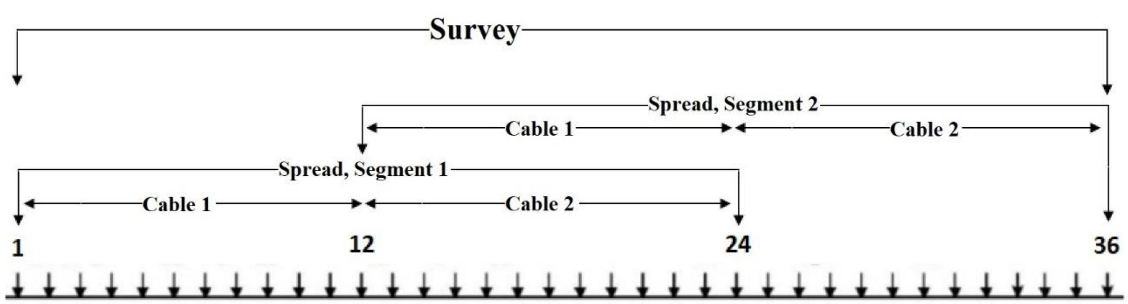

Figure 3.18: Illustration of DCR/IP spreads, segments and survey parameters.

spreads were 115 m long and 8 electrodes were advanced between each segment so that the segments overlapped 75 m. In June 2017, the 2 m Central Schlumberger survey was extended 12 m to the north and 12 m to the south which meant repositioning 6 electrodes of the spread for each extension.

Using IRIS software Electre II, survey sequences were programmed into the Syscal Junior Resistivity Unit using specific survey parameters based on the intended subsurface target. The instrument can store up to 5 sequences at a time. Figure 3.19 outlines the survey sequence design window corresponding to a Schlumberger survey carried out on June 25th, 2017. Note that this was not a "Wenner-Schlumberger survey as Figure 3.19 suggests,

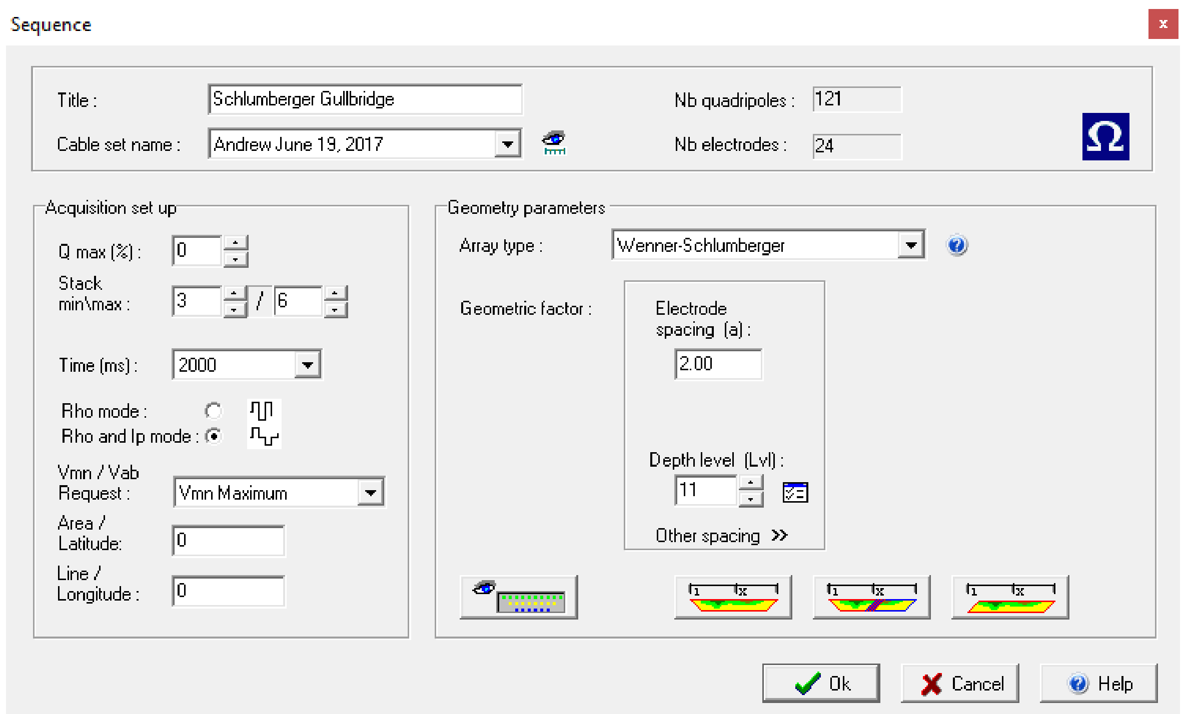

Figure 3.19: Automatic sequence creation window in Iris Instruments Electre II DCR software.

because no extra “b-spacings” were added to the array, as can be done in the “Other spacing” option.

Table 3.3 indicates the parameters used for each survey conducted over the Gullbridge TMA between June 2017 and July 2017. A minimum number of 3 stacks (repeat measurements) were conducted. If the standard deviation of these measurements was greater than Q_{max} (set to 0%, presumably meaning <0.5%), up to a maximum number of 6 stacks would be carried out. Q_{max} was chosen to be 0% to ensure reliable measurements. Injection times were between 1000-2000 ms. Longer cycling times provide the opportunity for transients due to IP effects and steady values of apparent resistivity to be better

Table 3.3: Parameters used for DCR/IP surveys conducted over the Gullbridge TMA. All DCR/IP surveys deployed a 24-electrode system using the following parameters not displayed: Q max (%) = 0, Stack (Min./Max.) = 3/6, and V_{MN}/V_{AB} = V_{MN} Maximum.

	June 2016 (Along Dam)	November 2016 (YLINE2)	June 2017 #1 (2 m Central)	June 2017 #2 (2 m Central, 2 m East)	June 2017 #3 (4 m Central)
Array Type	Wenner	Schlum.	Wennner	Schlum.	Schlum.
Injection Time (ms)	1000	2000	2000	2000	2000
Rho/IP	Both	Both	Rho	Both	Rho
Electrode Spacing (m)	5	2	2	2	4
Depth Level	7	5	7	11	11
Quadrupoles	84	85	84	121	121

measured. The "Vmn/Vab Request" refers to the user's preferences for the amount of voltage across the electrodes, and therefore relates to the total output of the transmitter. The V_{MN} maximum option ensured the highest voltage across the potential electrodes, thus the greatest signal to noise (and the largest drain on the batteries) (Iris Instruments). The positions of the electrodes (lat./long.) were not programmed into the survey.

DCR Survey Along the Dam Crest (June 2016)

In June 2016, a Wenner DCR survey was carried out over the length of the Gullbridge Dam crest (Table 3.3). Each segment consisted of 24 steel electrodes spaced at a station spacing of 5 meters over a total length of 115 m. The full survey consisted of a total of 18 segments measuring a total length of 795 m. Both measurements of resistivity and chargeability were recorded, and the resistivity meter was set to a depth level of 5, meaning that the a-spacing was varied by a factor of 5 from 5 m to 25 m.

DCR Surveys over the Seep Area

In November 2016, a 70 m long Schlumberger DCR survey consisting of two spreads (one extension to the north 24 m) was conducted over the seep area using an electrode spacing of 2 m (Table 3.3). The survey line was designated YLINE2 as it was collected over a line of the same name for another survey method (GPR).

In June 2017, 3 Schlumberger DCR surveys were conducted over the seep area (Table 3.3). The first "2 m Central" survey line consisted of 3 spreads and was conducted over the center of the dam crest using an electrode spacing of 2 m. The first spread was extended 12 m to the south and 12 m to the north for a total length of 70 m, requiring a total of 6 electrodes picked up and moved north and south of the original spread. A Wenner DCR survey was also conducted over the original 2 m Central spread..

A second parallel spread was conducted approximately 5 m to the east of the survey over the center of the dam. This spread had a total length of 46 m. This survey line was designated “2 m East” (Table 3.3).

A final DCR line, consisting of one spread, was conducted using an electrode spacing of 4 m over a spread distance of 92m, overlapping with the 2m Central line. The centre of this spread was 5 m south of the centre of the 2m line. The northernmost electrode was in the same location as the northernmost electrode of the 2 m central line, while the southernmost electrode was 22 m to the south of the southern end of the 2m line. This survey line was designated “4 m Central” (Table 3.3). In total there were 4 Schlumberger spreads carried out over the seep area.

The DCR surveys conducted on June 25th, 2017 did not extend over the old stream. Therefore, it is not possible to use the DCR method to characterize a suspected internally eroded area in the embankment over this area.

3.2.4 Ground-Penetrating Radar

GPR surveys were carried out over the Gullbridge Dam using a Sensors and Software pulseEKKO PRO GPR (Figure 3.20). The assembly consisted of a digital video logger/control module (DVL), one of three pairs of receiver and transmitter antennas,

Figure 3.20: GPR survey over the Gullbridge Dam in June 2016 deploying the pulseEKKO Pro GPR Smart-Cart assembly 100 MHz antennae setup.

cables and power supplies, usually mounted on a “Smart-cart”. The 50 and 100 MHz antennas used two fiber optic cables, and four 12 V lead based batteries used to power the transmitter and receiver. The 250 MHz transducers used coaxial cables instead of fibre optic cables. A handheld Garmin GPS attached to the DVL was also used to mark coordinates along the GPR transect. During surveys conducted over grids, RTK markers were positioned at the start and end of the survey lines.

GPR survey data were collected over both the wetland and the embankment Over the wetland individual survey lines were collected and stored as a set of lines in a particular directory. Over the embankment, data were collected using both survey line and grid acquisition. Grid acquisition stores a set of x and y-oriented survey lines beginning from a chosen origin and given fixed lengths and line separations.

A CMP/WARR survey commonly referred to as a “Common Mid-Point” survey was deployed in the bog area southwest of the embankment in June 2016 using two 100 MHz antennae to determine an accurate radar velocity for a GPR pulse travelling through the wetland area. Survey tape was laid out over a flat area of the bog, and the antennae, initially next to each other, were moved outwards over a total separation of 20 m. The step-size was 0.2 m and the CMP was carried out until the amplitudes of the reflections yielded were too weak to extract reliable velocity data.

Orange discoloured tailings water was observed flowing from the base of the dam near BH5 (see Figure 2.3, and to the right of label "Wetland” in Figure 1.1) during the July 2016 research trip. Drone imagery and field notes indicate the majority of reservoir water is pooled in the north between BH4 and BH6 resulting in a concentrated pressure load along the upstream slope. This is suspected to be a vulnerable region of the dam. A small, 10m×20m GPR grid was deployed on top of the dam over this area of observed leakage. The grid was collected using the 100 MHz antennae and consisted of 21W-E oriented Xlines and 11 S-N oriented Ylines with meter spacings. The origin of the grid (0,0) was originally in the northeast corner but was reassigned to the southwest to conform to labelling conventions used for other surveys. On this same trip in July 2016 the CMP profile was carried out in the bog area over a total length of the 20 m. This survey was also carried out using the 100 MHz antennae. GPR data was also collected along 3 parallel lines along the length of the dam approximately 10 m apart using the odometer wheel and 100 MHz antennae assembly with an assigned time-window of 200 ns.

. In September 2016 two GPR survey lines were acquired over the impoundment. These were both collected with the 100 MHz antennae, and a 400 ns time-window. A GPR survey was conducted S-N over the entire length of the Gullbridge Dam (973 m) approximately over the centre of the crest (GPR LINE00). A second survey was collected SE-NW for ~ 138 m, over the limestone barrier directing water from the spillway into the wetland at the outflow location (and proceeding along the old stream impression (GPR LINE05). The surveys were collected in free-run mode using the GPS feature, so the horizontal distance scale on the profiles, initially calculated based on an assumed, constant step-size per unit time, had to be corrected using the appropriate processing tools and a re-calculating the step-size based on GPS information.

In November 2016 GPR data was acquired along a (50x20 m) grid deployed over the seep area just north of BH3 using the 50 MHz antennae. The grid consisted of 5 S-N y-lines and 12 W-E x-lines. The line spacing in both directions was 5 m. The grid is approximately centered over the seep area. The origin of the grid (0,0) is in the SW corner.

In February 2017 GPR data was collected along 4 survey lines collected in the wetland area. Figure 3.21 displays the winter GPR survey setup in which the GPR antennae were within a large sled towed over the wetland by a snowmobile.

These surveys used the 100 MHz antennae with a 500 ns time-window. The surveyor was positioned in the center of the sled with an antenna on either side held at fixed

Figure 3.21: February 2017 Winter GPR assembly. Top: The author setting up the 250 MHz GPR transducers in the sled. Bottom-right: field assistant Joey Pittman navigating the snowmobile, towing the author operating the GPR. Note the 100 MHz antennae were used in the February 2017 research trip, and the top image was captured during a trip unrelated to this project.

positions, while operating the stationary DVL approximately at the center of the sled on the surveyor's lap. Not all lines collected on this trip were salvageable, as a handheld GPS positioned on the receiving antennae introduced low-frequency noise into the dataset over some lines. However, 4 survey lines (GPR LINE06-LINE09) were recovered with relatively high signal-to-noise.

In June 2017, a 20x140 m GPR grid was deployed over the Gullbridge Dam seep area. GPR data was collected along the grid using every available antennae frequency (50, 100 and 250 MHz). The GPR grid was originally 20x100 m with the origin (0, 0) in the southwest, and was extended another 20x40 m in the north on the last day. The grid consists of 28 20 meter W-E x-lines and 11 140-meter S-N y-lines.

3.2.5 Electromagnetic Ground Conductivity

Two models of controlled source, loop-loop electromagnetic equipment were used for conducting electromagnetic geophysical surveys over the Gullbridge TMA, a Geonics EM31-MK2 frequency-domain ground conductivity meter (Geonics Ltd., 2013) and a Geophex Limited GEM2, a portable multi-frequency electromagnetic sensor. Both are suited for shallow surveying. Frequency-domain EM surveys measure the complex ratio of the secondary induced field and the primary field generated by the transmitter, and from these the apparent electrical conductivity and (sometimes) the magnetic susceptibility of the top few meters of the ground can be found. For both instruments the penetration depth of a few metres is determined by the coil spacing s between the Tx and Rx (Subsurface Geotechnical, 2016).

The EM31-MK2 operates at 9.8 kHz. The measurements are operator-triggered, and the device can be rotated about its axis to take measurements at HMD and VMD orientations. Except during the July 2018 trip, measurements were taken in both the VMD and HMD orientations. The instrument was transported at hip-height throughout the entirety of the survey. Figure 3.22 displays an image of the author surveying with the EM31-MK2 in the wetland adjacent to the Gullbridge TMA.

The Geophex GEM2 system collected measurements at a constant time-interval using three different frequencies of 990 Hz, 6.21 kHz and 39.03 kHz. Data acquisition was controlled using a handheld data logger attached to the GEM2 board.

Figure 3.22: Andrew Blagdon conducting an EM31-MK2 electromagnetic ground conductivity survey in the wetland adjacent to the Gullbridge TMA.

Each instrument was carried along the survey line using a shoulder strap. Station positions were recorded either by a Topcon Hiper V DGPS or a hand-held Garmin GPS, operated by a field assistant following one station behind the EM system operator.

Table 3.4: Table of survey parameters used for EM31-MK2 surveys conducted over the Gullbridge Impoundment.

	Date	Boom Orientation	Dipole Orientation	Instrument Height	Station Spacing (m)	Survey Length (m)
GEM LINE00	Sept 2016	S-N	HMD	Hip	~0.5	810
EM LINE00	Sept 2016	S-N	Both	Hip	5	817.5
Base of Dam (TDS)	Feb 2017	S-N	Both	Hip	5	180
EM YLINE00, 05 and 09	June 2017	S-N and W-E	Both	Ground	5 (S-N) and 2 (W-E)	140 (S-N) and 20
EM XLINE00, 25, 50, 75, 100, and 120	June 2017	S-N and W-E	Both	Ground	2	20
EM LINE01	June 2017	S-N	Both	Hip	5	530
EM LINE02	June 2017	S-N	Both	Hip	5	550
EM LINE03	Nov 2017	S-N	Both	Hip	5	280
EM LINE04	July 2018	S-N	VMD	Hip	~6-7	~374
EM LINE05	July 2018	S-N	VMD	Hip	~6-7	~201

Table 3.4 indicates the survey parameters for the EM31-MK2 survey lines. In September 2016, GEM2 LINE00 was conducted along the center of the Gullbridge Dam the day before EM LINE00 was carried out approximately over the same line. On June 30th, 2017, EM surveys were carried out over the 5 most southerly (W-E) x lines of the June 2017 GPR grid. EM LINE TDS was collected along the southern toe of the downstream slope and crosses over the area containing water from the spillway. EM LINEs 01, 02 and 03 were carried out in the wetland over a partially frozen survey platform, while wetland lines EM LINEs 04 and 05 were carried out in the following summer.

An EM31 ground conductivity line was collected over the tailings reservoir on September 25th, 2016. The survey line was ~ 150 m long beginning on the northern edge of the embankment walking south onto the mining waste. However, only a short distance over the reservoir was achieved due to the loose nature of the tailings at the surface. Coordinates were not acquired over this survey line. The survey line was carried out with the intentions to test the response of the EM31-MK2 meter to tailings material.

EM LINEs 01 to 03, November 2017(fall)

Ideal ground conditions for surveying over the wetland required a complete freezing of the ground, as intervening streams and ponds made surveying a difficult task. At the Gullbridge site between November 9th-11th, 2017 the ground was not frozen and therefore only 3 survey lines (EM LINEs 01,02 and 03) were completed over the wetland.

Over this two day research trip, temperatures at the field site dropped as low as -4^0 C and were accompanied by strong gusts of wind. The survey team was often drenched in water in the wetland and flowing from the reservoir. Large ponds and meandering streams running W-E through the wetland made some station locations impossible to survey without damaging equipment, therefore some stations of survey lines were left out.

The stations over EM LINE01 and LINE02 were measured at 5 m increments using a survey tape to mark survey station locations. Each of the lines was separated by a distance of ~45 m on average. Station coordinates were obtained using a TopCon Hiper V RTK positioning system.

Marking survey stations was not an easy task over the wetland due to the heavily saturated bog soil. Over LINE02 the last 5 survey stations were not marked with an RTK waypoint. Stations along EM LINE01 and LINE02 were marked at 5m intervals using a survey tape. However due to particularly rugged terrain, survey stations along LINE03 were paced out. It was determined using linear interpolation that these station intervals were variable, sometimes as large as 8 and 9 m.

EM LINE02 is the longest of the wetland survey lines at 550 m. It lies over several treacherous surface features making obtaining measurements difficult. Such features include two small retaining ponds containing thickened sub-aerial copper tailings. At stations L2+10 & L2+15, water in the pond was estimated to be over a meter deep. Ground conductivity measurements were not acquired over stations L2+405-L2+425 and L2+450–L2+460 due to deep water.

RTK static data from the first day was used to perform base-station corrections along LINE01 and LINE02, and static data from the second day was used to perform base-station corrections on coordinates along LINE03. The base-stations were in the approximately same location but there a 0.9 m difference in height.

EM LINEs 04 and 05, July 2018 (summer)

EM LINE04 and LINE05 were collected in the wetland using only the VMD coil orientation. These lines were collected in the summer, when a heavily saturated bog material made surveying difficult. The stations were spaced using walking paces. Andrew Blagdon recorded the measurements operating the EM31-MK2, Dr. Alison Leitch marked the stations on the RTK, and Jacob Newman took notes and recorded values in a field book.

3.2.6 Bog and Water Sample Analysis

On July 15th, 2018 2 bog samples were collected with the Memorial University Geography Department's bog corer in the wetland and two water samples were collected using plastic bottles from the seep outflow area and the tailings reservoir, respectively.

Bog site #1 consisted of an initial core 1.10 m deep, starting at the surface, and a deeper core 1.2 m long, for depths 0.85 to 2.05 m. The cores were divided up into 5 sections, each of which was extracted using a long-bladed knife slipped under the sample, placed in a thick plastic sample bag, labeled, and sealed with electrical tape. The samples were soft, dark brown, organic and saturated with water, however cohesive. Little water was lost from the samples during extraction. Bog site #1 is located ~ 15 m southwest of the seep area. Figure 3.23 displays Andrew Blagdon and Jacob Newman collecting a bog sample with the probe instrument over bog site #1.

Figure 3.23: Andrew Blagdon and field assistant Jacob Newman collecting a bog sample over bog site #1 using a bog probe instrument. The top connection bar was used to extend the depth of the probe by interlocking caps and grooves. The bottom probe originally became stuck and required removal by hand. Note the drainage system placed over the seep in the background.

Site #2 was located over an area of shallow bog further from the embankment, ~ 200 m west of the embankment in the wetland. The corer penetrated only to a depth of 0.69 m, and only the top 0.36 cm of highly organic, greenish material was extracted.

Samples from Sites #1 and #2 were collected between 1 and 2pm, transported back to Memorial University at room temperature and were placed in a refrigerator at 10 pm on the same day.

At the time of the visit, on both 14^{th} and 15^{th} of July, water was observed emanating from the seep area over the filter fabric. Water samples were taken, and the flow rate measured on 15^{th} July 2018.

Two ~500 ml samples of water were collected in drinking containers. The containers had been used for the last week to hold drinking water for the field. They were rinsed out several times in the sampling water before being filled. A blue water bottle was filled with water from the tailings dam, just to the east of the seep site. A dark grey personal water bottle was filled with water running from the seep. The bottles were transported back to Memorial at room temperature and then placed in a refrigerator at 10 pm.

After collecting the samples, the flow rate from the seep was measured. To do this, water was constrained to flow from one low point in the filter fabric by propping up the lining on both sides with large rocks, and the bog underneath this point was excavated to allow space for a 20 litre bucket. The bucket was placed under the flow and allowed to fill for 2 minutes and 7 seconds. The water level in the bucket was then measured inside the bucket to be 23.3 cm from the bottom and 13 cm from the top.

On 17^{th} July 2018, aliquots of the water samples were analysed by John Allen in the Solution ICP-MS facility at Memorial University, and the pH of the water in the water samples was measured by Melissa Cook, PhD student of Dr Penny Morrill. On 19^{th} July

2018, the electrical conductivity of the water samples was measured by Leanne Fisher-Power, MSc, in Dr Tao Cheng's Hydrogeology Laboratory at Memorial University.

3.3 Data Processing

3.3.1 Spontaneous Potential

The processing techniques for the spontaneous survey method are primarily the base tie-in correction, the pot drift correction, the telluric drift correction (section 3.1.1.) and (in some circumstances) smoothing. In SP surveys, the drift and base tie-in corrections are added to the measured voltage (equation 3.22) (Corry, DeMoully, & Gerety, 1980; (Burr, 1982).

$$V_{abs} = V_{norm} + C_{base} + C_{drift} \tag{3.22}$$

The base tie-in correction is applied when the base electrode is moved to ensure all measurements have a common reference. The potential difference between base station locations is added to the dataset each time the base electrode is moved to a new location (Corry, DeMoully, & Gerety, 1980).

To monitor the effects of pot drift and telluric currents (section 3.1.1.), repeat measurements are generally required (Wynn & Sherwood, 1984). The drift error correction for each station can be calculated by interpolating the potential difference as a function of time between the beginning and end of the survey line, or measuring the pot drift before and after each line and averaging the total drift over the number of stations of each line (Lynch, 2017). The pot drift should not normally exceed 5 mV.

During the June 2016 SP surveys over the length of the Gullbridge Dam, the pot difference was measured before sections 1 and 3, and after sections 2 and 4 for SP Lines1 and Line 2. The distinct pot drifts were removed from the respective datasets.

Table 3.5 displays the drift measurements recorded through sections 1-2 and 3-4 of the June 2016 surveys. Cells containing “N/A” indicate a pot drift measurement was not made for the particular location.

Table 3.5: Drift measurements and correction calculations along sections 1-2 and 3-4 of SP Lines 1 and 2 collected in June 2016 over the Gullbridge Dam.

Section	Time (hr:min)	LINE1 (Initial) (mV)	LINE1 (Final) (mV)	LINE2 (Initial) (mV)	LINE2 (Final) (mV)	LINE1 Drift mV/st	LINE2 Drift mV/st
1	1:06 PM-5:32 PM	0.80	N/A	0.10	N/A	0.0093 *Station # + 0.80	0.016 *Station # + 0.10
2	6:01 PM-8:13 PM	N/A	1.5	N/A	1.3	0.0093 *Station # + 0.80	0.016 *Station # + 0.10
3	11:10 AM-12:48 PM	1.5	N/A	1.3	N/A	0.0051 *Station # + 2.9	0.0022 *Station # + 1.9
4	1:08 PM-3:16 PM	N/A	3.3	N/A	2.1	0.0051 *Station # + 2.9	0.0022 *Station # + 1.9

The drift correction for each station between sections 1 and 2 was calculated by determining the total drift through sections 1-2 over the duration of each line and dividing by the number of stations. All values were positive, and therefore the correction was subtracted from the normal voltage of all potential measurements. The pot differences indicated in Table 3.5 were all small and made no difference to the interpretation.

Drift corrections were not applied to the July 2018 SP grid data. Base station corrections were not necessary because the base-station at the center of the grid (0,0) was not moved.

3.3.2 Magnetics

The magnetic data collected along the Gullbridge Dam was processed using GEMLink 5.3 software. The TMI measurements were corrected for diurnal drift using base station data collected over the duration of the magnetic surveys, and the residual field was calculated using the average value of the local field measured at the base station as discussed below.

Figure 3.24 displays the results of the magnetic drift collected by the base station during the acquisition of two magnetic survey lines on July 17th, 2016. The surveys were completed in a relatively short period of time: the total drift was approximately 4 nT over 22 minutes and 32 seconds. This makes the diurnal correction almost negligible, but it was nevertheless applied to the dataset.

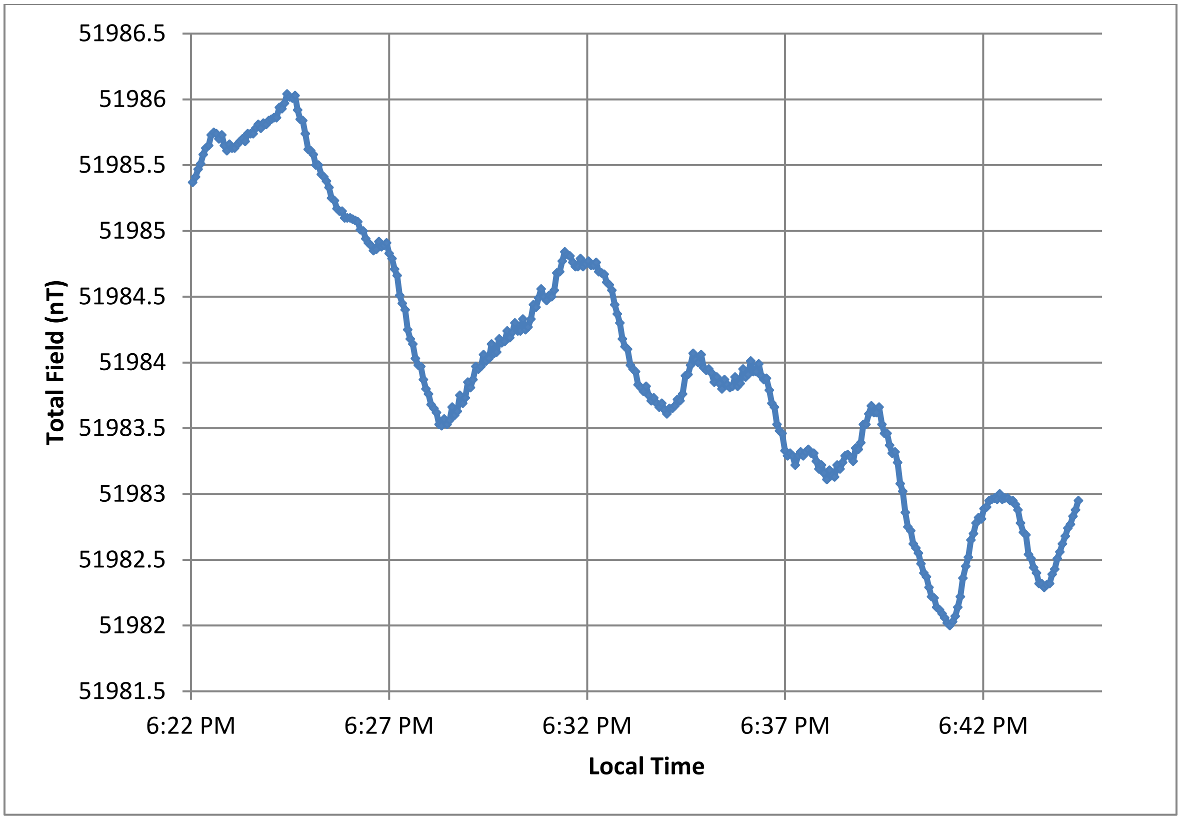

Figure 3.24: Magnetic drift over the Gullbridge Dam on July 17th, 2016.

For most magnetic surveys, it is customary to map the strength of magnetic anomalies relative to the International Geomagnetic Reference Field (IGRF). The IGRF is a data archive of the theoretical undisturbed magnetic field at any point on the Earth. This is particularly useful for tying in the results of localized magnetic surveys to broader surveys (Kearey, Brooks, & Hill, 2002) (GEM Systems Inc., 2008).

To separate the spatial variation in the TMI from temporal drift over a survey area, GemLink 5.3 software corrects the rover magnetic data based on the following equation:

$$\mathrm{TMI}_{(\mathrm{correct},\ x)} = \mathrm{TMI}_{(\mathrm{rover},\ t,\ x)} - \mathrm{TMI}_{(\mathrm{base},\ t)} + \mathrm{TMI}_{(\mathrm{offset})} \tag{3.23}$$

The base station value $TMI_{(base,\ t)}$ at time t is subtracted from the primary magnetic rover value $TMI_{(rover,\ t,\ x)}$ for a position *x* at a corresponding time *t*. Each of the mobile rover readings has an associated time stamp corresponding to the interpolated diurnal field measured at the base station at the time of the reading.

The $TMI_{(offset)}$ variable is a constant offset which is supposed to bring $TMI_{(correct,\ x)}$ values close to the time averaged field. If it is possible to place the base in a location where the time-average field is the IGRF, then $TMI_{(offset)} = TMI_{(IGRF)}$, which for the Gullbridge dam at the time of the survey on July 18th, 2016 was 52,277 nT +/- 152 nT (NOAA geomagnetic calculator). Surveyors generally attempt to place base stations away from known magnetic sources, in regions where the crustal magnetic field is flat, and so more likely to have a value close to the IGRF.

For our surveys, placement of the base-station was dictated by logistical convenience, which turned out to be in an area of low TMI (on a negative anomaly), so that setting $TMI_{(offset)} = TMI_{(IGRF)}$ in equation (3.23) would have resulted in a corrected TMI that was too high.

Since $TMI_{(offset)}$ does not equal the reference field in this study, ideally $TMI_{(offset)}$ should equal the time-averaged base station variations over the Gullbridge region, that is:

$$TMI_{(correct,\ x)} = TMI_{(rover,\ t,\ x)} - [TMI_{(base,\ t)} - TMI_{(base:\ time\ averaged)}] \qquad (3.24)$$

Ideally, to accurately calculate the time-averaged field the base-station should record measurement over several days. Our base-station recorded the local variations of the magnetic field for 1 hour, 19 minutes and 8 seconds, and the rover surveys were completed over 22 minutes and 32 seconds within this time frame. Because the time-variations over a day are typically in the order of tens of nT's, and the IGRF has an uncertainty of +/- 152 nT, it was decided that the $TMI_{(offset)}$ value assigned in the corrections would be the $TMI_{(base,\ averaged\text{-}over\text{-}survey\text{-}time)}$. This value, determined to be 51,986nT (791 nT less than the IGRF), was used as the datum in the final corrections in GEMLink 5.3.

One of the advantages of gradiometer measurements is that they do not require corrections because both sensors are affected equally by temporal variations. Magnetic gradient data represses regional magnetic trends and emphasizes shallow sources and does not require the removal of the Earth's main magnetic field (Mickus, 2014).

Each of the total field and magnetic gradient measurements were recorded with a corresponding Easting and Northing position. The distance along the dam required for generating profiles was calculated using a linear interpolation equation between each coordinate in Excel. The equation used was as follows:

$$\sqrt{(N_2 - N_1)^2 + (E_2 - E_1)^2} \tag{3.25}$$

where N is northing, and E is easting. Each of the distances calculated was then added to each of the subsequent distances to build an approximated distance along the crest of the embankment.

3.3.3 Direct-Current Resistivity and Induced Polarization

Processing of DCR and IP data involved three pieces of software: Prosys, RES2DINV and VES.

The DCR/IP data was uploaded from the Syscal Junior resistivity unit to computer using Prosys, a compatible Iris program capable of generating spreadsheets of resistivity and chargeability data in .txt file format. An example of the 20 first soundings of the June 2016 Wenner survey conducted along the length of the Gullbrige Dam is displayed in Table 3.6. Measurements of SP were deemed unreliable for this survey method.

Table 3.6: Example spreadsheet of DCR data uploaded from Syscal Junior resistivity unit in Prosys processing software. The data columns from left to right include the array type (El-array), the survey method measurement, the electrode positions *A*, *B*, *M* and *N* (m), values of apparent resistivity *Rho* (Ω*m), the standard deviation *Dev.*(%), the chargeability *M* (mV/V), the spontaneous potential *Sp* (mV), the potential between the electrodes M and N *Vp* (mV), and the current flowing between the current electrodes A and B *In* (mA).

	A	B	C	D	E	F	G	H	I	J	K	L	M
1		El-array		A	B	M	N	Rho	Dev.	M	Sp	Vp	In
2		Wenner	VES	0	75	25	50	4544.84	999	0	-50	0.345	0.012
3		Wenner	VES	0	60	20	40	301.76	0	0	-50	11.813	4.919
4		Wenner	VES	0	45	15	30	426.56	0	0	-50	19.15	4.231
5		Wenner	VES	0	30	10	20	684.42	0	0	-50	19.08	1.752
6		Wenner	VES	0	15	5	10	1035.51	0	0	-50	20.275	0.615
7		Wenner	VES	5	80	30	55	161.8	5	0	-50	1.796	1.744
8		Wenner	VES	5	65	25	45	337.2	0	0	-50	5.105	1.903
9		Wenner	VES	5	50	20	35	241.89	0	0	-50	4.81	1.874
10		Wenner	VES	5	35	15	25	639.57	0	0	-50	15.176	1.491
11		Wenner	VES	5	20	10	15	1160.29	0	0	-50	20.253	0.548
12		Wenner	VES	10	85	35	60	614.75	1	0	-50	14.836	3.791
13		Wenner	VES	10	70	30	50	327.31	0	0	-50	5.875	2.255
14		Wenner	VES	10	55	25	40	398.14	0	0	-50	19.989	4.732
15		Wenner	VES	10	40	20	30	525.71	0	0	-50	18.632	2.227
16		Wenner	VES	10	25	15	20	1128.59	0	0	-50	18.044	0.502
17		Wenner	VES	15	90	40	65	395.36	1	0	-50	15.818	6.285
18		Wenner	VES	15	75	35	55	5277.88	999	0	-50	0.067	0.002
19		Wenner	VES	15	60	30	45	338.62	0	0	-50	17.618	4.903
20		Wenner	VES	15	45	25	35	495.36	0	0	-50	20.501	2.6

The pseudo-depth or a-spacing a, the surface location of the mid-point between the potential pair x, and the distance between the potential pair b were calculated in Excel for Schlumberger (Equation 3.26) and Wenner (Equation 3.27) arrays respectively.

$$a = \frac{B - A}{2}, \quad x = \frac{A + B}{2}, \quad b = N - M \tag{3.26}$$

$$a = \frac{B - A}{3}, \quad x = \frac{A + B}{2}, \quad b = a \tag{3.27}$$

As a general rule, values of apparent resistivity with a standard deviation (Dev. column in Table 3.6) higher than 3 % were removed from the dataset.

In this survey (Table 3.6), quadrupoles with larger a-spacings had higher standard deviations. Data for a-spacings greater than 10 m were judged too noisy to be useful. The low signal to noise can be attributed to high current electrode contact resistance. With larger a-spacings the flow of current becomes deeper and spreads out over a larger volume, and there was insufficient battery power at large a-spacings to overcome this issue.

The ‘roll-over’ function in the Electre-II software automatically calculates electrode positions for multiple spreads. However, this function did not work for our equipment, so the positions of the electrodes in additional spreads had to be separately corrected in Excel.

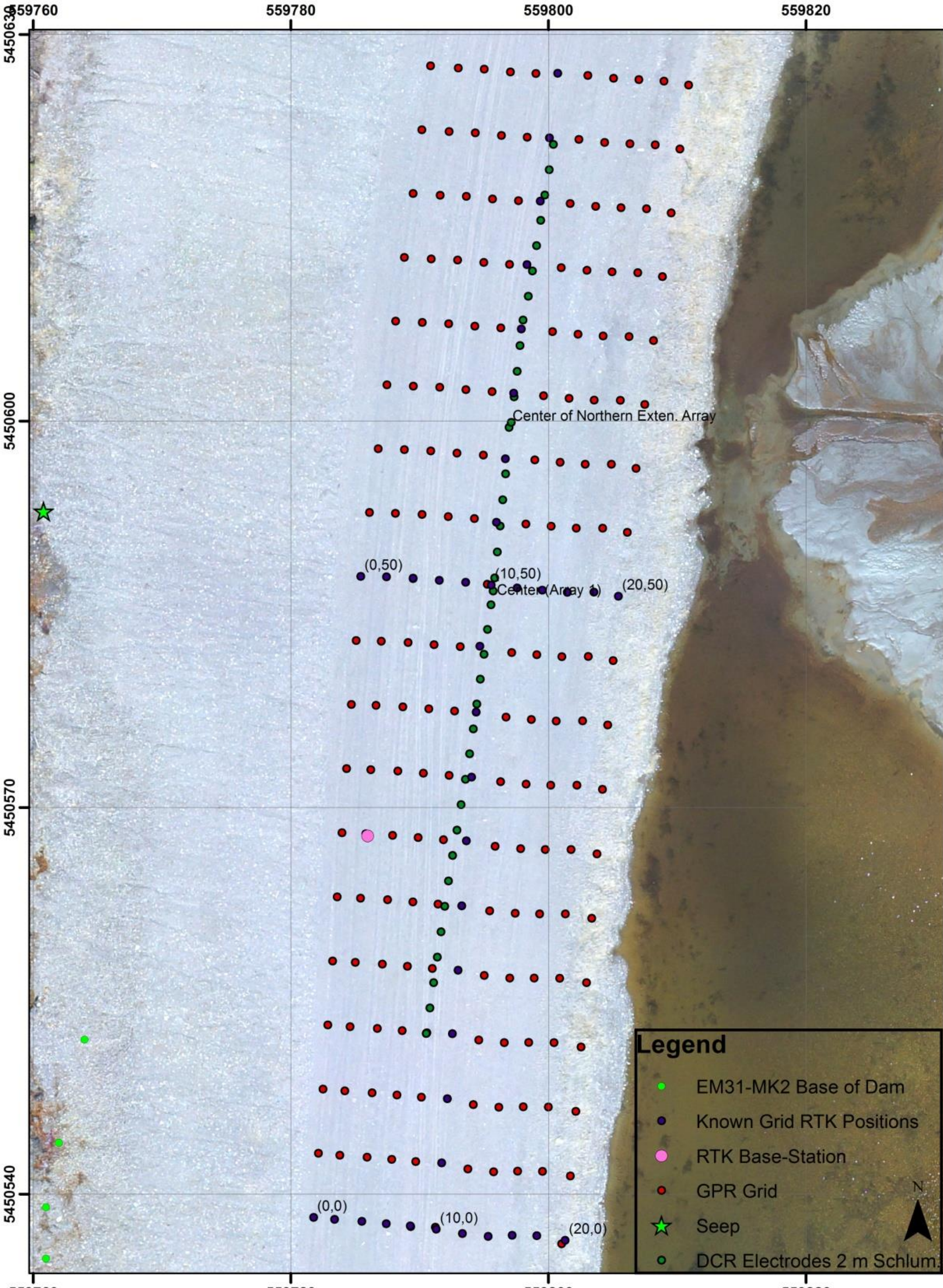

Figure 3.25: June 2017 2 m Schlumberger survey with north extension superimposed over the June 2017 GPR grid.

The June 2017 “2 m Central”, consisted of 3 overlapping spreads. (Figure 3.25) The electrode positions were first determined relative to the southernmost electrode.

To correlate results with other surveys, particularly the GPR grid over the seep, offsets were then added to electrode positions. The most southerly electrode was approximately located over station (8,15) on the GPR grid (see Fig. 3.25 above). Therefore, when formatting the DCR data, 15 m was added to every electrode position.

A DCR Wenner survey was also conducted over the seep area, with electrode positions at the same locations as the 2 m Schlumberger (center) spread. As for the seep center Schlumberger profile, 15 m was added to electrode positions over the Wenner array to correlate positions to the GPR grid.

A 3-point weighted running average was used to smooth out point-to-point zig-zags, which are a common feature of Wenner CSTs due to surface heterogeneities near the electrodes (Reynolds, 1997). The following formula was applied to the dataset:

$$\rho_{a\ smooth(x)} = 0.5 * \rho(x) + 0.25 * (\rho(x-1) + \rho(x+1)) \qquad (3.28)$$

Inversions of DCR-IP survey data measured over the Gullbridge Dam GPR grid were performed in *RES2DINV*. *RES2DINV* is a two-dimensional inversion modeling software produced by Geotomo (Geotomo Software, 2010) . It is important to note that the dam geometry does not perfectly satisfy the 2-D assumption for the inverse modelling code used in RES2DINV as variations in the resistivity structure across the dam are expected, and beyond the dam embankments there are highly conductive tailings on one side and highly resistive air on the other. The 2-D model assumes the subsurface resistivity structure does not change in the direction perpendicular to the survey line. Since the current is flowing in 3-D, the 3-D effect of the embankment geometry, the water table, and buried utilities violates the 2-D assumption of the inversion code leading to distortion of the model and an irregular resistivity distribution resulting in an increased interpretation error (Loke, 2004) (Nhu & Pham, 2018). Since the current is flowing sideways as much as downwards, distortions resulting from cross dam resistivity variations would be more pronounced at larger electrode spacings, and for spreads not at the center of the dam. This is particularly true for a-spacings larger than the width of the top of the dam crest (~20 m). DCR spreads were carried out mainly over the middle of the dam to minimize the effects of the finite dam width.

The software uses a mesh which divides the subsurface into numerous rectangular blocks which are arranged according to the distribution of data points in the apparent resistivity pseudo-section. Thus, the constraints assigned by the program are based on the mid-point of the quadrupole *x*, the a-spacing *a*, and the potential-pair spacing *b.* As an example, the depth of the bottom row of blocks is determined by the largest a-spacing and narrowest b-spacing electrode configuration. (Terraplus, 2001). For the array types used at Gullbridge, the thickness of the first layer of blocks is set at half the electrode spacing. The thickness of each of the following deeper layer is normally increased by 10% (Figure 3.26) (Geotomo Software, 2010). The inversion method is based on a smoothness-constrained least-squares optimization method (See Appendix A3.4).

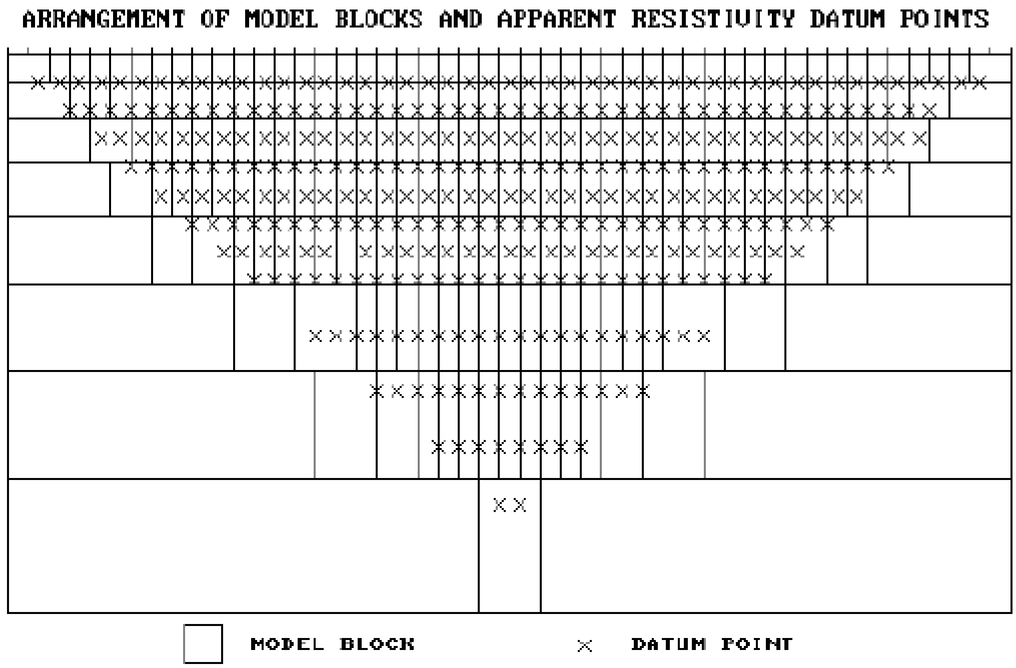

Figure 3.26: Arrangement of blocks in rectilinear mesh in *RES2DINV* with corresponding pseudo-section data point distribution (Geotomo Software, 2010).

It is possible to include topography in the inversion. However, since there is little to no variation in elevation over the crest of the dam between the electrodes of the DCR survey, it was not included.

One dimensional models of resistivity versus depth were generated from a subset of Schlumberger soundings, which were part of the DCR surveys. These models were generated using interactive freeware *VES*, written by G.R. Cooper of the University of Witwatersrand. *VES* assumes a one-dimensional stratigraphy of a finite number of homogeneous layers with sharp planar contact between them (Kilfoil, et al., 2018). The program takes as input apparent resistivity readings at multiple pseudo-depths (AB/2) over the same *x*-location, and calculates unit thicknesses and resistivities by manipulating these properties to generate a best fit. The program works best as a forward modeler, with the initial thickness estimates based on the *RES2DINV* inversion model results. The data misfit value guides the user during interactive adjustment of model properties.

3.3.4 Ground-Penetrating Radar

All the GPR data acquired for this study was processed using Sensors and Software's *Ekko_Project 5* software.

GPR line data is stored externally on an SD card inserted in the GPR's DVL unit during data acquisition. Data is uploaded to a computer using an external card reader.

Most processing of the GPR profiles is performed in the "Lineview" module illustrated in Figure 3.27. The horizontal axis gives the distance in meters along the GPR profile. The depth axis is based on the two-way travel time of a reflected radar pulse and

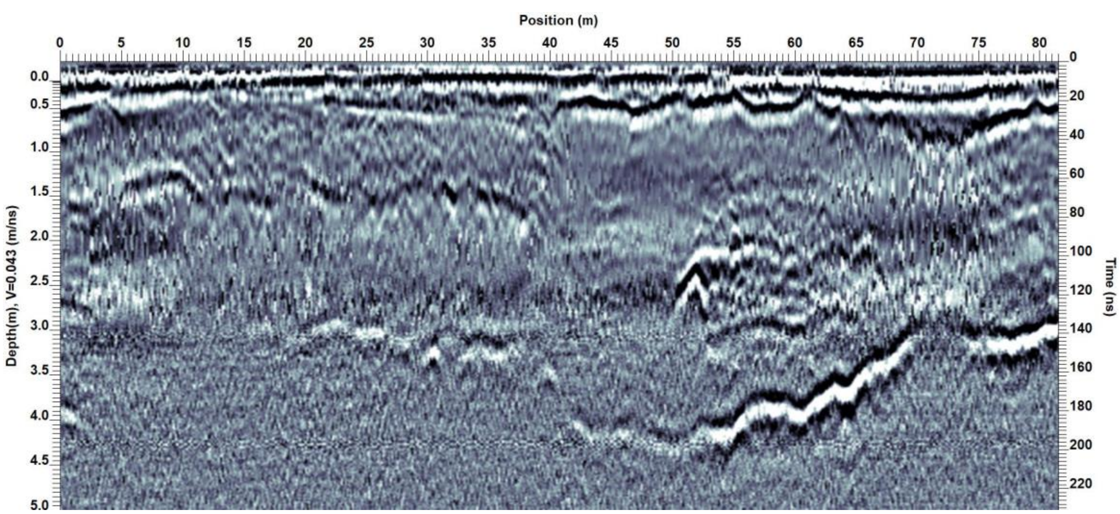

Figure 3.27: GPR LINE05 collected with 100 MHz antennae in September 2016 displayed in "LineView" mode (Sensors and Software Inc., 2017).

is a function of the radar velocity travelling through a particular medium in the ground (Sensors and Software Inc., 2017). GPR LINE05, illustrated here, was collected over the limestone berm in the wetland west of the dam in September 2016, and is featured in several of the processing steps described below.

Table 3.7 lists the processing steps performed on the GPR data using the Sensors and Software programs *Ekko_Project* and *GFP Edit*. The processing steps used for each survey line depend on several factors including the lithology of the subsurface, the amount of signal-to-noise and the subsurface target. Further details on the steps for individual lines are supplied in Appendix A3.5.

Table 3.7: Table of GPR processing procedures carried out with *EKKO Project* software.

Process	**Survey Line**
Repositioning	
Reversing Lines	**July 2016 Grid:** YLINE00, YLINE07, YLINE09 **September 2016**: **Dam**: LINE00 **February 2017: Wetland**: LINE06, LINE08 **June 2017:** YLINE03 (250 MHz), YLINE05 (100 and 50 MHz), YLINE07 (100 and 50 MHz), YLINE09 (All frequencies), XLINE03 (All frequencies), XLINE23 (50 MHz)

Renaming Lines (Swap X-Y)	**July 2016 Grid, November 2016 Grid**
Repositioning Grid (GFP Edit)	July 2016 Grid
Rescaling	
Reposition using GPS	**September 2016**: **Dam**: LINE00 **Wetland**: LINE05 **February 2017: Wetland:** LINE06, LINE07, LINE08, LINE09
Latency	**September 2016**: **Dam**: LINE00 **Wetland**: LINE05 **February 2017: Wetland:** LINE06, LINE07, LINE08, LINE09
Merge Lines	**June 2017:** YLINE00 (250 MHz), YLINE03 (100 MHz), YLINE05 (250 MHz)
Image Processing	
Dewow	**All Survey Lines**
Background Subtraction	**July 2016: Dam:** XLINE00, XLINE06, XLINE09, XLINE10, XLINE11, XLINE15, YLINE07, YLINE09 **September 2016**: **Dam**: LINE00 **Wetland**: LINE05 **November 2016: Dam:** YLINE02, YLINE03 **February 2017: Wetland**: LINE06, LINE07, LINE08, LINE09

	June 2017: Dam: YLINE00 (50 and 100 MHz) YLINE03 (All frequencies), YLINE05 (100 and 50 MHz), YLINE07 (All frequencies), YLINE08 (50 MHz), YLINE09 (100 and 50 MHz), XLINE03 (All frequencies), XLINE10 (All frequencies), XLINE16 (50 & 100 MHz), XLINE22 (100 and 50 MHz), XLINE23 (50 MHz)
AGC (Automatic Gain Control)	**All Survey Lines**
Depth Scaling	
Velocity Extraction (Hyperbola Curve Fitting)	**June 2016: Wetland:** CMP **September 2016: Dam:** LINE00

Repositioning Survey Lines

Not all survey lines were collected in the same orientation. For example, to save time, lines in a grid were surveyed by pushing the Smartcart along a line in one direction, and along the next parallel line in the opposite direction. Also, in some cases S-N lines were stored as x lines and W-E lines as y lines instead of the other way around.

The June 2017 GPR grid is a combination of two original grids, a 20x100 m grid and a 20x40 m grid extension to the north on the last day of surveying. The 20x40 m extension was stitched to the original grid in *GFP Edit*.

Rescaling Survey Lines

The GPR system sets a default step-size (distance between traces) based on the nominal frequency. If GPR data was collected using calibrated “Odometer” mode for positioning, then traces were stored at predetermined intervals, and the Position (m) axis gives the distance in meters from the beginning of the profile. In “Free-Run” mode with GPS, however, data is collected and stored continuously, with the time between traces determined by the depth of investigation and the stacking. Then the position (x) axis may be incorrect and require rescaling based on the number of traces in the profile and the length of the profile based on GPS positioning information. (Sensors and Software Inc., 2016). Such rescalings were performed under the tab “Process” menu.

The “Latency correction” was performed to correct for the difference in time between when the GPS receiver obtained a solution and when the data logger recorded the information (Sensors and Software Inc., 2016).

Signal Processing

The “Dewow” Filter was applied to the dataset to correct for DC bias and very low frequency components of each of the traces in the profile created by proximity of the transmitter and receiver and or inductive coupling effects between the ground and antennae (Appendix A.3.5).

The background subtraction filter is used to reduce near-surface horizontal banding caused by the direct and ground waves first arrivals and other system-generated coherent

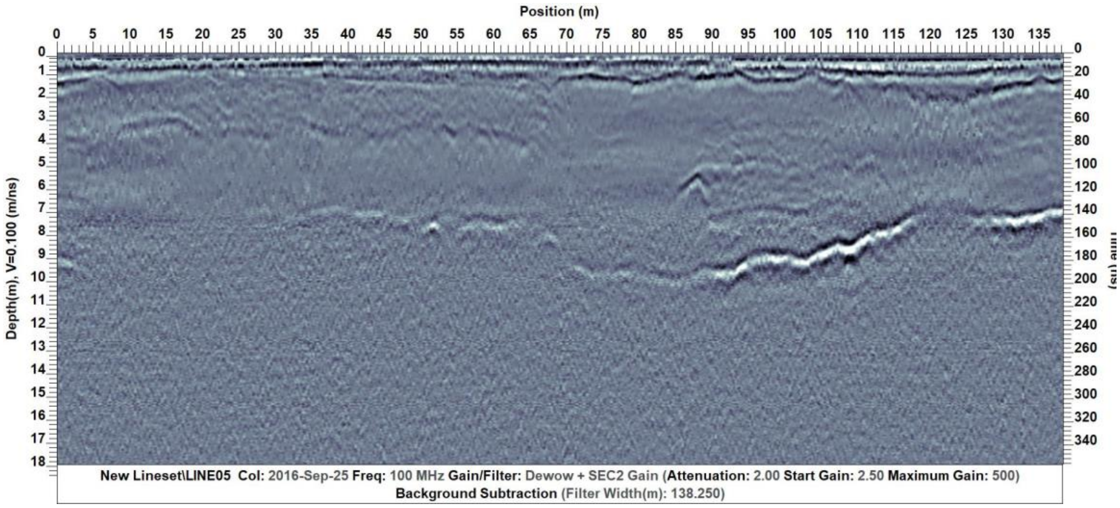

Figure 3.28: GPR LINE05 with application of local background subtraction filter (Sensors and Software Inc., 2017).

noise that appears at constant time intervals on the traces. The background subtraction filter works by taking a window of traces and averaging the amplitudes of each of the traces and subtracting the result from the trace at the center of the window. The window moves along one trace at a time and the process is repeated. The shallow black and white banding at the top of the profile can be observed over GPR LINE05 in Figure 3.27. Figure 3.28 displays Figure 3.27 after a background subtraction filter has been applied. It is important to note that using the background subtraction filter is not always practical as it may mask horizontal interfaces generated by flat-lying features of that extend across the entire length of the profile, or generate “ghost” interfaces along horizontal interfaces that extend part way along the profile.

Individual traces in each of the GPR profiles were examined in the “Traceview Window” which gives the wiggle trace plot of the amplitude (mV) versus two-way travel time (ns) of the selected GPR trace in the in the profile. There the appropriate values of the

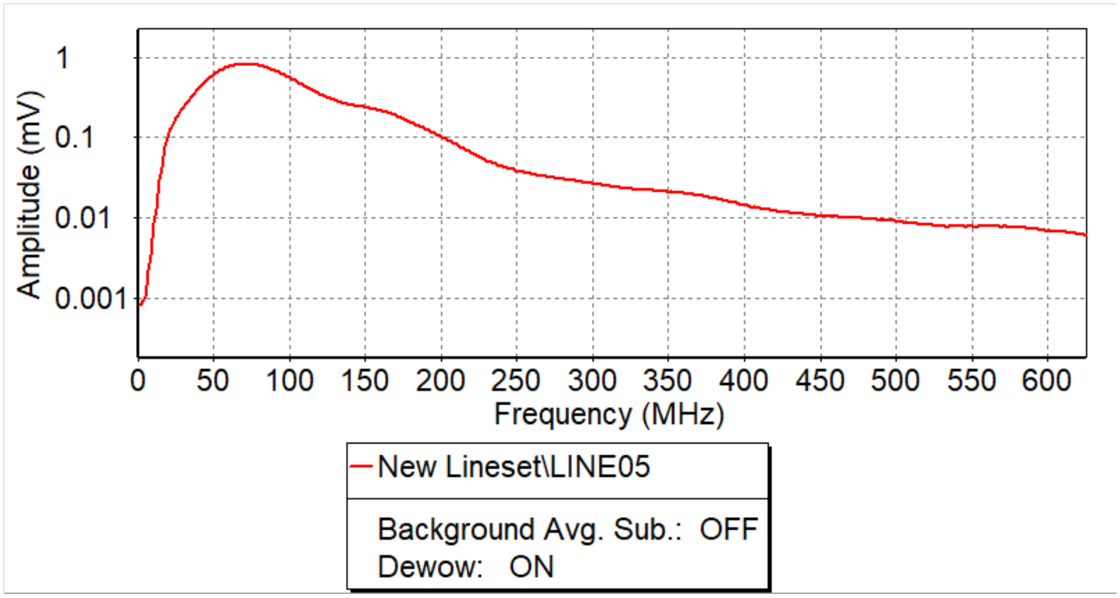

Figure 3.29: Average Frequency Spectrum Plot over GPR LINE05 collected over the Gullbridge Wetland area using 100 MHz antennae in September 2016 (Sensors and Software Inc., 2017).

start and max gain, as well as the attenuation variable were chosen based on the feature being investigated (see Appendix A3.5).

The GPR antennae actually transmit and receive a distribution of frequencies. The nominal antennae frequency is the center frequency of this distribution. Figure 3.29 provides the frequency content of LINE05, determined by the Average Frequency Spectrum tool in *EKKO Project* software. This tool provides information on whether a low pass, high pass, or bandpass filter should be used to remove unwanted frequencies contaminating the dataset. As Figure 3.29 displays, there is only a small amount of low frequency noise contaminating the dataset (Sensors and Software Inc., 2017).

Depth-Scaling

To determine the depth scale for the GPR surveys, most of the profiles collected over the Gullbridge Dam were assigned a velocity of 0.085, the speed of an EM radar pulse through partially water-saturated gravel assuming a homogeneous half-space. The radar pulse velocity for the wetlands was assumed to be that through a saturated bog: ~ 0.04 ns/m used throughout this study (Sensors and Software Inc., 2017).

The ground over Gullbridge was not homogenous as it contained variable materials (i.e. peat, till, gravel). An average velocity for the medium was determined using the hyperbola curve fitting tool (Sensors and Software Inc., 2017).

Common mid-point gather (CMP) data was used to extract a velocity in the wetland. The method is described in detail in Appendix A3.3. The observed moveout can be used to determine the radar pulse velocity by fitting a trendline in Ekko Project to the arrivals from observed two-way travel time reflections. (Jacob & Urban, 2015).

Figure 3.30 displays the CMP over the bog area to the west of the Gullbridge tailings embankment. This image displays a red hyperbola curve fitting tool superimposed over a diffraction hyperbola at normal incidence. This exercise yielded a velocity of 0.043 m/ns. This is a reasonable value for a moderately wet bog since the values of GPR wave pulses in bogs range between 0.03 ns/m and 0.05 ns/m (Sensors and Software Inc., 2006).

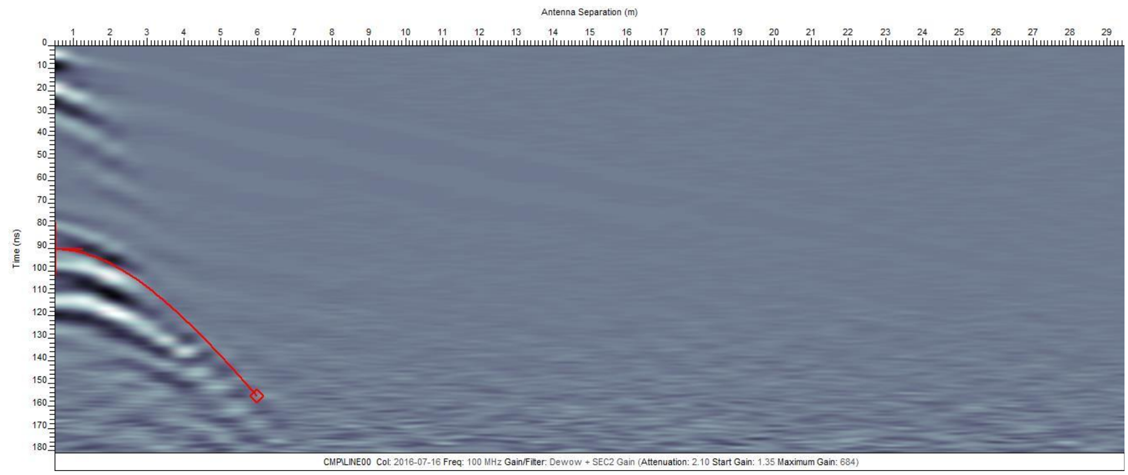

Figure 3.30: CMP over bog area to the west of the Gullbridge Tailings embankment (Sensors and Software Inc., 2017).

Interpretations

In LineView, the user can "interpret" a section by manually picking out a series of points along an interface. For each point the program stores the nominal (and, for Free Run profiles, incorrect) *x* location along the line, the (correct) GPS location in UTMs, latitude, longitude, and the depth of the interface. Each interpretation began by naming the interface based on the materials associated with the boundary. Each interface is drawn in Lineview with a different colour. This study applied a polyline template for clearly distinguishing the interfaces between differing materials.

The interpreted profile of GPR LINE05 in Figure 3.31 displays two marker horizons indicating the interface between the limestone and wetland soil (blue), and the interface between the wetland and the bedrock (green). These are valid assumptions as the

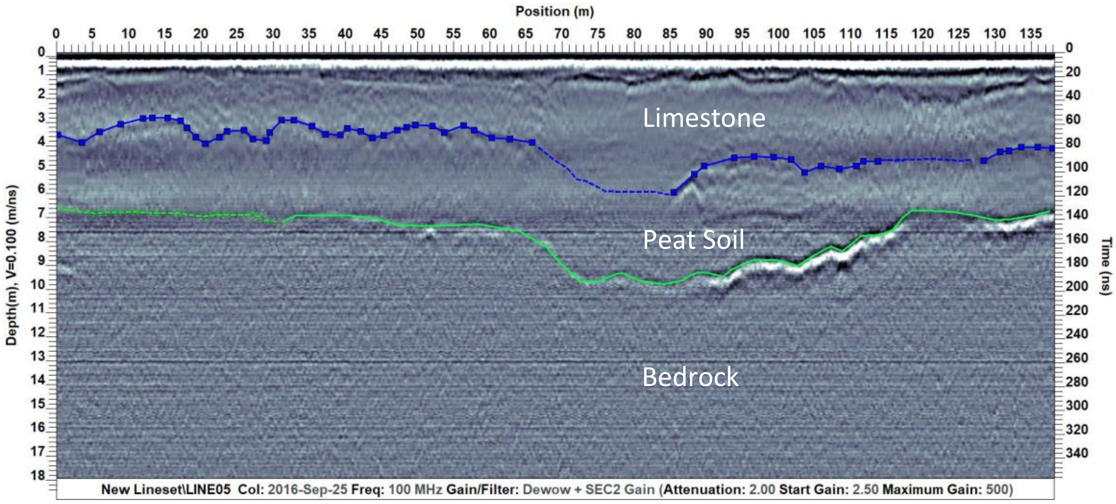

Figure 3.31: GPR LINE05 collected over the limestone berm of the Gullbridge wetland in September 2016 with active interpretations selected where marker horizons define the interfaces between differing materials (Sensors and Software Inc., 2017). Polylines with markers define known interfaces and dashed lines define inferred interfaces.

near surface lithology is well known in the area due to bog probes scattered along the bank of the downstream slope of the embankment. Table 3.8 displays the Excel spreadsheet of data exported from interpretation points in Figure 3.31. The spreadsheet displays each of the interpretations in the order they were completed.

Table 3.8: Excel spreadsheet of exported interpretation point data along GPR LINE05 collected in the wetland in September 2016 (Sensors and Software Inc., 2017).

	A	B	C	D	E	F	G	H	I	J	K	L	M	N	O	P	Q
1	Name	Description	Count														
2	Peat/Bedrock		2														
3																	
4	Tool	Interpretation	GPR Line	Position(m)	X(m)	Y(m)	Depth(m)	Time(ns)	Elevation(ı	Amplitude	Velocity(m	GPS-Eastin	GPS-North	Latitude	Longtitude	GPS-Elevat	Comment
5	Polyline	Peat	New Lines	1.209	47.808	154.529	2.702	124.56	154.498	0.137	0.043	559741	5450419	49.20366	-56.1799	157.2	
6	Polyline	Peat	New Lines	5.311	47.252	155.357	2.802	129.17	154.718	0.208	0.043	559740.5	5450420	49.20366	-56.1799	157.52	
7																	
8	Polyline	Peat	New Lines	28.224	42.961	163.649	3.111	143.47	153.289	0.04	0.043	559736.2	5450429	49.20374	-56.1799	156.4	
9	Polyline	Peat	New Lines	32.636	41.45	165.356	3.051	140.71	153.404	-0.018	0.043	559734.7	5450430	49.20375	-56.18	156.45	
10	Polyline	Peat	New Lines	34.958	40.547	166.245	2.911	134.25	153.589	0.035	0.043	559733.8	5450431	49.20376	-56.18	156.5	
11	Polyline	Peat	New Lines	38.132	39.668	167.32	2.842	131.02	153.203	0.072	0.043	559732.9	5450432	49.20377	-56.18	156.05	
12	Polyline	Peat	New Lines	40.222	39.248	167.964	2.981	137.48	152.824	-0.024	0.043	559732.5	5450433	49.20378	-56.18	155.81	
13	Polyline	Peat	New Lines	42.622	39.186	168.63	2.991	137.94	152.859	0.041	0.043	559732.4	5450433	49.20378	-56.18	155.85	
14	Polyline	Peat	New Lines	44.712	39.124	169.296	2.991	137.94	152.904	0.047	0.043	559732.4	5450434	49.20379	-56.18	155.89	
15	Polyline	Peat	New Lines	45.873	38.508	170.142	3.051	140.71	152.819	0.078	0.043	559731.7	5450435	49.2038	-56.18	155.87	
16	Polyline	Peat	New Lines	47.576	37.429	171.622	3.111	143.47	152.689	0.038	0.043	559730.7	5450436	49.20381	-56.18	155.8	
17	Polyline	Peat	New Lines	50.053	35.968	173.672	3.16	145.78	152.54	-0.041	0.043	559729.2	5450439	49.20383	-56.18	155.7	
18	Polyline	Peat	New Lines	52.375	35.224	175.147	3.14	144.86	152.56	0	0.043	559728.5	5450440	49.20384	-56.18	155.7	
19	Polyline	Peat	New Lines	53.846	34.852	175.884	3.359	155.01	152.341	0.002	0.043	559728.1	5450441	49.20385	-56.18	155.7	
20	Polyline	Peat	New Lines	55.858	34.158	177.136	3.13	144.4	152.63	0.012	0.043	559727.4	5450442	49.20386	-56.1801	155.76	
21	Polyline	Peat	New Lines	57.871	33.367	178.462	3.061	141.17	152.859	-0.053	0.043	559726.6	5450443	49.20387	-56.1801	155.92	
22	Polyline	Peat	New Lines	60.967	32.207	180.2	3.101	143.01	152.979	-0.035	0.043	559725.4	5450445	49.20389	-56.1801	156.08	
23	Polyline	Peat	New Lines	63.831	31.395	181.109	3.17	146.24	152.855	0.034	0.043	559724.6	5450446	49.2039	-56.1801	156.03	
24	Polyline	Peat	New Lines	65.612	30.368	181.765	3.25	149.93	152.78	-0.04	0.043	559723.6	5450447	49.2039	-56.1801	156.03	
25	Polyline	Peat	New Lines	67.857	28.172	182.742	3.319	153.16	152.846	0.005	0.043	559721.4	5450448	49.20391	-56.1801	156.16	
26	Polyline	Peat	New Lines	69.25	26.708	183.393	3.717	171.62	152.538	0.076	0.043	559719.9	5450448	49.20392	-56.1802	156.25	
27	Polyline	Peat	New Lines	71.185	25.929	183.607	3.916	180.84	152.359	0.06	0.043	559719.2	5450448	49.20392	-56.1802	156.28	
28	Polyline	Peat	New Lines	74.049	25.395	183.601	4.164	192.38	152.056	0.056	0.043	559718.6	5450448	49.20392	-56.1802	156.22	
29	Polyline	Peat	New Lines	76.526	24.646	184.371	4.085	188.69	152.175	0.061	0.043	559717.9	5450449	49.20393	-56.1802	156.26	

Peat

3.3.5 Electromagnetic Ground Conductivity

EM31-MK2

The Polycorder 600 digital data recorder connected to the EM31-MK2 ground-conductivity meter contains built-in software that controls the basic function of the survey equipment (Geonics Ltd., 1999). All data was acquired running a program labelled "*EM31-MK2*" and stored on the Polycorder.

The polycorder is easily disconnected from the conductivity meter and connected to a computer using a serial port to USB adapter cable. The data was downloaded and converted into asci format using the polycorder program "DUMPWIN" and Windows OS software DAT31W.

The data for each measurement consist of the coil orientation (VMD or HMD), the station number, and the apparent conductivity in mS/m. All data collected with the EM31-MK2 was analyzed in the form of scatterplot profiles and contour maps generated in ArcGIS.

Profiles of the EM31-MK2 data were plotted as a function of conductivity (mS/m) versus station with exception to EM LINEs 03, 04 and 05 which were plotted as a function of conductivity versus distance along the line (m) calculated from RTK measurements. Measurements in the VMD and HMD orientations were plotted on the same graph.

Contour maps of apparent conductivity were generated in Oasis Montaj and superimposed over drone imagery collected by DNR Mine's Branch in July 2017. Oasis

Montaj required a .csv data spreadsheet containing 3 columns including the easting, northing, and value of conductivity. The UTM coordinates were provided from RTK surveys of the stations (see section 3.2.5).

GEM2

GEM2 data was uploaded from the handheld data logger attached to the GEM2 board using Terraplus' software *WinGEM* and converted into .txt format. Similar to the EM31-MK2 data, profiles were generated in Microsoft Excel of the quadrature component along the survey. Data for all 3 frequencies were plotted on the same profiles for comparison.

3.3.6 Bog and Water Sample Analysis

Bog samples

The bog samples from 3 separate sites were weighed and analyzed for water content at Memorial University's Earth Science Department. Over the course of two days (July 17th-18th), the samples were weighed in their plastic sample bags, emptied into clean, weighed glass jars and weighed again. The sample bags were weighed after removal of the sample, after drying, and after cleaning, in order to allow for any material stuck to the inside of the bag to be considered. This correction was negligible, making a difference of less than 0.2% in the calculation of the water content. Because some water is suspected to have been lost in the extraction process, results are given to the nearest 1%. The jars containing the wet samples were placed in an oven at 100˚C overnight to dry, and then weighed again the following day.

The samples were also prepared for geochemical analysis. To prepare the samples for OES analysis, the dried samples were placed in a paper sample bag and crushed by striking with a rubber mallet, then shaken through a 160-micron sieve to filter out samples size too large for the experiment.

Water Samples

On 17th July 2018, aliquots of the water samples were filtered and prepared for geochemical analysis by John Allen in the Solution ICP-MS facility at Memorial University.

The samples were labelled as "Tailings Pond" and "Tailings Pond Leak". The samples were tested twice for quality control. Standard Deviation and % Relative Standard Deviation (RSD) were included in the results. Further details are provided in Appendix A3.2.

On 17th July 2018, the pH of the water in the water samples was measured by Melissa Cook, PhD student of Dr Penny Morrill, using a pH-Eh meter. The meter was calibrated before measurement. On 19th July 2018, the electrical conductivity of the water samples was measured by Leanne Fisher-Power, MSc, in Dr Tao Cheng's Hydrogeology Laboratory at Memorial University, using a VWR TRACEABLE conductivity meter, which was calibrated from 0 to 1000 μS/cm (microsiemens/cm) with a precision of ±5 μS/cm. Two readings were taken of each sample.

The results of the geochemical analysis for both the bog and water samples were plotted on graphs of depth (m) versus concentration (ppm & %) in Microsoft Excel.

4 Results

4.1 Spontaneous Potential

4.1.1 June 2016 Along the Embankment

The locations of the rover pot stations along SP Line 1 and SP Line 2 are displayed in Figure 4.1 over a drone image collected by DNR in June 2016. The survey lines are separated by a distance of ~ 10 m in the south and ~15 m in the north across the dam crest. The base station locations corresponding to each of the four sections are also included. The legend indicates several notable surface features (Appendix A2.1) including DNR drone spikes for flying drone surveys, the dam abutments, the old stream running beneath the dam and boreholes.

The results of SP Line 1 and 2 along the length of the dam embankment (Figure 4.1) are displayed in Figure 4.2 and 4.3 respectively. Distance is measured south to north, starting from UTM (559862, 5450268). The 4 sections along each line are separated by dashed vertical lines because the measurements in each section were not tied into a common reference point (Section 3.2.1). Thus, offsets between sections have no significance. The locations of the section breaks are indicated by large cyan dots in Figure 4.1. The blue, green and yellow stars in Figures 4.2 and 4.3 indicate the approximate locations of the spillway, seep and old stream/inlet channel respectively.

The profiles exhibit a high degree variability from station to station, with SP Line 2, nearer the tailings reservoir, showing significantly higher amplitude variability than Line

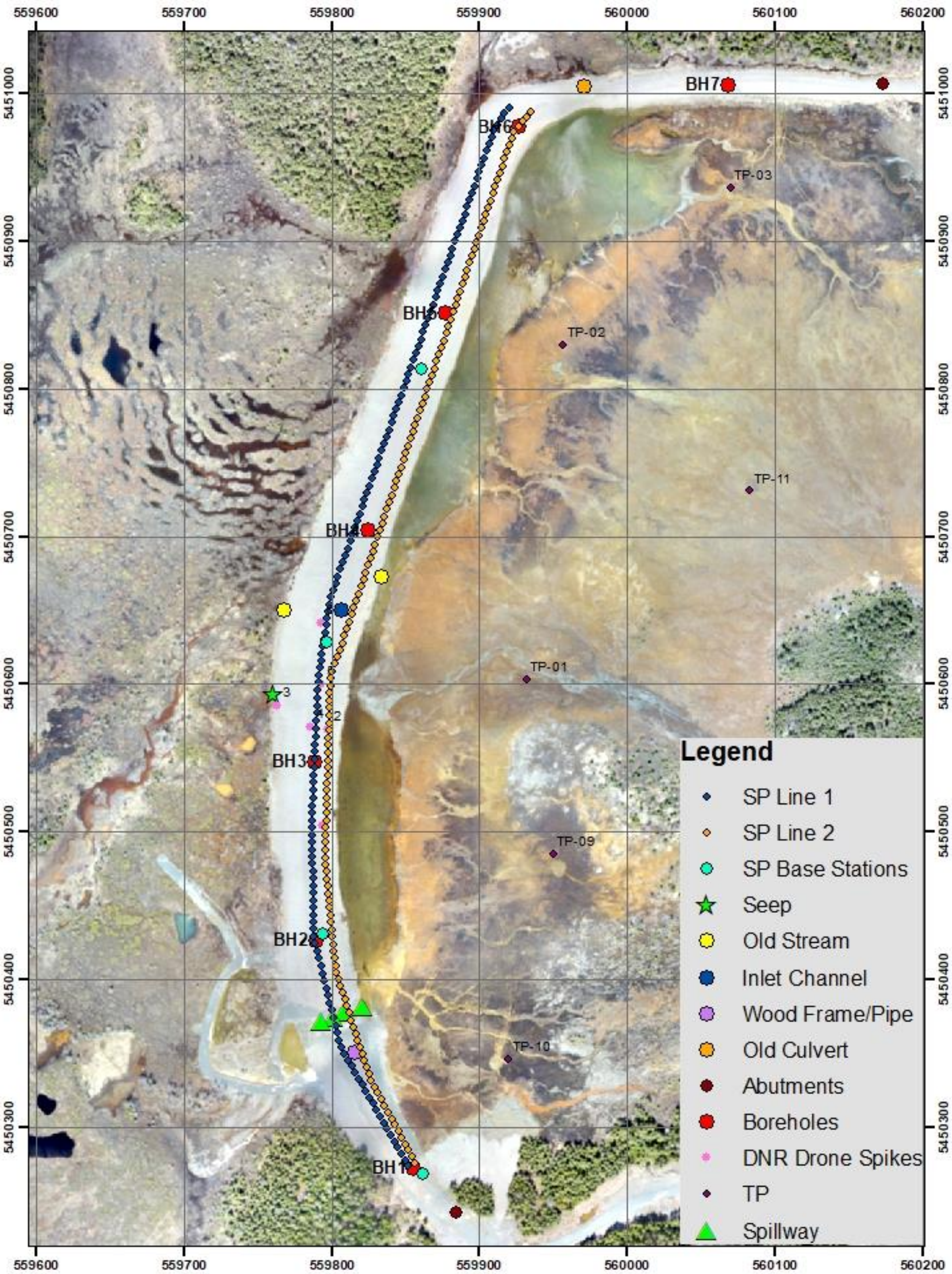

Figure 4.1: SP Line 1 and SP Line 2 collected over the Gullbridge Dam from June 19th-20th, 2016. Repeatability data over SP Line 2 was collected in the south from stations L2-+35 to L2+230 on July 18th, 2016.

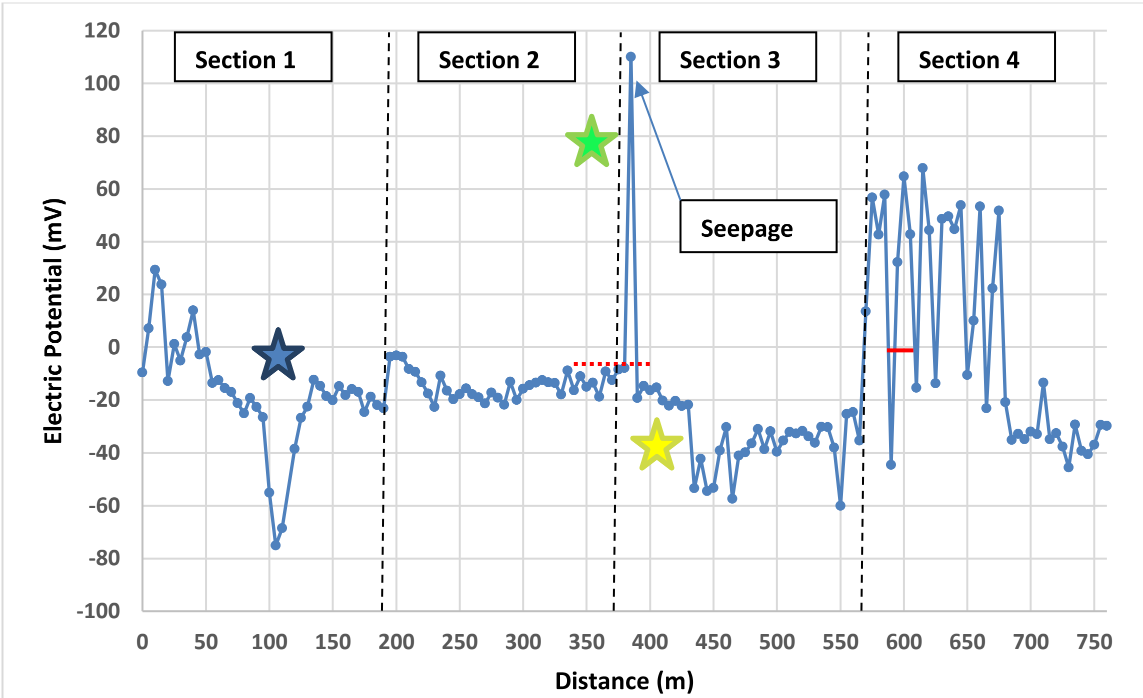

Figure 4.2: Drift corrected SP plotted in separate sections over Line 1, along the western (wetland) side of the dam crest (June 2016). Distance is measured S to N. ★ spillway, ★ seep, ★ old stream bed. The red dotted line between sections 2 and 3 is the approximate location of the July 2018 seep grid survey (see 4.1.2). The short red solid line in section 4 is the approximate location of the June 2016 GPR grid (see 4.4.2).

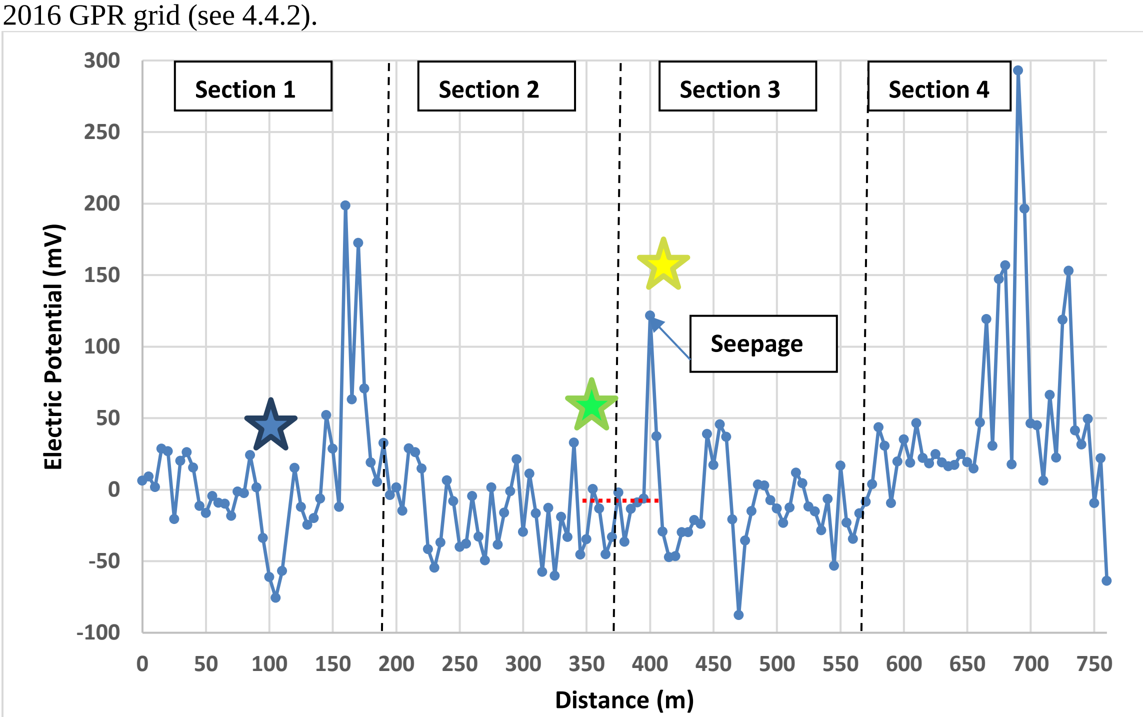

Figure 4.3: Drift corrected SP plotted in separate sections over Line 2, along the eastern (tailings reservoir) side of the dam crest (June 2016).

1. Note the difference in scales between the two figures. The profile over SP Line 2 also shows on average more positive values, indicating a potential gradient across the dam crest. This is likely because SP Line 2 is closer to SP sources associated with streaming potentials arising from reservoir water entering the embankment on the upstream side, and SP Line 1 is located further from this region and higher above the phreatic surface assuming a hydraulic gradient to the west.

The two most significant common anomalous features of the profiles are the negative peak at 105 m, and the sharp local high over station L1+385 m and L2+400 m.

The anomalous low of 50 to 60 mV between stations 95 m and 125 m within section 1 is the response to the spillway (blue star) (Figure 4.1). There are a number of possible mechanisms for generating this feature. It could be generated from topographic effects due to the variation in elevation over the spillway (Idris et al., 2015). The material beneath the spillway was reconstructed after the dam breach and is very low permeability, making streaming potentials within the embankment fill material an unlikely source, however, the data were collected during periods after heavy rain and therefore this anomalous low could be the response to the gradual discharge of rainwater over the limestone underlying the armoured channel rocks of the spillway. Alternatively, the source of the anomalous low may be an electrochemical potential over the interface between tailings imbued sediments and non-tailings imbued sediments, or limestone and quarry rock used in the construction of the spillway. Given the electrodes proximity to the tailings reservoir, it is possibly receiving a signal generated by diffusion potentials between the dam fill material and sulfide concentrated tailings water occupying the pore space of the dam soil nearest the reservoir.

The positive spike near the beginning of Section 3 is strong and narrow: ~ +140 mV and < 15 m wide on Line 2, and ~+120 mV and < 10 m wide on Line 1. It is likely sourced by streaming potentials generated by localized seepage through the dam. It occurs near the region of the observed seep on the toe of the dam; its sign (as it represents the potential difference in the direction of the seepage flow path) matches the E-W +ve gradient across the embankment; and local anomalous highs such as these match the conceptual behavior of streaming potentials in previous case studies using geophysical methods to detect anomalous seepage over tailings dams. Comparing the locations of the anomalous spikes and the seep at the toe of the dam, the seepage flow-path appears to be southwest beneath the embankment. It is unclear why the electric potential gradient is in the opposite direction expected across earth-filled embankments. Low measurements of SP near the downstream slope may indicate weathering of sulfide minerals within the embankment in the event that waste rock and tailings were used as construction materials when the dam was raised, as sulfide/mineral potentials are generally characterized by a negative SP response (Mainali, et al., 2015).More broadly, the patterns of variability with the sections show some similarity across the dam, particularly in sections 2 and 3. The values of SP over Section 4 show large-scale station to station variations in the southern portions of Line 1 and the northern portions of Line 2. This is likely the response to streaming potentials generated from small-scale leakage at periodic locations over a section of the embankment where seepage was identified at the at the toe of the downstream slope in July 2016. Again, the seepage would be in the southwest direction.

Repeatability Check

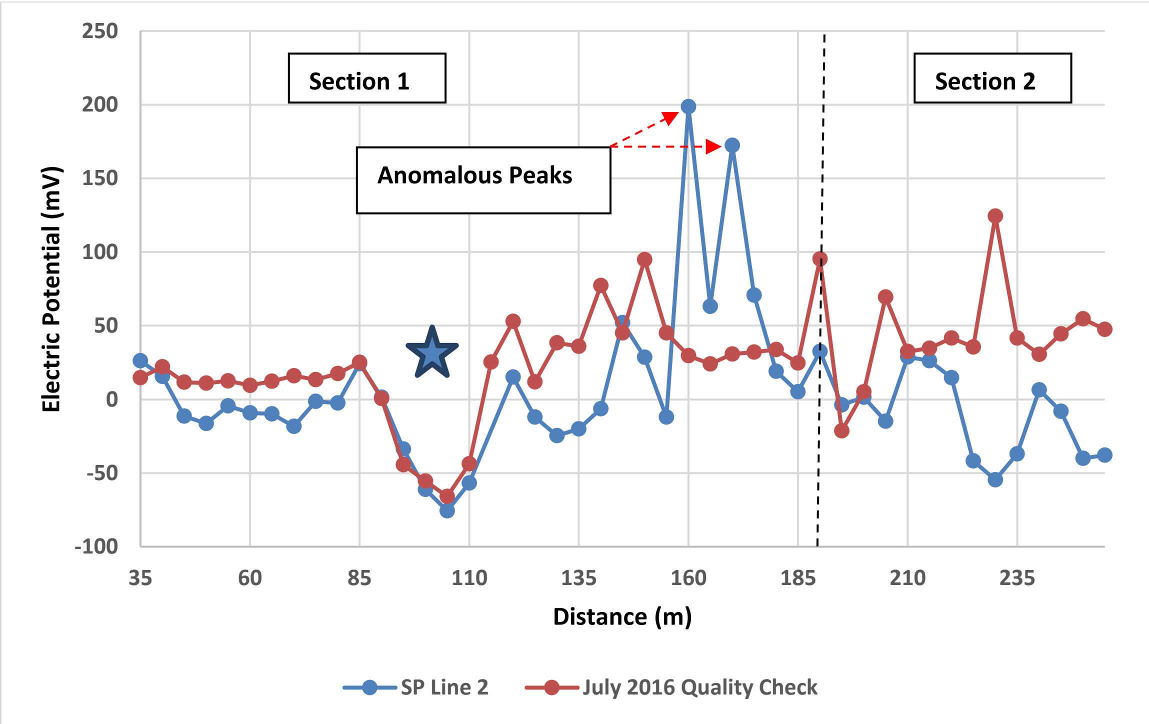

Figure 4.4: Profiles of electric potential over SP Line 2 and the July 18th, 2016 repeatability check over SP Line 2. Sections for the June 2016 profile are separated by a vertical dashed line. The blue star indicates the approximate location the survey line intersects the spillway.

The most striking difference between Lines 1 and 2 – apart from the generally larger station to station variability in Line 2 – is in section 1 north of the spillway.

Figure 4.4 displays the SP repeatability profile (red) located over stations L2+35 m – L2+255 m of SP Line 2 (blue). There is a strong correlation in the measured electric potential over the spillway along both profiles. The anomalous peaks (dashed red arrow) observed in June 2016 over L2+160 m and L2+170 m were not reproduced in the quality check. It is likely these peaks were related to rain events prior to the June 2016 surveys, resulting in the accumulation of water within the embankment and infiltration of tailings water. The reversal of polarity in the pattern of measurements in section 2, farther from the spillway, is a phenomenon that has previously been observed and attributed to changing redox conditions at interfaces within inhomogeneous ground after rainfall (Leitch & Boone, 2007).

4.1.2 July 2018 Seep Grid

Figure 4.5 displays the station location markers of the SP grid over the seep area. The labeling scheme of the stations designates that positive x is north and positive y is east of the base station. At several stations repeat measurements were made for quality control. Two DNR markers ("drone spikes") were located over stations (-8,-30) and (5,-30).

Figure 4.6 displays an electric potential contour map generated from SP data over the 60m×15m July 2018 grid, superimposed on drone imagery of the area with key anthropogenic features marked. The green star indicates the location of the observed seep to the west. Profiles of the measurements along YLINE 00 along the centre of the dam, and YLINE 05, closer to the reservoir, are shown in Figure 4.7. Other profiles in the x- and y-directions are provided in Appendix A4.1. The origin of the grid corresponds to approximately station 350 of the embankment profile 1 (Figure 4.2) and station 345 of embankment profile 2 (Figure 4.3). As for the embankment profiles, the data show considerable station to station variability.

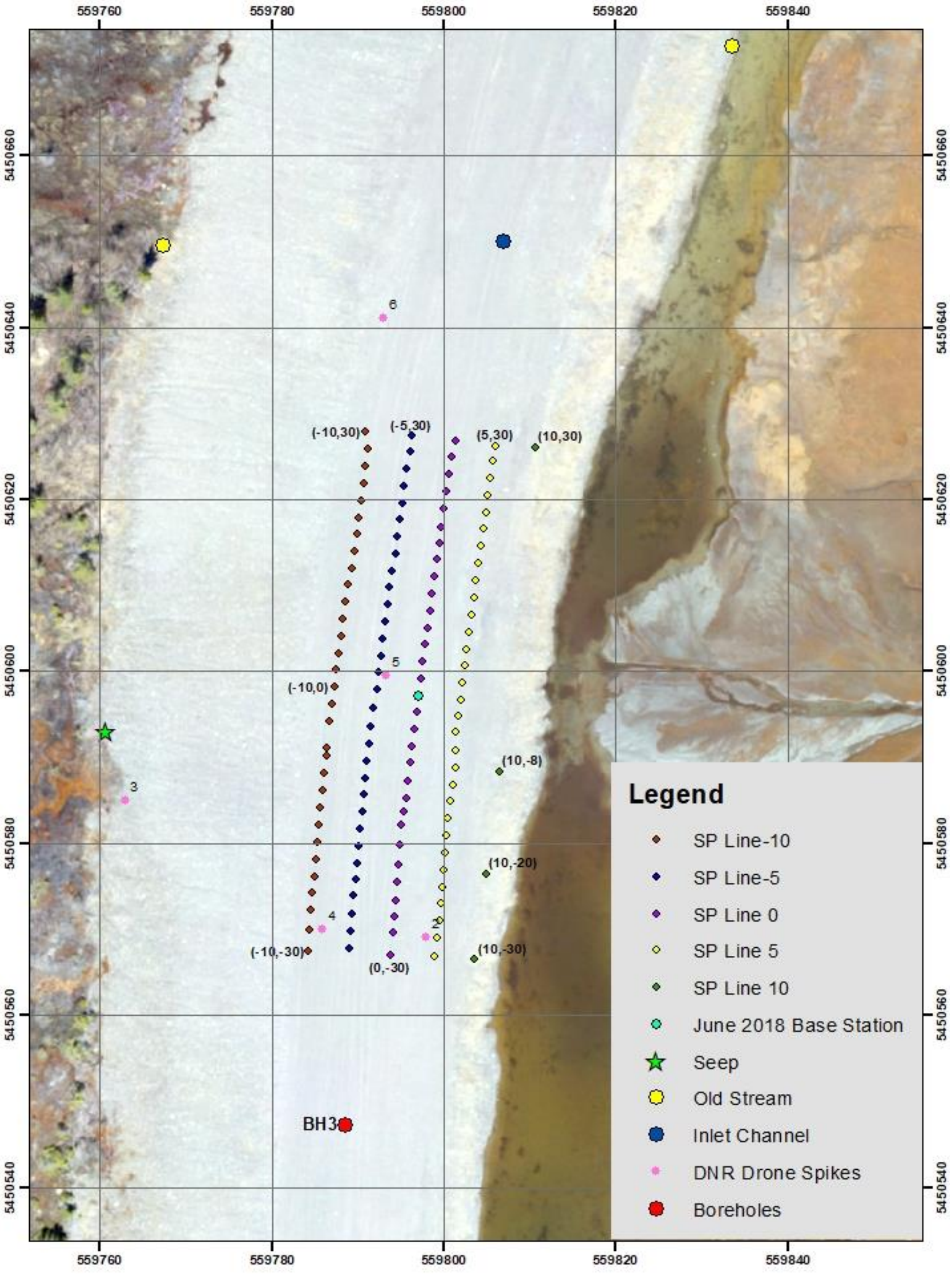

Figure 4.5: SP electrode positions collected over the seep area of the Gullbridge Dam on July 14th, 2018.

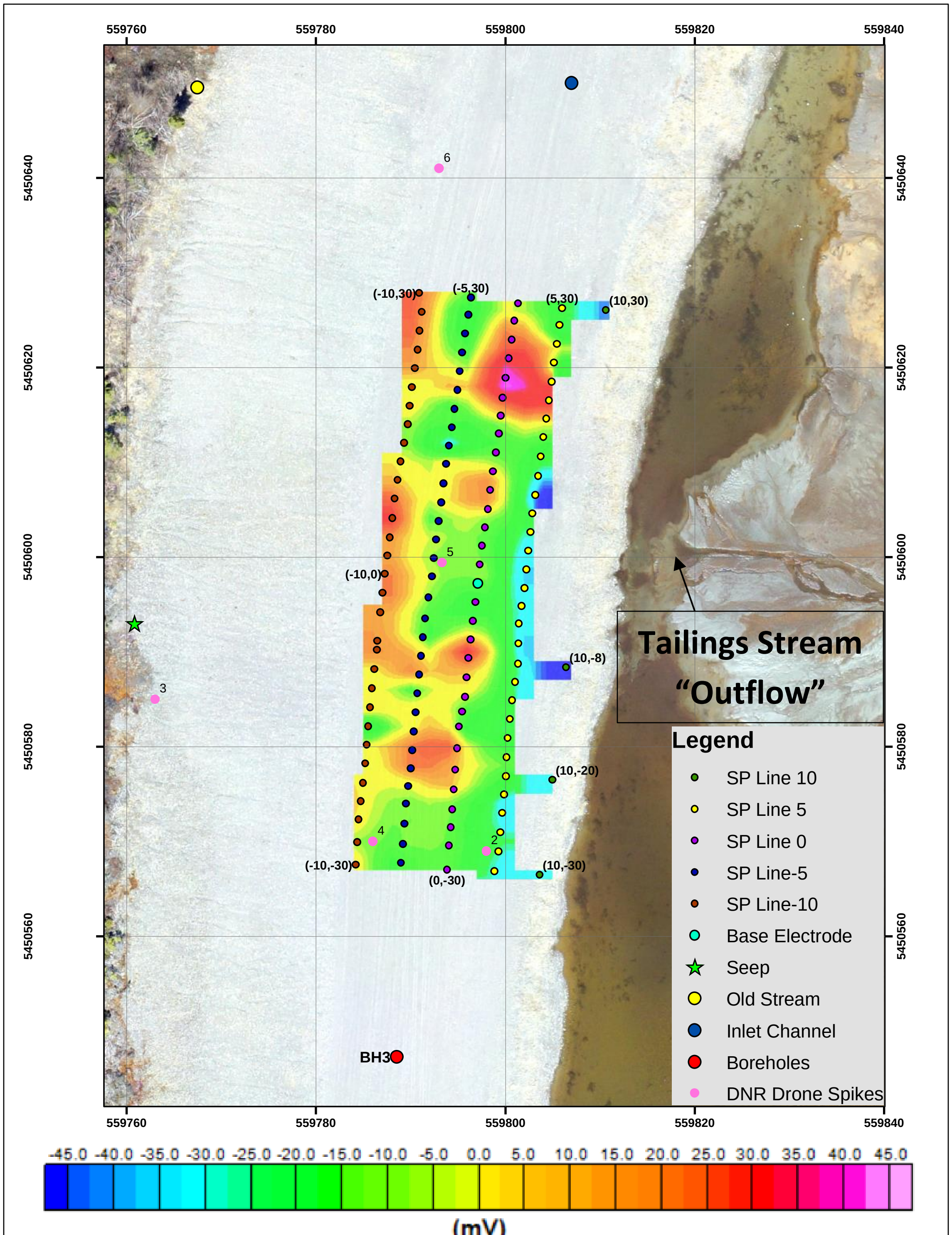

Figure 4.6: SP contour map over the July 2018 grid overlaying the drone imagery of the Gullbridge Impoundment.

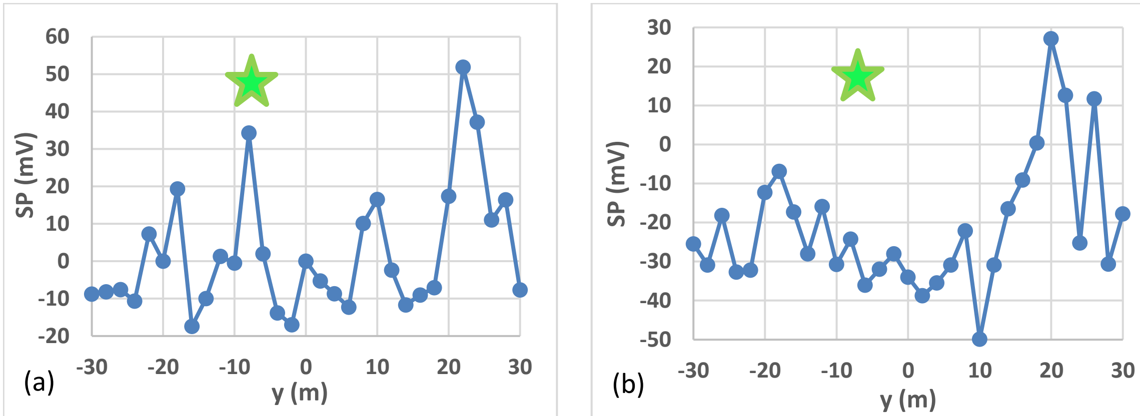

Figure 4.7: Profiles of SP versus station location over (a) YLINE00, (b) YLINE05 collected S-N over the 2018 seep grid. The green star indicates the approximate station location of the seep at the toe of the embankment.

The SP pattern over the grid in Figure 4.6 matches the conceptual behavior of streaming potentials over embankment dams (i.e., more positive on downstream side). The largest contrasts in SP are over the center of the dam along YLINE 00, which shows 4 sharp peaks. The largest measurement of electric potential obtained over the grid was at y = +22 m. This is the approximate location of the sharp peak in the 2016 embankment surveys, where measurements were taken every 5 m at less precisely determined positions (Figure 4.2). The more detailed grid survey suggests that seepage through the embankment has a complex geometry, as indicated in Figure 4.8. It is suspected that water flowing from the reservoir along the contributory flow path in this area has circulated within a loose region of core fines generating a subsequent streaming potential, resulting in a "developing stage" of seepage (Figure 2.14) where westward branching channels originate and diverge southwest to the observed seep. Other sharp anomalous spikes may be generated from streaming potentials as a result of small-scale, low-velocity, shallow fluid flow through the embankment.

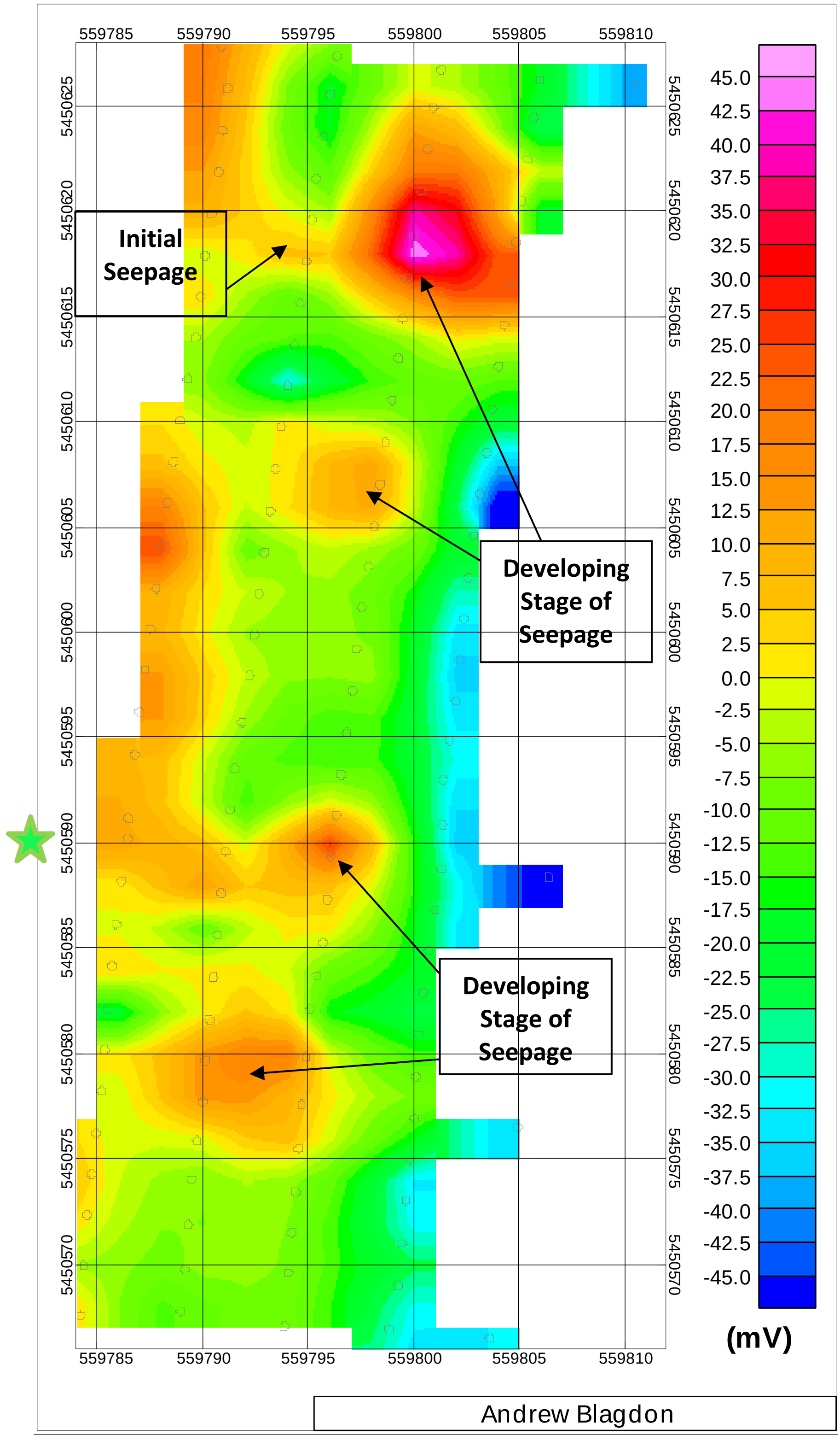

Figure 4.8: SP contour map over the July 2018 grid generated in Oasis Montaj, using minimum curvature gridding and a cell size of 2 m.

The data in the grid area show a general decrease in SP to the east. On average, SP Lines 1 and 2 collected along the embankment show the opposite trend (Figures 4.2 and 4.3), however, in the region of the seep the potential is more negative to the east, consistent with the grid survey data.

The map in Figure 4.8 suggests there are 4 distinct "development stage" zones where advancing seepage has accumulated in loose regions of the core. The high located at y= +22m along YLINE00 represents the largest development stage zone over the grid as a result of the substantial influx of water through the dam wall in this region due to the proximity of the discharge location of the surface stream carved through the tailings pond immediately to the east of the observed seep location. The location of the tailings stream outflow relative to the SP grid and observed seep is outlined in the map in Figure 4.6. East of YLINE00, the region of high SP extends from y= +20m to y= +22m over YLINE05 (Figure 4.7 (b)) marking the invasive seepage along the contributory flow path. West branching seepage appears to be emanating from the development stage zones.

Of particular note, the amount of drift dV/dt over each station of the grid was variable. After emplacement of the rover electrode, the potential was visually monitored and a measurement was recorded every 30 seconds until the SP value stopped changing.

Most stations exhibited a significant amount of monotonic drift over time, taking sometimes as long as 14 minutes before eventually stabilizing, while other stations produced potential differences that were stable after a minute.

Figure 4.9 displays profiles of v(t) over 3 stations chosen to exemplify large, medium and small drift. Station (0,-12) encountered the largest drift of 12.3 mV over 7.5 minutes. Station (-5,8) displayed the smallest drift of 0.5 mV over 30 seconds before stabilizing.

The values of the initial rate of change in SP (dV/dt_0) between the first two measurements are displayed in the contour map in Figure 4.10. The variation in SP over most stations was no more than 1 mV/min. The drift is greatest at locations bracketing the SP peaks. The proposed development stage saturation zone over YLINE00 in Figure 4.8 is centered between stations (0,-4) and (0,-12) in Figure 4.10 where the dV/dt_0 is greatest.

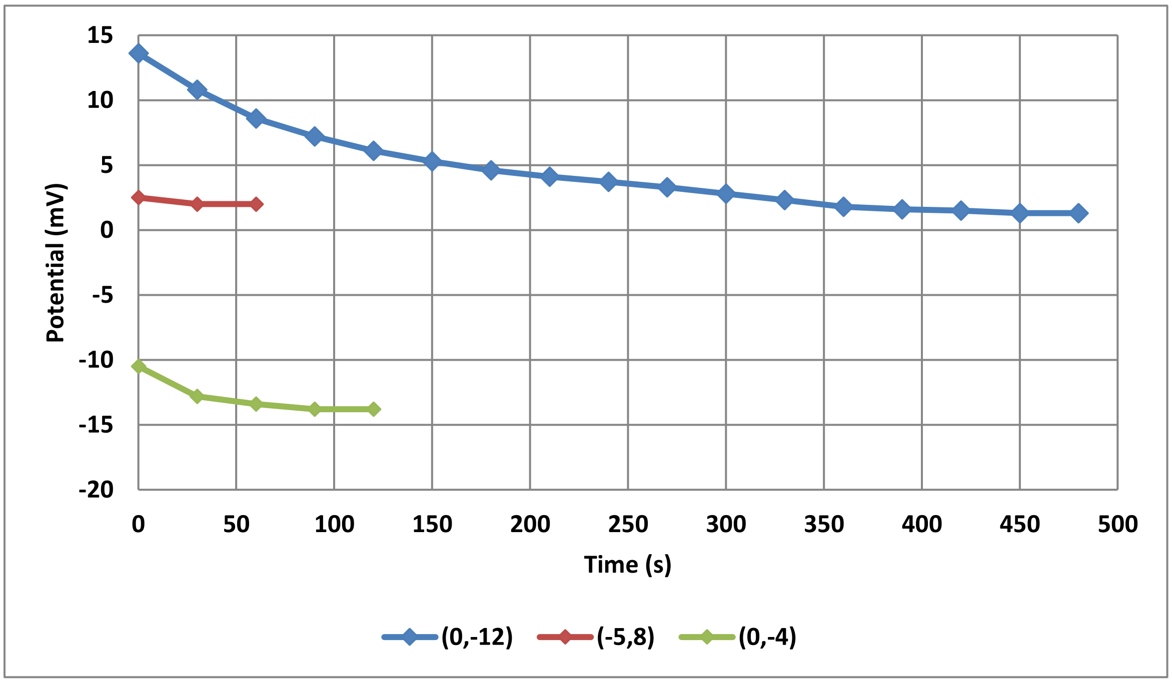

Figure 4.9: Graph displaying three separate profiles of the drift measured over time (seconds) v(t) over stations (0,-12), (-5, 8) and (0,-4) of the June 2018 SP grid.

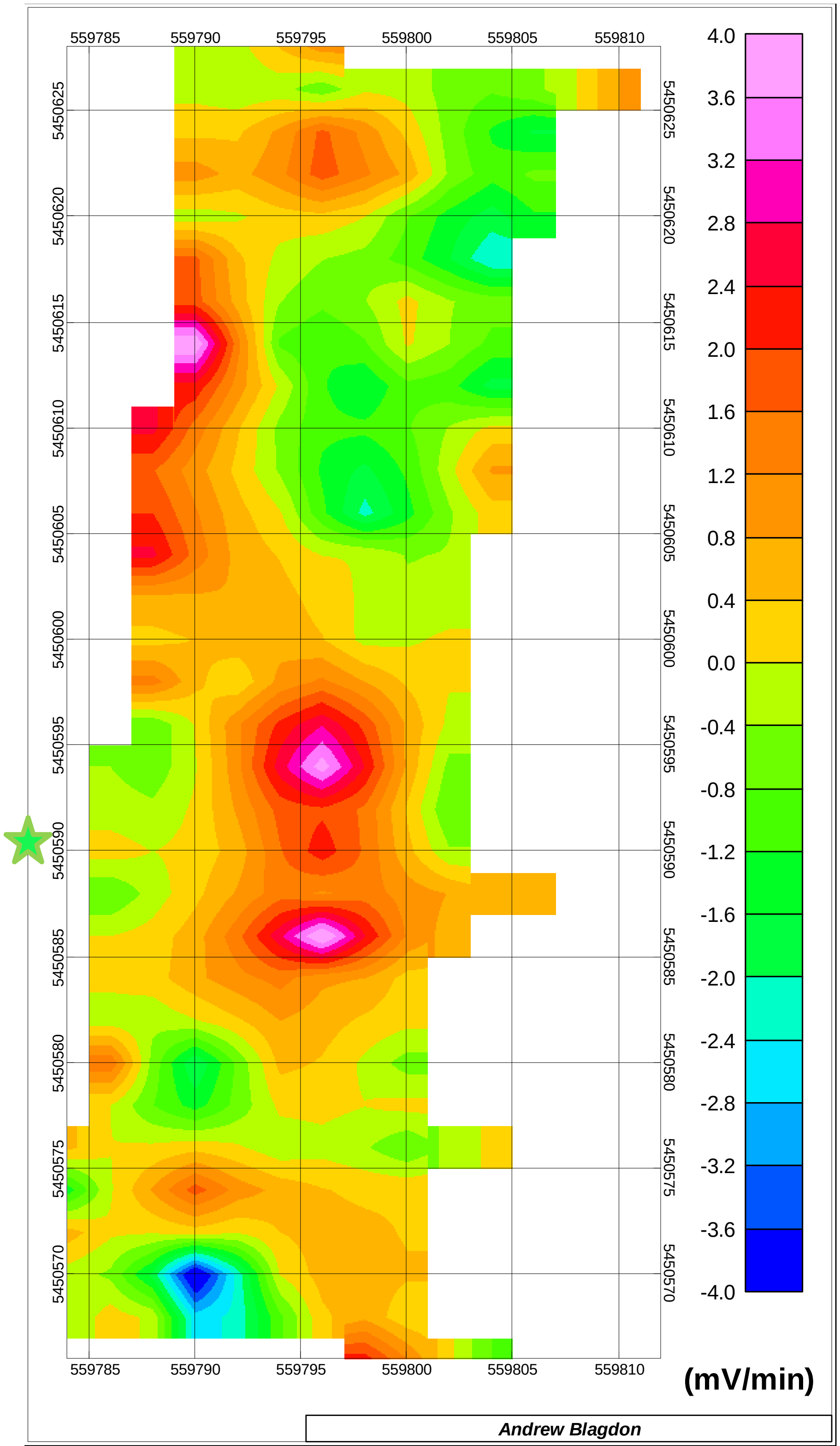

Figure 4.10: SP dV/dt₀ (mV/min) contour map over the July 2018 grid SP grid generated in Oasis Montaj, using minimum curvature gridding and a cell size of 2 m.

4.2 Magnetics

Figure 4.11 displays the regional TMI anomaly map over the Gullbridge area. The dam is sitting in a moderately low magnetization region, however an increase in TMI to the east over the tailings reservoir indicates the presence of magnetite in the tailings. It can be assumed that the anomalous magnetic highs with a northeasterly trend to the east of the impoundment are due to the multiple VMS deposits occupying the region. This is because these deposits as well as their host rocks contain varying quantities of magnetite (Morgan, 2010). At the scale of the survey, it appears there is an increase in the field to the north along the embankment.

Figure 4.12 displays Lines 1 and 2 of the magnetic survey over the Gullbridge Dam. Figure 4.13 displays the corresponding profiles of TMI measured over Lines 1 and 2 . The blue, green and yellow stars indicate the surface location intersecting the spillway, observed seep and old stream/inlet channel respectively. The figure shows a general increase in TMI to the north – expected from the regional data in Figure 4.11 – an unexpected increase in TMI to the west, and variability on a number of scales. The larger wavelength variations (> 20 m) are presumably sourced in the underlying bedrock, and smaller scale variations are sourced in magnetic materials within the embankment. Variations in the vertical magnetic gradient (VMG, Figure 4.14) emphasize sources within the embankment (section 3.2). The magnitude of the VMG and the change in sign from Line 1 to Line 2 is consistent with the change in TMI between the two lines.

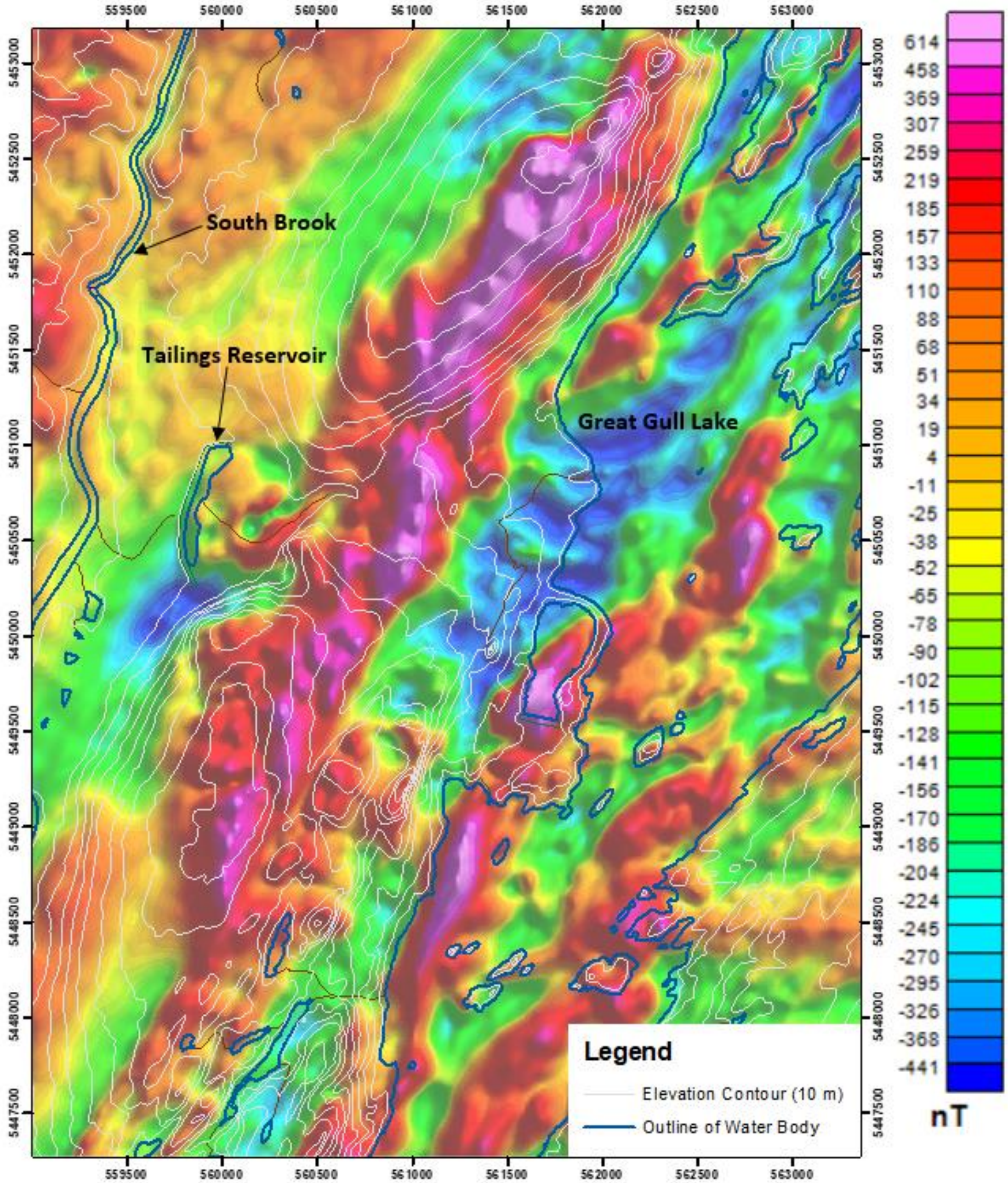

Figure 4.11: Residual magnetic field over the Gullbridge region (Geological Survey of Newfoundland, 2007). The grid was generated from residual magnetic field data collected by Fugro Geosurveys Inc. between March 1st-27th, 2007 in a survey flown at a line spacing of 100 m and a nominal terrain clearance of 40 m. It was acquired from the NL Mines Branch Geoatlas.

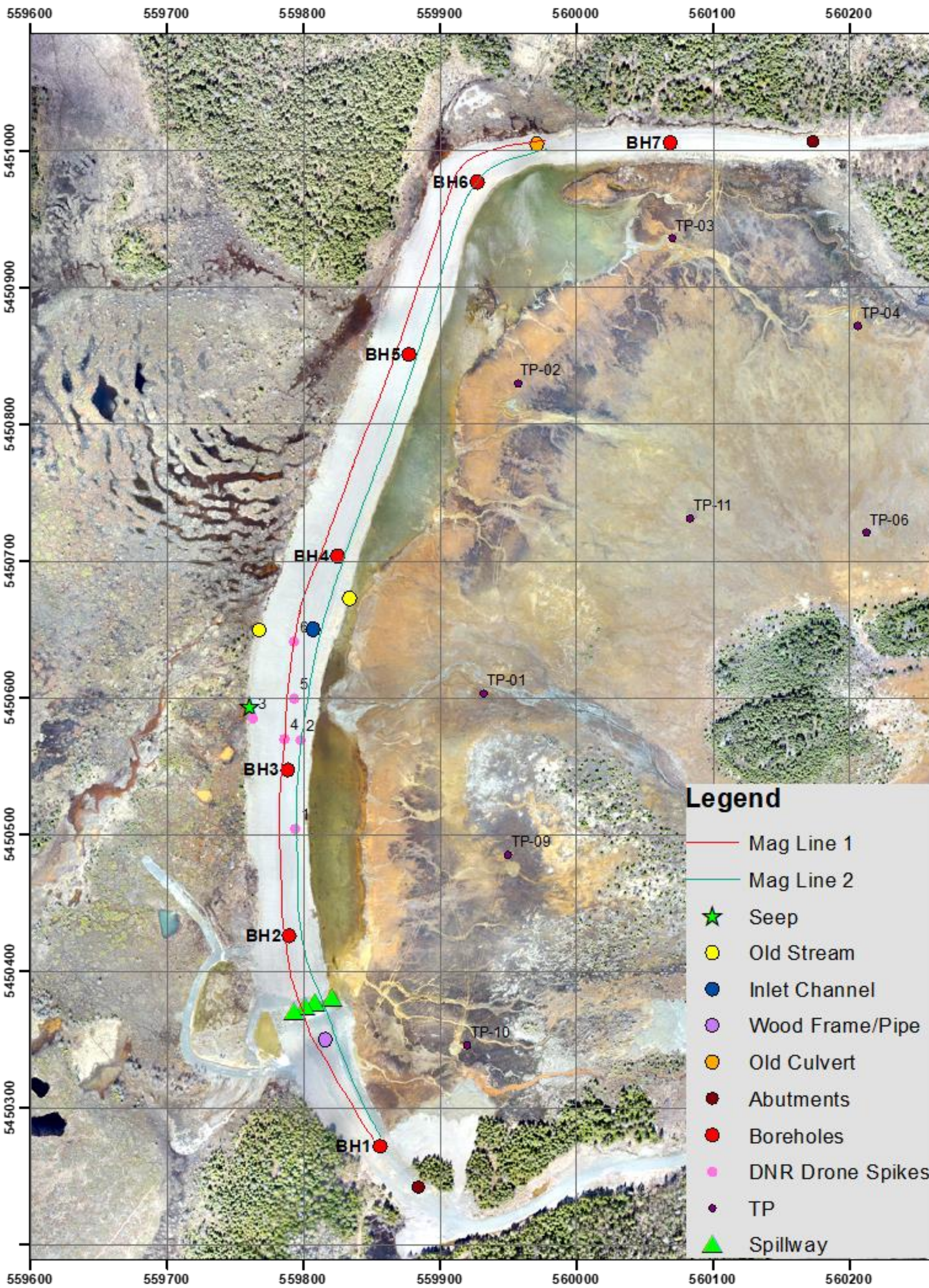

Figure 4.12: Magnetics Line 1 and 2 stations collected over the Gullbridge Dam on July 17th, 2016.

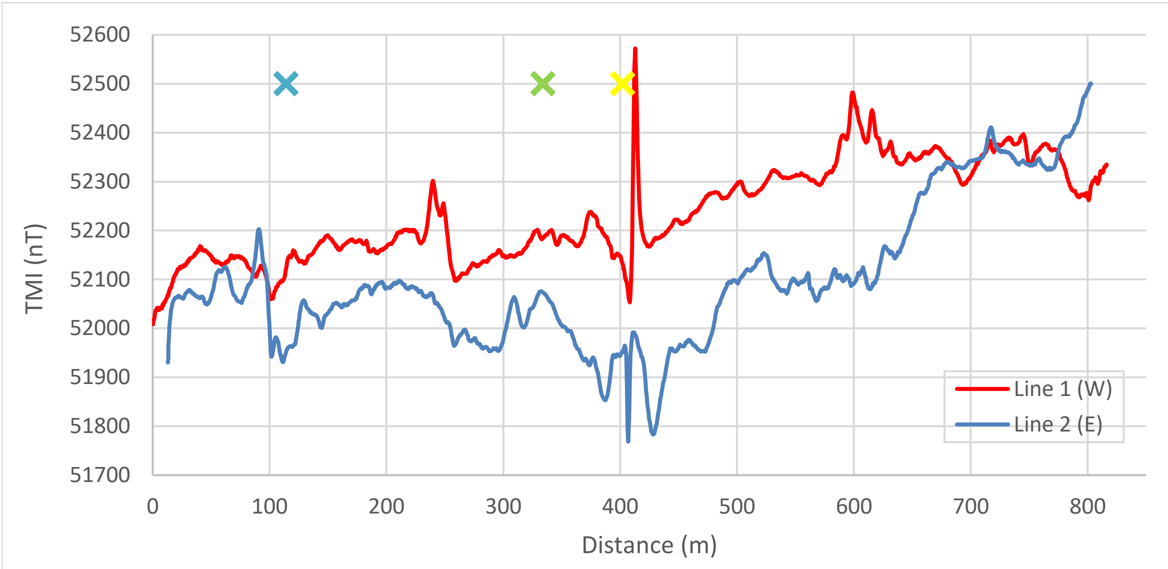

Figure 4.13: Corrected TMI (nT) collected S-N along the Gullbridge Dam. Distance measured along the embankment from ~6m north of BH1 (Fig. 3.21). Blue, green and yellow stars indicate approximate locations of spillway, seep and old stream/inlet respectively.

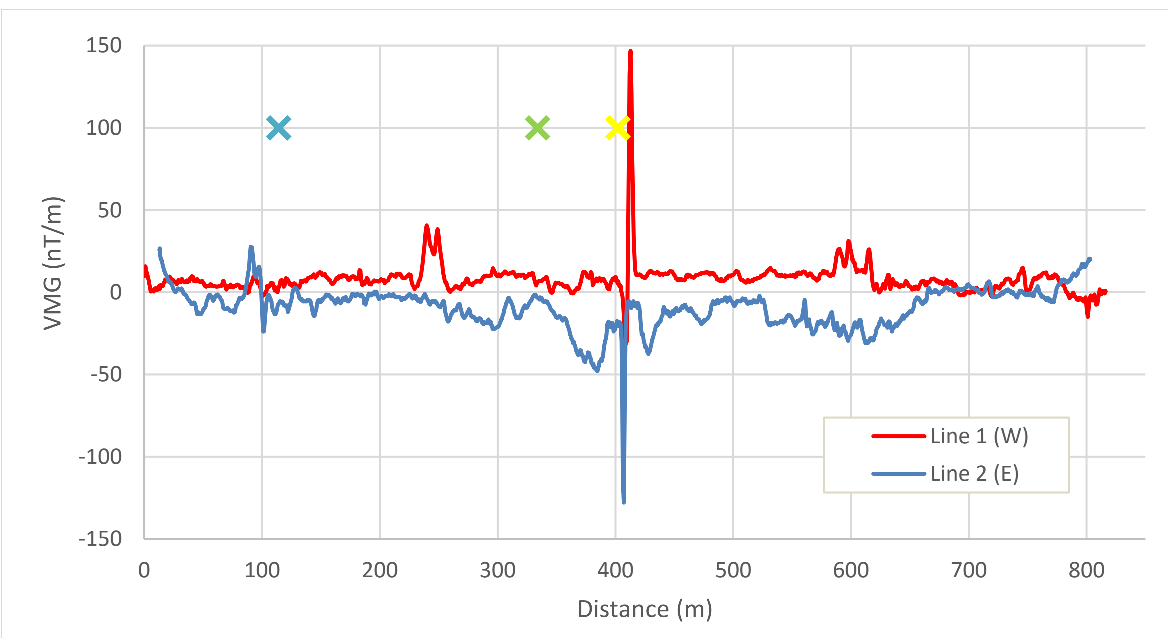

Figure 4.14: Corrected VMG (nT/m) collected S-N along the Gullbridge Dam.

A sharp and strong (several hundred nT) anomaly was recorded over the old stream/inlet channel region. The source of this short wavelength feature must be a small, near surface highly magnetic object. It is presumably anthropogenic iron, as anomalies in VMG of greater than 50 nT//m are typically anthropogenic in nature (Reynolds,1997). This anomaly is inferred to be the response to the inlet channel, whose design is not described in the currently available literature. It may be a historic decant structure. It is possible that during the initial phases of dam construction, a metal casing/decant was placed in the area to allow for water to flow freely beneath the embankment without eroding the dam fill materials. The anomaly is sharper on Line 2, suggesting it is a buried utility dipping to the west beneath the dam. The widths of the anomalies point to burial depths of about 3 to 4 m below Line 2 and 2 m below Line 2.

There is an abrupt drop in TMI over the spillway (blue star). This magnetic low could be the response to a lithological change as the spillway is underlain by limestone. Other sharp anomalies are more mysterious, but point to heterogeneities in the dam materials possibly related to "zoning" of materials used during repair work.

The data suggests the sharp variation in TMI south of the spillway is the response to the standpipe feature indicated in Figure 4.12. The anomaly is sharper on Line 2, suggesting it is a buried metal feature dipping to the west beneath the dam.

4.3 Direct-Current Resistivity and Induced Polarization

In the following sections the results of the DCR and IP surveys over the Gullbridge TMA are discussed. The surveys were taken along the embankment in late spring 2016, and over the seep area, in the winter of 2016 and the late spring of 2017. The data are presented as profiles of apparent resistivity ρ_a versus quadrupole midpoint location (x or y) at different pseudo-depths (a-spacings), two-dimensional inversion models generated in RES2DINV, and one-dimensional VES models.

4.3.1 June 2016 Along the Embankment

Figure 4.15 presents a map image indicating the midpoints (burgundy circles) of each of the Wenner DCR spreads arranged over the June 2016 survey line conducted along the embankment. Figure 4.16 displays profiles of the apparent resistivity versus *x* over the survey line in Fig. 4.15 for two a-spacings: a=5 and a=10 m. Measurements of ρ_a associated with pseudo-depths larger than a=10 were deemed unreliable due to low signal-to-noise. The surface locations where the survey line intersects the spillway, seep, and old stream/inlet channel are indicated by the blue, green and yellow stars respectively.

The values of ρ_a in Figure 4.16 range between 2,788 – 179 $\Omega * m$. Apparent resistivity measurements are weighted averages of the ground resistivities between the electrodes, so the resistivities of the dam materials would have a wider range than ρ_a. Resistivity decreases with depth, which is expected given the dam fill near the surface is drier, and dam fill beneath the water table is saturated with the tailings pond water.

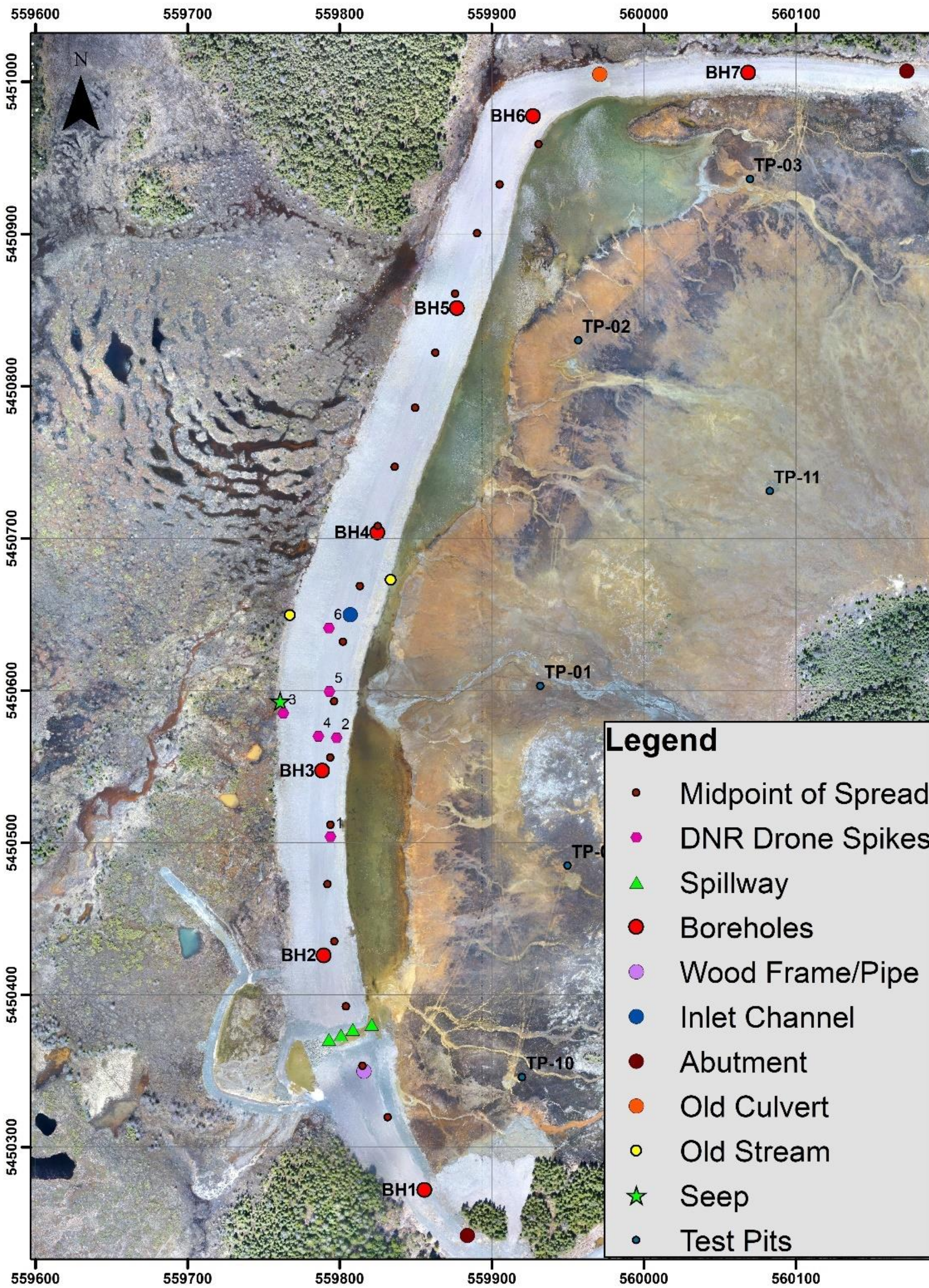

Figure 4.15: Midpoints of each DCR spread conducted over the Gullbridge TMA in June 2016.

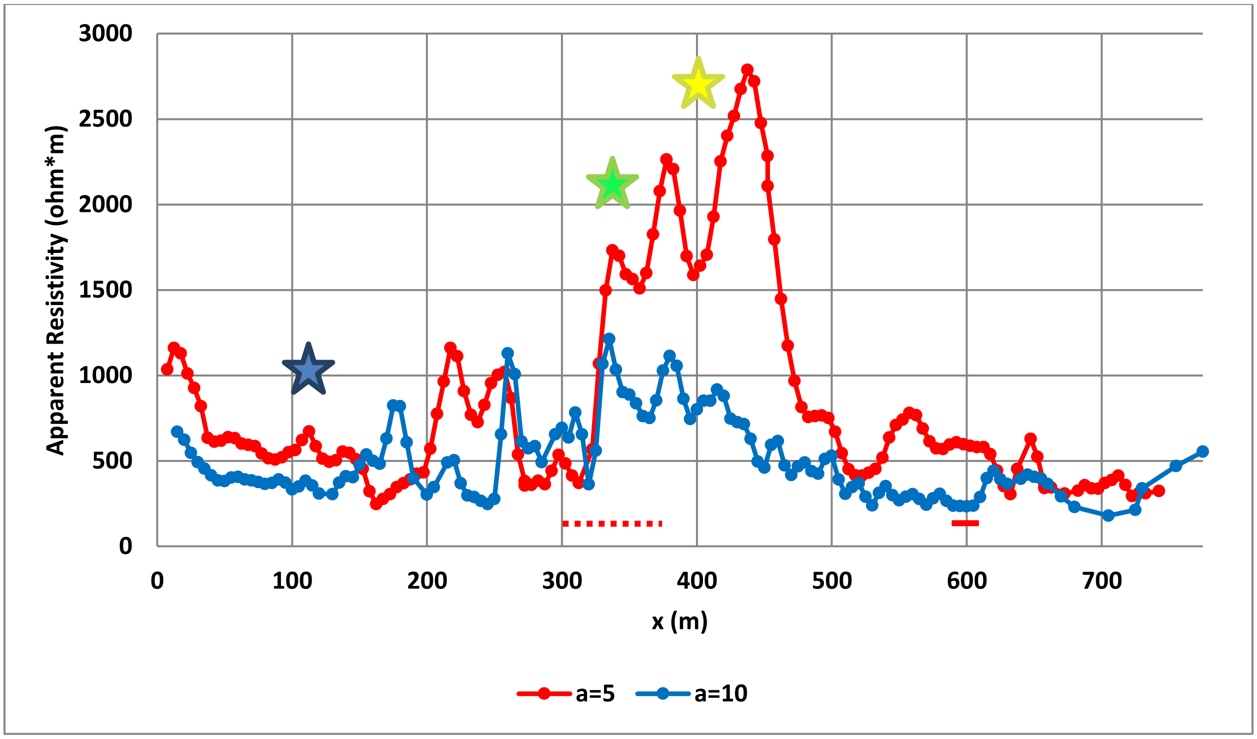

Figure 4.16: Profiles of ρ_a versus x for a-spacings (m) of 5m and 10m obtained from DCR Wenner CST survey along the middle of the Gullbridge Dam in June 2016. Blue, green and yellow stars indicate approximate locations of spillway, seep and inlet/old stream respectively. The dotted red line and shorter solid line indicate the approximate locations of the seep grids (section 4.3.2) and the northern GPR grid (section 4.4.2) respectively.

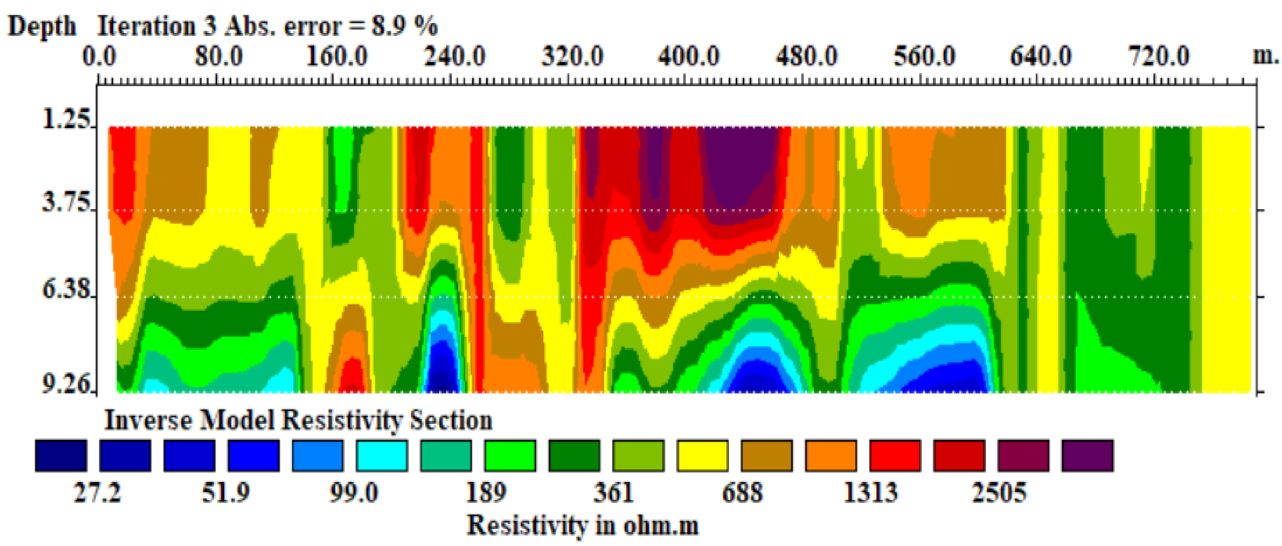

Figure 4.17: 2D Inversion model generated from DCR Wenner CST data plotted in Figure 4.16.

The most striking features in the profiles plotted in Figure 4.16 are the series of peaks between 320 m and 485 m. An anomalous region of increased porosity is inferred to be the subsurface property generating the peak over the seep region. In regions where dam fill has loosened due to seepage related erosion, the water table may sink, resulting in measurements of high resistivity near the surface as air replaces water in the pore space. The next two pronounced peaks overlie the location of the inlet channel. It is suspected these peaks are indicative of seepage related erosion around the inlet channel, and through the seep identified on the downstream slope. A small increase in apparent resistivity over the spillway (blue star) is reasonable due to the presence of resistive limestone fill lining the spillway. It is unclear what is causing the small peaks between x=150 m and x=300 m. These and other variations are presumably related to heterogeneities in dam fill, consistent with small scale variations in the magnetics (Figure 4.13).

Figure 4.17 displays the resultant inversion model generated from the Wenner CST data presented in Figure 4.16. It is important to note not to overinterpret this model due to the sparsity of the data. The inversion model shows the greatest contrast over the seep with depth. The high resistivity near surface feature between x=320 m and x=480 m is interpreted as a dry zone resulting from draw down of the water table over the seep. The two conductive features along the base of the dam underlying approximately x=450 m and x=560 m may represent seepage pathways beneath the embankment near the old stream and the region of observed seepage near BH5 in the north, respectively. A third anomalous zone of high conductivity underlying ~x=240 m may potentially indicate seepage beneath the embankment. The resistivities of the inferred seepage pathways are in agreement with the estimated value for tailings saturated sand and gravel calculated using Archie's Law ($93.8\ \Omega * m$).

4.3.2 Seep Surveys

Figure 4.18 displays the electrode positions of DCR spreads conducted over the Gullbridge Dam seep area during survey work conducted in November 2016 and June 2017. For the spread carried out in November 2016, YLINE2, slightly larger circle markers are used to distinguish it from the 2017 surveys. Note that in the figure, the dots marking YLINE2 are actually spaced at 5 m from one another, marking coordinates measured for the GPR survey carried out over the same line. YLINE2 actually extended approximately 20 m to the N-E of the marked circles. The approximated location of the last electrode along YLINE2 is indicated by the slightly larger circle marker and the dashed line indicating the inferred distance to last electrode. The centers of the northern and southern extension of the "2 m Central" survey line conducted in June 2017 are indicated by the red stars. It is worth noting the original "2 m Central" spread overlaps YLINE2 (Nov. 2016).

Some of the notable surface features in the area are the metal drone markers positioned by DNR (indicated by numbered pink dots), borehole BH3 and the inlet channel (blue dot in the north). Circles outlined in black indicate coordinates acquired by the RTK over the survey area in June 2017. The rest of the circles were calculated from a linear interpolation function used over the survey area.

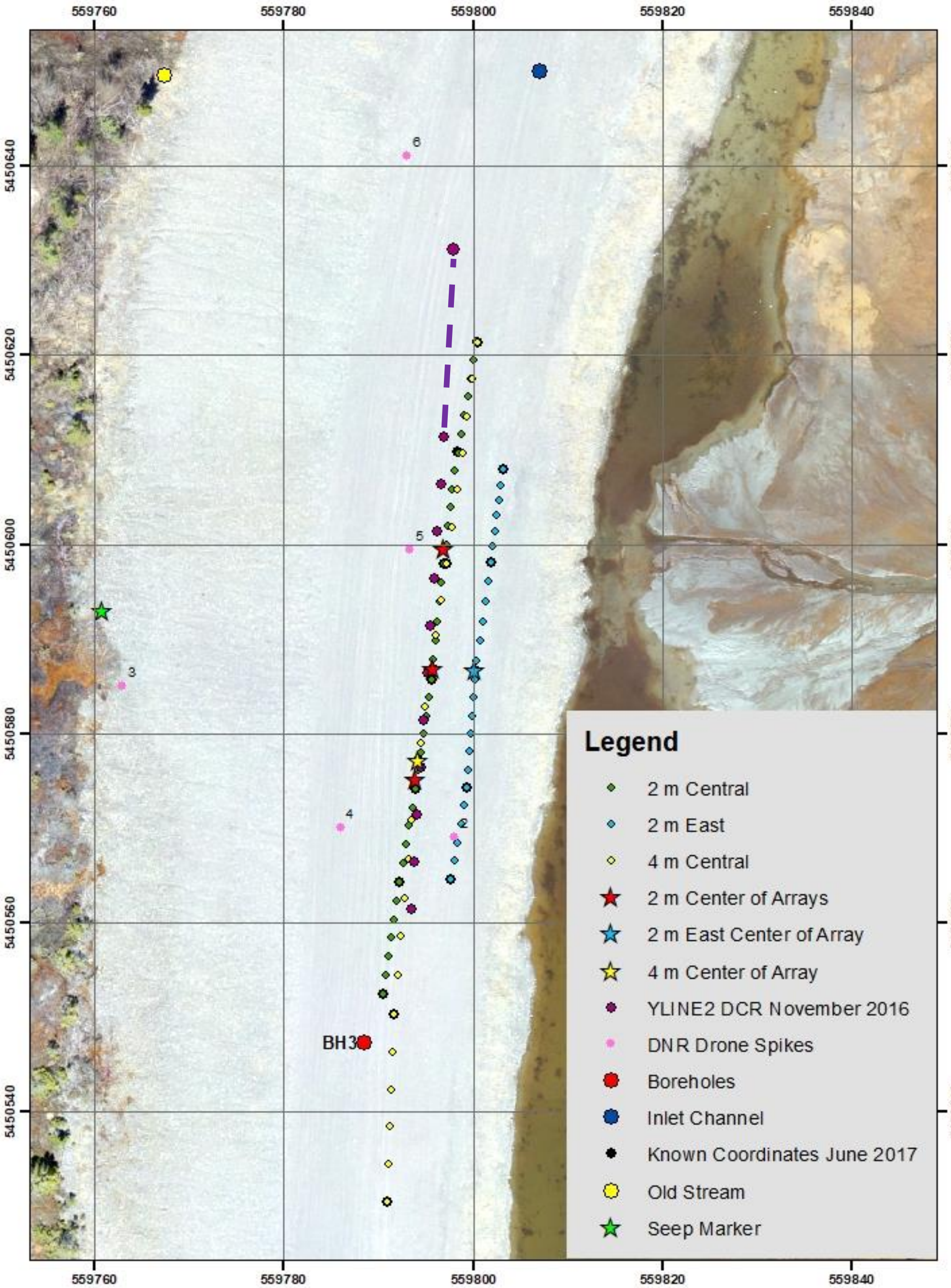

Figure 4.18: Electrode positions of DCR Schlumberger spreads conducted over the Gullbridge Dam seep area in November 2016 and June 2017, and other features of note in the area. The centers of overlapping spreads conducted in June 2017 are indicated by stars.

November 2016 (YLINE2)

Figure 4.19 displays the profiles of $\rho_a$versus x for 5 pseudo-depths acquired from a 2 m Schlumberger VES survey consisting of two overlapping spreads carried out over the seep area where the dam height is approximately 9 m in November 2016. Unreliable measurements due to low signal-to-noise particularly at greater pseudo-depths were omitted from the profiles. The profiles indicate decreasing resistivity with depth, resulting from increasing saturation of materials with depth. There is a general trend of increasing resistivity to the north. These features are consistent with the results of the embankment survey (Figure 4.16).

The values of ρ_a range between 14,572 and 114 $\Omega * m$ in Figure 4.19. The increase in ρ_a for the smallest a-spacing (a=3 m) compared with the June 2016 survey (Figure 4.16) is partly due to the smaller penetration depth of the current, more of which flows through the more resistive ground near the surface. Comparing the a=5 results for both surveys, the apparent resistivities in November are higher (~1655 to 4160 Ω.m cf 400 to 1025 Ω.m over the same ground) and the variations are not as extreme. The higher apparent resistivities are due to frozen ground. The June 2016 surveys were conducted during hot weather (26° C), and the November surveys were collected under freezing conditions. The resistivity of ice is orders of magnitude higher than typical ground water (Reynolds, 1997). The difference in magnitude of the peaks between the two surveys demonstrates a change in electrical structure with time: there was probably more seepage in the spring.

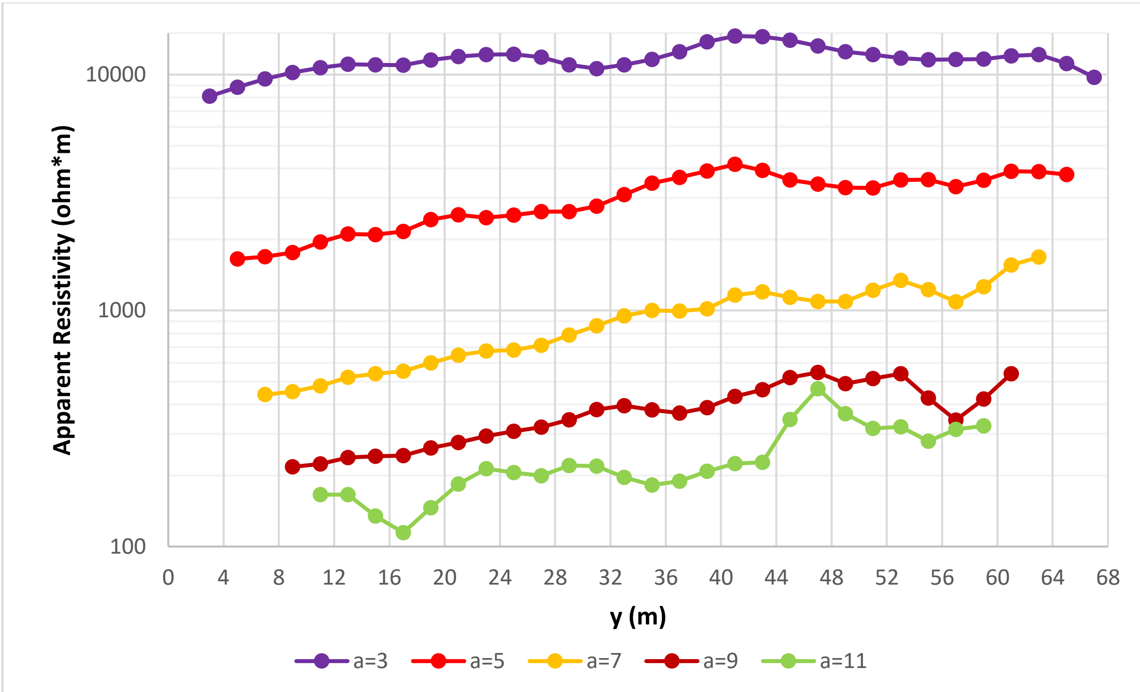

Figure 4.19: Log-linear graph displaying profiles of ρ_a versus *x* for 5 a-spacings (m)acquired from 2 m Schlumberger DCR survey collected S-N over the seep area in November 2016. *y*=0 corresponds to distance ~305 in Figure 4.12.

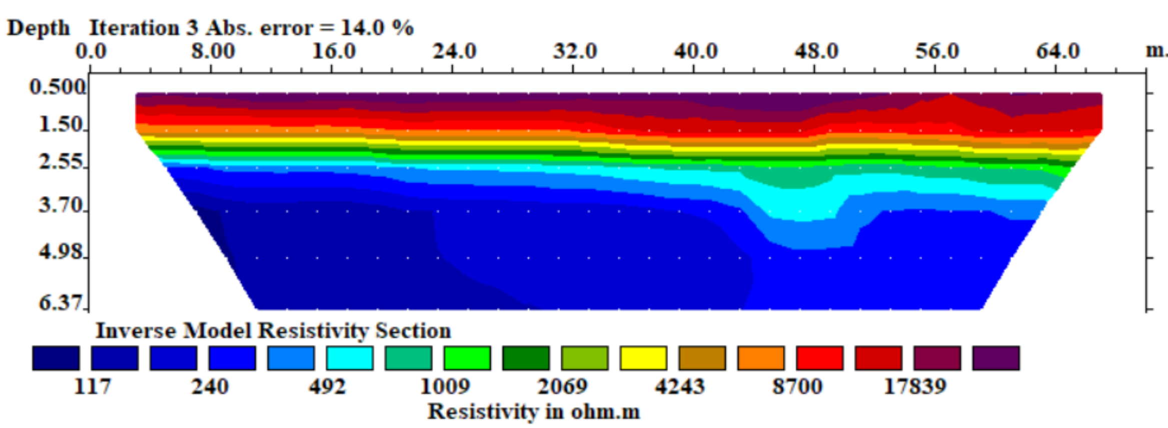

Figure 4.20: 2D inversion performed in RES2DINV on 2 m Schlumberger DCR data collected S-N over the seep in November 2016. The seep is located in the wetland adjacent to station *y*=30 m.

The corresponding 2-D inversion model of data displayed in Figure 4.19 is presented in Figure 4.20. The model extends to a depth of 6.4 m, which is over half of the embankment height of ~9 m at this location. The near surface is characterized by high resistivity due to the dry, frozen ground. This high resistivity layer thickens to the north. It is not possible to distinguish the water table boundary in this model, as no sharp changes in resistivity are displayed. It is estimated from piezometer and GPR data that the water table ranges in depth between approximately 2.2 m in the south and 2.7 m in the north. In that case, the water table in the inversion model would correspond roughly to the bottom of the dark green contour interval. Elevation of the water table in the south would indicate the presence of a hydraulic gradient to the north. .

Figure 4.21 displays the profiles of chargeability versus *x* for the 5 *a*-spacings. Negative values of chargeability and overlapping points were discarded. Chargeability increases with depth up to $a = 9$ (depth ~ 4 – 4 ½ m). Also, with depth, the profiles become increasingly erratic and zig-zag trends dominate the dataset. It is suspected this pattern is the response to surface anomalies. This zig-zag pattern was also observed during the June 2016 SP surveys over SP Line 1 and Line 2. A decrease in the signal to noise ratio would generate these trends.

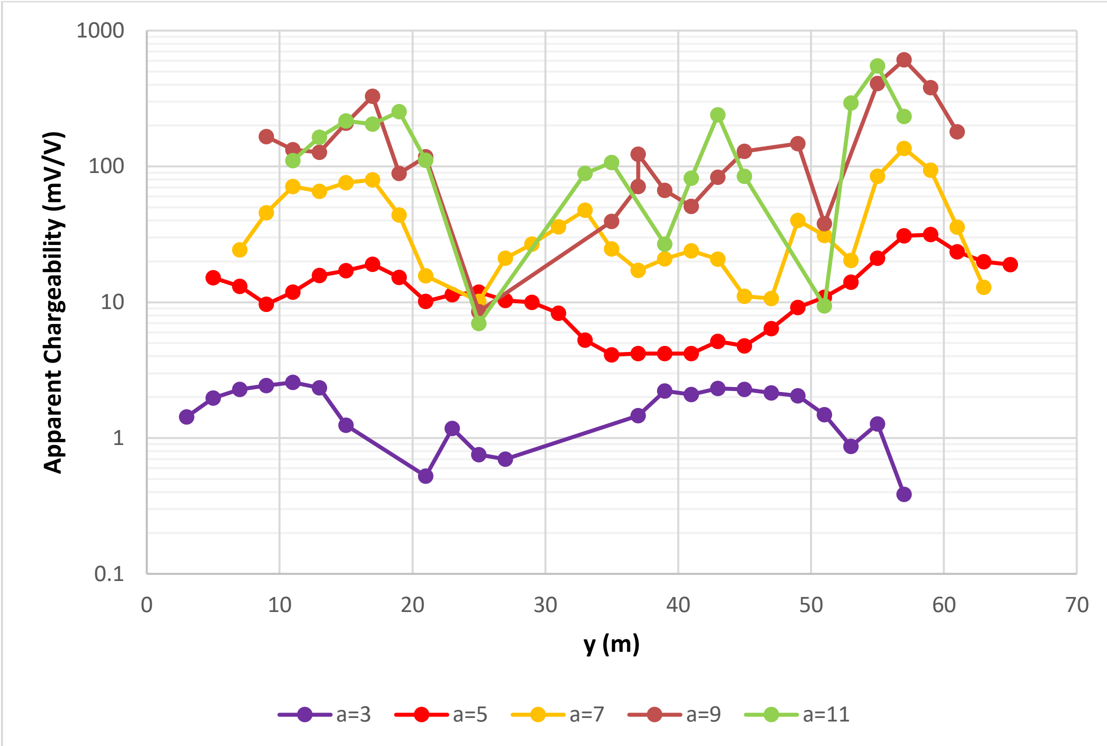

Figure 4.21: Graph displaying profiles of apparent chargeability versus y for 5 pseudo-depths acquired from 2 m Induced-Polarization survey collected S-N over the seep area in November 2016.

<u>*June 2017, 2m surveys along centre line of embankment*</u>

Figure 4.22 displays the profiles of apparent resistivity versus y acquired from the DCR surveys conducted in June 2017, using electrodes spaced at 2 m intervals along a S-N line in the centre of the embankment. The data locations y correspond to positions along YLINE05 of the GPR seep grid collected on the same trip. Two types of surveys were conducted: one using Schlumberger array soundings and consisting of three overlapping spreads, and one utilizing Wenner arrays over the central of the three spreads.Values of ρ_a for larger a-spacings and those associated with a "central artifact" were removed from the dataset. The central artifact (see Appendix A4.2) refers to soundings over the middle of the

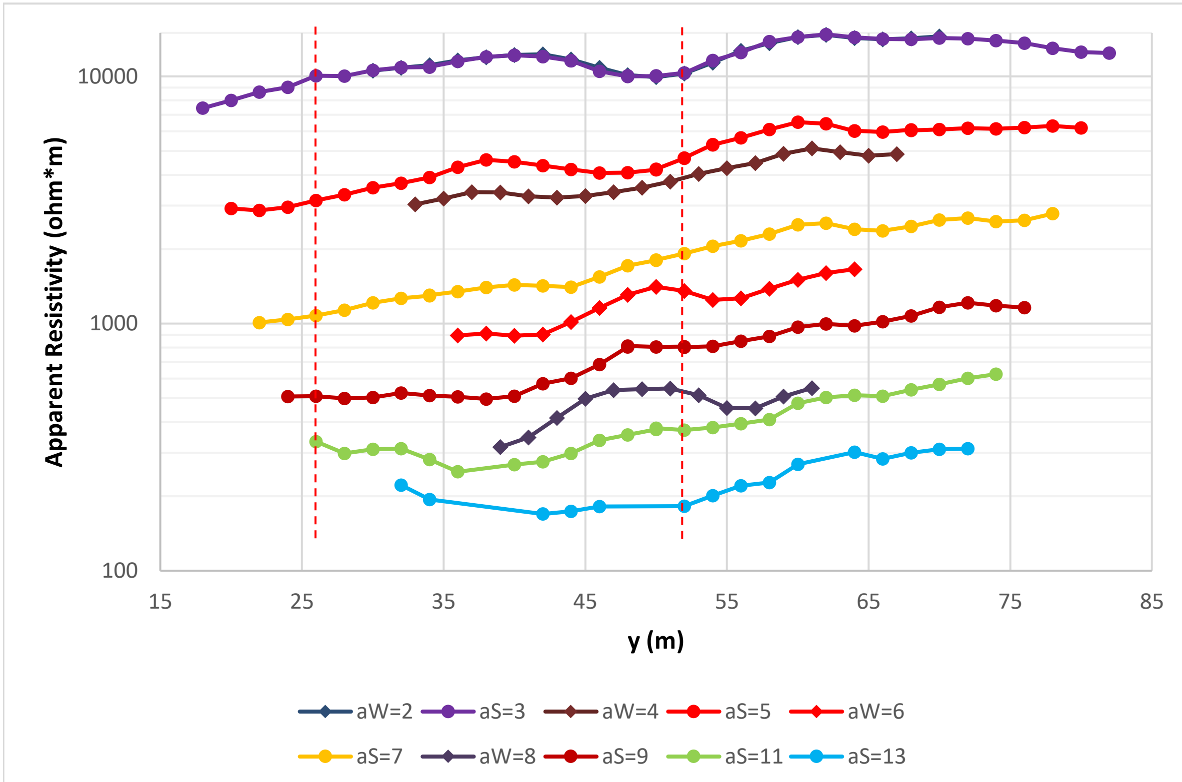

Figure 4.22: Graph of profiles of apparent resistivity versus y for different pseudo-depths obtained from the 2 m DCR surveys collected S-N over the June 2017 seep grid. Circles indicate Schlumberger array data, diamonds Wenner array data. Red dashed lines indicate data used in VES models (Figs. 4.18 and 4.19). Note that the a-spacing for Wenner is defined as current electrode spacing AB/3, whereas for Schlumberger it is AB/2, so $a_S = 3$ and $a_W = 2$ are coincident measurements. The seep is located west of x=53 m.

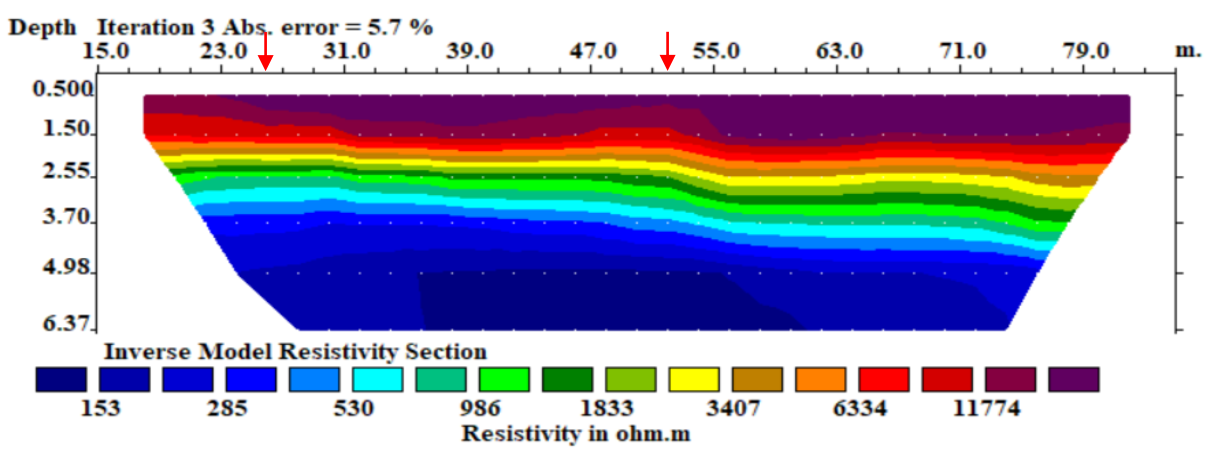

Figure 4.23: Inversion model generated from Schlumberger DCR data from three overlapping spreads shown in Figure 4.16. Red arrows indicate locations of data used for VES models below.

central array (potential electrodes at M=12 and N=13)that were inconsistent, presumably due to malfunction of one of the callouts at the ends of the multicore cables or a connection issue at the unit end. The location of the seep is immediately to the west of array location *y*=53 m.

The large values of ρ_a measured near the surface are a result of dry near-surface materials. Figure 4.23 depicts the inversion model of the ρ_a data. Similar to Figure 4.20, the highly resistive near surface layer is observed thickening to the north, and the estimated depth of penetration (~6.3 m) is much less than the height of the dam (~9-10 m at this location). The interface representing the water table is not well-defined. However, it appears there is a hydraulic gradient to the north inferred from the dipping resistivity contours. However, this could be related to the compaction of the materials at depth. There is a suggestion of lower resistivity over the seep area, however measurements of apparent resistivity at larger *a*-spacings are harder to interpret.

The RES2DINV algorithm, used to produce the 2D resistivity model in Figure 4.23 assumes smooth variations in ρ in two dimensions beneath the “2 m Central” Schlumberger VES survey conducted over YLINE05 of the June 2017 seep grid. In comparison, VES models assume a finite number of distinct horizontal layers of uniform ρ in one dimension. VES models were generated to assist in delineating the top of the saturation zone underlying the crest of the Gullbridge Dam.

Figure 4.24 and 4.25 are the 1-D VES models generated using values of ρ_a over *y*=26 m and *y*=52 m of the Schlumberger DCR survey assuming a 2-layer system

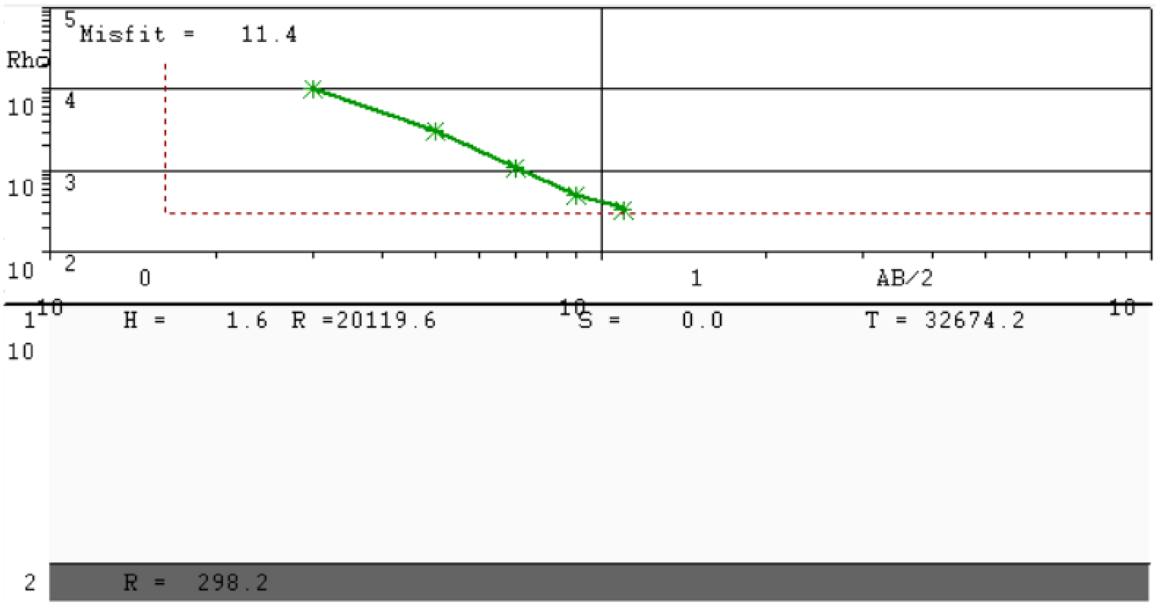

Figure 4.24: Schlumberger VES modelling of “2 m Central” DCR data at position *y*=26 m over YLINE05 along the June 2017 seep grid assuming a 2-layer system.

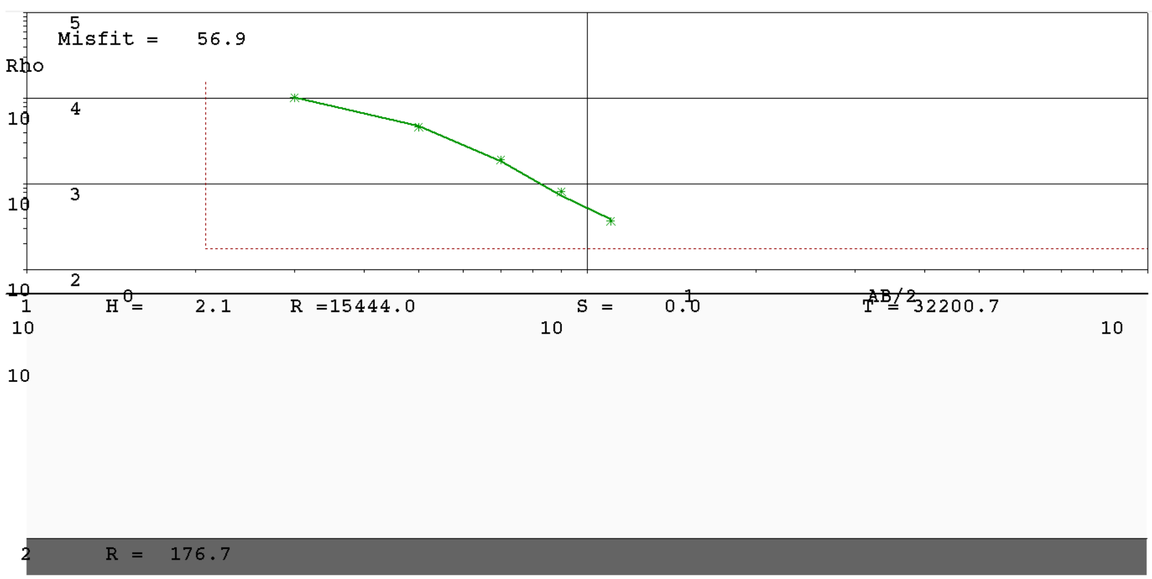

Figure 4.25: Schlumberger VES modelling of “2 m Central” DCR data at position *y*=52 m over YLINE05 along the June 2017 seep grid assuming a 2-layer system.

comprised of two uniform, electrically distinct units, saturated and unsaturated sand and gravel dam fill. The data provide insight into the resistivity structure of the top 5-6 m of the 8 m high dam wall.

The best fit model in Figure 4.24 gives an upper layer 1.6 m thick with resistivity ρ = ≈20,000 $\Omega * m$ corresponding to the dry near surface layer observed in Figure 4.23. Dam sediment located below the inferred water table at 1.6 m depth has resistivity ρ=≈300 $\Omega * m$. The VES model in Figure 4.25 gives the unit of near-surface dry material as 2.1 m thick, in general agreement with the deepening resistivity contours in Figure 4.23. The resistivity values of the bottom layer in the VES models are consistent with damp to wet sand and gravel. Given the contrast in the assigned values of ρ_a between the top and bottom layers, these models have generated a reasonable depth to the water table interface. The water table was encountered at an inferred depth of 2.2 m within BH3 located ~7.5 m south of electrode #1 and a depth of 5.7 m over BH4/MW located ~85 m north of electrode #24. This is consistent with the deepening of the water table to north in Figures 4.24 and 4.25, and the deepening resistivity contours in Figure 4.23.

Figure 4.26 presents the inversion model generated from both Wenner and Schlumberger data collected over the “2 m Central” survey line. This model also shows that the high resistivity, dry near surface layer thickens to the north. Applying the water table depths from the VES modelling, the red contour indicates the approximate location of the water table.The benefit of combining the Schlumberger and Wenner profiles is the increased precision resulting from additional data.

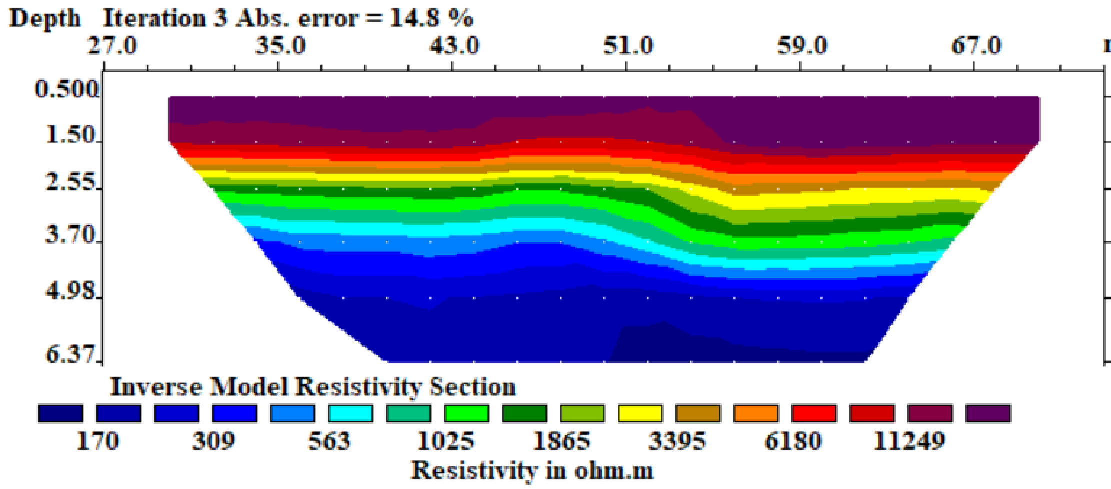

Figure 4.26: Inversion model of combined Schlumberger and Wenner DCR results over the 2 m Central spread displayed in Figure 4.22.

June 2017, 4m survey along centre line of embankment (4 m Central)

A Schlumberger DCR survey was undertaken using electrode spacing of 4 m, in the hope of obtaining a resistivity model for the entire thickness of the embankment. Unfortunately, large a-spacing measurements were very noisy. Figure 4.27 displays the profiles of ρ_a versus y obtained from the 4 m survey following removal of unreliable measurements (see Figure A4.3 for complete data). The first electrode position is is located ~6.75 m south of YLINE5 of the GPR grid. The values of ρ_a in the a=6 m and a=10 m profiles are consistent with measurements at 2m electrode spacing (Figure 4.22), with values falling between those of a=5 m and a=7 m, and a=11 m and a=13 m respectively. The a=14 m profile yields values of ρ_a very similar to those of a=13 m, hinting at highresitivity layers beneath the dam.

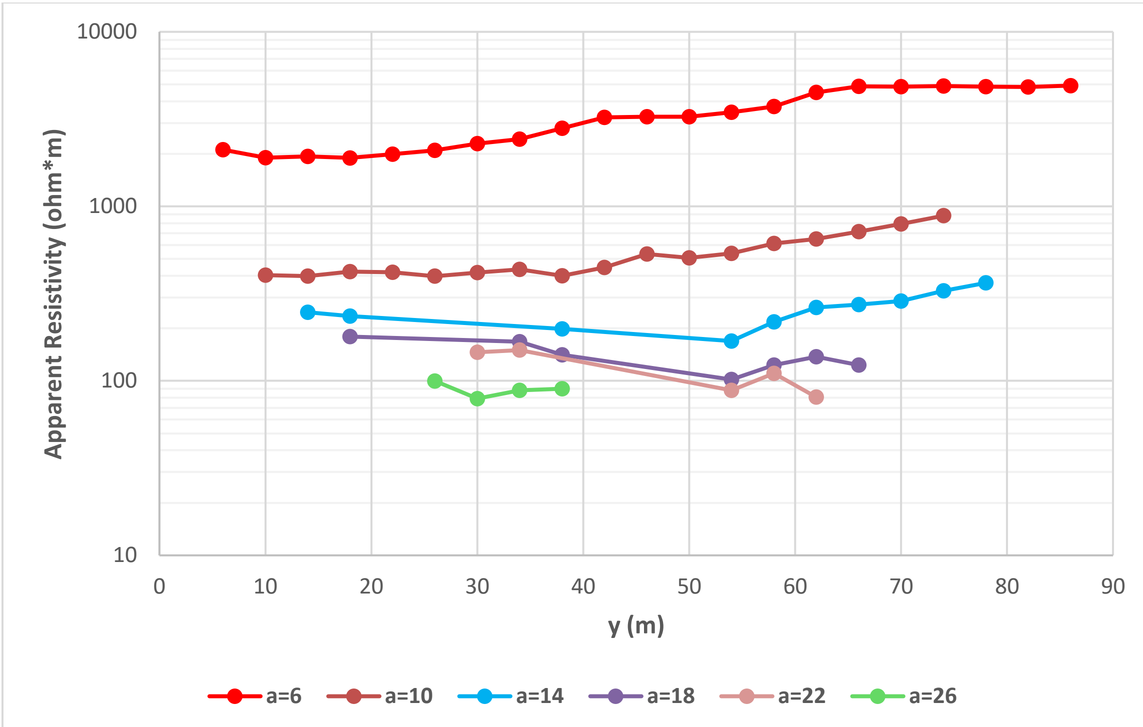

Figure 4.27: Selected points of ρ_a versus x profiles acquired over the "4 m Central" Schlumberger DCR survey collected S-N over the seep grid in June 2017. The array falls over YLINE05 of the June 2017 seep grid with exception to the first 6.75 m of the survey line located south of the grid**.** The seep is directly downstream of y=60 m.

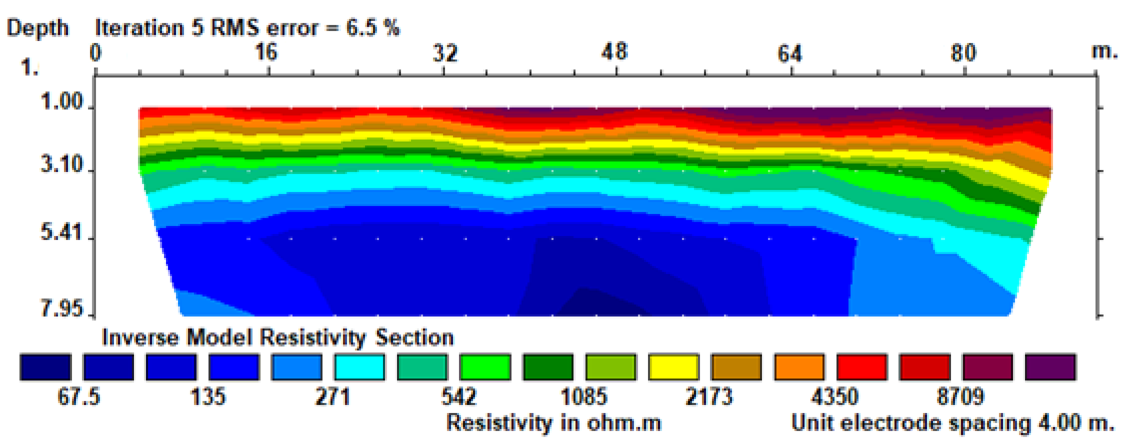

Figure 4.28: Inversion model generated from Schlumberer DCR data using values of ρ_a up to a=14 over the "4 m Central" survey line plotted in Figure 4.22.

Figure 4.28 is the inversion model generated from ρ_a data in Figure 4.27 up to and including a=14 m . Note the colour scale is much less compressed than previous models due to the extended depth of the model. It extends to a depth of approximately 8 m, close to the height of the dam. As for the other models, there are north-dipping resistivity contours near the surface. The resistive low centered over the base of the model is suspected to be an artifact associated with low signal-to-noise with large a-spacing. The boundary between the aqua and blue contours may indicate the top of the core materials which suggests increasing clay content with depth as indicated by borehole data from 2011 (Stantec Consulting Ltd., 2012)

June 2017, 2m survey east of centre line of embankment

Figure 4.29 displays the profiles of $\rho_a$versus y for 5 different a-spacings acquired from a 2 m Schlumberger DCR survey conducted over the "2 m East" line collected S-N approximately over YLINE07 of the June 2017 seep grid, that is, closer to the tailings than the "Central" lines. The observed seep is to the west of y=55. Values associated with the central artifact and high standard deviation have been removed (Appendix A4.4). The measured ρ_a are considerably lower than the ρ_a measured over the centre line of the dam (cf Figure 4.22). This is likely due to two factors: the water table being shallower closer to the reservoir, resulting in lower resistivities at smaller investigation depths, and more current being channeled through the lower resistivity tailings to the east. Figure 4.30 displays the inversion model generated from the ρ_a data plotted in Figure 4.29.

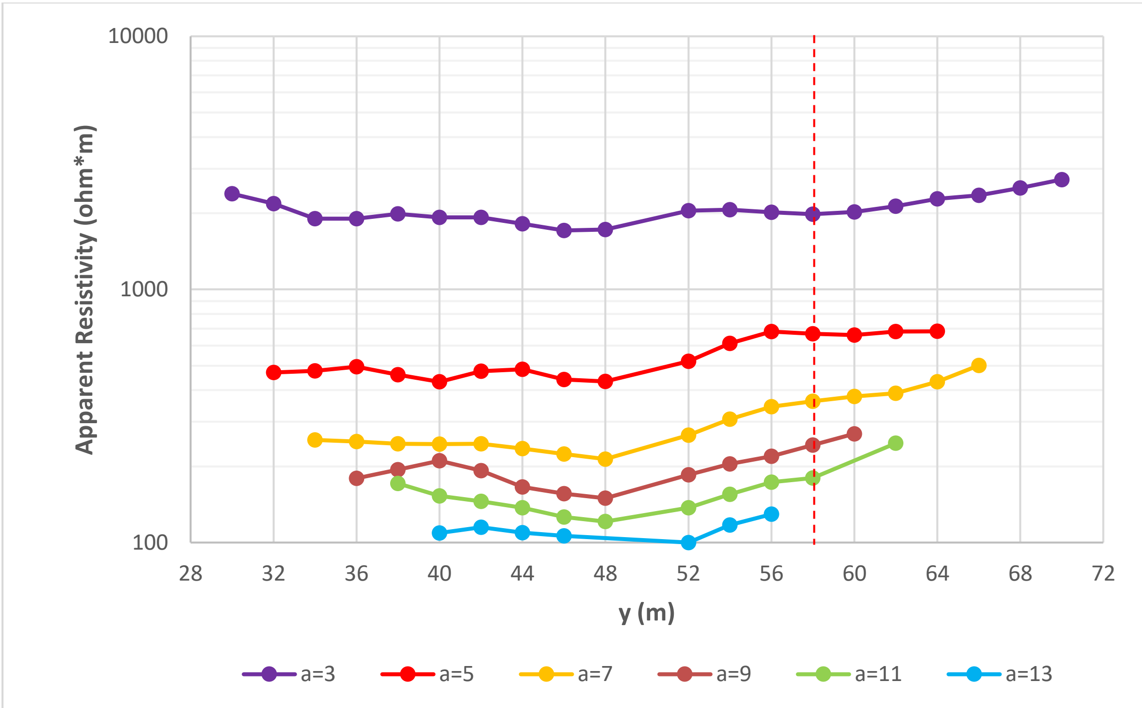

Figure 4.29: Smoothed ρ_a versus y profiles acquired over the "2 m East" Schlumberger DCR survey with the central artifact removed. Red dashed line indicates data used in VES modelling. The value of y corresponds to the y position along YLINE07 of the June 2017 seep grid.

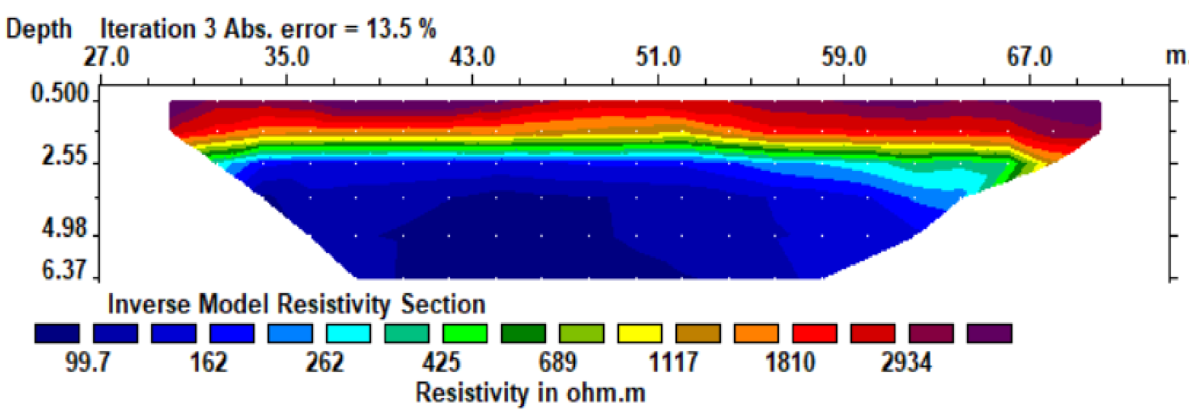

Figure 4.30: Inversion model generated from Schlumberger DCR data over the "2 m East" survey line plotted in Figure 4.29.

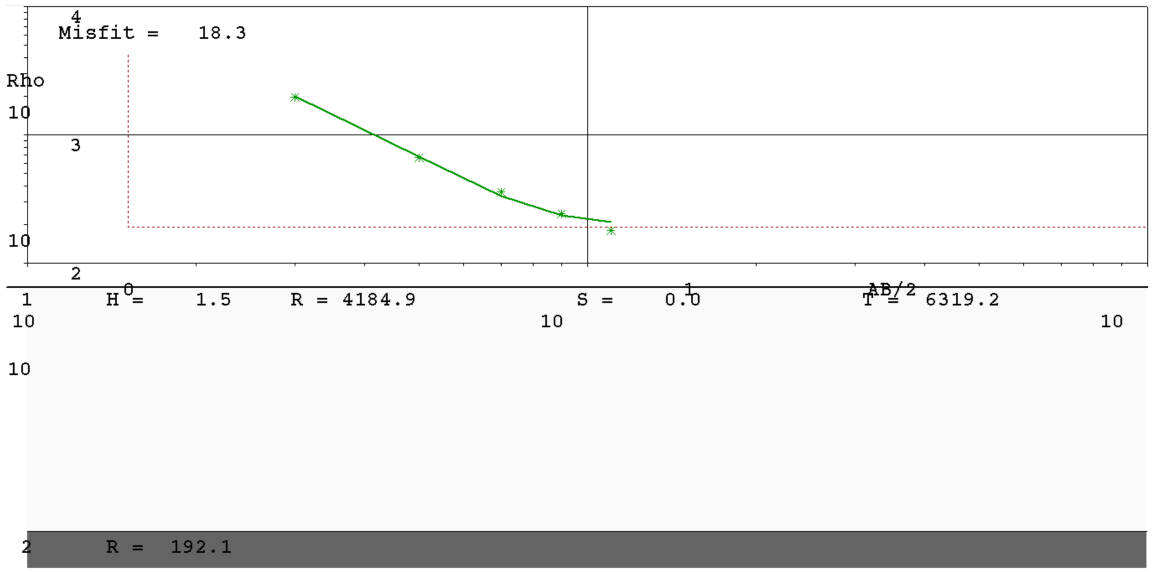

Figure 4.31: Schlumberger -1-D VES model of “2 m East” ρ_a data at position y=58 m along YLINE07 over the June 2017 seep grid assuming a 2-layer system.

Figure 4.31 displays the 1-D VES model generated from measurements of ρ_a over *y*=58 m (Figure 4.29), assuming a two layer subsurface. This model has the top layer 1.5 m thick with a resistivity of $\rho \approx 4{,}200\ \Omega * m$ representative of dry dam fill. In comparison, the value of ρ for the top unit over *y*=52 m along YLINE05 (Figure 4.25) was ≈15,500 $\Omega * m$ suggesting the shallow dam fill is damper to the east, and there is a hydraulic gradient to the west. The bottom unit value of $\rho \approx 200\ \Omega * m$, is consistent with it being saturated dam fill.

DCR surveys over the Gullbridge Dam encountered very high resistivity near the surface, of more than 2,000 Ωm and up to 10,000 Ωm. The material near the surface is dry as seen in previous models over the center of the dam. The resistivity decreased with depth in every instance, down to 100 Ωm or less largely influenced by infiltration of reservoir water through regions of loose core materials.

The ground water table interface is not clearly defined in the 2D DCR inversion models. VES modelling of ρ_a vs. a acquired from the 2 m Center Schlumberger survey predicted the depth to the water table was between 1.6 – 2.1 m over (10,26) and (10,52) of the GPR grid respectively. This supports the hypothesis that the water table is elevated south of the seep, and becomes depressed to the north approaching the seep region.

4.4 Ground-Penetrating Radar

Table 4.1: Selected GPR surveys at the Gullbridge Tailings Facility. Map locations given in Figures 3.27 and 3.29. Yoffsets for grids are relative to the origin of LINE 0.

Date	Antenna (MHz)	GPR Survey	Location	Yoffset	X/Y line spacings (m)
July 16, 2016	100	LINE00,01,02 along embankment.	Odometer wheel		
Sept 25, 2016	100	LINE 0 along embankment	Garmin GPS		
July 16, 2016	100	10 m x 20 m Grid near BH5.	Odometer wheel	600	5/2
Nov 26, 2016	50	50 m x 20 m Seep Grid	Odometer wheel	300	5/5
June 26-30, 2017	250 100 50	140 m x 20 m Seep + Old Stream Grid (Fig 3.29)	Odometer wheel	275	5/2
Sept 25, 2016	100	LINE05 over outlet in wetland	RTK GPS		
Feb 20, 2017	100	Wetland LINE06 - 09	RTK GPS		

Several GPR surveys were carried out at the Gullbridge TMA between June 2016 and June 2017. Some were imprecisely located or redundant. Those listed in Table 4.1 are discussed in this section. Their locations are illustrated in Figures 4.32, 4.45 and 4.56 in the following discussion.

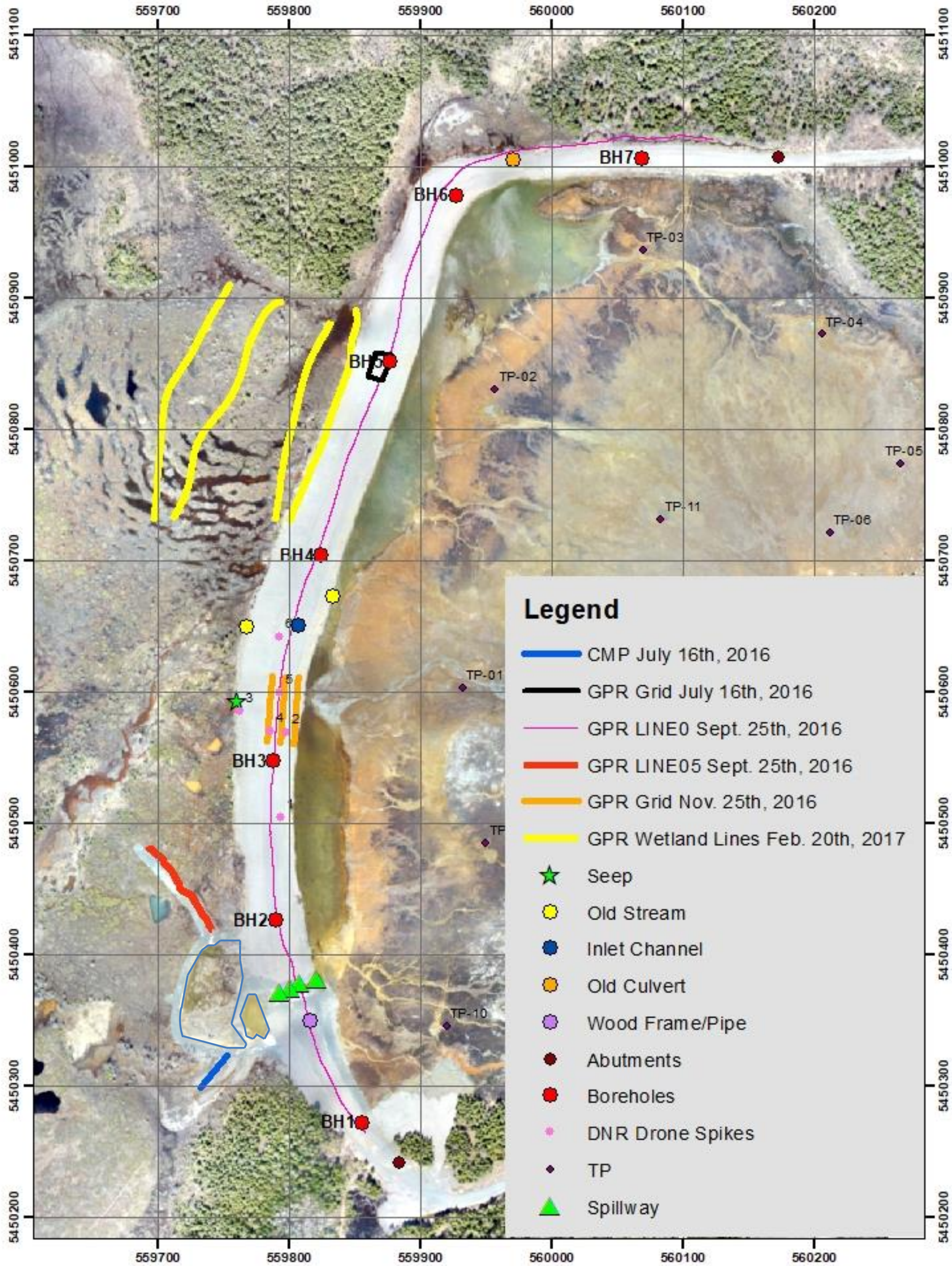

Figure 4.32: GPR surveys collected over the Gullbridge TMA between July 2016 and February 2017. The settling ponds in the south are outlined by the blue lines.

Figure 4.32 indicates the locations of the GPR survey lines conducted over the Gullbridge Tailings impoundment between July 2016 and February 2017. Orange discoloured tailings water is visible in Figure 4.32 discharging from the base of the downstream slope ~ 17.1 m west of the July 2016 grid. Note that the orange discolouration is likely due to reducing conditions in the wetland and iron precipitation. The July 2016 CMP is indicated by the thick blue line near the sediment ponds, which are outlined in blue. GPR LINE00 (pink line) and GPR LINE05 (red line) collected in September 2016 are also indicated.

Three orange lines in Figure 4.32 just north of BH3 indicate the perimeter of the November 2016 GPR grid. The orange dots correspond to lines YLINE0, YLINE02 and YLINE04 giving the general outline of the grid. The W-E x-lines were roughly 20 m long and mostly 5 m apart, but with XLINE10 midway between XLINE09 and XLINE11 with 2.5 m spacings. DNR marker 4 lies ~over YLINE00 between XLINE09 and XLINE10, DNR marker 5 lies ~over YLINE02 between XLINE02 and XLINE03, and DNR marker 2 was located approximately over YLINE03 between XLINE09 and XLINE10. The start of YLINE02 is located approximately over x=24 of the “2 m Central” DCR spread. The even x-lines cut across the electrode positions of the DCR, and YLINE02 is along the “2 m Central” DCR spread.

Figure 4.32 displays GPR LINE06 in the east and LINE09 in the west (yellow) collected in the wetland area in February 2017.

The variation in the intensity of the reflections in GPR profiles over unconsolidated materials are primarily related to water content and to a lesser extent the degree of compaction. In general, the intensity of the reflections increase nearer to the reservoir due to abrupt changes in the saturation and/or material properties of dam materials adjacent to the tailings pond. Strong, shallow reflections may result in the early attenuation of the radar pulse which can make reflections from deeper features appear weaker.

GPR surveys conducted over thin strata may produce an interference pattern generated by overlapping of reflection events. When the thickness of a sedimentary layer is much smaller than the wavelength of the GPR pulse it is difficult to distinguish reflections off the top and bottom of a stratum as separate reflection events given their overlap in time (Guha, 2004). However, major interfaces along the Gullbridge Dam are well-spaced and relatively easy to identify in the GPR profiles given the first positive (white) reflection peak is often significantly brighter than the second peak. These major interfaces are picked as the dark line above the bright reflections.

Hyperbolas are typically generated from large cobbles scattered throughout the dam fill as well as buried utilities used in the construction of the dam (e.g. pipes). The profiles were assigned a radar pulse velocity of 0.085 m/ns which was extracted from several hyperbolas distributed throughout the embankment (Appendix A3.3). As the dam material gets wetter and more conductive with depth, the velocity of the radar pulse will change. Therefore interpretations at greater depths may not be as precise.

4.4.1 July and September 2016, Along the Embankment

Figure 4.33 presents the GPR profile images generated from data collected over 3 parallel survey lines approximately 10 m apart spanning the length of the Gullbridge Dam in July 2016. The data was acquired using the odometer wheel (Table 4.1). The survey line locations correspond to three distinct positions along the top of the dam crest: (a) the eastern edge (reservoir side), (b) along the center, and (c) along the western edge (wetland side). The positions of the spillway, seep marker, old stream, and inlet channel are indicated in the legend. Correspondance with the July 2016 and June 2017 seep grids is indicated by the black and orange lines respectively. There is a strong correlation in the depths to the major interfaces between GPR LINE0 (September 2016) (Figure 4.32) and Figure 4.33 collected over the center of the embankment.

The profiles in Figure 4.33 emphasize three major boundaries: the water table (blue horizon), the top of the core (red horizon), and the dam base (green horizon). It is apparent that there is a considerable degree of variation in the depths to the major interfaces across the width of the dam crest. In addition, the strength of the reflections along the major interfaces vary significantly between the profiles as a result of the contrasts in soil saturation. Some features that are consistently detected by the GPR pulse include a wood frame/pipe, the spillway, and an inlet channel located over the capped stream bed. In contrast, isolated hyperbolas generally originate from large cobbles scattered throughout the dam soil.

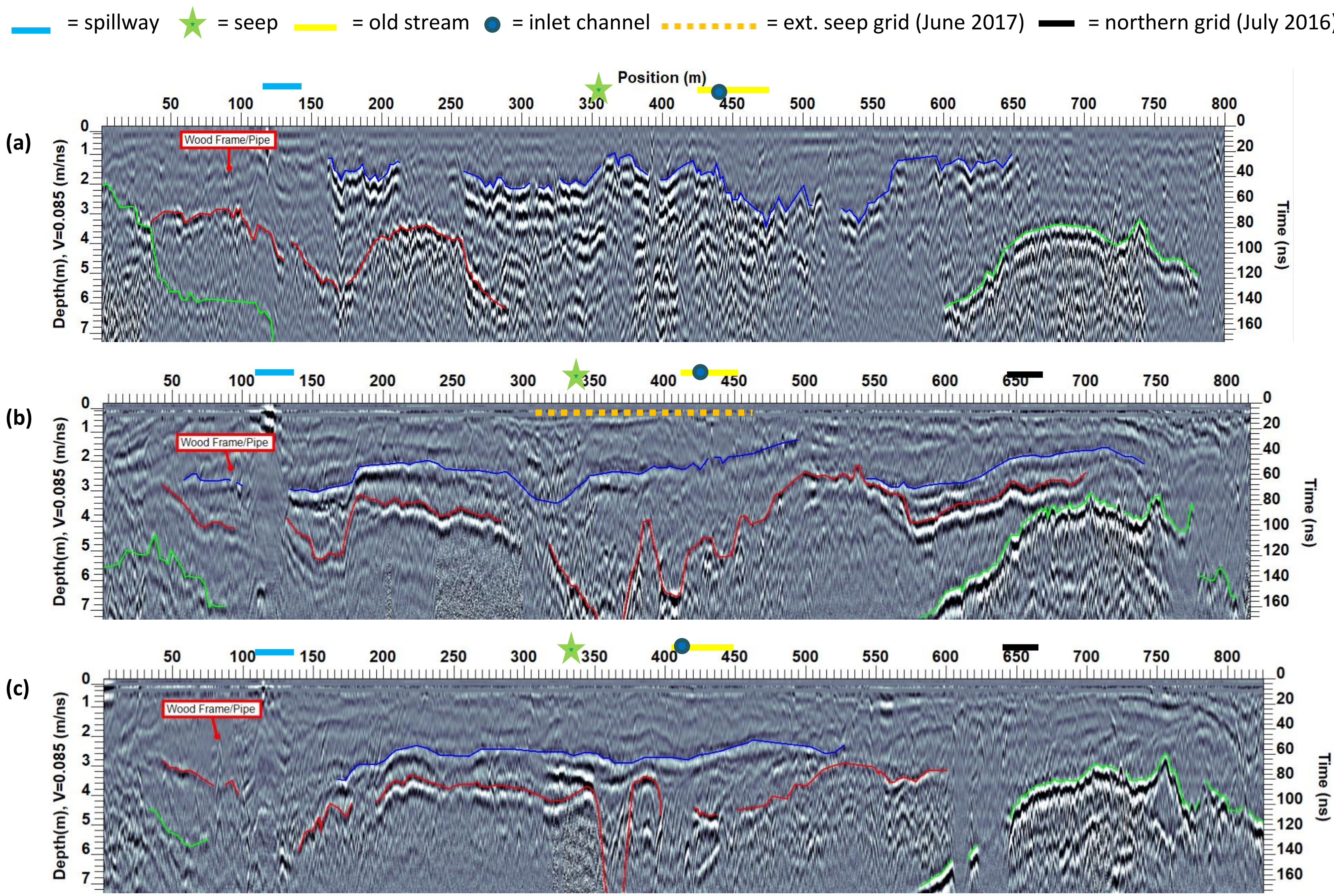

Figure 4.33: Profiles of three GPR survey lines collected S-N over the Gullbridge Dam in July 2016 along the (a) reservoir side, (b) center of the dam, and (c) wetland side. The blue, red, and green horizons indicate the water table, core, and dam base boundaries, respectively.

In September 2016, survey line denoted LINE 0 was carried out along the length of the embankment, using the 100 MHz antennas on the Smartcart, with location determined by a Garmin handheld GPS, which sent positioning information to the GPR through a cable. The approximate path of GPR LINE 0 south to north along the centreline of the embankment is indicated in Figure 3.27, and interpreted profile is displayed in four sections in Figures 4.34 to 4.37. Locations of the boreholes (BH1 to BH7) drilled in 2011 are indicated by labelled vertical yellow lines, and other noteworthy features are marked. Interpretations are guided by borehole data. The first major reflection at 1 to 3 m depth is interpreted as the water table (blue marker horizon); the lowest continuous reflection at 5 to 8 m depth as the interface between dam material and underlying compressed peat (green line). The dashed green lines indicate the approximate height of the dam based on borehole information assuming 1 m of the crest was excavated in 2011 (Section 2.2.4). Discrepancies between the dam height inferred from the borehole charts and the dam height interpreted from the GPR profile (solid green line) can be attributed to variations in the amount of dam crest excavated along the length of the dam. The interface marked with the red line is interpreted as the boundary between an upper very loose gravel with silt and sand and a lower 'core' layer of compact gravel with silt and sand section 2.3.1). GPR profiles without interpretations can be found in Appendix A4.5.

Figure 4.34 displays the profile of the first 243 m of GPR LINE00.The depth of the interpreted water table varies between ~ 1.5 m in the south and ~ 2.8 m north of the spillway, in general agreement with measured and inferred depths obtained in 2011 from boreholes BH1 and BH2. The water table depths recorded in 2011 are the same over BH1

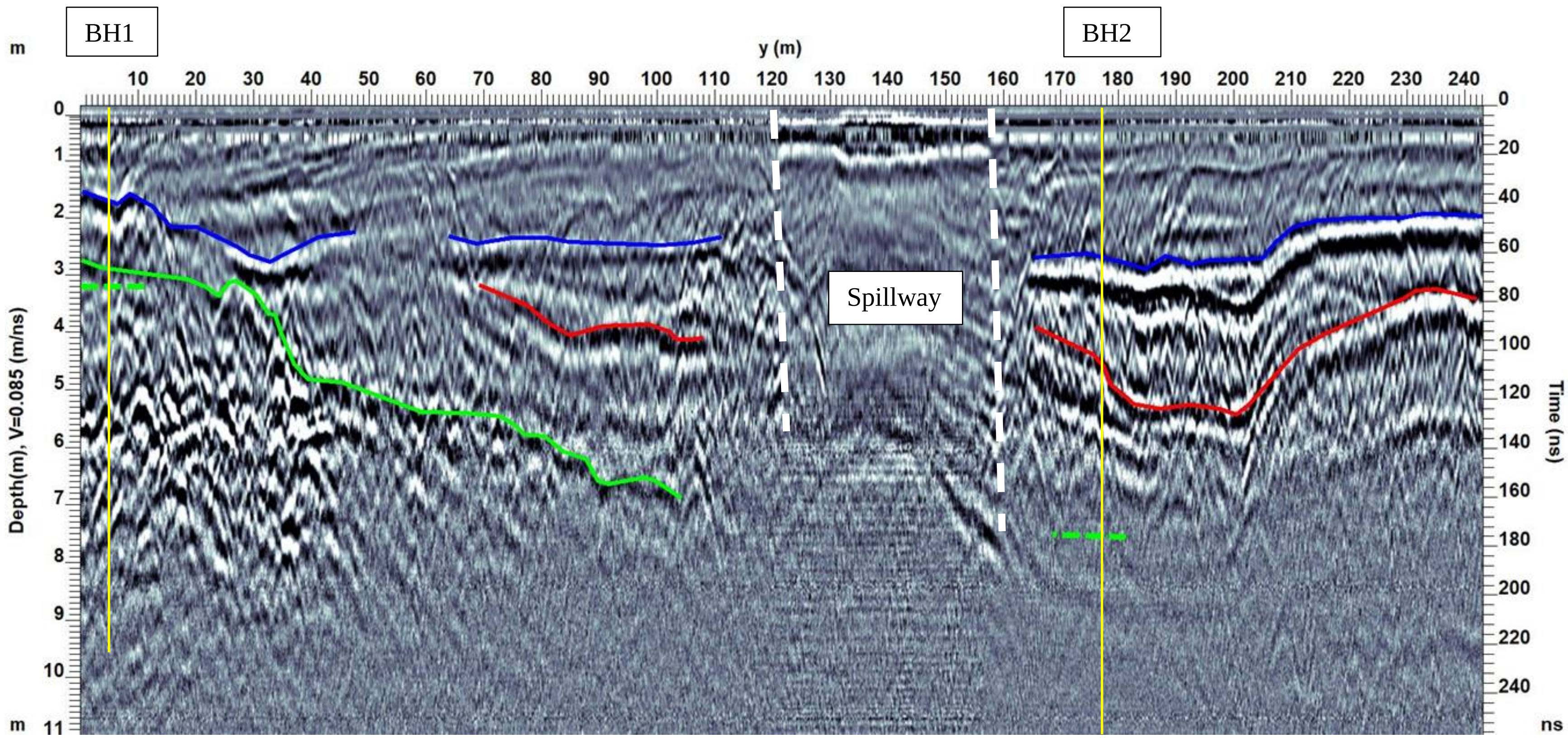

Figure 4.34: S-N oriented profile over GPR LINE00 collected in September 2016 along the center of the Gullbridge Dam between y=0 m and y=243 m with marker horizons indicating the water table (blue), a top of the core (red), and the dam/peat interface (green). The area between the vertical white lines indicates the spillway/replaced section of dam, and the vertical yellow lines represent BH1 and BH2, respectively. The dashed green lines indicate the approximate height of the dam based on borehole information assuming 1 m of the crest was excavated in 2011.

within resolution limitations and deeper over BH2 by 0.6 m. This difference is likely related to the lowering of the dam crest and the placement of the spillway in 2013, and seasonal fluctuations. A section of the dam was replaced in the region between the dashed white lines, and a spillway was subsequently installed over the breached area. There is an increase in reflection strength along the water table north of the spillway, potentially asociated with differences in material properties such as increased porosity. The core interface is deepest and also most pronounced north of the spillway, likely related to differences in the material properties of the dam fill north of the replaced section.

The green marker horizon between y=0 m and y=85 m indicates the boundary between the dam and underlying till which is rich in cobbles, as revealed by the cluster of overlapping hyperbolas. North of y=85 m, this interface transitions into the contact between lower fill and organic peat material. Strong shallow reflectors north of the spillway contribute to early signal loss resulting in the weakening of the dam/peat interface. The interpreted depth to the base of the dam over BH1 in Figure 4.34 is in agreement with the borehole data assuming 1 m of the crest was excavated to aid in reconstruction following the dam failure. The dam base is not clearly distinguishable over BH2 due to the enhanced reflection strength along the water table north of the spillway.

Figure 4.34 reveals a well-defined hyperbola within the dam at a depth of ~5.3 m at y=107 m, here interpreted to be a reflection multiple generated from an overlying standpipe and an old wood frame installed for controlling the pond water elevation. Correspondance with magnetics and Figure 4.26 indicates the standpipe is buried at an approximate depth of 2.3 m over the center of the dam and is dipping to the west. This location corresponds to the region of the suspected pre-construction primary drainage stream pathway (Stantec Consulting Ltd., 2011).

North of this feature, over the spillway, there is a strong reflection at the surface and some signal loss below. Changes in the surface material, that is, the constrasting dielectric constant of limestone lining the spillway and high conductivity of underlying dam soil saturated with conductive tailings water are responsible. Topography corrections were not applied to the profile due to unreliable elevation measurements obtained using the Garmin Handheld GPS. The dipping reflectors at the edges of the spillway are therefore a consequence of the surveyor pushing the GPR up and down the the slopes of the spillway.

Figure 4.35 presents the S-N profile of GPR LINE00 between y=250 m and y=493 m. The yellow stars indicate the locations of the old stream running NE-SW beneath the upstream (easterly) slope at y=440 m to the downstream slope at y=400 m.

The water table interface is located between a depth of 2.1 m and 3.1 m. The elevation of the water table (blue) above the base of the dam (green horizon) was compared to the inferred depth of the water table from the ground up over BH3, as it is assumed this material has remained undisturbed by construction. The GPR profile indicates the depth to the water table has not changed since 2011 over BH3.

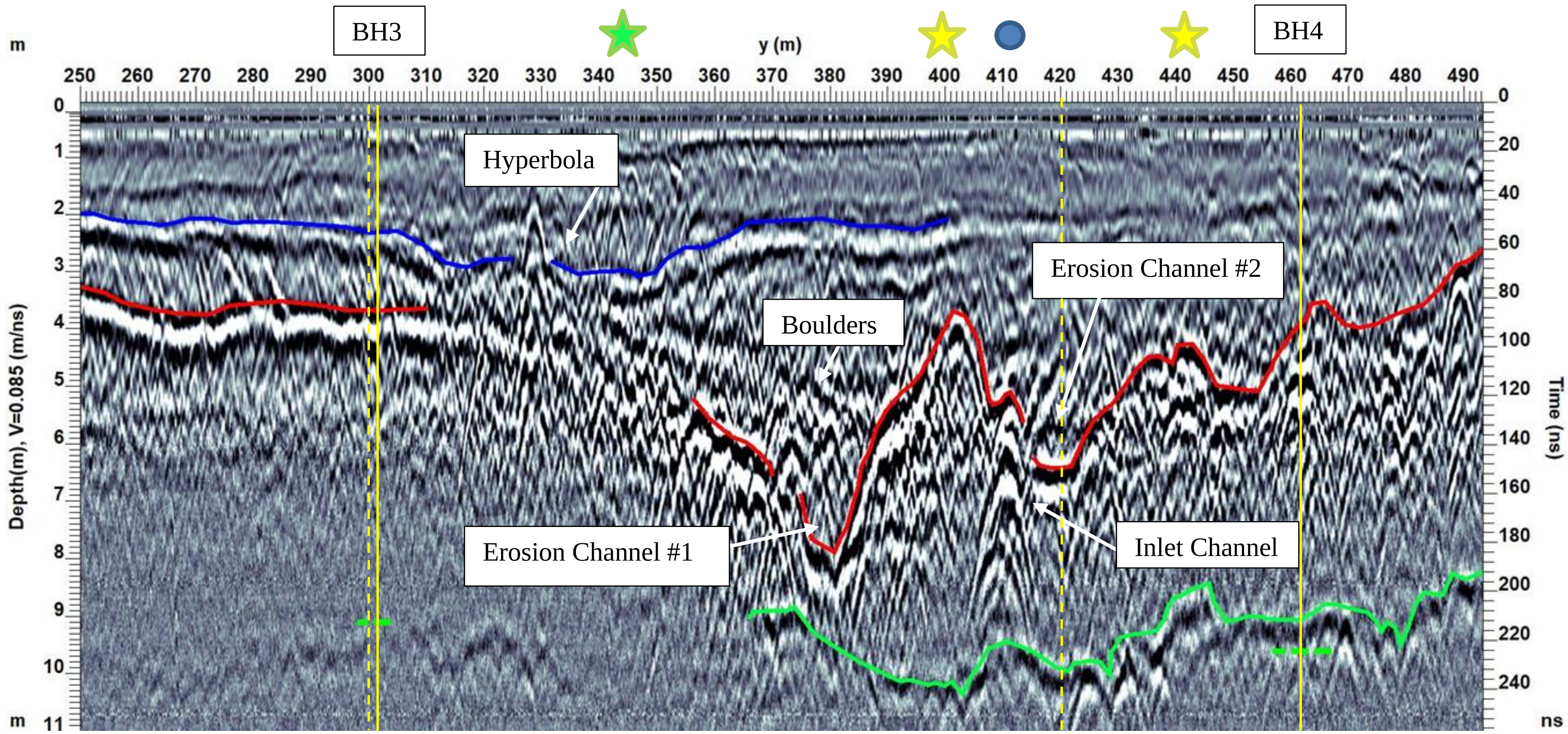

Figure 4.35: S-N oriented profile over GPR LINE00 collected in September 2016 along the center of the Gullbridge Dam between y=250 m and y=493 m with marker horizons indicating the water table (blue), a top of the core (red), and the dam/peat interface (green). The vertical yellow lines represent the locations of BH3 and BH4 respectively. The dashed vertical yellow lines represent the surface locations where GPR LINE00 overlaps YLINE03 of the June 2017 seep grid. The dashed green lines indicate the approximate height of the dam based on borehole information assuming 1 m of the crest was excavated in 2011. The blue circle marks the position of the suspected inlet channel between the old stream (yellow stars). The green star represents the surface location perpendicular to the observed seep at the downstream slope.

A series of hyperbolic diffractions at y~410 m at a depth of ~4 ½ to 5 m is believed to be the GPR response to a metal casing supporting the inlet channel, as it coincides with a strong magnetic signal. Strong hyperbolic diffractions encountered at y= 329 m indicate a highly reflective object at a depth of ~1 ½ m but this feature has no obvious magnetic signal.

The water table interface becomes more difficult to identify above the inlet channel. The faint reflector above the water table between y=250 m and y=370 m is interpreted as the top of the capillary transition zone, a broader vadose zone over the region resulting from changes in the compaction of the materials (Appendix A3.1). It is inferred that an increase in porosity surrounding the inlet channel makes this region of the core particularly susceptible to seepage related erosion. Water directed through the inlet channel could occupy the dam fill surrounding this decant structure and subsequently erode the core. This theory is supported by two inferred erosion channels marked by regions where the top of the core is anomalously deep due to the washing away of fines as a result of internal seepage. Erosion channel #1, centred at y~380 m, could be the main flow path to which reservoir water discharges to the observed seep location at the downstream slope. Strong overlapping hyperbolas in the region near erosion channel #1 and the inlet channel in Figure 4.35 suggest an increase in cobbles and boulders, or stronger reflections from them perhaps due to reduction of fines around them.

Water flowing along the old stream could be an additional mechanism for destabilizing the core in the region surrounding the inlet channel. It is proposed here that water flowing beneath the dam along the old stream has eroded sections along the base of the dam, in particular the peat and till foundation under the seep location (green star) where the lower interface (marked by green line) is not imaged. Poor foundation materials may have contributed to the December 2012 breach, as badly broken cores zones are often linked to unstable or eroded foundation materials (U.S. Army Corps of Engineers, 2004).

The depth to the base of the dam in Figure 4.35 ranges between 8.4 m and 10.2 m. This boundary is not clearly defined between y=250 m and y=360 m due to the enhanced reflection strength along the water table north of the spillway.

There are interesting correlations between the GPR and SP data (section 4.1) in this section of the dam. The distance coordinate for SP Line 1 (along the embankment, Figure 4.2) is offset by about 10 m from the *y* coordinates of GPR LINE 0. Thus, the location of the large positive SP spike at station 385 m corresponds to a position of *y*~375 m of GPR LINE 0. This lies above erosion channel #1 in Figure 4.28, and supports the interpretation that there is water flowing through there.

GPR LINE 0 crosses over the July 2018 SP grid, approximately in the middle of the grid, between y=318 m and y=378 m. The highest positive value of SP over this grid was measured over station +22 along SP LINE 0, corresponding to y~370 m in Figure 4.28. This is again interpreted to be the response to seepage through erosion channel #1. The SP map also shows a peak over stations -8, corresponding to a position of y=340 m in Figure 4.35 (see also Figure 4.7a). This SP anomaly is centered over the ‘seep’ region, where the core interface is obscured, and likely also generated from seepage.

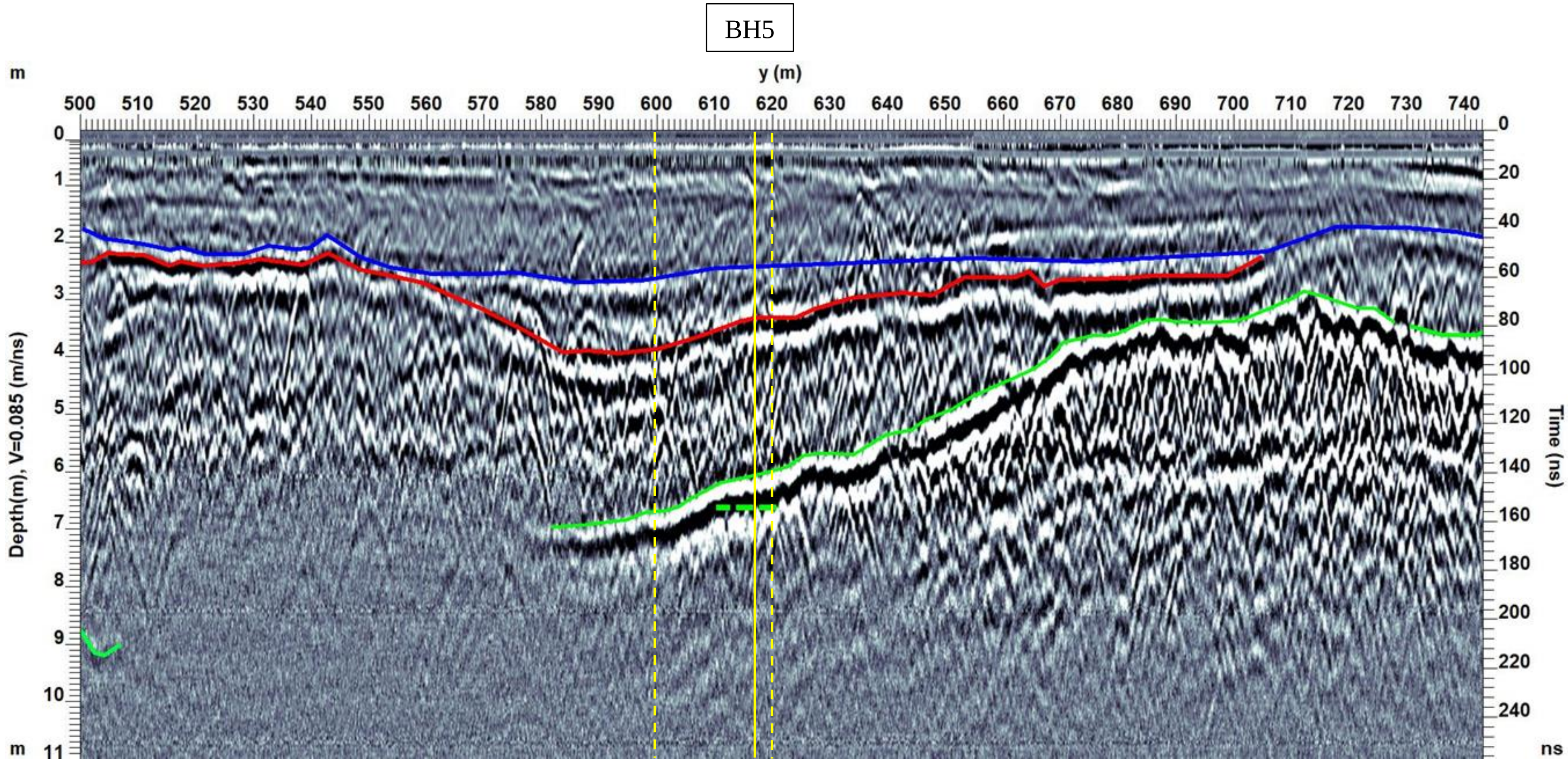

Figure 4.36: Profile of GPR LINE00 collected in September 2016 S-N along the center of the Gullbridge Dam between y=500 m and y=743 m with marker horizons indicating the water table (blue), and the base of the dam/peat (green). The yellow vertical line indicates the approximate location of BH5 in the cross-section. The dashed yellow vertical lines indicate the location where GPR LINE00 falls over YLINE09 of the July 2016 grid. The dashed green line indicates the approximate height of the dam based on borehole information assuming 1 m of the crest was excavated in 2011.

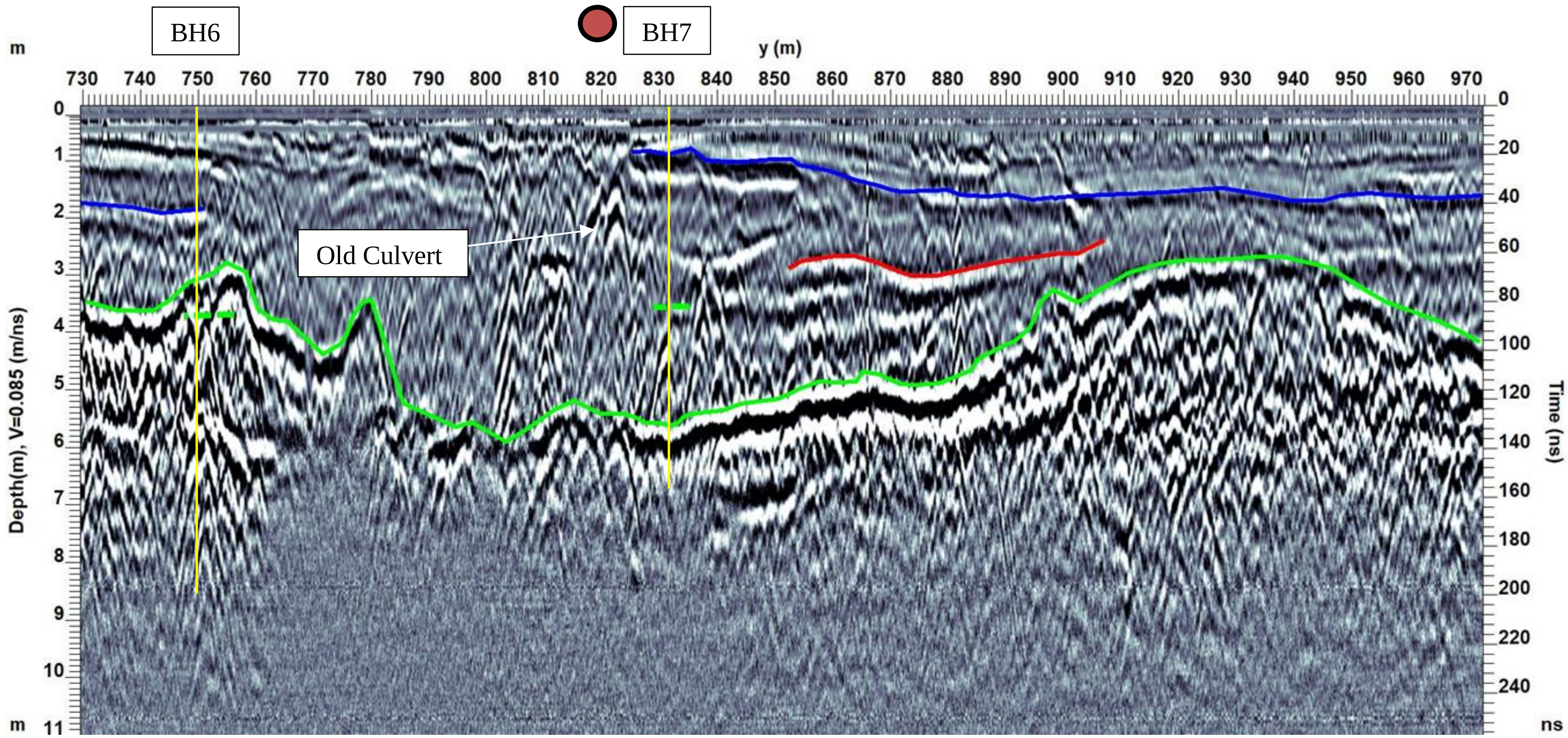

Figure 4.37: S-N oriented profile over GPR LINE00 collected in September 2016 along the center of the Gullbridge Dam between y=730 m and y=973 m. The marker horizons indicating the inferred water table (dashed blue), the top of the core (red), and the base of the dam/peat (green). The dashed green lines indicate the approximate height of the dam based on borehole information assuming 1 m of the crest was excavated in 2011. The orange circle indicates the position of the old culvert provided by DNR.

Figure 4.36 presents GPR LINE 0 between y=500 m and y=743 m. The height of the dam wall ranges between 2.8 m and 9.0 m, resulting from the cross-valley topography E-W across the impoundment. According to the data from BH5 (yellow line at y = 616m), the interpreted height of the dam is in general agreement with the borehole data.

Figure 4.37 presents GPR LINE 0 between y=730 m and the end of the survey line. The primarly S-N orientated survey line bends to the east north of BH6 approaching the northern abutment. The height of the dam wall ranges between 2.6 m and 5.6 m. The subsurface beneath the peat interface becomes increasingly rich in debris in the north as the height of the dam wall decreases.

The major feature of interest in Figure 4.37 is the subsurface region around the location of an old culvert/decant structure (location provided by NLDNR). The shallow hyperbola located at $y \approx 823$ m is believed to be this old culvert. It was employed prior to the installation of the twin-culverts which were installed sometime after 1996, and subsequently removed during dam rehabilitation in 2013.

Table 4.2 compares the depths to major interfaces obtained from borehole data with GPR LINE 0 boundary interpretations below the surface location where the survey line is in closest proximity to the borehole location. The uncertainty in the y-location of the boreholes relative to GPR LINE 0 ranges between 2 and 5 m, and there is additional uncertainty in the cross-dam direction.

The majority of comparisons indicate the water table depth was deeper relative to the crest in 2011. This is unsurprising given the subsequent excavation of the crest. Stantec

Table 4.2: Comparison of depths to major interfaces obtained from borehole data with GPR interpretations below the approximate surface location where LINE00 intersects the boreholes (* inferred depth, **not determined).

Borehole #/ Corresponding GPR LINE00 location (m)	Water Table Depth (m) obtained from BH/GPR LINE00	Top of Core Depth (m) obtained from BH/GPR LINE00	Dam Base Depth (m) obtained from BH/GPR LINE00
BH1/ y=6	*1.8 / 1.7	1.8 / **	4.2 / 5.0
BH2/ y=178	3.3 / 2.7	4.9 / 4.3	8.5 / **
BH3/ y=300	*2.3 / 2.3	2.4 / 3.6	10.1 / **
BH4/ y=460	5.7 / **	3.8 / 2.6	10.6 / 9.0
BH5/ y=616	2.7/ 2.4	4.3 / 3.4	7.6 / 6.0
BH6/ y=750	*1.5 / 1.8	2.4 / **	4.7 / 3.1
BH7/ =y=832	1.5 / 0.8	2.6 / **	4.5 / 5.6

do not explicity state the depth to the top of the dam core materials in the borehole record. Estimates of the core depth from the borehole charts are based on reported changes in the compaction and fine content of the dam soil. In every occurrence with exception to BH3 the GPR profile over LINE00 indicated the top of the core had become shallower over each of the borehole locations with exception to BH3, which is expected given the removal of ~ 1m of the dam crest during rehabilitation work. The discrepancy in the results over BH3 may be attributed to internal erosion of the core materials since 2011 as a result of seepage through this region.

4.4.2 July 2016 Northern Grid

In July 2016, a small (10m x 20m) GPR grid was constructed in the northern part of the embankment near BH5, over a secondary area of suspected seepage (see Figure 4.32) As in the previous section, the interpreted water table, the core and the dam base interfaces are outlined by the blue, red and green marker horizons respectively. Each of the profiles reaches a maximum depth of 7.2 m.

Figure 4.38 displays three YLINE profiles oriented S-N over the grid. YLINE00 is along the western edge of the grid nearest the wetland, while YLINE10 is near the eastern edge of the grid, near the centreline of the dam crest. Striking features of Figure 4.38 (a), near the centreline of the dam, are the parallel, horizontal reflective boundaries extending the length of the profile at depths of ~ 3-4 m. (It is on account of these horizontal interfaces that the background subtraction feature was not applied.) From Figures 4.34 and 4.37, the lower interface represents the core and the upper interface the water table. An interface at a depth of 6-7 m is interpreted as the base of the embankment, consistent with the embankment profiles, although in Figure 4.38 (a) the interface reflection is obscured by background noise south of y~14 m.

In Figures 4.38 (b) and (c), the dam base interface is seen at the ends of the profiles and a hint of the water table interface may be seen at the southernmost, but over most of these profiles these interfaces are not detected. This is consistent with the profile in Figure 4.33(c), which shows very low reflectivity in this region, interpreted here to result from a diffuse zone of increased electrical conductivity. This early attenuation of the radar pulse

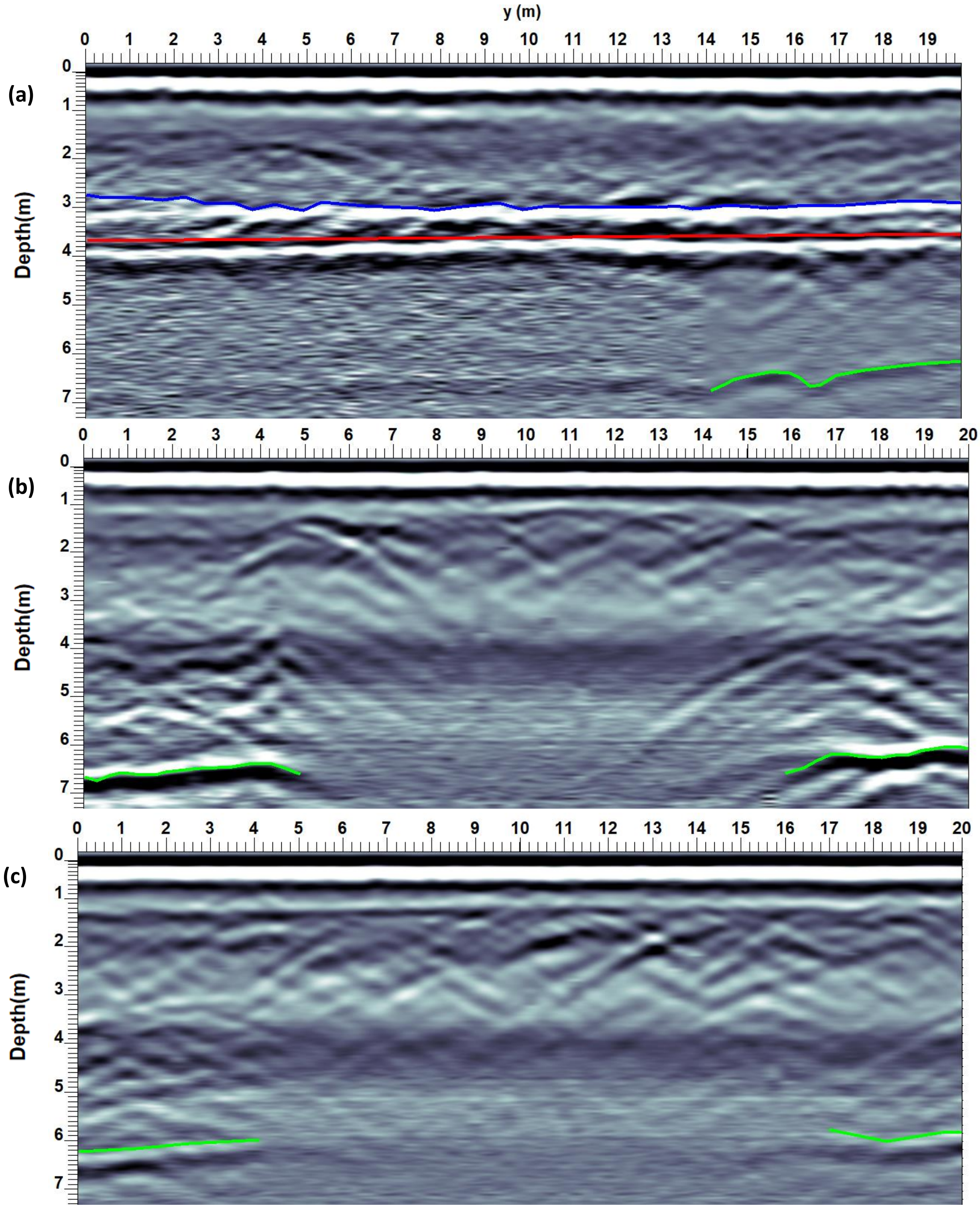

Figure 4.38: Profiles of GPR surveys collected S-N over the July 2016 GPR grid. (a) YLINE10 (b) YLINE03 (c) YLINE01. No background filter applied.

could be a result in higher amounts of conductive tailings water within the dam or a sudden increase in the clay content. It is also possible the shallow signal attenuation is influenced by the presence of iron-oxide minerals coating the dam fill. Sediments rich in iron-oxides can amplify reflections and result in dielectric losses, limiting the penetration depth (L. van Dam, 2001; Josh, et al., 2011). The profile in Fig. 4.38 (c) (YLINE01) indicates the region of limited penetration depth widens S-N to the west of YLINE03.

Figure 4.39 illustrates W-E XLINE profiles over the grid. XLINE20 (Figure 4.39 (a)) is along the northern perimeter of the grid. A series of west-dipping reflectors to the west is evidence that the downstream construction method was used in the raising of the embankment. Where it is detected, the water table is at a depth of about 3 m and the top of the core is at a depth of approximately 3.5 m. The dam base/peat soil interface is located at a depth of ~6 m which agrees with data from BH5.

The water table and peat boundaries are faint west of x=5 m. Figure 4.39 (c) and (d) present profiles respectively without and with the background subtraction filter, and are a good illustration of how the background subtraction filter, though it removes the distracting ground wave signal at shallow depths and longer wavelength patterns of light and dark, can generate artifacts or “ghost” interfaces. Presumably the loss of signal west of x=5 m is due to elevated conductivity resulting from seepage of tailings water through the dam.

There is little change in the elevation of the water table and the dam base between XLINE00 and and XLINE20. Figure 4.39 (b) displays the profile of XLINE14 which

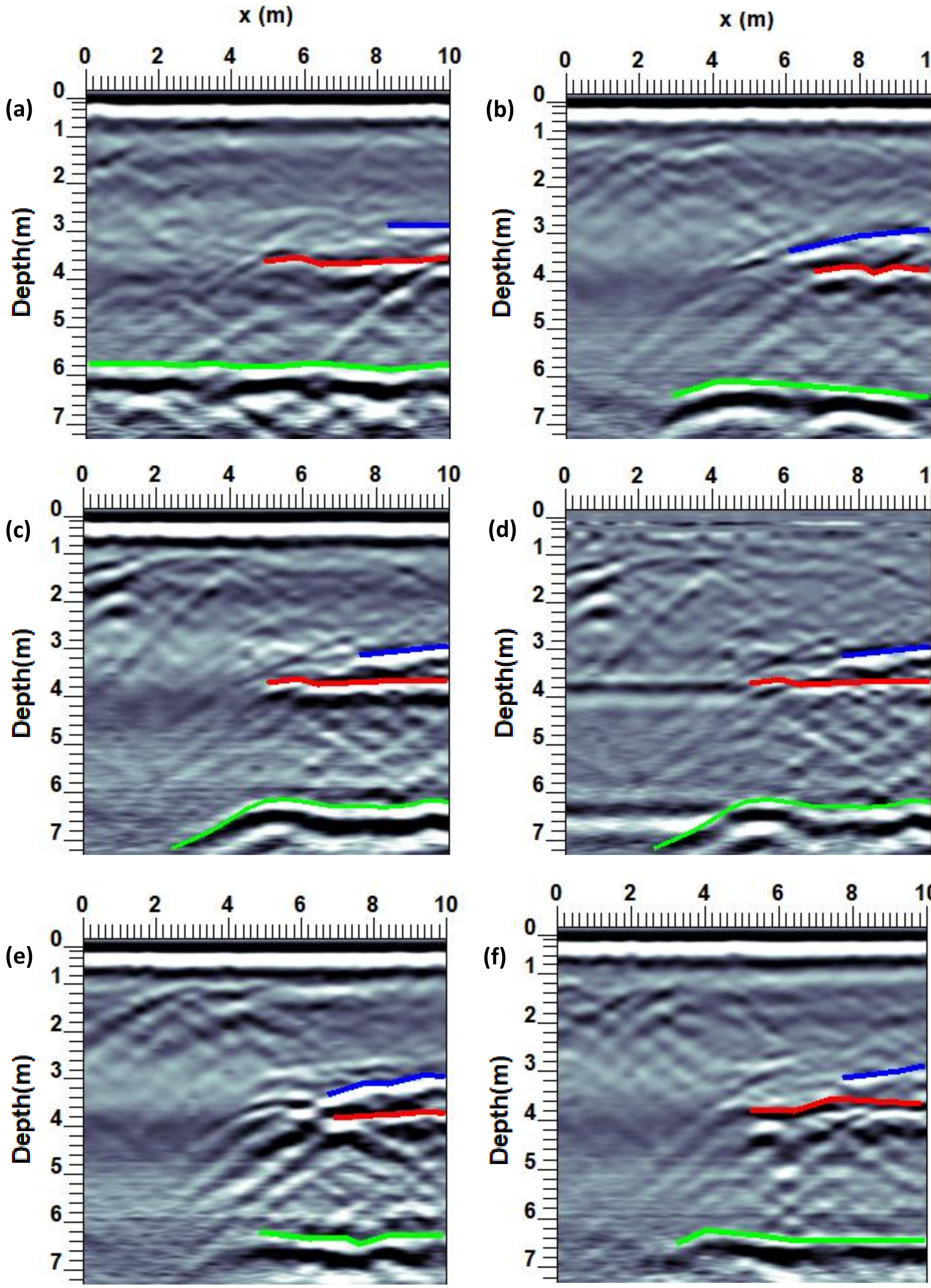

Figure 4.39: Profiles of GPR surveys collected E-W over the July 2016 GPR northern grid: (a) XLINE20 (b) XLINE14 (c) XLINE11 (d) XLINE11 with background subtraction filter (e) XLINE09 (f) XLINE05.

crosses BH5/MW at x~20 m. The depth of the water table in November 2011 in BH5 was 4.9 m above the base of the dam, about 1.4 m higher than the depth along XLINE14.

Evidence to support seepage in the vicinity of the northern grid is supplied by SP Line 1 (Figure 4.1). The GPR grid falls within an area of irregular SP values between stations 580 m and 675 m. In particular, the grid location between stations 580 and 610m (short red line in Figure 4.2) corresponds to a strong SP signal. This is consistent with the interpretation of the larger main ‘seepage’ anomaly (Figure 4.2) as the response to streaming potentials generated from leakage through the embankment. The presence of conductive materials such as tailings water, tailings sediment and clay is evidenced by the abrupt attenuation of the radar pulse west of x=5 m particularly over the x-line profiles in the middle of the grid.

Figure 4.40 shows a map of the Northern GPR grid. The region within the dashed lines indicates surface locations where the radar pulse is attenuated. This may represent a zone of saturation, where tailings water is draining west of the the sloping interface marked by blue in Figure 4.39. Small-scale leakage may then pass to the identified seep area at the base of the embankment.

Figure 4.41 displays the reflection energy contour plot over a planar slice at a depth of z= 4.25 m, just below the core interface. Dark blue shading indicates regions where there is little reflected energy corresponding to the elevated conductivity zone. The yellow-red regions indicate moderate to high amplitude reflections.

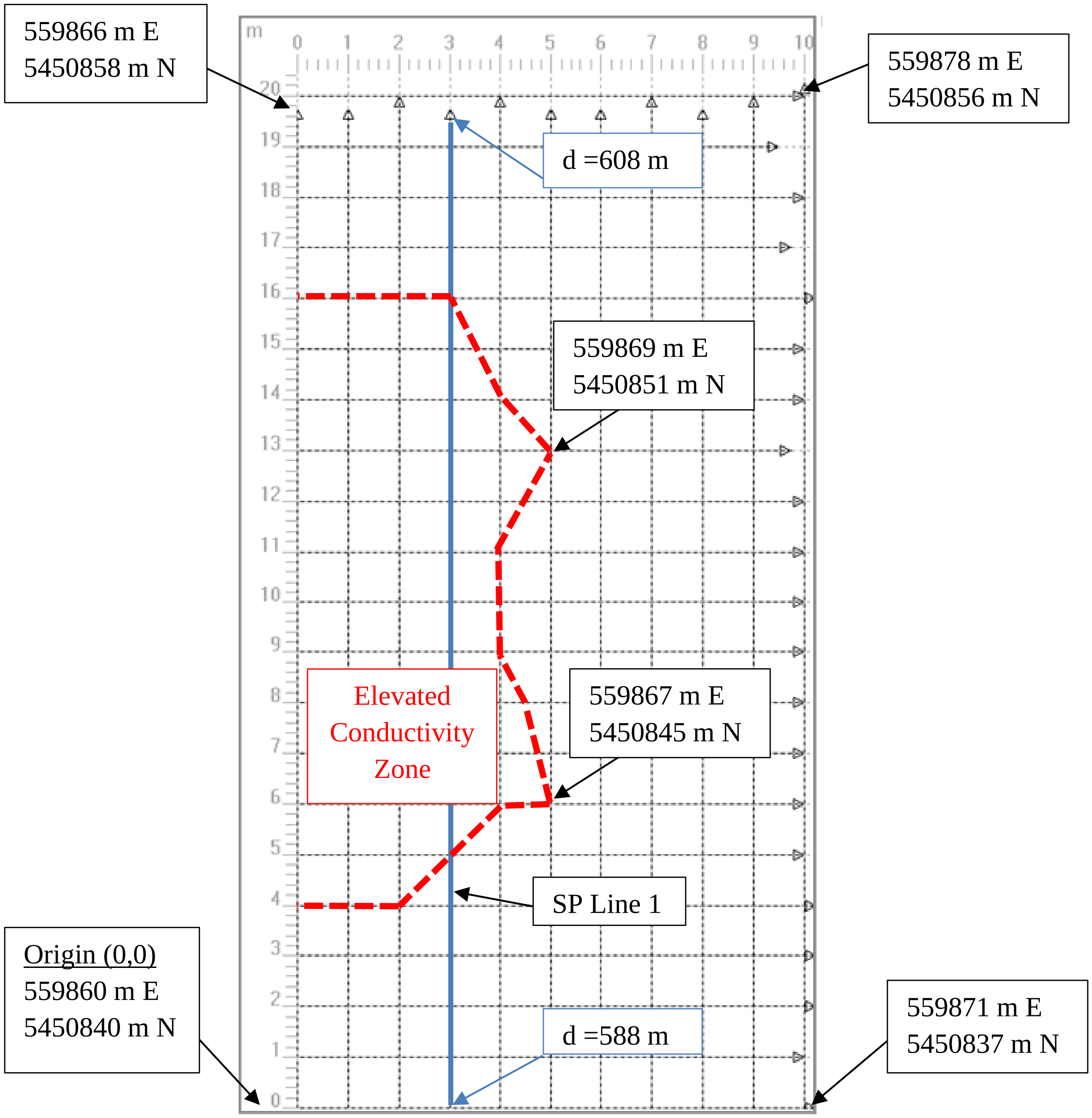

Figure 4.40: July 2016 grid generated in .GFP edit outlining the surface location where the radar pulse has attenuated. The positive directions are to the north and to the east.

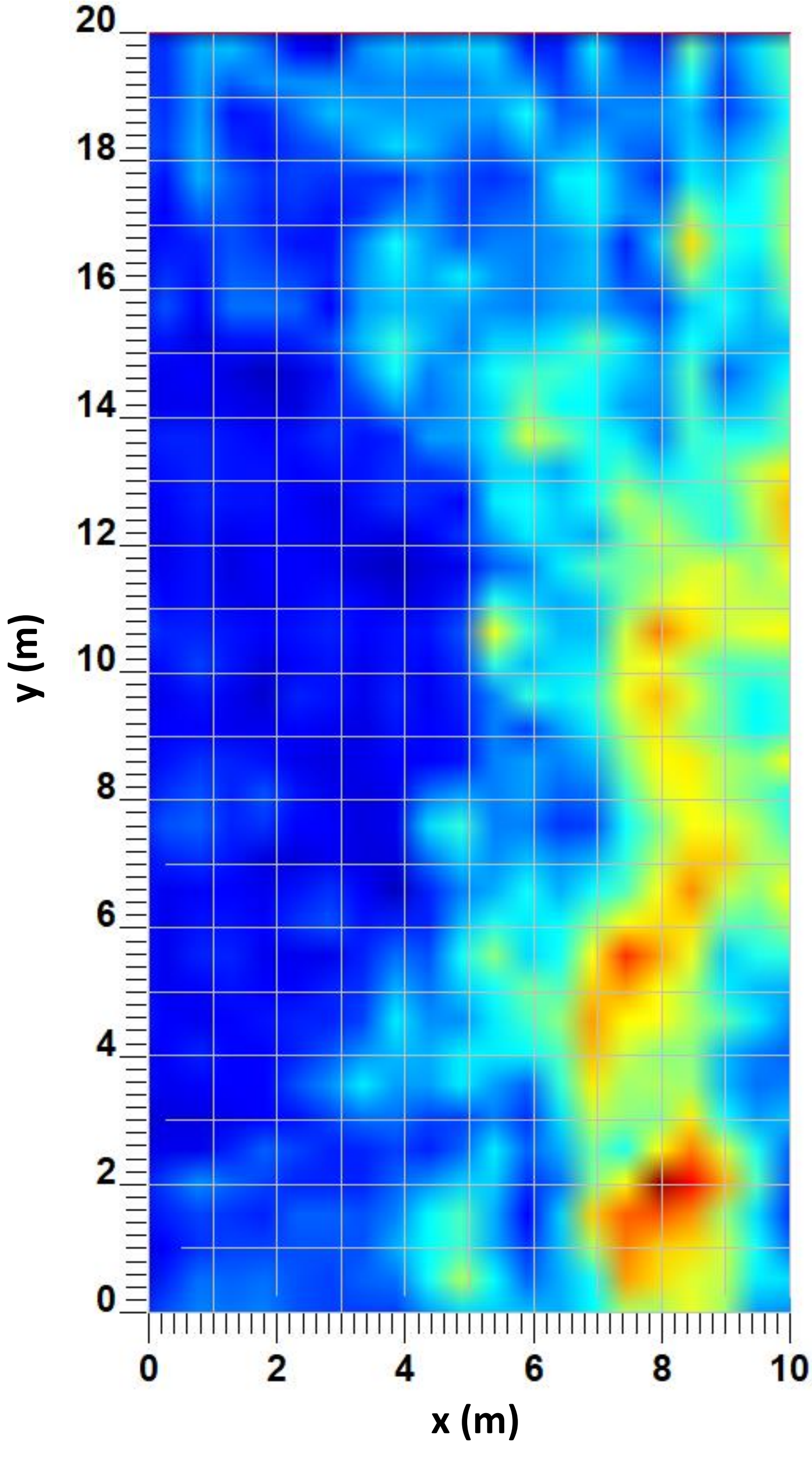

Figure 4.41: Reflection amplitude slice over the July 2016 GPR grid taken at a depth of 4.25 m. As for Fig. 4.33, the positive directions are to the north and to the east.

It is reasonable to assume that seepage of conductive tailings water through the dam is responsible for the low/no GPR signal in this area. However, one problem with this theory is that the dam base, core and water table are indeed visible closest to the tailings pond in the east. The reason for this is not well understood.

4.4.3 November 2016 Seep Grid

A 50 m x 20 m grid survey was carried out over the main seep area, using the 50 MHz antennae in the winter of 2016 (Figure 4.32). The 50 MHz antennae are capable of greater exploration depth at the cost of limited resolution, narrowing interpretations to larger-scale boundaries such as the dam base and bedrock foundation. It is expected the first few meters of dam soil underlying the crest was partially frozen at this time. The relative permittivity values of permafrost and wet sand are 4-8 and 10-30 respectively (Wu & Liu, 2013). Given this contrast, the reflection strength along the saturation zone during winter surveying is significant.

Figure 4.42 displays S-N profiles over the November 2016 gris YLINE00, closest to the wetland, is displayed in Figure 4.42(a). The fiduciary marker F1 indicates the location of DNR drone spike 4 ~ 2 m to the east. The interpreted water table extends across the profile at a depth of 3.5 m. The interpreted core is visible over the seep at a depth of ~5 m, masking the underlying dam base interface. There is a change in the pattern of reflections over the seep (green star) and to the north indicating a difference in the ground properties, possibly related to erosion of dam material.

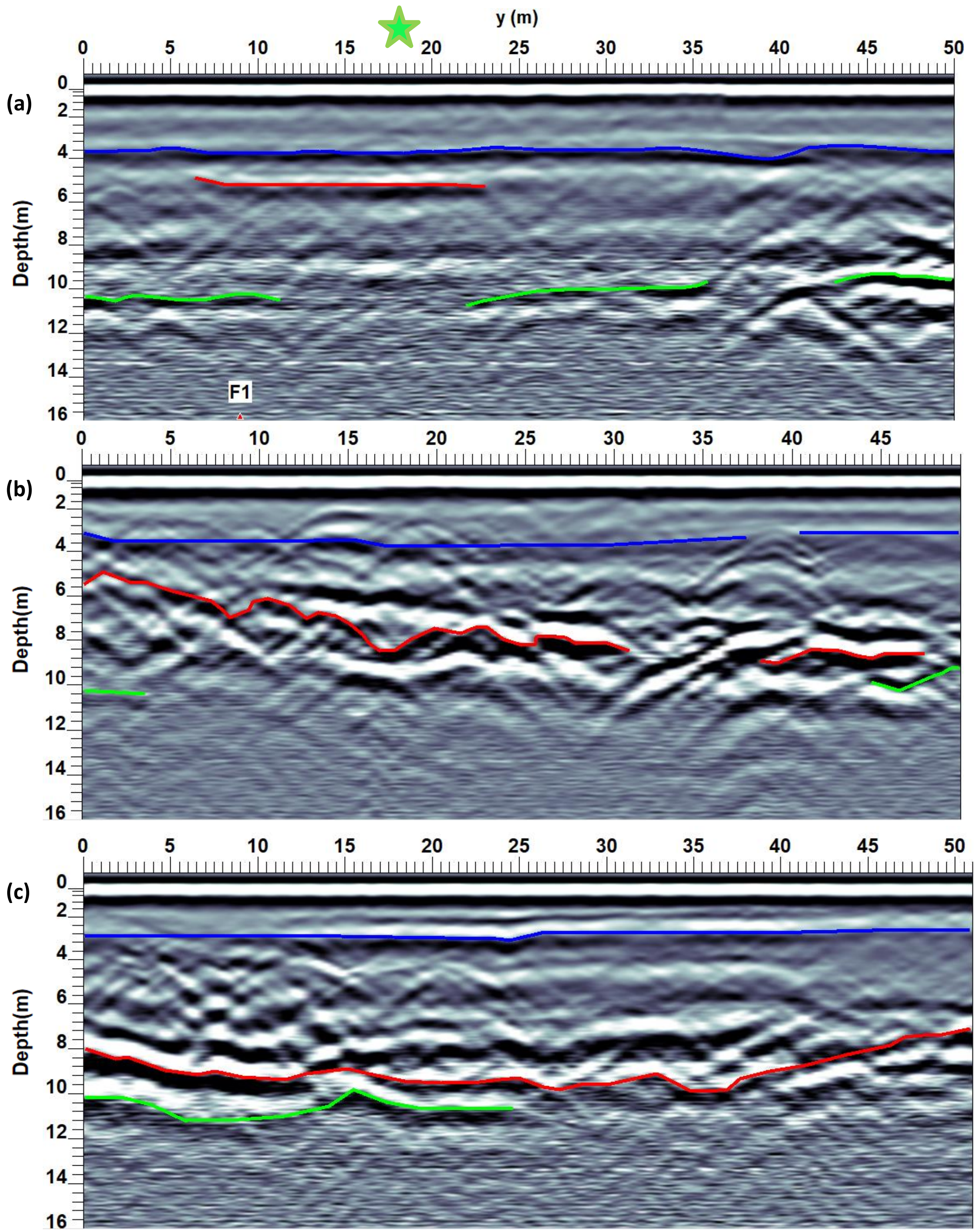

Figure 4.42: S-N GPR profiles collected over the November 2016 seep grid. a) YLINE00 (x=0); b) YLINE02 (x=10); c) YLINE03 (x=15). F1 is y location of drone spike 4. Seep is at y~18 m.

SP Line -10 of the July 2018 SP grid (Figures 4.4 and 4.6) falls approximately over YLINE00 starting at y≈7 m . The strongest SP anomalies corresponds to the regions north of the green star in Figure 4.42.

Figure 4.42 (b) is the S-N profile of YLINE02, approximately over the center of the dam crest. The red line marks the interpreted transition between loose, damp upper fill and saturated, very loose ‘core’ materials. The base of the dam is not easily recognizable over YLINE02, likely due to attenuation as a result of strong overlying reflections and conductive losses. There are a number of hyperbola, presumably related to large cobbles, above the core region (e.g., at y=39 m). This is consistent with their appearance in the profiles along the embankment.

Figure 4.42 (c) shows the GPR profile for YLINE03, 5 m east of YLINE02. The core interface is interpreted as the strong sub horizontal reflector extending the length of the profile at a depth of ~ 9m. Figure 4.42 indicates the dam core thins to the east. This suggests the core is relatively narrow and centered over the dam crest.

Figure 4.43 presents four of the twelve W-E oriented x-line profiles collected over the grid. These profiles were selected to provide a better understanding of the structure of the core over the seep area.

Figure 4.43 (a) is the southernmost W-E profile, and features an interface (marked red) that suggests an intact core, encountered at a depth of ~ 5m on the west and deepening to the east. The reflection corresponding to the base of the dam (marked in green) is located at a depth of approximately 10 m on average, which agrees with intersecting y-line data.

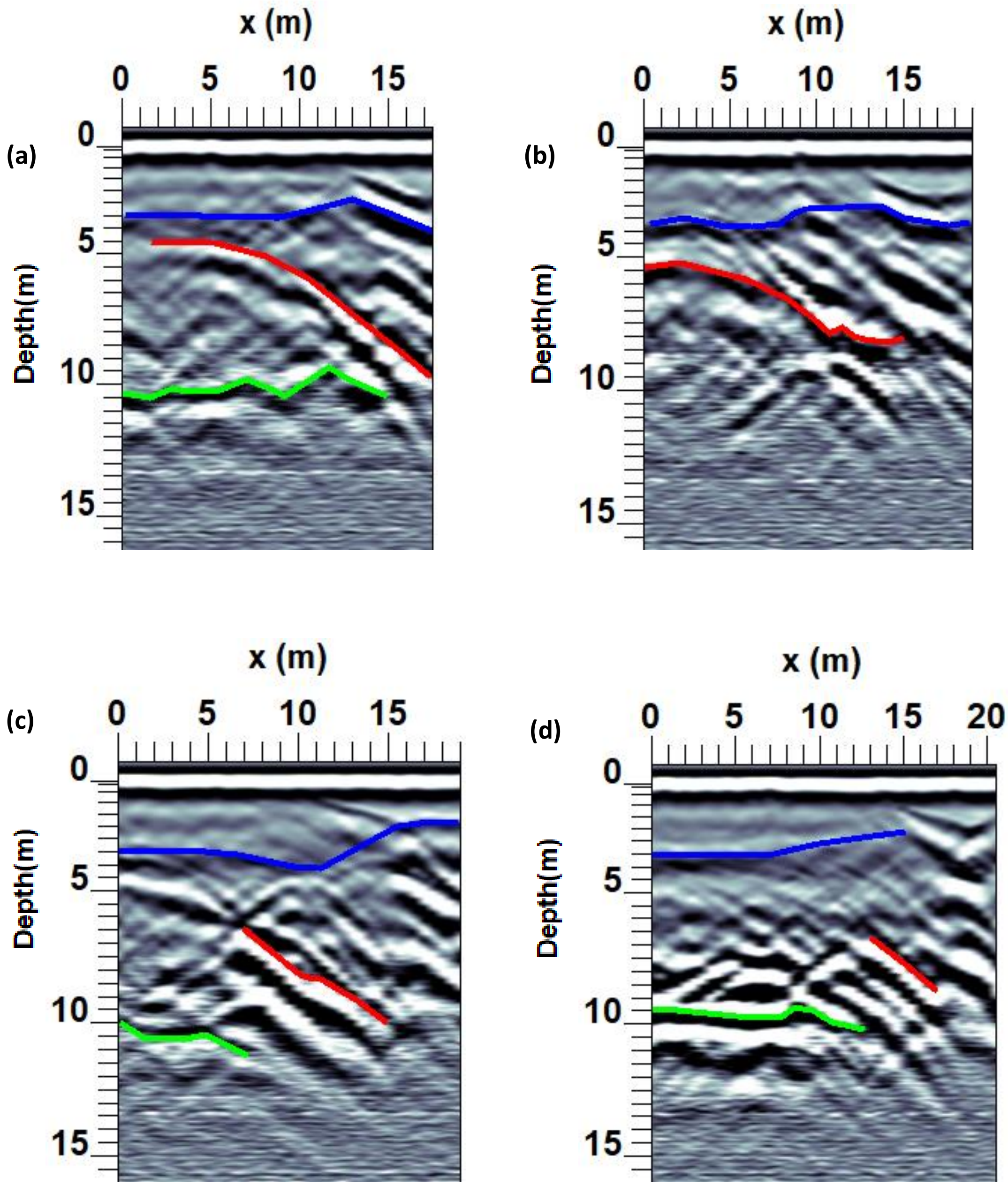

Figure 4.43: GPR profiles of (a) XLINE00 (y=0), (b) XLINE03 (y=15), (c) XLINE06 (y=30), and (d) XLINE10 (y=50), collected W-E over the November 2016 seep grid.

Figure 4.43 (b), collected 15 m north of XLINE00, shows east-dipping reflectors overlying the core, which indicates layers of tailings sediment that have adhered to the upstream slope following each dam lift. These interfaces are also seen in the other profiles of Figure 4.43.

Figure 4.43 (c) presents the W-E profile of XLINE06 collected immediately to the east of the seep . The series of strong, east-dipping reflectors underlying the eastern slope of the core indicate the stratigraphic layering of the dam soil. The increase in reflection strength along these layers is a consequence of increased porosity resulting from internal erosion of the core over this region. It is suspected water is flowing from the reservoir through the dam wall along a known seepage path approximately along XLINE06, resulting in increased water content and therefore larger dielectric contrasts that generate stronger reflections.

Figure 4.43 (d) presents the W-E profile of XLINE11, the northernmost x-line at y=50 m. The water table and dam base interfaces are visible in the west. The core interface sinks to the north of the seep region, as seen in the embankment profiles. Several deep east-dipping reflectors near the reservoir suggest gradational crossbedding within the till foundation.

Figure 4.44 displays reflection strength contour slices generated using y-line data at depths of (a) 4.00 m to 4.25 m and (b) 4.50 to 4.75m. The strong reflections in the slice images in Figure 4.39 indicate the top of the core. Seepage pathways are consistent with lowering of the dam core interface, therefore regions where the reflection is missing

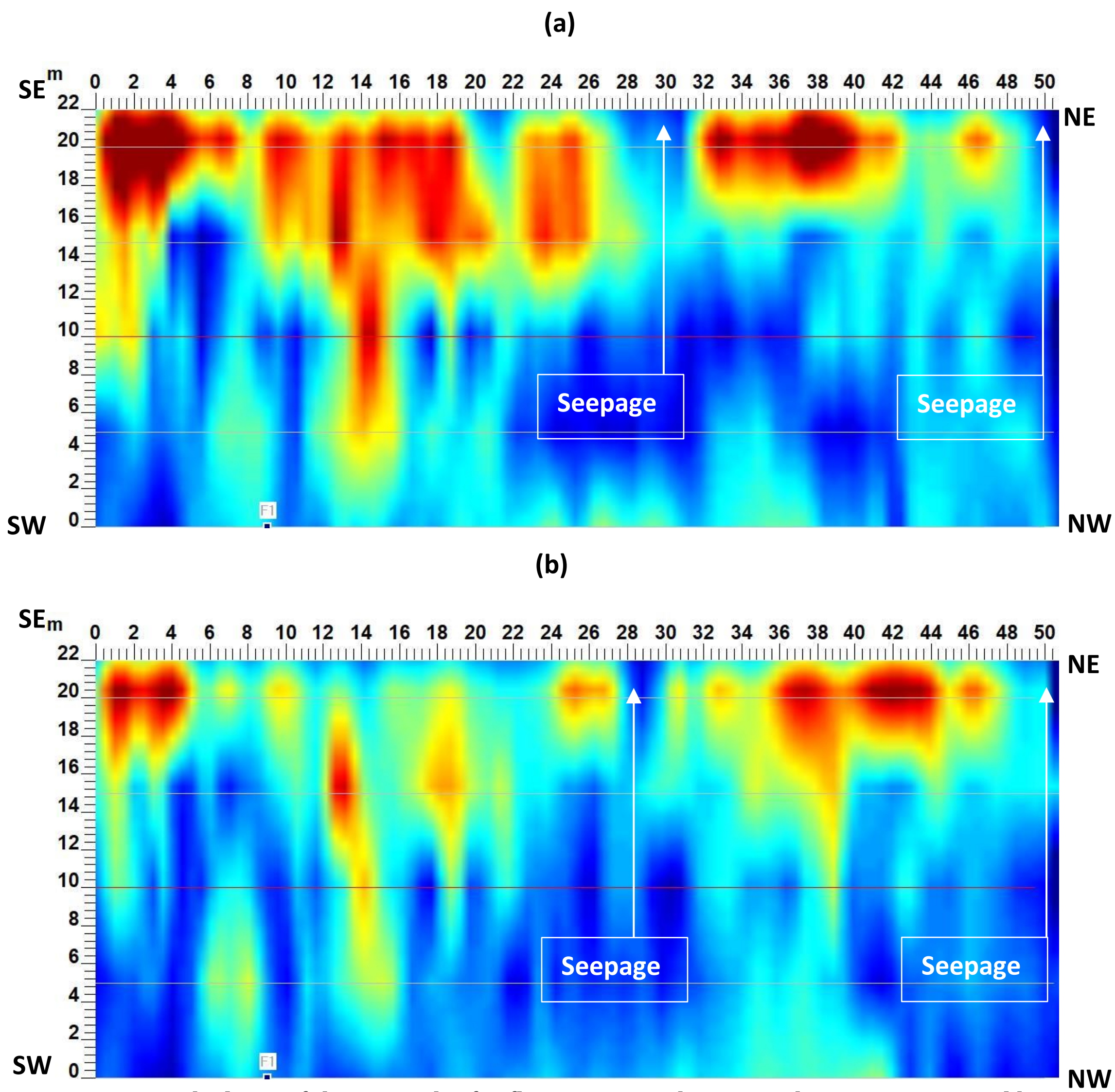

Figure 4.44: Depth slices of the strength of reflections over the November 2016 GPR grid between (a) z= 4.00 m and z= 4.25 m and (b) z= 4.50 m and z= 4.75 m. Horizontal lines indicate the y-lines used to generate the images. Generated in Ekko_Project.

indicates seepage. As an example, reflections from the top of the core are missing in the slice images at y=30 m and y=50 m, corresponding to the locations of the seep marker and a suspected erosion channel (erosion channel #1) within the embankment, respectively.

4.4.4 June 2017 Seep Grid

Figure 4.45 displays the station markers of a 20x140 m GPR grid conducted over the Gullbridge Dam seep area. The black markers define coordinates precisely determined by RTK and the positions of the red markers were calculated using a linear interpolation and correspond to fiducial markers displayed in each of the profiles. The fiduciary marker stations along the x lines are spaced at 2 m and the fiduciary markers stations along the y-lines are spaced at 5 m. The "2 m Center" DCR Schlumberger survey was collected approximately over YLINE05 between y=15 m and y=85 m.

Some notable surface features over the grid are BH3 located on (6,10) and BH4 just to the north of the grid. DNR marker 4 is between station (2,30) and (2,35), DNR marker 2 between station (14,30) and (14,35), DNR marker 5 between station (6,60) and (6,65) and DNR marker 6 between (0,100) and (0,105). It is assumed the former stream bud runs underneath the embankment NE-SW between XLINE20-XLINE27. It is estimated that a small inlet channel is located in the subsurface region underlying the blue circle. The coordinates for this feature were provided by NLDNR. GPR line XLINE13 runs parallel to the present-day stream depositing tailings on the eastern edge of the dam.

The correspondence between the June 2017 GPR grid and the November 2016 grid is displayed in Figure 4.46. The 2016 grid is offset approximately 25 m to the north relative to the 2017 grid, and has a slightly different orientation, such that the northernmost points of the lines are ~ 2m west of the 2017 grid lines. Sept. 2016 GPR LINE 0 is also displayed.

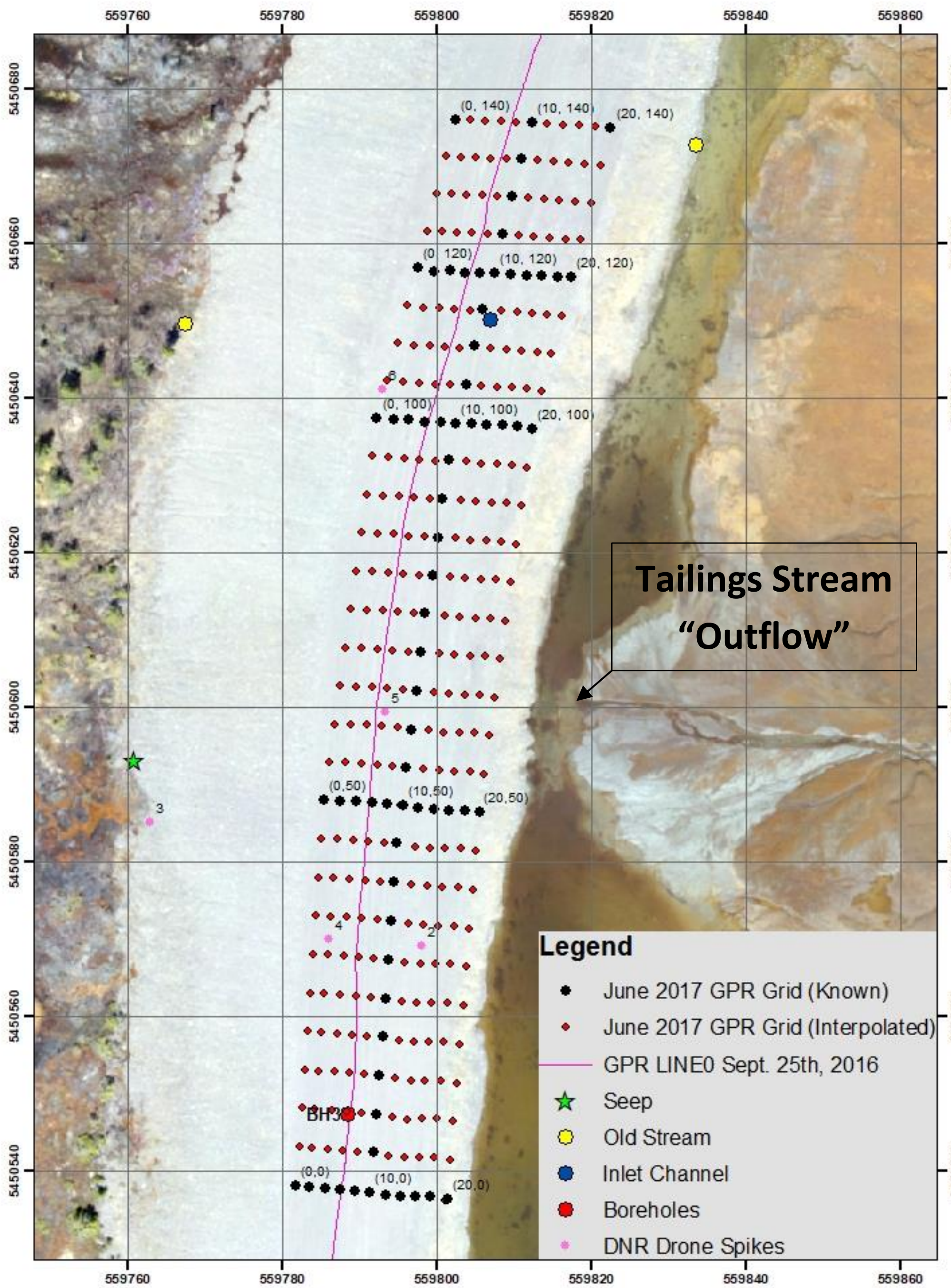

Figure 4.45: June 2017 GPR Survey Grid over the Seep area of the Gullbridge TMA.

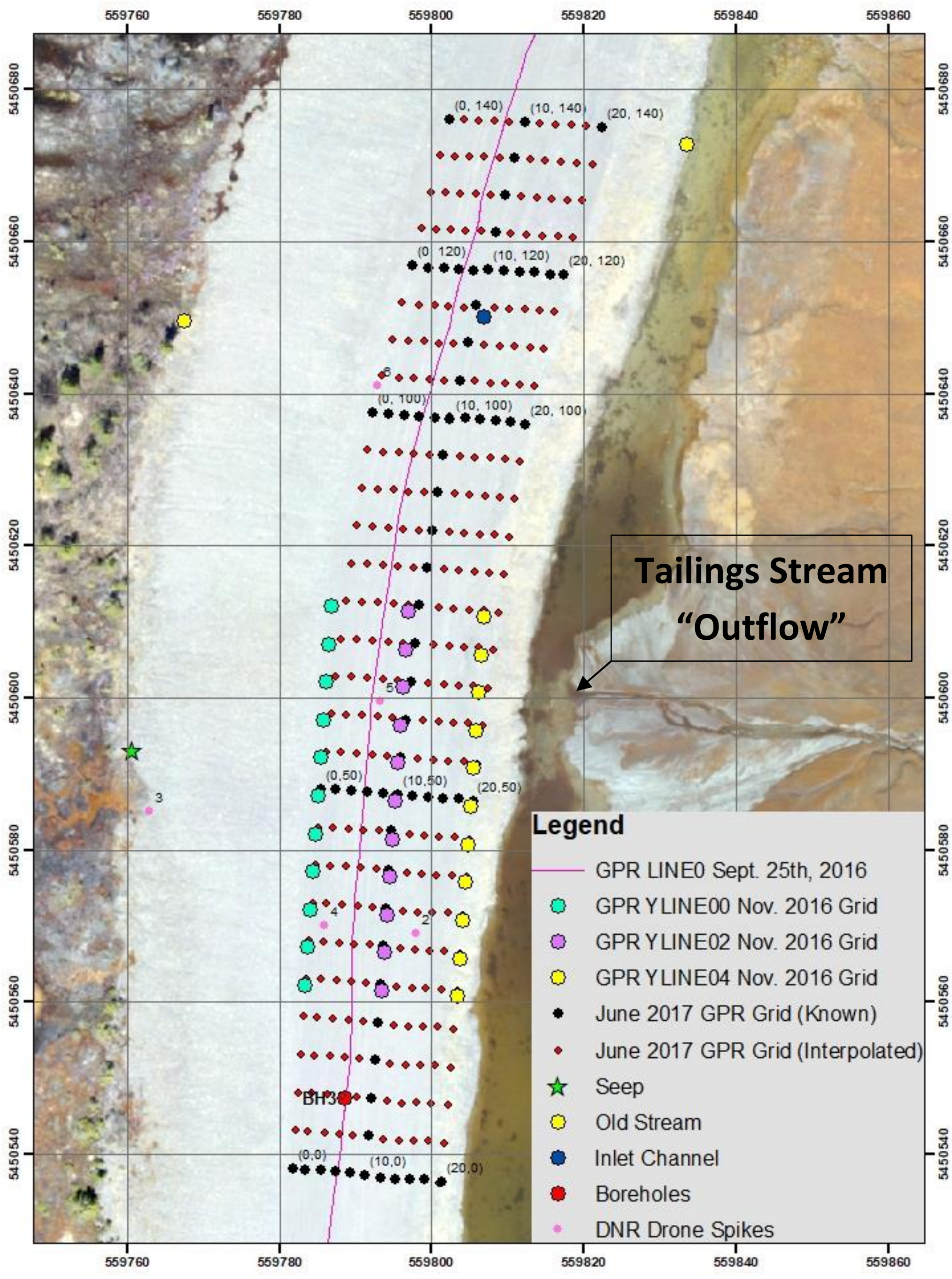

Figure 4.46: November 2016 grid location relative to the June 2017 GPR grid. Station designations (0,0) etc refer to the June 2017 grid.

The GPR grid surveyed over the main seep area in June 2017 was longer than the winter 2016 seep grid (140m vs 50m) and the y-lines (along the embankment) were more closely spaced (2m vs 5m). The origin of the winter 2016 grid corresponds to station (0,25) of the June 2017 grid, thus the June 2017 grid extends 25 m farther south and 65 m farther north. The grid was traversed with all three GPR antennae: 250 MHz, 100 MHz and 50 MHz, and results along y-lines on the west, centre and east of the embankment are presented in Figures 4.47, 4.49 and 4.50. Note the different depth scales in the figures. The blue, red and green lines mark respectively the interpreted water table, 'core' and dam base. The green and yellow stars indicate the positions along the dam crest where the survey line crosses the underlying seep and old streambed/inlet channel, respectively.

The frequency of the antenna chosen depends on the desired subsurface target. Higher frequency antennae generate waves that penetrate to shallow depths but produce higher resolution profile images. Profiles generated from reflection data collected using the 250 MHz antennae were examined mainly to delineate the top of the water table and to a lesser extent the variation in the structure of the top 2 m of dam soil. Lower frequency antennae (50 MHz) generate waves that penetrate to greater depths but produce lower resolution profile images. Profiles generated from reflection data collected using the 50 MHz antennae were examined mainly to delineate major interfaces at depth such as the base of the dam and its underlying foundation. GPR profiles generated from reflection data collected using the 100 MHz proved to be most effective in assisting to delineate the top of the core.

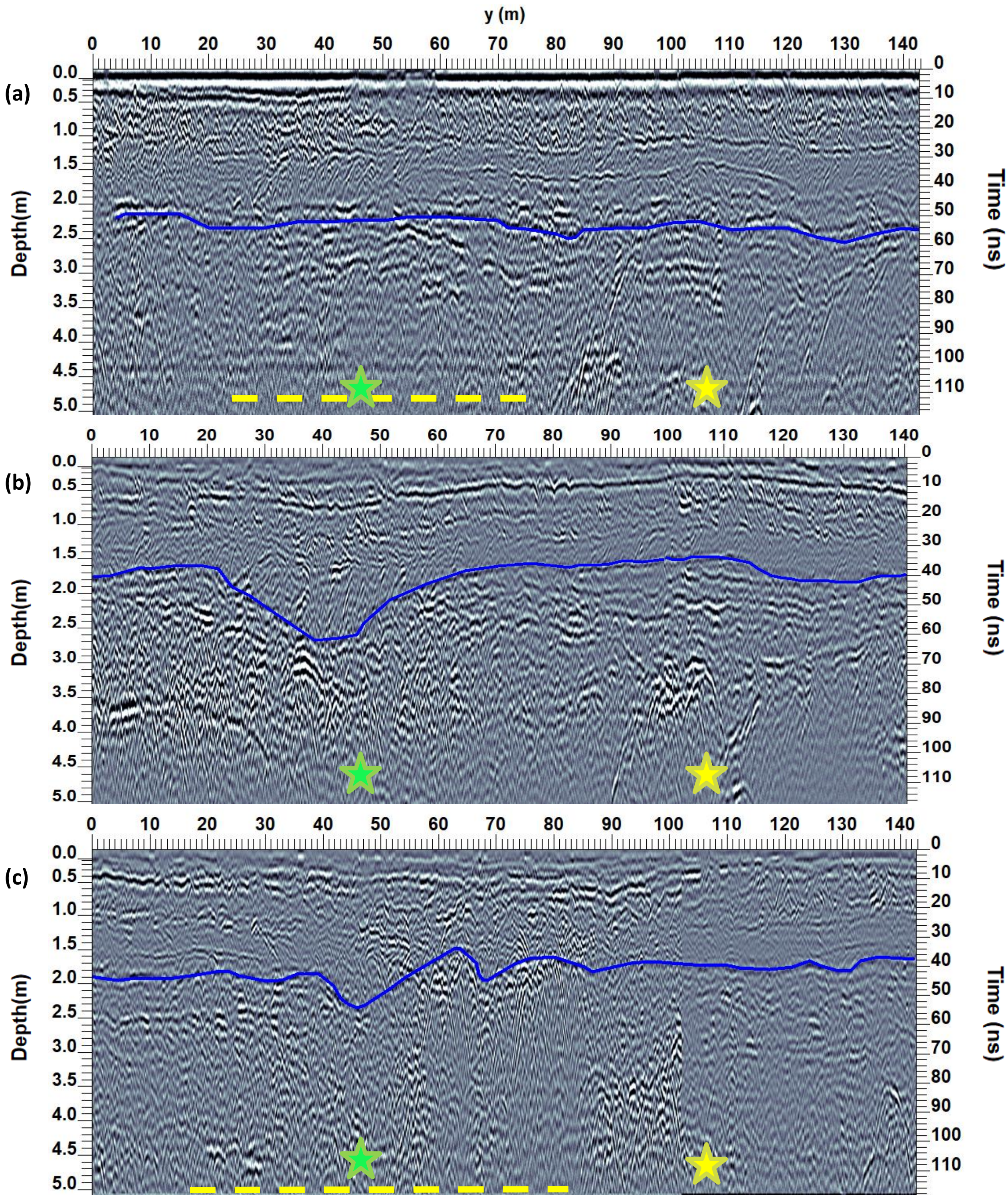

y (m)
(a)
(b)
(c)
Depth(m)
Time (ns)

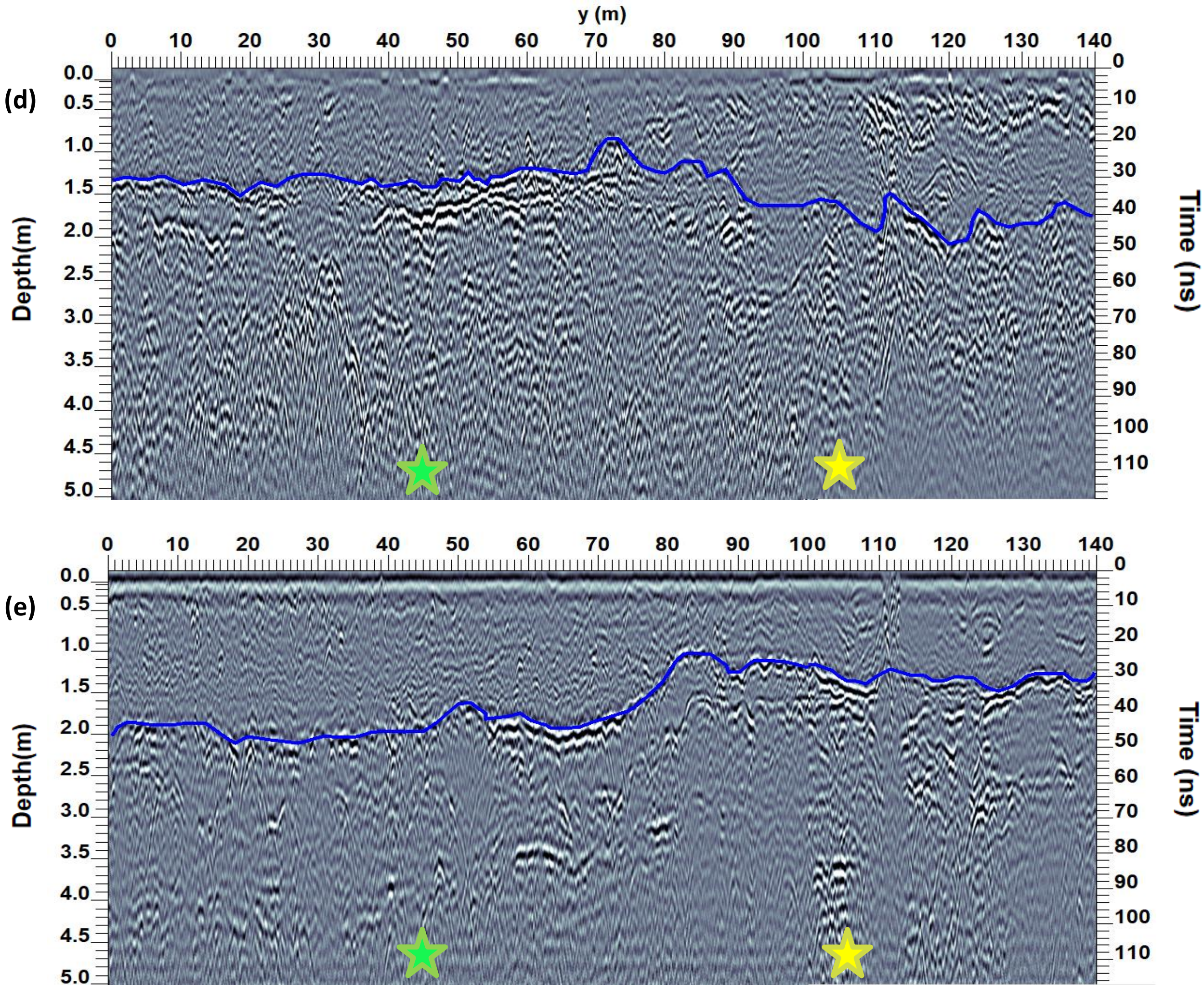

Figure 4.47: S-N profiles collected over the June 2017 seep grid using 250 MHz antennae. (a) YLINE00 (x=0) with no background subtraction; (b) YLINE03 (x=6) (c) YLINE05 (x=10) (d) YLINE07 (x=14) (e) YLINE09 (x=18). The thick dashed yellow lines in panel (a) and (c) indicate the coverage of the November 2106 seep grid (section 4.4.3) and the start and end positions of the "2 m Central" DCR Schlumberger survey (section 4.3.2) respectively.

GPR surveys conducted over clusters of closely spaced point sources (cobbles) may produce a profile image exhibiting an interference pattern characteristic of overlapping adjacent hyperbolas (crossing tails). It is important to note that the slopes of hyperbola tails depend on the vertical exaggeration of the profiles.

The 250 MHz profiles are shown in Figure 4.47. Figure 4.47 (a), taken nearest the wetland, reveals a continuous interface at a depth of 1-1.2 m. The ground above this hosts many small reflectors indicative of heterogeneous soil containing sand, gravel and cobbles. Other interfaces (e.g. between y= 55 m and y= 120 m) may indicate layers of varied compaction associated with the roller used to flatten the crest. The top of the water table is a moderately flat-lying reflector at an average depth of ~ 2 m across the profile. The ground above the water table is a dry upper unit illustrated as the highly resistive near surface layers in the DCR inversion models over the seep.

Figures 4.47 (b) and (c) reveal there are variations in the shallow subsurface layering east of YLINE00. The strong shallow reflector located between a depth of 0.2-0.7 m along the extent of YLINE03 and YLINE05 may be partly hidden by the ground wave. The water table in YLINE03 and YLINE05 descends in elevation near the seep location (green star). Borehole #3 is centered over y=10 m along YLINE03. The water table was inferred at a depth of 2.3 m in 2011 similar to estimates in Figure 4.47 at this location. The profile YLINE07 (see also Figure 4.49) exhibits a amplified horizontal reflective interface between y=37 m and y=70 m at a depth of ~ 2 m. This may be an area of shallow tailings saturation given its proximity to the adjacent seep marker.

Data from the 250 MHz GPR profiles in Figure 4.47 were used to produce the depth map of the water table surface over the grid shown in Figure 4.48. The general trend indicates a hydraulic gradient to the west, as would be expected with the impoundment to the east. This gradient may be influenced by the thickness of the upper fill materials and/or

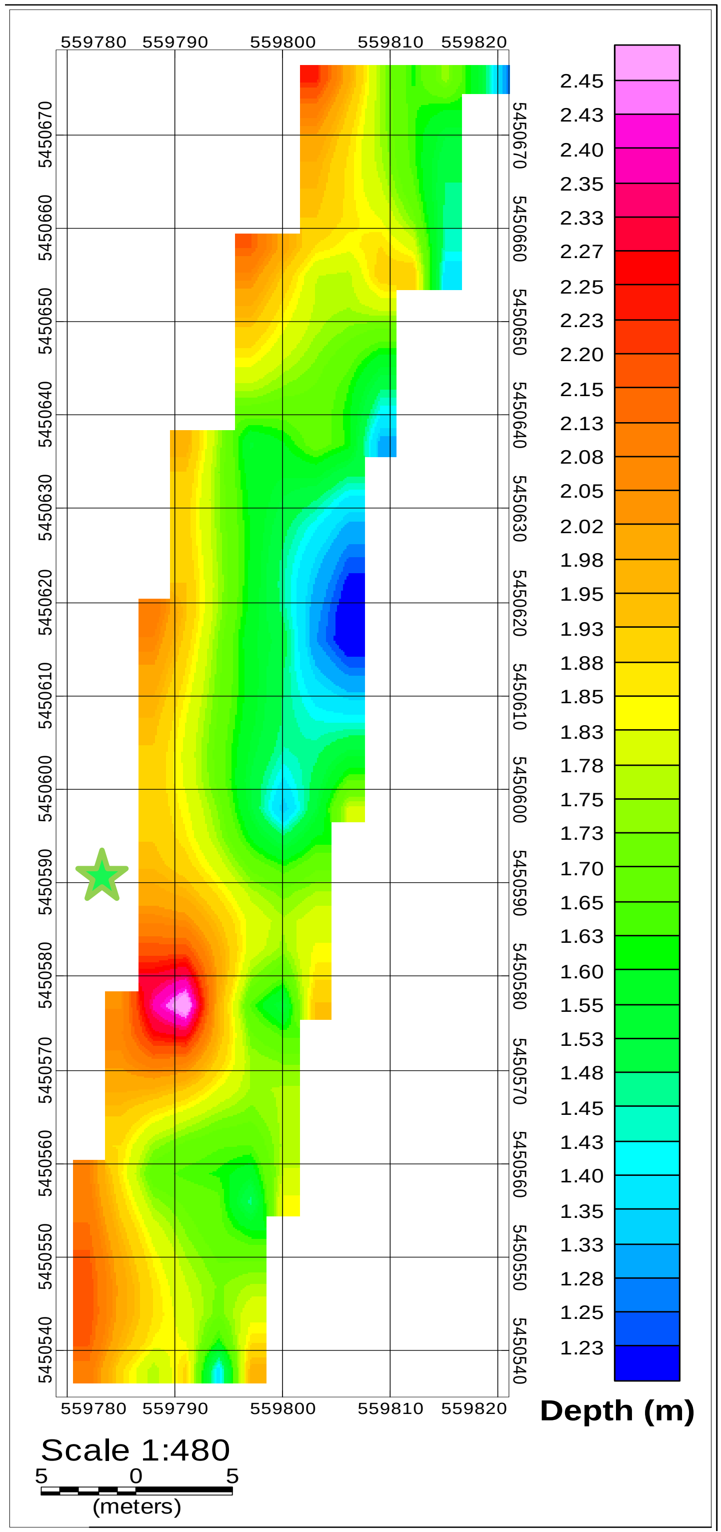

Figure 4.48: Depth contour map of the water table surface over the June 2017 seep grid.

the underlying topography of the impoundment. The dry dam fill is thickest in the vicinity of the seep (green star), suggesting the water table is being drawn down by the seep identified at the base of the downstream slope over this area. The water table elevation is at the impoundment level along the upstream slope, and at the wetland level at the downstream toe of the dam. Between these two locations the water table will be between these two elevations.

Using the 100 MHz antennae (Figure 4.49) major interfaces such as the water table and the core interface are more pronounced, and smaller-scale features such as the soil layering and are less resolved. Hyperbolas, presumably associated with cobbles, show up much more clearly in the 100 MHz profiles than the 250 MHz profiles. As for the 250 MHz profiles, these figures also show significant variations in the structures across the dam from YLINE00 nearest the wetland to YLINE05 over the centre of the embankment to YLINE09 near the tailings pond, however there are some persistent features.

Along YLINE00 (Figure 4.49(a)), three proposed erosion channels surrounding the subsurface region near the inlet channel and old stream are designated erosion channel #1, #2 and #3 S-N, respectively. These erosion channels are most pronounced over YLINE00 near the wetland as seepage progresses E-W through the embankment. Between y=90 m and y=110 m a series of hyperbolic reflections underlying the top of the core are ascribed to an agglomeration of erosion resistant cobbles and boulders. It is proposed in this research that the region underlying the boulders has high porosity generated from washing away of fines from the core that allows fluid flow to permeate west through a pathway that joins

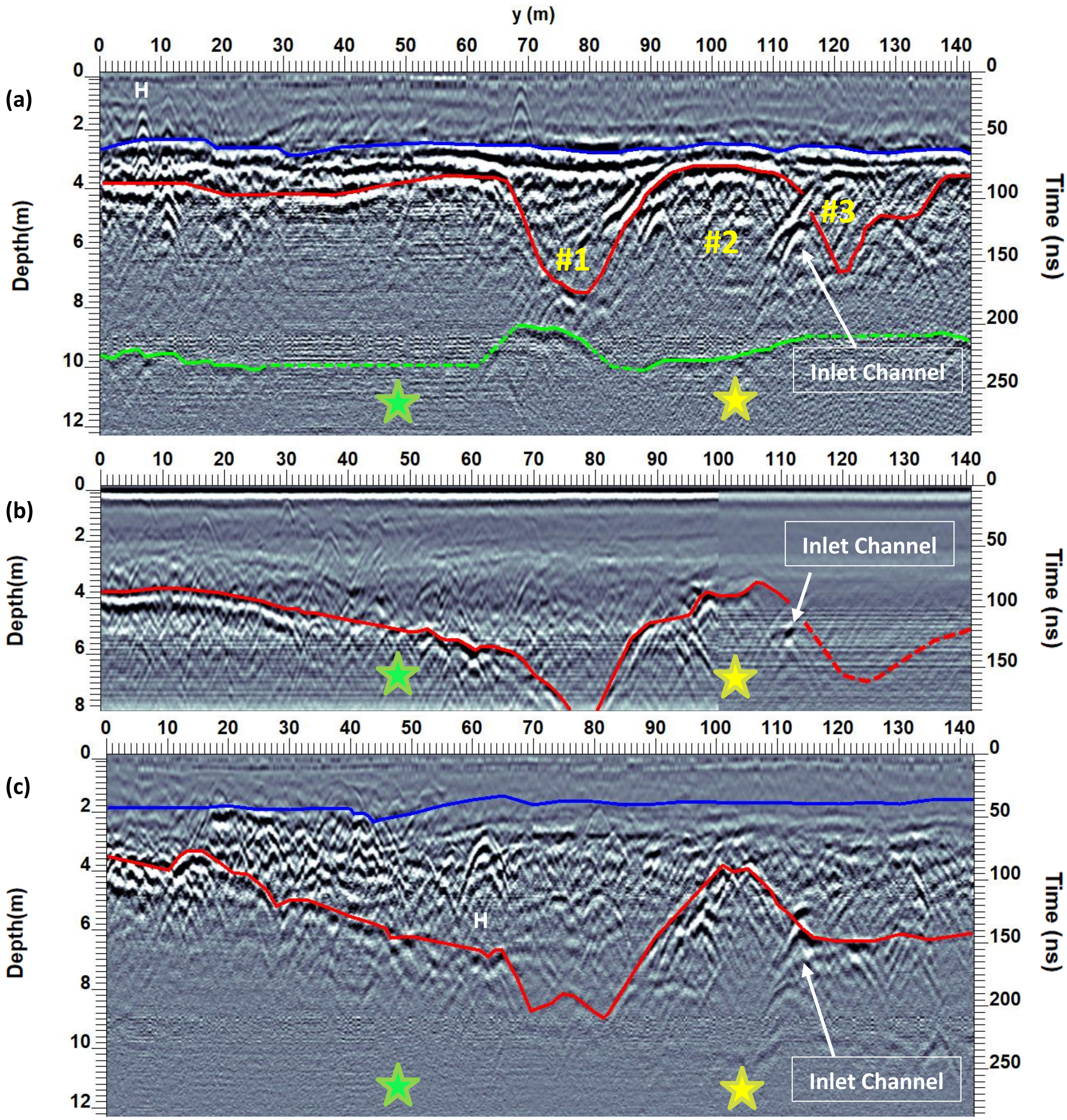

y (m)
(a)
(b)
(c)
H
#1
#2
#3
Inlet Channel
Depth(m)
Time (ns)

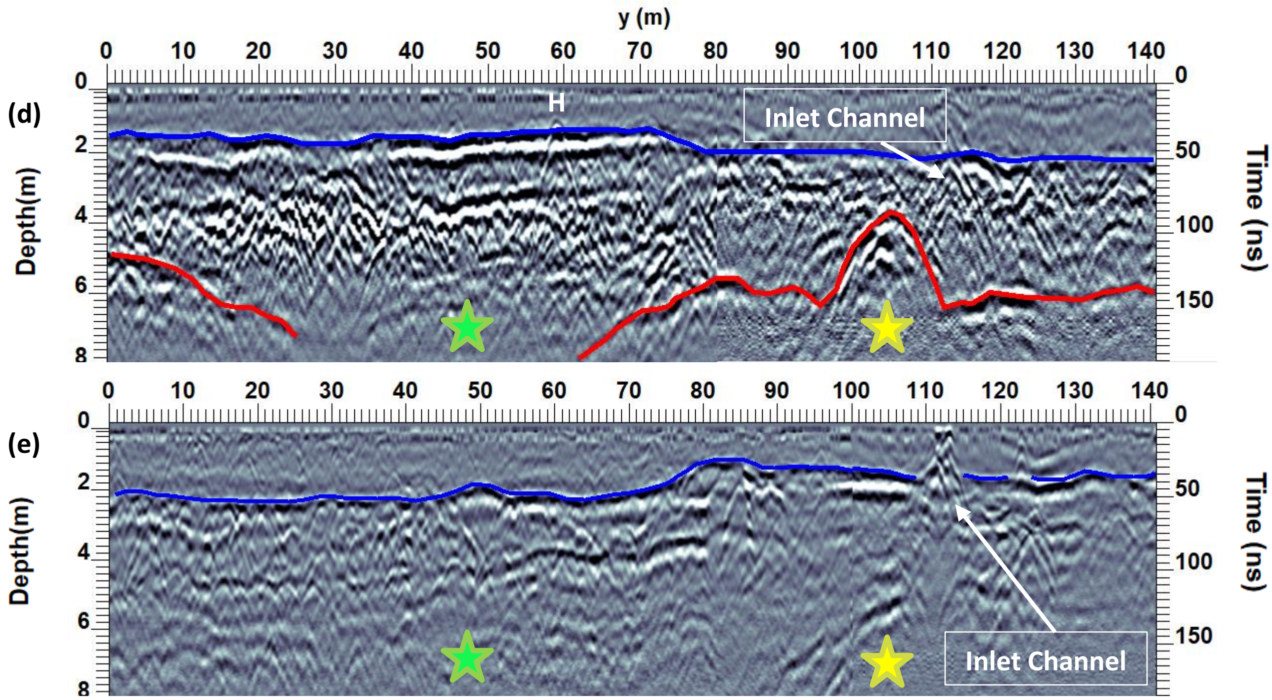

Figure 4.49: S-N profiles collected over the June 2017 seep grid using 100 MHz antenna frequency. (a) YLINE00 (x=0); (b) YLINE03 with no background subtraction (x=6); (c) YLINE05 (x=10); (d) YLINE07 (x=14); (e) YLINE09 (x=18).

erosion channel #1 over YLINE00 to the west. There is a consistent break in the reflection pattern underlying the core near the inlet channel. This feature lines up with channel #2 in YLINE00 (Figure 4.49 (a)).

It is likely the core material surrounding the inlet channel (section 2.2.3) is poorly compacted. Such a zone of high permeability is particularly vulnerable to seepage related erosion. The increased permeability in the subsurface region surrounding the inlet channel could well be the primary factor influencing seepage through the core in this area. It is interpreted that fine sediment has been progressively washed away due to prolonged seepage around loose materials surrounding the inlet channel.

The signal associated with the inlet channel under y~113 m is shallower to the east, as is particularly clear in Figures 4.49 (c) to (e). This dip to the west, to be expected from a decant structure, is consistent with the results of the magnetics (section 4.2), and indicates that if water flowing is actively flowing west through erosion channel #2, it is following the hydraulic gradient illustrated in the water table depth map.

The 50 MHz radar pulses (Figure 4.50) better illuminate deeper features such as the core interface and the dam base interface, the suspected seepage pathway through erosion channel #2 (fuchsia marker), and produces hyperbolas from larger cobbles only. For example, a cobble underlying y=62 m at a depth of 3 m produces a prominent hyperbola in the 100 and 50 MHz profile but not the 250 MHz profile. This cobble is hidden in the 250 MHz profile by reflections from overlying material that (due to its sizing) is less visible in the longer wavelengths. Figures 4.49 and 4.50 indicate little variation in the main core interface between YLINE03 and YLINE05. Strong reflection from the water table between y=17 m and y=41 m, results in shallow signal attenuation and subsequent weakening of the reflection from the underlying core interface.

Differences in the internal structure of the dam between YLINE05 and YLINE07 largely occur south of the inlet channel. The core boundary is more pronounced, flatter, and deeper over YLINE07. A dip at y=91 m corresponds to the location of erosion channel #1. YLINE09 is dominated by reflections associated with conductive tailings water and sediment occupying the adjoining reservoir. The core materials thin to the east, therefore

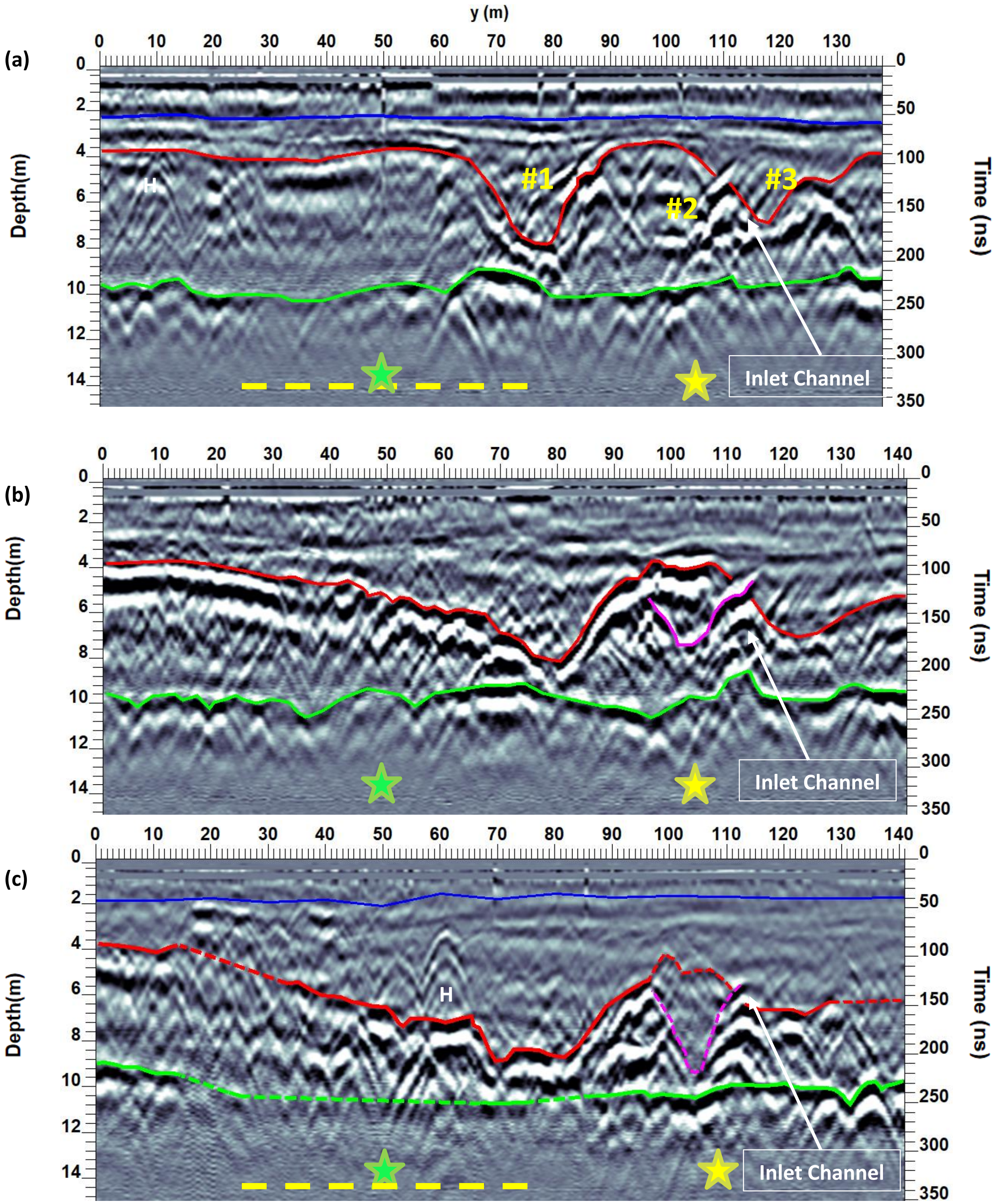

y (m)
(a)
(b)
(c)
Depth(m)
Time (ns)
#1
#2
#3
H
Inlet Channel

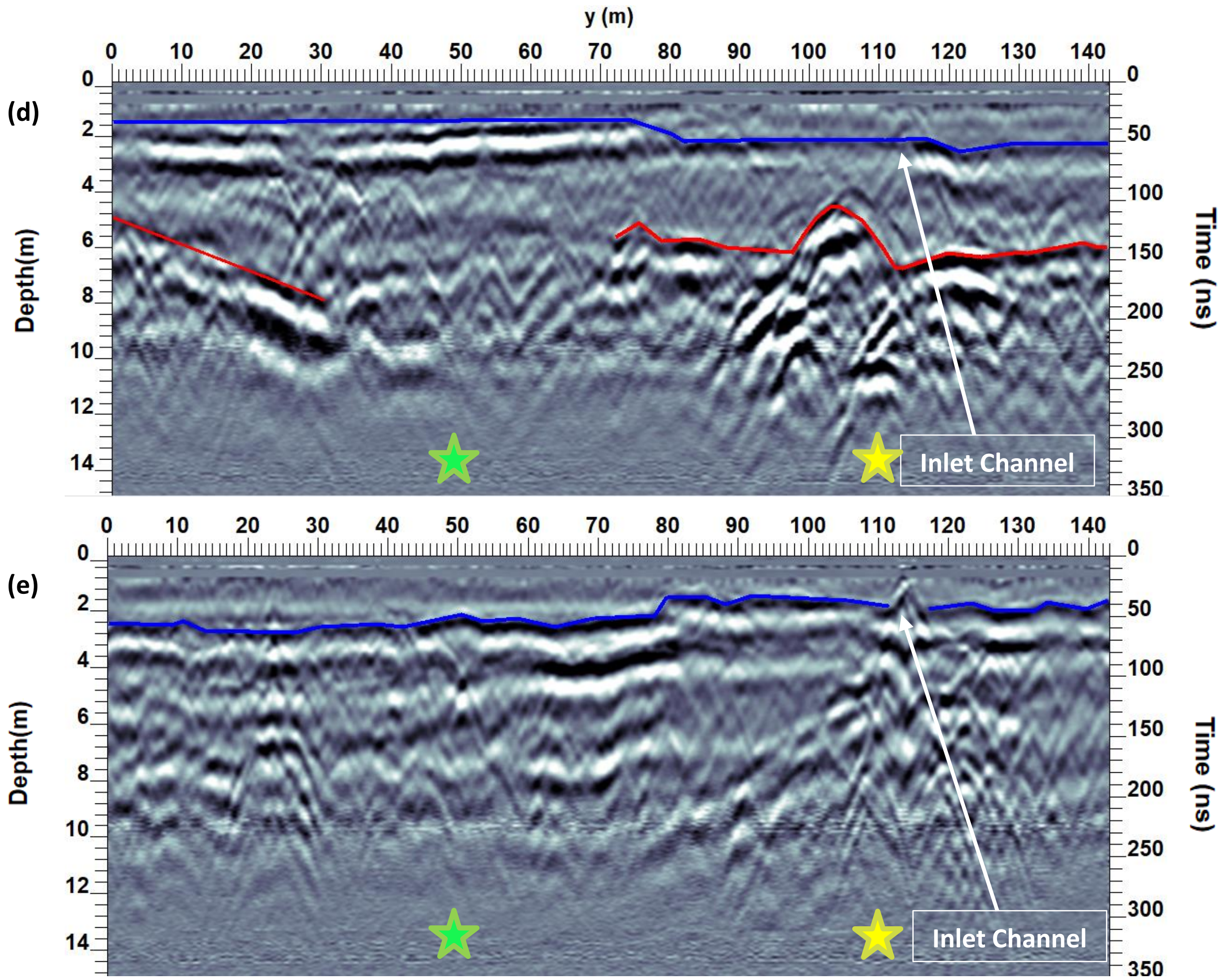

Figure 4.50 S-N profiles collected over the June 2017 seep grid using 50 MHz antenna frequency. (a) YLINE00 (x=0), (b) YLINE03 (x=6); (c) YLINE05 (x=10); (d) YLINE07 (x=14); (e) YLINE09 (x=18). The thick dashed yellow line indicates the coverage of the November 2106 seep grid (section 4.4.3).

this interface is not visible as far east as YLINE09. The base of the dam cannot be identified.

Figure 4.51 displays a reflection amplitude slice at a depth between 3.0 and 3.5 m over the southernmost 100 m of the 50 MHz seep grid. The conductivity of the dam soil

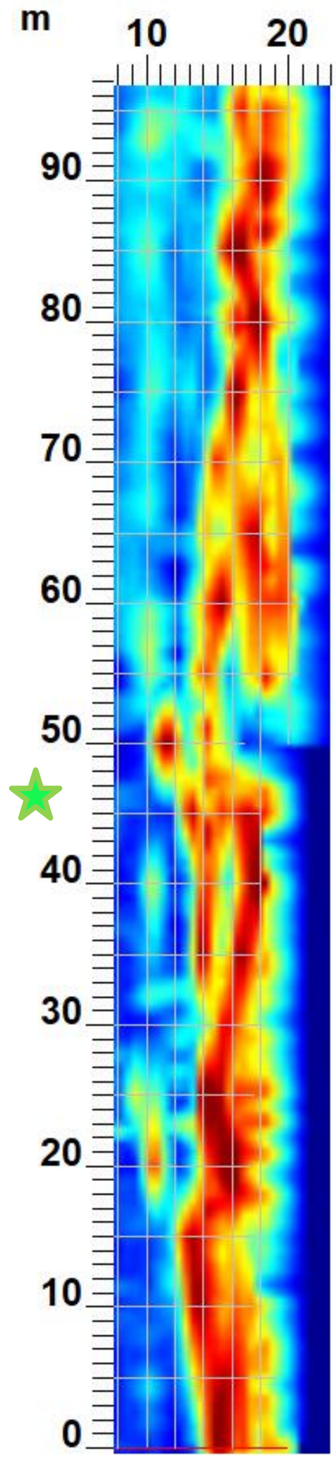

Figure 4.51: Reflection amplitude slice between z= 3.0 m and z=3.5 m over the June 2017 seep grid collected using the 50 MHz antennae. Grey lines indicate the locations of the profiles. Produced by EKKO Project 5 software.

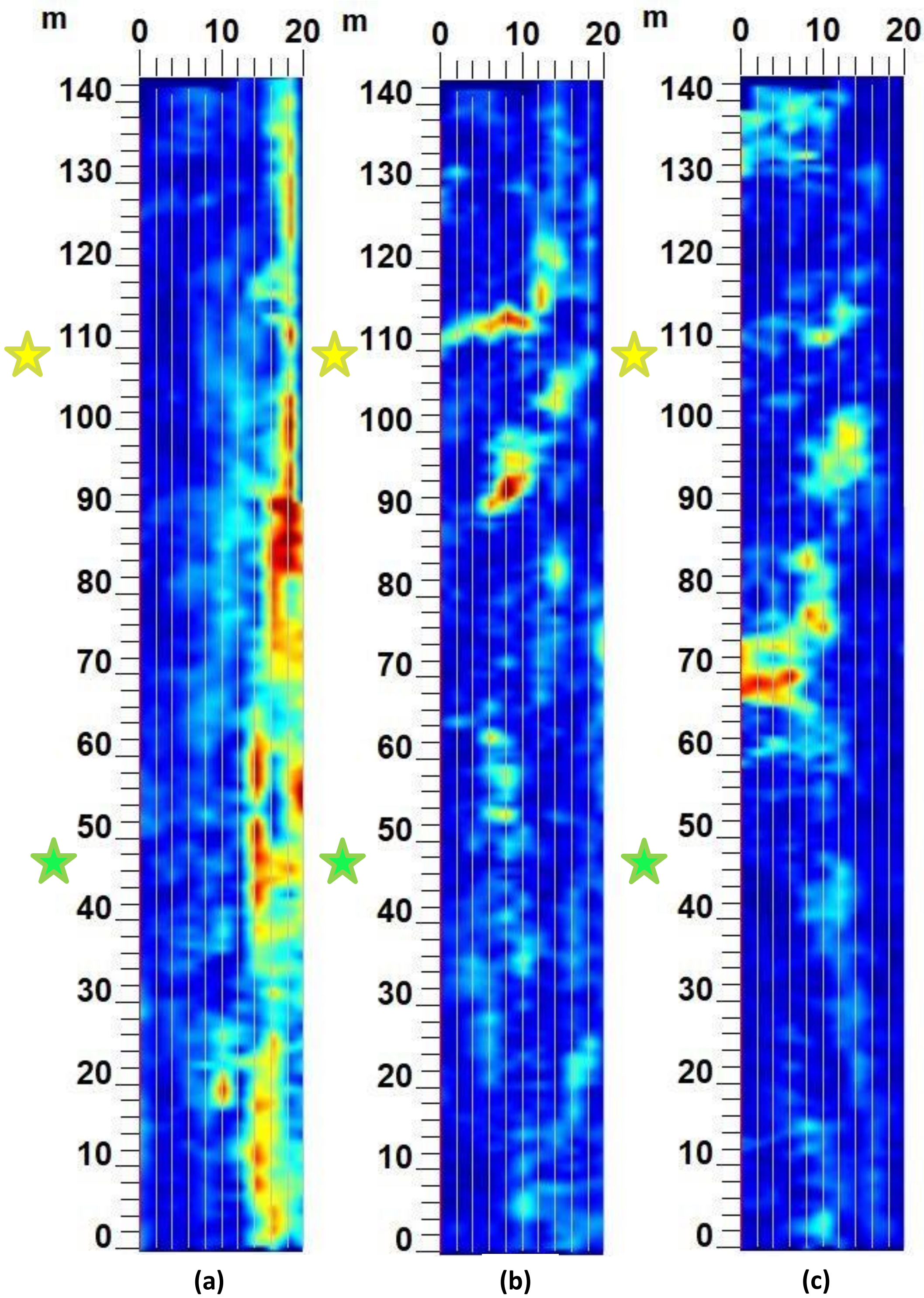

Figure 4.52: Reflection amplitude slices between (a) z= 2.5-3.0 m (b) z=7.0-7.5 m and (c) z=10.5-11 generated from y-line data over the June 2017 seep grid using the 50 MHz antennae.

increases with decreasing distance to the reservoir due to the infiltration of tailings water occupying the pore space of the pervious shell rocks flanking the upstream slope east of the core. Conductivity contrasts between the sand/gravel and tailings sediment result in high reflection strength that attenuate the GPR signal at depths below 3.5 m. Reflections from the top of the core are missing east of YLINE08 along y=50 m in the region adjacent to the seep marker. This was similarly observed in the slice image over the November 2016 grid in Figure 4.44.

Figure 4.52 presents reflection amplitude slices at three depths, through the full length of the seep grid, using y-line data exclusively. Figure 4.46 (a), a slice at 2.5 to 3 m, emphasizes regions of shallow elevated reflection strength along the eastern edge of the dam crest due to adhering of tailings sediment to the upstream slope. Figure 4.52 (b), a slice at 7 to 7.5 m, illustrates two strong reflectors in the north associated with the inlet channel and seepage along the old stream. Figure 4.52 (c) displays the depth slice at the base of the dam. The region of high reflection is near the proposed erosion channel #1.

Figures 4.53 to 4.55 presents the GPR profiles of XLINEs collected using the three antennae. The x-line profiles indicate there is a hydraulic gradient to the west. The steep east-dipping features are likely hyperbola tails.

Figure 4.53 (c) presents the W-E GPR profile of XLINE16 (intersecting y=80) collected using the 250 MHz antennae. XLINE16 runs W-E through erosion channel #1, and intersects the surface location where the largest SP high over the July 2018 SP grid (Figure 4.6) was measured at x=10 m. Fiduciaries F1 and F2 indicate the positions where

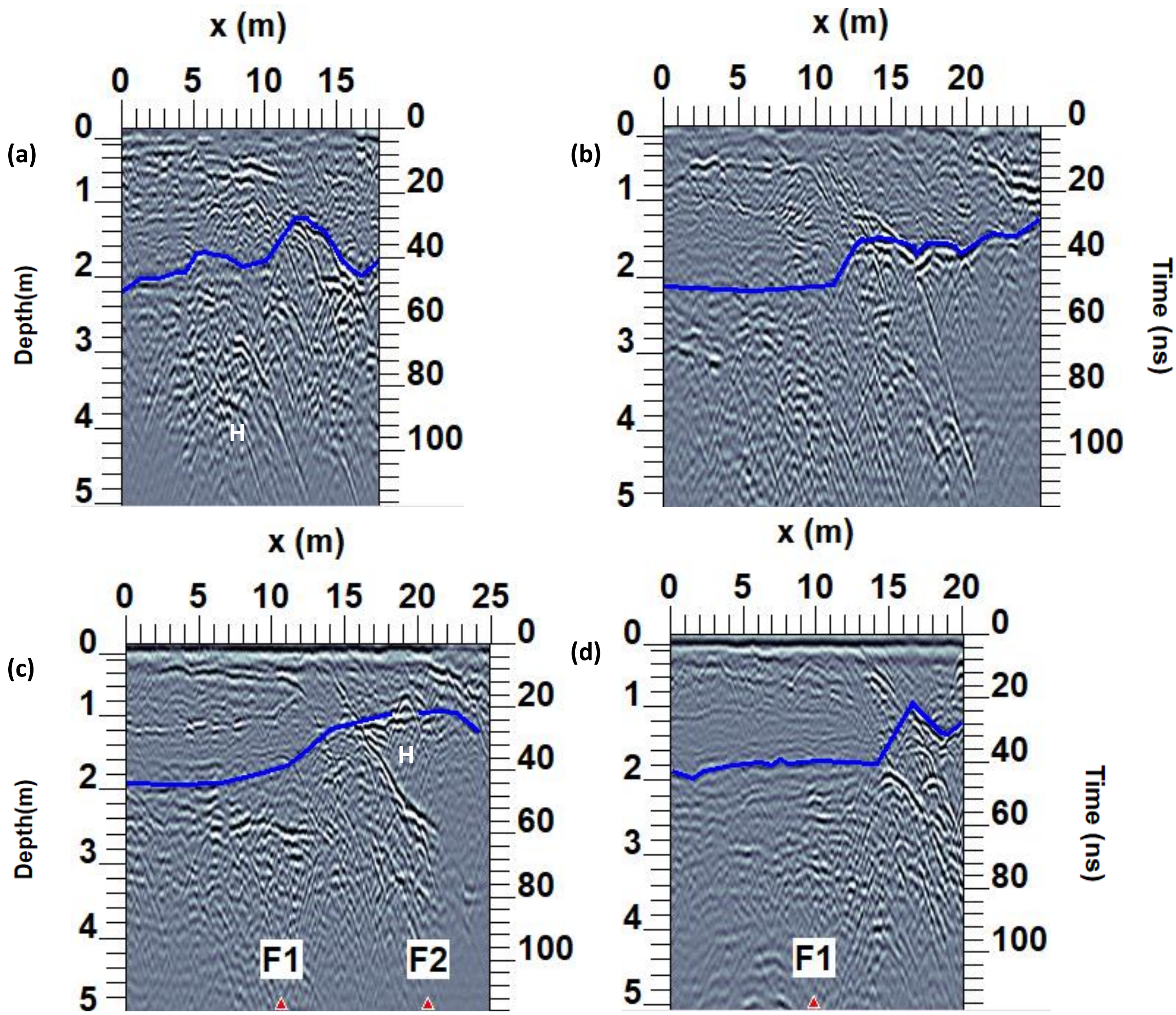

Figure 4.53: W-E profiles over the June 2017 seep grid using the 250 MHz antennae. (a) XLINE03 (y=15); (b) XLINE10 (y=50); (c) XLINE16 (y=80); (d) XLINE22 (y=110).

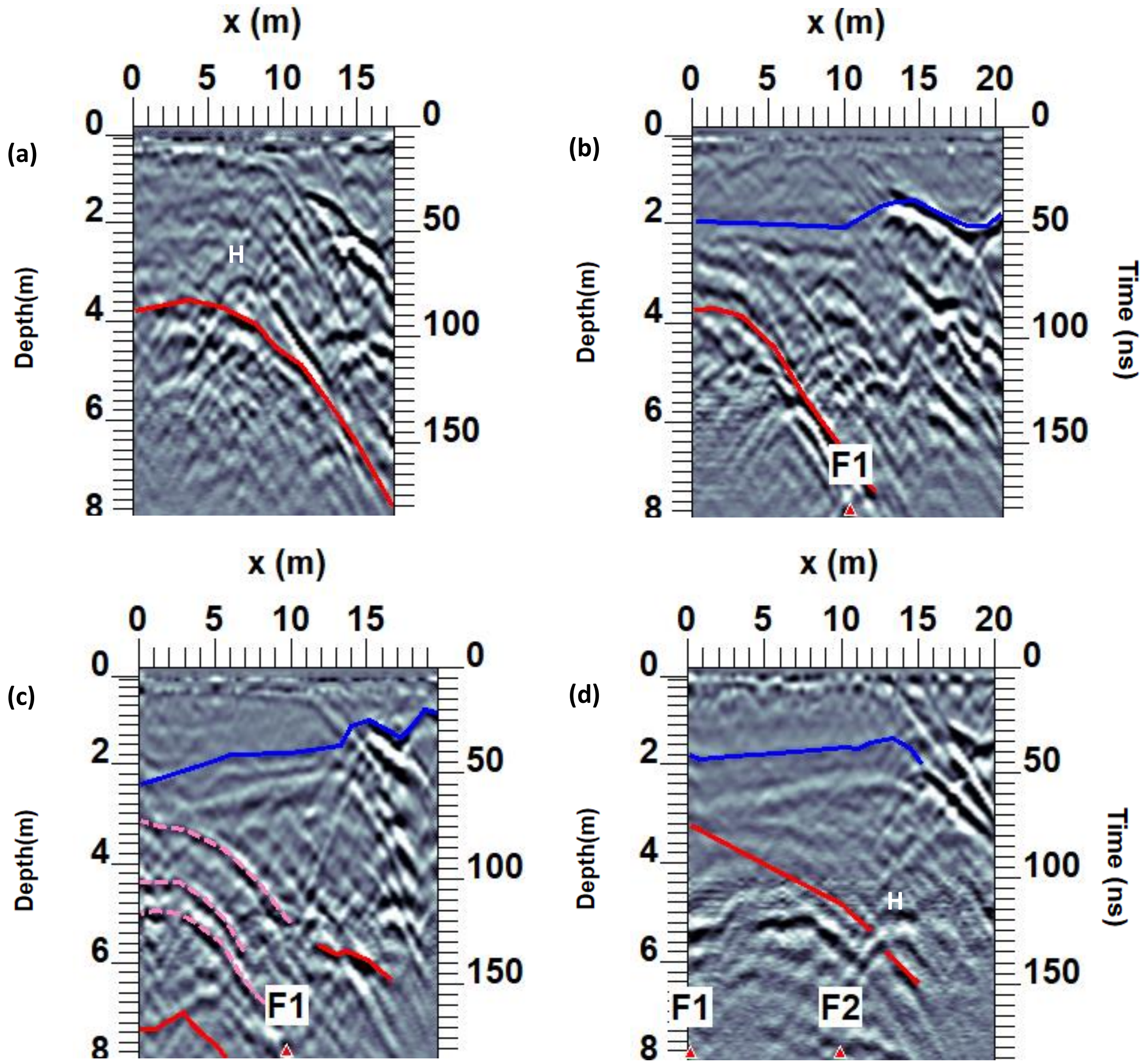

Figure 4.54: W-E profiles over the June 2017 seep grid collected using the 100 MHz antennae**.** (a) XLINE03 (y=15); (b) XLINE10 (y=50); (c) XLINE16 (y=80); (d) XLINE22 (y=110)**.**

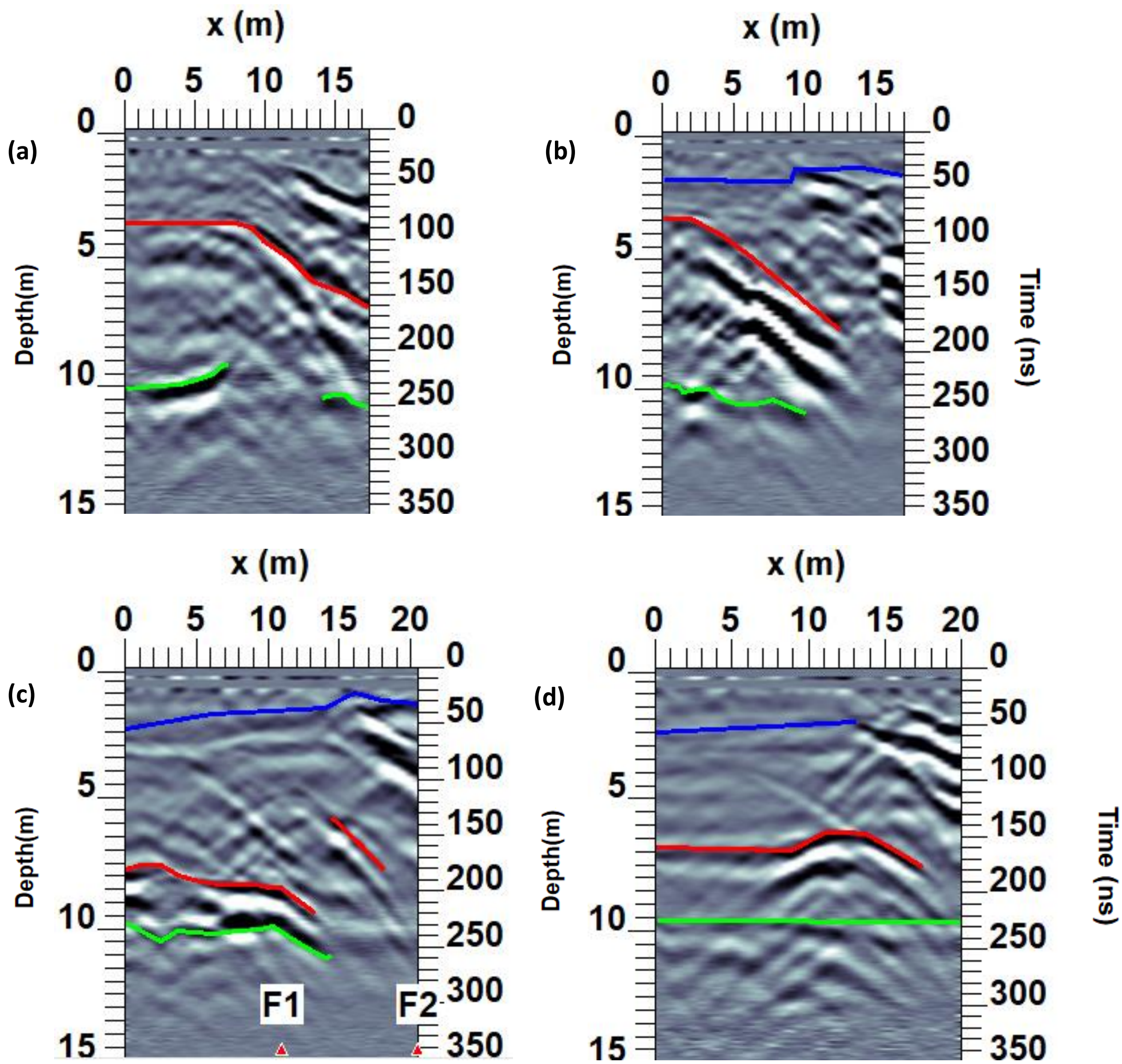

Figure 4.55: W-E profiles collected over the June 2017 seep grid using 50 MHz antennae. (a) XLINE03 (y=15); (b) XLINE10 (y=50); (c) XLINE16 (y=80); (d) XLINE23 (y=115).

the GPR crosses the SP high and the eastern edge of the dam crest, respectively. An interface interpreted as a boundary between upper compacted dam soil flattened by a roller and relatively looser underlying dam soil (see Figure 4.47) is located at a depth of ~1.2 m in the west. A hyperbola underlying x~19 m becomes visible over XLINE16, not previously seen over XLINE10 or XLINE03. The sudden descent in the water table to the west at F1 matches the surface location where the anomalous SP high was measured over the July 2018 grid.

Figure 4.54 presents the W-E x-line profiles collected over the June 2017 seep grid using the 100 MHz antennae. The core appears in-tact at a depth of ~ 4 m over the center of the dam crest.

In the profile of XLINE16 (Fig, 4.54 (c)), the top of the eroded core interface is only visible west of x~10 m. These depths were confirmed by intersecting y-line data. The dashed pink horizons may delineate the soil layering associated with successive dam lifts.

Figure 4.55 presents the W-E x-line profiles collected over the June 2017 seep grid using the 50 MHz antennae. The base of the dam becomes visible over XLINE03 (Fig.4.55 (a)) suggesting the height of the dam is approximately 10 m.

Figure 4.55 (c) presents the W-E profile of XLINE16 collected using the 50 MHz antennae. The height of the dam is 10 m on average (green marker horizon) and is visible between x=0 m and x~14 m. There is a break in the core interface between approximately x=13 m and x=15 m interpreted as seepage related erosion in the region. Figure 4.49 (d) presents the profile of XLINE23 located over the inlet channel and old stream.

(a)

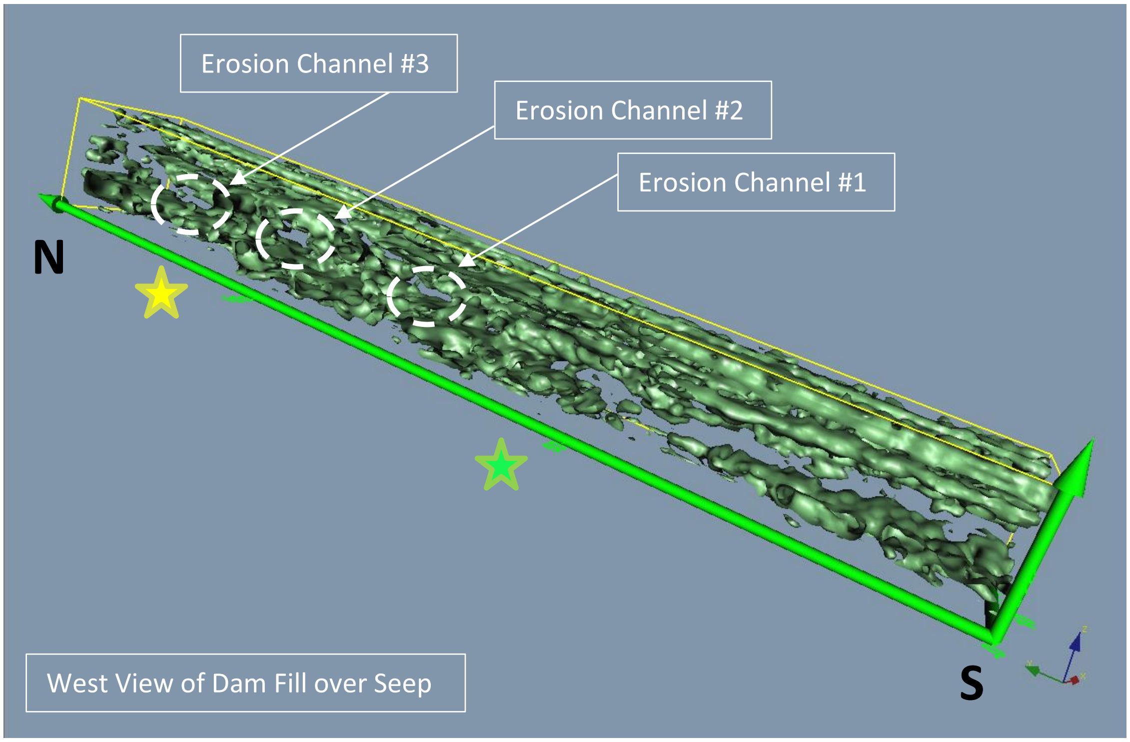

(b)

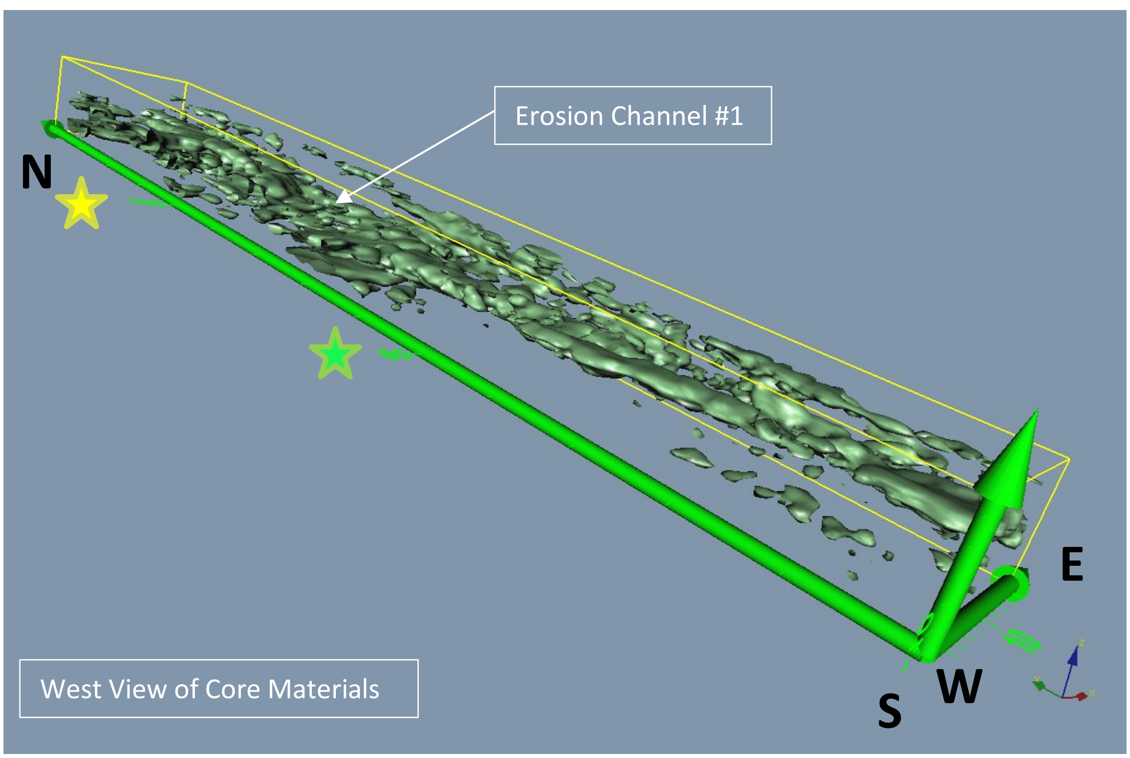

Figure 4.56: Voxler isosurface models generated using y-line data over the 50 MHz June 2017 GPR grid displaying (a) 10.01 mV reflectors and (b) 52.15 mV reflectors.

Figure 4.56 presents 3-D isosurface models generated in Voxler from trace-amplitude data from the 50 MHz antennae viewed from the (a) wetland and (b) southwest. The isosurfaces (green) consist of regions where the radar amplitude is constant (at a value of 10 mV) over various reflective interfaces. Reflection amplitudes along surfaces that are weaker than the selected isovalue are not displayed in the model.

Most reflections along the grid were stronger than this isovalue, allowing for the modeling of the dam wall looking east from the wetland. The subsurface region outlined by the dashed white circles in Figure 4.56 (a) correspond to areas of low reflectivity associated with erosion channels #1, #2 and #3. The model in Figure 4.50 (b) was assigned an isovalue of 52 mV and greater. Because the core/upper fill boundary is a strong reflector, weak reflections associated with small-scale heterogeneities in the upper dam fill are unseen while the surface along the top of the core is resolved. The interface is observed deepening to the north to a maximum depth corresponding to the location of erosion channel #1.

Comparison of SP and GPR

YLINE0 of the July 2018 SP grid lies approximately over YLINE05 of the June 2017 GPR seep grid. The highest recorded value of SP measured over the grid at station (0,22) corresponds to a position of y=82 m overlying erosion channel #1 in the GPR profiles over YLINE05.

YLINE07 crosses an anomalous SP high measured over the July 2018 grid (Figure 4.8) at y=80 m inferred to be related to water discharging through erosion channel #1. An anomalous SP high of 121.6 mV measured over L2+400 m (Figure 4.3) lies directly over y=108 m along YLINE07, corresponding to the location above the inlet channel and the old stream. This measured SP high is interpreted to be associated with streaming potentials generated from water discharging through erosion channel #2. The suspected seepage pathway (fuchsia marker) begins to narrow over YLINE07, and the inlet channel becomes concealed within the core.

YLINE08 marks the location across the dam crest where background noise begins to dominate the signal at lower depths east of YLINE07. We surmise the high and irregular values of electric potential along SP Line 2 (Figure 4.3) originate from the same source generating the background noise. It is likely this is due to the random distribution of tailings sediment along the base of the upstream slope. The location of the large SP anomaly encountered over SP Line 1 in June 2016 ('seepage' peak in Figure 4.2) was measured ~ 3 m SE of y=95 over YLINE00. This peak could have been generated by a streaming potential flowing through the inlet channel (erosion channel #2).

4.4.5 Wetland: September 2016 (GPR LINE05)

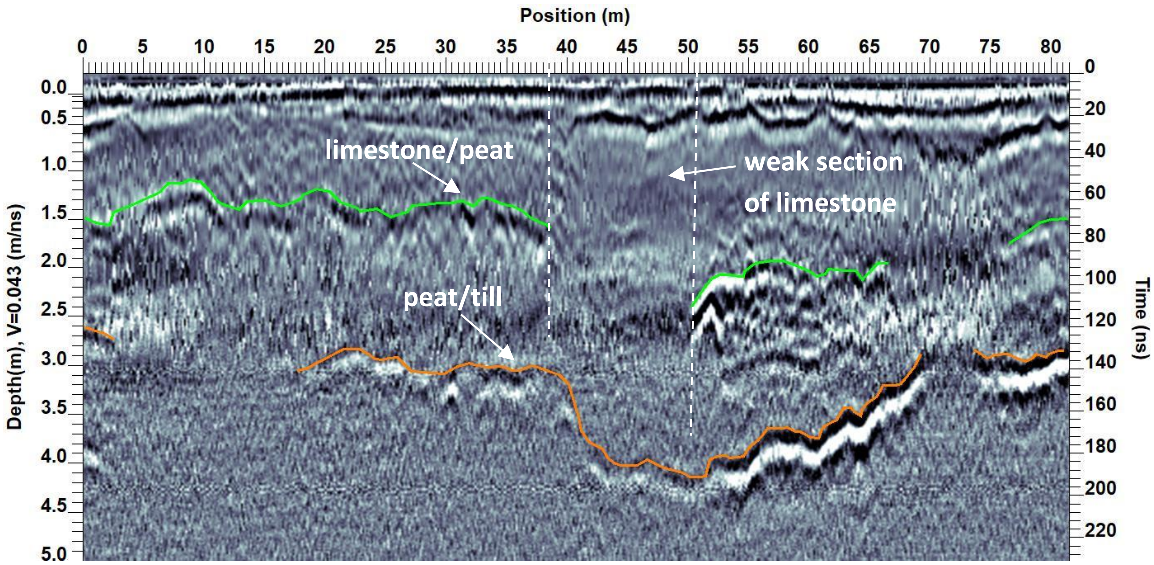

Figure 4.57: SE-NW profile of GPR LINE05 collected over the limestone barrier encompassing sediment pond 2 in the wetland in September 2016.

Figure 4.57 displays GPR LINE05 collected in September 2016 using the 100 MHz antennae over the limestone barrier encompassing the western perimeter of sediment pond 2. The peat thickness over GPR LINE05 ranges between 1.3 m and 1.7 m. BP-4 and BP-23 located just upstream of GPR LINE05 (Figure 2.3) indicate the peat thickness was 1.7 m over both probe locations. The region where the peat/till interface is discontinuous (dashed white line) is interpreted as a weak section of the limestone barrier where small-scale leakage of tailings water contained in sediment pond #2 is discharging into the wetland.

4.4.6 Wetland: February 2017

Figures 4.58 to 4.61 display the S-N profiles collected in the wetland along the northern edge of the downstreams slope. For their locations, see Figure 4.32. The data are unfortunately contaminated with low-frequency noise introduced when the Garmin GPS was laid on top of the transmitting antennae, limiting the interpretations of peat thickness.

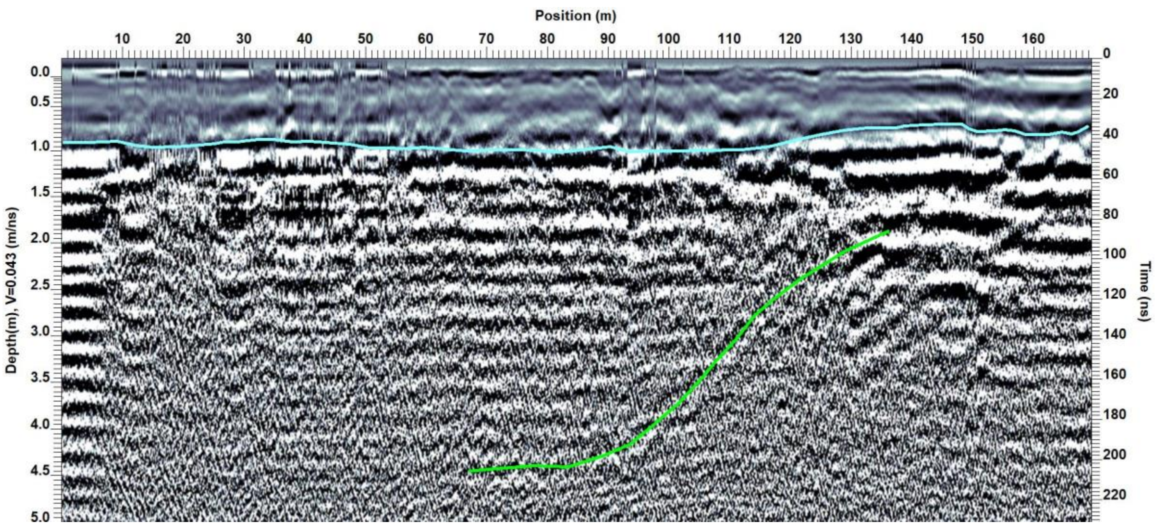

Figure 4.58: S-N oriented profile over GPR LINE06 collected in the wetland.

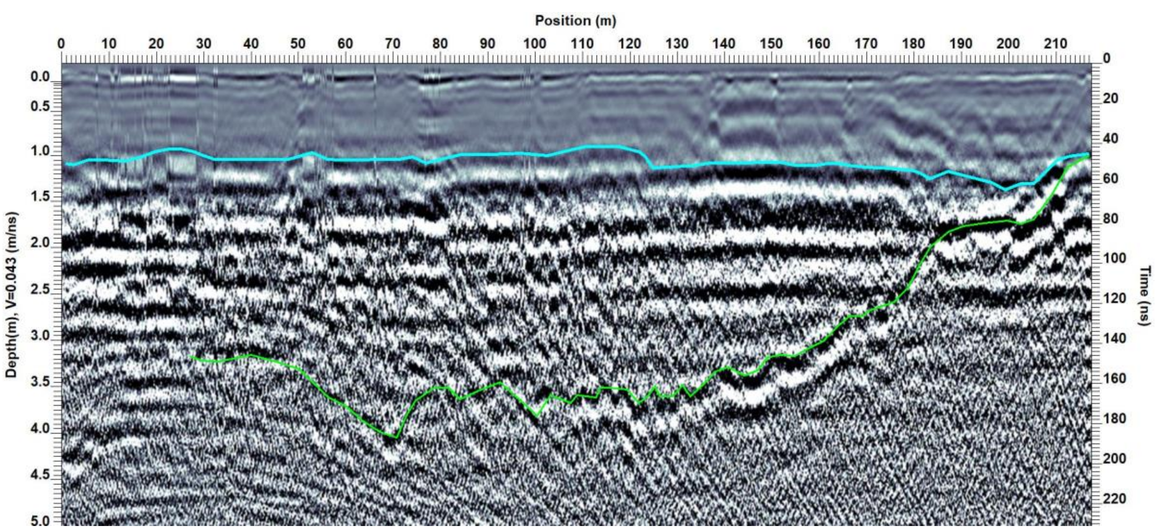

Figure 4.59: S-N oriented profile over GPR LINE07 collected in the wetland.

The snow thickness over LINE06 is approximately 1 m, as indicated by the aqua marker. The noise floor is located just below this depth. The peat/till interface (green horizon) is slightly visible between a position of 66 m and 137 m. Data from BP-9 indicated the peat thickness was 1.8 m just south of 0 m along the horizontal/surface position axis over GPR LINE06. Figure 4.58 suggests the peat thins to the north over GPR LINE06. It is expected that the peat thickness increases to the west towards the center of a shallow lake depression.

In the wetland, the snow was thicker to the west. Over GPR LINE07 (Figure 4.59), conducted ~25 m west of LINE06 in the wetland, the snow reached depths of ~1.3 m over the southern section of the profile. The peat is estimated to be as thick as 2.9 m in the south which is in close agreement with bog probe data from nearby BP-10 and BP-11. The peat layer is thicker on average over GPR LINE07.

GPR LINE08 (Figure 4.60) was conducted approximately 88 m west of the downstream slope. The survey line was collected over several small lakes/streams in the area concentrated along the southern section of the survey line between a position of 0 m and 85 m and into peat and vegetation beyond 85 m. The interface between the ice/frozen soil (mud and organic debris) and the ice/peat interface is not visible: it is suspected themud and soil lining the shallow lakes and the peat lining the till interface has completely frozen. The dielectric constants (dielectric permittivity ε) of ice, snow and frozen soil range between 3-4, 1.4-2.5 and 6 respectively, making an interface between these materials dificult to detect (Equation 3.25) (Robinson et al., 2013). The peat/till interface is

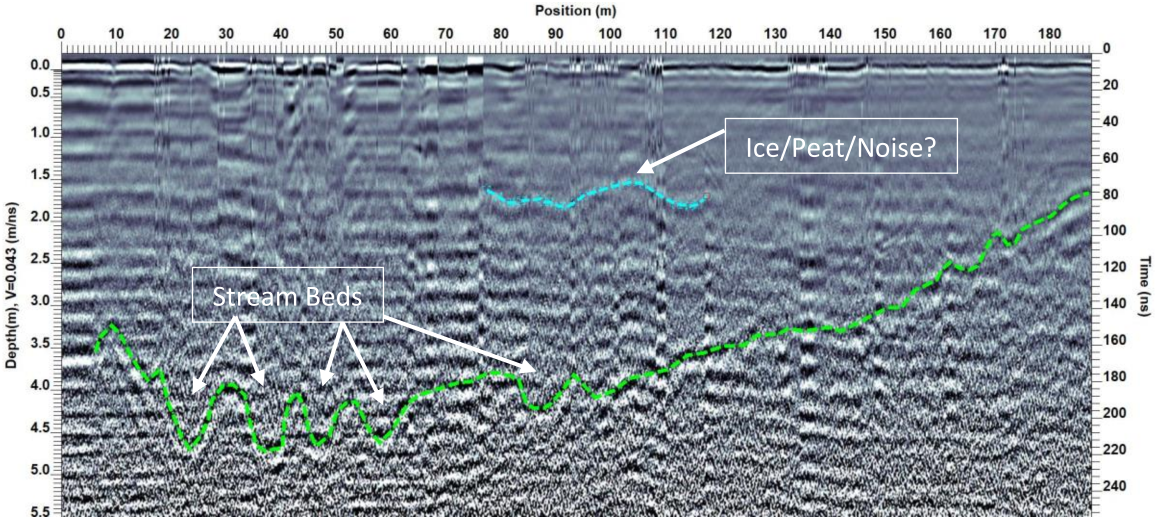

Figure 4.60: S-N oriented profile over GPR LINE08 collected in the wetland.

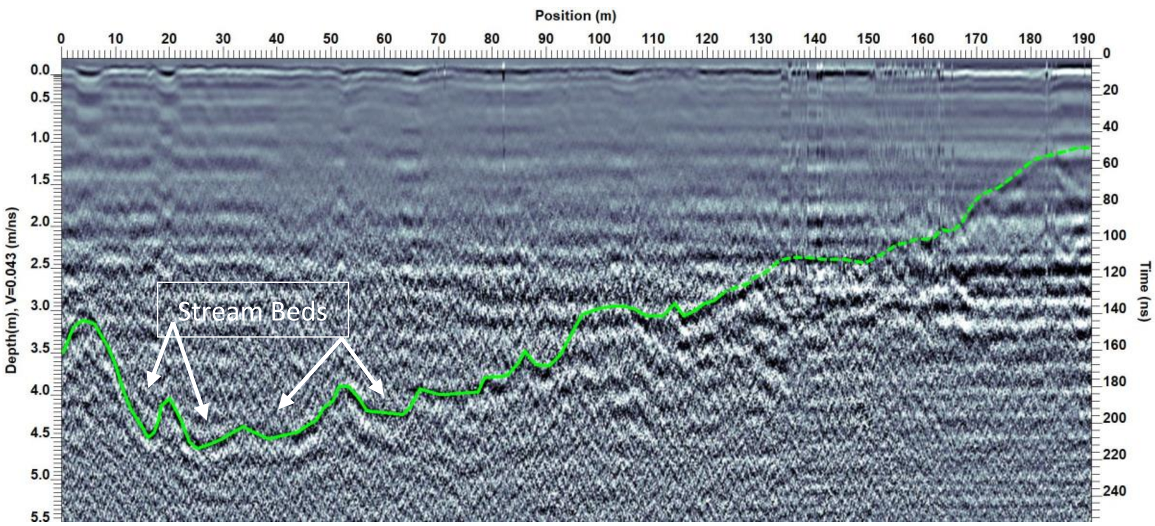

Figure 4.61: S-N oriented profile over GPR LINE09 collected in the wetland.

encountered at a maximum depth of 4.68 m over a position of 39 m. Note that the data hve not been topographically corrected. As a result the apparently jagged basal topography of the mud/till interface between a position of 0 m and 95 m is actually a consequence of the GPR crossing a small stream or lake.

Figure 4.61 displays LINE09, the westernmost line collected over the wetland ~ 100 m west of the downstream slope. Similar to LINE08, the ice/peat boundary is not visible. Between a surface position of 0 m and 65 m the survey line crosses several small lakes and streams (Figure 4.32). The profile looks very similar to LINE08, however the peat/till interface is not as irregular as LINE09 givens the survey line does not cross as many ponds in the south. The peat/till interface is deepest over at a position of 25 m at a depth of 4.6 m and is increasingly shallow to the north.

Based on the GPR surveys collected over the wetland in Februuary 2017 a total average of 1-1.5 m of snow covered the wetland at the time of the survey. Furthermore, it is estimated the peat layer thickens towards to the center of the wetland impression. The peat thickness is of importance to this research as wetlands can store water and naturally mitigate the impact of mining wastes. It is suspected that regions where peat is thick are favorable for passive mitigation of tailings water.

4.5 Electromagnetic Ground Conductivity

Figure 4.62 displays station markers of electromagnetic survey lines. Not shown in Figure 4.62 are EM31-MK2 surveys conducted over the seep area. An EM31 survey along the centre of the Gullbridge dam crest was undertaken in September 2016. LINE00 begins in the south approximately over BH1, and ends approximately at the location of the old culvert in the north. The instrument was carried at hip height, with the boom orientated along the survey path. Both VMD and HMD measurements were taken at 5 m intervals (section 3.2.5).

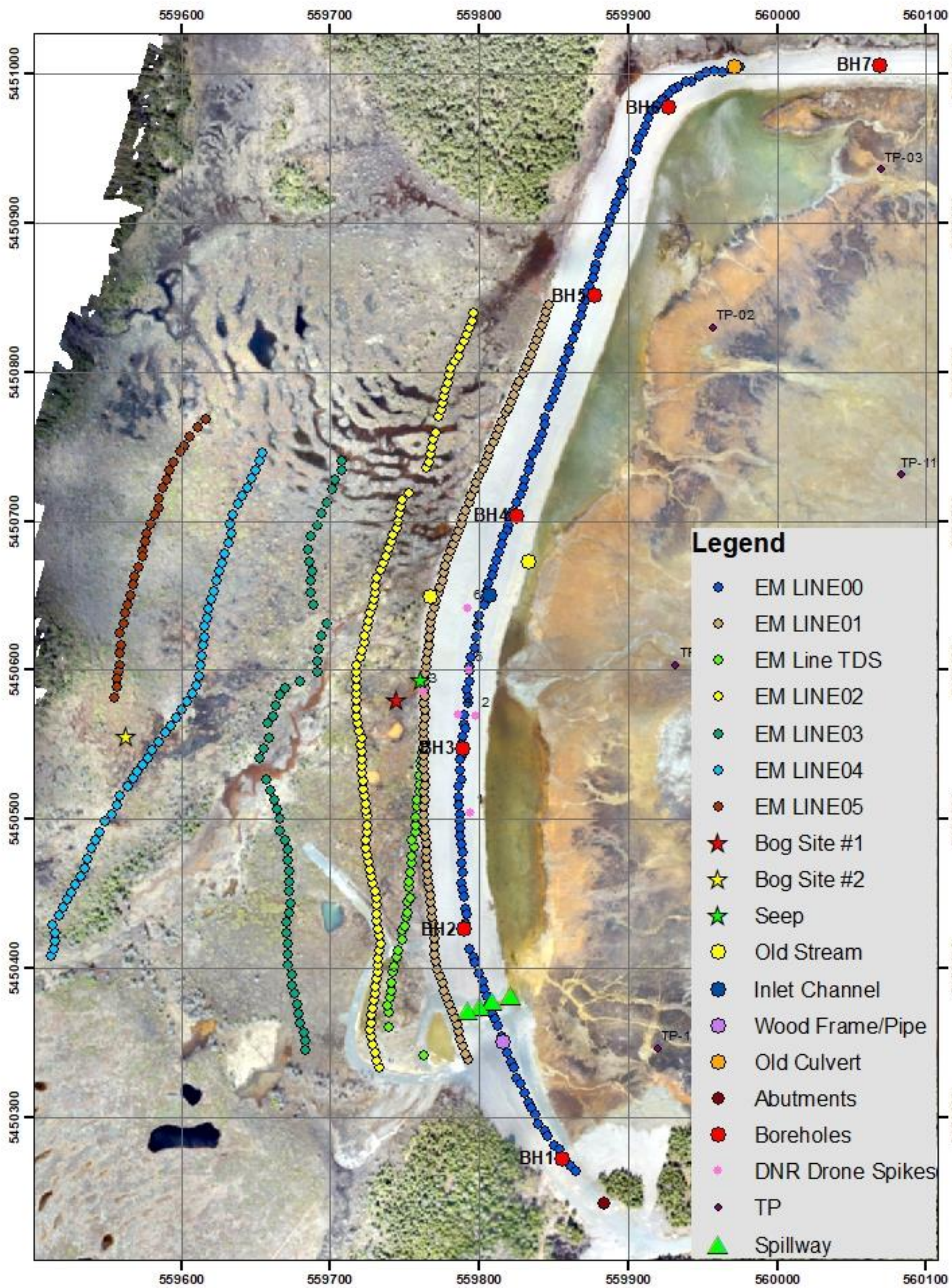

Figure 4.62: EM31-MK2 survey lines collected over the Gullbridge TMA between September 2016 and July 2018. Also pictured are the locations of two bog probe sites collected from the wetland in July 2018.

GEM2 LINE00 (also not shown in Figure 4.62) was conducted along the center of the Gullbridge Dam the day before EM LINE00 was carried out approximately over the same line (blue circles).

Figure 4.62 also displays the 6 S-N EM31 survey lines collected in the wetland. These are E-W the line collected along the toe of the downstream slope (TDS), and EM LINE01-LINE05. Also shown here are the locations of the two bog samples collected in June 2018.

Not shown in Figure 4.62 is an EM31 ground conductivity line collected on September 25th, 2016 over the tailings reservoir, as well as the June 2017 seep grid in which EM31 data was acquired over (see Figure 4.45).

4.5.1 EM Along the Embankment

Figure 4.63 displays the quadrature readings, that is, the apparent conductivity σ_a versus station spacing. The instrument has a greater penetration depth in the VMD orientation, so the fact that the VMD readings are higher than the HMD readings reflects the increase of conductivity with depth: otherwise the patterns are similar. Since the HMD samples a smaller volume of the subsurface, it is more sensitive to near surface variations, hence the greater station to station variation in the HMD.

The quadrature component of the EM31 and DCR respond to the same ground property, that is, the conductivity/resistivity, however their modes of interaction are different. DCR is most responsive to changes in resistive ground, whereas EM techniques

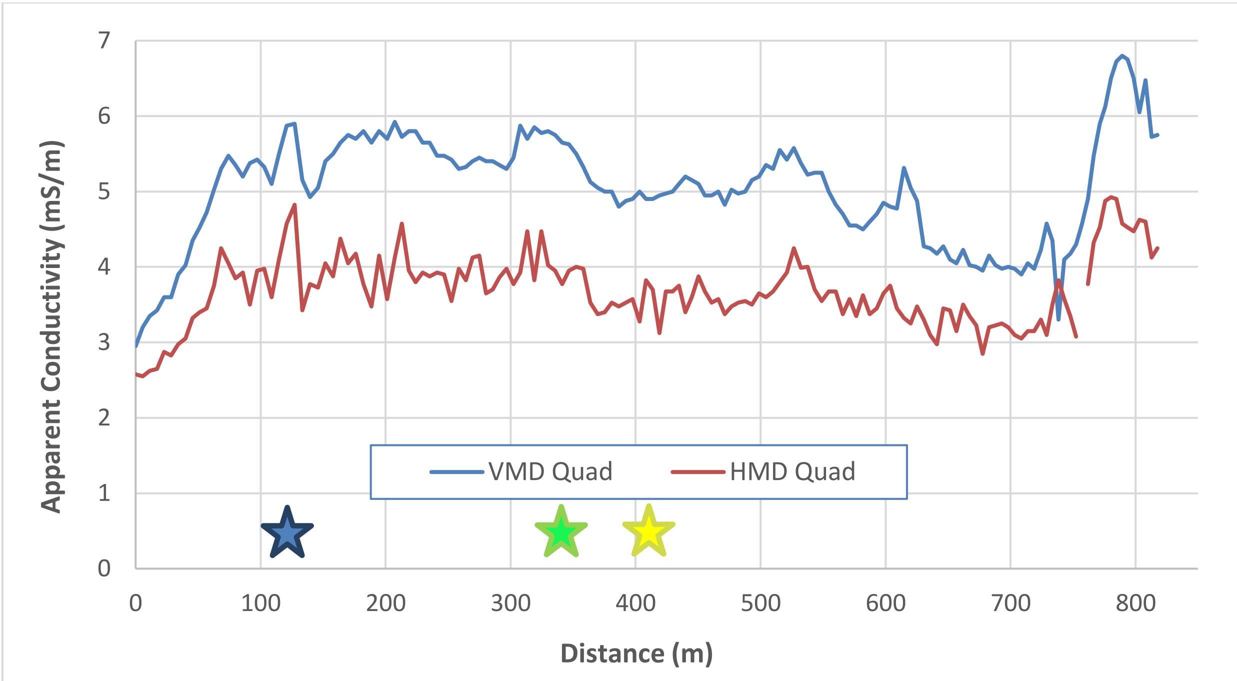

Figure 4.63: S-N profiles of σ_a versus station spacing along EM LINE00 collected using VMD and HMD orientations and a S-N instrument orientation. The blue, green and yellow stars give approximate locations of the spillway, seep, and old stream.

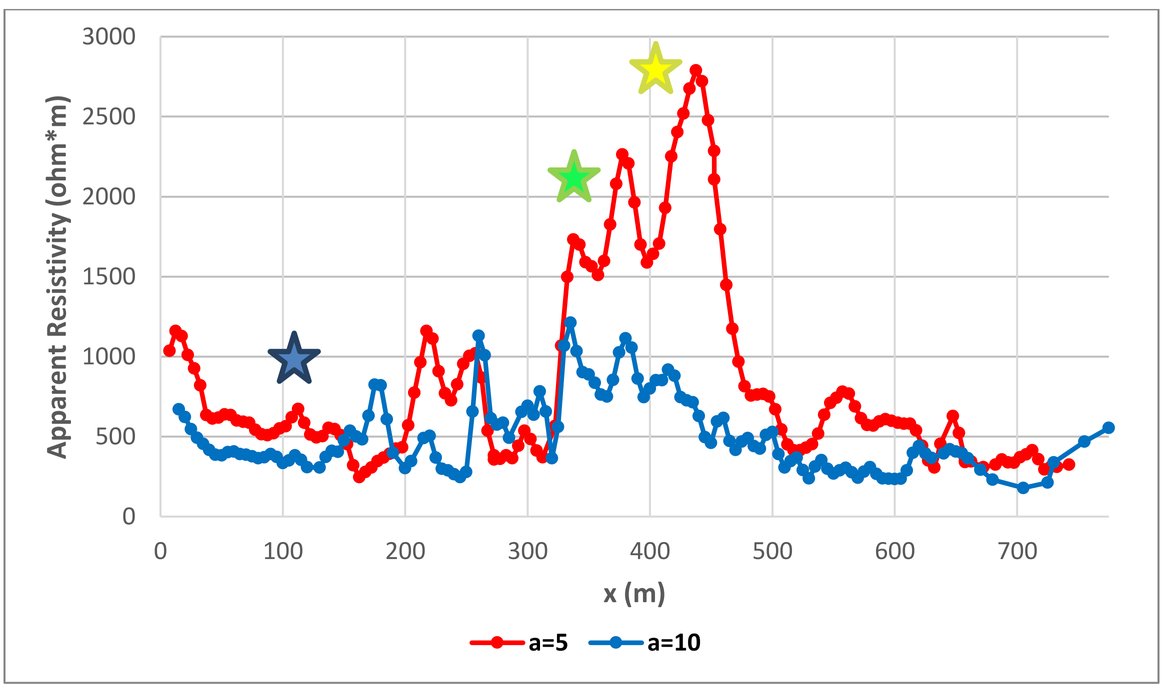

Figure 4.16: Profiles of ρ_a versus x for a-spacings (m) of 5m and 10m obtained from DCR Wenner CST survey along the middle of the Gullbridge Dam in June 2016 (see Section 4.3.1).

respond best to changes of conductivity in relatively conductive ground. Comparing Figures 4.63 and 4.12, the EM31 shows higher conductivity and less variability. The profiles show the same general features of low conductivity/high resistivity in the south where the profile is farther from the tailings, and high conductivity/low resistivity in the north, where the embankment swings around a pool of tailings water near the location of an old culvert. There is only a small decrease in apparent conductivity in the VMD data over the seep/old stream region where the DCR profiles show large increases in apparent resistivity. This is likely related to the difference in sensing depths between the DCR (a=5 m) and the EM31 (6 m).

The increase in conductivity over station +120 m marks the instruments response to the fordable spillway (blue star). The increase in σ_a is likely the result of tailings sediment settling in the spillway following precipitation events that result in the discharge of water into the wetland to control rising pond water in the reservoir. A sharp dip in apparent conductivity over station +280 m along the HMD profile represents an isolated conductive body embedded within the dam structure. The classic "pipe signature" for a loop-loop EM system is two highs separated by a sharp low or negative value in the quadrature. This feature likely does not appear in the VMD profile because it is buried in the top ~ 3 m of the dam soil.

Figures 4.64 and 4.65 displays the profiles of GEM2 LINE00 carried out along the Gullbridge Dam for three different operating frequencies: 990 Hz, 6.21 kHz and 39.03 kHz. Lower frequencies penetrate deeper into the subsurface. Measurements were taken

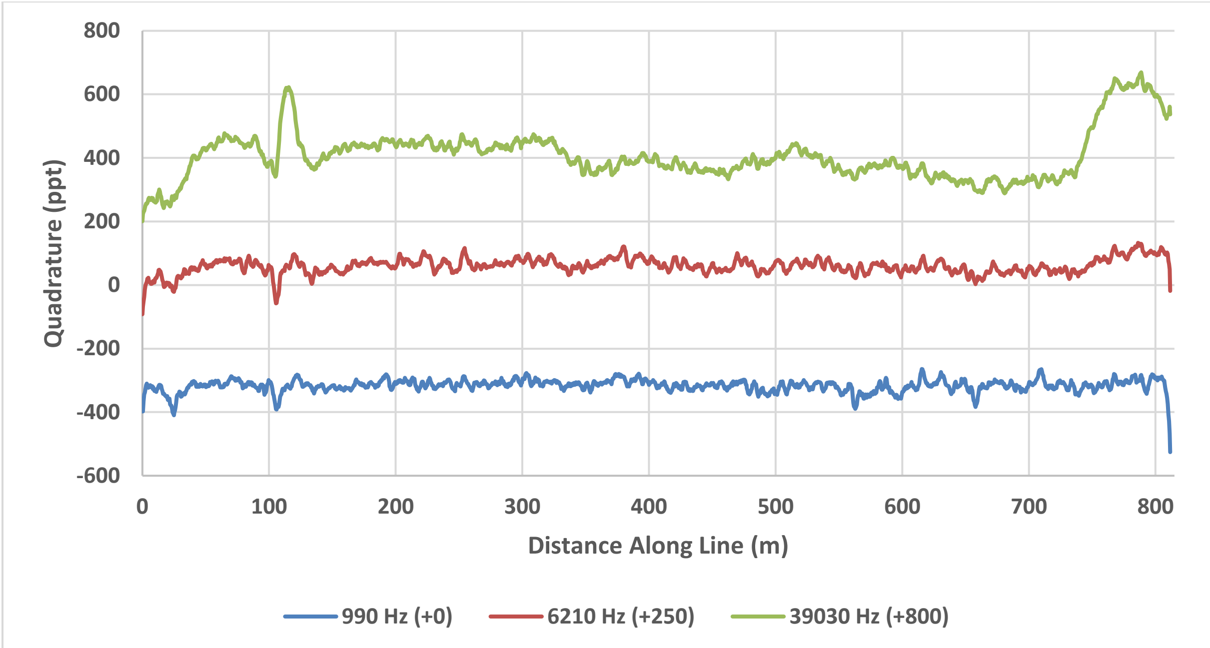

Figure 4.64: S-N profile GEM2 LINE00 displaying the quadrature component of $\vec{H}_s$ for three different operating frequencies. Offsets of +250 and +800 were applied to the 6210 Hz and 39030 Hz respectively to eliminate overlap in the data points.

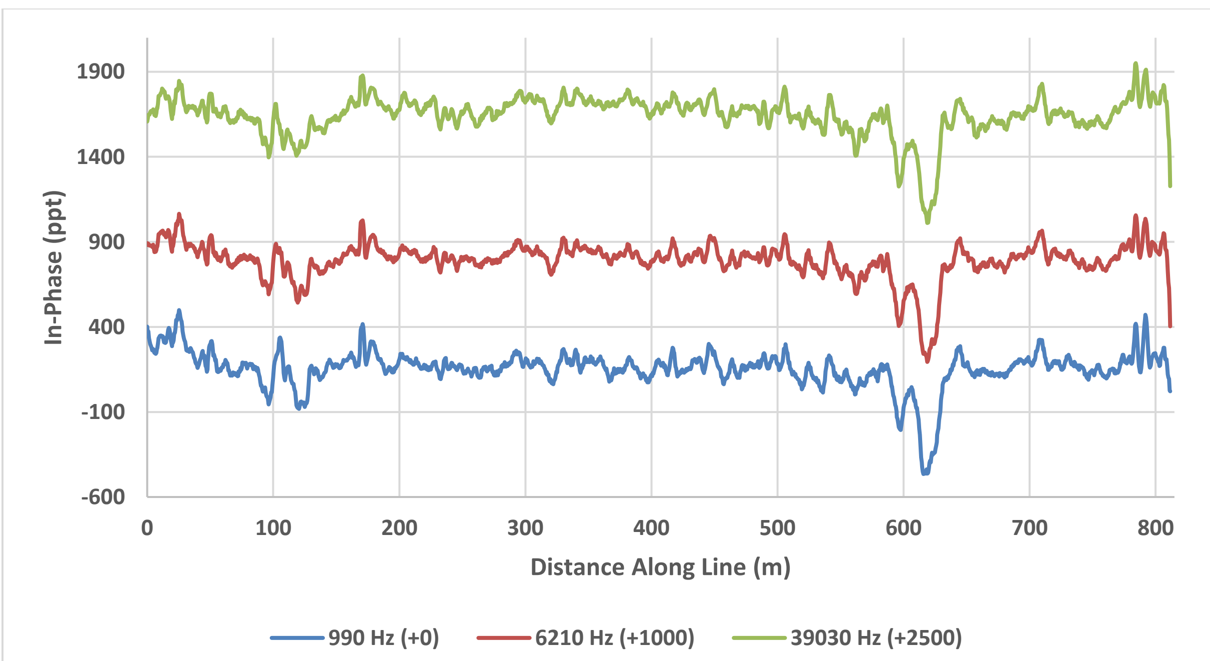

Figure 4.65: S-N profile GEM2 LINE00 displaying the in-phase component of $\vec{H}_s$ for three different operating frequencies. Offsets of +1000 and +2500 were applied to the 6210 Hz and 39030 Hz profile respectively to eliminate overlap in the data points.

approximately every 0.5 m. GEM2 LINE00 was collected approximately over EM LINE00.

There is good correspondence between the GEM2 39 kHz quadrature results (top, Figure 4.64) and the quadrature results of the 9.8 kHz EM31 (Figure 4.63). These include low conductivity at the southern end of the embankment, the conductive high over the spillway at station +115 m, more subtle variations over the seep region, and the conductivity high at the northern end of the embankment. For the lower frequencies (penetrating deeper and sampling a larger volume) these features are more muted, and lost in noise associated with the irregular motion of the boom during the walking survey.

Figure 4.65 displays the in-phase component of the GEM 2 data. The most distinct feature in these data is between stations 600 to 620 m, corresponding to the seepage region investigated by the July 2016 Northern GPR grid. This region is anomalous on the western (wetland) side of the embankment in GPR (Figure 4.33) and magnetics (Figure 4.13).

4.5.2 EM31 over the Reservoir, September 2016

On September 25th, 2016, an EM31 survey was carried out over the subaerial tailings themselves. The initial measurement was collected over the crest of the dam in the north near the abutment (several m east of the north end of LINE00, Figure 4.63) and the survey continued south towards the center of the reservoir. Figure 4.66 presents the profiles of apparent conductivity for two dipole orientations versus station distance. Measurements of apparent conductivity increase towards the center of the reservoir due to the increasing thickness of conductive sediment settling over the center of the reservoir. The values of σ_a

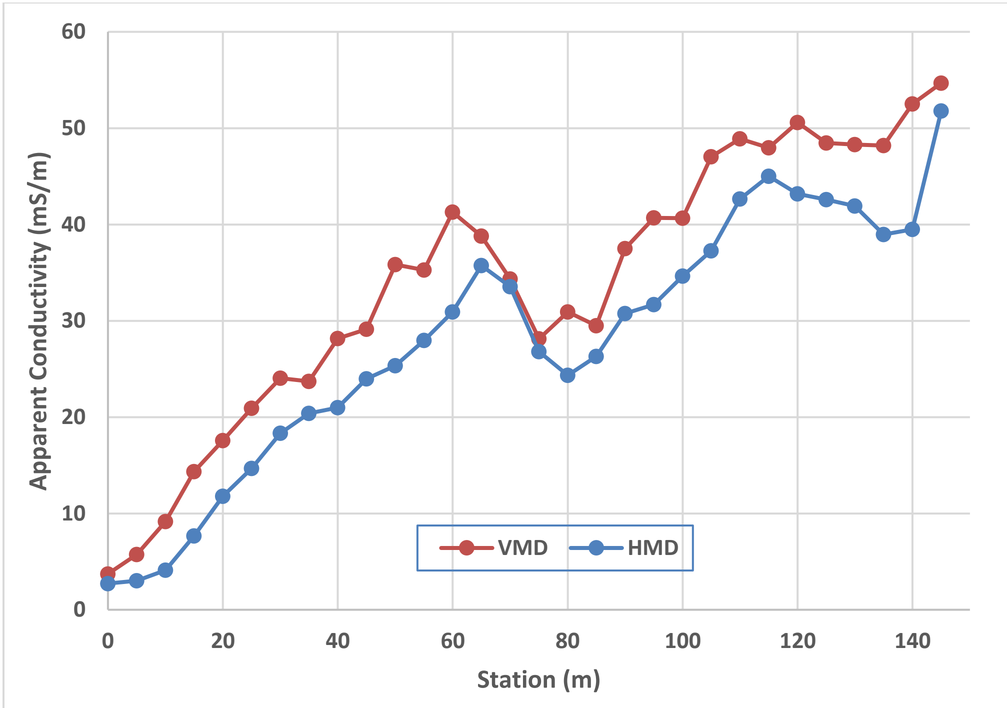

Figure 4.66: N-S profiles of the EM31 Quadrature component of $\vec{H}_s$ collected using VMD and HMD dipole orientations over the tailings reservoir.

measured over the reservoir are significantly higher than those measured over the embankment (Figure 4.63), and demonstrate the utility of the EM31-MK2 meter as a tool for delineating conductive tailings sediment/water. A dip in the trend over station +80 m is suspected to be the result of a change in the basal topography of the reservoir. The measurements recorded in the VMD orientation are higher than the HMD due to an increase in clay content and saturation of tailings with depth as indicated by test pit data. The data trend however remains consistent between dipole orientations.

4.5.3 EM31 June 2017 Seep Grid

Figure 4.67 and 4.68 display the Oasis Montaj VMD and HMD ground conductivity contour maps generated from EM31 data collected over the June 2017 GPR seep grid (Figure 4.45) using both VMD and HMD orientations at ground height. For consistency, all measurements of σ_a used in generating the contour map were collected using a W-E boom orientation with exception to YLINE00 and YLINE09. The maps indicate that σ_a is lowest over YLINE00 along the western edge of the dam crest (closest to the wetland) between the seep and the old stream, showing variations of less than 1 mS/m between stations. YLINE-10 of the June 2018 SP grid is located directly over YLINE00 between y=30 m and y=90 m and indicates no correlation between SP highs and the ground conductivity of the top 6 m of the dam wall. The conductivity is highest along the eastern edge of the dam closest to the tailings reservoir (YLINE09). The trend of high conductivity to the east resembles the trend of elevated reflection strength to the east over the reflection amplitude slice in Figure 4.51. It must also be kept in mind that currents induced in the tailings reservoir itself could contribute to the eastward increase in the apparent conductivity.

Figure 4.69 displays the profiles of ground conductivity collected along YLINE05 using two boom orientations. The HMD and VMD profiles of σ_aYLINE00, YLINE05, and YLINE09 are presented in Appendix A4.6. Comparison of the profiles indicate the ground is isotropic given the boom orientation has little effect on the value of σ_a. YLINE05, in the centre of the grid, is approximately coincident with LINE00 (section 4.5.1) and shows a

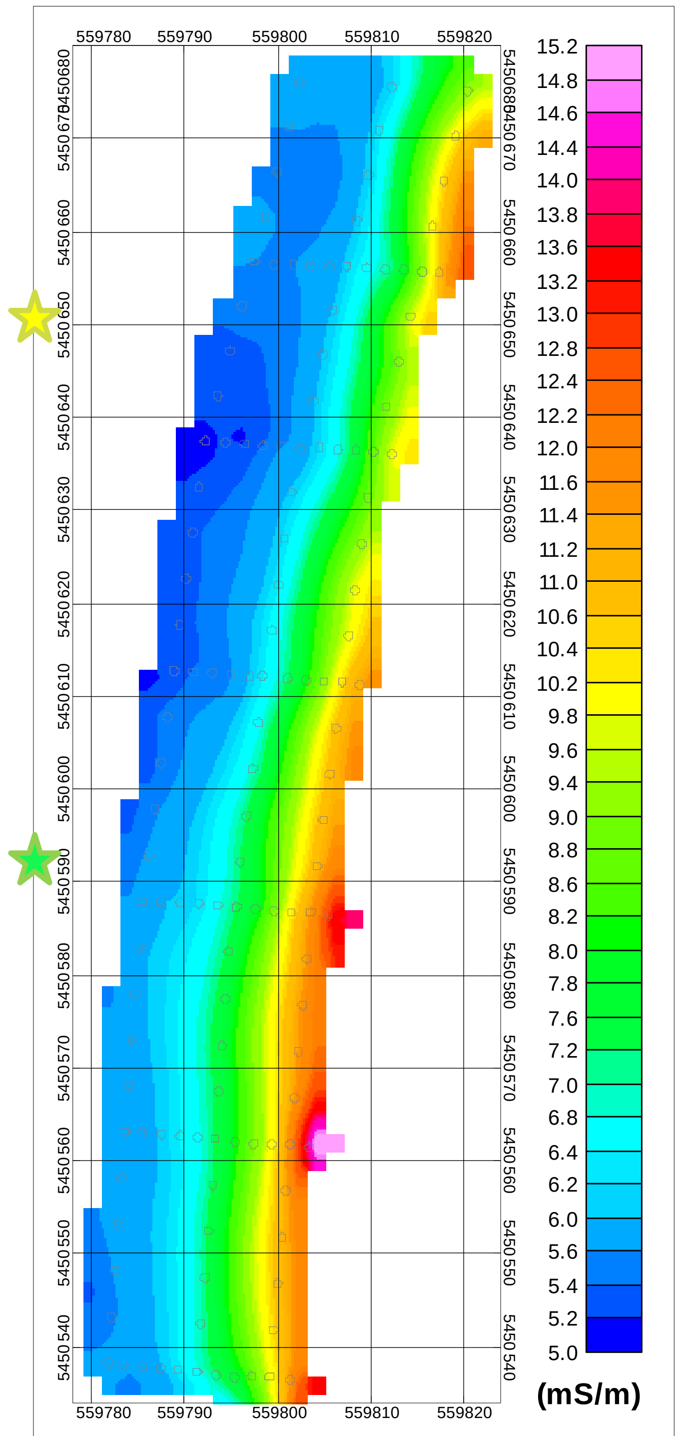

Figure 4.67: VMD Quad. phase apparent conductivity contour map over the June 2017 seep grid.

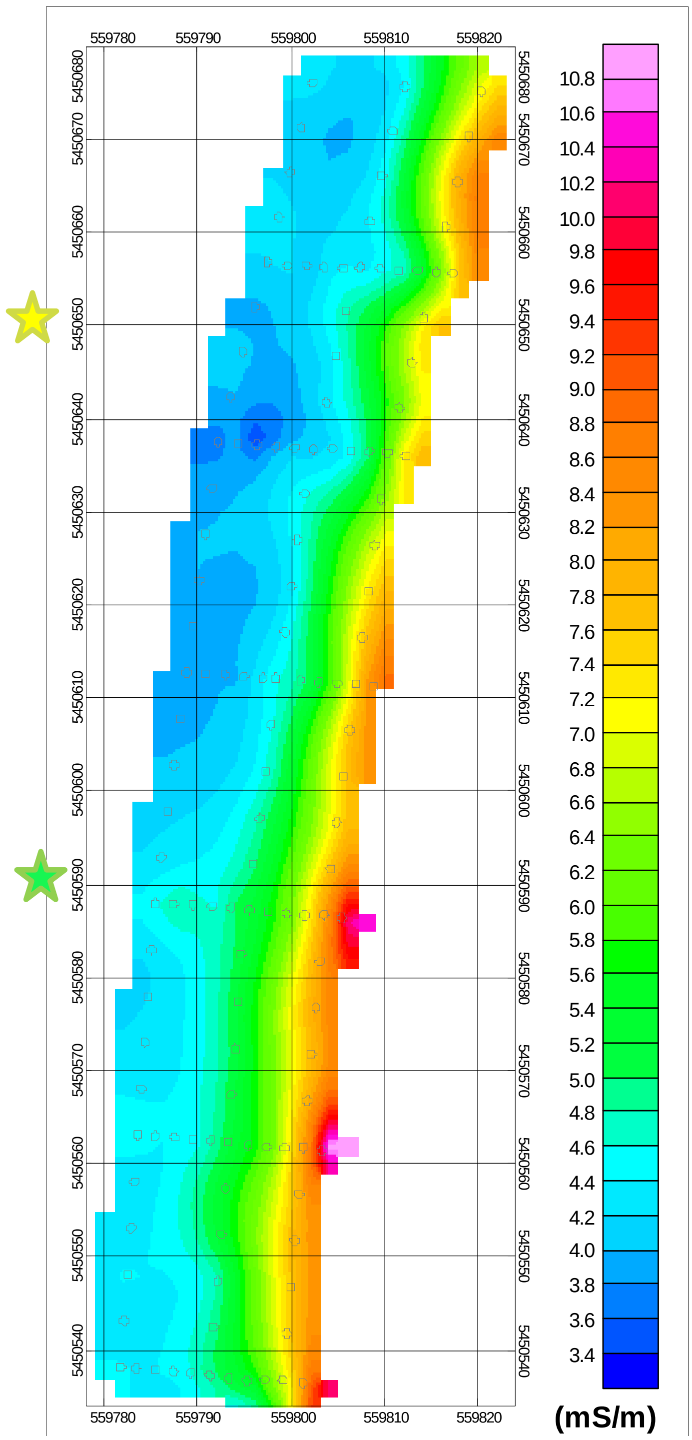

Figure 4.68: HMD Quad. phase apparent conductivity contour map over the June 2017 seep grid.

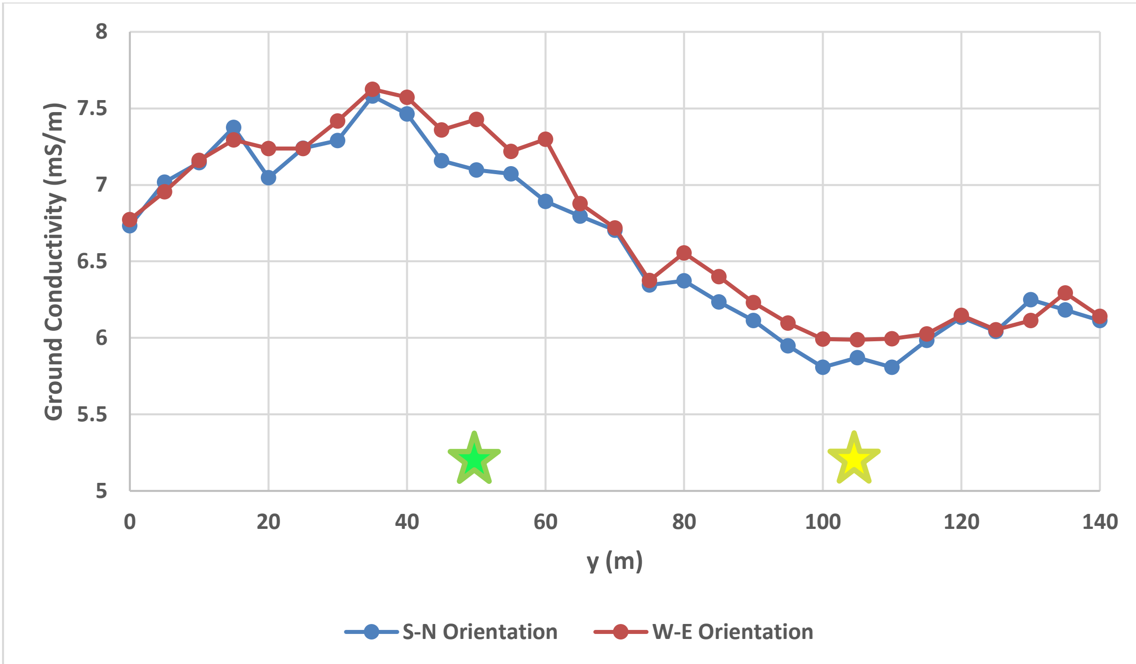

Figure 4.69: Profiles of σ_a versus station spacing over YLINE05 of the June 2017 seep grid collected S-N using the VMD orientation, with the boom aligned in two directions.

similar decrease in conductivity to the north, reaching a minimum over the old stream (yellow star). Apparent conductivity values are higher than for LINE00 because the instrument was at ground level over the grid. Profiles of σ_a versus station spacing along YLINE05 and YLINE09 exhibit a decreasing trend in σ_a over the old stream (yellow star). It is theorized the measured conductivity is lowest over the old stream as a result of conductive water being drawn down by the seep through erosion channel #2. The GPR profile of YLINE05 suggests the ground conductivity over the center of the dam may be influenced by the depth to the core, as the data trend of the EM31 profiles is similar in appearance to the depth to the core across the profile of GPR YLINE05. This decrease in conductivity is inferred to be influenced by the depth to the top of the core and the water

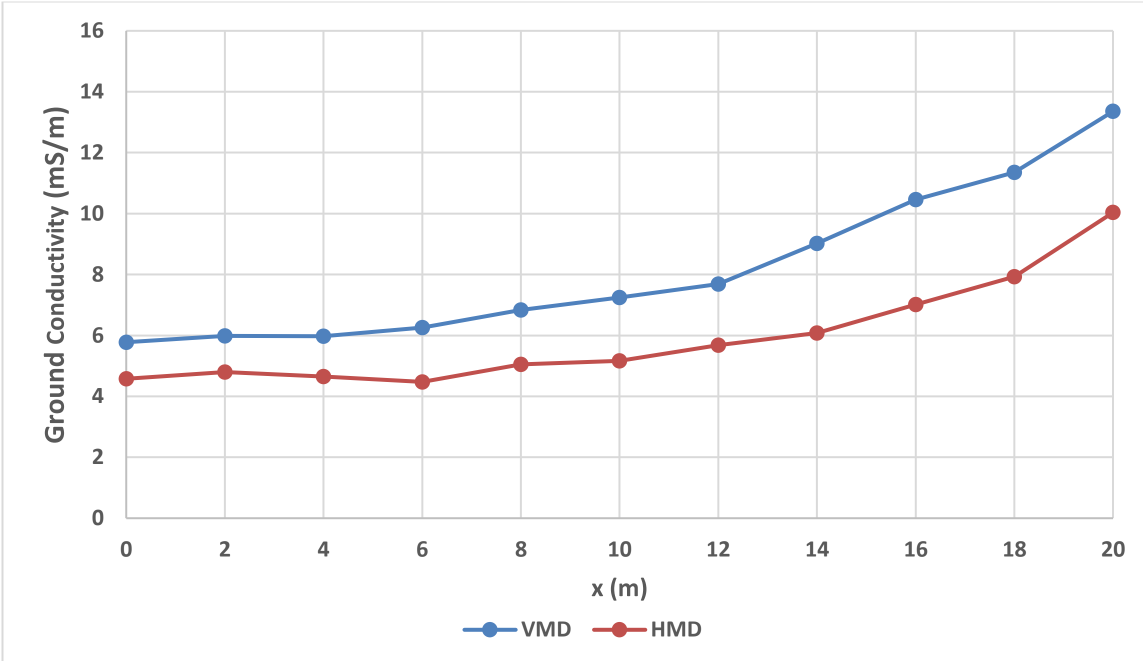

Figure 4.70: Profiles of σ_a versus station spacing over XLINE10 of the June 2017 seep grid collected W-E with the EM31-MK2 ground conductivity meter using VMD and HMD orientations aligned S-N.

table elevated in copper and zinc. Values of σ_a are higher to the east due to the rise in water table approaching the reservoir.

Figure 4.70 presents the W-E profiles of σ_a along XLINE10. All EM x-line profiles collected over the seep grid indicated the ground conductivity increased towards the reservoir. This is because tailings water from the reservoir containing conductive fines easily permeates through the coarse shell rocks east of the core flanking the upstream slope.

4.5.4 EM31 Wetland Survey Lines

A total of 6 survey lines were acquired in the wetland (Figure 4.62) over both the disturbed region downstream of the spillway and the undisturbed region containing some natural pools downstream of the dam. They are designated EM LINE01 – LINE05 E-W, and a survey line was carried out along the toe of the downstream slope (TDS). All were carried out at hip height using a S-N instrument boom, and most involved both VMD and HMD coil configurations (Table 3.4). Complete results are shown in Appendix A4.6. Figure 4.69 displays a contour map of all VMD measurements, and Figure 4.70 displays an elevation contour map over the wetland.. It is suspected that tailings sediment has settled within depressions in the wetland (i.e., anomalous regions of high conductivity are associated with topographic lows).

In Figure 4.71, σ_a is relatively low over the dam and elevated along the old stream impression. It is proposed this elevated σ_a is the result of conductive tailings sediment accumulating in the old stream bed. The old stream bed was capped during the initial placement of the dam, however GPR surveys collected above the old stream (section 4.4.4) indicate the core is damaged in this region, and such damage is often linked to unstable or eroded foundation materials. The eroded core in this area is cause for belief that the materials used to cap the old stream bed have loosened since the dam's operation, resulting in the flow of tailings water beneath the embankment and into the wetland along the old stream impression.

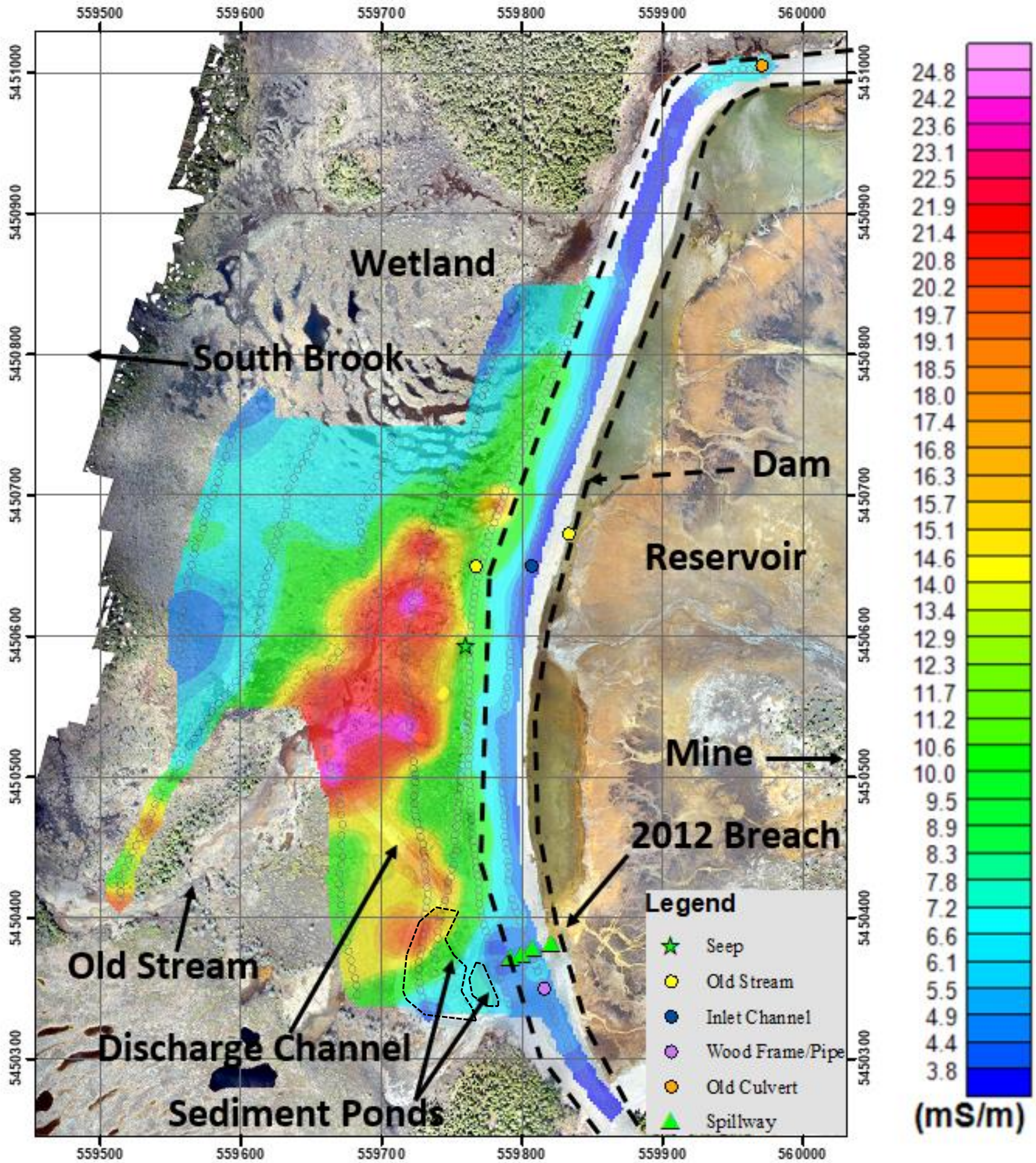

Figure 4.71: EM31 VMD ground-conductivity contour map over the Gullbridge embankment and wetland. All measurements were collected using a S-N boom orientation at hip-height.

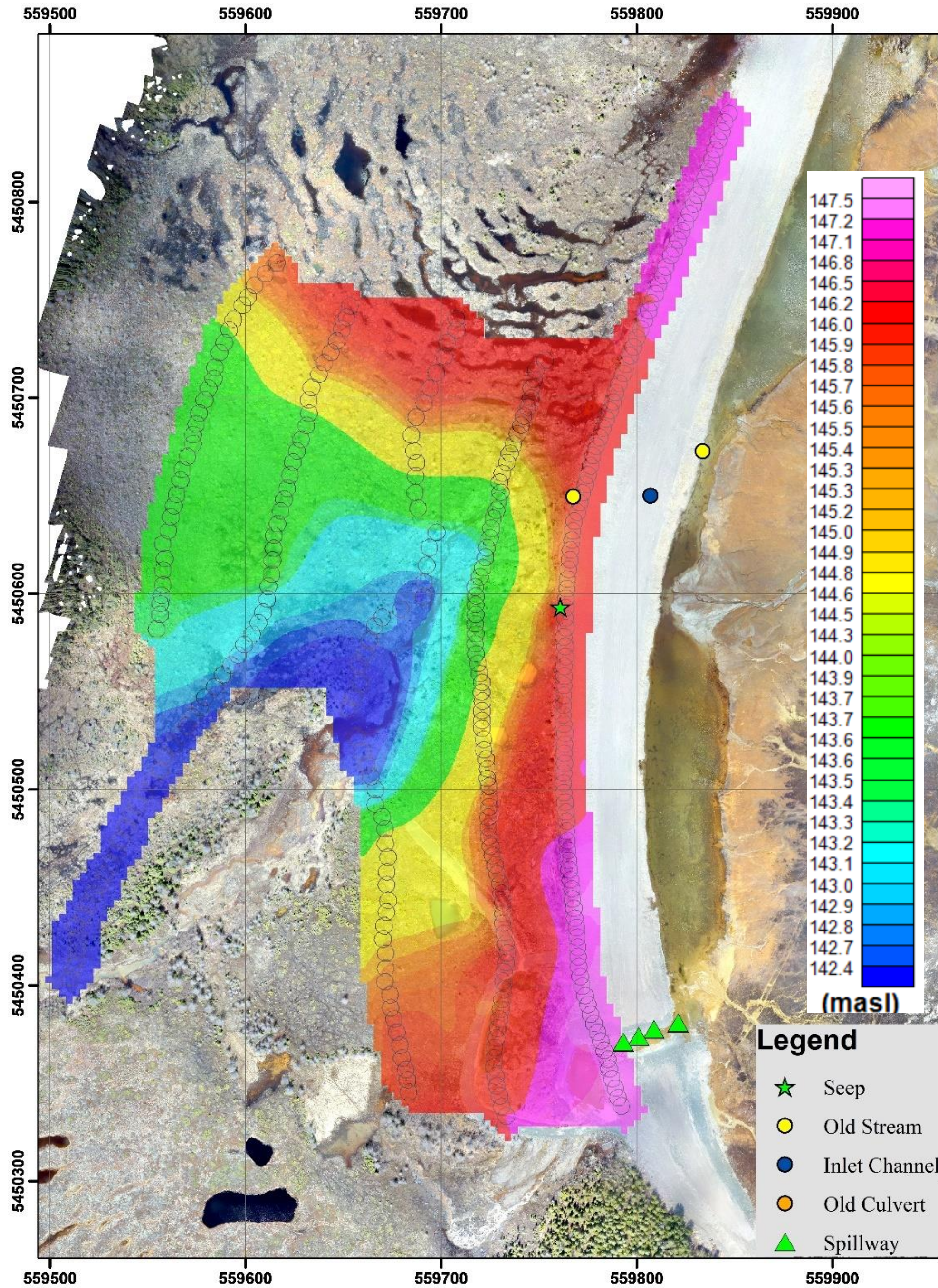

Figure 4.72: Elevation contour map over the wetland adjacent to the Gullbridge Tailings impoundment. This map was generated from elevation data over EM LINES01-05 E-W respectively.

Flow of tailings sediment into the wetland occurs primarily beneath the embankment along the old stream bed and along the discharge channel at the “outflow” location. During precipitation events, water discharging through the spillway enters the sediment ponds and is directed along the discharge channel and into the wetland north of the outflow location, where advancing tailings water eventually settles in the old stream impression. Secondary processes contributing to the increased volume of tailings sediment along the banks of the old stream include a combination of historic breaches and seepage. The degree to which this sedimentation occurs is likely proportional to the flow rate of water west of the embankment and the degree to which the wetland filters the tailings water. There is a general trend of decreasing conductivity to the west of the old stream impression.

EM LINE01 shows some of the lowest values of σ_a over the wetland, and indicates there are three regions of relatively high σ_a corresponding to the locations of the region along the toe of the downstream slope adjacent to the discharge channel north of the spillway, the observed seep (green star), and pooled tailings in a natural wetland depression near the embankment respectively.

LINE TDS (abbreviation for “Toe of Downstream Slope”) was conducted from south of sediment pond 2 to the base of the Gullbridge Dam. The region of high σ_a in the south was measured over sediment pond 2. As expected, the ground conductivity over this region is elevated due to consolidation of tailings sediment exiting the spillway. The ground conductivity decreases to the north until it reaches ~8 mS/m, corresponding to the values along EM LINE01 at similar locations along the bottom of the dam wall.

EM LINE02 shows an increase in ground conductivity west of EM LINE01. Measurements of σ_a in the south along stations located over sediment pond 2 were elevated in response to the accumulation of tailings along the discharge channel. There is a sharp increase in σ_a over the northwestern perimeter of sediment pond 2 (Northing ~ 5450390) followed by a sudden drop in σ_a marking the location the survey line traverses the limestone lined berm.

The ground conductivity along EM LINE02 steadily increases northward of the sediment ponds downstream of the spillway as the survey stations approach tailings water flow path emanating from the seep identified at the toe of the downstream slope (green star). The value of σ_a at Northing ~ 5450540 m is elevated due to the proximity of a depression containing pooled, discoloured water (Figure 4.62). The measured σ_a is particularly high over Northings ~5450620 and 5450660 corresponding to the old stream impression (yellow circle) and its north bank. The ground conductivity is relatively low north of the old stream, corresponding to the location where the survey line crosses a series of small freshwater ponds and streams occupying the wetland (Figure 4.62).

EM LINE03 was collected ~ 40 m west of EM LINE02. The survey line passes over the old stream bed between about Northings 545510 and 545540 where apparent conductivity values of ~22-23 mS/m are recorded. A region of pooled discoloured water is visible from the drone footage in Figure 4.62. The sharp increase in σ_a north of 545490 occurs at the “outflow” location where conductive tailings sediment is directed into the wetland along the discharge channel containing tailings in the sediment ponds to the east.

The ground conductivity reaches 25.4 mS/m at the outflow location, the highest measurement of σ_a recorded over the wetland. North of the stream bed, until about 5450585 where a low in apparent conductivity is encountered, the survey stations move progressively further west away from the old stream. Northward of this low, σ_a progressively increases as survey stations approach the old stream and is high and steady for several stations along the western edge of the old stream bed. Yet farther to the north there is a significant decrease in σ_a as survey stations move further away from the old stream into an area of the wetland concentrated in natural ponds and streams that aid in the passive treatment of potential tailings concentrated water.

The measured σ_a over EM LINE04 along the southern section of the line is elevated due to the proximity of the survey stations to the old stream bed transporting tailings sediment southwest through the wetland. North of the old stream σ_a decreases to moderate values between 7 and 8 mS/m indicating the majority of elevated σ_a measurements are confined to the old stream. The measured σ_a over EM LINE05 is low, varying from the values over the northern portion of EM LINE04 to values measured over the embankment. This suggests the groundwater in the wetland is diluted west of the old stream due to passive wetland mitigation processes.

4.6 Bog and Water Sample Analysis

4.6.1 Water Samples

In July 2018, water samples were collected at the seep, which was actively flowing at a rate of 6.4 litres/minute at the time, and in the tailings reservoir on the other side of the embankment. Table 4.3 presents the results of the ICP-MS analysis of these water samples (Allen, 2018), a second seep water sample collected in 2016 by DNR (Maxxam, 2016), Sample SW-01, which was collected by AMEC in the reservoir in July 2013, and the corresponding Schedule A concentrations. The details of how DNR sampled the seep water were not disclosed.

Values listed as $<$DL correspond to elements whose concentrations were below the detection limit of the chemical analysis. All physical parameters tested were in compliance with NL Schedule A regulations for storage of surface water, with exception to the measured pH and the concentration of copper (Cu).

Table 4.3 indicates there is no significant change in the measured conductivity between the seep and the tailings pond samples collected in 2018. In September 2016, a ground conductivity measurement of ~ 55 mS/m was collected over the reservoir at the station closest to the center of the tailings pond in Figure 4.64, the conductivity of the seep water in November 2016 was 57 mS/m. It should be noted that the increased copper concentration contributes to the elevated conductivity of the water samples. However, it is suggested in Table 4.3 this increased conductivity is primarily influenced by the increased

Table 4.3: Elemental concentrations (μg/L≈ppb), pH and conductivity (mS/m) of reservoir surface water and seep samples. The concentrations provided for the 2018 samples are the average of two measurements. The range reflects the difference between the two measurements.

Elements	Tailings Pond 2018	Tailings Pond SW-01 July 2013	Seep 2018	Seep 2016	Schedule A
As	0.210 ±0.032	<1.0	0.136	<DL	<500
Al	7,636 ± 165	N/A	703 ± 0	15,000	N/A
Ba	51.5 ± 2.1	44.9	29.7 ± 0.8	37	<5000
B	6.67 ± 0.28	<50	7.23 ±0.82	<DL	<5000
Cd	0.867 ± 0.033	0.314	1.42 ± 0.03	1.3	<50
Cr	<DL	<1.0	<DL	<DL	<50
Cu	984 ± 36	706	393 ± 4	1,800	<300
Fe	2,448 ± 36	200	<DL	300	<10,000
Pb	2.59 ± 0.13	<0.50	3.08 ± 0.01	<DL	<200
Ni	178 ± 7	79.8	83.8 ± 0.8	290	<500
Se	<DL	<1.0	<DL	<DL	<10
Ag	<DL	<0.10	<DL	N/A	<50
Zn	145 ± 4	73.7	86.7 ± 0.1	270	<500
pH	3.79	4.34	4.28	4.35	5.5-9
Conductivity	35.1 ± 0.4	34	35.1 ± 0.5	57	N/A

is the result of the elevated acidity in the pond increasing the solubility of iron. The pond water is more acidic than recorded in 2013, likely as a result of acid generation due to decreasing pond water cover. The conductivity in the reservoir has not changed since July 2013. The high conductivity is expected to correlate with elevated copper and iron concentrations in the tailings pond.

Table 4.3 indicates there have been significant improvements in the water quality at the seep between November 2016 and July 2018. This includes a major decrease in the concentration of aluminum, copper, iron, nickel, and zinc. The concentrations of all elements have decreased since November 2016 with exception to B, Cd and Pb. The concentrations of Al, Cu, Ni and Zn were higher in water emanating from the seep in November 2016 than the pond water in 2018.

The analysis of the July 2018 seep and tailings pond samples in Table 4.3 indicates that the tailings water emanating from the seep is sieved as it passes through the dam wall, as generally the concentration of all elements measured decreases at the seep location with exception to boron and lead. At the time of sampling there was a 90%, 60% and 40% decrease in the concentration of Al, Cu and Zn through the dam, respectively. Also, the concentration of Fe decreased from 2448 ppb to below the detection limit.

The results in Table 4.3 show an increase in pH through the dam wall to the seep location. The decreasing acidity between the impoundment and the seep indicates materials within the dam wall buffer the tailings seepage. As previously mentioned, limestone gravel was added to the spillway to neutralize potential acid-drainage. It is possible other areas of the dam wall contain small amounts of limestone gravel used in repair work. Alternatively, it may be due to the effect of dilution by meteoric water infiltrating the berm. The pH was approximately the same between 2016 and 2018.

4.6.2 Properties of Bog Samples

The locations of the bog probe sites are indicated in Figure 4.62 by the red star (bog site #1) and yellow star (bog site #2).

Tables A4.7.1 and A4.7.2 in the Appendices present the water content and geochemical analyses of bog soil collected at GB-1 and GB-2 at various depth intervals within the wetland adjacent to the Gullbridge Tailings Dam (Memorial Univerity Department of Earth Science, 2018). Bog Site #1 (GB-1) was approximately 20 m downstream of the observed seep, in a region of high conductivity and Bog Site #2 (GB-2) was roughly 200 m west of the Gullbridge Dam over a conductivity low. The calculated water content and LOI (loss on ignition) of the samples are shown in Figure 4.73 (a). The LOI indicates the organic matter content, which is volatilized in the preparation stages to the geochemical analysis. The high water and organic contents in GB-1 (dots) and the top section of GB-2 (triangles) are typical of wetlands in the summer months. The higher water content of the top measurement of GB-2 is likely due to the higher concentration of ponds and streams that occupy the region nearest South Brook. The lower measurement of GB-2, with much reduced organic content, is consistent with the bog corer reaching the bottom of the bog and sampling underlying wet soil.

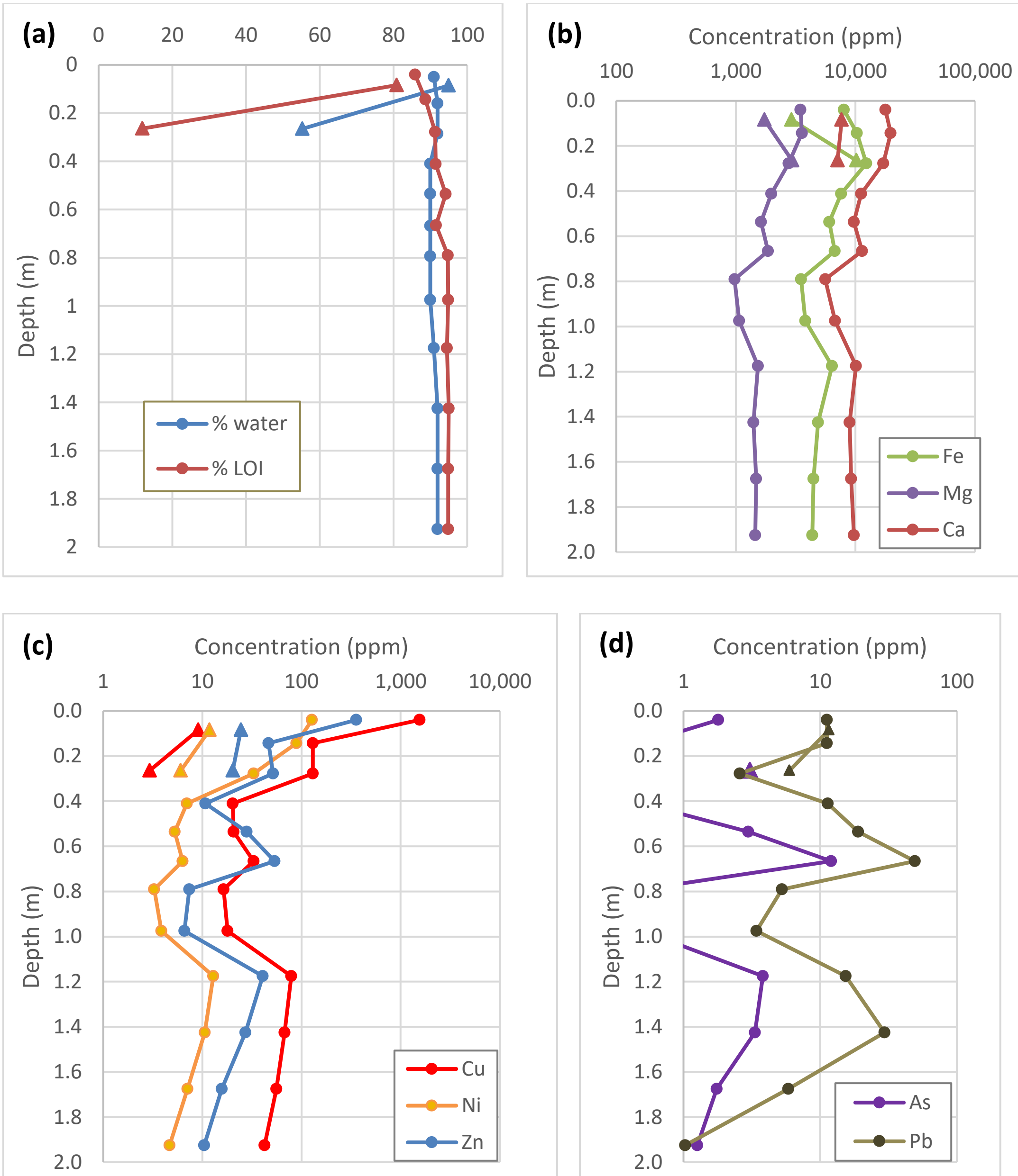

Figure 4.73: Profiles of concentrations versus core depths at bog site locations GB-01 (dots) and GB-02 (triangles). (a) Water and LOI contents, (b) Lithic elements, (c) Tailings elements, (d) Additional elements associated with tailings. LOI and element concentrations generated from OES analysis. Detection limits in (b) are 100 ppm, and in (c) and (d) are 1 ppm. Note that 10,000 ppm is 1 wt%.

The concentration of lithic elements (Figure 4.73 (b), basically indicating silicate soil) is generally low, reflecting the high organic content of the bog. It is higher in the top 0.7 m of GB-1, possibly as a result of higher sediment inflow following the mining activity. The concentrations of these elements are lower in the top most sections. It is possible this is due to cultivation of peat moss over small amounts of debris not recovered in the wetland following the December 2012 breach.

As expected, the lower section of GB-2 (triangles) shows higher lithic concentrations than the top.

The profiles of elements associated with the tailings (Figure 4.73 (c)) for GB-1 show a major decrease between the surface sample and a depth of 0.4 m, by a factor of 70 in the case of copper. The shallowest measurement, of the top 4 cm of bog in GB-1 near the seep, was particularly highly concentrated in copper. The concentration of copper over GB-1 plummets with depth, indicating the leachate does not easily penetrate the wetland bog. The concentration of zinc and nickel follows the same general trend with depth. The significant decrease in these metals in the bog at GB-2 is evidence to support the debris flow path is contained to the east of the old stream impression and/or the wetland is passively filtering advancing tailings water.

Figure 4.73 (d) presents the concentration of arsenic and lead versus sample depth. These elements show similar patterns, with peaks near the surface and at a depth of about 0.7 m. The lower peak is also seen, to a lesser degree, in panels (b) and (c). It is not uncommon for impoundments such as Gullbridge to release arsenic from stored tailings as a result of oxidation of sulfide minerals (Lim et al., 2009).

5 Summary and Discussion

The Gullbridge Tailings Facility (Figure 5.1) was designed to store sub-aqueous mining waste generated from the milling of copper-zinc ore excavated from one of the many pyritic VMS ore deposits occupying volcanic host-rocks of the Buchans-Roberts Arm Belt. The Gullbridge deposit was first discovered in 1905, and the mine was opened in 1967 (Rennie, 1998).

It is suspected that the Gullbridge Dam is a rolled-earth dam, that is, it was built up, in compacted layers of earth, around a more impermeable ‘core’. Borehole data from 2013 indicate the dam material is primarily composed of loose to compact sand and gravel with varying amounts of silt, and that the internal core has a similar composition with a relatively higher volume of poorly compacted fines. There are no design, modification, or repair records available for the Gullbridge Dam between the closure of the mine in 1971 and 1996 when a decant structure was washed out and subsequently repaired.

In December 2012, a section of dam collapsed**,** releasing an estimated 500 m^3 of solid Cu-Zn tailings into the adjacent wetland. The collapse was likely triggered by an unstable foundation and internal erosion of the dam resulting from seepage of water through the embankment.

Major repair and modifications to the dam in 2013 included the installment of a fordable, armoured spillway, lowering of the dam crest by between 1 and 2 m, and flattening of the downstream slope. The embankment is now approximately 1,050 m long,

Figure 5.1: Aerial view of the Gullbridge Tailings Facility with main features of the impoundment indicated. Key: (1) Reservoir; (2) Tailings Pond Surface Stream; (3) Dam; (4) Northern Seep; (5) Wetland; (6) Old Streambed; (7) Main Seep; (8) Approximate location of Inlet Channel; (9) Spillway/2012 Breach; (10) Sediment Pond 1; (11) Sediment Pond 2; (12) Approximate location of crack observed on downstream slope in 2011 by Stantec; (13) Armoured Discharge Channel

between ~2.6-10.2 m tall, with a width at the crest varying from 8 m in the north to 30 m in the south (AMEC, 2014). Water exits the reservoir via the armoured spillway before flowing through two sedimentation ponds and an armored discharge channel into the wetland (Figure 5.1).

Water was observed emanating from beneath the dam into the wetland at the “main seep” (location (7) in Figure 5.1) during all site visits conducted between 2016 and 2018. Immediately to the east of this seep, water flowing from a stream over the tailings (marked (2) in Figure 5.1) is discharged against the upstream slope.

Orange discoloured tailings water was observed flowing from the base of the dam at a second site in the north (marked (4) in Figure 5.1) and was designated the “northern seep” region. Based on previous geotechnical assesments and interpretation of geophysical data acquired over the course of this research, the embankment in this location is suspected to contain a historic decant structure that was decommissioned following the installation of twin-culverts sometime after 1996. The twin-culverts were located near the historic decant structure, and are suspected to have been removed during Winter 2013 rehabilitation work.

In air photos and during site visits, water was observed collecting in an old streambed running E-W beneath the embankment (location (6) in Figure 5.1). It is plausible that materials used to cap the streambed during the installment of the dam have weakened, resulting in small scale leakage of tailings water here.

As part of an ongoing dam monitoring study, several different geophysical techniques were used to survey the Gullbridge tailings dam and adjacent wetland, with the objectives of characterizing the dams internal structure– particularly in locations of leakage and potential failure – and mapping areas of tailings concentration in the wetland. Information from previous technical reports, provided by NLDNR, was of value in this project. The geophysical techniques used were self-potential (SP), magnetics, direct current resistivity (DCR), ground penetrating radar (GPR), and ground conductivity (EM31 and GEM2). A summary of the surveys is provided in Table 3.2.

SP surveys proved to be an effective tool at delineating fluid flow through the Gullbridge Dam near two regions associated with seepage. SP data was collected over two parallel lines along the top of the dam. In general, values of SP were more irregular and positive nearer the reservoir. This is attributed to increased seepage on the upstream side of the dam. SP surveys were also conducted on a grid centered over the main seep area, and this assisted in delineating regions of seepage.

Magnetics surveys conducted along the embankment assisted in identifying the structure, location, and orientation of an "inlet channel" whose origins are not well documented but is proposed by Stantec to have been installed during the initial phases of the dam construction and served as a decant to allow for water to flow freely beneath the embankment without eroding the dam fill materials. This research suggests the inlet channel which may play an important role in the development of the main seep.

All DCR surveys over the Gullbridge Dam showed the resistivity decreases with depth. The main factor influencing this phenomenon is the increase in tailings water concentrated in dissolved ions below the water table.

GPR surveys assisted in locating and identifying major interfaces (e.g., water table, core, dam base) and internal erosion within the dam wall. GPR data collected along the embankment assisted in locating several buried utilities, including a wooden frame in the south and the decant system used prior to the installment of the twin-culverts, as well as the suspected buried utility in the north. GPR data was also collected in grids over the northern seep region, and the main seep.

Electromagnetic ground conductivity surveys were deployed with the objective of mapping regions of elevated conductivity associated with increased concentrations of copper and zinc. A survey over the reservoir showed conductivity was greatest where the volume of tailings sediment is thickest.

Northern seep area

The most compelling evidence to suggest seepage through the dam wall in the region underlying the Northern grid is the attenuation of the GPR signal at shallow depths under the downstream part of the embankment. It is plausible that conductive tailings water is flowing through loosely compacted regions of the core to a location halfway across the dam, where it spreads out into the downstream part of the embankment along the drainage blanket and towards an unprotected exit where seepage was observed at the downstream toe in July 2016. The regions of limited penetration depth correspond to the locations of high and rapid spatial changes in SP measurements (Figures 4.2 and 4.3). GPR data indicated that the water table is approximately 2 m lower relative to the top of the dam than it was in 2011.

Main Seep Area

Figure 5.2 presents a S-N cross-section over the center of the dam over the main seep compiled from magnetic, DCR, GPR and borehole data. It is suspected the physical properties of the dam have been altered over this region as a result of pervasive seepage related erosion. Based on information from BH3, approximately 1.5 m of the dam crest was excavated here. The phreatic surface was delineated from Schlumberger VES modelling and in GPR profiles generally observed as a strong, shallow, continuous sub-horizontal reflector. The main distinction between the core and the overlying lower unit is an increase in the volume of fines. Within some regions of the core, a large volume of these fines have been washed away (i.e., internally eroded) as a result of prolonged seepage. This has subsequently loosened the core resulting in the flow of reservoir water through narrow seepage pathways. This is the mechanism believed to be responsible for the relatively loose nature of the core materials. The thin section of core between y=65 m and y=85 m accommodates sufficient pore space for the flow of reservoir water through the embankment to the observed seepage location at the base of the downstream slope. Water may be actively flowing beneath the dam along the old streambed, where the underlying foundation has been eroded.

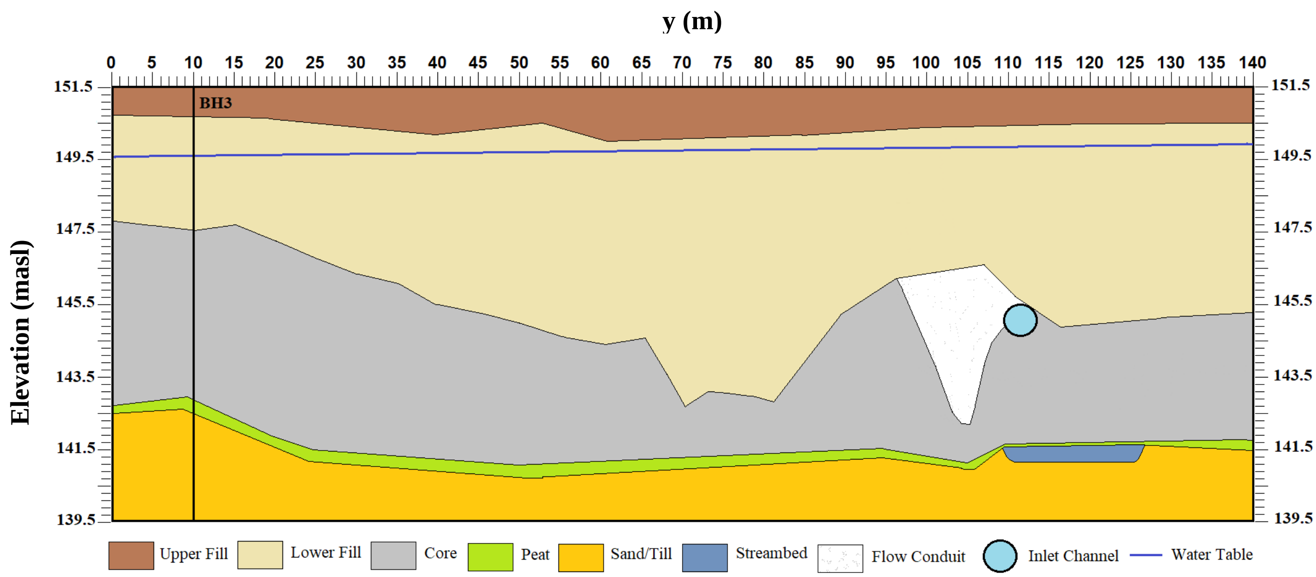

Figure 5.2: S-N section over YLINE05 of the June 2017 seep grid conducted over the main seep area of the Gullbridge Dam. BH3 indicates the location of borehole 3, drilled in 2011.

It is suspected water is still actively flowing through the inlet channel and the loose core materials surrounding it, resulting in a large flow conduit (erosion channel #2). The inlet channel was probably installed during the initial phases of the dam construction and served as a decant to allow for water to flow freely beneath the embankment without eroding the dam fill materials. Magnetics data indicate a shallow magnetized source dipping to the west close the location of the SP anomalies seen in the SP profiles along the embankment . The inlet channel is presumably supported by a metal casing, which is generating the strong magnetic anomalies characteristic of ferromagnetic materials in the vicinity. The anomalous SP high "spikes" located over L1+385 m and L2+400 m could be the response to "streaming potentials" associated with seepage related erosion through the inlet channel. An alternative possibility is that the SP response is generated by corrosion of the steel casing.

GPR data suggest a series of 3 erosion channels where the core is anomalously deep is responsible for small-scale leakage through the embankment. These seepage pathways extend E-W through the dam wall and widen to the west through loose and eroded sections of the core surrounding the inlet channel. This loose section of core is particularly vulnerable to seepage related erosion, which is interpreted to be the primary factor influencing the disintegration of the core in this area. The Wenner DCR survey encountered a series of resistivity highs at surface locations corresponding to the positions overlying the suspected erosion channels. These resistivity highs are inferred to be associated with a drawing down of the water table and consequently increased air within pore spaces, related to loosening of the core materials. Active flow through the inlet channel will further escalate the vulnerability of the surrounding fill material to seepage related erosion. A prominent SP peak corresponds to a surface position overlying erosion channel #1 underlying y=80 m in Figure 5.2.

Figure 5.3 presents a plan view map of the suspected seepage flow path through the Gullbridge Dam compiled primarily from SP and GPR data obtained over the main seep area. It is evident that seepage is occurring through the dam wall as it can be observed emanating from the mouth of the drainage system at the toe of the downstream slope in the wetland. One of the aims of this research is to delineate seepage flow paths in the event maintenance and repair to the structure is required. It is suspected one of the major factors influencing seepage in this area is water flowing from the mouth of a stream that has been carved through the reservoir denoted as the “tailings stream outflow” in Figure 5.3. Precipitation events resulting in increased flow of water through the tailings stream

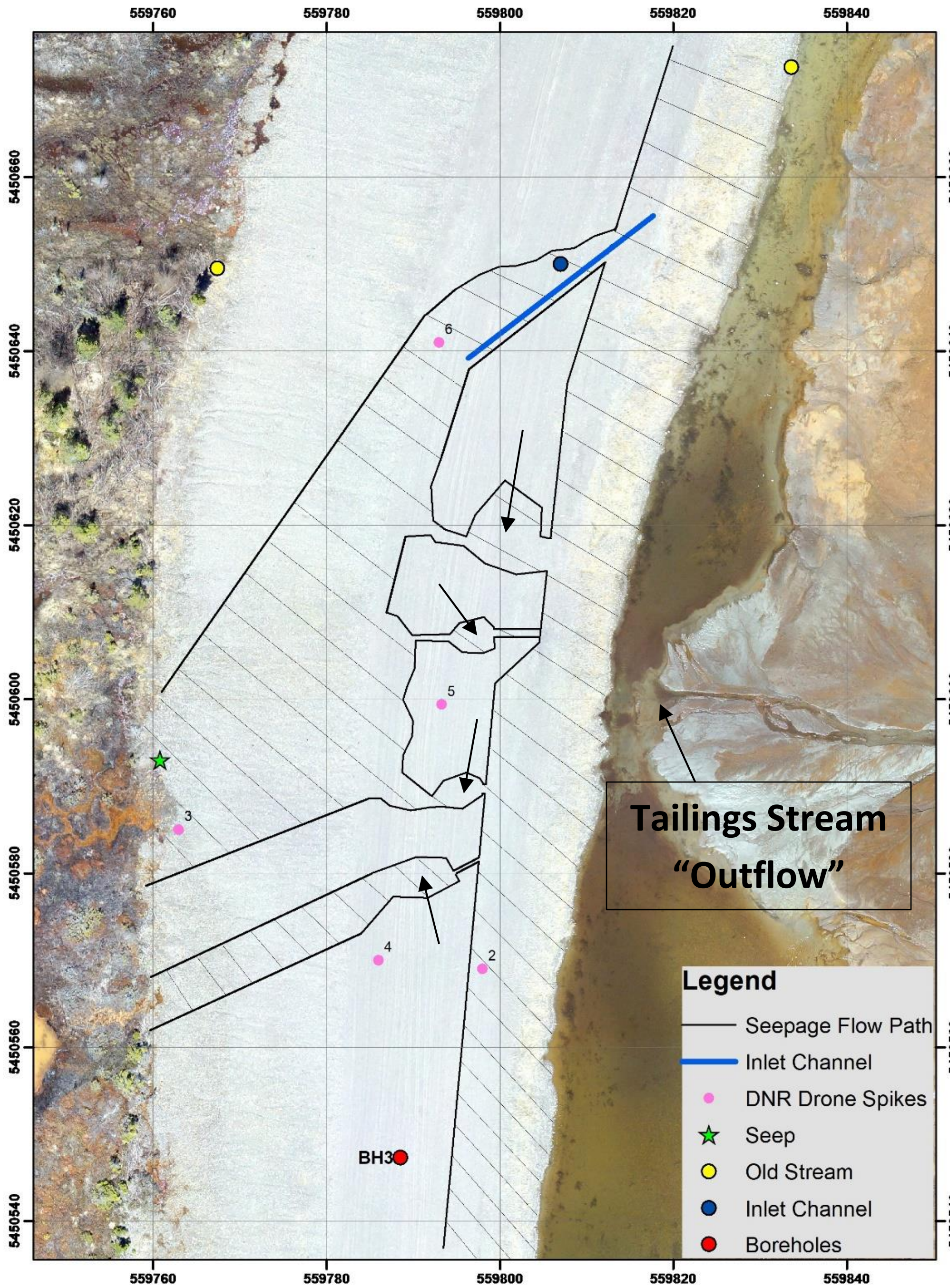

Figure 5.3: Delineation of suspected seepage flow paths compiled from SP and GPR surveys conducted over the main seep area. The area within the seepage flow path (black lines) is accentuated using a cross-hatching pattern for visual aid.

increases the risk for seepage related erosion on a small-scale. The progressive seepage through the dam wall in this region has resulted in the gradual wash out of fine sediment and an increase in the pore space of the core. These loose sections of core provide sufficient space for water to pool, referred to as "developing stages of seepage". Given the elevated reflection strength of the core interface in the GPR profiles here, it is possible reservoir water containing conductive tailings water has pooled within loose regions of the core. In Figure 5.3, there are 4 suspected seepage development stage zones indicated by the arrows. We suggest the contributory flow paths feeding the seepage development zones are narrow feeder conduits emanating from the reservoir through loose sections of coarse shell rocks lining the upstream slope. Given the significantly higher SP measured along the dam crest nearest the reservoir combined with the enhanced reflectivity along the upstream slope, water has likely invaded the pore space underlying the eastern perimeter of the dam crest. This occurs as shallow as 2.0- 2.5 m along the dam crest straddling the upstream slope.

This analysis suggests that the inlet channel serves as the main flow path for tailings water emanating from the reservoir to the base of the downstream slope at the observed seep location. In a study conducted by *Adamo et al.* 2020 regarding seepage through conduits, the authors state "Similarly, such paths may develop along the contact surfaces of conduits installed under dams as outlet structures due to the low degree of compaction as a result of narrow trench dimensions". In Figure 5.3 the location and orientation of the inlet channel (blue line) was delineated from sharp SP highs over SP Line 1 and 2. It is suspected that water has been discharging through the inlet channel since its installation. In Figure 5.3, the inlet channel is oriented NE-SW and directed towards the observed seepage at the base of the downstream slope observed as orange-discoloured water. It is suspected water also flows beneath the dam along the old stream where foundation materials have become unstable, contributing to the seepage in the region to a lesser degree. However, this cannot be validated by the limited geophysical data.

GPR survey lines collected W-E over the dam crest in the main seep region provided insight into the construction process required to raise the dam to accommodate increasing tailings volume in the reservoir. The downstream construction method was carried out by installing benches into the existing structure on the downstream side every 2 m until the desired height of the dam crest was reached. Each time the dam was extended, material was subsequently cast onto the downstream slope. When the dam was flattened during rehabilitation work in winter 2013, material excavated from the crest was used to extend and reshape the upstream slope (AMEC, 2014) covering tailings sediment adhered to the surface of the dam fill. This was characterized by elevated reflection strength in the vicinity of the upstream slope.

Figure 5.4 displays the location of an elevation profile collected across the main seep area. The profile begins in the wetland near the area of observed seepage. This elevation profile was used to construct a W-E cross-section of the dam. There was a total change in elevation of 6.3 masl over the survey line.

Figure 5.5 presents a cross-section through the Gullbridge Dam of the subsurface region underlying the elevation profile plotted in Figure 5.4 constructed from GPR data. The red boundary lining the downstream slope indicates shell rocks of unknown thickness.

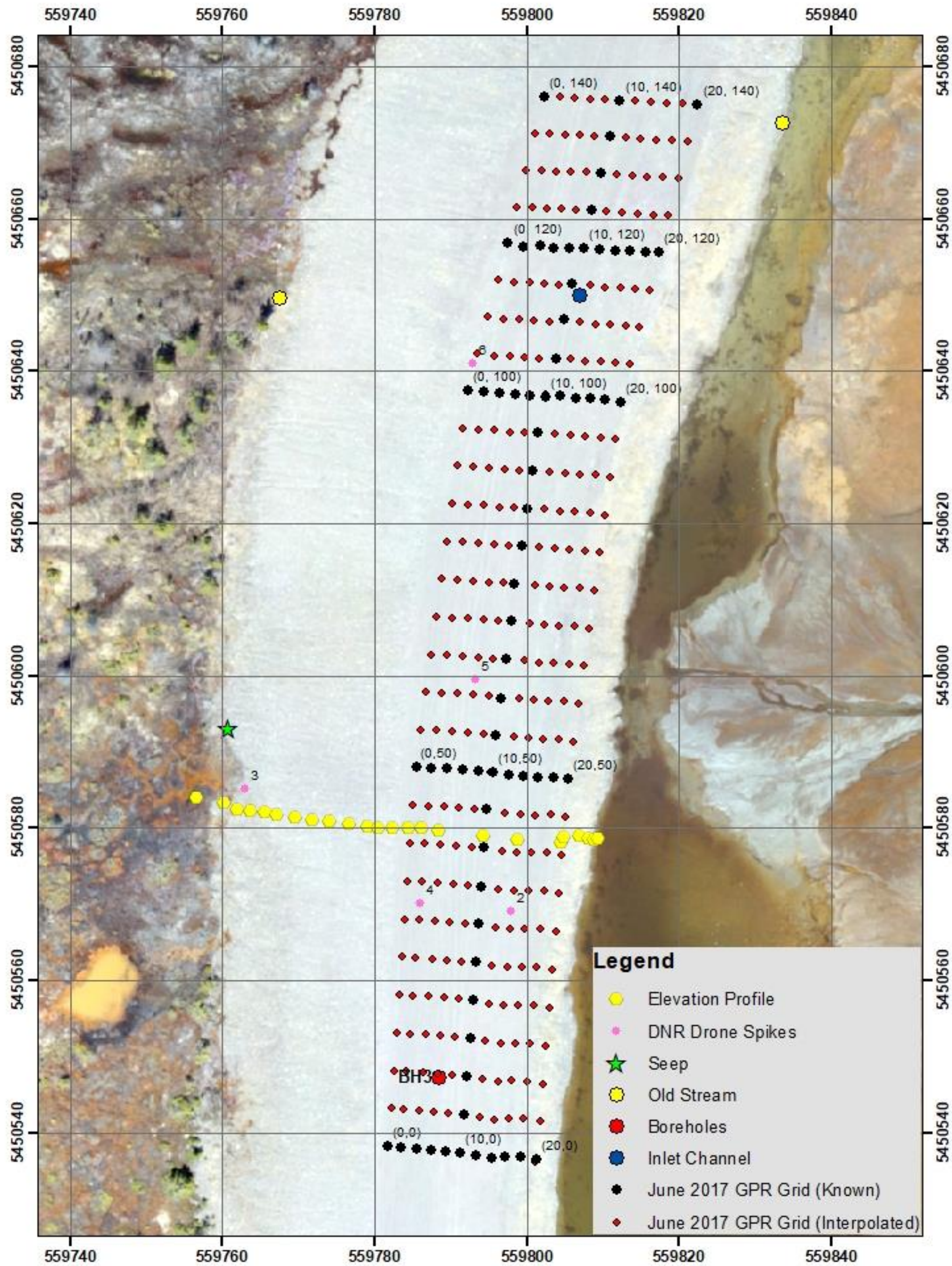

Figure 5.4: Coordinates of an elevation profile collected W-E across the Gullbridge Dam starting in the wetland at the toe of the downstream slope, and crossing near XLINE08 of the June 2017 GPR seep grid.

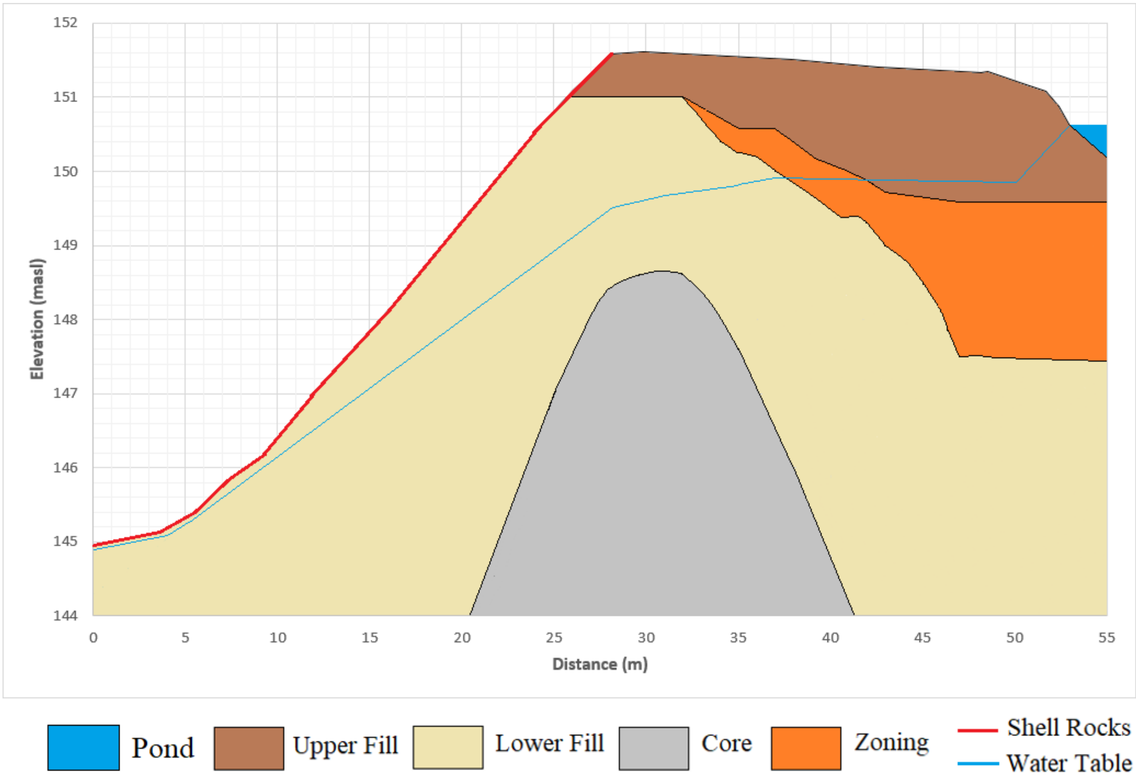

Figure 5.5: W-E cross-section of the Gullbridge Dam over the elevation profile indicated in Figure 5.4. Note that there is no water cover east of the survey line in Figure 5.4.

The blue line presents the depth to the water table, which indicates a hydraulic gradient to the west which is controlled by the drainage blanket. The Gullbridge Dam was originally constructed as a core dam, and during dam raises fines/clay materials were not added to increase the height of the core. As a result, water flows above the fine material normally used to impede the flow of water from the reservoir. The dry, high-resistivity unit indicated in Figure 5.2 thickens to the east. The orange unit indicates zoned material that was excavated from the crest and cast upstream to extend and reshape the upstream slope when the dam was flattened during winter 2013 rehabilitation work.

Southern Section of Embankment (~ 65 m north of the Spillway)

In addition to the geophysical signals associated with seep areas, the spillway, and the ends of the embankment, there was a significant degree of variation in the measurements of SP, DCR, and Magnetics between ~ 200 m and 250 m (measured from the south) along the embankment surveys, particularly on the wetland side of the embankment. There was also shallow attenuation of the GPR signal in this area. It is possible these anomalies indicate a change in the dam's structure. Shallow slope failure was observed in this region prior to the breach (Figure 5.1). The regional magnetic trendindicates the tailings pond is more magnetic than the embankment, suggesting the presence of magnetite in the tailings. If increased volumes of tailings sediment occupy the pore space of the dam materials in this region, it may be responsible for the elevated TMI in the area.

The Wetland

EM31-MK2 surveys conducted in the wetland revealed the ground conductivity was elevated over the sediment ponds and the path of the old stream due to settling of tailings fines. Tailings water is transported from the reservoir into the wetland along two main flow paths: beneath the dam along the old stream and through the spillway into the sediment ponds. It should be noted that historic seepage and breaches have resulted in the transport of sediment into the wetland. This research indicates ongoing seepage is contributing to the concentration of metals in the wetland, however it was not possible to distinguish recent contributions from historical : further studies to determine changes with time would be needed.

ICP-MS analysis of surface water samples collected from the tailings pond and the main seep in July 2018 indicated all tested parameters were in compliance with Schedule A concentrations except for copper and pH.

Comparison of the July 2018 tailings pond and seep samples suggests that tailings seepage is filtered through the dam wall, given the concentration of all elements is lower at the seep with the exception of boron and lead. Comparison of pH measurements over the tailings pond and at the seep showed an increase in pH through the dam wall suggesting materials within the dam wall buffer the tailings seepage. Alternatively, it may be due to the effect of dilution by meteoric water and/or snow melt infiltrating the dam.

OES analysis of bog samples GB-1 located near the seep and GB-2 west of the old stream indicated the near-surface concentrations of Cu, Zn, Fe, Ni, and Pb all higher near the seep. The top 4 cm of bog soil over GB-1 was highly concentrated in copper and to a lesser degree zinc. This elevated concentration, the primary factor influencing the elevated conductivity over this area, is restricted to a thin veneer over the surface of GB-1. The relatively low base metal concentrations over GB-2 coupled with low measurements of ground conductivity show that tailings are restricted in their coverage of the wetland.

All earth-filled dams are prone to seepage over time, and prolonged seepage leads to instabilities within the dam wall. The use of non-invasive, geophysical survey methods proved to be an effective procedure for identifying regions of the core destabilized by seepage related erosion over the Gullbridge Dam. Seepage through the dam wall is believed to occur through poorly compacted regions of the core, particularly surrounding the inlet channel. This is supported primarily by GPR surveys and streaming potentials detected by the SP method. Ground conductivity surveys assisted in delineating the distribution of tailings sediment in the wetland.

References

Actlabs. (n.d.). *Enviromining and Acid Base Accounting*. Retrieved August 22, 2018, from Actlabs: Quality Analyses Innovative Technologies: http://www.actlabs.com/page.aspx?menu=69&app=251&cat1=650&tp=2&lk=no

Adamo, N., Al-Ansari, N., Sissakian, V., Laue, J., Knutsson, S. (2020). Dam Safety Problems Related to Seepage. *Journal of Earth Sciences and Geotechnical Engineering,* 191-239.

Allen, J. (2018). *Results of Analysis of Tailings Pond and Seep Water.* Gullbridge: Memorial University Solutions ICP-MS Facility.

Allred, B. J., Daniels, J. J., & Ehsani, M. R. (2008). *Handbook of Agricultural Geophysics.* Boca Raton: CRC Press.

AMEC. (2014). *Gullbridge Mine-Tailings Management Area Project Summary Report.* St. John's: Department of Natural Resources Canada.

AMEC. (2013). *Gullbridge Mine - Tailings Management Area Closure Options Analysis.* St. John's.

AMEC. (2013 (c)). *Gullbridge Mine Tailings Management Area Slope Stability Assessment of the Proposed Rehabilitation Design Draft Prelminary Results.* St. John's.

AMEC. (2013 (b)). *Invitation to Tender for Gullbridge Mine Tailings Closure.* St. John's.

AMEC. (2014 (c)). *Gullbridge Mine - Tailings Management Area Geochemical Water Quality Model Results.* St. John's.

AMEC. (2014 (b)). *Gullbridge Mine, Newfoundland Assessment of Spillway Capacity.* St. John's.

Arthur, M., & Saffer, D. (n.d.). *Aquifer Anatomy*. Retrieved from Pennsylvania State University: https://www.e-education.psu.edu/earth111/node/910

Babechuk, M. (2018, July 19). Email reharding ICP-MS Procedures. St. John's, NL, Canada.

Bagshaw, H. (2012). Spark Optical Emission Spectroscopy. Dublin, Ireland: Center for Microscopy and Analysis.

Bazilio, A., & Weinrich, J. (2012). *The Easy Guide To: Inductively Coupled Plasma - Mass Spectrometry (ICP-MS).* Amherst: University of Massachusetts.

Blowes, D., Ptacek, C., & Jurjovek, J. (2003). Mill Tailings: Hydrogeology and Geochemistry in Environmental Aspects of Mine Wastes. Mineralogical Association of Canada Short Course Series Volume 31.

Blundell, S. (2001). *Magnetism in Condensed Matter.* Oxford: Oxford University Press.

Boak, J., & Sibbick, S. (2014). *Gullbridge Tailings Facility Geochemical Water Quality Modelling Results Final Draft.* St. John's: AMEC.

Boss, C. B., & Fredeen, K. J. (2004). *Concepts, Instrumentation and Techniques in Inductively Coupled Plasma Optical Emission Spectrometry.* Shelton: PerkinElmer.

Brewster, H. D. (2009). *Electrostatics.* Oxford Book Co.

Brittanica Encyclopedia. (2017). *Magnetic Susceptibility*. Retrieved from Physics: https://www.britannica.com/science/magnetic-susceptibility

Brown, I., Wood, P., & Elmouttie, M. (2016). *Estimation of in situ strength from back-analysis of pit slope failure.* Perth: Austrailian Centre for Geomechanics.

Burr, S. (1982). *A Guide to Prospecting by the Self-Potential Method.* Toronto: Ontario Geological Survey.

Burridge, A. (2014, January 14). *Effluent Discharge Schedule Determination Policy.* Retrieved June 4, 2018, from Government of Newfoundland and Labrador Municipal Affairs and Environment: http://www.mae.gov.nl.ca/env_protection/PD-PP2013-01%20-%20Effluent%20Discharge%20Schedule%20Determination%20Policy.pdf

Butler, D. K. (2005). *Near-Surface Geophysics, Volume 13.* SEG Books.

Byrd, W. E. (1967). *Potential Applications of Magnetic Gradients to Marine Geophysics.* Cambridge: Massachusetts Institute of Technology.

Calamak, M., Bingol, A., & Yanmaz, A. (2016). Effect of Drainage Properties on Seepage Behavior of Earth-Fill Dams. *12th International Congress on Advances in Civil Engineering (ACE2016)*, (pp. 1-8). Istanbul.

Callegary, J. B., Ferre, T. P., & Groom, R. (2007). Vertical Spatial Sensitivity and Exploration Depth of Low-Induction -Number Electromagnetic Induction Instruments. *Vadose Zone Journal*, 158-167.

Camacho, A. (2009). *Encyclopedia of Inland Waters.* Elsevier Inc.

Champagne, P., Ong, R. S., Bhandari, A., Tyagi, R., & Lo, I. (2008). *Natural Processes and Treatment for Hazardous Waste Treatments.* Kingston: American Society of Civil Engineers.

Circuit Globe. (2019, June 16). *Difference Between Magnetic Field & Magnetic Flux*. Retrieved from Circuit Globe: https://circuitglobe.com/difference-between-magnetic-field-and-magnetic-flux.html

Conrad, C. (2011, March 10). *Lecture 11: Magnetic Surveys.* Retrieved October 7, 2016, from University of Hawaii: http://www.soest.hawaii.edu/GG/FACULTY/conrad/classes/GG304_S11/handouts/Lecture_11.pdf

Cooper, G. (2000). VES 1.30 Freeware Modelling Software. *VES 1.30*. VES.

Corry, C. E., DeMoully, G. T., & Gerety, M. T. (1980). *Field Procedure Manual for Self-Potential Surveys.* Tucson: Zonge Engineering and Research Organization.

Corwin, R. (1990). The self-potential method for environmental and engineering applications. In Ward, S.H. (ed.), *Geotechnical and Environmental Geophysics: Volume I, Review and Tutorial,Investigations in Geophysics Series, Society of Exploration Geophysicists*.

Das, S., & Chakraborty, S. (2010). Effect of Finite Electric Double Layer Conductivity on Streaming Potential and Electroviscous Effect in Nanofluidic Transport. *20th National and 9th International ISHMT-ASME Heat and Mass Transfer Conference.* Mumbai.

DATAQ Instruments Inc. (2017). *FFT (Fast Fourier Transform) Waveform Analysis.* Retrieved from General Education and Tutorials: https://www.dataq.com/data-acquisition/general-education-tutorials/fft-fast-fourier-transform-waveform-analysis.html

de Hoffman, E., & Stroobant, V. (2007). *Mass Spectrometry: Principles and Applications .* West Sussex: John Wiley and Sons Ltd.

Dec, T., Swinden, S. H., & Dunning, G. R. (1997). Lithostratigraphy and Geochemistry of the Cottrells Cove Group, Buchans - Roberts Arm Volcanic Belt: New Constraints for the Paleotectonic Setting of the Notre Dame Subzone, Newfoundland Appalachians. *Canadian Journal of Earth Science*, 86-103.

Dordio, A., Carvalho, A. P., & Pinto, A. P. (2008). *Wetlands: Water “living filters”?* Évora: University of Évora.

Dou, Q., Wei, L., Magee, D. R., & Cohn, A. G. (2016). Real-Time Hyperbola Recognition and Fitting in GPR Data. *IEE Transactions on Geoscience and Remote Sensing Data Volume 55 Issue 1*, 51-62.

Dunnivant, F. M. (2008). *Components of an Inductively Coupled Plasma—Atomic Emission Spectrometry System (ICP-AES).* Retrieved October 9, 2018, from Whitman College: http://people.whitman.edu/~dunnivfm/FAASICPMS_Ebook/CH3/3_3_3.html

Durham University. (2021, May 12). *Embankment Dams - Seepage*. Retrieved from Durham University: https://community.dur.ac.uk/~des0www4/cal/dams/emba/seep.htm

Earle, S. (2019). *Physical Geology - 2nd Edition.* BCcampus Open Education. Retrieved from BC.

Engels, J. (2017). *Conventional Impoundment Storage - The Current Techniques*. Retrieved June 18, 2018, from Tailings.info: http://www.tailings.info/disposal/conventional.htm

Engels, J. (2017 (b)). *Water Management Considerations for Conventional Storage*. Retrieved November 16, 2017, from Tailings info: http://www.tailings.info/technical/water.htm

Engineers Edge. (2017). *Factors of Safety FOS Review*. Retrieved April 19, 2017, from Engineers Edge: www.engineersedge.com/analysis/factor-of-safety-review.htm

Fey, D. C. (2003, June 1). *Acid-Base Accounting*. Retrieved May 9, 2017, from United States Geological Survey: http://pubs.usgs.gov/of/2003/ofr-03-210/Section508/IX_Acid-base_Accounting-508.pdf

Fitzpatrick, A. (2013). Dam Went More Than a Year Without Repairs Before Failure. *The Telegram*.

Fitzpatrick, R. (2006, February 2). Magnetic Susceptibility and Permeability. Austin, Texas, U.S.A.

Ford, K. (2003). *Passive Treatment Systems for Acid Mine Drainage.* Lincoln: University of Nebraska.

Fugro Geosurveys Inc. (2007). Residual Total Magnetic Field North Gullbridge 2007. St. John's, Newfoundland, Canada.

Gedeon, G. (2004). *Design and Construction of Earth and Rock-Fill Dams.* Stony Point: CED.

GEM Systems Inc. (2008). *GEM Overhauser Magnetometer Brochure*. Retrieved from Gemsys: http://www.gemsys.ca/pdf/GSM-19%20Overhauser%20v7.0.pdf?lbisphpreq=1

GEM Systems Inc. (2008). *GSM-19 v7.0 Instruction Manual.* Markham.

Geological Association of Canada. (n.d.). Regional Geological Map of Newfoundland. Newfoundland, Canada: Geological Association of Canada.

Geological Survey of Canada. (1988). *Magnetic Anomaly Map, Great Gull Pond, Newfoundland.* St. John's: Department of Mines and Energy.

Geological Survey of Newfoundland. (2007, March 1-27). *Newfoundland and Labrador Department of Natural Resources.* Retrieved from Geoscience Atlas: https://www.geosurv.gov.nl.ca/airborne/disp_airborne.asp?SURVEY_ID=DN09903

Geological Survey of Newfoundland and Labrador. (2007). *Geoscience Atlas: Government of Newfoundland and Labrador.* Retrieved November 4, 2016, from Residual Mag - Gullbridge North: http://geoatlas.gov.nl.ca/Default.htm

Geomatrix Earth Science Ltd. (2021, May 24). *Syscal Junior from Iris Instruments*. Retrieved from Geomatrix Earth Science Ltd.: https://www.geomatrix.co.uk/land-products/electrical-resistivity/syscal-junior/

Geonics. (2013). *EM31 MK2*. Retrieved October 27, 2017, from Geonics Limited: Leaders in Electromagnetics: http://www.geonics.com/html/em31-mk2.html

Geonics Ltd. (1999). *EM31-MK2 Ground Conductivity Data Logger Operating Instructions.* Mississauga.

Geonics Ltd. (2003). *Computer Program Manual (Survey Data Reduction Manual) DAT31W Version 1.20.* Mississauga.

Geonics Ltd. (2013). *EM31-MK2 | EM31-SH*. Retrieved December 14, 2017, from Geonics Ltd: Leaders in Electromagnetics: http://www.geonics.com/html/em31-mk2.html

Geonics training for EM-61 EM-31 EM-34 EM-38: https://geonicstraining.com/exploration-depth-geonics equipment/#:~:text=The%20accumulative%20response%20of%20the,reduced%20to%20approximately%203%20meters.

GeoSci Developers. (2015). *Direct Current Resistivity*. Retrieved from EM: https://em.geosci.xyz/content/geophysical_surveys/dcr/survey.html

GeoSci Developers. (2017). *Ground-Penetrating Radar*. Retrieved from Geophysics for Practicing Geoscientists: https://gpg.geosci.xyz/content/GPR/GPR_fundamental_principles.html

GEO-SLOPE International Ltd. (2012). *Stability Modeling with SLOPE/W.* Calgary.

Geotomo Software. (2010). *RES2DINV - Rapid 2-D Resistivity & IP Inversion using the least-squares method.* Penang: Geotomo Software.

Gillis, G. (2016). *Oil Field Glossary*. Retrieved from Schulmberger: http://www.glossary.oilfield.slb.com/en/maincredits.aspx

Glover, P. W. (2016). *Archie's Law - a reappraisal.* Leeds: University of Leeds.

Google Earth. (2018). Gullbridge, Newfoundland.

Government of Newfoundland and Labrador. (2018, February 26). *Gullbridge Dam.* Retrieved May 28, 2018, from Newfoundland and Labrador Municipal Affairs and Envrionment: http://www.mae.gov.nl.ca/waterres/southbrook/gullbridgedam.html

Government of Oregon. (2014, April). *Appendix F - Rational Method.* Retrieved from Oregon Department of Transportation: https://www.oregon.gov/ODOT/GeoEnvironmental/Docs_Hydraulics_Manual/Hydraulics-07-F.pdf

Goyal, V. C., Niwas, S., & Gupta, P. K. (1991). Theoretical Evaluation of Modified Wenner Array for Shallow Resisitivity Exploration. *National Groundwater Association*, 582-586.

Gregersen, E. (2019). *Magnetic Dipole*. Retrieved from Encycloppaedia Britannica: https://www.britannica.com/science/magnetic-dipole

Griffiths, D. J. (1999). *Introduction to Electrodynamics.* Upper Saddle River, New Jersey: Prentice-Hall Inc.

Gubbins, D., Herrero-Bervara, E., Reeves, C., & Korhonen, J. V. (2005). Magnetic Anomalies for Geology and Resources. *Encyclopedia of Geomagnetism and Paleomagnetism*, 477-480.

Hollett, A. (2014, April). Gullbridge Mine Tailings Management Area Closure Option Analysis Gullbridge, NL. *TMA Overview with Closure Boundary*. Newfoundland, Canada: AMEC Environment and Infrastructure.

Hudson, K. A., & Swinden, S. H. (1990). The Lake Bond Deposit: Superimposed Volcanogenic and Synorogenic Base and Precious Metal Mineralization in the Robert Arm Group, Central Newfoundland. *Atlantic Geology*, 11-25.

Hunter, R. (1981). *Zeta Potential in Colloids Science.* New York: Academic Press.

Idris, M., Abba, S., Said, B., & Abdullahi, M. (2015). The Underground Water Investigations using Self-Potential Geophysical Survey: A Case Study of Buk Old Campus by the Application of Computer Modeling Software (Matlab). *International Journal of Advanced Technology in Engineering and Science*, 680-691.

Iris Instruments. (n.d.). Electre II Software Help. Orleans, France.

Jacob, R. W., & Urban, T. (2015). *Ground-Penetrating Radar Velocity Determination and Precision Estimates Using Common Mid-Point (CMP) Collection with Hand-Picking,* *Semblance Analysis, and Cross-Correlation Analysis: A Case Study and Tutorial for Archaeologists.* Lewisburg: Bucknell University.

Jain, S., & Singh, V. (2003). *Developments in Water Science.*

Jika, H., & Mamah, L. (2014). Application Of Electromagnetic Method And Electrical Resistivity Sounding in Hydrogeological Studies, A Case Study Of Vandeikya Area, Central Nigeria. *International Journal of Scientific and Technology Research*, 179-190.

Johnson, C., Albrecht, G., Ketterings, Q., Beckman, J., & Stocken, K. (2005). Nitrogen Basics - The Nitrogen Cycle. Ithica, New York, U.S.A.

Jol, H. M. (2009). *Ground Penetrating Radar Theory and Applications.* Amsterdam: Elsevier.

Jones, F. (2007, June 28). *Electrical Resistivity of Geologic Materials*. Retrieved from University of BC: Department of Earth, Ocean and Atmospheric Sciences: https://www.eoas.ubc.ca/ubcgif/iag/foundations/properties/resistivity.htm

Josh, M., Lintern, M. J., Kepic, A. W., & Verrall, M. (2011). Impact of grain-coating iron minerals on dielectric response of quartz sand and implications for ground-penetrating radar. *Society of Exploration Geophysicists*, J27-J34.

Jouniaux, L., Maineult, A., Naudet, V., Pessel, M., & Sailhac, P. (2009). Review of Self-potential methods in Hydrogeophysics. *Comptes Rendus Géoscience*, 928-936.

Kashani, A., & Mostaghimi, J. (2016). *Aerosol Characterization of Concentric Pneumatic Nebulizer Used in Inductively Coupled Plasma - Mass Spectrometry (ICP-MS).* Toronto: University of Toronto.

Kearey, P., Brooks, M., & Hill, I. (2002). *An Introduction to Geophysical Exploration.* Oxford: Blackwell Publishing.

Khan Academy. (2018). *Intro to the imaginary numbers*. Retrieved September 27, 2018, from Khan Academy: https://www.khanacademy.org/math/algebra2/introduction-to-complex-numbers-algebra-2/the-imaginary-numbers-algebra-2/a/intro-to-the-imaginary-numbers

Kilfoil, G., Blagdon, A., Leitch, A., Campbell, H., Irvine, M., Batterson, M., . . . Baker, B. (2018). *The Application and Testing of Two Geophysical Methods (Direct-Current Resistivity and Ground-Penetrating Radar) as part of the Coastal Monitoring Program to Assess Terrain Stability.* St. John's: Newfoundland and Labrador Department of Natural Resources Geological Survey.

Kochmann, S. (2018). *ICP-OES: Why spectral lines are true peaks and how this can fool the user*. Retrieved October 7, 2018, from The Winnower: https://thewinnower.com/papers/217-icp-oes-why-spectral-lines-are-true-peaks-and-how-this-can-fool-the-user

L. van Dam, R. (2001). *Causes of ground-penetrating radar reflections in sediment.* Amsterdam: Vrije Universiteit.

LearnGPR. (2016). *What are High Pass/ Low Pass Filters for GPR!* Retrieved from Youtube: https://www.youtube.com/watch?v=hqOVq_Pw4RI

Leitch, A. (2008). EASC 3172 Lectures Notes. *Ground Penetrating Radar*. St. John's, Newfoundland, Canada: Memorial University of Newfoundland.

Leitch, A. (2015). Electrostatics and SP. St. John's, Newfoundland: Memorial University of Newfoundland.

Leitch, A. (2016). Module 2: DC Resitivity. *Earth Science 3172 Lecture*. St. John's, NL, Canada: Memorial Univerisity of Newfoundland.

Leitch, A. (2019). *Low Induction Number and the EM31.* St. John's.

Leitch, A., & Boone, C. (2007). A study of the SP geophysical technique in a campus setting. *Atlantic Geology*, 91-111.

Lenntech. (2019, April 26). *Iron (Fe) and Water*. Retrieved from Water Treatment and Purification: https://www.lenntech.com/periodic/water/iron/iron-and-water.htm

Lim, M., Han, G.-C., Ahn, J.-W., You, K.-S., & Kim, H.-S. (2009). Leachability of Arsenic and Heavy Metals from Mine Tailings of Abandoned Metal Mines. *International Journal of Environmental Research and Public Health*, 2865–2879.

LLC, Landviser;. (2012, August 17). *Formatting Array Input Data File in RES2DINV: surface electrodes for any geometry*. Retrieved November 7, 2017, from Landviser Enlightening Research: http://www.landviser.net/content/formatting-array-input-data-file-res2dinv-surface-electrodes-any-geometry

Loke, M. (1999). *Electrical imaging surveys for Environmental and Engineering Studies.* Houghton: Michigan Technology University.

Loke, M. (2004). *Tutorial : 2-D and 3-D electrical imaging surveys.*

Loperte, A., Bavusi, M., Cerverizzo, G., Lapenna, V., & Soldovieri, F. (2011). Ground Penetrating Radar in Dam Monitoring: The Test Case of Acerenza (Southern Italy). *International Journal of Geophysics*, 1-9.

Lowrie, W. (2007). *Fundamentals of Geophysics Second Edition.* New York: Cambridge University Press.

Lucius, J. E., Langer, W. H., & Ellefsen, K. J. (2006). *An Introduction to Using Surface Geophysics to Characterize Sand and Gravel Deposits.* Reston: USGS.

Lynch, N. (2016). *DCR Guide.* St. John's: Memorial University of Newfoundland Department of Earth Sciences.

Lynch, N. (2017). *Geophysical Detection of Reducing Springs Using Magnetics and a Newly Developed Self Potential System.* St. John's: Memorial University of Newfoundland.

Lyons, W. C. (2010). *Working Guide to Reservoir Engineering.* Elsevier.

Magnet Academy. (2015, Janaury 28). *Diamagnetism and Paramagnetism.* Retrieved December 20, 2017, from National Magnet Lab: https://nationalmaglab.org/education/magnet-academy/watch-play/interactive/diamagnetism-and-paramagnetism

Mainali, G. (2006). *Monitoring of Tailings Dams with Geophysical Methods.* Luleå: Luleå University of Technology.

Mainali, G., Nordlund, E., Knuttson, S., & Thunehed, H. (2015). Tailings Dam Monitoring in Swedish Mines using Self-Potential and Electrical Resistivity Methods. *Electronic Journal of Geotechnical Engineering*, 5859-5875.

Marescot, L. (2013). *Electrical Surveying Part III: Spontaneous Potential Method.* Swiss Federal Insititude of Technology Zurich.

Mariita, N. (2007). *The Magnetic Method.* Naivasha: Kenya Electricity Generating Company Ltd. (KenGen).

Martinex, A., & Byrnes, A. P. (2001). *Modeling Dielectric-constant values of Geologic Materials: An Aid to Ground-Penetrating Radar Data Collection and Interpretation.* Lawrence: Kansas Geological Survey.

Maxxam. (2016). *Results of Analysis of Water: Gullbridge.* St. John's.

McNeill, J. (1980). *Electromagnetic Terrain Conductivity Measurement at Low Induction Numbers.* Mississauga: Geonics Ltd.

Memorial Univerity Department of Earth Science. (2018). *Reults of Bog Sample OES Analysis.* Gullbridge: Memorial University Department of Earth Science.

Mickus, K. (2014). *Magnetic Method.* Springfield: Missouri State University.

Mills, C. (2017, May 9). *Acid Base Accounting (ABA)*. Retrieved May 9, 2017, from Infomine.com: technology.infomine.com/enviromine/ard/acid-base%20accounting/ABAdiscussion.htm

Minsley, B., Burton, B., Ikard, S., & Powers, M. (2011). Hydrogeophysical investigations at Hidden Dam, Raymond, California. *Journal of Environmental and Engineering Geophysics 16*, 145-164.

Morgan, L. A. (2010). *Geophysical Characteristics of Volcanogenic Massive Sulphide Deposits.* Reston, Virginia: U.S. Geological Survey.

Mussett, A., & Khan, M. (2000). *Looking into the Earth: An Introduction to Geological Geophysics.* Cambridge: Cambridge University Press.

Nagatsuma, T. (2002). Geomagnetic Storms. *Journal of the Communications Research Laboratory*, 139-154.

National Instruments Corporation. (2011, JUNE). *Filter Specifications (Digital Filter Design Toolkit).* Retrieved from LabVIEW 2011 Digital Filter Design Toolkit Help: http://zone.ni.com/reference/en-XX/help/371325F-01/lvdfdtconcepts/dfd_filter_spec/

National Wetlands Working Group. (1997). *The Canadian Wetland Classification System Second Edition.* Waterloo: University of Waterloo.

Natural Resources Canada. (2013). *Tailings Management at NRCan.* Retrieved May 10, 2018, from Natural Resources Canada Mining/Materials Publications: https://www.nrcan.gc.ca/sites/www.nrcan.gc.ca/files/mineralsmetals/pdf/mms-smm/pubr-pubr/pdf/NRCan-TailingsMgmt_FS-eng.pdf

Natural Resources Canada. (2019, May 16). *Precise Point Positioning*. Retrieved from Natural Resources Canada: https://webapp.geod.nrcan.gc.ca/geod/tools-outils/ppp.php

Naudet, V., Revil, A., Bottero, J.-Y., & Bégassat, P. (2003). *Relationship between self-potential (SP) signals and redox conditions in contaminated groundwater.* AGU100.

Ness, I., Janin, A., & Stewart, K. (2014). *Passive Treatment of Mine Impacted Water in Cold Climates: A Review.* Whitehorse: Yukon Research Center.

Nhu, T. N., & Pham, K. N. (2018). Correcting the distortion of apparent resistivity pseudosection produced by 3D effect of the embankment geometry. *Environmental Earth Sciences*, 1-13.

NLDNR. (2012). *Geochemistry of Tailings, Gullbridge Tailings Pond.* Government of Newfoundland and Labrador.

NLDNR. (2012 (b)). *Field Inspection Report - Gullbridge Dam and South Brook Watershed.*

Nobes, D., & Warner, B. (1991). *The Characterization of Bogs using Ground Penetrating Radar.* Ontario Geological Survey.

O'Brien, B. (2007). *Geology of the Buchans-Roberts Arm Belt, Near Great Gull Lake.* Department of Natural Resources Newfoundland. St. John's: Geological Survey of Newfoundland.

O'Kane, M., Tallon, L., & Meiers, G. (2014). *Low Permeability Barrier Layers and Cover System.* Saskatoon: O'Kane Consultants Inc., Canada.

Oliver, P. (2015). *The frequency dependence of Magnetic Susceptibility Applied to the Non-Destructive Characterization of Stony Meteorites.* Ottawa: Carleton University.

Open EI. (2013, April). *Exploration Technique: DC Resistivity Survey (Wenner Array)*. Retrieved October 30, 2017, from DC Resistivity Survey (Wenner Array): https://openei.org/wiki/DC_Resistivity_Survey_(Wenner_Array)

Or, D., & Tuller, M. (2005). Capillarity. *Encyclopedia of Soils in the Environment*.

Orogen Department of Transportation. (2014, April). *GeoEnvironmental: Hydraulics Manual.* Retrieved August 8, 2018, from Orogen Department of Transportation: https://www.oregon.gov/ODOT/GeoEnvironmental/Docs_Hydraulics_Manual/Hydraulics-07-F.pdf

Palla, N., Gudavalli, S., Subedi, B., & Jao, M. (2008). A Comparison among SPT, CPT, and Texas Cone Penetration Test. *ASCE Texas Section Spring Meeting*, (pp. 1-10).

Parsons, S., & Warford, W. (2008, March). Dam Safety. Newfoundland and Labrador, Canada: Stantec Ltd.

Prouty, M., Hrvoic, I., & Vershovski, A. (2013). *Instruments and Methodologies for Measurement of the Earth's Magnetic Field.* GEM.

Rennie, R. (1998). Mining. Retrieved from Heritage Newfoundland and Labrador: https://www.heritage.nf.ca/articles/economy/mining.php

Revil, A., Karaoulis, M., Srivastava, S., & Byrdina, S. (2013). Thermoelectric self-potential and resistivity data localize the burning front of underground coal fires. *Geophysics*, B259-B273.

Reynolds International. (2011, March). *EM31 electro-magnetic ground conductivity mapping.* Retrieved December 14, 2017, from Reynolds International: http://www.reynolds-international.co.uk/uploads/files/04tssem31.pdf

Reynolds International Ltd. (2011, March). EM31 Electromagnetic Ground Conductivity Mapping. *Technical Summary Sheet No.4*. United Kingdom: Reynolds International Ltd.

Reynolds, J. M. (1997). *An Introduction to Applied and Environmental Geophysics.* Las Vegas: Wiley.

Richmond, A. (1979). Ionospheric Wind Dynamo Theory: A Review . *Journal of Geomagnetism and Geoelectricity*, 287-310.

Richmond, A. D. (2016). *Ionospheric Electrodynamics.* University Corporation for Atmospheric Research.

Riddihough, R. (1971). Diurnal Corrections to Magnetic Surveys - An Assesment of Errors. *Geophysical Prospecting, Vol. XIX*, 551-567.

Risch, M. R., & Robinson, B. A. (2001). *Use of Borehole and Surface Geophysics to Investigate Ground-Water Quality near a Road-Deicing Salt-Storage Facility,Valparaiso, Indiana.* Indianapolis: U.S. Geological Survey.

Robinson, M., Bristow, C., McKinley, J., & Ruffell, A. (2013). *Ground-Penetrating Radar.* British Society for Geomorphology.

Rogers, N., van Staal, C., Zagorevshki, I., Skulski, T., Piercey, S., & McNicoll, V. (2007). Timing and Tectonic Setting of Valcongenic Massive Sulphide Bearing Terranes within the Central Mobile Belt of the Canadian Appalachians. *Proceeedings of Exploration 07: Fifth Dicennial International Conference in Mining Exploration* (pp. 1199-1205). Toronto: Regional Exploration.

Saintenoy, A., & Hopmans, J. (2011). Ground Penetrating Radar: Water Table Detection Sensitivity to Soil Water Retention Properties. *Journal of Selected Topics in Applied Earth Observations and Remote Sensing*, 748-753.

Salim, A. A. (2012). *Application of Magnetic Suceptibility Measurements to Oilfield Scale Management.* Edinburgh: Heriot Watt University.

Schenck, J. F. (1996). The role of magnetic susceptibility in magnetic resonance imaging: MRI magnetic compatbility of the first and second kinds. *Medical Physics*, 815-850.

Schlumberger Ltd. (2017). *Automatic Gain Control.* Retrieved April 26, 2017, from Schlumberger: http://www.glossary.oilfield.slb.com/Terms/a/automatic_gain_control.aspx

Science Applications International Corporation. (2006). *Shallow Land Disposal Area Geophysical Investigation.* Twinsburg.

Sensors and Software Inc. (2006). *pulseEKKO PRO User's Guide.* Mississauga: Sensors and Software Inc.

Sensors and Software Inc. (2015). *Ekko_Project Sliceview Module.* Mississauga.

Sensors and Software Inc. (2016). 3-Day GPR Short Course Notes. *Sensor and Software 3-Day GPR Short Course Notes* (p. 5). Mississauga: Sensors and Software Inc.

Sensors and Software Inc. (2016). *Ekko_Project LineView and Interpretation Modules User's Guide.* Mississauga: Sensors and Software Inc.

Sensors and Software Inc. (2016). *Ekko_Project with Processing, Bridge Deck Condition and Pavement Structure Modules.* Mississauga.

Sensors and Software Inc. (2017). *Ekko_Project Software*. Retrieved April 25, 2017, from Sensors and Software: https://www.sensoft.ca/products/ekko-project/detailsfeatures/

Sensors and Software Inc. (2017). *Sensors and Software Resources*. Retrieved May 19, 2017, from FAQ: How Can Velocity be Extracted from Hyperbolas?: https://www.sensoft.ca/resources/faq/

Sensors and Software Inc. (2018, September 12). Interpreting GPR Data: The Basics Part 2. Mississauga, Ontario, Canada.

Sharma, P. (1997). *Environmental and Engineering Geophysics.* Cambridge University Press.

Sheffer, M. R. (2007). *Forward modelling and inversion of streaming potential for the interpretation of hydraulic conditions from self-potential data.* Victoria: University of British Columbia.

Sheppard, L., Leith, I., Leeson, S., can Dijk, N., Field, C., & Levy, P. (2013). Fate of N in a peatland, Whim bog: immobilisation in the vegetation and peat, leakage into pore water and losses as N2O depend on the form of N. *Biogeosciences*, 149-160.

Shimadzu Corp. (2018). *Principle of Optical Emission Spectrometry*. Retrieved October 7, 2018, from Shimadzu: Excellence in Science: https://www.shimadzu.com/an/elemental/oes/oes.html

Skrede, K. (2012). *Magnetic susceptibility of sedimentary rocks from Bjørnøya.* Trondheim: Norwegian University of Science and Technology.

Sonnenberg, S. A., & Selley, R. C. (2015). *Elements of Petroluem Geology 3rd Edition.* Academic Press.

Space Weather Live. (2019). *The Kp-Index.* Retrieved from Space Weather Live: Real-Time Auroral and Solar Activity: https://www.spaceweatherlive.com/en/help/the-kp-index

Srigutomo, W. (2016). 2D Resistivity and Induced Polarization Measurement for Manganese Ore Exploration. *Journal of Physics: Conference Series 739*.

Stantec Consulting Ltd. (2011). *Dam Safety Review Various Former Mine Sites.* St. John's: Government of Newfoundland and Labrador.

Stantec Consulting Ltd. (2011 (b)). *Preliminary Dam Safety Review (DSR) Gullbridge Mine, Newfoundland.* St. John's.

Stantec Consulting Ltd. (2012). *Dam Safety Review (DSR) Gullbridge Mine, Newfoundland.* Fredericton.

Stantec Consulting Ltd. (2012 (b)). *Hydrotechnical Assessment of the Former Gullbridge Copper Mine.* St. John's.

Stantec Consulting Ltd. (2012 (c)). *Supplementary Report Dam Safety Review (DSR) Gullbridge Mine, Newfoundland.* St. John's: Government of Newfoundland and Labrador.

State of Tasmania. (2008, November). Guidelines for the Construction of Earth-Filled Dams. Hobart, Tasmania, Australia.

Subsurface Geotechnical. (2016). Retrieved October 20, 2016, from Electromagnetic Methods: http://www.geophysical.biz/electromagnetic-method.htm

Syltie, P. W. (2002). *How Soils Work: A Study into the God-Plane Mututalism of Soils and Crops.* Xulon Press.

Szymczyk, M., & Szymczyk, P. (2013). Preprocessing of GPR Data. *Image Processing and Communication Vol. 18 No. 2-3*, 83-90.

Taylor, C. D., Zierenberg, R. A., Goldfarb, R. J., Kilburn, J. E., Seal II, R. R., & Kleinkopf, M. D. (1995). *Volcanic-Associated Massive Sulfide Deposits.* United States Geological Survey.

TechTarget. (2007, July). *Magnetic Field Strength*. Retrieved from WhatIs: https://whatis.techtarget.com/definition/magnetic-field-strength

Terraplus. (2001). *Rapid 2-D Resistivity and IP inversion using the least-squares method.* Geotomo Software.

Tysmbal, E. (2006, February 10). Section 15: Magnetic properties of materials. *Physics 927*. Lincoln, Nebraska, U.S.A.

U.S. Army Corps of Engineers. (2004). *General Design and Construction Considerations for Earth and Rock-Fill Dams.* Washington.

U.S. Department of the Interior Bureau of Reclamation. (2012). *Reclamation: Managing Water in the West - Embankment Dams.* U.S. Department of the Interior Bureau of Reclamation.

U.S. Department of the Interior Bureau of Reclamation. (2014, December 10). *Dam Safety.* Retrieved August 6, 2018, from United States Department of the Interior Bureau of Reclamation: https://www.usbr.gov/ssle/damsafety/risk/BestPractices/Presentations/IV-4-20141210-PP.pdf

U.S. Department of the Interior Bureau of Reclamation. (2015). *IV-4. Internal Erosion Risks for Embankments and Foundations.*

U.S. Geological Survey. (2016, December 9). *Floods: Recurrence Intervals and 100-year Floods*. Retrieved May 16, 2017, from The USGS Water Science School: water.usgs.gov/edu/100yearflood.html

UBC. (2007, June 6). *University of British Columbia Department of Earth, Oceans and Atmosphere Science.* Retrieved September 18, 2018, from Introduction to Induced Polarization Surveying: https://www.eoas.ubc.ca/~fjones/aglosite/objects/meth_2/index.htm

United States Environmental Protection Agency. (2016, May 24). *Frequency-Domain Electromagnetic Methods.* Retrieved 10 20, 2016, from Environmental Geophysics: https://archive.epa.gov/esd/archive-geophysics/web/html/frequency_domain_electromagnetic_methods.html

University of Birmingham. (2019). *Chapter 4: Classification of Magnetic Materials Lecture Notes.* Retrieved from University of Birmingham: https://www.birmingham.ac.uk/Documents/college-eps/metallurgy/research/Magnetic-Materials-Background/Magnetic-Materials-Background-4-Classification-of-Magnetic-Materials.pdf

University of British Columbia. (2005). *UBC Geophysical Inversion Facility.* Retrieved January 25, 2018, from Inversion Concepts: Outline of Inversion: https://www.eoas.ubc.ca/ubcgif/iag/tutorials/invn-concepts/index.htm

University of British Columbia Geophysical Inversion Facility. (2014). *Principles of Electromagnetic (EM) Induction*. Retrieved October 20, 2016, from Geophysics for

Praciticing Geoscientists: http://gpg.geosci.xyz/content/electromagnetics/principles_of_em_induction.html

University of Guelph. (2019, April 28). *Bogs*. Retrieved from University of Guelph: http://www.aquatic.uoguelph.ca/wetlands/chapter2/bogpage2.htm

University of St. Andrews. (1997). *Applied Geophysics for Groundwater Studies.* St. Andrews: University of St. Andrews.

Upadhyay, H., & Smitheringale, W. (1972). Geology of the Gullbridge Copper Deposit, Newfoundland: Volcanogenic Sulfides in Cordierite-Anthophyllite Rocks. *Canadian Journal of Earth Sciences*, 1061-1073.

USEPA. (2015). *INDUCTIVELY COUPLED PLASMA—MASS SPECTROMETRY.* Retrieved from United States Environmental Protection Agency: https://www.epa.gov/sites/production/files/2015-12/documents/6020b.pdf

Vick, S. G. (2001). Stability aspects of long-term closure for sulfide tailings. *Safe Tailings Dams Constructions.* Gällivare.

Wright, S. H. (2004). Generation of resting membrane potential. *Advances in Physiology Education*, 139-142.

Wu, Z., & Liu, S. (2013). Imaging the debris internal structure and estimating the effect of debris layer on ablation of Glacier ice. *Journal of the Geological Society of India*.

Wynn, J. C., & Sherwood, S. I. (1984). *The Self-Potential (SP) Method: An Inexpensive Reconnaissance and Archaeological Mapping Tool.* Taylor and Francis.

Zhao, G.-d., & Liuc, Q. (2010). Leaching of copper from tailings using ammonia/ammonium chlorida solution and its dynamics. *2010 International Conference on Chemistry and Chemical Engineering.* Kyoto: IEEE Xplore.

Zogala, B., Mendecki, M. J., Zuberek, W. M., & Robak, M. (2012). Application of Self Potential Method in the Area Contaminated with Oil Derivatives. *Acta Geodyn. Geomater*, 179-189.

Table of Contents for Appendices

Appendix 1A Table of Variables for Chapter 3 325

Appendix 2A Tables and Technical Notes for Chapter 2 328

A2.1 Notable Surface Features of the Gullbridge Impoundment 328

A2.2 Acid-Base Accounting 330

A2.3 Penetration Tests 331

A2.4 Borehole Records 332

A2.5 Factor of Safety and Slope Stability Analysis 339

A2.6 The Rational Formula 341

A2.7 Surface Water Sampling Results 342

A2.8 Tailings Sampling Results 343

A2.9 Peat Thickness Measurements 345

A2.10 Seep Water Analysis 346

Appendix 3A Tables of Technical Notes for Chapter 3 347

A3.1 The Vadose Zone 347

A3.2 Supplementary ICP-OES and ICP-MS Notes 349

A3.3 Supplementary GPR Field Method Notes 352

A3.4 Supplementary DCR Data Processing Notes 357

A3.5 Supplementary GPR Data Processing Notes 361

A3.6 Supplementary EM31-MK2 Data Processing Notes 371

A3.7 Supplementary ICP-MS Data Processing Notes 372

Appendix 4A Supplementary Data for Chapter 4 374

A4.1 SP over the Seep Grid 374

A4.2 Central artifact associated with DCR surveys over the Gullbridge Dam . 376

A4.3 Complete smoothed ρ_a versus x dataset plotted in Fig. 4.21 377

A4.4 Original Dataset for “2 m East” DCR Schlumberger Survey 378

A4.5 GPR profiles without interpretation lines 379

A4.6 Supplementary EM31 ground conductivity data 398

A4.7 Supplementary Bog Sample data 405

Appendix 1A Table of Variables for Chapter 3

Table A1: Table of variables

Symbol	Equation	Units	Definition
V	3.2, 3.8	Volts (V, mV)	Electric potential
$\vec{M}$	3.1, 3.15	Magnetic moment per unit volume (A/m)	Magnetization
χ	3.1	ppm	Magnetic Susceptibility
$\vec{H}$	3.1, 3.15, 3.16	A/m	Magnetic Intensity
H_p	3.19, 3.20	A/m	Primary Magnetic Field
H_s	3.19, 3.20	A/m	Secondary Magnetic Field
Δ	3.2, 3.4, 3.8	N/A	Change/difference
∇	3.13, 3.14, 3.16	N/A	Gradient
I	3.2, 3.4	Amperes	Electric Current
R	3.2, 3.3	$\Omega = \mathrm{V/A}$	Resistance
ρ	3.3, 3.31	(Ω*m)	Resistivity
ρ_a	3.4	(Ω*m)	Apparent Resistivity
ρ_r	3.7	(Ω*m)	Resistivity of water-saturated rock
ρ_w	3.7	(Ω*m)	Resistivity of water
F	3.7	N/A	Formation Factor
L	3.3	Meters (m)	Length of circuit element
A	3.3	m^2	Cross-sectional area of a circuit
A	3.8	m^2	Area under electric potential decay curve
K	3.4, 3.5, 3.6	N/A	Geometric Factor
a	3.5, 3.6, 3.26, 3.27	m	a-spacing (pseudo-depth)
b	3.5, 3.26, 3.27	m	b-spacing (potential electrode spacing)
M	3.8	ms	Chargeability
t	3.8, 3.9a, 3.9b, 3.10a, 3.10b, 3.13, 3.14, 3.16	s	Time
∂	3.9a, 3.9b, 3.13, 3.14, 3.16	N/A	Derivative

$\vec{E}$	3.9a, 3.10a, 3.13, 3.14, 3.17	Newtons/Coulomb (N/C)	Electric Field
$\vec{B}$	3.9b, 3.10b, 3.13, 3.14	Teslas (N*m/A)	Magnetic Field
$\vec{B}$	3.14	Teslas (N*m/A)	Magnetic Flux Density
z	3.9a, 3.9b, 3.10a, 3.10b	m	Vertical Distance
μ	3.9a, 3.9b, 3.11a, 3.11b, 3.18	N/A^2	Magnetic Permeability
ε	3.9a, 3.9b, 3.11a, 3.11b, 3.12	Farads per meter (F/m)	Dielectric Permittivity
σ	3.9a, 3.9b, 3.11a, 3.11b, 3.17, 3.19	Siemens per meter (S/m)	Electrical conductivity
σ_a	3.21, 3.23	Siemens per meter (S/m)	Apparent Conductivity
κ	3.10a, 3.10b, 3.11b	N/A	Decay Rate
k	3.10a, 3.10b, 3.11a	m	Wave Number
ω	3.10a, 3.10b, 3.11a, 3.11b, 3.18, 3.20,	Hz (rads./s)	Angular Frequency
δ_E	3.10a, 3.10b	Degrees (°)	Initial phase angle of the electric field $\vec{E}$
ϕ	3.10b	N/A	Phase Delay of the Magnetic Field $\vec{B}$
ε_r	3.12	N/A	Dielectric Constant
ε_0	3.12, 3.14	Farads per meter (F/m)	Permittivity of free space
μ_0	3.14, 3.15, 3.19, 3.20	N/A	Permeability of Free Space
$\vec{J}$	3.14, 3.19, 3.17	A/m^2	Current Density
$\vec{D}$	3.16	C/m^2	Electric Displacement
β	3.18	N/A	Induction number
s	3.18, 3.19, 3.20	m	Intercoil spacing
δ	3.18	m	Skin Depth
R	3.21	N/A	Response of Secondary Magnetic Field

φ	3.21	V	Electric Potential
A	3.26, 3.27	m	Surface location of Current Electrode A
B	3.26, 3.27	m	Surface location of Current Electrode B
M	3.26	m	Surface Location of Potential Electrode M
N	3.26	m	Surface Location of Potential Electrode N
x	3.26, 3.27	m	Midpoint of Quadrupole

Appendix 2A Tables and Technical Notes for Chapter 2

A2.1 Notable Surface Features of the Gullbridge Tailings Impoundment

Table A2.1: UTM Coordinates of notable features (NAD83, UTM Zone 21N)

Feature	Easting	Northing
Seep	559761	5450593
Old Stream (Upstream)	559833	5450673
Old Stream (Downstream)	559767	5450649
South Abutment	559884	5450242
Northeast Abutment	560173	5451007
Inlet Channel	559807	5450650
Old Culvert	559971	5451005
Old Wood Frame and Pipe	559816	5450350
Spillway	559800	5450373
BH1	559856	5450272
BH2	559790	5450426
BH3	559789	5450547
BH4	559825	5450704
BH5	559877	5450851
BH6	559927	5450977
BH7	560069	5451006
DNR Drone Marker #1	559794	5450504
DNR Drone Marker #2	559798	5450569
DNR Drone Marker #3	559763	5450585
DNR Drone Marker #4	559786	5450570
DNR Drone Marker #5	559793	5450599
DNR Drone Marker #6	559793	5450641

Figure A2.1: Twin-culverts on the upstream side of the embankment in the north (July 2013) (AMEC, 2014).

Figure A2.1 is a photo captured in July 2013 indicating the extent of the corrosion of the twin-culverts in the north.

A2.2 Acid Base Accounting (ABA)

Acid Base Accounting is an analytical technique used to assess the degree to which acid generation has occurred calculated by the balance between acid-production and acid-neutralizing potential (Mills, 2017). Acid-generating sulfides such as pyrite at the Gullbridge site react with water and oxygen to produce sulfuric acid which is detrimental to water quality. Each mole of sulfur produces two moles of acid which can be neutralized by one mole of $CaCO_3$. The standard Sobek method calculates acid potential values based on the samples sulfur concentration in kg $CaCO_3$/t, where the sample is reacted with H_2O_2 to oxidize any sulfide minerals present. The neutralization potential value is calculated by reacting the sample with HCl and back-titrating with NaOH to determine the amount of unreacted HCl in kg $CaCO_3$/t (Actlabs, n.d.). The ratio of the neutralization potential to the acid production potential is calculated as the Neutralization Potential Ratio (NPR) in kg $CaCO_3$/t. If the NPR value is less than 1, the sample is considered acid generating as the acid potential exceeds the neutralization potential (Fey, 2003).

A2.3 Penetration Tests

The Dynamic Cone Penetration Test (DCPT) method involves dropping a sliding hammer attached to a rod with a steel cone fixed to the base. The number of blows required from the hammer to penetrate the ground 300 mm is recorded as the Dynamic Penetration Index (DPI) and plotted versus depth to provide a record of the shearing resistance of the dam materials. 13 DCPTs were carried out over the crest of the Gullbridge dam in the immediate vicinity of the boreholes (Figure 2.3).

Standard Penetration Tests (SPT) were conducted in each of the boreholes using a 50 mm split spoon sampler, similarly, measuring the "blow count" or number of blows required to drive a steel rod 300 mm. The blow count or N-value were plotted on the borehole charts and provided information on the density of the materials (Palla, Gudavalli, Subedi, & Jao, 2008) (Stantec Consulting Ltd., 2012).

Data from DCPT and SPT analysis was used to derive the shearing resistance (kPa) of the material at 0.5 m depth intervals. The undrained shearing resistance was calculated by converting the blows/mm to kips/sq. ft. The undrained shear strength was plotted as mGal on the borehole charts (force per unit area).

A2.4 Borehole and Penetration Test Records

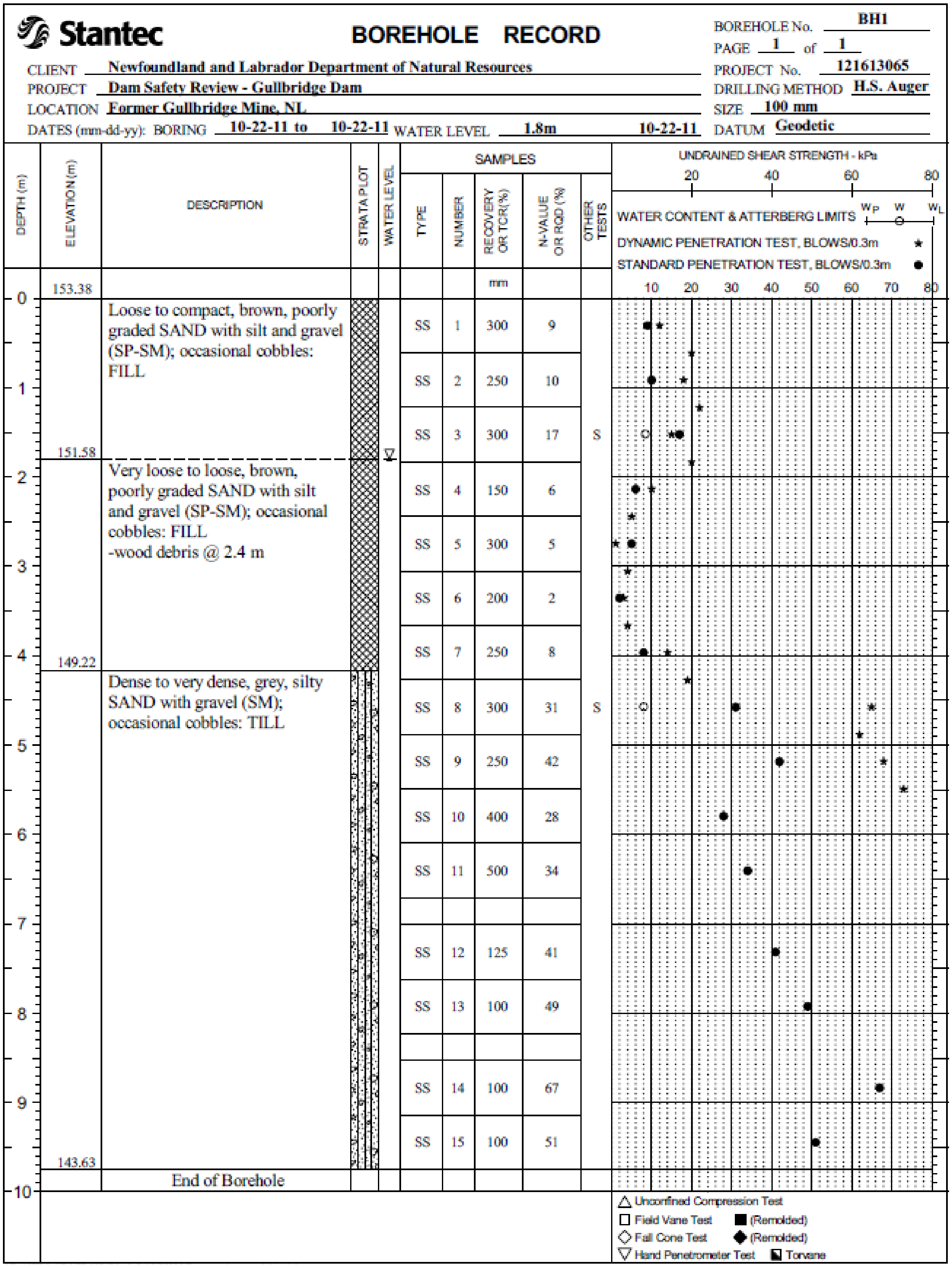

Figure A2.2: Borehole stratigraphy chart over BH1 (Stantec Consulting Ltd., 2012).

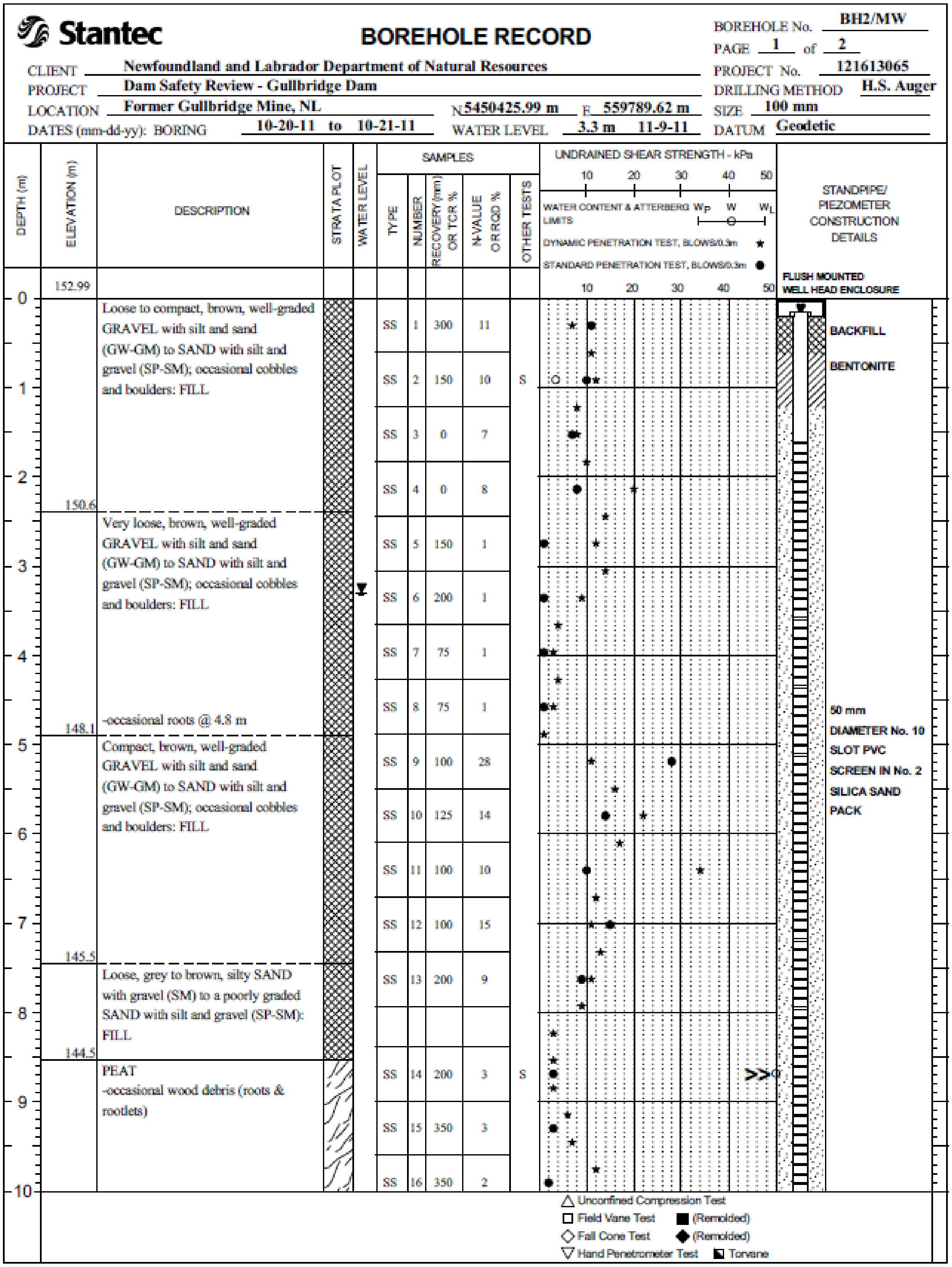

Figure A2.3 (a): Borehole stratigraphy chart over BH2/MW (Stantec Consulting Ltd., 2012).

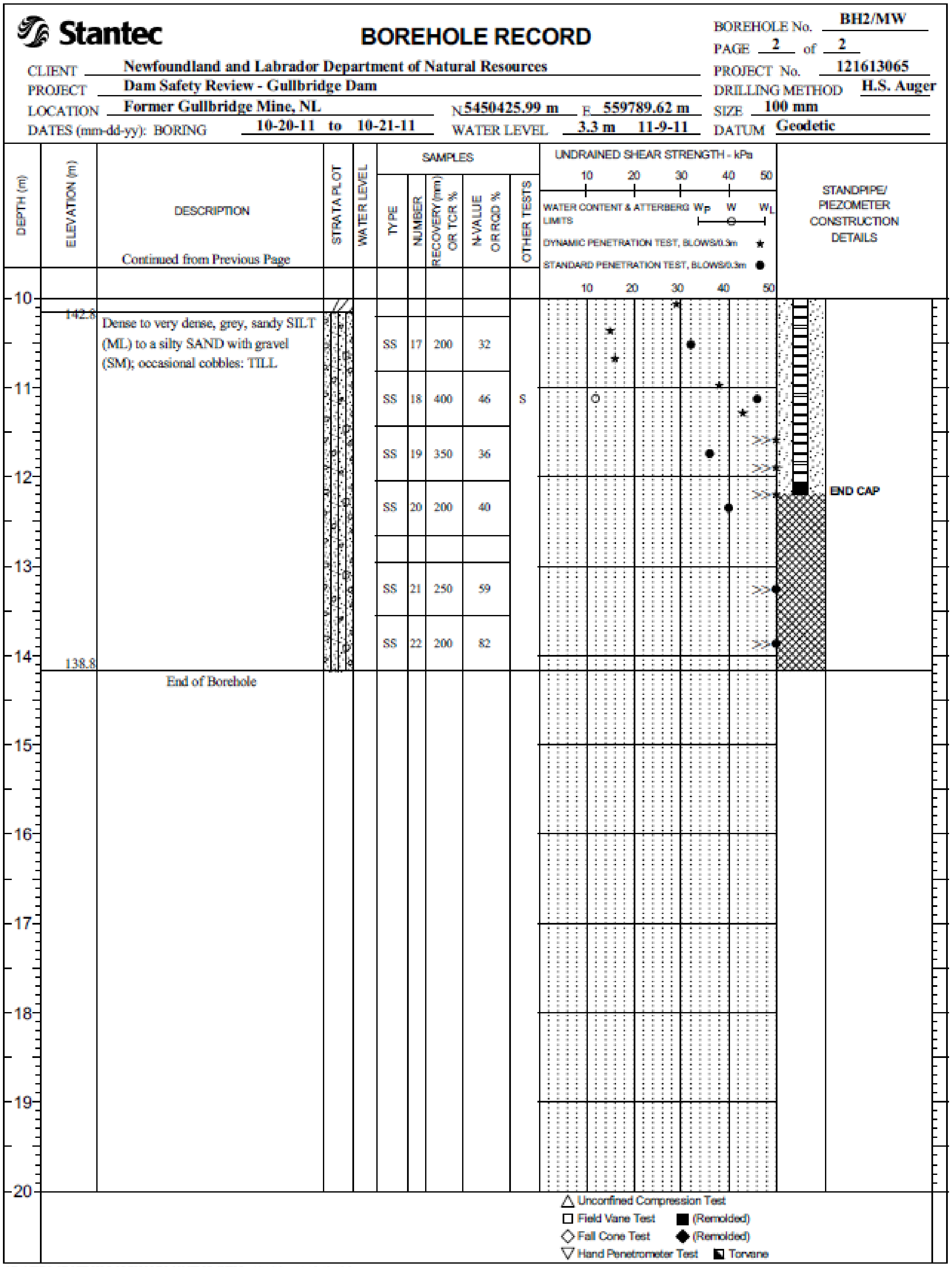

Stantec

BOREHOLE RECORD

BOREHOLE No. BH2/MW
PAGE 2 of 2
PROJECT No. 121613065
DRILLING METHOD H.S. Auger
SIZE 100 mm
DATUM Geodetic

CLIENT Newfoundland and Labrador Department of Natural Resources
PROJECT Dam Safety Review - Gullbridge Dam
LOCATION Former Gullbridge Mine, NL N 5450425.99 m E 559789.62 m
DATES (mm-dd-yy): BORING 10-20-11 to 10-21-11 WATER LEVEL 3.3 m 11-9-11

DEPTH (m)	ELEVATION (m)	DESCRIPTION	STRATA PLOT	WATER LEVEL	TYPE	NUMBER	RECOVERY (mm) OR TCR %	N-VALUE OR RQD %	OTHER TESTS
		Continued from Previous Page							
10	142.8	Dense to very dense, grey, sandy SILT (ML) to a silty SAND with gravel (SM); occasional cobbles: TILL			SS	17	200	32	
11					SS	18	400	46	S
					SS	19	350	36	
12					SS	20	200	40	
13					SS	21	250	59	
14	138.8				SS	22	200	82	
		End of Borehole							

UNDRAINED SHEAR STRENGTH - kPa: 10 20 30 40 50
WATER CONTENT & ATTERBERG LIMITS W_P W W_L
DYNAMIC PENETRATION TEST, BLOWS/0.3m ★
STANDARD PENETRATION TEST, BLOWS/0.3m ●
10 20 30 40 50

STANDPIPE/ PIEZOMETER CONSTRUCTION DETAILS

END CAP

△ Unconfined Compression Test
□ Field Vane Test ■ (Remolded)
◇ Fall Cone Test ◆ (Remolded)
▽ Hand Penetrometer Test ◪ Torvane

Figure A2.3 (b): Borehole stratigraphy chart over BH2/MW (Stantec Consulting Ltd., 2012).

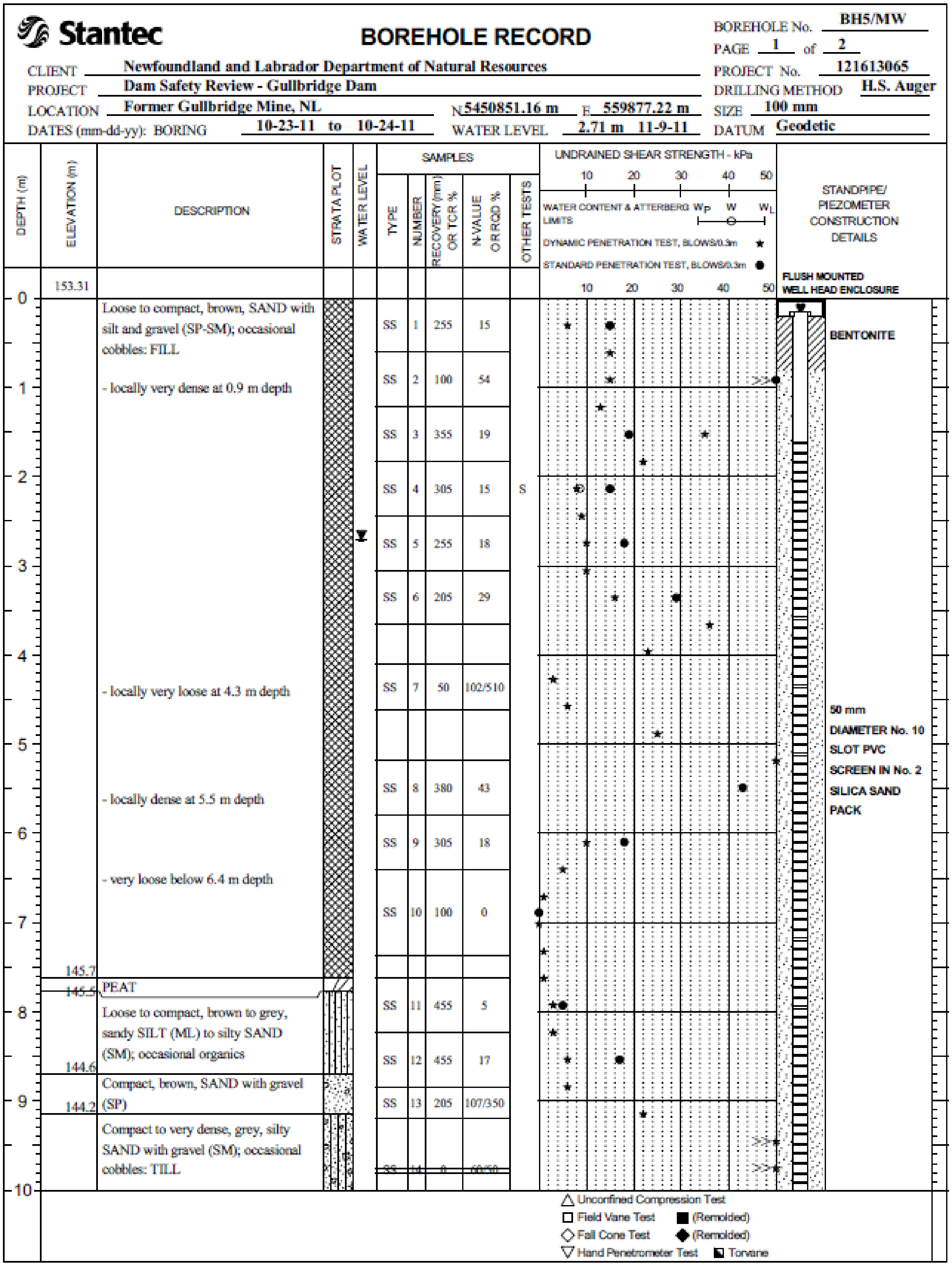

Figure A2.4 (a): Borehole stratigraphy chart over BH5/MW (Stantec Consulting Ltd., 2012).

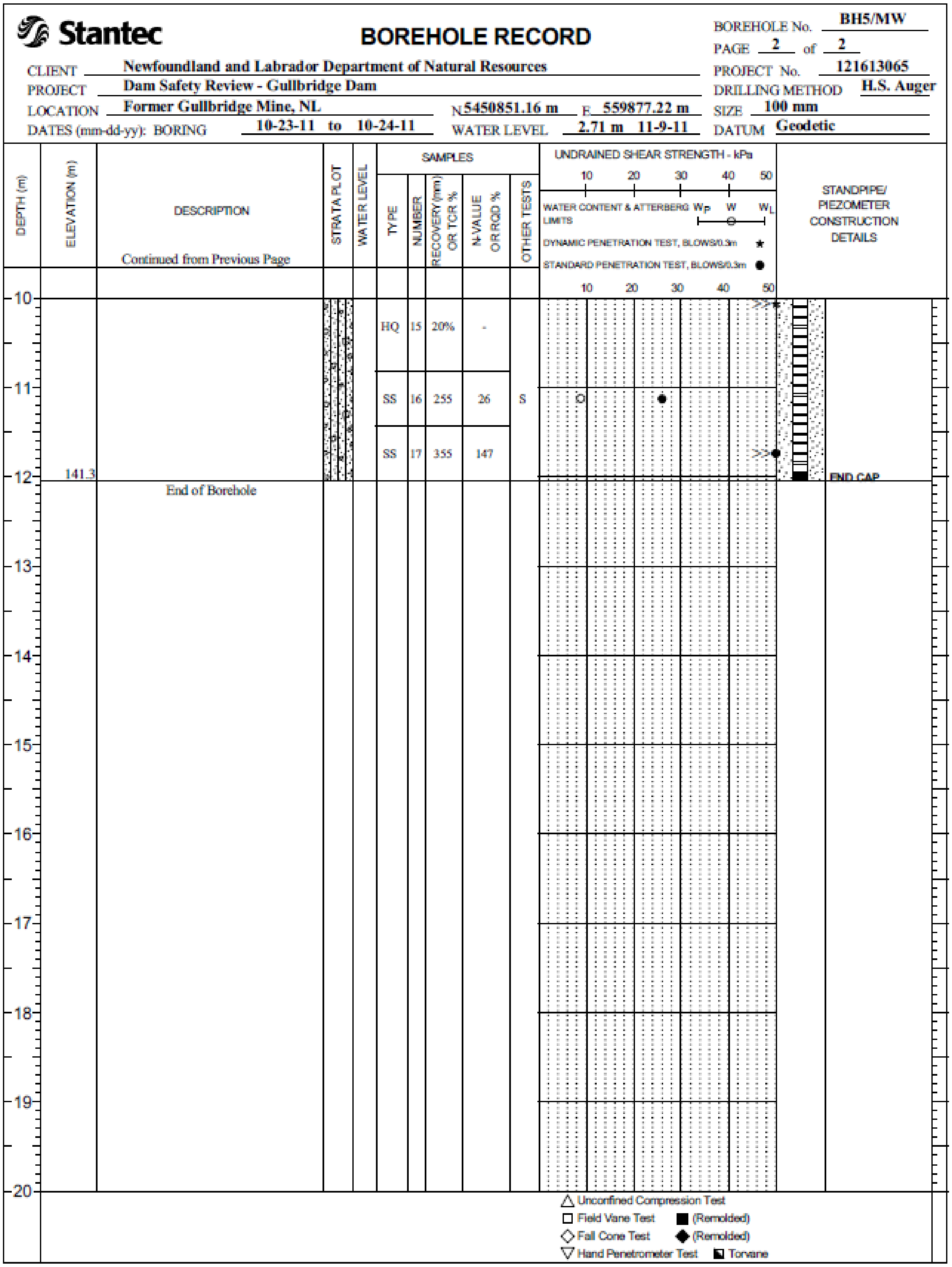

Figure A2.4 (b): Borehole stratigraphy chart over BH5/MW (Stantec Consulting Ltd., 2012).

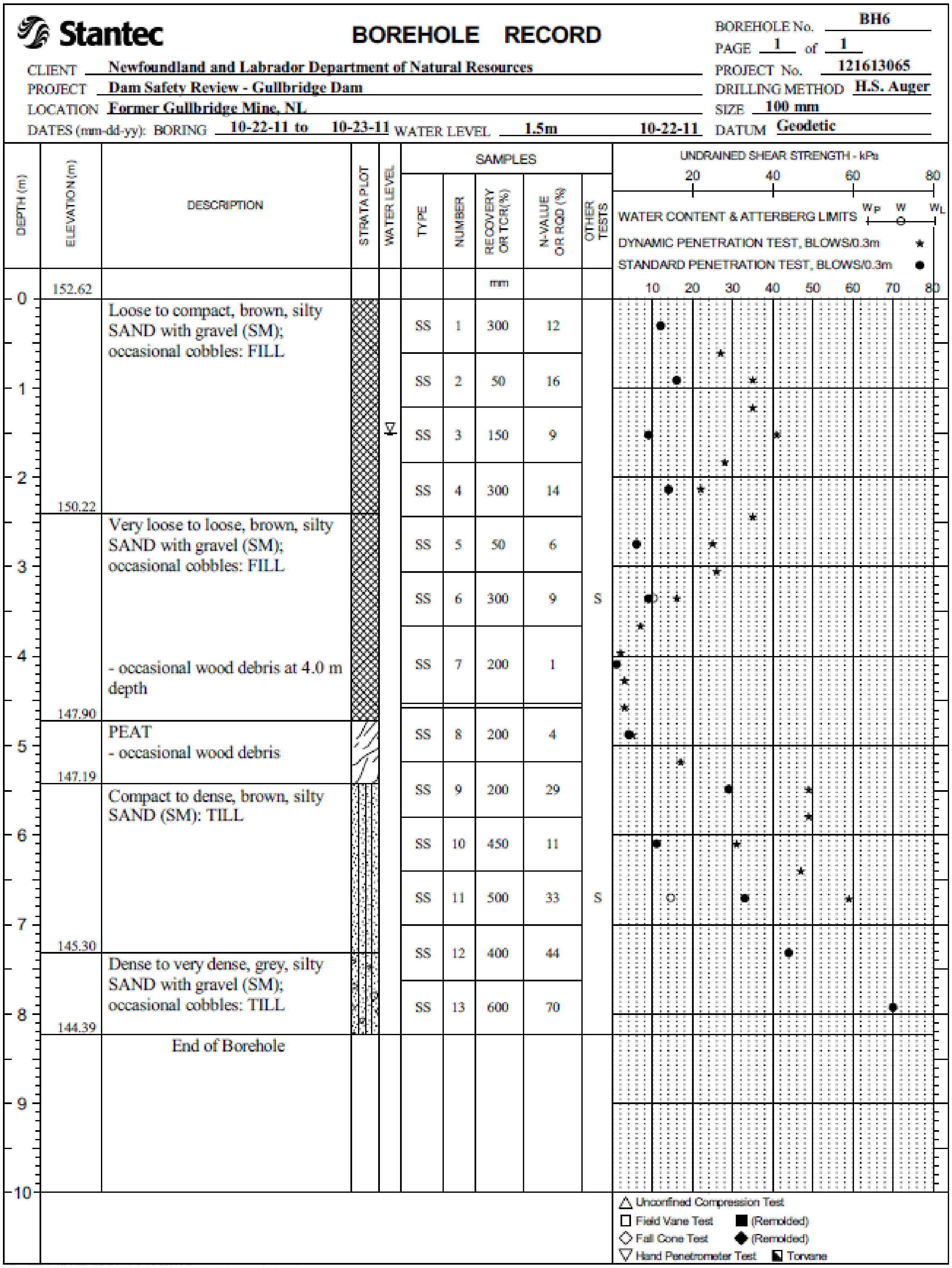

Figure A2.5: Borehole stratigraphy chart over BH6 (Stantec Consulting Ltd., 2012).

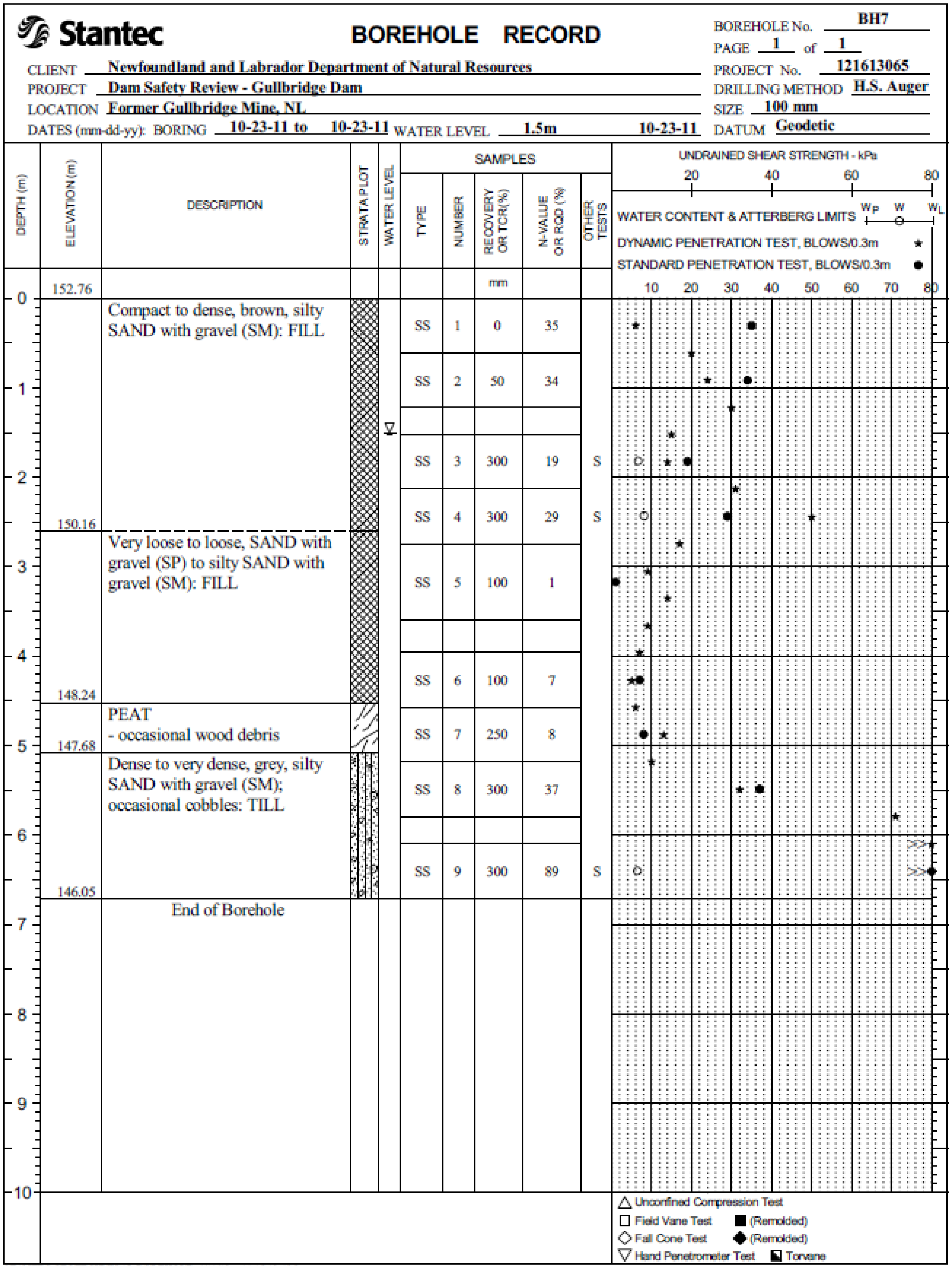

Figure A2.6: Borehole stratigraphy chart over BH7 (Stantec Consulting Ltd., 2012).

A2.5 Factor of Safety & Slope Stability Analysis

The FOS is calculated using slope stability analysis, annual exceedance probabilities and the "Inflow Design Flood" (IDF). IDF uses meteorological data and hydrographs (discharge versus time in the spillway) to determine the hypothetical maximum flood in which the dam could sustain overtopping and subsequent failure. The IDF is also used to estimate spillway capacity and is directly linked to dam classification. These parameters determine whether dams are in compliance with CDA guidelines regulations for safety (Jain & Singh, 2003; Stantec Consulting Ltd., 2012).

The FOS is a commonly used parameter for earth-filled embankments in Canada. It is determined by the ratio of the strength of a material and the stress it is subjected to. In the case of earth-filled dams, it determines whether the embankment has the capacity to carry the load subjected to it by the pressure in the reservoir. The definition is given by:

$$FOS = s_m/s_w \tag{A2.1}$$

where s_m indicates the maximum stress the material can handle before shearing. This material property is normally determined by applying a force to the material in the lab and calculating the magnitude needed to induce structural strain. The parameter s_w indicates the working stress that is subjected to the slope. The CDA guidelines have enforced a minimum FOS of 1.5 to be considered stable (Engineers Edge, 2017; AMEC Environment and Infrastructure, 2013 (c)).

The slope stability analysis for Gullbridge dam was carried out using Geo-Slope International Ltd.'s SLOPE/W software which calculates the FOS based on the Morgenstern-Price two-dimensional limited equilibrium method (1965). This software numerically computes the FOS by descritizing sections of the embankment into vertical slices and assigning each their respective physical properties. The Morgenstern-Price method of analysis considers all interslice forces possible in the slope stability model. The software uses two factor of safety equations: (A2.2) The FOS with respect to the moment equilibrium and (A2.3) the FOS with respect to the horizontal force equilibrium:

$$F_m = \frac{\sum(c'\beta R + (N - u\beta)R \ tan\emptyset')}{\sum Wx - \sum Nf \pm \sum Dd} \tag{A2.2}$$

$$F_f = \frac{\sum(c'\beta cos\alpha + (N - u\beta) \ tan\emptyset' cos\alpha)}{\sum Nsin\alpha - \sum Dcos\omega} \tag{A2.3}$$

where c' is the effective cohesion, $\emptyset'$ is the effective angle of friction, u is the pore water pressure, N is the slice base normal force, W is the slice weight, D is the concentrated point load, α is the inclination of the slice base, and β, R, x, f, d and ω are geometric parameters (GEO-SLOPE International Ltd., 2012).

Values of shear strength were calculated for both drained and undrained peat for the slope stability. Values varied depending on the friction angles and cohesion values used in the calculation of the slope stability analysis.

A2.6 The Rational Formula

The Rational Formula is a commonly used equation that accurately predicts the peak flow of small watersheds. It is an important hydrological tool in the preliminary dam design stages, and is given by:

$$Q = C_f C i A \tag{A2.4}$$

where Q is the peak discharge in L/s, i is the rainfall intensity given in L/s/m^2 and A is the drainage area in m^2. The variable C is the runoff coefficient, a dimensionless quantity relating the total amount of rainfall to surface runoff. The value of the runoff coefficient is dependent on several physical properties influencing losses from the watershed including infiltration, ground slopes, and soil types. The variable C_f is the runoff coefficient adjustment factor used to correct for the occurrence of less frequent, higher intensity storms where losses such as infiltration have a considerably smaller influence on the total runoff (Orogen Department of Transportation, 2014).

A2.7 Surface Water Sampling Results

Table A2.2: July 2013 AMEC Surface Water Sampling Results (AMEC Environment and Infrastructure Ltd., 2014)

			Sample ID	GB-SW01	GB-SW05	GB-SW08	GB-SW02	GB-SW07	GB-SW09	GB-SW03	GB-SW04	GB-SW10
			Easting	0559821	559971	559787	0559771	559970	559780	0560076	560549	560320
			Northing	5450402	5451000	5450677	5450397	5450819	5450680	5450537	5450768	5450400
			Description	Tailings Pond		Tailings Seepage	Downstream Toe		Diluted Seepage	Tailings Creek		
Physical Parameters	**Units**	**Sched A***	**MISA****									
pH	pH	5.5 - 9		**4.34**	**3.89**	**4.68**	7.17	7.25	7.14	6.06	7.23	6.02
Conductivity	uS/cm			340	350	280	340	67	210	250	82	210
Total Suspended Solids	mg/L	30	30	2.6	5.4	30	18	3.4	2.4	**74**	<1.0	**42**
Nitrate (N)	mg/L	10		<0.050	<0.050	0.22	0.074	0.15	<0.050	0.058	<0.050	<0.050
Anions												
Dissolved Chloride (Cl)	mg/L			2.8	3.0	2.8	2.7	2.8	1.4	1.9	3.0	2.4
Nitrogen (Ammonia Nitrogen)	mg/L	2		<0.050	<0.050	0.14	0.37	0.29	0.097	0.098	0.057	0.13
Orthophosphate (P)	mg/L	1		<0.010	<0.010	<0.010	<0.010	<0.010	0.010	<0.010	<0.010	<0.010
Dissolved Sulphate (SO4)	mg/L			150	150	110	37	8.7	70	110	5.6	88
Metals												
Total Arsenic (As)	ug/L	500	1000	<1.0	<1.0	<1.0	8.9	<1.0	<1.0	<1.0	<1.0	<1.0
Total Barium (Ba)	ug/L	5000		44.9	39.9	26.4	25.4	12.7	19.7	91.0	45.4	54.5
Total Boron (B)	ug/L	5000		<50	<50	<50	<50	<50	<50	<50	<50	<50
Total Cadmium (Cd)	ug/L	50		0.314	0.249	0.202	0.057	0.023	0.024	0.107	<0.010	0.100
Total Chromium (Cr)	ug/L	50		<1.0	2.2	27.0	1.2	<1.0	1.3	2.4	1.2	<1.0
Total Copper (Cu)	ug/L	300	600	***706***	***733***	89.5	4.8	3.4	12.6	**442**	13.6	45.6
Total Iron (Fe)	ug/L	10000		200	481	1540	**13700**	1640	1350	**20900**	2110	1830
Total Lead (Pb)	ug/L	200	400	<0.50	<0.50	<0.50	<0.50	<0.50	<0.50	<0.50	<0.50	<0.50
Total Nickel (Ni)	ug/L	500	1000	79.8	81.5	30.1	<2.0	<2.0	5.9	34.8	<2.0	36.7
Total Phosphorus (P)	ug/L	0.5		<100	<100	<100	<100	<100	<100	<100	<100	<100
Total Selenium (Se)	ug/L	10		<1.0	<1.0	<1.0	<1.0	<1.0	<1.0	<1.0	<1.0	<1.0
Total Silver (Ag)	ug/L	50		<0.10	<0.10	<0.10	<0.10	<0.10	<0.10	<0.10	<0.10	<0.10
Total Zinc (Zn)	ug/L	500	1000	73.7	72.6	74.0	<5.0	12.9	15.4	39.8	<5.0	33.8

A2.8 Tailings Sampling Results

Table A2.3: Total Metal Contents of Tailings Solids (AMEC, 2013)

		Average Continental Crust	Location #3-30 cm	Location #3-60 cm	Location #5-30 cm	Location #5-60 cm	GB-TP1-1	GB-TP2-1	GB-TP3-1	GB-TP4-1	GB-TP5-1	GB-TP6-1	GB-TP7-1	GB-TP8-1	GB-TP9-1	GB-TP10-1	GB-TP11-1	Deep Samples Minimum	Deep Samples Average	Deep Samples Median	Deep Samples Maximum
Hg	µg/g	0.09	-	-	-	-	0.08	<0.05	<0.05	0.06	<0.05	<0.05	0.06	0.06	0.08	0.07	<0.05	<0.05	0.06	0.06	0.08
Al	µg/g	82300	73862	70453	73159	65854	37000	36000	26000	30000	25000	27000	25000	25000	33000	36000	28000	25000	40755	33000	73862
As	µg/g	1.8	3.6	5.0	7.6	9.2	5.6	6.1	6.2	5.4	5.9	8.0	6.0	6.7	6.2	5.5	5.9	3.6	6.2	6.0	9.2
Ba	µg/g	425	560	507	289	472	390	240	230	330	160	190	160	200	240	360	200	160	302	240	560
Be	µg/g	3.0	0.4	0.3	0.3	0.3	0.10	0.11	0.09	0.10	0.09	0.09	0.07	0.08	0.09	0.10	0.11	0.07	0.15	0.10	0.35
Bi	µg/g	0.01	<5	<5	<5	<5	**1.2**	**0.86**	**0.71**	**1.1**	**0.76**	**0.96**	**0.82**	**0.88**	**1.0**	**1.0**	**0.66**	0.66	2.0	1.0	5.0
Ca	µg/g	41500	9451	9256	5992	8799	7700	5600	7400	6000	4900	5600	3200	4600	5300	6600	7800	3200	6547	6000	9451
Cd	µg/g	0.2	0.6	0.7	0.4	0.5	0.42	0.35	0.26	0.43	0.38	0.49	0.29	0.28	0.32	0.38	0.40	0.26	0.41	0.40	0.69
Co	µg/g	25	151	133	192	148	96	93	98	110	110	140	130	130	120	89	93	89	122	120	192
Cr	µg/g	102	277	278	389	389	120	130	140	170	180	220	240	220	190	120	170	120	215	190	389
Cu	µg/g	60	1058	1038	1926	836	**1300**	510	**830**	**1100**	**910**	**1100**	**1560**	**1200**	**740**	**1000**	**610**	510	1048	1038	1926
Fe	µg/g	56300	172940	182790	200731	216421	120000	120000	130000	130000	140000	180000	160000	190000	150000	120000	140000	120000	156859	150000	216421
K	µg/g	20850	2929	2339	1822	2000	770	540	610	850	430	450	450	700	600	790	510	430	1053	700	2929
Li	µg/g	20	17.7	17.4	13.6	16.2	10	9	7	8	6	7	5	7	7	9	8	5.00	10	8.0	18
Mg	µg/g	23300	39578	42161	42910	39277	26000	24000	17000	20000	16000	18000	17000	17000	23000	25000	20000	16000	25795	23000	42910
Mn	µg/g	950	1333	1560	1384	1504	560	550	430	470	420	490	420	440	520	530	630	420	749	530	1560
Mo	µg/g	1.2	1.0	1.1	1.1	1.0	2.0	2.1	1.7	1.9	2.3	2.0	1.6	1.7	1.5	1.6	1.8	1.0	1.6	1.7	2.3
Na	µg/g	23550	4018	3613	1974	2549	330	260	230	280	180	160	180	230	230	330	230	160	986	260	4018
Ni	µg/g	84	150	139	170	137	69	76	72	81	97	110	110	100	91	56	81	56	103	97	170
P	µg/g	1050	935	998	907	933	1400	1100	1500	1100	870	890	750	850	860	1400	1000	750	1033	935	1500
Pb	µg/g	14	5.3	5.6	4.5	4.6	16	5.6	5.6	15	7.3	11	7.6	7.7	8.1	9.8	7.3	4.5	8.1	7.3	16
Sb	µg/g	0.2	<2	<2	<2	<2	<0.8	<0.8	<0.8	<0.8	<0.8	<0.8	<0.8	<0.8	<0.8	<0.8	<0.8	<0.8	1.1	0.8	2.0
Se	µg/g	0.1	-	-	-	-	**8.8**	**7.6**	**10**	**2.6**	**12**	**15**	**16**	**16**	**13**	**8.1**	**8.6**	2.6	11	10	16
Sn	µg/g	2.3	<2	<2	3	<2	0.5	0.6	<0.5	0.5	<0.5	0.7	<0.5	0.5	<0.5	0.5	0.6	0.50	1.0	0.5	3
Sr	µg/g	370	48	52	31	40	15	14	15	14	11	11	8.2	11	11	15	14	8.2	21	14	52
Ti	µg/g	5650	6408	6676	6457	6986	680	570	610	510	380	450	380	440	510	650	520	380	2148	570	6986
Tl	µg/g	0.9	<5	<5	<5	<5	0.04	0.03	0.03	0.04	0.03	0.04	0.02	0.03	0.03	0.05	0.04	0.02	1.4	0.04	5
U	µg/g	2.7	0.68	0.64	0.87	0.72	0.20	0.23	0.19	0.17	0.14	0.17	0.16	0.13	0.17	0.17	0.15	0.13	0.32	0.17	1
V	µg/g	120	230	243	258	280	120	130	160	150	190	240	210	230	170	120	170	120	193	190	280
Y	µg/g	33	19	25	19	21	7.7	7.4	9.0	6.1	5.4	5.4	4.6	5.2	5.3	7.6	7.0	5	10	7.4	25
Zn	µg/g	70	191	221	123	137	100	83	59	100	74	85	62	69	72	87	84	59	103	85	221

Figure A2.7: Image of TP-7 captured on July 10th, 2013 (NL. AMEC Environment & Infrastructure, 2014).

Figure A2.7 displays an image captured at the site of TP-7 on the eastern extent of the reservoir, dug to the maximum depth of 7 m. This was achieved due to the solidity of the ground relative to other test pits. Two geochemically distinct layers were encountered. From the surface to a depth of 0.5 m a sandy and dusty layer with a thick reddish-orange-yellow hardpan was encountered. An underlying damp grey-black tailings unit extending depth was found to be less saturated than previous tailings within the test pit trench. The degree of saturation in all test pits was quite variable. Similar to TP-2, the pH increased from the red layer (3.4) to the grey-black layer (6) (AMEC, 2013).

A2.9 Peat Thickness Measurements

Table A2.4 Locations of boreholes (BH) and bog probes (BP) and corresponding peat thickness measurements (m) under and near the Gullbridge dam embankment (Figure 1.1). “Dist.” is the distance (m) measured along the embankment from BH1 for the boreholes, and for the bog probes where they would be if extrapolated back perpendicular to the embankment.

Embankment					Toe						Downstream			
Station	Depth	Easting	Northing	Dist.	Station	Depth	Easting	Northing	Dist.	Station	Depth	Easting	Northing
BH1	0	559856	5450272	0									
					BP-24	0.6	559820	5450292	32				
					BP-1	1.5	559805	5450333	76	BP-2	1.5	559795	5450327
BH2	1.6	559790	5450426	168	BP-3	2.1	559783	5450408	151	BP-4	1.7	559770	5450405
					BP-22	1.5	559780	5450464	205	BP-23	1.7	559770	5450462
BH3	0.4	559789	5450547	289	BP-5	1.8	559774	5450537	278	BP-6	1.5	559760	5450537
					BP-7	1.8	559789	5450650	393	BP-8	1.8	559776	5450650
BH4	0.6	559825	5450704	450	BP-9	1.8	559809	5450696	435	BP-10	3	559796	5450701
									450	BP-11	3	559793	5450709
					BP-20	1.5	559838	5450783	534	BP-21	3	559828	5450785
BH5	0.2	559877	5450851	606	BP-12	1.5	559859	5450845	595	BP-13	1.8	559850	5450847
BH6	0.7	559927	5450977	742	BP-14	1.2	559905	5450974	731	BP-15	0.6	559897	5450975
					BP-16	1.8	559960	5451005	780	BP-17	2	559957	5451013
BH7	0.6	560069	5451006	886	BP-18	1.8	560010	5451015	830	BP-19	1.8	560008	5451024

A2.10 Seep Water Analysis, 2016

Table A2.5: Chemical analysis results of water samples collected in November 2016 at the seep location and within the impoundment respectively.

Maxxam ID		DJZ474		DJZ475		
Sampling Date		2016/11/02		2016/11/02		
COC Number		N/A		N/A		
	UNITS	SEEP	QC Batch	IMPOUNDMENT	RDL	QC Batch
Metals						
Total Aluminum (Al)	mg/L	15	4746360	32	0.0050	4746538
Total Antimony (Sb)	mg/L	ND	4746360	ND	0.0010	4746538
Total Arsenic (As)	mg/L	ND	4746360	ND	0.0010	4746538
Total Barium (Ba)	mg/L	0.037	4746360	0.028	0.0010	4746538
Total Boron (B)	mg/L	ND	4746360	ND	0.050	4746538
Total Cadmium (Cd)	mg/L	0.0013	4746360	0.0022	0.000010	4746538
Total Calcium (Ca)	mg/L	45	4746360	45	0.10	4746538
Total Chromium (Cr)	mg/L	ND	4746360	0.0034	0.0010	4746538
Total Copper (Cu)	mg/L	1.8	4746360	2.7	0.0020	4746538
Total Iron (Fe)	mg/L	0.30	4746360	10	0.050	4746538
Total Lead (Pb)	mg/L	ND	4746360	0.00054	0.00050	4746538
Total Magnesium (Mg)	mg/L	29	4746360	44	0.10	4746538
Total Manganese (Mn)	mg/L	1.3	4746360	1.7	0.0020	4746538
Total Nickel (Ni)	mg/L	0.29	4746360	0.49	0.0020	4746538
Total Potassium (K)	mg/L	0.86	4746360	1.0	0.10	4746538
Total Selenium (Se)	mg/L	ND	4746360	ND	0.0010	4746538
Total Sodium (Na)	mg/L	3.4	4746360	4.1	0.10	4746538
Total Strontium (Sr)	mg/L	0.064	4746360	0.067	0.0020	4746538
Total Uranium (U)	mg/L	ND	4746360	0.00021	0.00010	4746538
Total Zinc (Zn)	mg/L	0.27	4746360	0.47	0.0050	4746538

RDL = Reportable Detection Limit
QC Batch = Quality Control Batch
ND = Not detected

Appendix 3A Tables and Technical Notes for Chapter 3

A3.1 The Vadose Zone

A sharp interface could be masked due to capillary fringe within the dam wall.

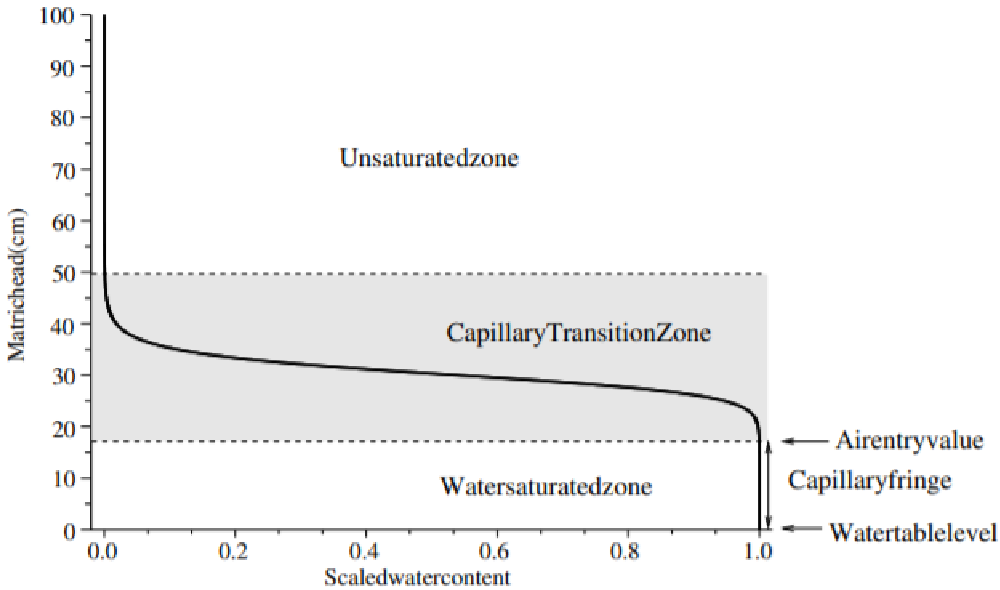

Figure A3.1: Theoretical Model of capillary fringe between water saturated and unsaturated zones within the dam wall displaying soil water retention curve (Saintenoy & Hopmans, 2011).

Capillarity occurs when liquid from the water table rises through the pore space of a material due to due to a combination of interfacial cohesive and adhesive forces at the water/solid interface quantified collectively as "surface tension". Figure A3.1 displays a theoretical model of capillary fringe and the corresponding water retention curve which relates water content θ to the soil water potential or the height of the water column (cm) corresponding to a particular pressure h. In the figure, the water table depth is defined by the depth where the water pressure h=0 (bottom of the vertical axis). The capillary fringe is located within the saturated zone but occurs at low soil pressures. The base of the capillary fringe marks the air-entry value at which the soil begins to de-saturate. The area between the air-entry value and the unsaturated (vadose) zone is the capillary transition zone, which is believed to be the primary mechanism behind masking the water table interface in the DCR inversions. In the capillary transition zone, θ decreases sharply as h decreases along the retention curve. This progressive infiltration of water through the pore space of the dam upwards will increase in materials as the pore space decreases. It is believed the capillary transition zone extend upwards to the base of the highly resistive near-surface layer in the inversion models in Section 4.3, masking the sharp interface between the dam fill and the saturation zone (Or & Tuller, 2005) (Sonnenberg & Selley, 2015) (Arthur & Saffer, n.d.) (Saintenoy & Hopmans, 2011).

A3.2 Supplementary ICP-OES and ICP-MS Notes

The ICP-OES is a quick and reliable method with a good limit of detection, and is an effective tool in particular for determining concentrations of base metals such as copper and zinc.

In ICP-OES analysis, a finely ground sample is heated by a high-voltage electrical source to temperatures in the range of several thousand degrees Celsius. This excites the atoms in the sample to a high-energy vaporized state within a discharge plasma. The atoms subsequently relax and emit electromagnetic radiation in the UV and visible spectrum and this light is analysed by a spectrometer (Shimadzu Corp., 2018) (Kochmann, 2018)

The OES computer is designed to handle large amounts of wavelength and intensity data. The analyst can construct graphs of peak intensity versus wavelength to determine the elemental composition and concentration. Figure A3.2 illustrates an example (Kochmann, 2018).

Inductively coupled plasma – mass spectrometry (ICP-MS) was the analytical tool used to measure trace elements of metals present in the groundwater samples collected at the Gullbridge site. Mass spectrometry determines the elemental composition of a sample by converting liquid samples to gas-phase ions and separating the ions based on their mass to charge ratio (de Hoffman & Stroobant, 2007). The general setup of the equipment used in the ICP-MS process is illustrated in Figure A3.3.

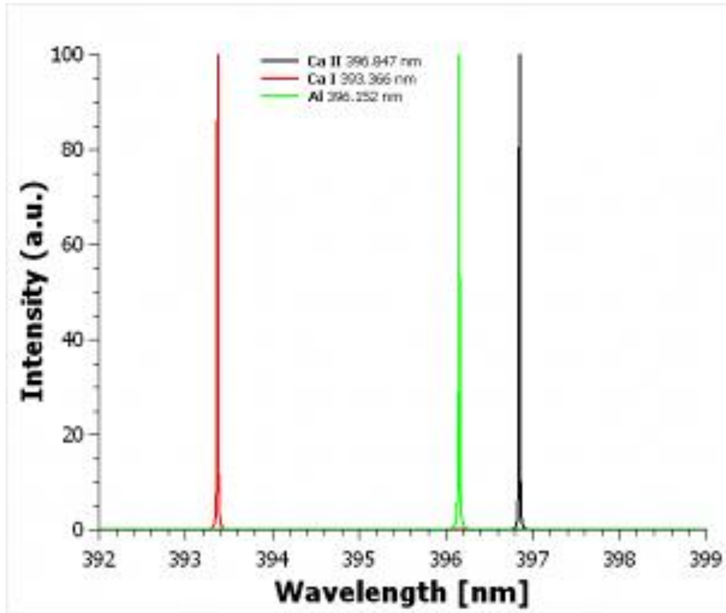

Figure A3.2: Example of spectral analysis graph displaying light intensity peaks associated with calcium (in two oxidation states) and aluminum (Kochmann, 2018).

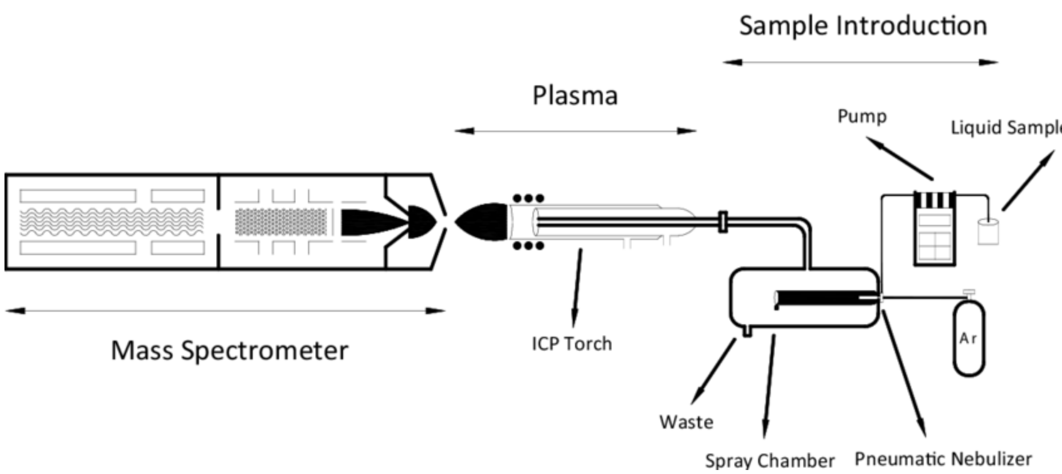

Figure A3.3: General setup of ICP-MS method (Kashani & Mostaghimi, 2016).

Droplets of the liquid sample are pumped through a pneumatic nebulizer chamber where they are nebulized into an aerosol using Argon gas. Only a fraction of the aerosol is actually introduced to the ICP torch, and the majority is caught in a waste drain (Bazilio & Weinrich, 2012).

The aerosol sample is next passed into the ICP-torch (Figure A3.3) which converts the atoms of the elements in the sample to ions. (Bazilio & Weinrich, 2012) (Dunnivant, 2008).

In the spectrometer, ions are separated and detected based on their mass to charge (m/z) ratios. A detector receives this information and sends a digital signal to a computer recorder, which generate elemental composition data based on the intensity of the spectra versus the m/z ratio (de Hoffman & Stroobant, 2007).

A3.3 Supplementary GPR Field Method Notes

The GPR survey parameters are chosen based on the nature of the investigation, and can be manipulated to enhance particular features based on the geometry of the subsurface. The acquisition mode used to collect data over the Gullbridge dam and the bogs to the west was the “reflection mode”, which continually collects reflection traces along the line creating a profile image of the subsurface (Sensors and Software Inc., 2006).

The triggering method used for the data acquisition over the Gullbridge Dam varied between “free-run” and odometer mode. The free-run mode setting triggers electromagnetic pulses at a constant time-interval (Sensors and Software Inc., 2006). The time interval is chosen based on the velocity at which the GPR is pushed along the ground. The GPR can only collect UTM coordinates from a GPS if the “free-run” acquisition method is enabled. Therefore, it was the appropriate choice for acquiring GPR data in in large surveys where it is impractical to lay out straight lines or grids, and/or where the surface is not suitable for the smart-cart. The odometer setting triggers electromagnetic pulses based on a fixed distance measured by a spinning odometer wheel interlocked to the rear-wheel of the Smart-cart assembly.

It is necessary before beginning a survey using the odometer wheel that the odometer wheel be calibrated ensuring the horizontal axis of the acquired GPR profiles yields true surface distances. Therefore, for Smart-cart surveys along the dam crest, 100 m of survey tape was laid out flat along the dam, and the GPR was pushed along the tape from x=0 to x=100 m in the odometer calibration mode on the digital video logger.

The time window chosen determines how long the electromagnetic pulses will probe the subsurface. Therefore it determines how deep the pulses will penetrate the ground (Sensors and Software Inc., 2016). During the first trip to Gullbridge, data was acquired using the default time-window for the 100 MHz antenna of 200 ns, but this was not long enough to probe the area underneath the embankment. The following trips employed time-windows varying from 200 – 800 ns in an attempt to further the investigation depth of the survey (Sensors and Software Inc., 2006).

The signal to noise ratio decreases with depth, limiting the effective depth penetration. A way of increasing depth penetration is by increasing the system stacking. This allows for the GPR to record multiple readings at each data collection point and add the data traces for improved signal to noise (Sensors and Software Inc., 2006). The GPR surveys conducted over the Gullbridge TMA were carried out using 16 stacks, as well as research the DynaQ stacking option. The DynaQ stacking option chooses stacking relative to the speed of the smart-cart. Over areas of particular interest the GPR was pushed slowly in order to increase the number of stacks, effectively increasing the signal-to-noise (Sensors and Software Inc., 2006).

The step size is the sampling distance the antennae pair will be moved before the system collects a new trace, and the optimum step size is chosen based on the antenna wavelength. If the step size is too large, certain subsurface targets of interest will be lost due to too little sampling, and step-sizes too small result in the collection of redundant data (Sensors and Software Inc., 2006).

Figure A3.4 displays the scope mode screen of the DVL used in the initial setup of a GPR survey. The scope mode is a calibration tool used to time-zero the radar pulse after the survey parameter have been chosen and is generally done to correct a time offset associated with the first large reflection, arrival or “first break” in the radar trace. This is an important step to perform especially after switching equipment such as fiber optic cables and the antennae frequency, as different electrical components change the transmission rate of the radar pulse. The time-zero is essentially a reference point of for the start of the trace. If time-zero is off, may be discrepancies in the depths of interpreted interface.

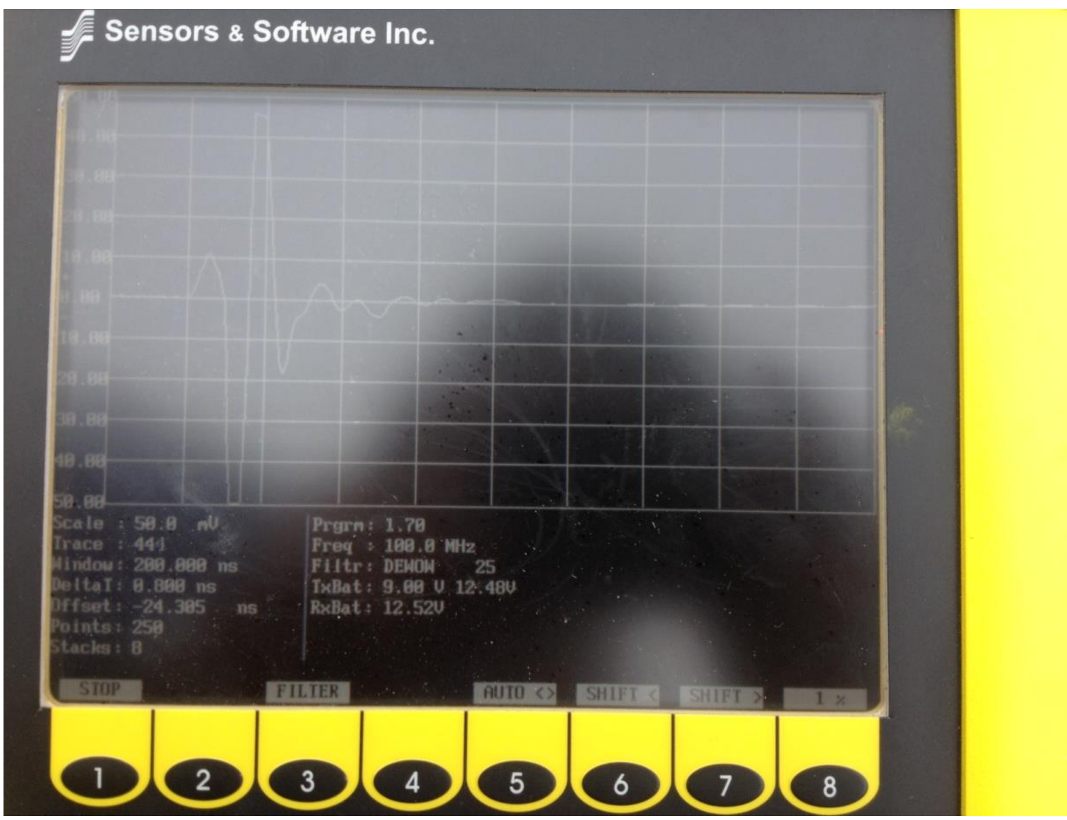

Figure A3.4: DVL screen displaying “scope mode” during the survey setup phase of the GPR survey.

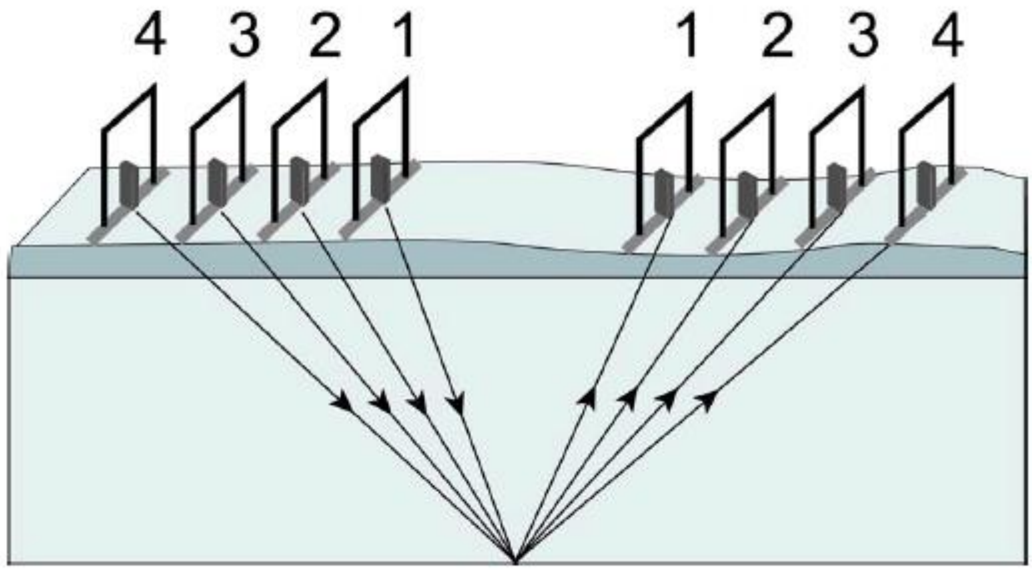

Figure A3.5: CMP survey geometry used to determine the GPR radar velocity in a particular subsurface medium (Sensors and Software Inc., 2006).

A CMP/WARR is performed by changing the antennae separation from a "common mid-point" on the surface and using a line of best fit in specified software to derive an average velocity from a series of reflectors. It is best used in an area of flat-lying reflectors. The geometry of the CMP survey is conveyed in Figure A3.5. The survey is conducted by laying out a survey tape and continually changing the antennae separation starting from the middle by a fixed increment. The longer the survey tape used, and thus the more measurements taken generally yields a more accurate velocity, as the greater the change in the antennae separation results in more reflections effectively increasing the signal path length/time from the mid-point reflector. The travel time is averaged out and the average velocity for the subsurface is calculated. The antennae are not fixed to the smart-cart in this case, but rather are carried separately by the surveyor. The survey generally requires two people or more, and requires the 20 m fiber optical cables rather than the standard 5 m. One person continually changes the antennae separation by a fixed increment while another person stands at the common mid-point triggering each individual trace using the DVL (Sensors and Software Inc., 2006).

The step size for a CMP/WARR is typically programmed for double the distance each antenna will move. For the 100 MHz antennae, the step-size is normally set to 0.25 m.

A3.4 Supplementary DCR Data Processing Notes

Prosys

Prosys software has the capability of generating pseudo-sections of resistivity and chargeability. In a pseudo-section, the apparent resistivity or chargeability is plotted at a position of *x* corresponding to the center of the quadrupole at a pseudo-depth of a. The Wenner array emphasizes near-surface lateral variations in chargeability and resistivity, whereas the Schlumberger array generates a pseudo-section that “sees” deeper as the current electrodes expand about the potential pair. The Wenner array displays a total depth level of n=7 and the Schlumberger reaches a total depth level of n=11, consistent with the maximum depth level achieved by the Memorial University DCR system. Each of the a-spacings (a=1, a=2, a=3) will generate data points in the first 3 rows respectively using different potential pairs across the spread with the same a-spacing. Each of the columns of data points over the same location of *x* at different a-spacings are the data points used in VES modelling (Geotomo Software, 2010).

RES2DINV

Designed by deGroot-Hedlin and Constable 1990, and Sasaki 1992, the RES2DINV inversion follows the equation:

$$(J^T J + uF)d = J^T g \tag{A3.1}$$

where $F = f_{xx}{}^{T} + f_{zz}{}^{T}$, f_x =horizontal flatness filter and f_z =vertical flatness filter, J =matrix of partial derivatives, u =damping factor, d =model perturbation vector and g =discrepancy vector (Terraplus, 2001).

This method works by trying to reduce the difference between the calculated and measured apparent resistivity values by modifying the resistivity of the model blocks by minimizing the sum the squares of the residuals. The measure of this difference is given by the RMS error. However, these models are non-uniform and often RMS error alone is not enough to indicate the reliability of the model, as models with low RMS error can show large and variations in subsurface resistivity models that are unrealistic from a geological perspective (Terraplus, 2001).

The inversion requires a specific formatting to address the constraints of the inversion and the type of inversion being performed. Table A3.1 indicates both the "general array format" which can be used for any array, and the "index-based format" used for conventional array styles such as Wenner and Schlumberger.

Table A3.1: Data formatting for RES2DINV using the "general array" and "index based" format.

General Array Format										Index Based Data Format			
	A		B		M		N		rho	x	b	n	rho
4	15	0	21	0	17	0	19	0	7440	18	2	1	7440
4	15	0	25	0	19	0	21	0	2920	20	2	2	2920

As an example, the general array format uses the positions of the A, B, M and N electrodes along with the corresponding apparent resistivity at that geometrical configuration. The index-based data format instead uses 3 different parameters. The first column is the midpoint of the sounding x. The second column is the b-spacing. Lastly, the n-factor or the skin depth (depth level) of the reading is calculated by dividing the distance between the outer current electrode and the closest potential electrode (C_1-P_1 or C_2-P_2) over the distance between the two inner potential electrodes. As an example:

$$n = \frac{(M-A)}{(N-M)} \text{ or } n = \frac{(B-N)}{(N-M)} \tag{A3.2}$$

Table 3A displays the difference between formatting data points using a general array data format and index-based data format. To match the DCR line to YLINE5 of the GPR grid as previously demonstrated, 15, 27, and 39 were added to the positions along A,B,M and N of the south, center and northern extension respectively to correlate to YLINE5. For the index-based format, 15 was added to each midpoint of the array. As you can see, the n-factor changes when the a-spacing changes. Therefore, as the a-spacing increases the n-factor increases. Note there is no change in the b-spacing signifying that the Schlumberger array was used.

Table A3.2 is similar to Table A3.1 with the addition of rows containing the surface locations of each of the soundings *x* and their corresponding elevation values in meters above sea level (masl). The extension of the inversion sheet begins with a heading labelled “topography” used as a header to indicate a separate data file within the inversion sheet. The cell labelled 2 indicates that the distance is measured in surface distances, and the cell

Table A3.2: Table displaying additional elevation information required for RES2DINV format for displaying topography along the 2 m electrode spacing Schlumberger DCR survey over the seep area.

4	62	0	68	0	64	0	66	0	12539
4	64	0	70	0	66	0	68	0	12436
Topo...									
2									
36									
15	151.52								
17	151.53								
83	151.50								
85	151.50								
1									
0									
0									
0									
0									

labelled 36 indicates there are 36 elevation points being added to the dataset. The first two and last two elevation stations along YLINE5 of the June 2017 GPR grid are displayed in Table A3.2 with the station number along YLINE5 and the associated elevation listed in the immediate column. The cell 1 indicates that the first elevation point lies over electrode 1, and as a formatting requirement for the general array a column of 4 zeroes are added to the data (LLC, Landviser;, 2012).

A3.5 Supplementary GPR Data Processing Notes

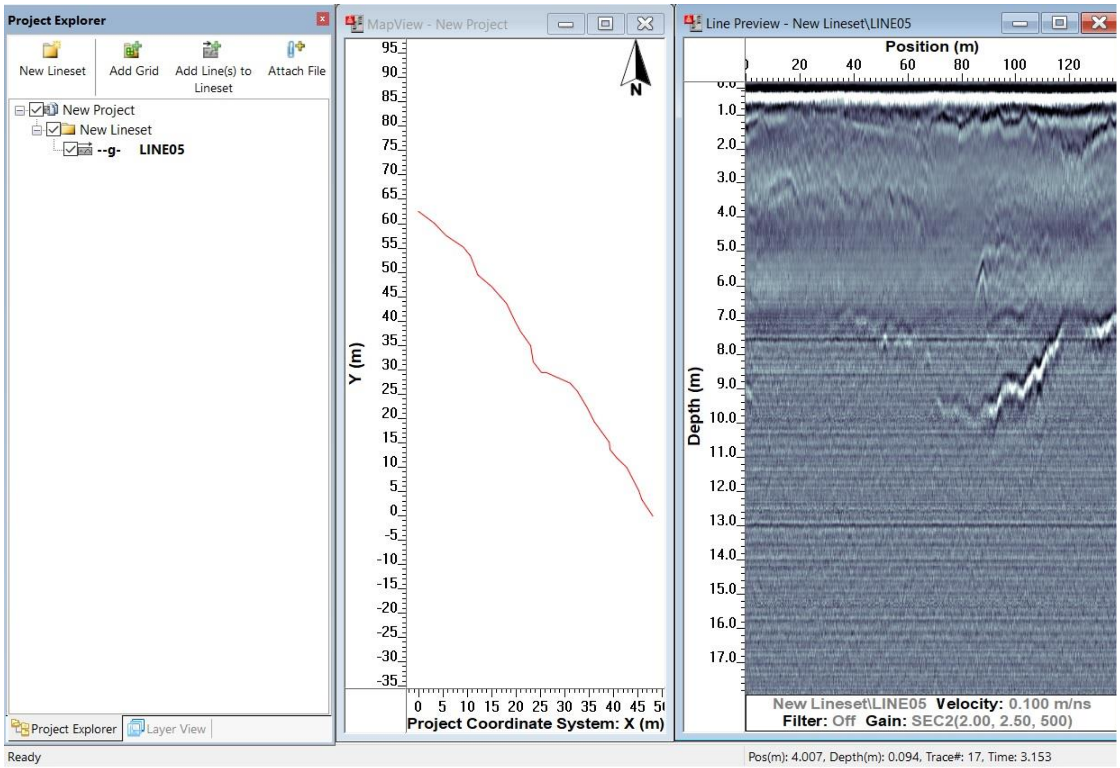

Figure A3.6: *Ekko_Project* interface showing Project Explorer, Line Preview and Mapview windows for GPR LINE05 collected over the dam in September 2016 (Sensors and Software Inc., 2017).

The project explorer menu (Figure A3.6) is where all survey metadata is accessed. The “Line Preview” window displays a compressed profile image of a selected line. The paths of the survey lines in the project space coordinate system is displayed in the Mapview window.

Dewow

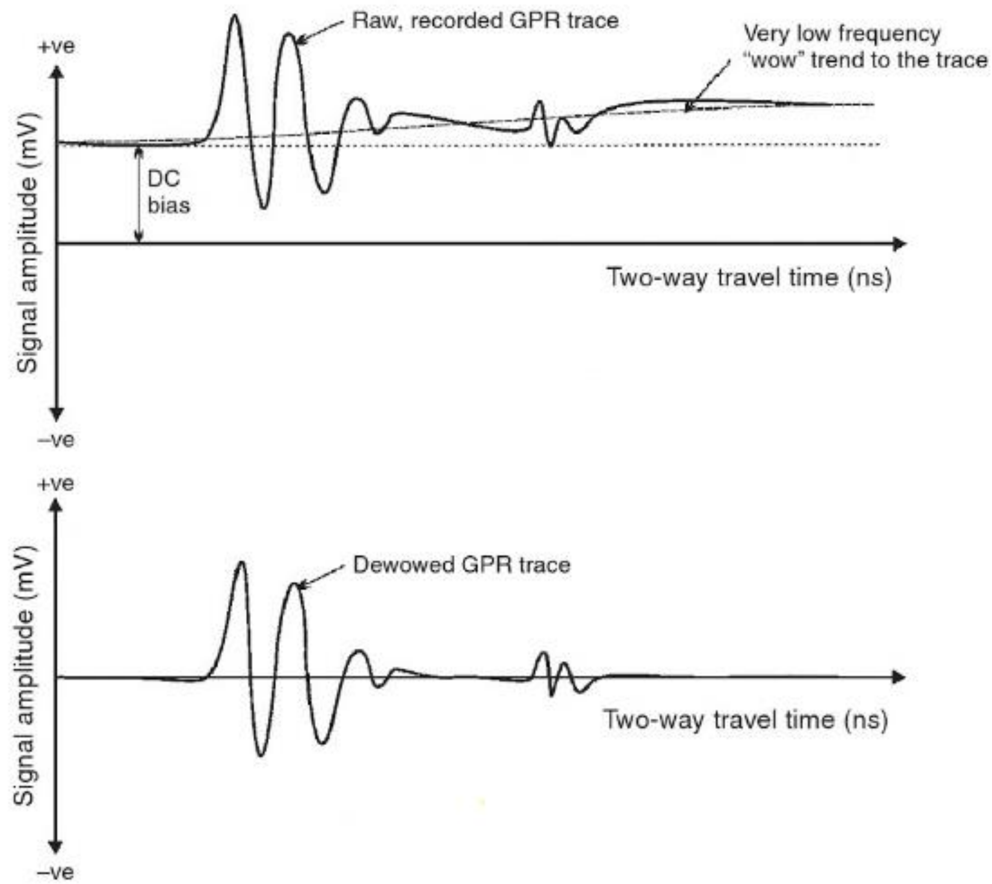

Figure A3.7: Raw GPR trace before Dewow (Top) and After (Bottom) (Jol, 2009).

Wow is created by the saturation of the recorded signal by early reflection arrivals caused by proximity of the transmitter and receiver and or inductive coupling effects between the ground and antennae. This requires the removal of the DC bias and low frequency components from the signal using a low-cut or median filter for correction while preserving the high frequency signal (Sensors and Software Inc., 2016). Dewow is applied to each trace automatically and applies a running average filter to each of the traces (Jol, 2009) (Szymczyk & Szymczyk, 2013).

In Figure A3.6, the top illustration displays how signal saturation causes a DC offset or "bias" that creates a low frequency trend in the data. In the bottom illustration, this offset is corrected, and the signal now has the desired mean amplitude of zero. The low frequency trend is removed and the high frequency signal is preserved as the signal traces become centered over the zero amplitude trend line (Sensors and Software Inc., 2017) (Sensors and Software Inc., 2016).

Automatic Gain Control

AGC is used to enhance the visibility of late-arrival attenuated reflections. An AGC value from 1-12 can be selected in the Lineview window (Schlumberger Ltd., 2017) (Allred, Daniels, & Ehsani, 2008).

Attenuation, Start Gain and Max Gain

The Traceview window (Figure A3.8) is shown displaying the raw trace (black), processed trace (red), and the gain function (blue). When the gain is increased the amplitude of reflections along the trace especially at late penetration times become stronger to enhance weak reflectors at depth as displayed by the superimposed red plot over the raw signal. The early high-amplitude reflections of the raw trace are seen dampened by background subtraction filter and dewow filter as displayed by the processed trace.

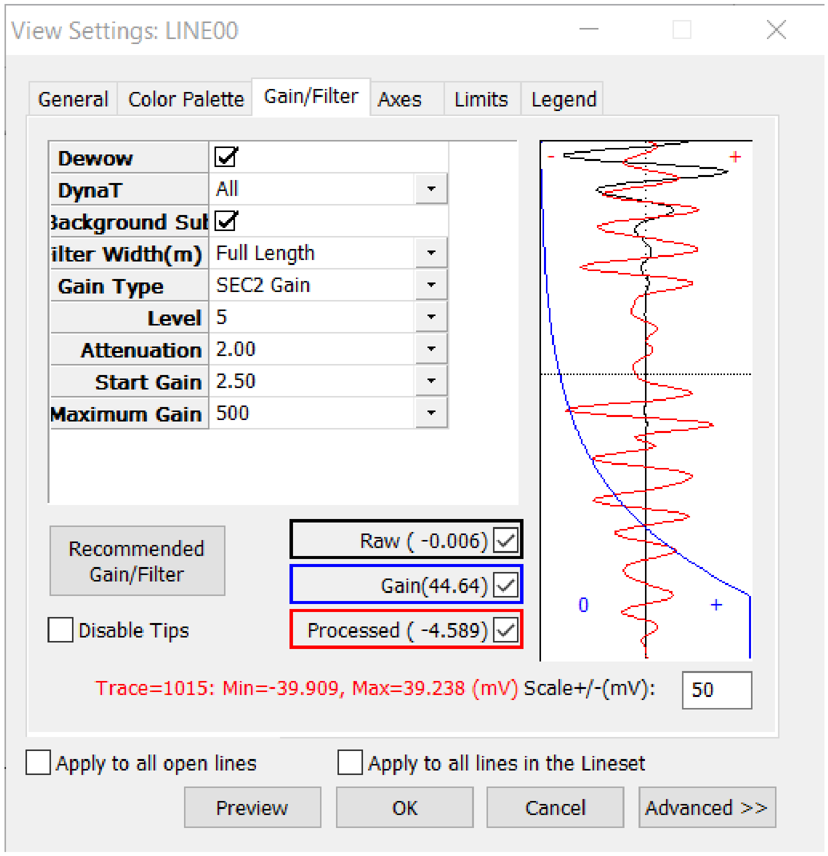

Figure A3.8: Gain/Filter Tab in Ekko Project's Lineview Mode (Sensors and Software Inc., 2016).

The shape of the gain plot will change depending on the gain parameters and type used. The blue pot represents the gain function, specifically SEC2 gain which was used for the majority of this research (Sensors and Software Inc., 2016). The SEC2 gain or "Spreading Exponential Calibrating Compensation" uses an exponentially increasing gain as a function of depth. As shown in Figure A3.8, the gain increases exponentially until it reaches the maximum gain level and plateaus where it will not increase any further, which is set to 500 mV (Sensors and Software Inc., 2017).

Manipulating the signal attenuation variable allows the user to increase the gain of the radar signal reflecting from deeper targets thus enhancing reflections where the signal has attenuated, especially in lossy materials (Sensors and Software Inc., 2016). The value for the attenuation used in the profile determines the steepness of the SEC2 gain ramp. The lower the attenuation value chosen the more gradual the slope, and the higher the value the steeper the slope of the SEC2 gain function. The attenuation value should typically be low with a gradually increasing slope as it is not necessary in most cases to amplify the signal at early propagation times.

Higher attenuation values create a steep SEC2 gain ramp, meaning the signal at earlier propagation times is amplified. Higher values are normally used to enhance deeper targets. The user must manipulate this variable with caution as to not “overgain” the profile making it more complicated (Sensors and Software Inc., 2016).

The start gain is the amplitude of the gain at the beginning of the SEC2 ramp at zero depth in the profile. The ramp defined by the attenuation begins at the start gain, and a dataset with a high degree of attenuation over a lossy environment may require a higher value than the default value. The start gain value is a multiplier for the attenuation, therefore increasing the start gain increases the steepness of the SEC2 ramp (Sensors and Software Inc., 2016).

EKKO Project Slice View

The SliceView feature of EKKO Project 5 builds a 3D volume underneath a regular grid and fills the volume with values of the reflection amplitude (Sensors and Software Inc., 2015). The user can then scroll through the volume, viewing depth slices of user defined thicknesses producing images of the average GPR signal reflection amplitudes over the area.

Figure A3.9 displays a depth slice image window and corresponding LineView window taken from GPR grid data that was collected over the Gullbridge Dam seep in November 2016. Red areas indicate high reflection amplitudes. The red horizontal lines in the LineView window indicate the depth interval of the slice.

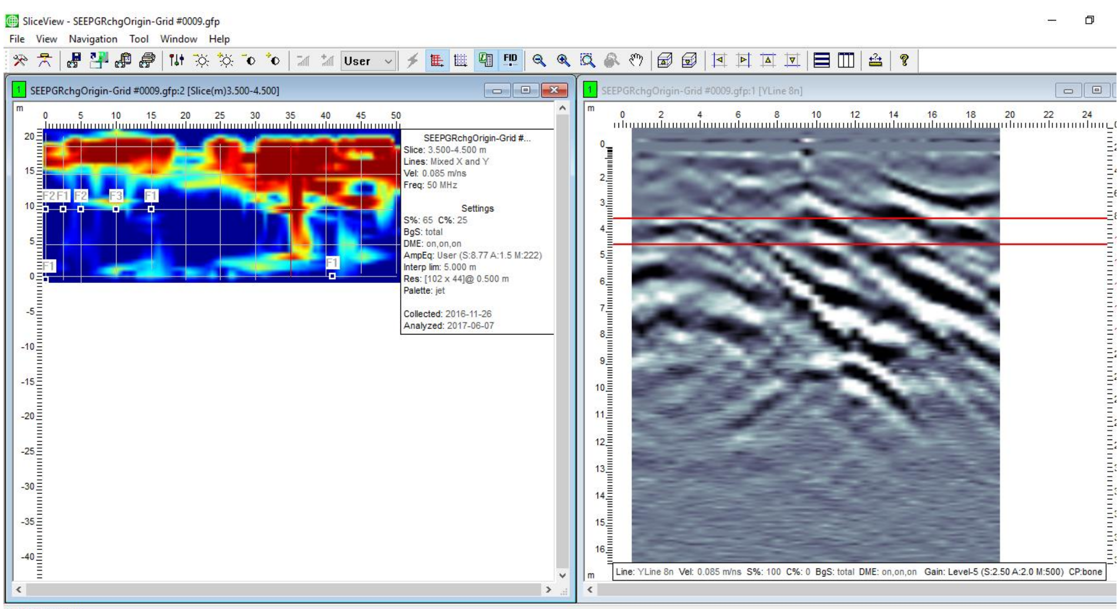

Figure A3.9: Sliceview module displaying Depth Slice window (left) and GPR Line View window (right) (Sensors and Software Inc., 2015).

Depth Scale

One of the most important steps before beginning any data interpretation is to determine the proper depth scale for the particular GPR profile being examined. The parameters of the depth axis are chosen based on the velocity of the EM pulse travelling through a particular medium at the time of the survey. This is essential to yield an accurate target depth since each reflection in the profile is based on two-way travel time and thus the equation for velocity v=2d/t.

To gain the most accurate depth estimates of subsurface targets in a particular medium, two velocity extraction exercises were performed using data acquired over the Gullbridge TMA. These were the Common Mid-Point Gather performed over the wetland area and the Hyperbola Velocity Calibration Tool performed over the Gullbridge Dam (Sensors and Software Inc., 2017).

A practical tool for estimating the signal velocity is the hyperbolic fitting to a local target approach. There are two basic pattern shapes in all GPR profiles, linear segments and hyperbolic curves (Dou, Wei, Magee, & Cohn, 2016).

The GPR will produce hyperbolas in the profile if the GPR system traverses perpendicular to linear features at a “point scatter” (Jacob & Urban, 2015). From determining the parameters of the hyperbolic response or the depth and time information, an average propagation velocity can be extracted (Sensors and Software Site).

To extract a velocity the depth to the interface must vary, where the distance between the radar antennae and reflector vary in a regular progressive pattern (Jacob & Urban, 2015). Figure A3.10 illustrates the path of a GPR over a pipe perpendicular to the traverse creating a hyperbolic response (Sensors and Software Inc., 2017).

To determine the velocity at each location x along the traverse and thus determine the average velocity over the hyperbola the operator may use the equation:

$$T = 2\frac{(x^2 + d^2)^{\frac{1}{2}}}{v} \tag{A3.3}$$

where T is the time to the reflector, x is the surface distance, d is the depth to the interface and v is the velocity of the radar pulse. The variables may be manipulated to solve for v.

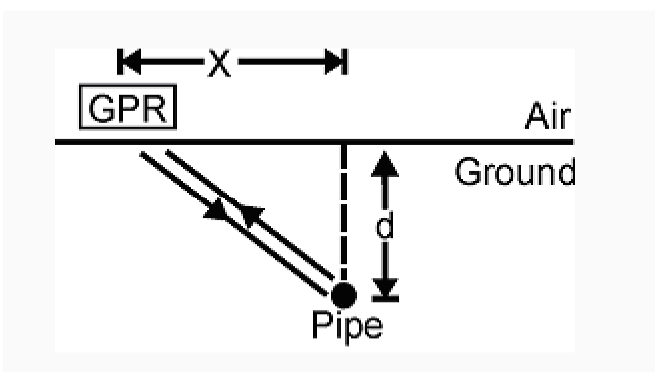

Figure A3.10: GPR transect over linear object perpendicular to the traverse (Sensors and Software Inc., 2017).

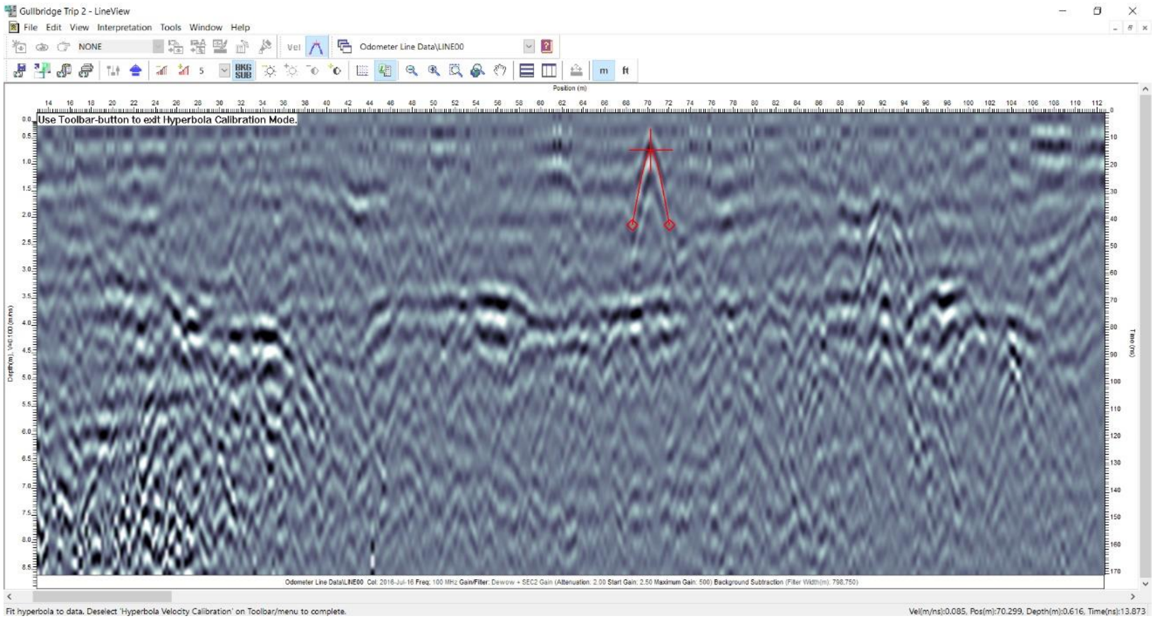

Figure A3.11: Hyperbola curve fitting exercise over LINE00 collected in July 2016.

In Ekko Project, a hyperbola curve fitting exercise uses the algorithm in equation (43) to automatically generate a velocity for a radar pulse in the medium above the hyperbolic response. This was performed by moving a red hyperbola in Ekko Project and matching this shape as close to the apex of a prominent hyperbolic response in the data as possible. Figure A3.11 illustrates a hyperbola curve fitting exercise performed using data acquired over the crest of the Gullbridge Dam. This exercise yielded a radar velocity of 0.085 m/ns. However, this velocity is only practical for a wave pulse travelling through material above hyperbola. Below the water table the speed of the radar pulse will decrease, and the depth scaling becomes inconsistent. Given the velocity of saturated sand is 0.06 m/ns and most soil/rock is 0.100 m/ns this is a reasonable assumption, regardless of how shallow the hyperbola is within the dam material. The velocity of a radar pulse in dry sand is 0.150 m/ns, however the top 2-3 m of the dam is generally saturated by the water table.

The red curve was fitted to a hyperbola in the north over LINE00 collected in July 2016 which is believed to represent the old culvert. This line was collected using Odometer mode and therefore the survey location is unclear.

A3.6 Supplementary EM31-MK2 Data Processing Notes

Table A3.3: Spreadsheet of EM31-MK2 data uploaded from ground conductivity meter.

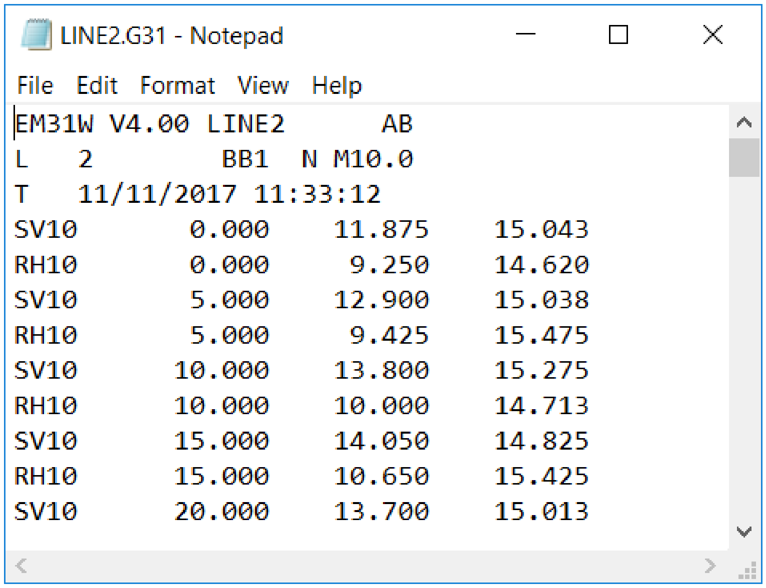


```
EM31W V4.00 LINE2       AB
L    2         BB1   N M10.0
T   11/11/2017 11:33:12
SV10        0.000    11.875    15.043
RH10        0.000     9.250    14.620
SV10        5.000    12.900    15.038
RH10        5.000     9.425    15.475
SV10       10.000    13.800    15.275
RH10       10.000    10.000    14.713
SV10       15.000    14.050    14.825
RH10       15.000    10.650    15.425
SV10       20.000    13.700    15.013
```

The data was uploaded using DAT31W, originally a DOS based program converted for use with Windows OS. DAT31W generates a file containing all relevant survey data in. G31 format, exclusive to Geonics acquisition systems. The .G31 file is easily converted to .txt using any .txt based application.

Table A3.3 gives an example of the spreadsheet generated from a .G31 file. The first row gives the instrument name, version number, the name assigned to the line collected, and the initials of the instrument operator. The second row specifies the line name again (i.e. L 2), and the survey parameters revealed by the letters BB1. The first "B" indicates that "both" quadrature and in-phase data was collected, the second "B" indicates that "both" VMD and HMD instrument orientations were collected, and the 1 specifies the data was acquired using only 1 instrument orientation. The letter “N” indicates the line orientation was to the north, and field “M10.0” indicates the data was collected in manual mode (Geonics Ltd., 2003). The row beginning with the letter T indicates the data and time the survey was acquired on.

The following rows contain the survey results. The letter S in the first column indicates the data points contain just the station number and values of values of conductivity and susceptibility. The second letter which is either “V” or “H” indicates the dipole orientation, the letter 1 refers to the single instrument orientation used and the 0 indicates that no fiduciary marker was applied to the dataset. The second column refers to the station. It is evident in this dataset that the station spacing over LINE02 as 5 m. The third column of values indicates the conductivity in mS/m and the fourth column indicates the in-phase susceptibility (ppt).

A3.7 Supplementary ICP-MS Data Processing Notes

The instrument used was a PerkinElmer Elan DRC-ii. The first step involved syringe filtering an aliquot of 50 mLs of water into a separate, pre-leached/cleaned polypropylene test tube (to remove any existing metals) through a 0.45 um filter (removes particles, leaving truly dissolved element fraction and colloidally bound fraction).

John subsequently acidified the waters to the equivalent of 2% HNO_3 v/v using a concentrated or 8 M HNO_3 source that is 1x purified through sub-boiling distillation. This step was necessary to preserve all dissolved metals in solution for analysis and also places the sample in a matrix that is compatible with all of the calibration solutions ready for ICP-

MS analysis. For analysis, the package formerly described on the CREAIT web page was used.

USGS T-193 Reference Materials were tested along with the samples to verify the data. The reference materials are laboratory control samples (LCS) containing known concentrations of analytes used to ensure that the instrument is accurately measuring the samples tested (USEPA, 2015).

Appendix 4A Supplementary Data for Chapter 4

A4.1 SP over the Seep Grid

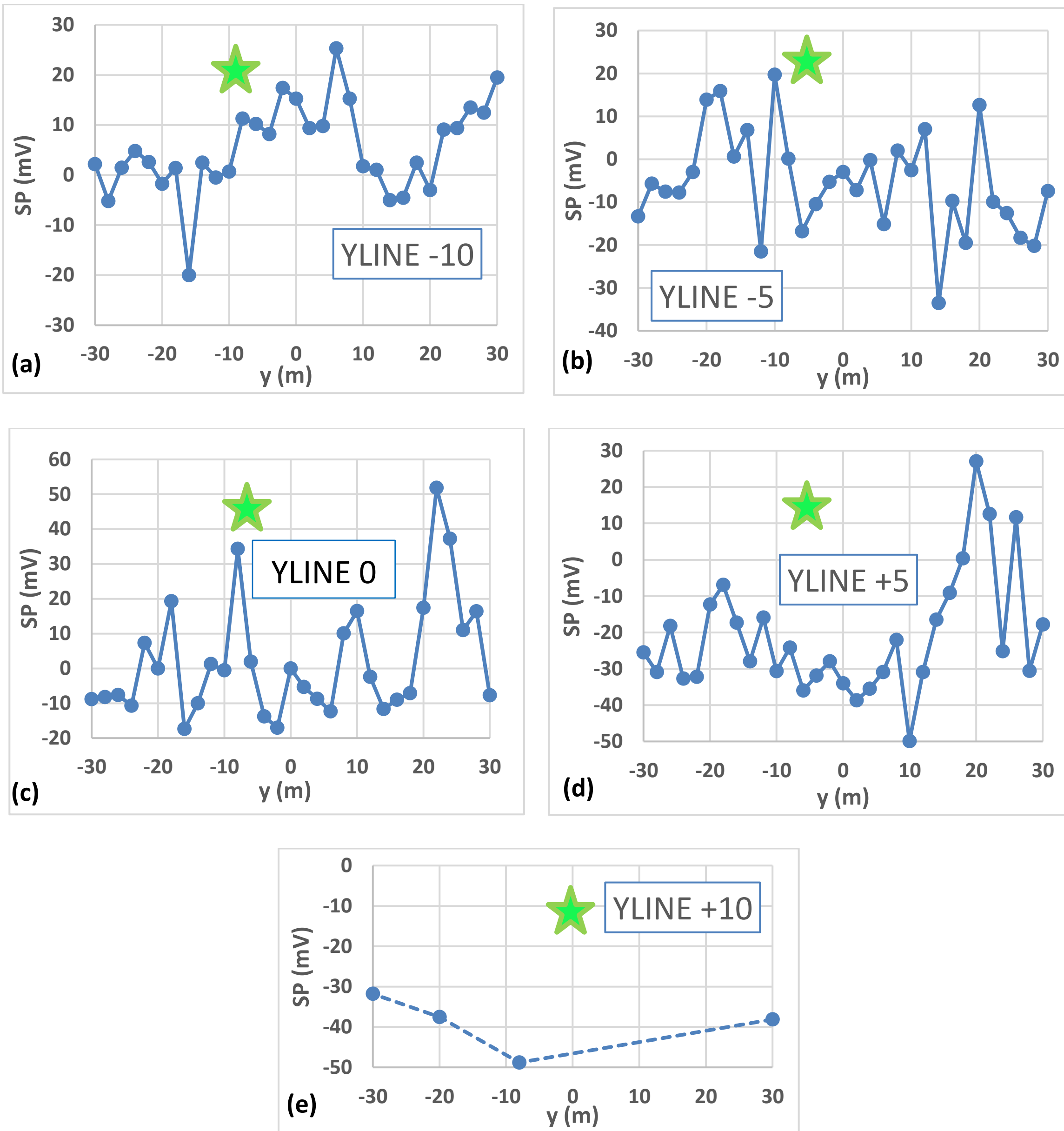

Figure A4.1.1: Profiles of SP versus station spacing (m) over y-lines collected S-N over the 2018 seep grid. The green star indicates the location of the observed seep downstream (Figure 3.20).

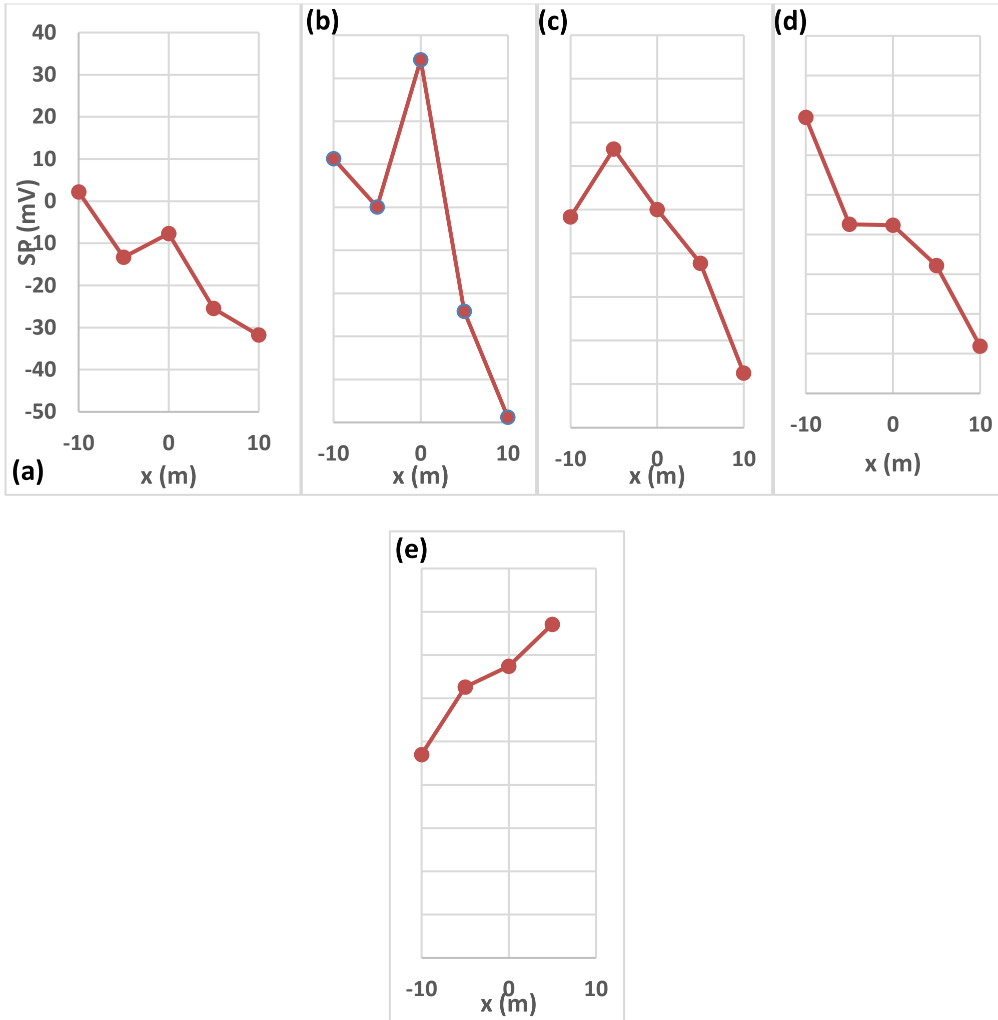

Figure A4.1.2: Profiles of SP versus station (m) over x-lines (a) XLINE-30, (b) XLINE-20, (c) XLINE-8, (d) XLINE20 and (e) XLINE30 collected W-E over the 2018 seep grid.

A4.2 Central Artifact associated with DCR surveys over the Gullbridge Dam

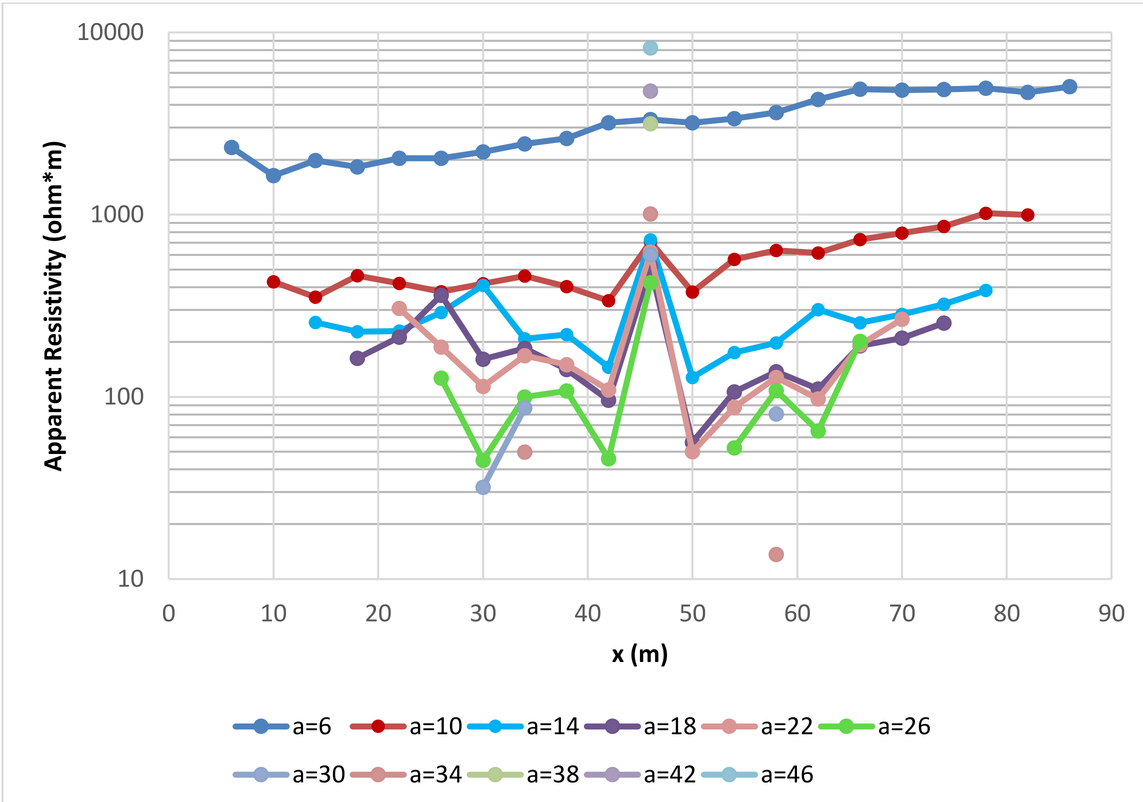

Figure A4.2: Unprocessed ρ_a versus x profiles for 11 pseudo-depths acquired from a 4 m Schlumberger DCR survey conducted over the seep grid in June 2017.

Figure A4.2 highlights the central artifact associated with soundings recorded at the center of the array (potential electrodes at M=12 and N=13). In this example, the central artifact was recorded over x=46 m along the "4 m Central" Schlumberger array carried out in June 2017. This inconsistency is presumably due to a malfunction of one of the multicore cable callouts or a connection issue at the side of the Syscal resistivity unit.

A4.3 Complete smoothed ρ_a versus x dataset plotted in Figure 4.27

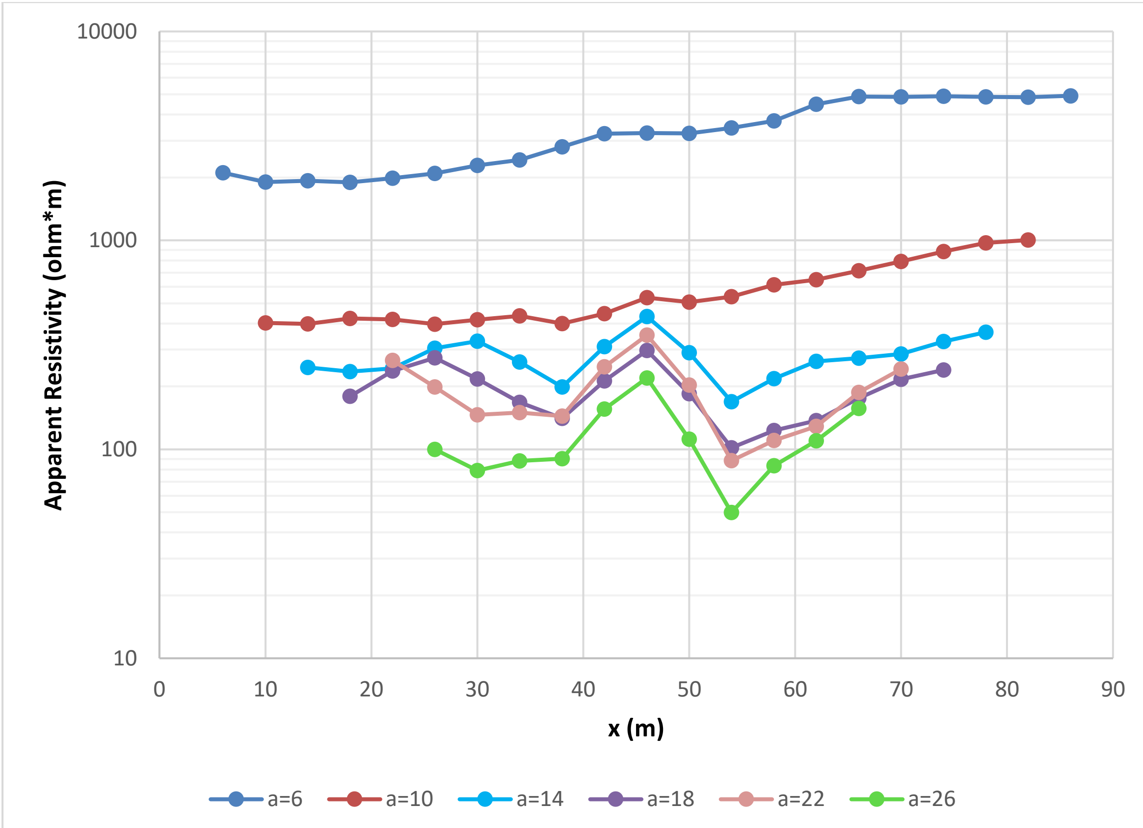

Figure A4.3: Processed ρ_a versus x profiles for 6 pseudo-depths acquired from a 4 m Schlumberger DCR survey conducted over the seep grid in June 2017. Values of ρ_a that were omitted in Figure 4.27 due to high deviation and low signal-to-noise associated with the central artifact are included in Figure A4.3.

A4.4 Original Dataset for "2 m East" DCR Schlumberger Survey

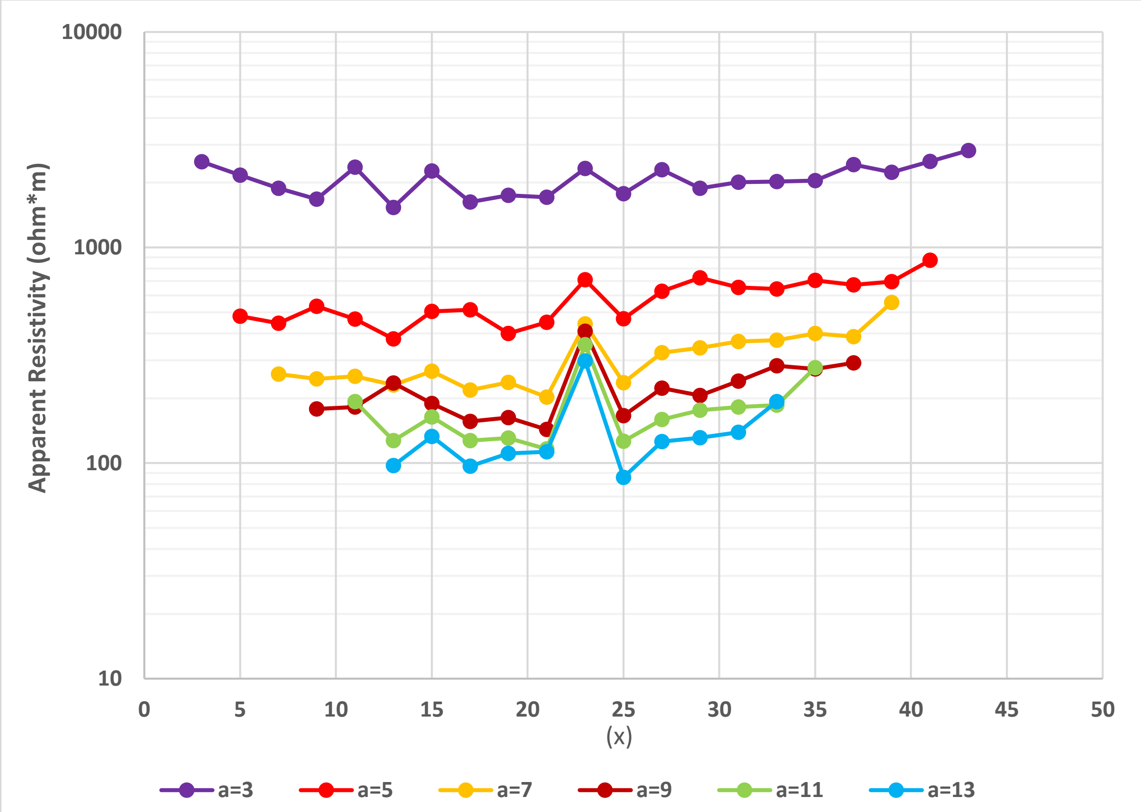

Figure A4.4: Unprocessed ρ_a versus x profiles for 6 pseudo-depths acquired from the "2 m East" Schlumberger DCR survey conducted approximately over YLINE07 of the seep grid in June 2017 with pronounced central artifact. Values of ρ_a that were omitted in Figure 4.29 due to high deviation and the central artifact are included in Figure A4.4. Note the original x values used in this graph differ from those used in Figure 4.29 corresponding to the y position along YLINE07 of the June 2017 seep grid.

A4.5 Supplementary GPR Profiles

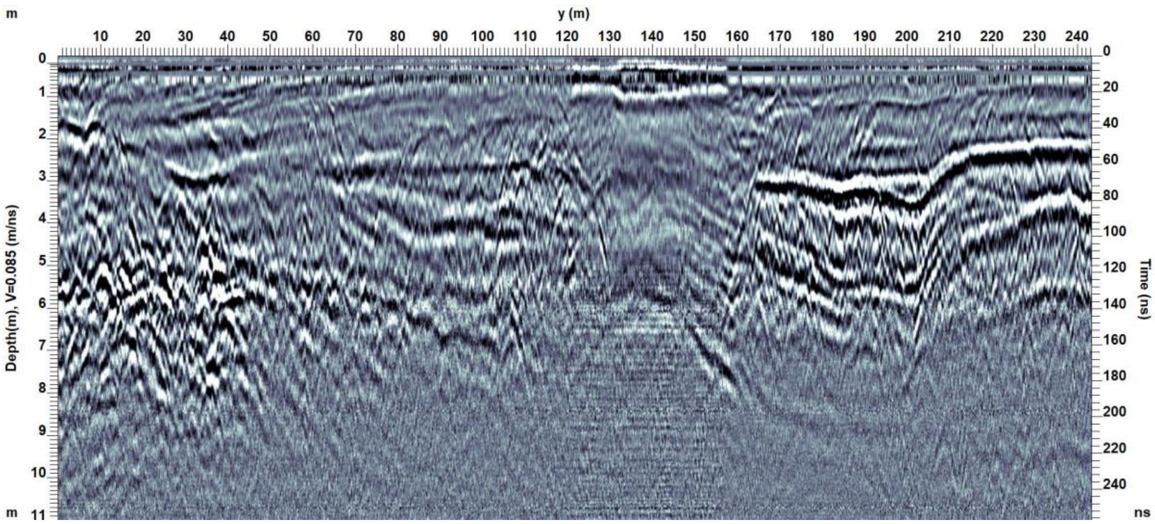

Figure A4.5: GPR LINE00 profile between y=0 m and y=243 m (Figure 4.28) without interpretation lines displayed.

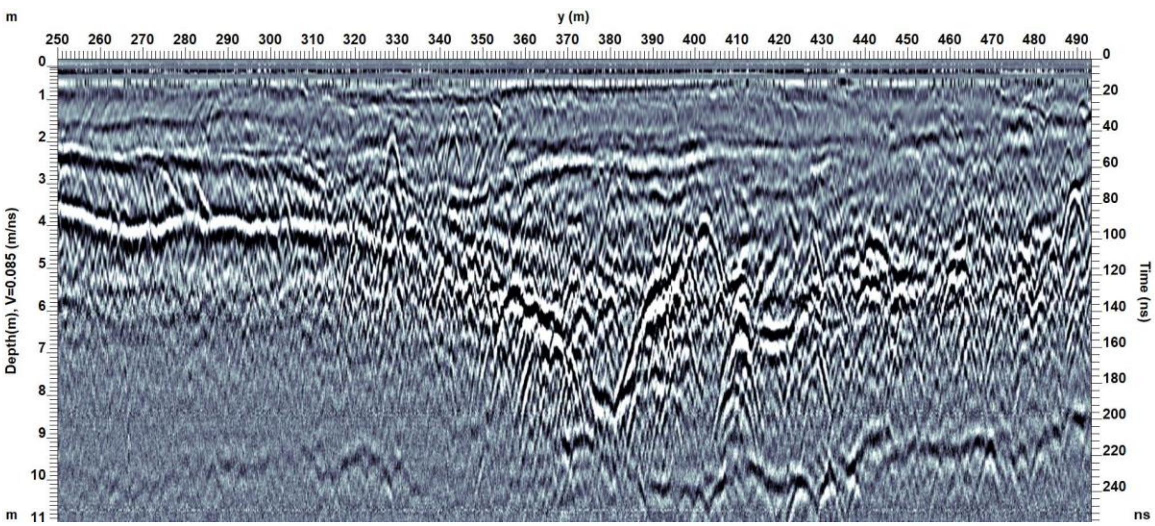

Figure A4.6: GPR LINE00 profile between y=250 m and y=493 m (Figure 4.29) without interpretation lines displayed.

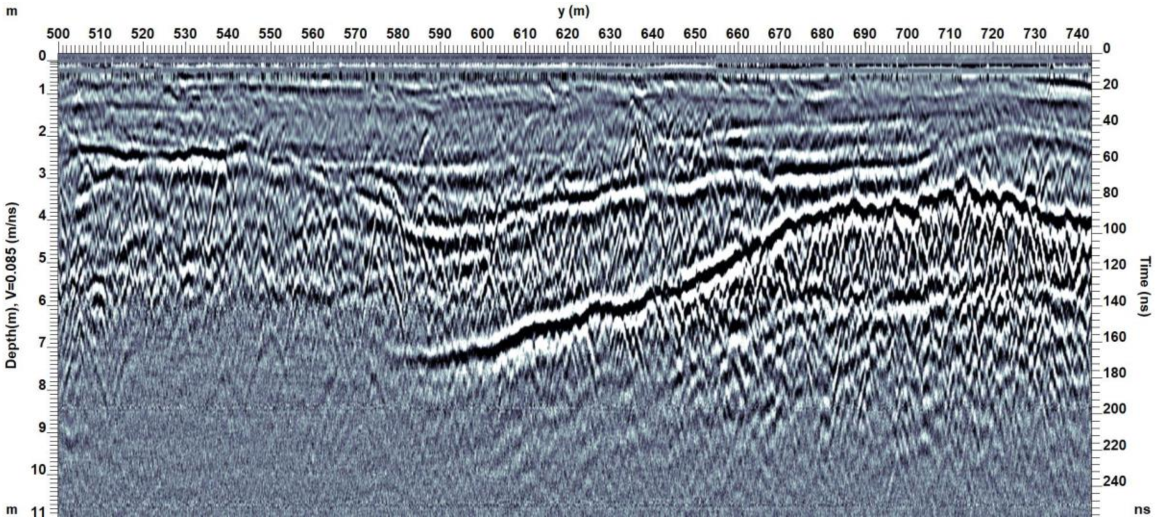

Figure A4.7: GPR LINE00 profile between y=500 m and y=743 m (Figure 4.30) without interpretation lines displayed.

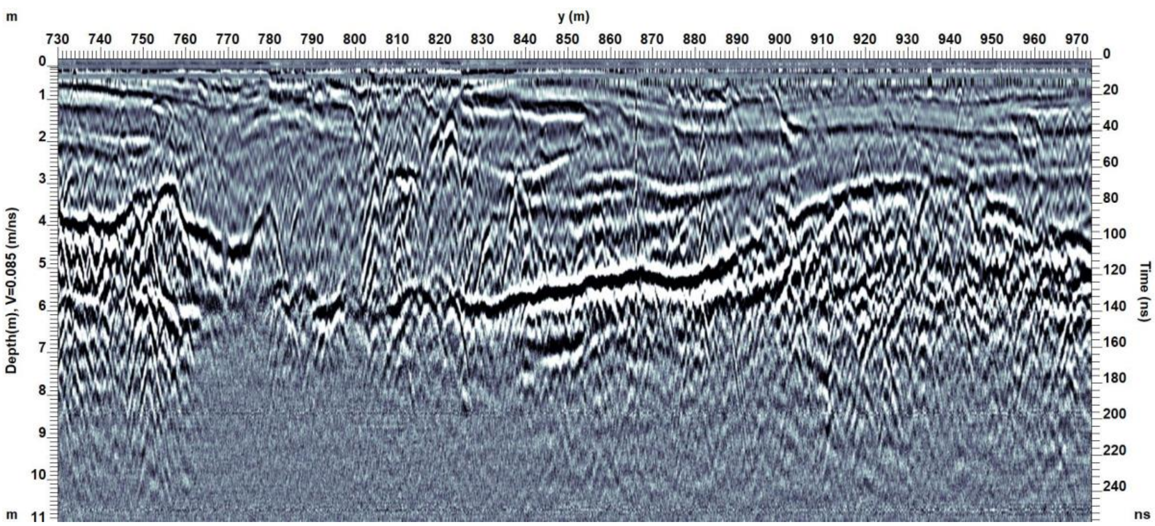

Figure A4.8: GPR LINE00 profile between y=750 m and y=973 m (Figure 4.31) without interpretation lines displayed.

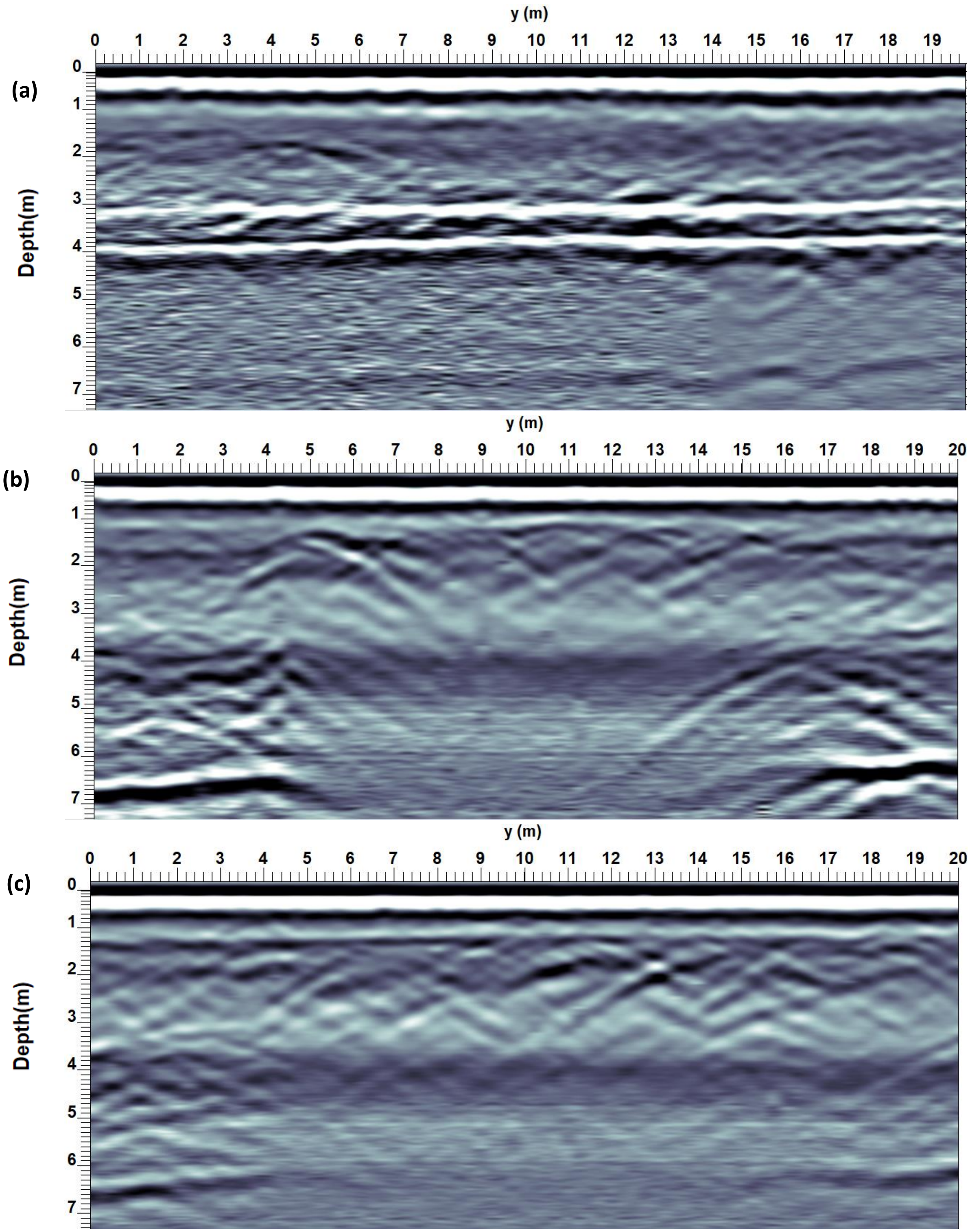

Figure A4.9: Profiles of GPR surveys collected S-N over the July 2016 GPR grid with the removal of interpretation lines: (a) YLINE10 (b) YLINE03 (c) YLINE01. A signal velocity of 0.085 m/ns was assigned as the depth scale.

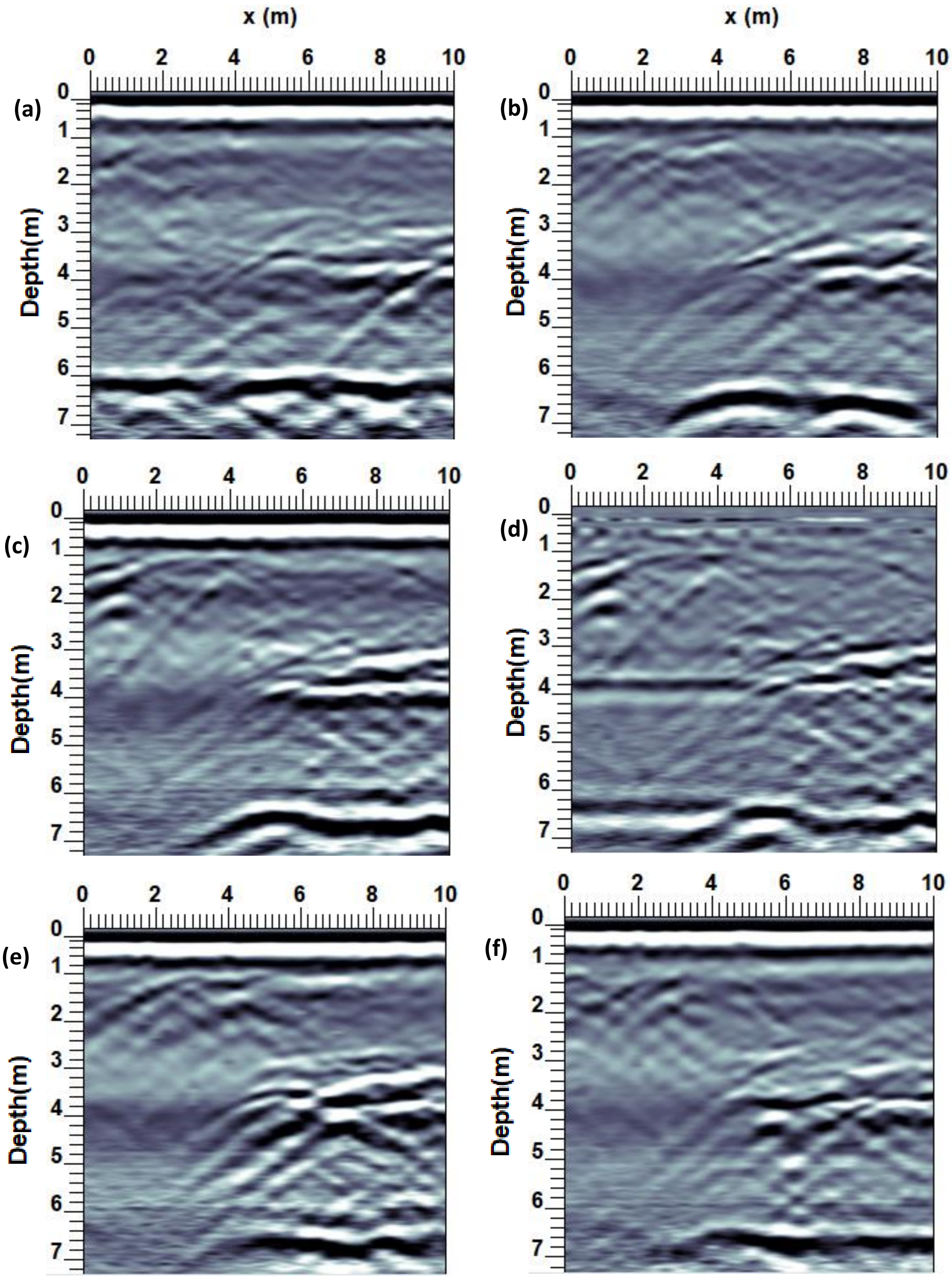

Figure A4.10: Profiles of GPR surveys collected E-W over the July 2016 GPR northern grid with the removal of interpretation lines: (a) XLINE20 (b) XLINE14 (c) XLINE11 (d) XLINE11 with background subtraction filter (e) XLINE09 (f) XLINE05.

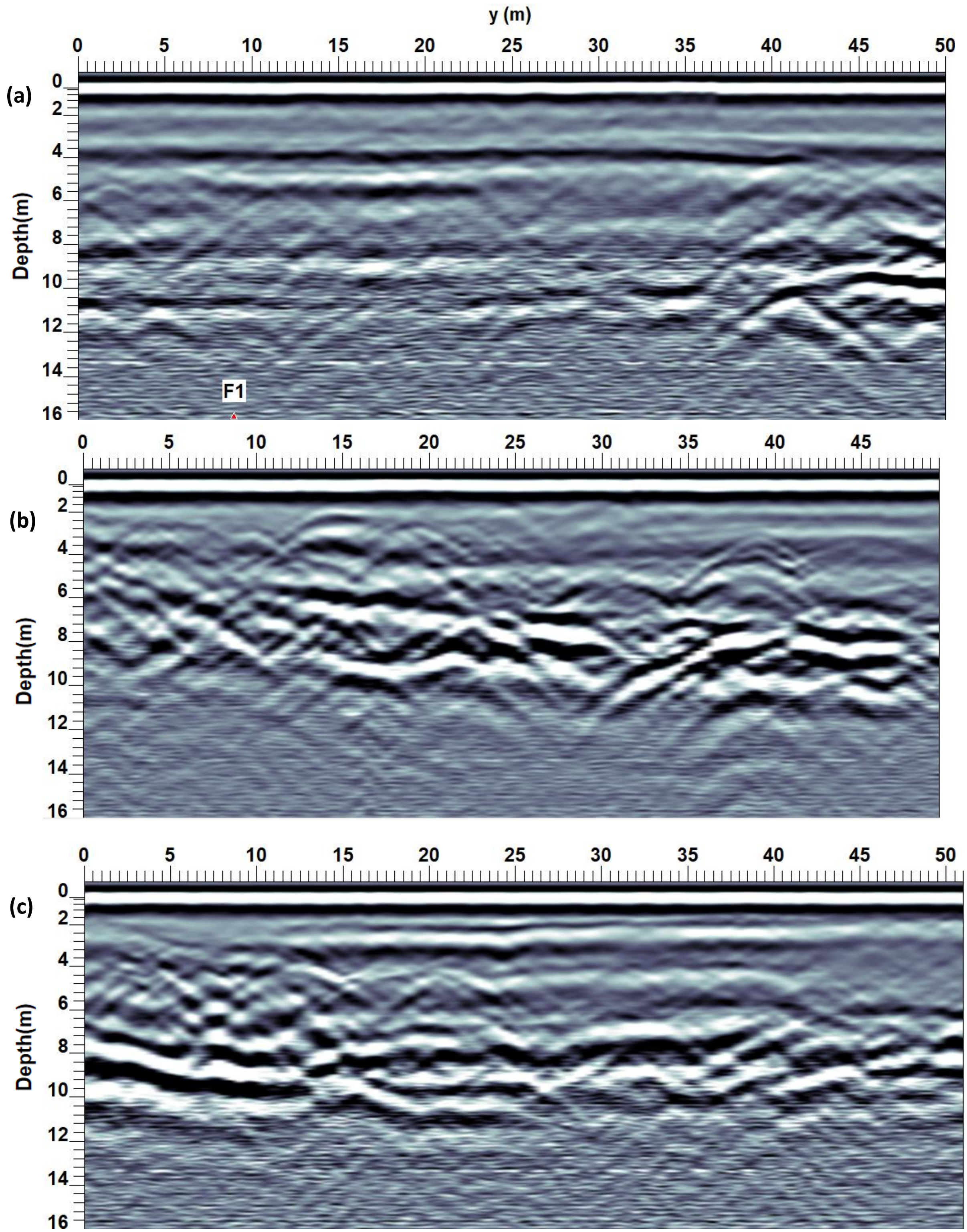

Figure A4.11: S-N profiles of (a) YLINE00, (b) YLINE02 and (c) YLINE03 collected over the November 2016 seep grid with the removal of interpretations.

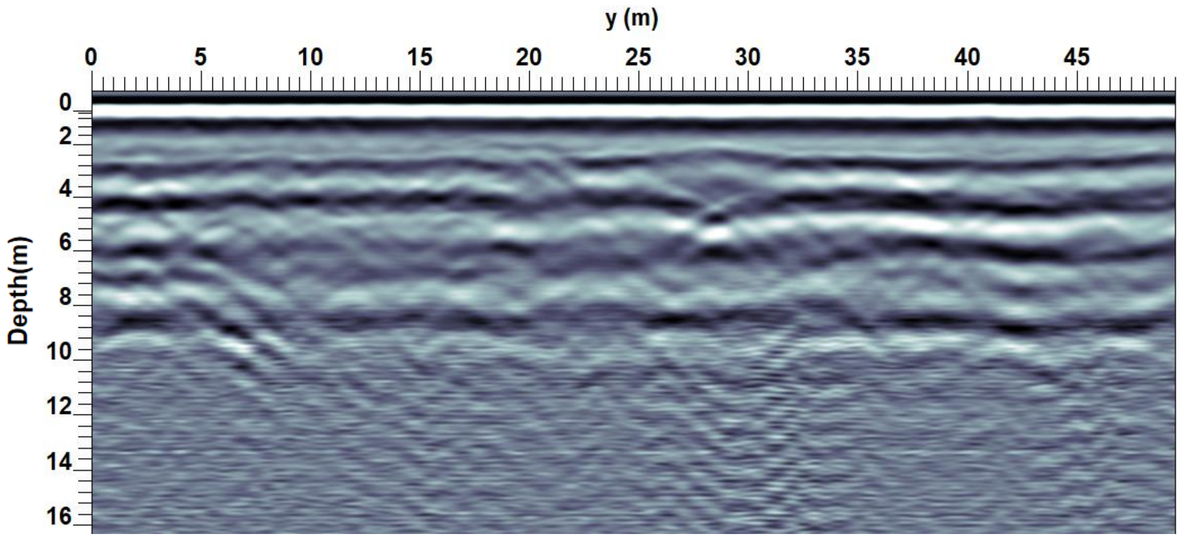

Figure A4.12: GPR profile of YLINE04 collected S-N over the November 2016 GPR grid.

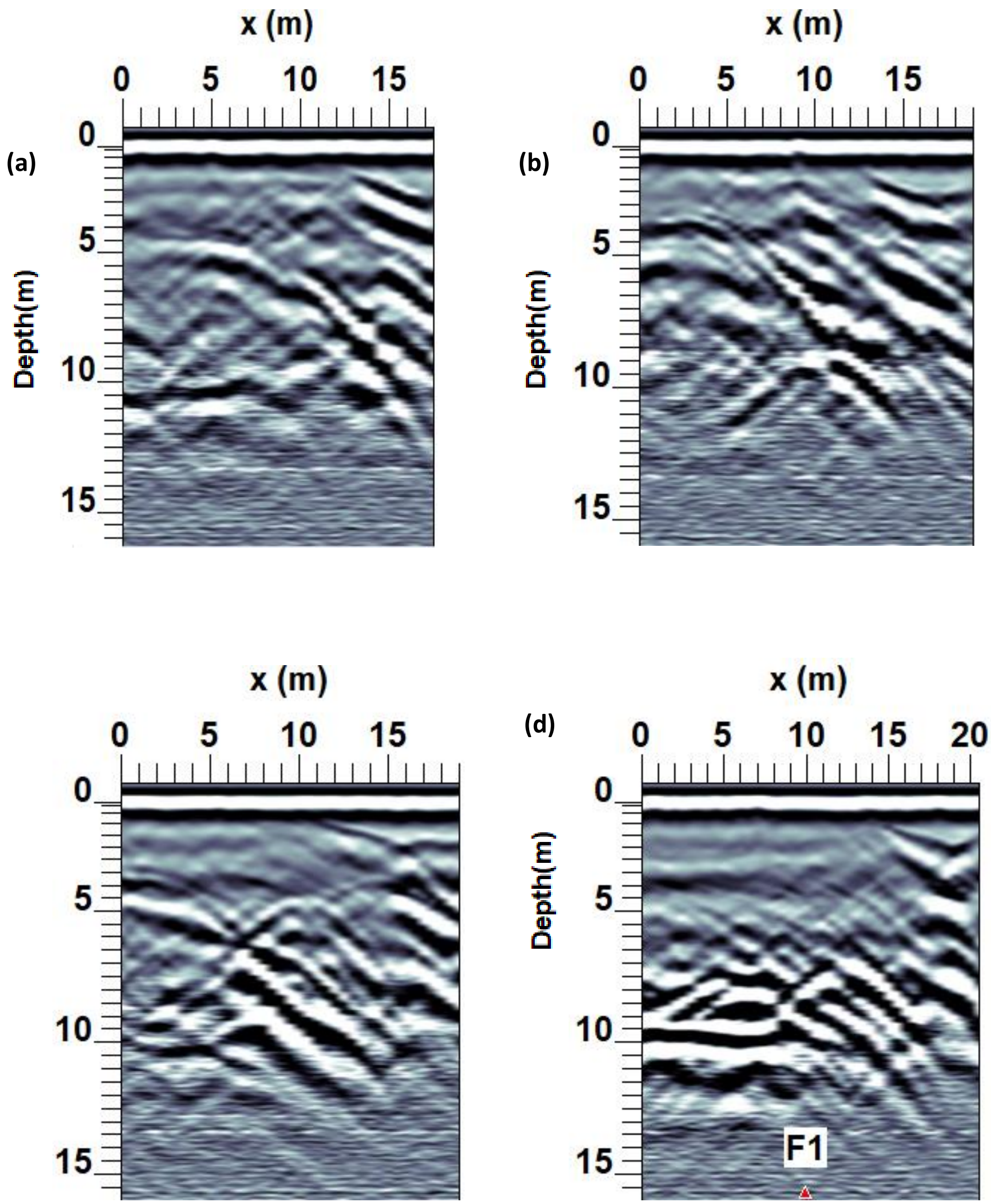

Figure A4.13: GPR profiles of (a) XLINE00 (y=0), (b) XLINE03 (y=15), (c) XLINE06 (y=30), and (d) XLINE10 (y=50), collected W-E over the November 2016 seep grid without interpretation lines.

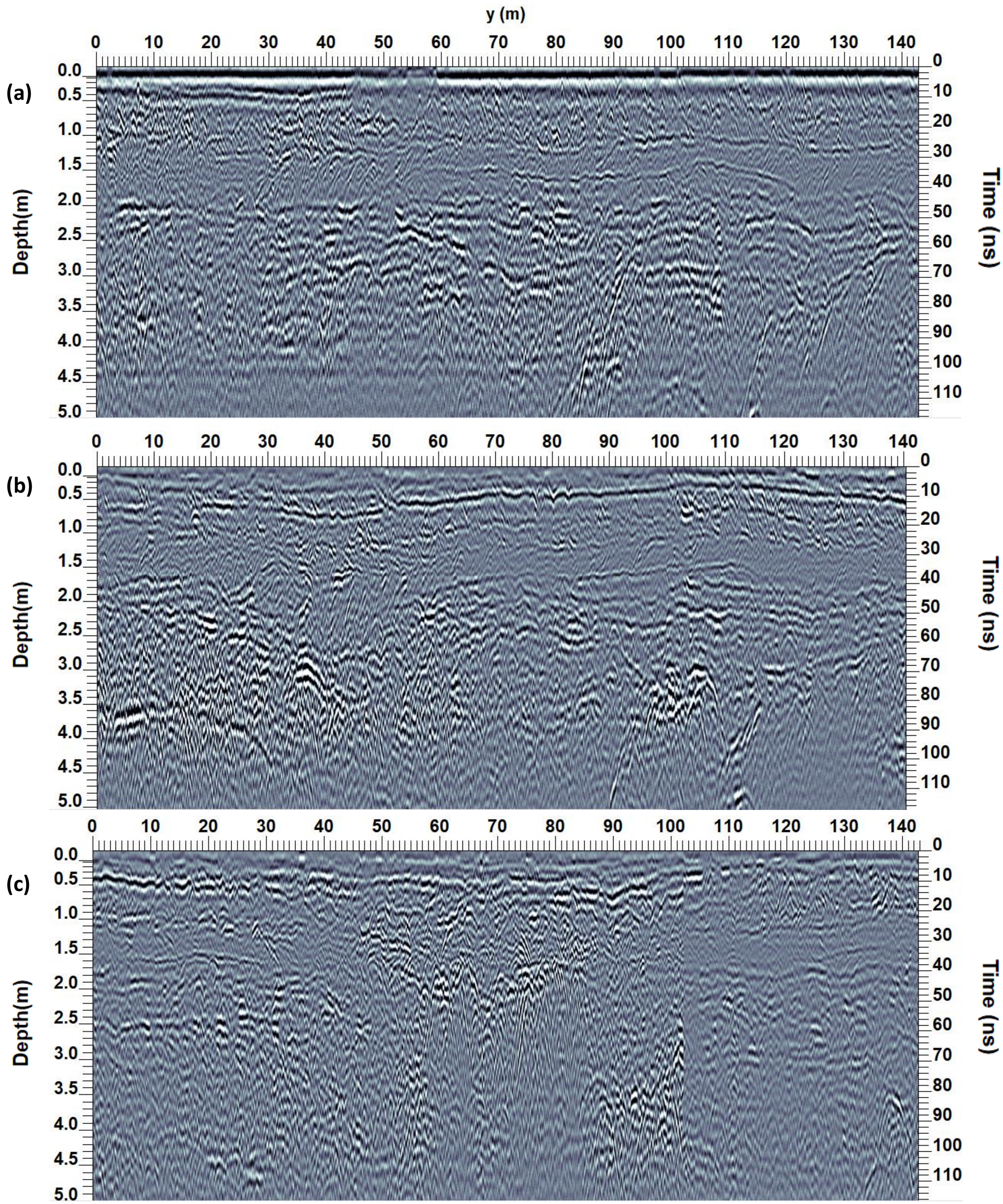

y (m)
0 10 20 30 40 50 60 70 80 90 100 110 120 130 140
(a)
(b)
(c)
Depth(m)
Time (ns)
0.0 0.5 1.0 1.5 2.0 2.5 3.0 3.5 4.0 4.5 5.0
0 10 20 30 40 50 60 70 80 90 100 110

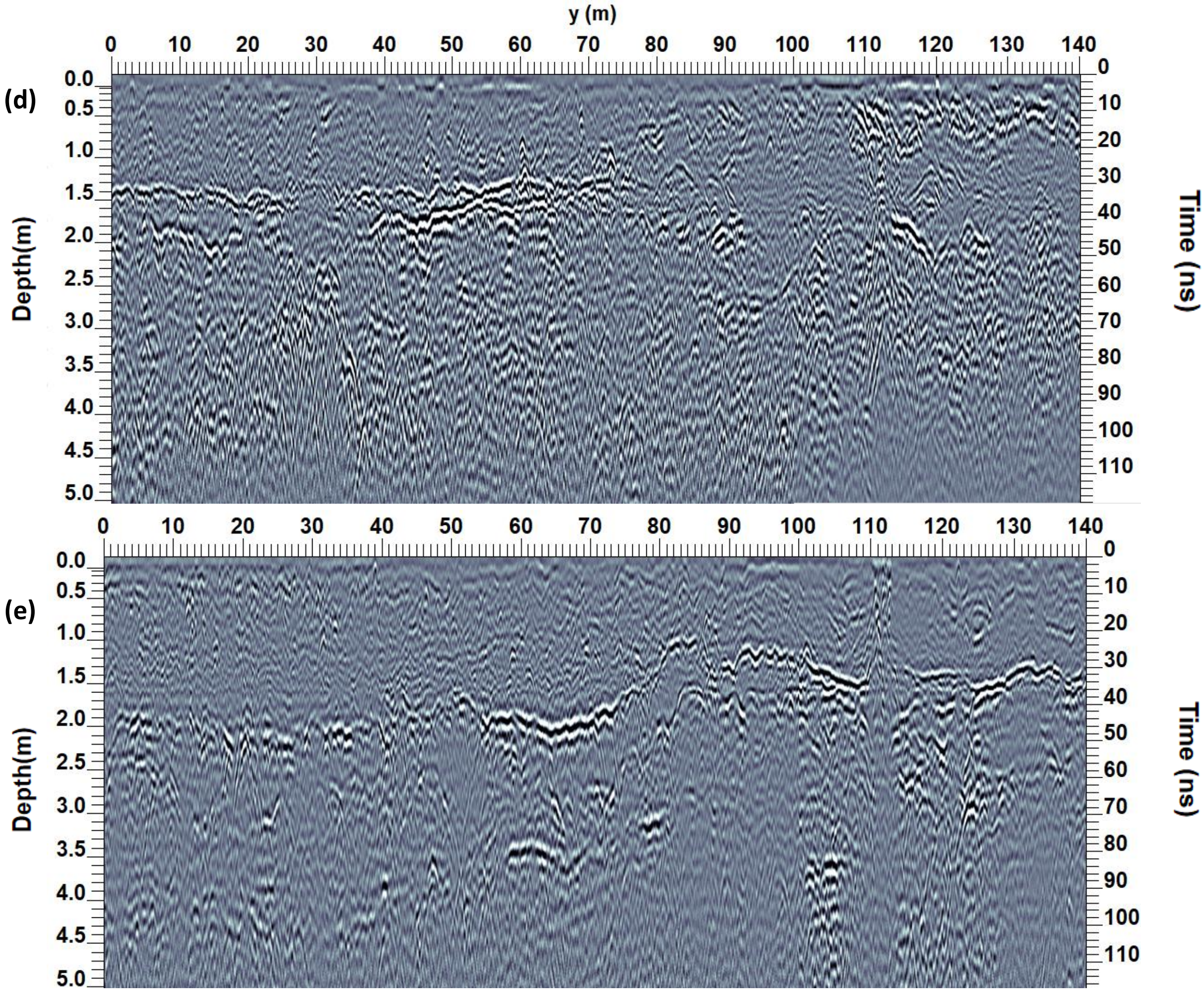

Figure A4.14: S-N profiles collected over the June 2017 seep grid using 250 MHz antennae without interpretation lines: (a) YLINE00 (x=0) with no background subtraction; (b) YLINE03 (x=6) (c) YLINE05 (x=10) (d) YLINE07 (x=14) (e) YLINE09 (x=18).

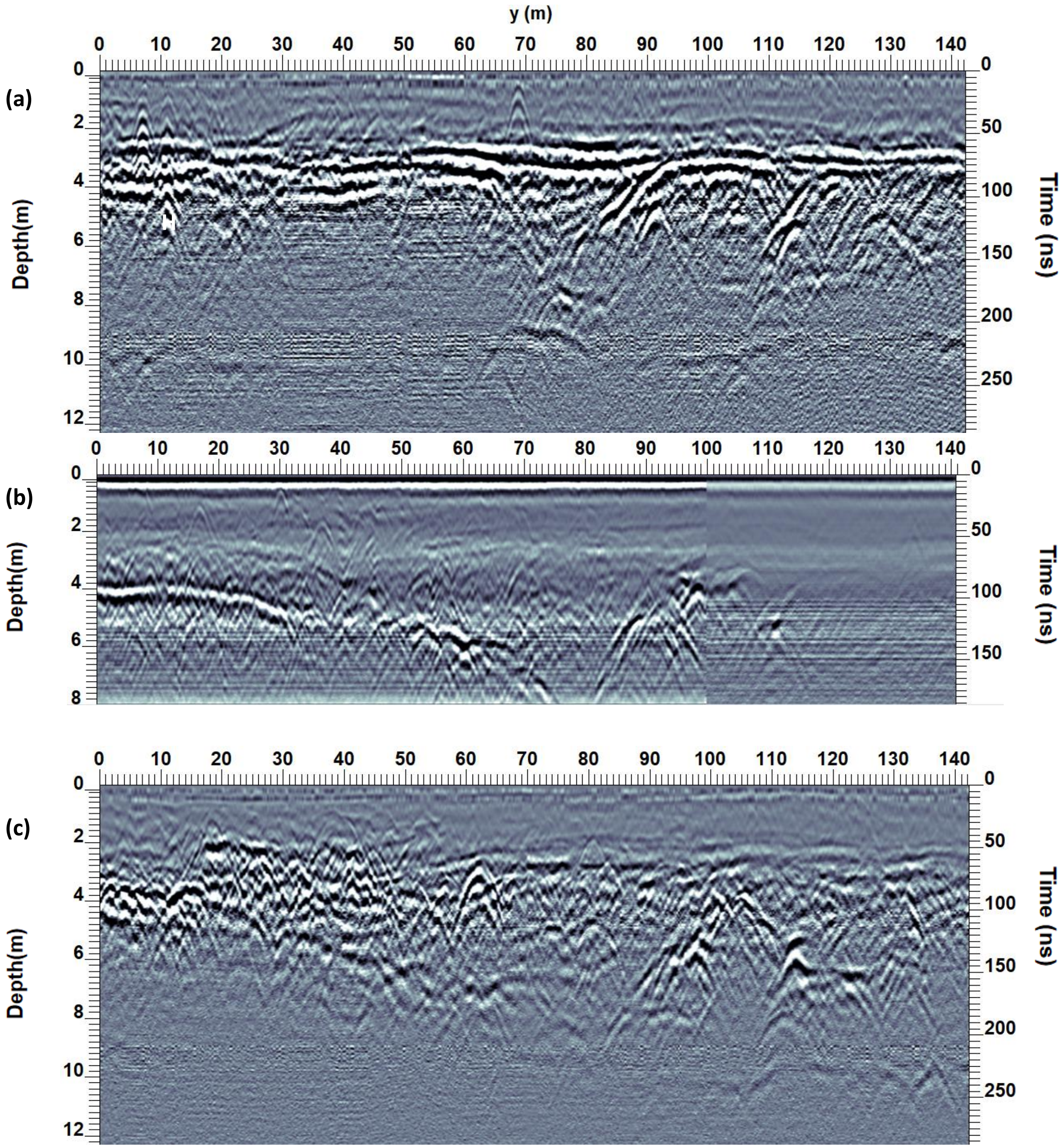

y (m)
(a)
(b)
(c)
Depth(m)
Time (ns)

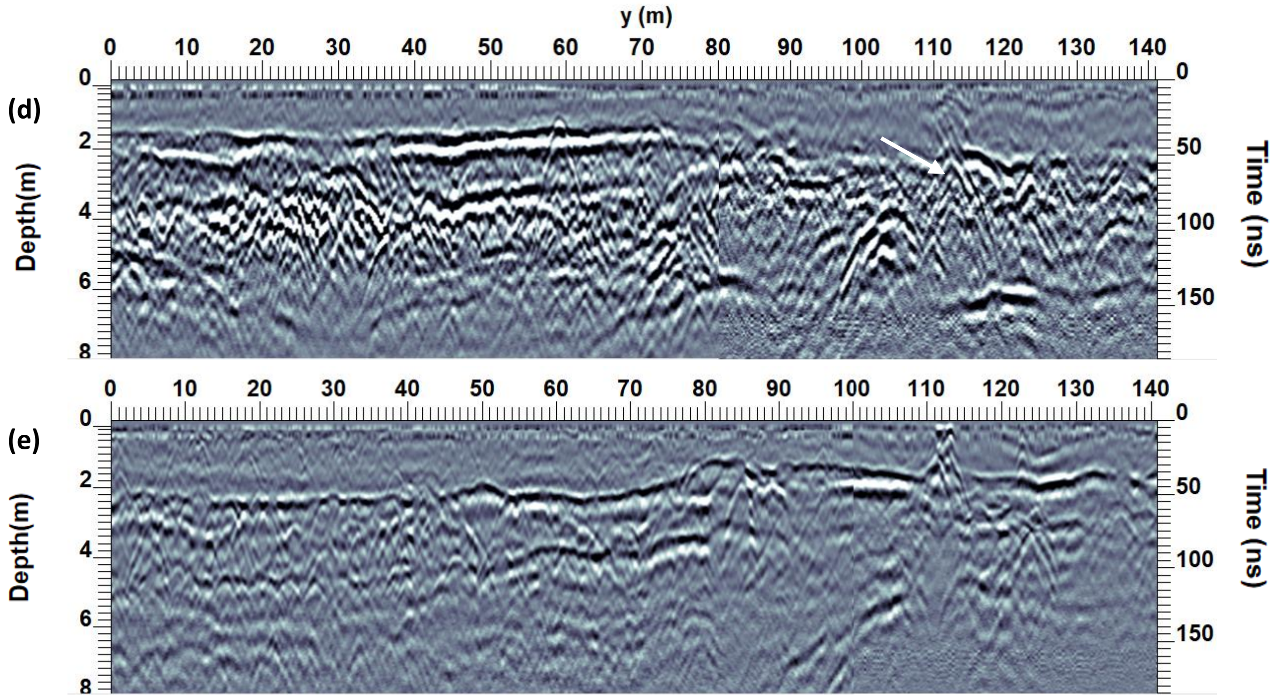

Figure A4.15: S-N profiles collected over the June 2017 seep grid using 100 MHz antenna frequency without interpretation lines: (a) YLINE00 (x=0); (b) YLINE03 (x=6); (c) YLINE05 (x=10); (d) YLINE07 (x=14); (e) YLINE09 (x=18).

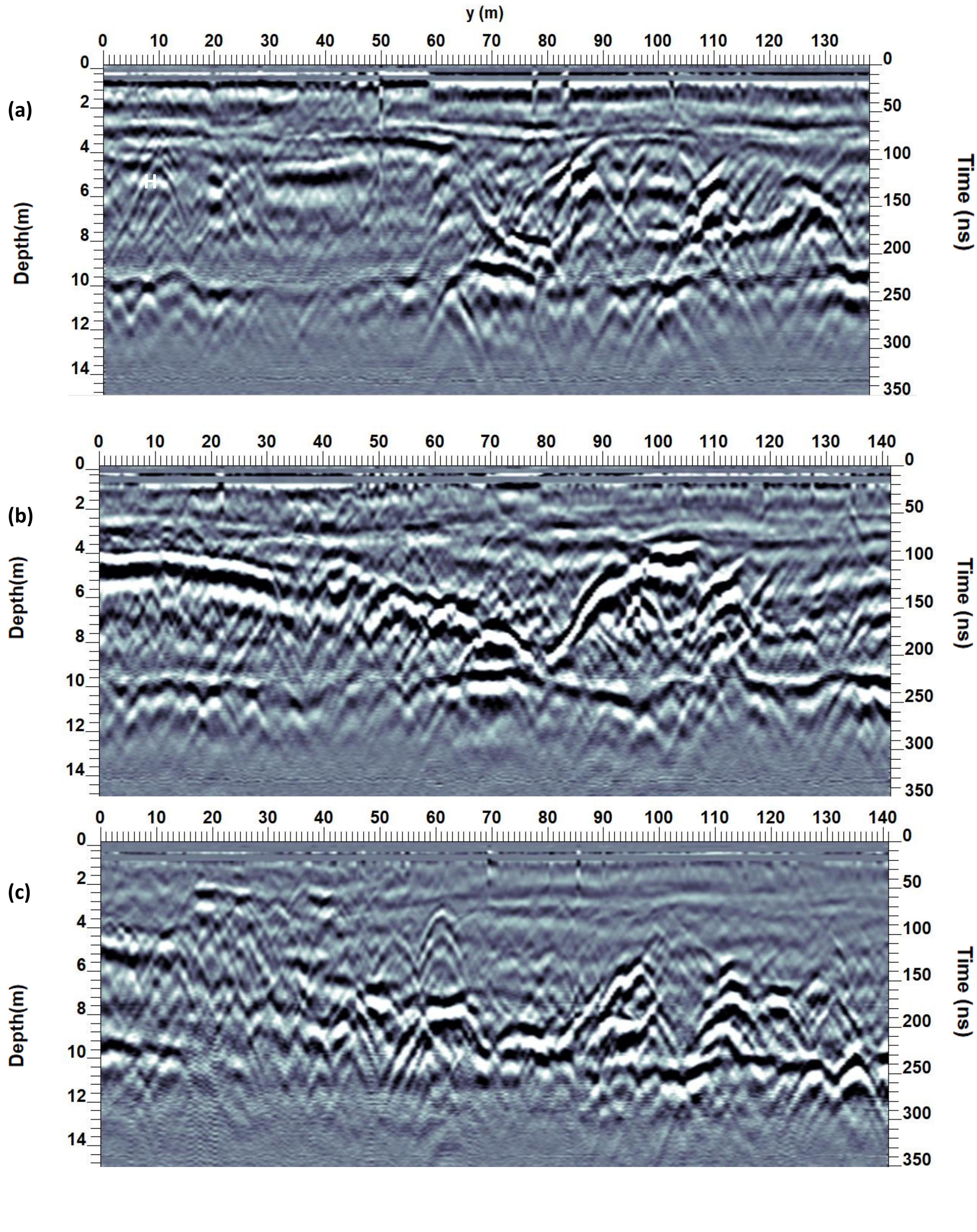
y (m)
(a)
(b)
(c)
Depth(m)
Time (ns)
H

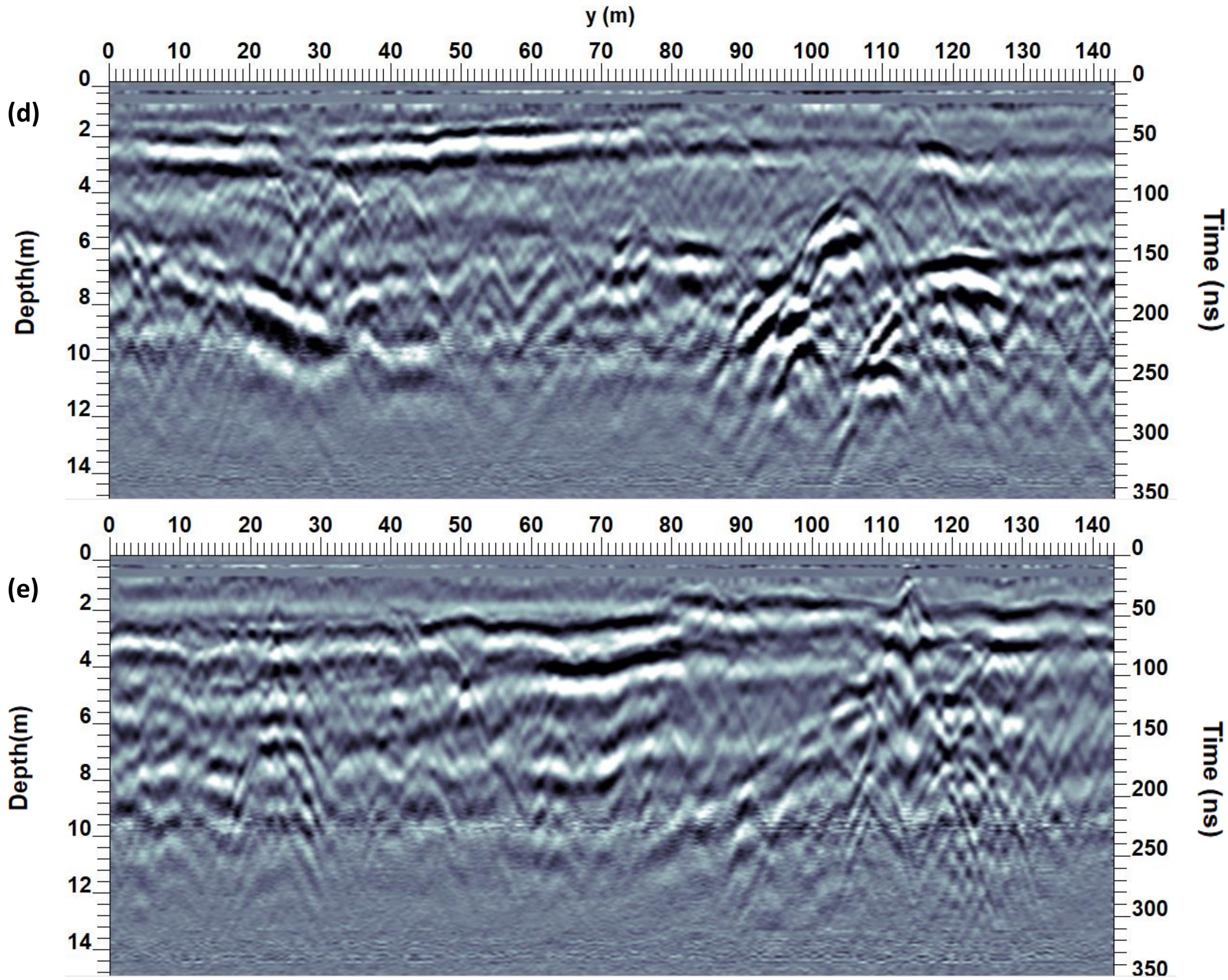

Figure A4.16: S-N profiles collected over the June 2017 seep grid using 50 MHz antenna frequency without interpretation lines: (a) YLINE00 (x=0), (b) YLINE03 (x=6); (c) YLINE05 (x=10); (d) YLINE07 (x=14); (e) YLINE09 (x=18).

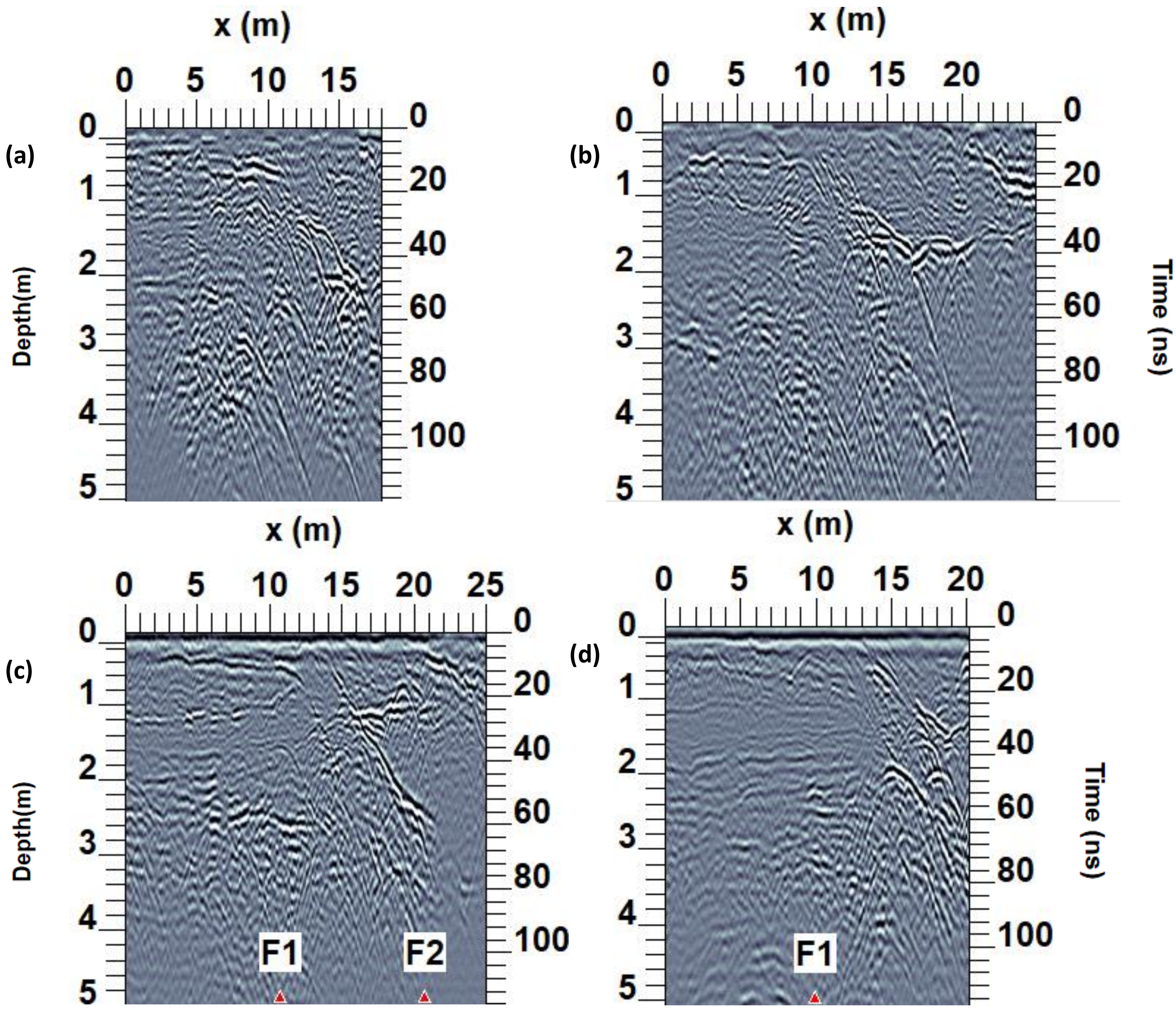

Figure A4.17: W-E profiles over the June 2017 seep grid using the 250 MHz antennae without interpretation lines: (a) XLINE03 (y=15); (b) XLINE10 (y=50); (c) XLINE16 (y=80); (d) XLINE22 (y=110).

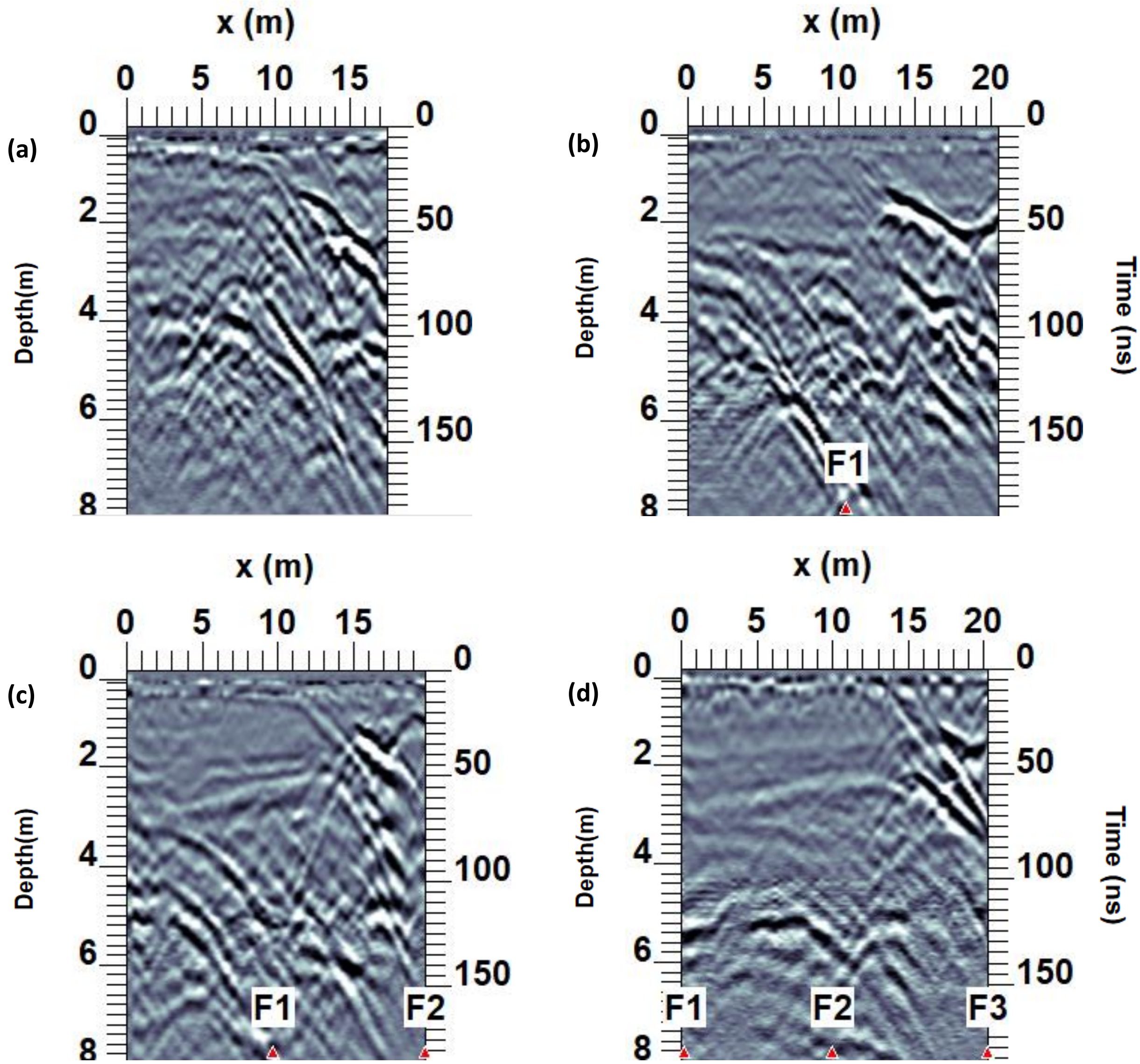

Figure A4.18: W-E profiles over the June 2017 seep grid collected using the 100 MHz antennae without interpretation lines**:** (a) XLINE03 (y=15); (b) XLINE10 (y=50); (c) XLINE16 (y=80); (d) XLINE22 (y=110)**.**

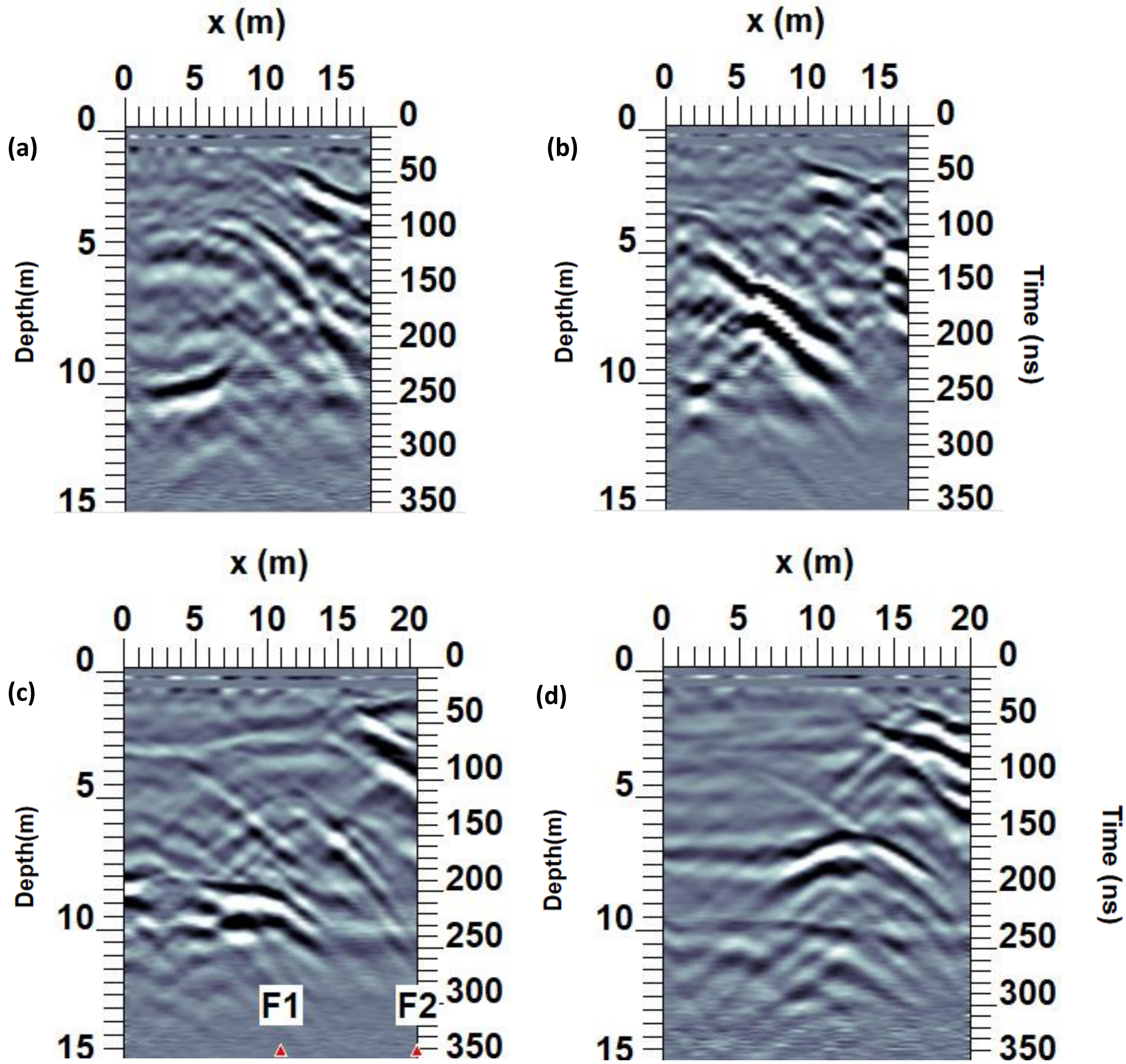

Figure A4.19: W-E profiles collected over the June 2017 seep grid using 50 MHz antennae without interpretation lines: (a) XLINE03 (y=15); (b) XLINE10 (y=50); (c) XLINE16 (y=80); (d) XLINE23 (y=115).

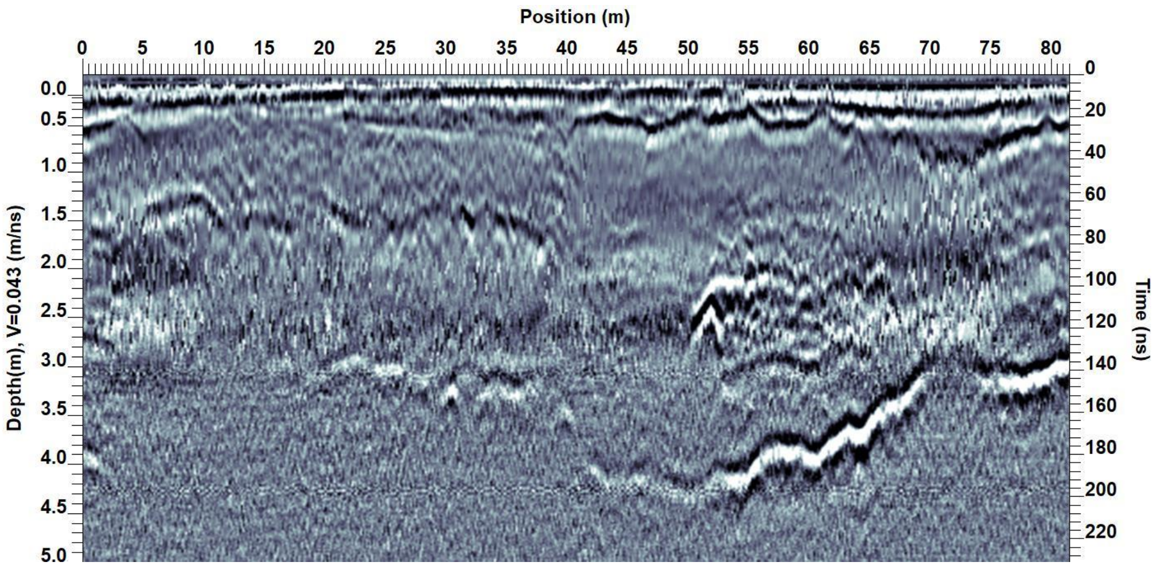

Figure A4.20: SE-NW profile of GPR LINE05 collected over the limestone barrier encompassing sediment pond 2 in the wetland in September 2016 without interpretation lines.

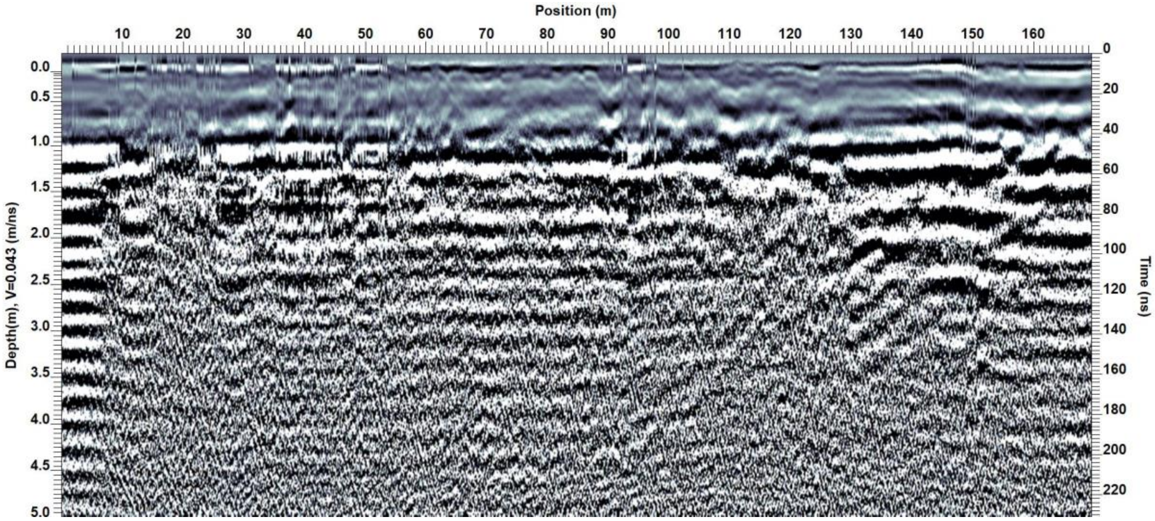

Figure A4.21: S-N oriented profile over GPR LINE06 collected in the wetland without interpetation lines.

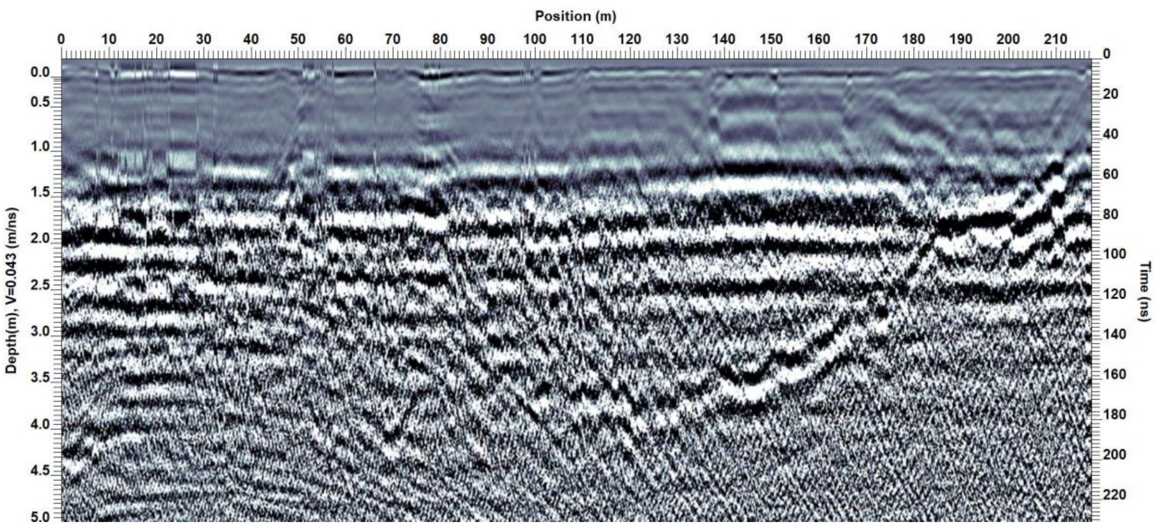

Figure A4.22: S-N oriented profile over GPR LINE07 collected in the wetland without interpretation lines.

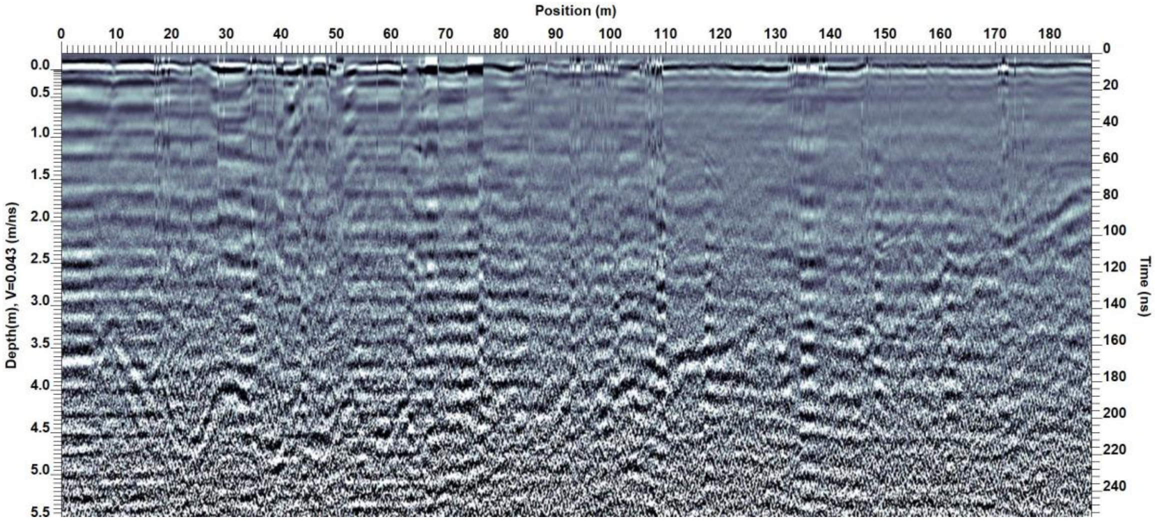

Figure A4.23: S-N oriented profile over GPR LINE08 collected in the wetland without interpretation lines.

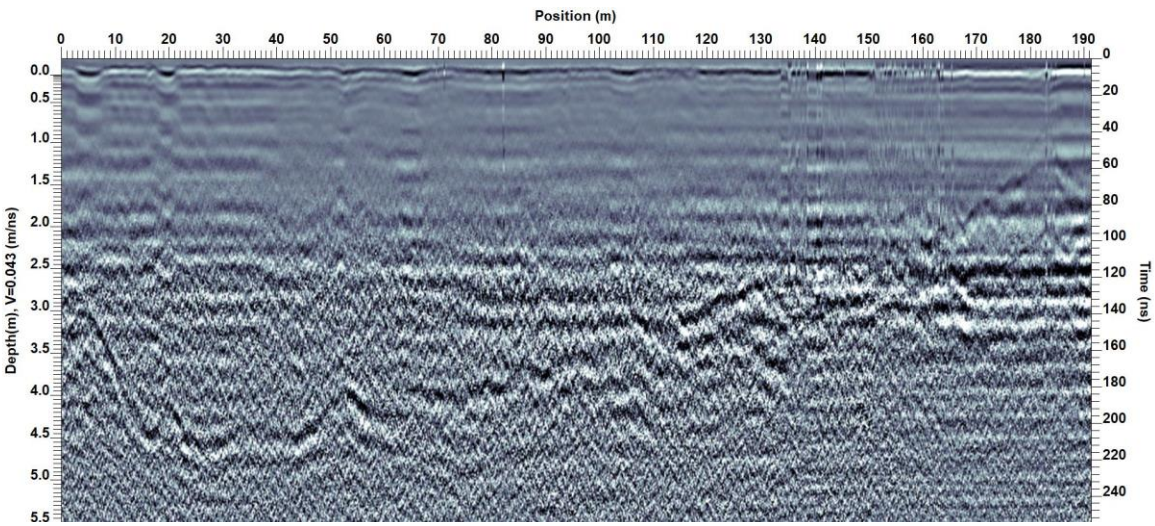

Figure A4.24: S-N oriented profile over GPR LINE09 collected in the wetland without interpretation lines.

A4.6 Supplementary EM31 Ground Conductivity Data

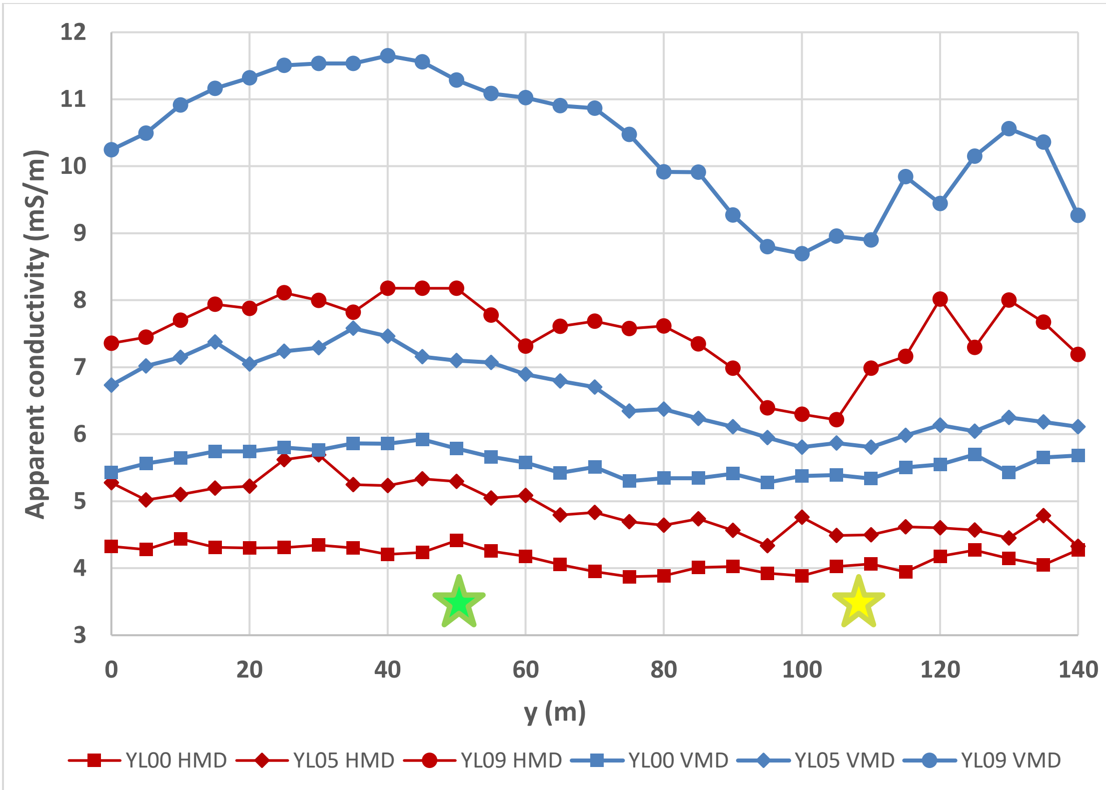

Figure A4.25 Profiles of σ_a versus station spacing over YLINEs00, 05 and 09 of the June 2017 seep grid collected S-N with the EM31-MK2 ground conductivity meter using VMD (blue symbols) and HMD (dark red symbols) orientations and a S-N boom orientation. The green and yellow stars give approximate locations of the seep and old stream respectively.

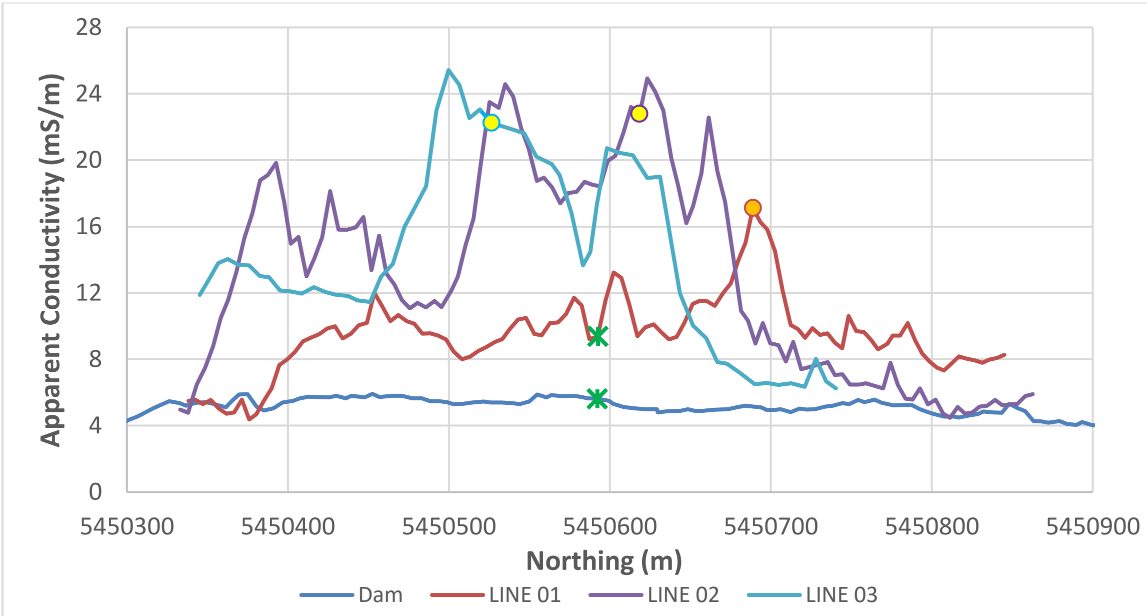

Figure A4.26: Profiles of σ_a versus northing along the embankment (Dam) and in the wetland, with VMD coil orientation and a S-N boom orientation. The green star, yellow dots and orange dot indicate the northerly position in the wetland of the observed seep, the banks of the old stream and a region of pooled tailings in a natural wetland depression near the embankment respectively.

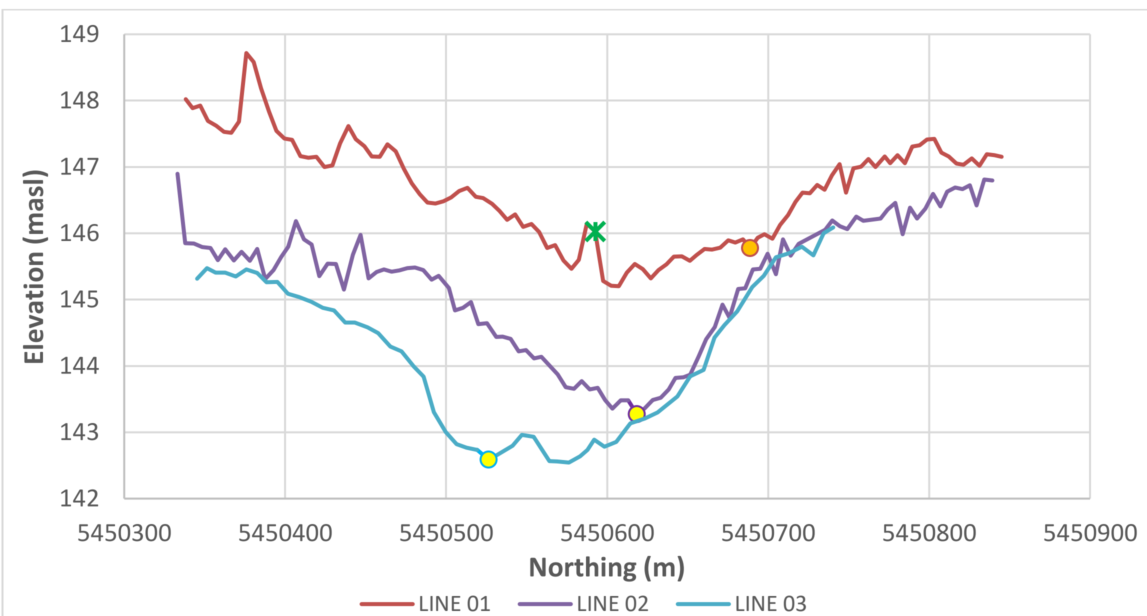

Figure A4.27: Elevation profiles versus northing for EM31 survey lines in the wetland corresponding to those in Figure A4.26.

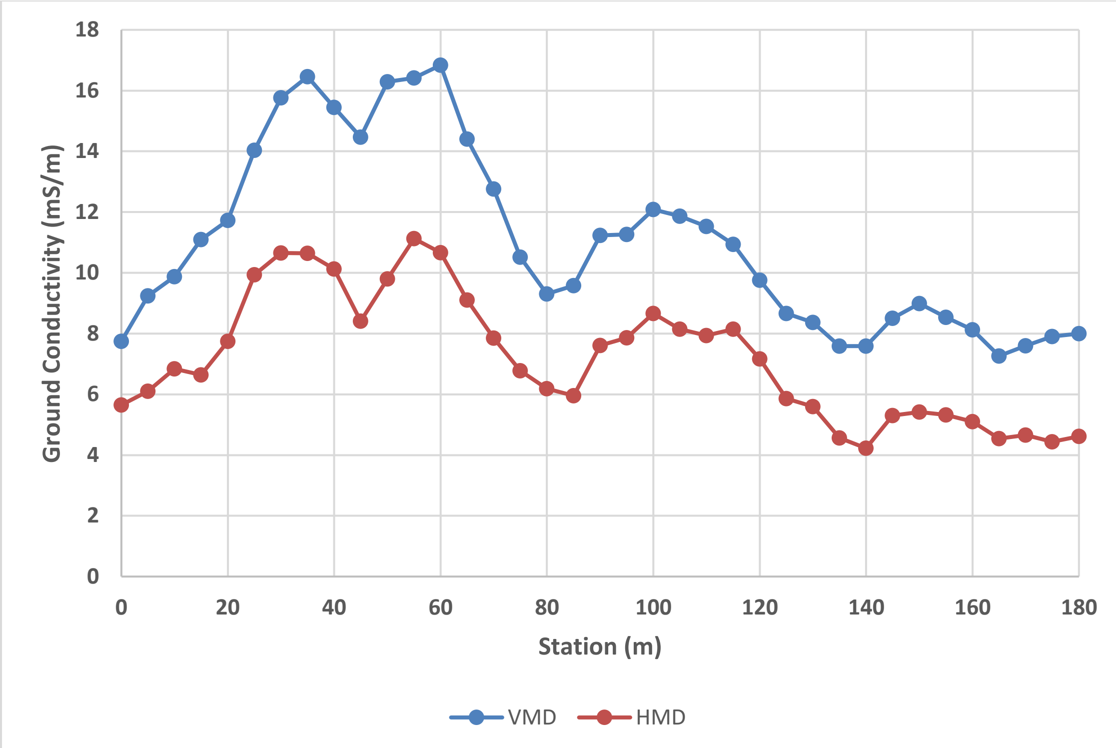

Figure A4.28: S-N profiles of σ_a versus station spacing over a survey line collected along the toe of the downstream slope (TDS) of the Gullbridge Dam in February 2017 using VMD and HMD orientations and a S-N instrument boom. See Figure 4.5.8 for line locations.

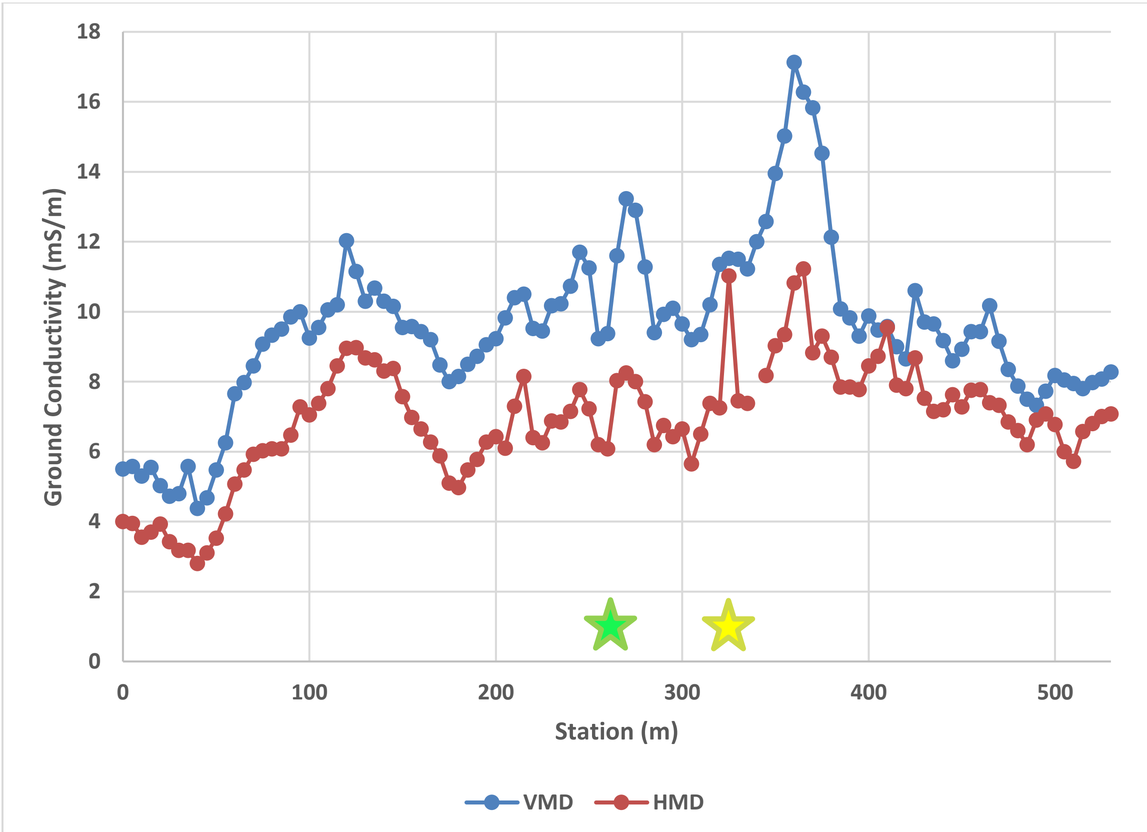

Figure A4.29: S-N profiles of σ_a versus station spacing along EM LINE01 collected along the base of the dam in the wetland using VMD and HMD orientations and a S-N instrument boom. The green star indicates the location where the survey line crosses the seep and the yellow star indicates where the survey line overlaps the old stream. See Figure 4.5.8 for line locations.

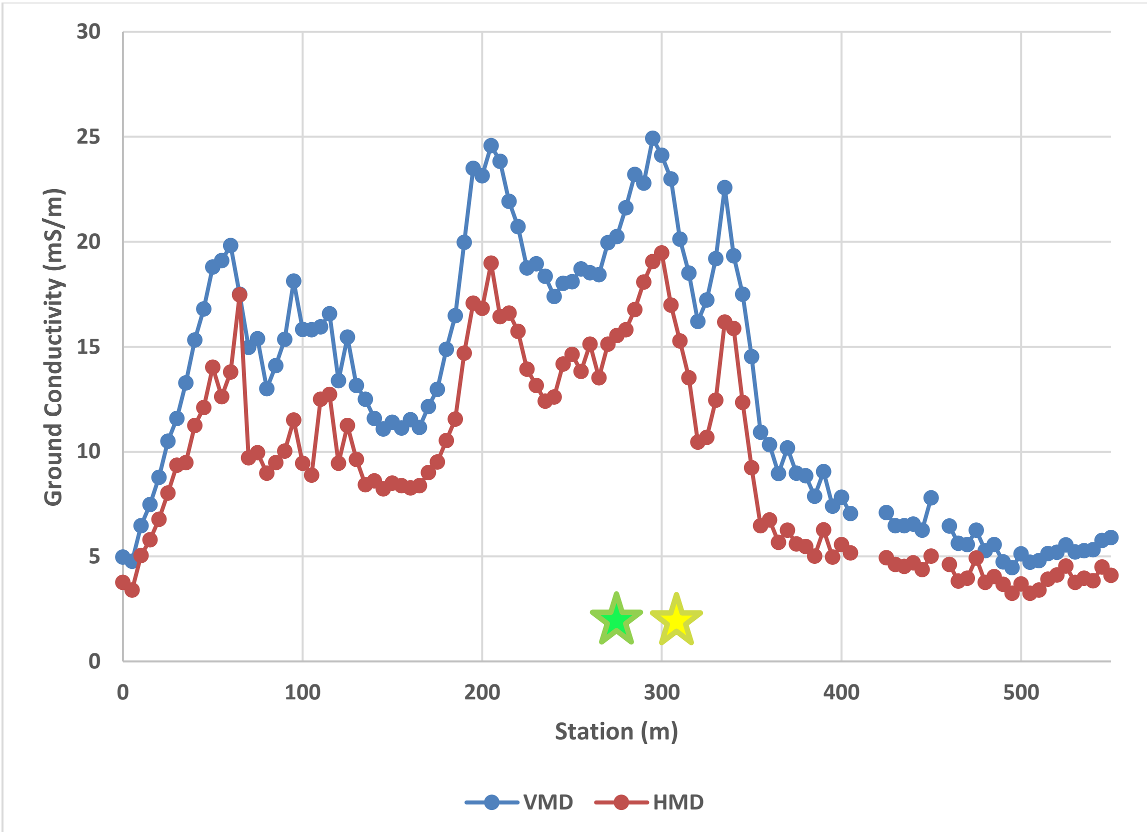

Figure A4.30: S-N profiles of σ_a versus station spacing along EM LINE02 collected in the wetland using VMD and HMD orientations and a S-N instrument boom. The green star indicates the location of the seep ~ 45 m east of station +265 m. The yellow star indicates where the survey line overlaps the center of the old stream impression. See Figure 4.5.8 for line locations.

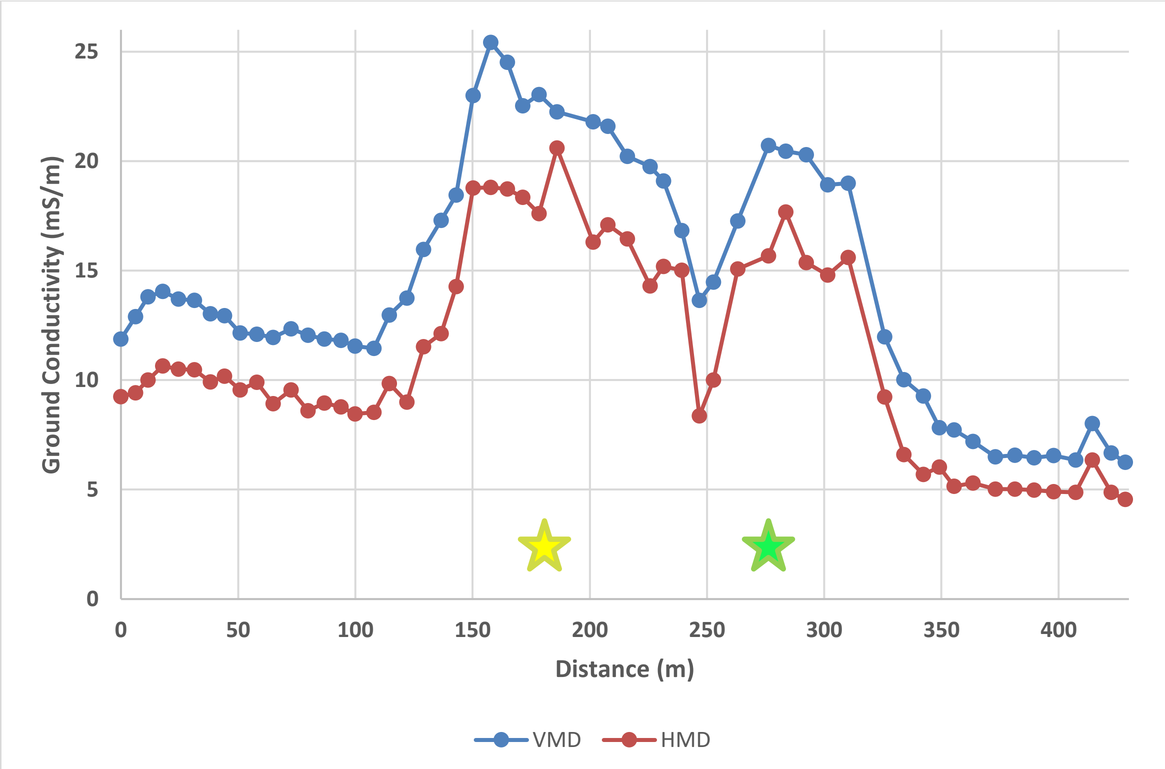

Figure A4.31: S-N profiles of σ_a versus station spacing along EM LINE03 collected in the wetland using VMD and HMD orientations and a S-N instrument boom. The green star indicates the location of the seep ~ 70 m east of station +276 m. The yellow star indicates where the survey line overlaps the center of the old stream impression. See Figure 4.5.8 for line locations.

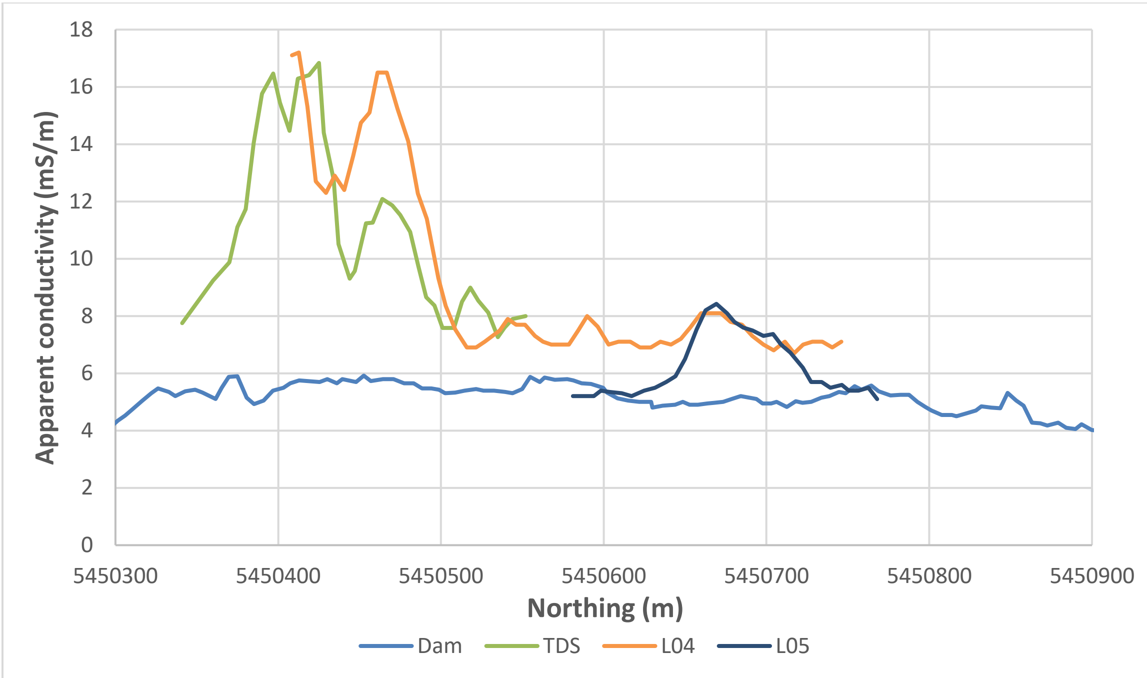

Figure A4.32: Profiles of σ_a versus northing along the embankment (Dam) and in the wetland, with VMD coil orientation and a S-N boom orientation. See Figure 4.5.8 for line locations.

A4.7 Supplementary Bog Sample Data

Table A4. 1: Water content of bog samples collected in the wetland adjacent to the Gullbridge Tailings Impoundment.

Site	Sample Interval (m)	Depth (m)	Wet mass (g)	Dry Mass (g)	% water
1	0 – 0.1	0 – 0.1	49.69	4.42	91
1	0.1 – 0.35	0.1 – 0.22	75.79	5.90	92
1		0.22 – 0.35	87.05	7.33	92
1	0.35 – 0.60	0.35 – 0.47	85.73	8.79	90
1		0.47 – 0.60	88.54	8.65	90
1	0.60 – 0.85	0.60 – 0.735	92.18	9.28	90
1		0.735 – 0.85	83.75	8.56	90
1	0.85 – 1.10	0.85 – 1.10	149.49	15.55	90
1d	0 – 0.2	0.85 – 1.05	116.29	8.39	93
1d	0.2 – 0.45	1.05 – 1.3	146.59	13.38	91
1d	0.45 – 0.7	1.3 – 1.55	134.65	10.47	92
1d	0.7 – 0.95	1.55 – 1.80	137.03	11.01	92
1d	0.95 – 1.2	1.80 – 2.05	126.04	10.03	92
3	0 – 0.17	0 – 0.17	110.44	12.36	95
3	0.17 – 0.36	0.17 – 0.36	126.65	67.98	55

Table A4.2: Elemental concentrations of bog samples collected at sites GB-01 (red) and GB-02 (yellow) generated from OES analysis.

Site	Average Depth	Al %	As ppm	Ba ppm	Be ppm	Ca %	Cd ppm	Ce ppm	Co ppm	Cr ppm	Cu ppm	Dy ppm	Fe %	Fe ppm
GB-1	0.040	1.15	1.8	90	1.0	1.78	1.6	15	102	15	1548	1.2	0.80	8017.40
GB-1	0.143	0.41	0.5	52	0.3	1.98	0.3	5	88	8	130	-0.5	1.03	10292.91
GB-1	0.278	0.22	0.5	30	0.2	1.71	0.3	-5	17	5	130	-0.5	1.24	12360.10
GB-1	0.411	0.38	0.5	42	0.1	1.12	-0.1	-5	3	8	20	-0.5	0.76	7629.24
GB-1	0.536	0.17	3.0	24	-0.1	0.97	0.1	-5	2	4	21	-0.5	0.61	6059.46
GB-1	0.665	0.33	12.1	76	0.1	1.14	0.2	-5	3	6	33	-0.5	0.67	6724.84
GB-1	0.790	0.37	0.5	23	0.1	0.56	-0.1	6	1	5	16	0.6	0.35	3514.23
GB-1	0.975	0.43	0.5	24	0.1	0.68	0.1	7	2	6	18	0.7	0.38	3813.54
GB-1	1.175	0.19	3.8	31	0.1	1.02	0.2	-5	10	3	79	-0.5	0.64	6377.45
GB-1	1.425	0.25	3.3	27	0.1	0.90	h	-5	8	6	68	-0.5	0.49	4872.98
GB-1	1.675	0.31	1.8	25	0.1	0.92	0.3	-5	5	4	56	0.5	0.45	4459.11
GB-1	1.925	0.35	1.3	20	0.1	0.97	0.3	-5	2	6	42	0.7	0.44	4377.64
GB-2	0.084	0.65	-1.0	89	0.2	0.77	0.2	-5	34	8	9	-0.5	0.29	2927.48
GB-2	0.264	4.11	3.1	325	1.2	0.71	-0.1	14	3	28	3	2.5	1.02	10210.00

Table A4.3: Elemental concentrations of bog samples collected at sites GB-01 (red) and GB-02 (yellow) generated from OES analysis continued.

Site	Average Depth	K %	La ppm	Li ppm	Mg %	Mg ppm	Mn ppm	Mo ppm	Na %	Nb ppm	Ni ppm	P ppm	Pb ppm
GB-1	0.040	0.09	19	1.1	0.35	3468.51	808	-1	0.18	-1	128	419	11
GB-1	0.143	0.05	3	0.8	0.36	3576.91	664	-1	0.11	-1	89	319	11
GB-1	0.278	0.03	2	0.7	0.28	2773.70	474	-1	0.07	-1	33	220	3
GB-1	0.411	0.06	2	0.6	0.20	1983.00	256	-1	0.11	-1	7	233	11
GB-1	0.536	0.04	-1	0.7	0.16	1631.47	240	-1	0.07	-1	5	159	19
GB-1	0.665	0.08	2	1.3	0.19	1856.84	255	-1	0.11	-1	6	168	49
GB-1	0.790	0.05	3	0.3	0.10	976.57	159	-1	0.07	-1	3	263	5
GB-1	0.975	0.03	4	0.3	0.11	1067.10	170	-1	0.07	-1	4	281	3
GB-1	1.175	0.03	2	0.6	0.15	1533.39	263	-1	0.05	-1	13	182	15
GB-1	1.425	0.03	2	0.5	0.14	1402.37	250	-1	0.04	-1	11	232	30
GB-1	1.675	0.02	2	0.3	0.15	1479.04	282	-1	0.04	-1	7	217	6
GB-1	1.925	0.02	2	0.3	0.15	1457.69	325	2	0.04	-1	5	201	1
GB-2	0.084	0.16	2	0.8	0.17	1737.19	247	-1	0.13	2	12	462	12
GB-2	0.264	1.26	7	3.4	0.30	2961.50	344	-1	1.34	11	6	137	6

Table A4.4: Elemental concentrations of bog samples collected at sites GB-01 (red) and GB-02 (yellow) generated from OES analysis continued.

Site	Average Depth	Rb ppm	S ppm	Sc ppm	Sr ppm	Ti ppm	V ppm	Y ppm	Zn ppm	Zr ppm	LOI %
GB-1	0.040	-5	7088	2.1	67	572	17	21	356	4	85.9
GB-1	0.143	-5	10025	1.2	67	326	11	3	47	3	88.7
GB-1	0.278	-5	7402	0.5	54	131	4	2	52	2	91.3
GB-1	0.411	-5	5325	1.1	50	326	9	1	11	3	91.5
GB-1	0.536	-5	5034	0.5	31	122	4	2	28	2	94.2
GB-1	0.665	-5	4552	0.9	34	261	7	4	54	5	91.6
GB-1	0.790	-5	2938	2.0	21	188	6	3	7	4	94.8
GB-1	0.975	-5	3294	2.4	26	195	7	4	7	3	94.8
GB-1	1.175	-5	5776	0.6	30	83	3	3	41	2	94.5
GB-1	1.425	-5	5032	1.3	25	95	4	4	27	2	95.0
GB-1	1.675	-5	6100	1.8	26	66	4	4	16	3	94.8
GB-1	1.925	-5	6395	1.9	26	53	12	5	10	3	94.9
GB-2	0.084	-5	3422	1.9	33	1377	13	4	25	28	80.9
GB-2	0.264	45	217	7.4	91	5767	63	17	20	122	11.9